Mathematical Problems in Engineering

Theory, Methods, and Applications

Special Issue
Nonlinear Time Series: Computations and Applications 2012

Guest Editors: Ming Li, Massimo Scalia, Carlo Cattani, S. C. Lim, Bin Fang, and Thomas T. Yang

Hindawi Publishing Corporation
http://www.hindawi.com

Nonlinear Time Series: Computations and Applications 2012

Mathematical Problems in Engineering

Nonlinear Time Series: Computations and Applications 2012

Guest Editors: Ming Li, Massimo Scalia, Carlo Cattani, S. C. Lim, Bin Fang, and Thomas T. Yang

Editorial Board

Contents

Hindawi Publishing Corporation
Mathematical Problems in Engineering
Volume 2012, Article ID 738258, 4 pages
doi:10.1155/2012/738258

Editorial

Nonlinear Time Series: Computations and Applications 2012

Ming Li,[1] Massimo Scalia,[2] Carlo Cattani,[3] S. C. Lim,[4] Bin Fang,[5] and Thomas T. Yang[6]

[1] *School of Information Science & Technology, East China Normal University, Shanghai 200241, China*
[2] *Department of Mathematics, University of Rome "La Sapienza", Piazzale Aldo Moro 2, 00185 Rome, Italy*
[3] *Department of Mathematics, University of Salerno, Via Ponte Don Melillo, 84084 Fisciano, Italy*
[4] *Faculty of Engineering, Multimedia University, 63100 Cyberjaya, Selanger, Malaysia*
[5] *College of Computer Science, Chongqing University, Chongqing 400044, China*
[6] *Department of Electrical, Computer, Software, & Systems Engineering, Embry-Riddle Aeronautical University, Daytona Beach, FL 32114, USA*

Correspondence should be addressed to Ming Li, ming_lihk@yahoo.com

Received 19 November 2012; Accepted 19 November 2012

Nonlinear time series attracts the interests of scientists and engineers in both research and applications in various fields, ranging from hydrology to computer science. It is a powerful tool for revealing interesting phenomena in natural science and engineering regarding challenging issues in, for instances, fractal random functions, differential equations of fractional order, fractional calculus, prediction of random functions, technologies in denoising for both signals and images, pattern recognition, wavelets, and so forth. The aim of this special issue is to collect high quality papers with respect to nonlinear time series, its computations, and applications. There are 28 papers collected in this special issue in the related topics. We introduce them by six paragraphs below.

A.-J. Shi and J.-G. Lin's paper entitled "*Tail dependence for regularly varying time series*" studies regularly varying time series to describe heavy-tailed phenomena from a view of tail dependence by introducing a dependence function and establishing a relationship between the dependence function and the intensity measure with discussions of their present expressions about dependence parameters. J. Xue et al.'s paper "*Bound maxima as a traffic feature under DDOS flood attacks*" provides a novel method to characterize the traffic features with and without attacking packets. The paper entitled "*A novel fractional-discrete-cosine-transform-based reversible watermarking for healthcare information management systems*" by L.-T. Ko et al. presents a new method of watermarking to reconstruct host images by using the technique of discrete cosine transform of fractional order. I. Cherif et al.'s paper "*Nonlinear*

blind identification with three-dimensional tensor analysis" deals with the blind identification of a second-order Volterra-Hammerstein series using the analysis of three-dimensional tensor. The paper "*Online health management for complex nonlinear systems based on hidden semi-markov model using sequential Monte Carlo methods*" by Q. Liu and M. Dong introduces a new approach of multisteps ahead health recognition based on joint probability distribution for health management of a complex nonlinear system with the technique combining hidden semi-Markov model with sequential Monte Carlo methods. H. Bayiroğlu et al.'s paper "*Nonlinear response of vibrational conveyers with nonideal vibration exciter: superharmonic and subharmonic resonance*" gives the theoretical and numerical analysis of the working ranges of oscillating shaking conveyers with nonideal vibration exciter for superharmonic and subharmonic resonances in multiple scales.

Wavelets remain a powerful tool in nonlinear time series. The paper entitled "*A new texture synthesis algorithm based on wavelet packet tree*" by H. C. Hsin et al. presents an efficient method of texture synthesis with wavelet packet tree, providing a useful technique for investigating the issue of multiresolution representation for fractal images. Y. Huang et al.'s paper "*Minimum-energy multiwavelet frames with arbitrary integer dilation factor*" explains the research of the minimum-energy multiwavelet frame.

J. Yang et al. presented their study in the construction of affine invariant functions in the paper entitled "*Construction of affine invariant functions in spatial domain*", which is satisfactorily used for pattern recognition of Chinese words. The paper "*Adaptive binary arithmetic coder-based image feature and segmentation in the compressed domain*" by H. C. Hsin et al. gives a modification of the compression-based texture merging algorithm to alleviate the influence of overmerging problem by making use of the rate distortion information so that the computational cost because of the segmentation of an image may be reduced considerably. R. Wang and B. Fang's paper "*A combined approach on RBC image segmentation through shape feature extraction*" proposes a combined approach for complex surface segmentation of red blood cell based on the techniques of shape-from-shading and multiscale surface fitting, which is promising for the pattern recognition of red blood cell in the sense of 3-dimensional modeling by taking into account multiscale surface features of red blood cell segments. S. Hu et al. in their paper "*Reducing noises and artifacts simultaneously of low-dosed X-ray computed tomography using bilateral filter weighted by Gaussian filtered sinogram*" proposed an efficient method to obtain satisfied denoising results for sinogram restoration of low-dosed X-ray computed tomography by weighing the similarity using Gaussian smoothed sinogram. The paper entitled "*Image denoising based on dilated singularity prior*" by S. Hu et al. gives an approach to preserve edges and textures in image denoising by adding dilated singularity prior to noisy images. Y.-Y. Zhu et al.'s paper "*Detection and recognition of abnormal running behavior in surveillance video*" gives a method of identifying abnormal running behavior based on spatiotemporal parameters by taking into account real-time systems and multitarget tracking in surveillance videos. The paper entitled "*Data matrix code location based on finder pattern detection and bar code border fitting*" by Q. Huang et al. presents an algorithm for locating data matrix code based on finder pattern detection and bar code border fitting, which has applications to locating a 2D bar code quickly and precisely in an image with complex background, such as poor illumination. B. Chen et al.'s paper "*A multiplicative noise removal approach based on partial differential equation model*" contributes a method of removing speckle noise by introducing a four-order partial differential equation, which may obtain better edge-preserve performance.

Packet-delay analysis gains interests of scientists in computer-network engineering from the point of view of real-time systems in particular as well as applied statistics with

respect to queuing systems driven by fractal arrival time series. D. Pan et al.'s paper entitle "*Buffer management and hybrid probability choice routing for packet delivery in opportunistic networks*" contributes a hybrid probability choice routing protocol with buffer management for opportunistic networks. The authors developed a delivery probability function based on continuous encounter duration time, which is used for selecting a better node to relay packets. By combining the buffer management utility and the delivery probability, they attained a total utility that is used to decide whether the packet should be kept in the buffer or be directly transmitted to the encountering node. H. Wu et al.'s paper "*Location updating schemes for high-speed railway cellular communication systems*" proposes two useful methods regarding location updating, namely, "clustering location management" and "mobile group location management," towards solving the problems caused by the existing location updating schemes in high speed railway cellular private network without occupying more frequency resources and impacting the mobile subscribers' paging. In addition, the paper gives analysis of useful specifications, such as channel request number of stand-alone dedicated control channel, average waiting time of location updating, cost of location updating, and paging. The paper "*Applying semigroup property of enhanced Chebyshev polynomials to anonymous authentication protocol*" by H. Lai et al. presents an anonymous authentication protocol that is efficient in low computational complexity and cost in the initialization phase by using semigroup property of enhanced Chebyshev polynomials. H.-Y. Lin et al. presented a paper entitled "*An adaptive test sheet generation mechanism using genetic algorithm*", where an adaptive test sheet generation is given from a view of time series. That may be the first paper noticing that there may be fractal phenomena, such as statistical self-similarity of genetic algorithm's fitness scores, in the assessment of information provided by computerized testing systems.

The paper entitled "*Hypothesis testing in generalized linear models with functional coefficient autoregressive processes*" by L. Song et al. studies the hypothesis testing in generalized linear models with functional coefficient autoregressive processes by introducing quasi-maximum likelihood estimators. T.-S. Tsay's paper "Automatic regulation time series for industry processes" proposes a nonlinear digital control scheme for analyses and designs of stable industry processes, which can be applied to servo systems, time delay systems, and so on. D. Xiang et al.'s paper "*Degenerate-generalized likelihood ratio test for one-sided composite hypotheses*" gives a method with respect to the degenerate-generalized likelihood ratio test for one-sided composite hypotheses in cases of independent and dependent observations. Their method has less overall expected sample sizes and less relative mean index values in comparison with the sequential probability ratio test and double sequential probability ratio test.

Research of theory and tools of time series prediction is encouraged. The paper by X.-H. Yang and Y.-Q. Li, which is entitled "*DNA optimization threshold autoregressive prediction model and its application in ice condition time series*", presents a new DNA (deoxyribonucleic acid) optimization threshold autoregressive prediction model (DNAOTARPM) by combining threshold autoregressive method with DNA optimization. It may be useful for the calibration of the threshold autoregressive prediction model for nonlinear time series with prediction precision improving and prediction uncertainty reducing. The paper entitled "*Design of deep belief networks for short-term prediction of drought index using data in the Huaihe River Basin*" by J. Chen et al. contributes a short-term drought prediction model based on deep belief networks for predicting the time series at different time scales. Their prediction model has applied to predict the real drought time series in the Huaihe River Basin, China. J.-L. Wu and P.-C. Chang's paper "*A trend-based segmentation method and the support vector regression for financial time series forecasting*" presents a trend-based segmentation method and the support vector

regression for financial time series forecasting. S.-S. Yang et al. in their paper entitled "*New optimal weight combination model for forecasting precipitation*" introduced a new optimal weight combination model to increase accuracies in precipitation forecasting. The present model, which consists of three forecast submodels, namely, rank set pair analysis model, radical basis function model, and autoregressive one, may significantly improve the forecast accuracy of precipitation in terms of the error sum of squares in comparison with the single model of rank set pair analysis, or radical basis function, or autoregressive system.

Acknowledgments

The guest editors are grateful to the authors of the special issue for their contributions and the reviewers for their valuable comments on the submissions. They highly appreciate the editorial members of Mathematical Problems in Engineering as well as the editorial staff of Hindawi Publishing Corporation. M. Li acknowledges the 973 plan under the Project Grant no. 2011CB302800, and the National Natural Science Foundation of China under the Project Grants nos. 61272402, 61070214, and 60873264.

Ming Li
Massimo Scalia
Carlo Cattani
S. C. Lim
Bin Fang
Thomas T. Yang

Hindawi Publishing Corporation
Mathematical Problems in Engineering
Volume 2012, Article ID 454823, 17 pages
doi:10.1155/2012/454823

Research Article

Applying Semigroup Property of Enhanced Chebyshev Polynomials to Anonymous Authentication Protocol

Hong Lai,[1,2,3] Jinghua Xiao,[1] Lixiang Li,[2,3] and Yixian Yang[2,3]

[1] *School of Science, Beijing University of Posts and Telecommunications, Beijing 100876, China*
[2] *Information Security Center, Beijing University of Posts and Telecommunications, Beijing 100876, China*
[3] *National Engineering Laboratory for Disaster Backup and Recovery, Beijing University of Posts and Telecommunications, Beijing 100876, China*

Correspondence should be addressed to Lixiang Li, li_lixiang2006@yahoo.com.cn

Received 15 May 2012; Accepted 22 June 2012

Academic Editor: Ming Li

We apply semigroup property of enhanced Chebyshev polynomials to present an anonymous authentication protocol. This paper aims at improving security and reducing computational and storage overhead. The proposed scheme not only has much lower computational complexity and cost in the initialization phase but also allows the users to choose their passwords freely. Moreover, it can provide revocation of lost or stolen smart card, which can resist man-in-the-middle attack and off-line dictionary attack together with various known attacks.

1. Introduction

With rapid developments in limits and possibilities of communications and information transmissions, there is a growing demand of authentication protocol, which has greatly spurred research activities in authentication protocols' study. In general, the server authenticates the users by matching the user's identity and password after establishing a secure channel [1]. Since the server establishes a secure channel before asking identity/password information, an attacker can open a connection to a server that does not respond when identity/password information is inquired by the server, which results in the consumption of the resources of the server. Moreover, the attacker can set up many connections and consume all the resources of the server. However, this method is vulnerable to denial of service (DoS) attack and cannot discriminate an impostor who fraudulently obtains access privileges (e.g., user's identity and password) from the real user. Later, Li and Hwang [2]

proposed a biometrics-based remote user authentication scheme using smart cards. Soon, Li et al. [3, 4] improved Li and Hwang's scheme. There is no doubt that most existing authentication protocols only achieve "heuristic" security, that is, the underlying hardness assumptions of these protocols are not perfect. However, we discover the references [5–9], which contain the detection of the DDOS attacks by consuming all, or mostly, the resources of the server can be assured, providing a more hopeful line of investigation for us to future study.

Later, Bellovin and Merritt [10] firstly presented a two-party password authenticated key exchange (2PAKE) protocol which permits a user and a server to establish a session key over an insecure channel to address the problem mentioned above. In their protocol, each user just shares an easy-to-remember password with the trusted server. Regretfully, Patel [11] pointed out that it was easy for an adversary to guess the passwords used for authentication in Bellovin and Merritt's protocol. In order to avoid these attacks, many 2PAKE protocols with weak passwords for authentication have been presented by the researchers [12–18]. However, in these 2PAKE protocols, every user has to share a different password with his/her peer. It is usually rather inconvenient for applications in large-scale communication environments. To surmount this weakness, three-party PAKE (3PAKE) protocols have been proposed in [19–22]. Unlike 2PAKE protocols, 3PAKE protocol is a very practical mechanism to establish secure session key through authenticating each other with a trusted server's help. There are two common weaknesses in these schemes as follows. (1) They needs more communications rounds to reduce computational load. However, as early as in 1995, Gong pointed out that the number of rounds is a key standard for weighing against the performance of a protocol. (2) The sensitive table that stores the shared secret between the server and the designed users will be an attractive target leading to potential server compromise. In 2008, Chen et al. [23] proposed a round and computation-efficient three-party authenticated key exchange protocol, which addressed the above mentioned problems. However, we find that their scheme still exist following four drawbacks. (1) It has computational efficiency problems in initialization phase. (2) User has no choice in choosing his password. (3) It cannot protect user anonymity. (4) There is no provision for revocation of lost or stolen smart card, which is susceptible to man-in-the-middle attack.

Therefore, in this paper, password-based anonymous authentication protocol defined over enhanced Chebyshev polynomials is proposed. A number of outstanding mathematicians and numerical analysts have said that Chebyshev polynomials are everywhere dense in numerical analysis. There is scarcely any area of numerical analysis where Chebyshev polynomials do not drop in like surprise visitors, and indeed there are now a number of subjects in which these polynomials take a significant position in modern developments [24]. One is taken on a journey which leads into all areas of numerical analysis by studying Chebyshev polynomials. Moreover, due to the semigroup property of enhanced Chebyshev polynomials, the well-known discrete logarithm problem and the Diffie-Hellman problem are proved to hold in enhanced Chebyshev polynomials [25]. Thus, we apply semigroup property of enhanced Chebyshev polynomials to present an anonymous authentication protocol. Moreover, our proposed protocol has the following features.

(1) It has much lower computational complexity and cost in the initialization phase.

(2) It allows the users to choose their passwords freely.

(3) It can provide revocation of lost or stolen smart card, which can resist man-in-the-middle attack.

(4) There is no need to find primitive elements, large prime, and even large number.

The rest of this paper is organized as follows. Section 2 gives description of enhanced Chebyshev polynomials and some hard problems based on them. Section 3 briefly reviews Chen et al.'s protocol and describes its disadvantages. In Section 4, we apply semigroup property of enhanced Chebyshev polynomials to design an anonymous authentication protocol. We analyze the security of proposed scheme in Section 5, and computational efficiency analysis is made in Section 6. Finally, we conclude this paper in Section 7.

2. Preliminaries

In this section, we review some basic definitions concerning enhanced Chebyshev polynomials and some hard problems based on the enhanced Chebyshev polynomials [26].

Definition 2.1 (Chebyshev polynomials). The Chebyshev polynomials of degree n are defined as

$$T_n(x) = \cos(n \times \arccos(x)), \quad \{x \mid -1 \leq x \leq 1\}, \tag{2.1}$$

The recurrent formulas are

$$T_n(x) = 2xT_{n-1}(x) - T_{n-2}(x), \tag{2.2}$$

where $n \geq 2$, $T_0(x) = 1$, and $T_1(x) = x$.

The first few Chebyshev polynomials are

$$\begin{aligned} T_2(x) &= 2x^2 - 1, \\ T_3(x) &= 4x^3 - 3x, \\ T_4(x) &= 8x^4 - 8x^2 + 1. \end{aligned} \tag{2.3}$$

It can be identified that Chebyshev polynomial has the following properties:

(1) semigroup property as

$$T_r(T_s(x)) = \cos r * \arccos(\cos(s * \arccos(x))) = \cos rs * \arccos(x) = T_s(T_r(x)) = T_{rs}(x), \tag{2.4}$$

(2) chaotic property,

When $n > 1$, Chebyshev polynomials map $T_n(x) : [-1, 1] \rightarrow [-1, 1]$ of degree n is a chaotic map with its invariant density as

$$f^*(x) = \frac{1}{\pi\sqrt{1 - x^2}}, \tag{2.5}$$

for Lyapunov exponent $\lambda = \ln n > 0$.

Table 1: Some of the notations used in Chen et al.'s protocol.

Symbol	Definition
ID_A, ID_B	Identities of users A and B, respectively
ID_S	Identity of the authentication server S
p, q, g	The large primes p and q, a generator g of group G with the order q
x, y	The long-term key of S, and $y = g^x \bmod p$
δ_A, δ_B	Components of authentication information V_A and V_B
a, b	Random number privately chosen by A and B, respectively
R_A, R_B	Components of session key, where $R_A = g^a \bmod p$ and $R_B = g^b \bmod p$
$h(\cdot)$	Collision-free one-way hash function
C_{XY}	Evidence generated by user X for user Y

Definition 2.2 (enhanced Chebyshev polynomials). In order to enhance the property of the Chebyshev chaotic map, Zhang [27] proved that the semigroup property holds for Chebyshev polynomials defined on interval $(-\infty, +\infty)$. This paper uses the following enhanced Chebyshev polynomials:

$$T_n(x) = 2xT_{n-1}(x) - T_{n-2}(x) \pmod N, \tag{2.6}$$

where $n \geq 2$, $x \in (-\infty, +\infty)$, and N is a large prime number. Obviously,

$$T_r(T_s(x)) = T_s(T_r(x)) = T_{rs}(x). \tag{2.7}$$

So the semigroup property still holds and the enhanced Chebyshev polynomials also commute under composition.

Definition 2.3 (the discrete logarithm problem (DLP)). DLP is explained by the following. Given an element α, find the integer r, such that $T_r(x) = \alpha$.

Definition 2.4 (the Diffie-Hellman problem (DHP)). DHP is explained by the following. Given an element x, and the values of $T_r(x)$, $T_s(x)$, what is the value of $T_{rs}(x)$?

3. Review of Chen et al.'s Protocol

This section reviews Chen et al.'s protocol (showed in Figure 1). Some of the notations used in this protocol are defined in Table 1.

3.1. Initialization Phase

In this phase, A and B ought to register with S to be legal participants, and S should choose issue secret keys, which will be used in the subsequent phase. Through taking A for an example, S executes the following steps to authorize A:

(1) Randomly choose $1 \leq \delta_A < q$ and calculate $V_A = h(ID_A, \delta_A)$.

(2) Generate signature (e_A, s_A) as A's self-verified token, where $r_A = g^{\delta_A} \bmod p$, $e_A = h(r_A, ID_A)$, and $s_A = (\delta_A - xe_A) \bmod q$.

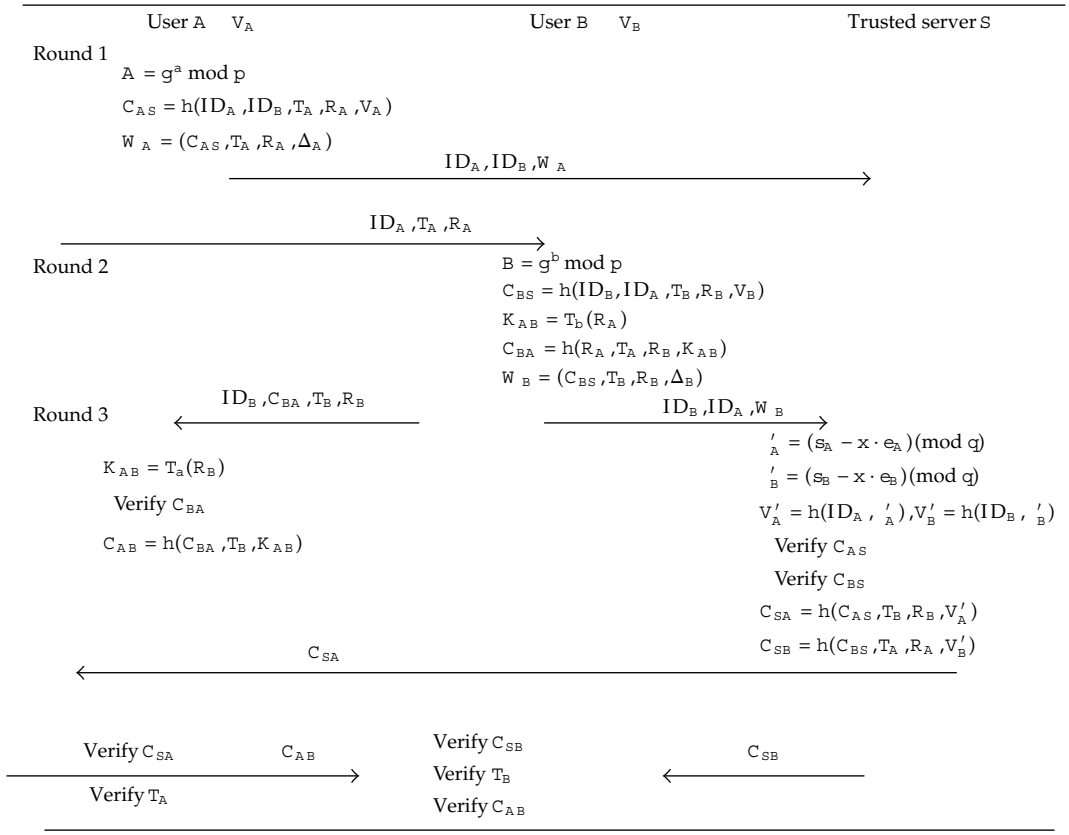

Figure 1: Authenticated key exchange phase in Chen et al.'s protocol.

(3) Store the authentication information $(V_A, (e_A, s_A))$ into a smart card and then deliver it to A in a secure way.

To test whether (e_A, s_A) is authorized by S, A retrieves r'_A as $r'_A = g^{s_A} \cdot y^{e_A} \bmod p$, and then verifies $h(r'_A, \mathrm{ID}_A) \stackrel{?}{=} e_A$.

Similarly, after B obtains the authorization information $(V_B, (e_B, s_B))$ stored in the smart card from S, he can ensure that whether (e_B, s_B) is valid by using the method mentioned above.

3.2. Authentication key Exchange Phase

This phase aims to establish the session key SK with S's help. It just needs three rounds to achieve this goal.

Round 1:

$$\begin{aligned} A &\longrightarrow S : (\mathrm{ID}_A, \mathrm{ID}_B, W_A), \\ A &\longrightarrow B : (\mathrm{ID}_A, T_A, R_A). \end{aligned} \tag{3.1}$$

(1) Randomly choose an integer a and compute $R_A = g^a \bmod p$, $C_{AS} = h(\mathrm{ID}_A, \mathrm{ID}_B, T_A, R_A, V_A)$, then transmits $\mathrm{ID}_A, \mathrm{ID}_B$ and $W_A = (C_{AS}, T_A, R_A, (e_A, s_A))$ to S; where T_A is the time stamp obtained by A from the local clock to ensure the freshness of the message.

(2) A transmits ID_A, T_A and R_A to B.

Round 2:

$$\begin{aligned} &B \longrightarrow S : (\mathrm{ID}_B, \mathrm{ID}_A, W_B), \\ &B \longrightarrow A : (\mathrm{ID}_B, T_B, R_B, C_{BA}). \end{aligned} \tag{3.2}$$

After receiving the message from A, B does the following steps.

(1) Randomly choose an integer b and compute $R_B = g^b \bmod p$, $C_{BS} = h(\mathrm{ID}_B, \mathrm{ID}_A, T_B, R_B, V_B)$, and send $W_B = (C_{BS}, T_B, R_B, (e_B, s_B))$ to S, where T_B is the time stamp obtained by B from the local clock to ensure the freshness of the message.

(2) Calculate the session key $SK = (R_A)^b \bmod p$ and then transmit $C_{BA} = h(T_A, R_A, R_B, SK)$ to A.

Round 3:

$$\begin{aligned} &S \longrightarrow A : C_{SA}, \\ &S \longrightarrow B : C_{SB}, \\ &A \longrightarrow B : C_{AB}. \end{aligned} \tag{3.3}$$

In this round, S does the following steps.

(1) Verify whether T_A is fresher than the one received in the last request. If so, apply x to computing $\delta'_A = (s_A + xe_A) \bmod q$ and $V'_A = h(\mathrm{ID}_A, \delta'_A)$, and then compute $C'_{SA} = h(\mathrm{ID}_A, \mathrm{ID}_B, T_A, R_A, V'_A)$. In the following, test $C'_{AS} \stackrel{?}{=} C_{AS}$ to authenticate the identity of A; if it holds, S calculates $C_{SA} = h(C_{AS}, T_B, R_B, V'_A)$ and transmits it to A.

(2) Test whether T_B is fresher than the one received in the last request. If so, S calculates $V'_B = h(\mathrm{ID}_B, \delta'_B)$ and computes $C'_{BS} = H(\mathrm{ID}_A, \mathrm{ID}_B, T_B, R_B, V'_B)$. Then, check $C'_{BS} \stackrel{?}{=} C_{BS}$ to authenticate the identity of B; if it holds, S calculates $C_{SB} = h(C_{BS}, T_A, R_A, V'_B)$ and transmits it to B.

(3) Independently, A tests whether $(T - T_A)$ is in a valid period, where T is the time when the message transmitted from B after Round 2 was received. If so, A uses the received R_B to compute the session key $SK' = (R_B)^a \bmod p$. Then, it computes $C'_{BA} = h(T_A, R_A, R_B, SK')$ and checks $C'_{BA} \stackrel{?}{=} C_{BA}$ to authenticate B; if it holds, A computes $C_{AB} = h(C_{BA}, T_B, SK')$ and sends it to B.

After this round, A tests whether $(T' - T_A)$ is in a valid period, where T' is the time when C_{SA} was received. If so, A calculates $C'_{SA} = h(C_{AS}, T_B, R_B, V_A)$ and tests $C'_{SA} \stackrel{?}{=} C_{SA}$ to verify the correctness of C_{SA}. If it holds, A finishes this protocol.

Similarly, B tests if $(T'' - T_B)$ is in a valid period, where T'' is the time when C_{SB} was received. If so, B calculates $C'_{SB} = h(C_{BS}, T_A, R_A, V_B)$ and tests $C'_{SB} \stackrel{?}{=} C_{SB}$ to verify the correctness of C_{SB}. If it holds, B completes this protocol.

3.3. Disadvantages of Chen et al.'s Protocol

In this section, we argue that Chen et al.'s scheme still has four disadvantages. The detailed description of the weaknesses is as follows.

3.3.1. Computational E ciency Problem

In the initialization phase of Chen et al.'s protocol, S has to compute all the authenticated information $(\delta_A, r_A, e_A, s_A)$ for A and $(\delta_B, r_B, e_B, s_B)$ for B. Server has to perform two modular exponentiation operations, which are more expensive than other operations in Chen et al.'s protocol. Hence, it has low efficiency in this phase.

3.3.2. Lack of User Friendliness

In Chen et al.'s scheme, the password is chosen by the server S without the consent of A/B, thus, A/B can only passively accept the password from S. It is not practical for real life applications, such as on-line banking and e-mail subscription. Moreover, $\delta_A/\delta_B \in [1, q]$ chosen by the server could be long and random (e.g., 160 bits), which might be difficult for a registered user A/B to remember easily, and it is most likely that A/B may forget this long and random password if he is not frequently using the system. Hence, Chen et al.'s scheme has lack of user friendliness.

3.3.3. No Protecting User Anonymity

In authenticated key exchange phase of Chen et al.'s scheme, $\mathrm{ID}_A, \mathrm{ID}_B$ are sent to S over insecure channel in the authentication message: $(\mathrm{ID}_A, \mathrm{ID}_B, W_A)$, $(\mathrm{ID}_B, \mathrm{ID}_A, W_B)$. In certain authentication scenarios, such as e-voting and secret online-order placement, it is fairly crucial to protect the privacy of a user. Once an attacker sniffs the communication parties involved in the authentication process, he can easily analyze the transaction being performed by users. Hence, Chen et al.'s scheme fails to provide the user anonymity in the authentication phase.

3.3.4. No Provision for Revocation of Lost or Stolen Smart Card

In case the smart card is lost or stolen, the attacker may impersonate the legal user using the lost or stolen smart card, so there should be a mechanism to ensure that the system can revoke the lost or stolen smart card to avoid the possible attacks. Providing for revocation is also one of the requirements of smart card-based authentication protocols. By keeping

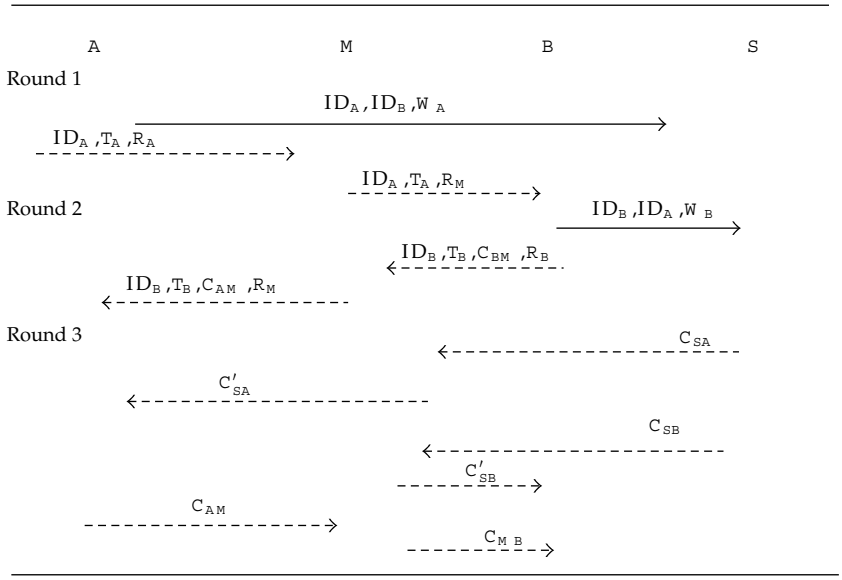

Figure 2: Man-in-the-middle attack in Chen et al.'s protocol.

record of valid card identifier of every registered user, the authentication system can tell the valid card from the invalid one. Regretfully, Chen et al.'s scheme ignored this feature and there is no mechanism to revoke the lost smart card. Moreover, the drawback would become catastrophic if an attacker has got the lost smart card by accident and has revealed the authentication message of a legal user by any means to login into the system for performing secure transaction, such as on-line banking and e-commerce. Thus, Chen et al.'s scheme failed to provide the important feature of smart card-based authentication for revoking the lost smart cards without changing the user's identities.

3.3.5. Man-in-the-Middle Attack

Due to Section 3.3.4, unqualified users can easily launch a man-in-the-middle attack when the smart card is stolen. The steps of the attack is outlined in Figure 2 and explained as follows.

Suppose an adversary M had stolen the smart card from the legal user, then he can obtain the authenticated values V_A and V_B. Let $R_M = g^m \bmod p$ be M's ephemeral public key, and $m \in z_p^*$ is chosen by M. Then, he replaces C_{SA} and C_{SB} with C'_{SA} and C'_{SB} in Round 3. The notation "$\dashrightarrow$" denotes the transmitted message that is manipulated by M. The purpose of M is to share a session key with A by posing as B and to share a session key with B by posing as A. The specific process is as follows.

Round 1:

$$\begin{aligned} A &\longrightarrow S : (\mathrm{ID}_A, \mathrm{ID}_B, W_A), \\ A &\dashrightarrow M(B) : (\mathrm{ID}_A, T_A, R_A), \\ M(A) &\dashrightarrow B : (\mathrm{ID}_A, T_A, R_M). \end{aligned} \tag{3.4}$$

Round 2:

$$\begin{aligned} &B \longrightarrow S : (\mathrm{ID}_B, \mathrm{ID}_A, W_B), \\ &B \dashrightarrow M(A) : (\mathrm{ID}_B, T_B, R_B, C_{BM}). \\ &M(B) \dashrightarrow A : (\mathrm{ID}_B, T_B, R_M, C_{MA}). \end{aligned} \tag{3.5}$$

When receiving the message from $M(A)$, B calculates the session key with $M(A)$, as $SK_{MB} = g^{bm} \bmod p$, $C_{BM} = h(T_A, R_M, R_B, SK_{MB})$, then M calculates the session key with A as $SK_{AM} = g^{am} \bmod p$, $C_{AM} = h(T_A, R_M, R_B, SK_{AM})$.

Round 3:

$$\begin{aligned} &S \dashrightarrow M(A) : C_{SA}, \\ &M(S) \dashrightarrow A : C'_{SA}, \\ &S \dashrightarrow M(B) : C_{SB}, \\ &M(S) \dashrightarrow B : C'_{SB}, \\ &A \dashrightarrow M(B) : C_{AM}, \\ &M(A) \dashrightarrow B : C_{MB}. \end{aligned} \tag{3.6}$$

In this round, because M obtains the value V_A, he can compute $C'_{SA} = h(C_{AS}, T_B, R_M, V_A)$ for mutual authentication with A; similarly, M can also use V_B to calculate $C'_{SB} = h(C_{BS}, T_A, R_M, V_B)$ for mutual authentication with B.

When receiving the values C'_{SA} and C'_{SB}, A and B authenticate the server using their own parameters. Then A computes $C_{MB} = h(C_{BM}, T_B, SK_{AM})$ for $M(B)$, it confirms if C_{MB} is valid from its own knowledge. M calculates $C_{MB} = h(C_{MA}, T_B, SK_{MB})$ and sends it to B to achieve session key agreement.

Finally, M has shared the session key $SK_{AM} = g^{am}\, p$ with A and $SK_{BM} = g^{bm} \bmod p$ with B. In this case, the authenticate mechanism of the Chen et al.'s protocol does not help.

4. An Anonymous Authentication Protocol Using Semiproperty of Enhanced Chebyshev Polynomials

To surmount serious latency security problems in the Chen et al.'s protocol, we apply semigroup property of enhanced Chebyshev polynomials to designing a new anonymous authentication protocol.

4.1. Notations

In the section, we describe some of the notations used in our protocol (Table 2).

Table 2: Some of the notations used in our paper.

Symbol	Definition
ID_A, ID_B	Identities of users A and B, respectively
ID_S	Identity of the authentication server S
N	The large prime N
x_1, y, n	The long-term key of S, and $y = T_{x_1}(x)$
x	x is the seed of the enhanced Chebyshev polynomial
P_A, P_B	Passwords of A and B, respectively
a, b	Random large integer number chosen by A and B, respectively
R_A, R_B	Components of session key, where $R_A = T_a(x)$ and $R_B = T_b(x)$
$H(\cdot)$	Collision resistant secure one-way chaotic hash function
C_{XY}	Evidence generated by user X for user Y

4.2. Initialization Phase

In this phase, the users and the server need some intercommunication for user's registration.

We take A for an example. To register with S to become a valid user A, A and S will do the following steps.

(1) $A \rightarrow S$: (D_A, ID_A)

A freely chooses an easy-to-remember password P_A and identity ID_A, then computes $D_A = T_{P_A}(x)$ and sends (D_A, ID_A) to S.

(2) When receiving D_A from A, S first tests if $D_A \stackrel{?}{=} D_I$. If $D_A = D_I$, S should ask A to submit a different password.

(3) $S \rightarrow A$: $(\Delta_A, H(\cdot))$

Then, S computes $\Delta_A = E_n(T_{P_A}(x) \| ID_A)$, for convenience, S stores $(\Delta_A, H(\cdot))$ into a smart card and then delivers it to A face to face.

Of course, B registers with S in the same way.

4.3. Authentication Key Exchange Phase

This phase aims to establish a session key SK. To achieve this goal, A and B first compute $V_A = H(T_{P_A}(y))$ and $V_B = H(T_{P_B}(y))$ using their own passwords and the public key of S as their authentication information respectively. Note that V_A, V_B can be precomputed. This phase also includes three rounds (shown phase in Figure 3) and the detailed descriptions are as follows.

Round 1:

$$\begin{aligned} A &\longrightarrow S : (ID_A, \Delta_A, W_A) \\ A &\longrightarrow B : (\Delta_A, T_A, R_A). \end{aligned} \tag{4.1}$$

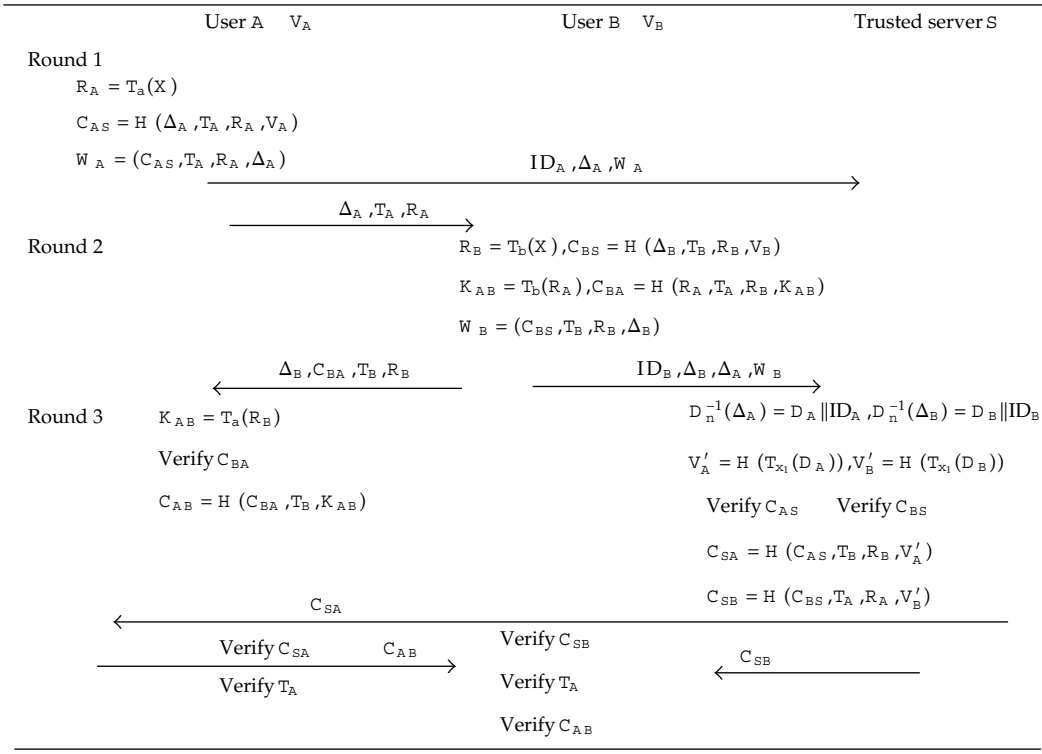

Figure 3: Authenticated key exchange phase in our proposed protocol.

(1) Calculates $C_{AS} = H(\Delta_A, T_A, R_A, V_A)$ and $W_A = (C_{AS}, T_A, R_A, \Delta_A)$, then transmits Δ_A and W_A to S; where the meaning of T_A is the same as that in the Chen et al.'s protocol.

(2) A transmits Δ_A, T_A and R_A to B.

Round 2:

$$\begin{aligned} B &\longrightarrow S : (\mathrm{ID}_B, \Delta_A, \Delta_B, W_B) \\ B &\longrightarrow A : (\Delta_B, T_B, R_B, C_{BA}). \end{aligned} \tag{4.2}$$

On receiving the request transmitted from A, B does the following steps.

(1) B calculates $C_{BS} = H(\Delta_B, T_B, R_B, V_B)$ and sends $W_B = (C_{BS}, T_B, R_B, \Delta_B)$ to S; the meaning of T_B is the same as that in the Chen et al.'s protocol.

(2) B calculates the session key $SK = T_b(R_A)$ and transmits $C_{BA} = H(T_A, R_A, R_B, SK)$ to A.

Round 3:

$$S \longrightarrow A : C_{SA},$$
$$S \longrightarrow B : C_{SB}, \tag{4.3}$$
$$A \longrightarrow B : C_{AB}.$$

In this round, S does the following steps.

(1) Verify if T_A is in a valid time interval. If so, S decrypts Δ_A, Δ_B with his private key n to reveal $T_{P_A}(x)\|\mathrm{ID}_A$ and $T_{P_B}(x)\|\mathrm{ID}_B$. Then, S calculates $V'_A = H(T_{x_1}(D_A))$ and computes $C'_{SA} = H(\Delta_A, T_A, R_A, V'_A)$. Finally, test $C'_{AS} \stackrel{?}{=} C_{AS}$, if it holds, S calculates $C_{SA} = H(C_{AS}, T_B, R_B, V'_A)$ and transmits it to A.

(2) Test whether T_B is in a valid time interval. If so, S calculates $V'_B = H(T_{x_1}(D_B))$ and computes $C'_{BS} = H(\Delta_B, T_B, R_B, V'_B)$. Then, he tests $C'_{BS} \stackrel{?}{=} C_{BS}$, if it holds, S calculates $C_{SB} = H(C_{BS}, T_A, R_A, V'_B)$, and transmits it to B.

(3) Independently, A tests if $(T - T_A)$ is in a valid period, where T is the time when B received the message from S. If so, A calculates $SK' = T_a(R_B)$ and $C'_{BA} = H(T_A, R_A, R_B, SK')$; then, tests $C'_{BA} \stackrel{?}{=} C_{BA}$; if it holds, A calculates $C_{AB} = H(C_{BA}, T_B, SK')$ and sends it to B.

After this round, A tests if $(T' - T_A)$ is in a valid period, where T' is the time when C_{SA} was received. If so, A calculates $C'_{SA} = H(C_{AS}, T_B, R_B, V_A)$ and tests $C'_{SA} \stackrel{?}{=} C_{SA}$ to verify the correctness of C_{SA}. If it holds, A finishes this protocol.

Similarly, B tests if $(T'' - T_B)$ is in a valid period, where T'' is the time when C_{SB} was received. If so, B calculates $C'_{SB} = H(C_{BS}, T_A, R_A, V_B)$ and tests $C'_{SB} \stackrel{?}{=} C_{SB}$ to verify the correctness of C_{SB}. If it holds, B finishes this protocol.

5. Security Analysis

The enhanced scheme is a modified form of the Chen et al.'s scheme. Hence, we just discuss the enhanced and some important security features of the proposed scheme instead of discussing the security analysis that has been already shown in [23]. Before analyzing the security properties, we stress the following two facts to prove security that authenticated key agreement protocol should meet. (1) It is widely believed that there is no polynomial-time algorithm to solve DLP and DHP based on enhanced Chebyshev polynomials with nonnegligible probability. (2) The chaotic hash function has collision-free and irreversible properties.

5.1. Securely Chosen and Update Password

In our proposed scheme, A/B is able to freely choose and change his password without any hassle of contacting the server S. Any users except A/B cannot change or update the password without knowing the corresponding valid $\mathrm{ID}_A/\mathrm{ID}_B$ and P_A/P_B of the smart card holder.

5.2. Revocation of Smart Card

In our proposed scheme, if (A/B)'s smart card is stolen or lost, he can request the server S to revoke his smart card for future use. S can revoke the smart card directly. If an adversary who steals (A/B)'s smart card wants to derive P_A from $\Delta_A = E_n(T_{P_A}(x)\|\mathrm{ID}_A)$, this will be impossible, because just S knows the secret key n, and he is faced with the discrete logarithm problem (DLP) too. Hence, the old smart card becomes useless for future use.

5.3. The Proposed Protocol Can Resist Man-in-the-Middle Attack

Due to $V_A = H(T_{P_A}(y)) = H(T_{x_1}(D_A))$, if the adversary attempts to login to S, it needs to derive x_1/P_A from y/Δ_A. However, it is widely believed that there is no polynomial-time algorithm to solve DLP based on enhanced Chebyshev polynomials with nonnegligible probability. Moreover, because just S knows the secret key n, he even cannot obtain D_A. So the adversary cannot compute V_A. Due to the same reason, the adversary cannot calculate V_B either, that is, our protocol can resist man-in-the-middle attack.

5.4. Protection of User Anonymity

The anonymity feature of users is that the real identity of user should be protected from being revealed by any other entity except S. Our protocol can preserve the identity anonymity for any user which can be explained as follows.

ID_A is hidden in $\Delta_A = E_n(T_{P_A}(x)\|\mathrm{ID}_A)$. Because just S knows the secret key n, even if adversary can obtain Δ_A from the stolen smart card, he still cannot decrypt Δ_A.

5.5. The Proposed Protocol Can Provide Mutual Authentication

Similarly to Chen et al.'s scheme, we analyze this property from three aspects: authentications among A, B, and S.

Case 1. A and B To authenticate A, S needs to suppose that they own the same session key. In this protocol, S is responsible for confirming both the origin and integrity of the received message in step (2) to help them authenticate each other. S ensures that the received messages T_A, R_A, V_A and T_B, R_B, V_B are truly sent from A and B, respectively, and that no modification has occurred. Meanwhile, S sends the respective evidence C_{SA} and C_{SB} for the origin and the integrity of (T_A, R_A) and (T_B, R_B). Based on the premise that S is trustworthy, A/B is convinced that the origin of $(T_B, R_B)/(T_A, R_A)$ is B/A when the validity of C_{SA}/C_{SB} is verified. As only A/B knows the secret a/b of R_A/R_B, the common session key is generated by A/B as $T_a(R_B)/T_b(R_A)$. Because the session key is only known by A/B, no one can forge a valid $C_{BA} = H(T_A, R_A, R_B, SK)$ or $C_{AB} = H(C_{BA}, T_B, SK')$. Therefore, mutual authentication between A and B is achieved while the session key confirmation is guaranteed.

Case 2. A and S To achieve the mutual authentication between A and S, on the one hand, S has to verify the validity of the evidence $C_{AS} = H(\Delta_A, T_A, R_A, V_A)$. On the other hand, A must

test the validity of $C_{SA} = H(C_{AS}, T_B, R_B, V'_A)$ to authenticate S. These evidences are computed with the common secret key. Because only A and S know the common secret key V_A, where V_A equals V'_A, no one can counterfeit the evidence. When validity of C_{AS} and C_{SA} is tested by S and A, respectively, the integrity of the transmitted message from S that contains T_A, R_A is confirmed by S and the integrity of evidence C_{SA} from S is confirmed by A. Thus, mutual authentication between A and S is achieved.

Case 3. B and S The analysis of the mutual authentication between B and S is done likewise. Except B and S, no one knows the secret key V_B. Therefore, mutual authentication between B and S is achieved by verifying the validity of $C_{BS} = H(\Delta_B, T_B, R_B, V_B)$ and $C_{SB} = H(C_{BS}, T_A, R_A, V'_B)$, respectively.

5.6. The Proposed Protocol Can Resist Bergamo et al.'s Attack

In addition, because our protocol is based on semigroup property of enhanced Chebyshev polynomials, we should consider Bergamo et al.'s attack [20]. Bergamo et al.'s attack is based on the condition that an adversary can obtain the related elements $x, N, T_a(x)$ and $T_b(x)$. In the proposed protocol, an attacker could get x and N easily, but they cannot obtain $T_a(x)$ and $T_b(x)$, even though the attacker is a legal user. Besides, the proposed protocol utilizes the enhanced Chebyshev polynomials, in which the periodicity of the cosine function is avoided by extending the interval of x from $(-1, +1)$ to $(-\infty, +\infty)$. Therefore, the attacker have no way to perform a successful attack using Bergamo et al.'s method.

5.7. The Proposed Protocol Can Resist Off-Line Dictionary Attack

In the off-line dictionary attack, the adversary can recode all transmitted messages in the initialization phase and attempt to guess using $A's/B's$ identities $\mathrm{ID}_A/\mathrm{ID}_B$ and passwords P_A/P_B from the recorded massages. An attacker tries to obtain identity and password verification information from Δ_A, he must guess n, P_A, ID_A correctly at the same time. However, the probability of guessing the three numbers correctly in the same attempt is nearly zero. Furthermore, even if the attacker guesses one parameter correctly, he or she cannot verify it with any password verifier information. Hence, the proposed protocol is secure against off-line dictionary attack.

According to the above analysis, we list the security properties' comparison of Chen et al.'s protocol and our protocol in Table 3.

6. Computational Efficiency Analysis

The proposed protocol is achieved through DLP and DHP problems based on enhanced Chebyshev polynomials. It enjoys the following advantages. (1) In the initial phase, we take A for example, S only needs to test $D_A \stackrel{?}{=} D_I$, where D_I denotes the users' component of authentication information and computes Δ_A. However, in Chen et al.'s protocol, S has to compute (V_A, r_A, e_A, s_A). In a word, our protocol greatly reduces the computational complexity and computational cost. Hence, our scheme is more efficient and practical. (2) V'_A, V'_B can be precomputed off-line in our protocol, which improves the computational

Table 3: Comparison of security properties.

Security properties	Chen et al.'s protocol	Our protocol
Anonymity	No	Yes
Man-in-the-middle attack	No	Yes
DoS attack	Yes	Yes
Mutual authentication among three parties	Yes	Yes
Perfect forward secrecy	Yes	Yes
Provision for revocation of lost or stolen smart card	No	Yes
Insider attack	Yes	Yes
User friendliness	No	Yes
Replay attack	Yes	Yes

Table 4: Comparison of computation overhead in initialization phase.

	Chen et al.'s protocol	Our protocol
Random number $(A/B/S)$	$0/0/0$	$1/1/0$
Symmetric encryption/decryption $(A/B/S)$	$0/0/0$	$0/0/2$
Modular exponentiation $(A/B/S)$	$1/1/2$	$0/0/0$
Hash operation $(A/B/S)$	$1/1/4$	$1/1/2$
Chebyshev polynomial computing $(A/B/S)$	$0/0/0$	$1/1/0$

efficiency and saves communication bandwidth. The detailed comparison is shown in Table 4.

7. Conclusion

In this paper, we have applied semigroup property of enhanced Chebyshev polynomials to present a novel authenticated key exchange protocol. To the best of our knowledge, it is the first time to realize three-party authenticated key exchange protocol preserving user anonymity with semigroup property of enhanced Chebyshev polynomials. First, we argued that Chen et al.'s protocol has computational efficiency problem in initialization phase and cannot protect user anonymity, user has no choice in choosing his password, and there is no provision for revocation of lost or stolen smart card leading to man-in-the-middle attack. To surmount these identified drawbacks, we have proposed an enhanced protocol to reduce computational complexity and computational cost in initialization phase and improve security. Hence, our proposed protocol is more efficient and practical. Furthermore, analysis shows that our protocol can resist various kinds of attacks.

Acknowledgments

The authors are grateful to the anonymous referees for their valuable comments and suggestions to improve the presentation of this paper. This work is supported by the National Basic Research Program of China (973 Program) (Grant no. 2010CB923200), the National Natural Science Foundation of China (Grant nos. 61003285, 61121061), the Foundation for the Author of National Excellent Doctoral Dissertation of PR China (Grant no. 200951), the Asia Foresight Program under NSFC Grant (Grant no. 61061040320), and the Specialized Research Fund for the Doctoral Program of Higher Education (Grant no. 20100005110002).

References

[1] T. Dierks, "The transport layer security (tls) protocol version 1.2 s," no. 5246, August 2008, http://www.ietf.org/rfc/rfc5246.txt.

[2] C. T. Li and M. S. Hwang, "An efficient biometrics-based remote user authentication scheme using smartcards," *Journal of Network and Computer Applications*, vol. 33, no. 1, pp. 1–5, 2010.

[3] X. Li, J. W. Niu, J. Ma, W. D. Wang, and C. L. Liu, "Cryptanalysis and improvement of a biometrics-based remote user authentication scheme using smart cards," *Journal of Network and Computer Applications*, vol. 34, no. 1, pp. 73–79, 2011.

[4] X. Li, Y. P. Xiong, J. Ma, and W. D. Wang, "An efficient and security dynamic identity based authentication protocol for multi-server architecture using smart cards," *Journal of Network and Computer Applications*, vol. 35, no. 2, pp. 763–769, 2012.

[5] M. Li and W. Zhao, "A model to partly but reliably distinguish DDOS flood traffic from aggregated one," *Mathematical Problems in Engineering*, vol. 2012, Article ID 860569, 12 pages, 2012.

[6] M. Li, "An approach to reliably identifying signs of DDOS flood attacks based on LRD traffic pattern recognition," *Computers and Security*, vol. 23, no. 7, pp. 549–558, 2004.

[7] M. Li, "Change trend of averaged Hurst parameter of traffic under DDOS flood attacks," *Computers and Security*, vol. 25, no. 3, pp. 213–220, 2006.

[8] M. Li and W. Zhao, "Representation of a stochastic traffic bound," *IEEE Transactions on Parallel and Distributed Systems*, vol. 21, no. 9, pp. 1368–1372, 2010.

[9] R. Bettati, W. Zhao, and D. Teodor, "Real-time intrusion detection and suppression in ATM networks," in *Proceedings of the 1st USENIX Workshop on Intrusion Detection and Network Monitoring*, Santa Clara, Calif, USA, April 1999.

[10] S. M. Bellovin and M. Merritt, "Encrypted key exchange: password-based protocols secure against dictionary attacks," in *Proceedings of IEEE Computer Society Symposium on Research in Security and Privacy*, pp. 72–84, Oakland, Calif, USA, 1992.

[11] S. Patel, "Number theoretic attacks on secure password schemes," in *Proceedings of IEEE Symposium on Security and Privacy*, pp. 236–247, 1997.

[12] N. McCullagh and P. S. L. M. Barreto, "A new two-party identity-based authenticated key agreement," in *Topics in Cryptology—CT-RSA 2005*, vol. 3376 of *Lecture Notes in Computer Science*, pp. 262–274, Springer, Berlin, Germany, 2005.

[13] M. Abdalla, D. Catalano, C. Chevalier, and D. Pointcheval, "Efficient two-party password-based key exchange protocols in the UC framework," in *Topics in Cryptology—CT-RSA 2008*, vol. 4964 of *Lecture Notes in Computer Science*, pp. 335–351, Springer, Heidelberg, Germany, 2008.

[14] G. Xie, "Cryptanalysis of Noel McCullagh and Paulo S.L.M. Barretos twoparty identity-based key agreement, Cryptology ePrint Archive," Report 2004/308, 2004, http://eprint.iacr.org/2004/308.

[15] N. McCullagh and P. S. L. M. Barreto, "A new two-party identity-based authenticated key agreement, Cryptology ePrint Archive," Report 2004/122, 2004, http://eprint.iacr.org/2004/122.

[16] J. Kwon, K. Sakurai, and D. Lee, "One-round protocol for two-party verifierbased password-authenticated key exchange," in *Communications and Multimedia Security*, H. Leitold and E. Markatos, Eds., vol. 4237 of *Lecture Notes in Computer Science*, pp. 87–96, Springer, Heidelberg, Germany, 2006.

[17] K. P. Xue and P. L. Hong, "Security improvement on an anonymous key agreement protocol based on chaotic maps," *Communications in Nonlinear Science and Numerical Simulation*, vol. 17, pp. 2969–2977, 2012.

[18] J. Kwon, K. Sakurai, and D. Lee, "One-round protocol for two-party verifierbased password-authenticated key exchange," in *Communications and Multimedia Security*, H. Leitold and E. Markatos, Eds., vol. 4237 of *Lecture Notes in Computer Science*, pp. 87–96, Springer, Heidelberg, Germany, 2006.

[19] O. K. Jeong, I. R. Jeong, K. Sakurai, and D. H. Lee, "Efficient verifierbased password-authenticated key exchange in the three-party setting," *Computer Standards and Interfaces*, vol. 29, pp. 513–520, 2007.

[20] C. L. Lin, H. M Sun, M. Steiner, and T. Hwang, "Three-party encrypted key exchange without server public-keys," *IEEE Communication Letters*, vol. 5, pp. 497–499, 2001.

[21] C. C. Chang and Y. F. Chang, "A novel three-party encrypted key exchange protocol," *Computer Standards and Interfaces*, vol. 26, pp. 471–476, 2004.

[22] D. Wang and X. Wei, "A new key exchange scheme based on extended chebyshev polynomials," in *Proceedings of the 4th WSEAS International Conference on Applied Mathematics and Computer Science*, pp. 1–5, Rio de Janeiro, Brazil, 2005.

[23] T. H. Chen, W. B. Lee, and H. B. Chen, "A round- and computation-efficient three-party authenticated key exchange protocol," *The Journal of Systems and Software*, vol. 81, pp. 1581–1590, 2008.

[24] G. J. Fee and M. B. Monagan, "Cryptography using chebyshev polynomial," Maple Summer Workshop, Burnaby, Canada, 2004, http://oldweb.cecm.sfu.ca/CAG/papers/Cheb.pdf.
[25] H. Tseng, R. Jan, and W. Yang, "A chaotic maps-based key agreement protocol that preserves user anonymity," in *Proceedings of the IEEE International Conference on Communications (ICC '09)*, pp. 1–6, 2009.
[26] E.-J. Yoon and I.-S. Jeon, "An efficient and secure Diffie-Hellman key agreement protocol based on Chebyshev chaotic map," *Communications in Nonlinear Science and Numerical Simulation*, vol. 16, no. 6, pp. 2383–2389, 2011.
[27] L. Zhang, "Cryptanalysis of the public key encryption based on multiple chaotic systems," *Chaos, Solitons and Fractals*, vol. 37, no. 3, pp. 669–674, 2008.

Hindawi Publishing Corporation
Mathematical Problems in Engineering
Volume 2012, Article ID 640789, 37 pages
doi:10.1155/2012/640789

Research Article

Minimum-Energy Multiwavelet Frames with Arbitrary Integer Dilation Factor

Yongdong Huang,[1] Qiufu Li,[1] and Ming Li[2]

[1] *Institute of Information and System Science, Beifang University of Nationalities, Yinchuan 750021, China*
[2] *School of Information Science & Technology, East China Normal University, Shanghai 200241, China*

Correspondence should be addressed to Yongdong Huang, nxhyd74@126.com

Received 15 May 2012; Accepted 26 June 2012

Academic Editor: Carlo Cattani

In order to organically combine the minimum-energy frame with the significant properties of multiwavelets, minimum-energy multiwavelet frames with arbitrary integer dilation factor are studied. Firstly, we define the concept of minimum-energy multiwavelet frame with arbitrary dilation factor and present its equivalent characterizations. Secondly, some necessary conditions and sufficient conditions for minimum-energy multiwavelet frame are given. Thirdly, the decomposition and reconstruction formulas of minimum-energy multiwavelet frame with arbitrary integer dilation factor are deduced. Finally, we give several numerical examples based on B-spline functions.

1. Introduction

Wavelets transform has been widely applied to information processing, image processing, computer science, mathematical physics, engineering, and so on. As you all know, it is not possible for any orthogonal scaling wavelet function with compact support to be symmetric, except for the Haar wavelets. In 1993, Goodman and Lee [1] established the multiwavelet theory by introducing the multiresolution analysis (MRA) with multiplicity r, and gave the spline multiwavelet examples. Using the fractal interpolation technology, Geronimo et al. [2] constructed the GHM multiwavelet which have short support, (anti)symmetry, orthogonality and vanishing moment with order 2 in 1994. From then on, multiwavelet has been a hot research area. In 1996, Chui and Lian [3] reconstructed the GHM multiwavelet without using the fractal interpolation technology, and they gave the general method on constructing the multiwavelet with short support, (anti)symmetry, and orthogonality. After that, Plonka and Strela [4] used two-scale similarity transforms (TSTs) to raise the approximation order of multiwavelet and gave the important conclusions of the two-scale matrix symbol's

factorizations and so on. And, by Lawton et al. [5], the construction of multiwavelet has been transformed into matrix extension problem in 1996. The construction theory of multiwavelet had a great development after Jiang [6, 7] putting forward a series of effective methods. Whether wavelets or multiwavelet, they require that the integer shifts of the scaling function form Riesz bases, orthogonal basis, or biorthogonal basis for its span space. And this will cause some defects: (1) the computational complexity can be increased during the course of decomposition and reconstruction; (2) the numerical instability can be caused during the procedure of reconstructing original signal (3) in the biorthogonal case, the analysis filter bank can not replaced by the synthetic filter bank, and vice verse.

Fortunately, besides orthogonal wavelets and multiwavelet minimum-energy frames can effectively avoid the difficulty which is caused by different bases functions during the course of decomposition and reconstruction, still use the same wavelets both for analysis and synthesis. The theory of frames comes from signal processing firstly. It was introduced by Duffin and Schaffer to deal with problems in nonharmonic Fourier series. But in a long time after that, people did not pay enough attention to it. After Daubechies et al. [8] defined affine frames (wavelets frames) by combining the theory of continuous wavelets transforms and frames while wavelets theory was booming, people start to research frames and its application again. Benedetto and Li [9] gave the definition of frame multiresolution analysis (FMRA), and their work laid the foundation for other people's further investigation. Frames cannot only overcome the disadvantages of wavelets and multiwavelet, but also increase redundancy properly, then the numerical computation become much more stable using frames to reconstruct signal. With well time-frequency localization and shift invariance, frames can be designed more easily than wavelets or multiwavelet. Nowadays frames have been used widely in theoretical and applied domain [10–22], such as signal analysis, image processing, numerical calculation, Banach space theory, Besov space theory, and so on.

In 2000, Chui and He [11] proposed the concept of minimum-energy wavelets frames. The minimum-energy wavelets frames reduce the computational complexity, maintain the numerical stability, and do not need to search dual frames in the decomposition and reconstruction of functions (or signals). Therefore, many people pay a lot of attention to the study of minimum-energy wavelets frames. Huang and Cheng [15] studied the construction and characterizations of the minimum-energy with arbitrary integer dilation factor. Gao and Cao [18] researched the structure of the minimum-energy wavelets frames on the interval and its application on signal denoising systematically. Liang and Zhao [23] studied the minimum-energy multiwavelet frames with dilation factor 2 and multiplicity 2 and gave a characterization and a necessary condition of minimum-energy multiwavelet frames. Unfortunately, the authors did not give the sufficient conditions of minimum-energy multiwavelet frames. In fact, people need to pay close attention to the existence of sufficient conditions of minimum-energy wavelet frames in most cases. On the other hand B-spline functions which are the convolution of Shannon wavelets [24–26]. It can be seen that also Shannon wavelets are minimum-energy wavelets. In this paper, in order to organically combine the minimum-energy frame with the significant properties of multiwavelet, minimum-energy multiwavelet frames with arbitrary integer dilation factor are studied. Firstly, we define the concept of minimum-energy multiwavelet frame with arbitrary dilation factor and present its equivalent characterizations. Secondly, some necessary conditions and sufficient conditions for minimum-energy multiwavelet frame are given; Thirdly, the decomposition and reconstruction formulas of minimum-energy multiwavelet frame with arbitrary integer dilation factor and the multiplicity r are deduced. Finally, we give several numerical examples based on B-spline functions.

Let us now describe the organization of the material that as follows. Section 2 is preliminaries and basic definitions. Section 3 is main result. In Section 4, we give the decomposition and reconstruction formulas of minimum-energy multiwavelet frame. Section 5 is numerical examples.

2. Preliminaries and Basic Definitions

Throughout this paper, let $\mathbb{Z}$, $\mathbb{R}$, and $\mathbb{C}$ denote the set of integers, real numbers, and complex numbers respectively; $a \in \mathbb{Z}$ with $a \geqslant 2$, $\omega_j = \cos(2j\pi/a) + i\sin(2j\pi/a)$, $j = 0, 1, \ldots, a-1$.

A multiscaling function vector (refinable function vector) is a vector-valued function:

$$\Phi = \left(\phi_1(x), \ldots, \phi_r(x)\right)^T, \qquad \phi_l(x) \in L^2(\mathbb{R}), \quad l = 1, \ldots, r, \tag{2.1}$$

which satisfies a two-scale matrix refinement equation of the form:

$$\Phi(x) = \sum_{k\in\mathbb{Z}} P_k \Phi(ax - k), \quad x \in \mathbb{R}, \tag{2.2}$$

r is called the multiplicity of Φ, the integer a is said to be dilation factor. The recursion coefficients $\{P_k\}_{k\in\mathbb{Z}}$ are $r \times r$ matrices.

The Fourier transform of the formula (2.2) is

$$\widehat{\Phi}(\omega) = P(z)\widehat{\Phi}\left(\frac{\omega}{a}\right), \quad z = e^{-i\omega/a}, \tag{2.3}$$

where

$$P(z) = \frac{1}{a}\sum_{k\in\mathbb{Z}} P_k z^k. \tag{2.4}$$

$P(z)$ is the symbol of the matrix sequence $\{P_k\}_{k\in\mathbb{Z}}$.

The multiresolution analysis (MRA) with multiplicity r and dilation factor a generated by $\Phi(x)$ is defined as

$$\{V_j\} = \overline{\operatorname{span}}\left\{\phi_{\tau,j,k} : 1 \leqslant \tau \leqslant r,\ k \in \mathbb{Z},\ j \in \mathbb{Z}\right\}, \tag{2.5}$$

where $\phi_{\tau,j,k} = a^{j/2}\phi_\tau(a^j x - k)$, and the sequence of closed subspace of $L^2(\mathbb{R})$ has the following properties:

(1) $V_j \subset V_{j+1}$, $j \in \mathbb{Z}$.

(2) $\overline{\bigcup_{j\in\mathbb{Z}} V_j} = L^2(\mathbb{R})$, $\bigcap_{j\in\mathbb{Z}} V_j = \{0\}$;

(3) $f(x) \in V_j \Leftrightarrow f(ax) \in V_{j+1}$, for all $j \in \mathbb{Z}$;

(4) $f(x) \in V_j \Leftrightarrow f(x - a^{-j}k) \in V_j$, for all $k, j \in \mathbb{Z}$;

(5) $\{\phi_{\tau,0,k} : 1 \leqslant \tau \leqslant r, k \in \mathbf{Z}\}$ forms a Riesz basis of V_0;

Definition 2.1. A finite family vector-valued function $\Psi^i = (\psi_1^i, \ldots, \psi_r^i)^T$, $i = 1, \ldots, N$ generates a multiwavelet frames for $L^2(\mathbb{R})$, if there exist constants $0 < A \leqslant B < \infty$ such that for any $f(x) \in L^2(\mathbb{R})$

$$A\|f\|^2 \leqslant \sum_{i=1}^{N} \sum_{\tau=1}^{r} \sum_{j,k\in\mathbb{Z}} \left|\left\langle f, \psi_{\tau,j,k}^i \right\rangle\right|^2 \leqslant B\|f\|^2, \tag{2.6}$$

where $\psi_{\tau,j,k}^i = a^{j/2}\psi_\tau^i(a^j x - k)$.

Definition 2.2. A nested subspace generated by a multiscaling vector-valued function $\Phi(x)$ satisfies formula (2.5) and its additional conditions, then finite family vector-valued function $\{\Psi^1, \ldots, \Psi^N\}$ generates a frame multiresolution analysis associated the vector-valued function $\Phi(x)$, if the finite family $\Psi^i = (\psi_1^i, \ldots, \psi_r^i)^T$, $i = 1, \ldots, N$ satisfies the formulation (2.6) with $\psi_\tau^i \in V_1$, $i = 1, \ldots, N$; $\tau = 1, \ldots, r$.

Definition 2.3. Let $\Phi(x) = (\phi_1(x), \ldots, \phi_r(x))^T$, with $\widehat{\phi}_\tau \in L^\infty(\mathbb{R}) \cap L^2(\mathbb{R})$, $\tau = 1, \ldots, r$, $\widehat{\Phi}$ continuous at 0 and $\widehat{\Phi}(0) \neq 0$, be a multiscaling vector-valued function that generates the nested subspace $\{V_j\}_{j\in\mathbf{Z}}$ in the sense of (2.5). Then a finite family vector-valued function $\{\Psi^1, \ldots, \Psi^N\} \subset V_1$ is called a minimum-energy multiwavelet frames associated with $\Phi(x)$, if for for all $f \in L^2(\mathbb{R})$

$$\sum_{\tau=1}^{r} \sum_{k\in\mathbb{Z}} \left|\langle f, \phi_{\tau,1,k}\rangle\right|^2 = \sum_{\tau=1}^{r} \sum_{k\in\mathbb{Z}} \left|\langle f, \phi_{\tau,0,k}\rangle\right|^2 + \sum_{i=1}^{N} \sum_{\tau=1}^{r} \sum_{k\in\mathbb{Z}} \left|\left\langle f, \psi_{\tau,0,k}^i \right\rangle\right|^2. \tag{2.7}$$

Remark 2.4. By the Parseval identity, minimum-energy multiwavelet frames $\{\Psi^1, \ldots, \Psi^N\}$ must be tight frames for $L^2(\mathbb{R})$ with frames bound equal to 1.

Remark 2.5. The formula (2.7) is equivalent to the following formulas:

$$\sum_{\tau=1}^{r} \sum_{k\in\mathbb{Z}} \langle f, \phi_{\tau,1,k}\rangle \phi_{\tau,1,k} = \sum_{\tau=1}^{r} \sum_{k\in\mathbb{Z}} \langle f, \phi_{\tau,0,k}\rangle \phi_{\tau,0,k} + \sum_{i=1}^{N} \sum_{\tau=1}^{r} \sum_{k\in\mathbb{Z}} \left\langle f, \psi_{\tau,0,k}^i \right\rangle \psi_{\tau,0,k}^i. \tag{2.8}$$

The interpretation of minimum energy will be clarified later.

3. Main Result

In this section, we will give a complete characterization of minimum-energy multiwavelet frames associated with some given multiscaling vector-valued function in term of their two-scale symbols. Let $\Phi(x) = (\phi_1(x), \ldots, \phi_r(x))^T$ with $\widehat{\phi}_\tau \in L^\infty(\mathbb{R}) \cap L^2(\mathbb{R})$, $\tau = 1, \ldots, r$, $\widehat{\Phi}$ continuous at 0, and $\widehat{\Phi}(0) \neq 0$ be a multiscaling vector-valued function which satisfies (2.2)–(2.5). Consider $\{\Psi^1, \ldots, \Psi^N\} \subset V_1$, then

$$\Psi^l(x) = \sum_{k\in\mathbb{Z}} Q_k^l \Phi(ax - k), \tag{3.1}$$

where $\{Q_k^l\}_{k\in\mathbb{Z}}$, $l = 1,\ldots,N$ are $r \times r$ matrices. Using Fourier transform on (3.1), we can get their symbols as follows:

$$Q_l(z) = \frac{1}{a}\sum_{k\in\mathbb{Z}} Q_k^l z^k, \quad l = 1,\ldots,N. \tag{3.2}$$

With $P(z)$, $Q_l(z)$, $l = 1,\ldots,N$, we formulate the $(N+1)r \times ar$ block matrix as follows:

$$R(z) = \begin{bmatrix} P(z) & P(\omega_1 z) & \cdots & P(\omega_{a-1} z) \\ Q_1(z) & Q_1(\omega_1 z) & \cdots & Q_1(\omega_{a-1} z) \\ \vdots & \vdots & & \vdots \\ Q_N(z) & Q_N(\omega_1 z) & \cdots & Q_N(\omega_{a-1} z) \end{bmatrix}, \tag{3.3}$$

and the $R^*(z)$ denotes the complex conjugate of the transpose of $R(z)$.

The following theorem presents the equivalent characterizations of the minimum-energy multiwavelet frames with arbitrary integer dilation factor.

Theorem 3.1. *Suppose that every element of the symbols, $P(z)$, $Q_l(z)$, $l = 1,\ldots,N$, in* (2.4) *and* (3.2) *is a Laurent polynomial, and the multiscaling vector-valued function $\Phi(x)$ associated with $P(z)$ generates a nested subspace $\{V_j\}_{j\in\mathbf{Z}}$. Then the following statements are equivalent:*

(1) *$\{\Psi^1,\ldots,\Psi^N\}$ is a minimum-energy multiwavelet frames associated with $\Phi(x)$:*

(2)

$$R^*(z)R(z) = I_{ar} \quad \text{for } \forall |z| = 1; \tag{3.4}$$

(3)

$$\alpha_{ml,ij} = 0, \quad \forall m,l \in \mathbb{Z};\ i,j = 1,\ldots,r, \tag{3.5}$$

where

$$\begin{aligned} \alpha_{ml,ij} &= \sum_{k\in\mathbf{Z}}\sum_{\tau=1}^{r}\left(P_{l-ak}^{\tau i*}P_{m-ak}^{\tau j} + \sum_{t=1}^{N} Q_{l-ak}^{t,\tau i*} Q_{m-ak}^{t,\tau j}\right) - a\delta_{ml,ij}, \\ \delta_{ml,ij} &= \begin{cases} 1, & m = l,\ i = j, \\ 0, & else. \end{cases} \end{aligned} \tag{3.6}$$

Proof. By using the two-scale relations (2.2) and (3.1) and notation $\alpha_{ml,ij}$ for for all $f \in L^2(\mathbb{R})$, (2.8) can be written as

$$\sum_{l\in\mathbb{Z}}\sum_{m\in\mathbb{Z}}\sum_{i=1}^{r}\sum_{j=1}^{r}\alpha_{ml,ij}\langle f, \phi_i(ax-m)\rangle\phi_j(ax-l) = 0. \tag{3.7}$$

On the other hand, (3.4) can be reformulated as

$$\begin{gathered}
P^*(z)P(z) + \sum_{t=1}^{N} Q_t^*(z)Q_t(z) = I_r, \\
P^*(z)P(\omega_j z) + \sum_{t=1}^{N} Q_t^*(z)Q_t(\omega_j z) = 0_r, \\
j = 1, 2, \ldots, a-1; \quad \forall |z| = 1,
\end{gathered} \tag{3.8}$$

and it is equivalent to

$$\begin{gathered}
\sum_{k=0}^{a-1} P^*(\omega_k z)P(z) + \sum_{t=1}^{N}\sum_{k=0}^{a-1} Q_t^*(\omega_k z)Q_t(z) = I_r, \\
\left(P^*(z) - \sum_{k=1}^{a-1} P^*(\omega_k z)\right)P(z) + \sum_{t=1}^{N}\left(Q_t^*(z) - \sum_{k=1}^{a-1} Q_t^*(\omega_k z)\right)Q_t(z) = I_r, \\
\left(\sum_{k=0}^{a-1} P^*(\omega_k z) - 2P^*(\omega_l z)\right)P(z) + \sum_{t=1}^{N}\left(\sum_{k=0}^{a-1} Q_t^*(\omega_k z) - 2Q_t^*(\omega_l z)\right)Q_t(z) = I_r, \\
l = 1, 2, \ldots, a-1; \quad \forall |z| = 1.
\end{gathered} \tag{3.9}$$

With $|z| = 1$, $\overline{z}^k = z^{-k}$, $\omega_l^k = \omega_k^l = \omega^{kl}$, and

$$\sum_{l=0}^{a-1} \omega_l^k = \sum_{l=0}^{a-1} \omega_k^l = \begin{cases} 0 & \omega_k \neq 1 \\ a & \omega_k = 1, \end{cases} \tag{3.10}$$

the formulation (3.9) is equivalent to

$$\begin{gathered}
\sum_{k\in\mathbb{Z}} P_{-ak}^* z^{ak} P(z) + \sum_{t=1}^{N}\sum_{k\in\mathbb{Z}} Q_{-ak}^{t*} z^{ak} Q_t(z) = I_r, \\
\left(\sum_{l=1}^{a-1}\sum_{k\in\mathbb{Z}} P_{l-ak}^* z^{ak-l}\right)P(z) + \sum_{t=1}^{N}\left(\sum_{l=1}^{a-1}\sum_{k\in\mathbb{Z}} Q_{l-ak}^{t*} z^{ak-l}\right)Q_t(z) = (a-1)I_r, \\
\left(\sum_{l=1}^{a-1} e^{-(2sl\pi/a)i}\sum_{k\in\mathbb{Z}} P_{l-ak}^* z^{ak-l}\right)P(z) + \sum_{t=1}^{N}\left(\sum_{l=1}^{a-1} e^{-(2sl\pi/a)i}\sum_{k\in\mathbb{Z}} Q_{l-ak}^{t*} z^{ak-l}\right)Q_t(z) = -I_r, \\
s = 1, 2, \ldots, a-1; \quad \forall |z| = 1.
\end{gathered} \tag{3.11}$$

Using the properties of roots of unity, the Vandermonde matrix and Cramer's rule, the above equation is equivalent to

$$\begin{aligned}
\sum_{k\in\mathbb{Z}} P^*_{-ak} z^{ak} P(z) + \sum_{t=1}^{N}\sum_{k\in\mathbb{Z}} Q^{t*}_{-ak} z^{ak} Q_t(z) &= I_r,\\
\sum_{k\in\mathbb{Z}} P^*_{1-ak} z^{ak-1} P(z) + \sum_{t=1}^{N}\sum_{k\in\mathbb{Z}} Q^{t*}_{1-ak} z^{ak-1} Q_t(z) &= I_r,\\
&\vdots\\
\sum_{k\in\mathbb{Z}} P^*_{a-1-ak} z^{ak-a+1} P(z) + \sum_{t=1}^{N}\sum_{k\in\mathbb{Z}} Q^{t*}_{a-1-ak} z^{ak-a+1} Q_t(z) &= I_r.
\end{aligned} \tag{3.12}$$

We multiply the identities in (3.12) by $\widehat{\Phi}(\omega/a)z^l$, $l = 0, 1, \ldots, a-1$, respectively, where $z = e^{-i\omega/a}$, to get

$$\sum_k \left\{ P^*_{l-ak} z^{ak} P(z)\widehat{\Phi}\Big(\frac{\omega}{a}\Big) + \sum_{t=1}^{N} Q^{t*}_{l-ak} z^{ak} Q_t(z)\widehat{\Phi}\Big(\frac{\omega}{a}\Big) \right\} = \widehat{\Phi}\Big(\frac{\omega}{a}\Big) z^l, \quad l = 0, \ldots, a-1. \tag{3.13}$$

Hence, (3.12) is equivalent to

$$\sum_k \left\{ P^*_{l-ak} z^{ak} \widehat{\Phi}(\omega) + \sum_{ti=1}^{N} Q^{t*}_{l-ak} z^{ak} \widehat{\Psi}^t(\omega) \right\} = \widehat{\Phi}\Big(\frac{\omega}{a}\Big) e^{-il\omega/a}, \quad l = 0, \ldots, a-1 \tag{3.14}$$

or

$$\sum_k \left\{ P^*_{l-ak} z^{ak} \Phi(x-k) + \sum_{t=1}^{N} Q^{t*}_{l-ak} z^{ak} \Psi^t(x-k) \right\} = a\Phi(ax-l), \quad l = 0, \ldots, a-1, \tag{3.15}$$

which can be reformulated as

$$\sum_k \left\{ P^*_{l-ak} z^{ak} \Phi(x-k) + \sum_{t=1}^{N} Q^{t*}_{l-ak} z^{ak} \Psi^t(x-k) \right\} = a\Phi(ax-l). \tag{3.16}$$

By using the two-scaling relations (2.2) and (3.1), we can rewrite (3.16) as

$$\sum_m \sum_{j=1}^{a} \alpha_{ml,ij} \phi_j(ax-m) = 0, \quad i = 1, \ldots, r;\ \forall l \in \mathbb{Z}. \tag{3.17}$$

In conclusion, the proof of Theorem 3.1 reduces to the proof of the equivalence of (3.5), (3.7), and (3.17).

It is obvious that (3.5)⇒(3.17)⇒(3.7). To show (3.7)⇒(3.5), let $f \in L^2(\mathbb{R})$ be any compactly supported function. By using the properties that for every fixed m, $\alpha_{ml,ij} = 0$ expect for finitely many l, i, j, then the functional

$$\beta_{lj}(f) = \sum_m \sum_{i=1}^{r} \alpha_{ml,ij} \langle f, \phi_i(ax - m) \rangle \tag{3.18}$$

just has finite nonzero for $l \in \mathbb{Z}$, $j = 1, \ldots, r$.

Using the property of Fourier transform, we obtain

$$\sum_l \sum_{j=1}^{r} \beta_{lj}(f) \widehat{\phi}_j(\omega) e^{-il\omega/a} = 0. \tag{3.19}$$

Since $\widehat{\phi}_l(\omega)$ is nontrivial function, then $\beta_{lj}(f) = 0$, $l \in \mathbb{Z}$, $j = 1, \ldots, r$, in other words, we have

$$\left\langle f, \sum_m \sum_{i=1}^{r} \alpha_{ml,ij} \phi_i(ax - m) \right\rangle = 0, \quad l \in \mathbb{Z},\ j = 1, \ldots, r. \tag{3.20}$$

Then the series in the above equation is a finite sum and hence represents a compactly supported function in $L^2(\mathbb{R})$. By choosing f to be this function, it follows that

$$\sum_m \sum_{i=1}^{r} \alpha_{ml,ij} \phi_i(ax - m) = 0, \tag{3.21}$$

which implies that the trigonometric polynomial $\sum_m \sum_{i=1}^{r} \alpha_{ml,ij} \widehat{\phi}_i(\omega) e^{-im\omega}$ is identically equal to 0 so that $\alpha_{ml,ij} = 0$, for all $m, l \in \mathbb{Z}$; $i, j = 1, \ldots, r$.

We complete the proof of Theorem 3.1 because the set of compactly supported functions is dense in $L^2(\mathbb{R})$. □

Theorem 3.1 characterizes the necessary and sufficient condition for the existence of the minimum-energy multiwavelet frames associated with Φ. However it is not a good choice to use this theorem to construct the minimum-energy multiwavelet frames. For convenience, we need to present some sufficient conditions in terms of the symbols.

In this paper, we just discuss the minimum-energy frames with compact support, that is, every element of symbols is Laurent polynomial.

Theorem 3.2. *A compactly supported refinable vector-valued function $\Phi(x) = (\phi_1(x), \ldots, \phi_r(x))^T$, with $\widehat{\Phi}$ continuous at 0 and $\widehat{\Phi}(0) \neq 0$. Let $\{\Psi^1, \ldots, \Psi^N\}$ be the minimum-energy multiwavelet frames associated with it, then*

$$\sum_{i=1}^{r} \left| p_{ij}(\omega_l z) \right|^2 \leqslant 1 \quad \forall |z| = 1,\ 1 \leqslant j \leqslant r,\ 0 \leqslant l \leqslant a - 1, \tag{3.22}$$

$$\sum_{l=0}^{a-1} \sum_{j=1}^{r} \left| p_{ij}(\omega_l z) \right|^2 \leqslant 1 \quad \forall |z| = 1,\ 1 \leqslant i \leqslant r. \tag{3.23}$$

Proof. Using Theorem 3.1, it is clear to show that the l^2-norm of every row vector of the symbol for Φ is less than 1, in other words, (3.22) is valid. In order to prove (3.23), let $i = 1$. First, we set

$$f(z) = \left[p_{11}(z) \ \cdots \ p_{1r}(z) \ \cdots \ p_{11}(\omega_{a-1}z) \ \cdots \ p_{1r}(\omega_{a-1}z)\right], \tag{3.24}$$

and the rest of $R(z)$ removed $f(z)$ as $F(z)$. Then we can reformulate (3.4) as

$$f(z)^* f(z) + F(z)^* F(z) = I_{ar}, \tag{3.25}$$

or equivalently, $F(z)^*F(z) = I_{ar} - f(z)^* f(z)$, which is a nonnegative definite Hermitian matrix for $|z| = 1$ so that

$$\det\left(I_{ar} - f(z)^* f(z)\right) \geqslant 0 \quad \forall |z| = 1, \tag{3.26}$$

and this gives

$$\sum_{l=0}^{a-1}\sum_{j=1}^{r}\left|p_{1j}(\omega_l z)\right|^2 \leqslant 1 \quad \forall |z| = 1. \tag{3.27}$$

In fact, we have

$$\begin{aligned}
\begin{pmatrix} I_{ar} & f(z)^* \\ f(z) & 1 \end{pmatrix}\begin{pmatrix} I_{ar} & -f(z)^* \\ -f(z) & 1 \end{pmatrix} &= \begin{pmatrix} I_{ar} - f(z)^* f(z) & 0 \\ 0 & 1 - f(z)f(z)^* \end{pmatrix}, \\
\det\left(\begin{pmatrix} I_{ar} & f(z)^* \\ f(z) & 1 \end{pmatrix}\right) &= \det\left(\begin{pmatrix} I_{ar} & f(z)^* \\ 0 & 1 - f(z)f(z)^* \end{pmatrix}\right), \\
\det\left(\begin{pmatrix} I_{ar} & -f(z)^* \\ -f(z) & 1 \end{pmatrix}\right) &= \det\left(\begin{pmatrix} I_{ar} & -f(z)^* \\ 0 & 1 - f(z)f(z)^* \end{pmatrix}\right),
\end{aligned} \tag{3.28}$$

then

$$\det\left(I_{ar} - f(z)^* f(z)\right)\left(1 - f(z)f(z)^*\right) = \left(1 - f(z)f(z)^*\right)^2, \tag{3.29}$$

and it gives $1 - f(z)f(z)^* \geqslant 0$, for all $|z| = 1$, that is,

$$\sum_{l=0}^{a-1}\sum_{j=1}^{r}\left|p_{ij}(\omega_l z)\right|^2 \leqslant 1 \quad \forall |z| = 1,\ 1 \leqslant i \leqslant r. \tag{3.30}$$

The proof of Theorem 3.2 is completed. □

Remark 3.3. By the proof of Theorem 3.2, we know that the restriction in Theorem 3.2 on the two-scale symbol $P(z)$ of a refinable vector-valued function $\Phi(x)$ is a necessary condition for

the existence of a minimum-energy frames associated with $\Phi(x)$ via the rectangular unitary matrix extension approach, even if $\Phi(x)$ is not compactly supported.

Remark 3.4. For a certain compactly supported refinable vector-valued function, it cannot exist in minimum-energy frames.

We write $P(z)$, $Q_j(z)$, $j = 1, \ldots, N$ in their polyphase forms:

$$P(z) = \frac{\sqrt{a}}{a}\Big(P_1(z^a) + zP_2(z^a) + \cdots + z^{a-1}P_a(z^a)\Big), \tag{3.31}$$

$$Q_j(z) = \frac{\sqrt{a}}{a}\Big(Q_{j1}(z^a) + zQ_{j2}(z^a) + \cdots + z^{a-1}Q_{ja}(z^a)\Big), \quad j = 1, \ldots, N, \tag{3.32}$$

where $P_i(z)$, $Q_{ij}(z)$, $i = 1, \ldots, a$; $j = 1, \ldots, N$ are $r \times r$ matrices and their every element is Laurent polynomial. Observe that

$$R(z)\frac{\sqrt{a}}{a}\begin{bmatrix} I_r & z^{-1}I_r & \cdots & z^{1-a}I_r \\ I_r & (\omega_1 z)^{-1}I_r & \cdots & (\omega_1 z)^{1-a}I_r \\ \vdots & \vdots & & \vdots \\ I_r & (\omega_{a-1} z)^{-1}I_r & \cdots & (\omega_{a-1} z)^{1-a}I_r \end{bmatrix} = \begin{bmatrix} P_1(z^a) & P_2(z^a) & \cdots & P_a(z^a) \\ Q_{11}(z^a) & Q_{12}(z^a) & \cdots & Q_{1a}(z^a) \\ \vdots & \vdots & & \vdots \\ Q_{N1}(z^a) & Q_{N2}(z^a) & \cdots & Q_{Na}(z^a) \end{bmatrix}. \tag{3.33}$$

Therefore, we have

$$\begin{aligned} & a\begin{bmatrix} P_1(z^a) & P_2(z^a) & \cdots & P_a(z^a) \\ Q_{11}(z^a) & Q_{12}(z^a) & \cdots & Q_{1a}(z^a) \\ \vdots & \vdots & & \vdots \\ Q_{N1}(z^a) & Q_{N2}(z^a) & \cdots & Q_{Na}(z^a) \end{bmatrix}^* \begin{bmatrix} P_1(z^a) & P_2(z^a) & \cdots & P_a(z^a) \\ Q_{11}(z^a) & Q_{12}(z^a) & \cdots & Q_{1a}(z^a) \\ \vdots & \vdots & & \vdots \\ Q_{N1}(z^a) & Q_{N2}(z^a) & \cdots & Q_{Na}(z^a) \end{bmatrix} \\ & = \begin{bmatrix} I_r & z^{-1}I_r & \cdots & z^{1-a}I_r \\ I_r & (\omega_1 z)^{-1}I_r & \cdots & (\omega_1 z)^{1-a}I_r \\ \vdots & \vdots & & \vdots \\ I_r & (\omega_{a-1} z)^{-1}I_r & \cdots & (\omega_{a-1} z)^{1-a}I_r \end{bmatrix}^* R(z)^* R(z) \begin{bmatrix} I_r & z^{-1}I_r & \cdots & z^{1-a}I_r \\ I_r & (\omega_1 z)^{-1}I_r & \cdots & (\omega_1 z)^{1-a}I_r \\ \vdots & \vdots & & \vdots \\ I_r & (\omega_{a-1} z)^{-1}I_r & \cdots & (\omega_{a-1} z)^{1-a}I_r \end{bmatrix}, \end{aligned} \tag{3.34}$$

and it follows from (3.4), that

$$\begin{bmatrix} P_1(z^a) & P_2(z^a) & \cdots & P_a(z^a) \\ Q_{11}(z^a) & Q_{12}(z^a) & \cdots & Q_{1a}(z^a) \\ \vdots & \vdots & & \vdots \\ Q_{N1}(z^a) & Q_{N2}(z^a) & \cdots & Q_{Na}(z^a) \end{bmatrix}^* \begin{bmatrix} P_1(z^a) & P_2(z^a) & \cdots & P_a(z^a) \\ Q_{11}(z^a) & Q_{12}(z^a) & \cdots & Q_{1a}(z^a) \\ \vdots & \vdots & & \vdots \\ Q_{N1}(z^a) & Q_{N2}(z^a) & \cdots & Q_{Na}(z^a) \end{bmatrix} = I_{ar}, \quad \forall |z| = 1. \tag{3.35}$$

And it is easy to obtain (3.35) from (3.4).

For convenience, we denote $z^a = u$. Next, we present some theorems to give several sufficient conditions for existence of minimum-energy multiwavelet frames.

Theorem 3.5. *A compactly supported vector-valued function* $\Phi(x) = (\phi_1(x), \ldots, \phi_r(x))^T$ *with* $\widehat{\Phi}$ *continuous at 0 and* $\widehat{\Phi}(0) \neq 0$*, its symbol* $P(z)$ *satisfies*

$$\sum_{i=1}^{r} \sum_{l=0}^{a-1} \sum_{j=1}^{r} \left| p_{ij}(\omega_l z) \right| < 1, \quad \forall |z| = 1. \tag{3.36}$$

Then there exist minimum-energy multiwavelet frames associated with Φ*.*

Proof. Let $P_j(z),\ j = 1, \ldots, a$ be the polynomial components of $P(z)$, that is,

$$P(z) = \frac{\sqrt{a}}{a} \Big(P_1(z^a) + z P_2(z^a) + \cdots + z^{a-1} P_a(z^a) \Big). \tag{3.37}$$

Using (3.34) and (3.35), we can get

$$\sum_{i=1}^{r} \sum_{l=1}^{a} \sum_{j=1}^{r} \left| p_l^{ij}(u) \right|^2 < 1. \tag{3.38}$$

Then we can find r real numbers $x_1, x_2, \ldots, x_r$, with

$$\sum_{i=1}^{r} x_i = 1, \qquad \sum_{l=1}^{a} \sum_{j=1}^{r} \left| p_l^{ij}(u) \right|^2 < x_i, \quad 1 \leqslant i \leqslant r. \tag{3.39}$$

By the Riesz lemma [27, Lemma 6.13], we can find Laurent polynomials $P_{a+1}^i(z),\ i = 1, \ldots, r$ satisfying

$$\sum_{l=1}^{a} \sum_{j=1}^{r} \left| p_l^{ij}(u) \right|^2 + \left| p_{a+1}^i(u) \right|^2 = x_i, \quad 1 \leqslant i \leqslant r. \tag{3.40}$$

For every $i \in \{1, \ldots, r\}$, using the method in the reference [15, Theorem 3] on the unit vector

$$\frac{1}{\sqrt{x_i}} \left(P_1^{i1}(z) \ \cdots \ P_1^{ir}(z) \ \cdots \ P_a^{i1}(z) \ \cdots \ P_a^{ir}(z) \ \ P_{a+1}^i(z) \right), \tag{3.41}$$

we can get a matrix

$$\widetilde{R}^i(z) = \frac{1}{\sqrt{x_i}} \begin{pmatrix} P_1^{i1}(z) & \cdots & P_1^{ir}(z) & \cdots & \mathrm{P}_a^{i1}(z) & \cdots & P_a^{ir}(z) & P_{a+1}^i(z) \\ Q_{11}^{i1}(z) & \cdots & Q_{11}^{ir}(z) & \cdots & Q_{1a}^{i1}(z) & \cdots & Q_{1a}^{ir}(z) & Q_{1,a+1}^i(z) \\ \cdots & & \cdots & & \cdots & & \cdots & \\ Q_{a1}^{i1}(z) & \cdots & Q_{11}^{ar}(z) & \cdots & Q_{aa}^{i1}(z) & \cdots & Q_{aa}^{ir}(z) & Q_{a,a+1}^i(z) \end{pmatrix}, \tag{3.42}$$

which satisfies $\widetilde{R}^i(z)^* \widetilde{R}^i(z) = I_{ar+1}$.

Therefor, the block matrix

$$\widetilde{R}(z) = \begin{pmatrix} \sqrt{x_1}\widetilde{R}^1(z) \\ \sqrt{x_2}\widetilde{R}^2(z) \\ \vdots \\ \sqrt{x_a}\widetilde{R}^a(z) \end{pmatrix} \tag{3.43}$$

satisfies $\widetilde{R}(z)^*\widetilde{R}(z) = I_{ar+1}$.

We can get matrix $R(z)$ which satisfies $R(z)^*R(z) = I_{ar}$, after adjusting the rows of $\widetilde{R}(z)$ and removing the last column of it, and the r rows in the front of matrix $R(z)$ are the polynomial components of the symbol $P(z)$.

Then we complete proof of Theorem 3.5 using the formulas (3.34), (3.32), and Theorem 3.1. □

Theorem 3.5 requests the sum of l^2-norm for every row in the matrix symbol $P(z)$ associated with the vector-valued function Φ. Then we can find a minimum-energy multiwavelet frames associated with the function using the theorem. The condition in Theorem 3.5 is too stringent compared with the sufficient conditions in Theorem 3.2. We can get the following theorem by strengthening the structure of the matrix symbol $P(z)$.

Theorem 3.6. *Let $\Phi(x) = (\phi_1(x), \ldots, \phi_r(x))^T$ with $\widehat{\Phi}$ continuous at 0 and $\widehat{\Phi}(0) \neq 0$ a compactly supported multiscaling vector-valued function. If the block matrix*

$$\begin{bmatrix} P(z) & P(\omega_1 z) & \cdots & P(\omega_{a-1} z) \end{bmatrix} \tag{3.44}$$

satisfies standard orthogonal by row, then there exist a minimum-energy multiwavelet frames associated with the function Φ.

Proof. Let $P_j(z)$, $j = 1, \ldots, a$ are the polynomial components of $P(z)$, that is,

$$P(z) = \frac{\sqrt{a}}{a}\Big(P_1(z^a) + zP_2(z^a) + \cdots + z^{a-1}P_a(z^a)\Big), \tag{3.45}$$

with (3.34) and (3.35), we can know that the block matrix

$$N(u) = \begin{bmatrix} P_1(u) & P_2(u) & \cdots & P_a(u) \end{bmatrix}_{r \times ar} \tag{3.46}$$

satisfies standard orthogonal by row.

Now, we use the method in the reference [15, Theorem 3] to deal with the first unit row vector $N_1(u)$ in the matrix $N(u)$. And, we can find a paraunitary matrix $H_1(u)$ which satisfies $N_1(u)H_1(u) = e_1 = (1, 0, \ldots, 0)_{ar}$ and

$$N(u)H_1(u) = \begin{pmatrix} 1 & \\ & \widetilde{N}(u) \end{pmatrix}, \tag{3.47}$$

with $\widetilde{N}(u)$ also a matrix standard orthogonal by row.

By mathematical induction, there are r paraunitary matrices $H_1(u), \ldots, H_r(u)$ satisfying

$$N(u)H_1(u)\cdots H_a(u) = \begin{pmatrix} 1 & \cdots & 0 & 0 & \cdots & 0 \\ \vdots & \ddots & \vdots & \vdots & \ddots & \vdots \\ 0 & \cdots & 1 & 0 & \cdots & 0 \end{pmatrix}_{r\times ar}, \tag{3.48}$$

then the matrix $N(u)$ is equivalent to the front r rows in the paraunitary matrix $H_1(u)^* H_2(u)^* \cdots H_a(u)^*$.

Using the formulation (3.34), (3.35), and Theorem 3.1, we completed the proof of this theorem. □

Theorem 3.6 requests that the multiscaling vector-valued function's symbol $P(z)$ satisfies standard orthogonal by row. This means the l^2-norm of every row in $P(z)$ is 1. If the l^2-norm of every row in $P(z)$ is less than 1 strictly, and we can find a matrix $P_{a+1}(u)$ to make the block matrix

$$\left[P_1(u) \;\; P_2(u) \;\; \cdots \;\; P_a(u) \;\; P_{a+1}(u)\right] \tag{3.49}$$

satisfy standard orthogonal by row, then there exist minimum-energy multiwavelet frames associated with the function Φ.

Corollary 3.7. *Let $\Phi(x) = (\phi_1(x), \ldots, \phi_r(x))^T$ with $\widehat{\Phi}$ continuous at 0 and $\widehat{\Phi}(0) \neq 0$ a compactly supported multiscaling vector-valued function. If the l^2-norm of every row in $P(z)$ is less than 1 strictly, that is,*

$$\sum_{l=0}^{a-1}\sum_{j=1}^{r} \left|p_{ij}(\omega_l z)\right|^2 < 1, \quad \forall |z| = 1,\ 1 \leqslant i \leqslant r, \tag{3.50}$$

and there exists a matrix $P_{a+1}(u)$ to make (3.49) *satisfy standard orthogonal by row, then there exist minimum-energy multiwavelet frames associated with the function Φ.*

By Theorem 3.1, if we can find some row vectors $\alpha_1(z), \ldots, \alpha_n(z)$ with multiplicity ar and the matrix in (3.3) formed by the vectors and the symbol of Φ satisfies standard orthogonal by column, there exist a minimum-energy multiwavelet frames associated with Φ, and vice versa. However, the number of columns in the symbol of Φ is so larger, that it is not easy to find the frames using Theorem 3.1. Corollary 3.7 requests some column vectors $\beta_1(u), \ldots, \beta_m(u)$ with multiplicity r and the matrix in (3.49) formed by the vectors and the polynomial components of $P(z)$ satisfies standard orthogonal by row, then we can find a minimum-energy frames associated with Φ. Obviously, the problem is vastly simplified.

For some multiscaling vector-valued function with small multiplicity which satisfies the conditions in Theorem 3.2, the matrix $P_{a+1}(u)$ that makes the block matrix in (3.49) satisfied standard orthogonal by column can be found using the method of undetermined coefficients. We will give some examples later.

4. Decomposition and Reconstruction Formulas of Minimum-Energy Multiwavelet Frames

Suppose the multiscaling vector-valued function Φ has an associated minimum-energy multiwavelet frames $\{\Psi^1, \ldots, \Psi^N\}$. Now, we consider the projection operators $\mathbf{P}_j$ of $L^2(\mathbb{R})$ onto the nested subspace V_j defined by

$$\mathbf{P}_j f := \sum_{\tau=1}^{r} \sum_{k\in\mathbb{Z}} \langle f, \phi_{\tau,j,k}\rangle \phi_{\tau,j,k}. \tag{4.1}$$

Then the formula (2.8) can be rewritten as

$$\mathbf{P}_{j+1} f - \mathbf{P}_j f := \sum_{i=1}^{N} \sum_{\tau=1}^{r} \sum_{k\in\mathbb{Z}} \left\langle f, \psi^i_{\tau,j,k} \right\rangle \psi^i_{\tau,j,k}. \tag{4.2}$$

In other words, the error term $g_j = \mathbf{P}_{j+1} f - \mathbf{P}_j f$ between consecutive projections is given by the frame expansion:

$$g_j = \sum_{i=1}^{N} \sum_{\tau=1}^{r} \sum_{k\in\mathbb{Z}} \left\langle f, \psi^i_{\tau,j,k} \right\rangle \psi^i_{\tau,j,k}. \tag{4.3}$$

Suppose that the error term g_j has other expansion in terms of the frames $\{\Psi^1, \ldots, \Psi^N\}$, that is,

$$g_j = \sum_{i=1}^{N} \sum_{\tau=1}^{r} \sum_{k\in\mathbb{Z}} c_{\tau,j,k} \psi^i_{\tau,j,k}. \tag{4.4}$$

Then by using both (4.3) and (4.4), we have

$$\langle g_j, f\rangle = \sum_{i=1}^{N} \sum_{\tau=1}^{r} \sum_{k\in\mathbb{Z}} \left| \left\langle f, \psi^i_{\tau,j,k} \right\rangle \right|^2 = \sum_{i=1}^{N} \sum_{\tau=1}^{r} \sum_{k\in\mathbf{Z}} c_{\tau,j,k} \overline{\left\langle f, \psi^i_{\tau,j,k} \right\rangle}, \tag{4.5}$$

and this derives

$$\begin{aligned} 0 &\leqslant \sum_{i=1}^{N} \sum_{\tau=1}^{r} \sum_{k\in\mathbf{Z}} \left| c_{\tau,j,k} - \left\langle f, \psi^i_{\tau,j,k} \right\rangle \right|^2 \\ &= \sum_{i=1}^{N} \sum_{\tau=1}^{r} \sum_{k\in\mathbf{Z}} \left| c_{\tau,j,k} \right|^2 - 2 \sum_{i=1}^{N} \sum_{\tau=1}^{r} \sum_{k\in\mathbf{Z}} c_{\tau,j,k} \overline{\left\langle f, \psi^i_{\tau,j,k} \right\rangle} + \sum_{i=1}^{N} \sum_{\tau=1}^{r} \sum_{k\in\mathbb{Z}} \left| \left\langle f, \psi^i_{\tau,j,k} \right\rangle \right|^2 \\ &= \sum_{i=1}^{N} \sum_{\tau=1}^{r} \sum_{k\in\mathbf{Z}} \left| c_{\tau,j,k} \right|^2 - \sum_{i=1}^{N} \sum_{\tau=1}^{r} \sum_{k\in\mathbb{Z}} \left| \left\langle f, \psi^i_{\tau,j,k} \right\rangle \right|^2. \end{aligned} \tag{4.6}$$

This inequality means that the coefficients of the error term g_j in (4.3) have minimal l^2-norm among all sequences $\{c_{\tau,j,k}\}$ which satisfy (4.4).

We next discuss minimum-energy multiwavelet frames decomposition and reconstruction. For any $f \in L^2(\mathbb{R})$, define the vector coefficients as follows:

$$\mathbf{c}_{j,k} := \langle f, \Phi_{j,k} \rangle, \qquad \mathbf{d}_{j,k} := \left\langle f, \Psi^i_{j,k} \right\rangle \quad i = 1, \ldots, N. \tag{4.7}$$

The inner product of f with vector-valued $\Phi_{j,k}$, $\Psi^i_{j,k}$, $i = 1, \ldots, N$ is a vector, its every component is the inner product of f with the corresponding component of $\Phi_{j,k}$, $\Psi^i_{j,k}$, $i = 1, \ldots, N$.

(1) Decomposition Algorithm

suppose the vector coefficients $\{\mathbf{c}_{j+1,l} : l \in \mathbf{Z}\}$ are known. By the two-scale relations (2.2) and (3.1), we have

$$\Phi_{j,l}(x) = \frac{1}{\sqrt{a}} \sum_{k \in \mathbb{Z}} P_{k-al} \Phi_{j+1,k}(x), \qquad \Psi^i_{j,l}(x) = \frac{1}{\sqrt{a}} \sum_{k \in \mathbb{Z}} Q^i_{k-al} \Psi^i_{j+1,k}(x), \quad i = 1, \ldots, N. \tag{4.8}$$

Then, the decomposition algorithm is given as

$$\mathbf{c}_{j,l} = \frac{1}{\sqrt{a}} \sum_{k \in \mathbb{Z}} P_{k-al} \mathbf{c}_{j+1,k}, \qquad \mathbf{d}^i_{j,l} = \frac{1}{\sqrt{a}} \sum_{k \in \mathbb{Z}} Q^i_{k-al} \mathbf{d}^i_{j+1,k}, \quad i = 1, \ldots, N. \tag{4.9}$$

(2) Reconstruction Algorithm

from (3.16), it follow that

$$\Phi_{j+1,l}(x) = \frac{1}{\sqrt{a}} \sum_{k} \left\{ P^*_{l-ak} \Phi_{j,k}(x) + \sum_{i=1}^{N} Q^{i*}_{l-ak} \Psi^i_{j,k}(x) \right\}. \tag{4.10}$$

Taking the inner products on both sides of this equality, we get

$$\mathbf{c}_{j+1,l} = \frac{1}{\sqrt{a}} \sum_{k} \left\{ P^*_{l-ak} \mathbf{c}_{j,k} + \sum_{i=1}^{N} Q^{i*}_{l-ak} \mathbf{d}^i_{j,k} \right\}. \tag{4.11}$$

5. Numerical Examples

By Theorem 3.6, the orthogonal multiwavelet always have minimum-energy multiwavelet frames associated with them, for example, DGHM multiwavelet and Chui-Lian multiwavelet. These examples are trivial. In this section, we will construct some minimum-energy multiwavelet frames in general sense.

It is well known that the mth-order cardinal B-spline $N_m^a(x)$ with dilation factor a has the two-scale relation as follows:

$$\widehat{N}_m^a(\omega) = P_m^a(z)\widehat{N}_m^a\left(\frac{\omega}{a}\right), \qquad P_m^a(z) = \left(\frac{1+z+\cdots+z^{a-1}}{a}\right)^m, \quad z = e^{-i\omega/a}. \tag{5.1}$$

In addition, if a scale wavelet $\phi(x)$ satisfies the refinable function

$$\phi(x) = \sum_{k=k_0}^{k_1} p_k \phi(ax-k), \tag{5.2}$$

and let $\Phi(x) = (\phi(x), \phi(x-1), \ldots, \phi(x-r+1))^T$, then the vector-valued function Φ satisfies (2.2) with some matrixes $\{P_k\}$.

Below, upon these conclusions, using Theorem 3.5 and Corollary 3.7 in Section 3, the minimum-energy multiwavelet frames be presented with the dilation factors $a = 2$, $a = 3$, $a = 4$, respectively.

5.1. $a = 2$

Example 5.1. With $a = 2$, the symbol of the B-spline $N_2^2(x)$ is

$$P_2^2(z) = \frac{1}{4} + \frac{1}{2}z + \frac{1}{4}z^2. \tag{5.3}$$

Take $\phi(x) = N_2^2(x)$, and the support of this function is $[0,2]$. The function satisfies

$$\phi(x) = \frac{1}{4}\phi(2x) + \frac{1}{2}\phi(2x-1) + \frac{1}{4}\phi(2x-2). \tag{5.4}$$

Let $\Phi(x) = (\phi(x), \phi(x-1))^T$, and

$$\Phi(x) = \begin{pmatrix} \frac{1}{2} & \frac{1}{2} \\ 0 & 0 \end{pmatrix}\Phi(2x) + \begin{pmatrix} \frac{1}{2} & \frac{1}{2} \\ 0 & 0 \end{pmatrix}\Phi(2x-1) + \begin{pmatrix} 0 & 0 \\ \frac{1}{2} & \frac{1}{2} \end{pmatrix}\Phi(2x-2) + \begin{pmatrix} 0 & 0 \\ \frac{1}{2} & \frac{1}{2} \end{pmatrix}\Phi(2x-3). \tag{5.5}$$

The coefficient matrixes in (5.5) are not unique.

And the symbol of Φ has polyphase components as follows:

$$P_1(u) = P_2(u) = \frac{\sqrt{2}}{2}\left(\begin{pmatrix} \frac{1}{2} & \frac{1}{2} \\ 0 & 0 \end{pmatrix} + u\begin{pmatrix} 0 & 0 \\ \frac{1}{2} & \frac{1}{2} \end{pmatrix}\right). \tag{5.6}$$

Take

$$P_3(u) = \frac{\sqrt{2}}{2}\left(\begin{pmatrix} \frac{\sqrt{2}}{2} & \frac{\sqrt{2}}{2} \\ 0 & 0 \end{pmatrix} + u\begin{pmatrix} 0 & 0 \\ -\frac{\sqrt{2}}{2} & -\frac{\sqrt{2}}{2} \end{pmatrix}\right), \tag{5.7}$$

which satisfies

$$P_1(u)P_1(u)^* + P_2(u)P_2(u)^* + P_3(u)P_3(u)^* = I_2. \tag{5.8}$$

Using Theorem 3.5, we can get matrix the following:

$$C(u) = \frac{\sqrt{2}}{2}\begin{pmatrix} \frac{1}{2} & \frac{1}{2} & \frac{1}{2} & \frac{1}{2} \\ \frac{u}{2} & \frac{u}{2} & \frac{u}{2} & \frac{u}{2} \\ -1 & 0 & 1 & 0 \\ 0 & -1 & 0 & 1 \\ -\frac{1}{2} & \frac{1}{2} & -\frac{1}{2} & \frac{1}{2} \\ -\frac{u}{2} & \frac{u}{2} & -\frac{u}{2} & \frac{u}{2} \end{pmatrix}, \tag{5.9}$$

which satisfy the formula (3.35). Then we take symbols as

$$\begin{aligned} Q_1(z) &= \frac{1}{2}\left(\begin{pmatrix} -1 & 0 \\ 0 & -1 \end{pmatrix} + z\begin{pmatrix} 1 & 0 \\ 0 & 1 \end{pmatrix}\right), \\ Q_2(z) &= \frac{1}{2}\left(\begin{pmatrix} -\frac{1}{2} & \frac{1}{2} \\ 0 & 0 \end{pmatrix} + z\begin{pmatrix} -\frac{1}{2} & \frac{1}{2} \\ 0 & 0 \end{pmatrix} + z^2\begin{pmatrix} 0 & 0 \\ -\frac{1}{2} & \frac{1}{2} \end{pmatrix} + z^3\begin{pmatrix} 0 & 0 \\ -\frac{1}{2} & \frac{1}{2} \end{pmatrix}\right). \end{aligned} \tag{5.10}$$

The graphs of Φ and its minimum-energy frames are shown in Figure 1.

We may discover from Figure 1 that every component of minimum-energy frames is (anti)symmetrical.

Example 5.2. With $a = 2$, the symbol of the B-spline $N_3^2(x)$ is

$$P_3^2(z) = \frac{1}{8} + \frac{3}{8}z + \frac{3}{8}z^2 + \frac{1}{8}z^3. \tag{5.11}$$

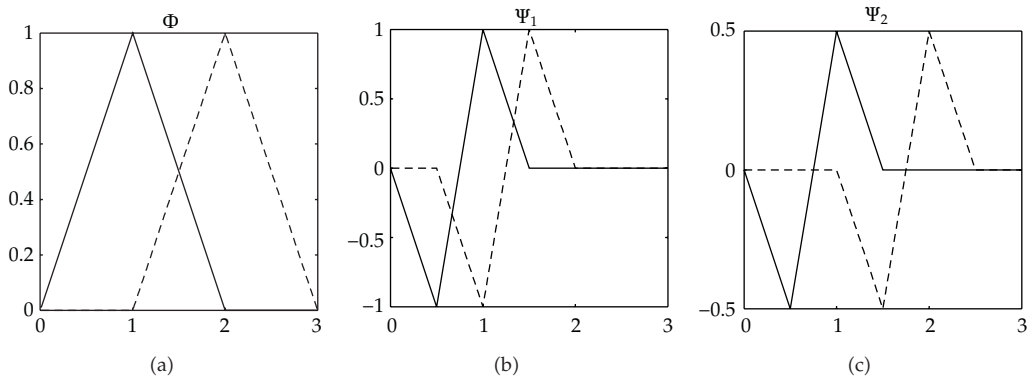

Figure 1

Take $\phi(x) = N_3^2(x)$, and the support of this function is $[0,3]$.

(1) Let $\Phi(x) = (\phi(x), \phi(x-1))^T$, and

$$\begin{aligned}\Phi(x) = {} & \begin{pmatrix} \frac{1}{4} & \frac{1}{4} \\ 0 & 0 \end{pmatrix} \Phi(2x) + \begin{pmatrix} \frac{1}{2} & \frac{1}{2} \\ 0 & 0 \end{pmatrix} \Phi(2x-1) + \begin{pmatrix} \frac{1}{4} & \frac{1}{4} \\ \frac{1}{4} & \frac{1}{4} \end{pmatrix} \Phi(2x-2) \\ & + \begin{pmatrix} 0 & 0 \\ \frac{1}{2} & \frac{1}{2} \end{pmatrix} \Phi(2x-3) + \begin{pmatrix} 0 & 0 \\ \frac{1}{4} & \frac{1}{4} \end{pmatrix} \Phi(2x-4). \end{aligned} \tag{5.12}$$

The symbol of Φ has polyphase components as follows:

$$\begin{aligned} P_1(u) &= \frac{\sqrt{2}}{2} \left(\begin{pmatrix} \frac{1}{4} & \frac{1}{4} \\ 0 & 0 \end{pmatrix} + u \begin{pmatrix} \frac{1}{4} & \frac{1}{4} \\ \frac{1}{4} & \frac{1}{4} \end{pmatrix} + u^2 \begin{pmatrix} 0 & 0 \\ \frac{1}{4} & \frac{1}{4} \end{pmatrix} \right), \\ P_2(u) &= \frac{\sqrt{2}}{2} \left(\begin{pmatrix} \frac{1}{2} & \frac{1}{2} \\ 0 & 0 \end{pmatrix} + u \begin{pmatrix} 0 & 0 \\ \frac{1}{2} & \frac{1}{2} \end{pmatrix} \right). \end{aligned} \tag{5.13}$$

Take

$$P_3(u) = \begin{pmatrix} -\frac{\sqrt{2}}{4} - \frac{\sqrt{2}}{4}u & -\frac{\sqrt{2}}{2} & -\frac{1}{2} + \frac{u}{2} & 0 \\ \frac{\sqrt{2}}{4}u + \frac{\sqrt{2}}{4}u^2 & \frac{\sqrt{2}}{2}u & 0 & -\frac{u}{2} + \frac{u^2}{2} \end{pmatrix}, \tag{5.14}$$

which satisfies $P_1(u)P_1(u)^* + P_2(u)P_2(u)^* + P_3(u)P_3(u)^* = I_2$. Using Theorem 3.5, we can get the following symbols:

$$
\begin{aligned}
Q_1(z) &= \frac{\sqrt{2}}{2}\left(\begin{pmatrix} 1 & -1 \\ 0 & 0 \end{pmatrix} + z\begin{pmatrix} 0 & 0 \\ -1 & 1 \end{pmatrix}\right),\\
Q_2(z) &= \frac{\sqrt{2}}{2}\left(\begin{pmatrix} -\frac{\sqrt{2}}{4} & -\frac{\sqrt{2}}{4} \\ 0 & 0 \end{pmatrix} + z^2\begin{pmatrix} \frac{\sqrt{2}}{4} & \frac{\sqrt{2}}{4} \\ \frac{\sqrt{2}}{4} & \frac{\sqrt{2}}{4} \end{pmatrix} + z^4\begin{pmatrix} 0 & 0 \\ -\frac{\sqrt{2}}{4} & -\frac{\sqrt{2}}{4} \end{pmatrix}\right),\\
Q_3(z) &= \frac{\sqrt{2}}{2}\left(\begin{pmatrix} -\frac{1}{4} & -\frac{1}{4} \\ 0 & 0 \end{pmatrix} + z\begin{pmatrix} \frac{1}{2} & \frac{1}{2} \\ 0 & 0 \end{pmatrix} + z^2\begin{pmatrix} -\frac{1}{4} & -\frac{1}{4} \\ \frac{1}{4} & \frac{1}{4} \end{pmatrix} + z^3\begin{pmatrix} 0 & 0 \\ -\frac{1}{2} & -\frac{1}{2} \end{pmatrix} + z^4\begin{pmatrix} 0 & 0 \\ \frac{1}{4} & \frac{1}{4} \end{pmatrix}\right).
\end{aligned}
\tag{5.15}
$$

Then, we get the minimum-wavelet frames associated with Φ. The graphs of them are shown in Figure 2.

We can discover from Figure 2 that every component of the minimum-energy frames is (anti)symmetrical and smooth.

(2) Take $\Phi(x) = (\phi(x), \phi(x-1), \phi(x-2))^T$, which satisfies

$$
\begin{aligned}
\Phi(x) = \frac{1}{4}\Bigg(&\begin{pmatrix} 0 & 0 & \frac{1}{3} \\ 0 & 0 & 0 \\ 0 & 0 & 0 \end{pmatrix}\Phi(2x+2) + \begin{pmatrix} 0 & \frac{1}{3} & 1 \\ 0 & 0 & 0 \\ 0 & 0 & 0 \end{pmatrix}\Phi(2x+1) + \begin{pmatrix} \frac{1}{3} & 1 & 1 \\ 0 & 0 & \frac{1}{3} \\ 0 & 0 & 0 \end{pmatrix}\Phi(2x)\\
&+ \begin{pmatrix} 1 & 1 & \frac{1}{3} \\ 0 & \frac{1}{3} & 1 \\ 0 & 0 & 0 \end{pmatrix}\Phi(2x-1) + \begin{pmatrix} 1 & \frac{1}{3} & 0 \\ \frac{1}{3} & 1 & 1 \\ 0 & 0 & \frac{1}{3} \end{pmatrix}\Phi(2x-2)\\
&+ \begin{pmatrix} \frac{1}{3} & 0 & 0 \\ 1 & 1 & \frac{1}{3} \\ 0 & \frac{1}{3} & 1 \end{pmatrix}\Phi(2x-3) + \begin{pmatrix} 0 & 0 & 0 \\ 1 & \frac{1}{3} & 0 \\ \frac{1}{3} & 1 & 1 \end{pmatrix}\Phi(2x-4)\\
&+ \begin{pmatrix} 0 & 0 & 0 \\ \frac{1}{3} & 0 & 0 \\ 1 & 1 & \frac{1}{3} \end{pmatrix}\Phi(2x-5) + \begin{pmatrix} 0 & 0 & 0 \\ 0 & 0 & 0 \\ 1 & \frac{1}{3} & 0 \end{pmatrix}\Phi(2x-6) + \begin{pmatrix} 0 & 0 & 0 \\ 0 & 0 & 0 \\ \frac{1}{3} & 0 & 0 \end{pmatrix}\Phi(2x-7)\Bigg)
\end{aligned}
\tag{5.16}
$$

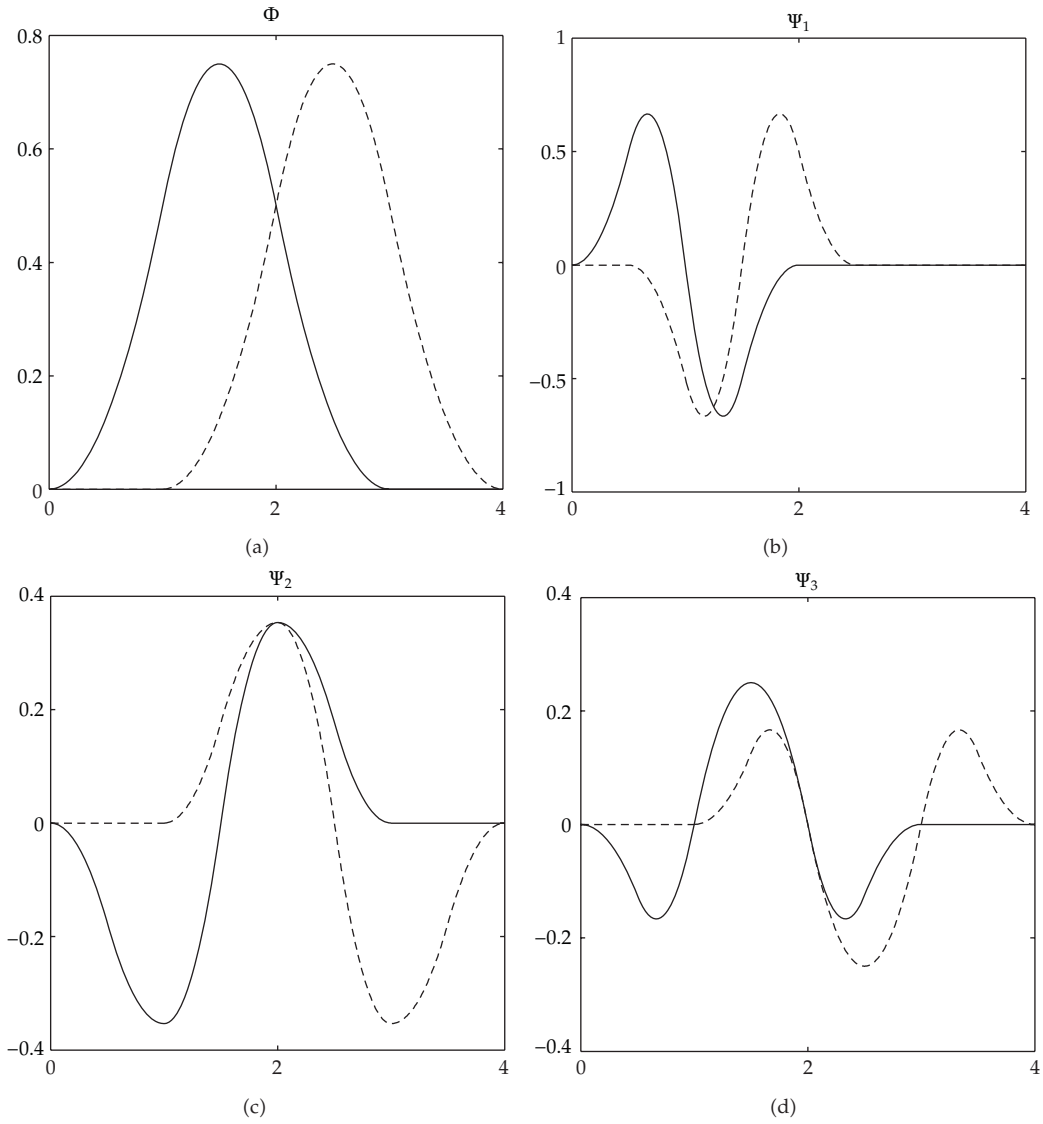

Figure 2

and the symbol of this multiscaling vector-valued function has the following polyphase components:

$$P_1(u) = \frac{\sqrt{2}}{8}\left(\begin{pmatrix} 0 & 0 & \frac{1}{3} \\ 0 & 0 & 0 \\ 0 & 0 & 0 \end{pmatrix} + \begin{pmatrix} \frac{1}{3} & 1 & 1 \\ 0 & 0 & \frac{1}{3} \\ 0 & 0 & 0 \end{pmatrix} u + \begin{pmatrix} 1 & \frac{1}{3} & 0 \\ \frac{1}{3} & 1 & 1 \\ 0 & 0 & \frac{1}{3} \end{pmatrix} u^2 + \begin{pmatrix} 0 & 0 & 0 \\ 1 & \frac{1}{3} & 0 \\ \frac{1}{3} & 1 & 1 \end{pmatrix} u^3 + \begin{pmatrix} 0 & 0 & 0 \\ 0 & 0 & 0 \\ 1 & \frac{1}{3} & 0 \end{pmatrix} u^4 \right),$$

$$P_2(u) = \frac{\sqrt{2}}{8}\left(\begin{pmatrix} 0 & \frac{1}{3} & 1 \\ 0 & 0 & 0 \\ 0 & 0 & 0 \end{pmatrix} + \begin{pmatrix} 1 & 1 & \frac{1}{3} \\ 0 & \frac{1}{3} & 1 \\ 0 & 0 & 0 \end{pmatrix} u + \begin{pmatrix} \frac{1}{3} & 0 & 0 \\ 1 & 1 & \frac{1}{3} \\ 0 & \frac{1}{3} & 1 \end{pmatrix} u^2 + \begin{pmatrix} 0 & 0 & 0 \\ \frac{1}{3} & 0 & 0 \\ 1 & 1 & \frac{1}{3} \end{pmatrix} u^3 + \begin{pmatrix} 0 & 0 & 0 \\ 0 & 0 & 0 \\ \frac{1}{3} & 0 & 0 \end{pmatrix} u^4 \right). \tag{5.17}$$

Let

$$P_3(u) = \frac{\sqrt{2}}{8} \times \begin{pmatrix} \sqrt{6} + \frac{\sqrt{6}}{3}u & 0 & -\left(\sqrt{6} + \frac{\sqrt{6}}{3}u\right) & \sqrt{6}u - \sqrt{6} & 0 & 0 \\ -(\mathcal{A}) & \mathcal{A} & 0 & 0 & \sqrt{6}u^2 - \sqrt{6}u & 0 \\ 0 & -(\mathcal{B}) & \mathcal{B} & 0 & 0 & \sqrt{6}u^3 - \sqrt{6}u^2 \end{pmatrix}, \tag{5.18}$$

where $\mathcal{A}$ denotes $\sqrt{6}u + (\sqrt{6}/3)u^2$, and $\mathcal{B}$ denotes $\sqrt{6}u^2 + (\sqrt{6}/3)u^3$, which satisfies $P_1(u)P_1(u)^* + P_2(u)P_2(u)^* + P_3(u)P_3(u)^* = I_3$. Using Theorem 3.5, we can get

$$\begin{aligned} Q_1(z) = {} & \frac{\sqrt{2}}{2}\left(\begin{pmatrix} -0.23547806816473105 & -0.1969247665800399 & -0.14891401559609693 \\ 0.08212785057744523 & -0.18555493781122898 & -0.19106026688126101 \\ 0.027375950192481735 & -0.061851645937076295 & -0.07928888488639749 \end{pmatrix}\right. \\ & + z\begin{pmatrix} 0.9033589710742332 & -0.07112938093948917 & -0.016506887733618497 \\ -0.0608286139211068 & 0.905683150972805 & -0.03808257781757404 \\ -0.020276204640368934 & -0.04704107893504214 & 0.9404994196162103 \end{pmatrix} \\ & + z^2\begin{pmatrix} -0.20402395049705468 & -0.05175658881673616 & 0.01828281901756732 \\ -0.2489115696557434 & -0.0979600599918386 & -0.016863228869914655 \\ -0.0700638169224561 & -0.12222299444169772 & -0.11122693740098887 \end{pmatrix} \\ & + z^3\begin{pmatrix} -0.05175658881673616 & 0.01828281901756732 & 0.006094273005855774 \\ -0.0979600599918386 & -0.016863228869914655 & -0.005621076289971551 \\ -0.12222299444169776 & -0.11122693740098887 & -0.03707564580032962 \end{pmatrix} \\ & + z^4\begin{pmatrix} 0.018282819017567314 & 0.0060942730058557715 & 0 \\ -0.016863228869914648 & -0.005621076289971549 & 0 \\ -0.11122693740098877 & -0.03707564580032959 & 0 \end{pmatrix} \\ & \left. + z^5\begin{pmatrix} 0.0060942730058557715 & 0 & 0 \\ -0.005621076289971549 & 0 & 0 \\ -0.03707564580032959 & 0 & 0 \end{pmatrix}\right), \end{aligned}$$

$$
\begin{aligned}
&Q_2(z)\\
&=\frac{\sqrt{2}}{2}\left(\begin{pmatrix}-0.09986325103103813 & 0.31589881995517033 & 0.0052538925646165024\\ 0.0854124922234307 & -0.26079578287935323 & 0.2998893006031239\\ 0.014450758807607454 & -0.05510303707581709 & -0.30514319316774036\end{pmatrix}\right.\\
&\quad+z\begin{pmatrix}-0.016309066862055847 & 0.005908379170891813 & 0.019381713326762175\\ 0.0045583062090611155 & -0.010950091637853966 & -0.0031215427310982043\\ 0.011750760652994713 & 0.005041712466962157 & -0.016260170595664\end{pmatrix}\\
&\quad+z^2\begin{pmatrix}-0.20916114471771918 & -0.051515547612800944 & 0.02048043820474356\\ -0.023639974479628924 & -0.01950964138878848 & -0.013083356132526147\\ 0.23280111919734814 & 0.07102518900158937 & -0.007397082072217509\end{pmatrix}\\
&\quad+z^3\begin{pmatrix}-0.051515547612800944 & 0.02048043820474356 & 0.006826812734914536\\ -0.019509641388788437 & -0.013083356132526147 & -0.00436111871084204\\ 0.07102518900158936 & -0.007397082072217509 & -0.0024656940240724914\end{pmatrix}\\
&\quad+z^4\begin{pmatrix}0.020480438204743462 & 0.006826812734914494 & 0\\ -0.013083356132526154 & -0.004361118710842047 & 0\\ -0.0073970820722173754 & -0.002465694024072461 & 0\end{pmatrix}\\
&\quad\left.+z^5\begin{pmatrix}0.006826812734914494 & 0 & 0\\ -0.004361118710842047 & 0 & 0\\ -0.002465694024072461 & 0 & 0\end{pmatrix}\right),\\
&Q_3(z)\\
&=\frac{\sqrt{2}}{2}\left(\begin{pmatrix}-0.04725690064321836 & 0.21949688473386203 & 0.1639130739275549\\ 0.2523328524498961 & -0.7281995751316489 & 0.15918487102463674\\ -0.003904624220396051 & 0.054187773506410915 & -0.7337722255518694\end{pmatrix}\right.\\
&\quad+z\begin{pmatrix}-0.07772611828042069 & -0.06662667519576504 & 0.0330957179061223\\ -0.02879898221803944 & -0.07331833791750912 & 0.008051002298630018\\ -0.042473900845222755 & -0.03375725777108183 & 0.037548046190520684\end{pmatrix}\\
&\quad+z^2\begin{pmatrix}-0.6930584034579804 & -0.08791155686974436 & 0.16099639981828018\\ -0.0287070169546376 & 0.06098379400257172 & 0.07937189961088224\\ 0.06463681665260418 & 0.11607547646429853 & 0.10634610477760928\end{pmatrix}\\
&\quad+z^3\begin{pmatrix}-0.08791155686974436 & 0.16099639981828018 & 0.053665466606093386\\ 0.06098379400257172 & 0.07937189961088224 & 0.026457299870294076\\ 0.11607547646429858 & 0.10634610477760928 & 0.03544870159253642\end{pmatrix}\\
&\quad+z^4\begin{pmatrix}0.16099639981828012 & 0.05366546660609337 & 0\\ 0.07937189961088217 & 0.026457299870294056 & 0\\ 0.10634610477760917 & 0.035448701592536394 & 0\end{pmatrix}\\
&\quad\left.+z^5\begin{pmatrix}0.05366546660609337 & 0 & 0\\ 0.026457299870294056 & 0 & 0\\ 0.035448701592536394 & 0 & 0\end{pmatrix}\right).
\end{aligned}
\tag{5.19}
$$

They are the symbols of the minimum-energy multiwavelet frames associated with Φ. The graphs of them are shown in Figure 3.

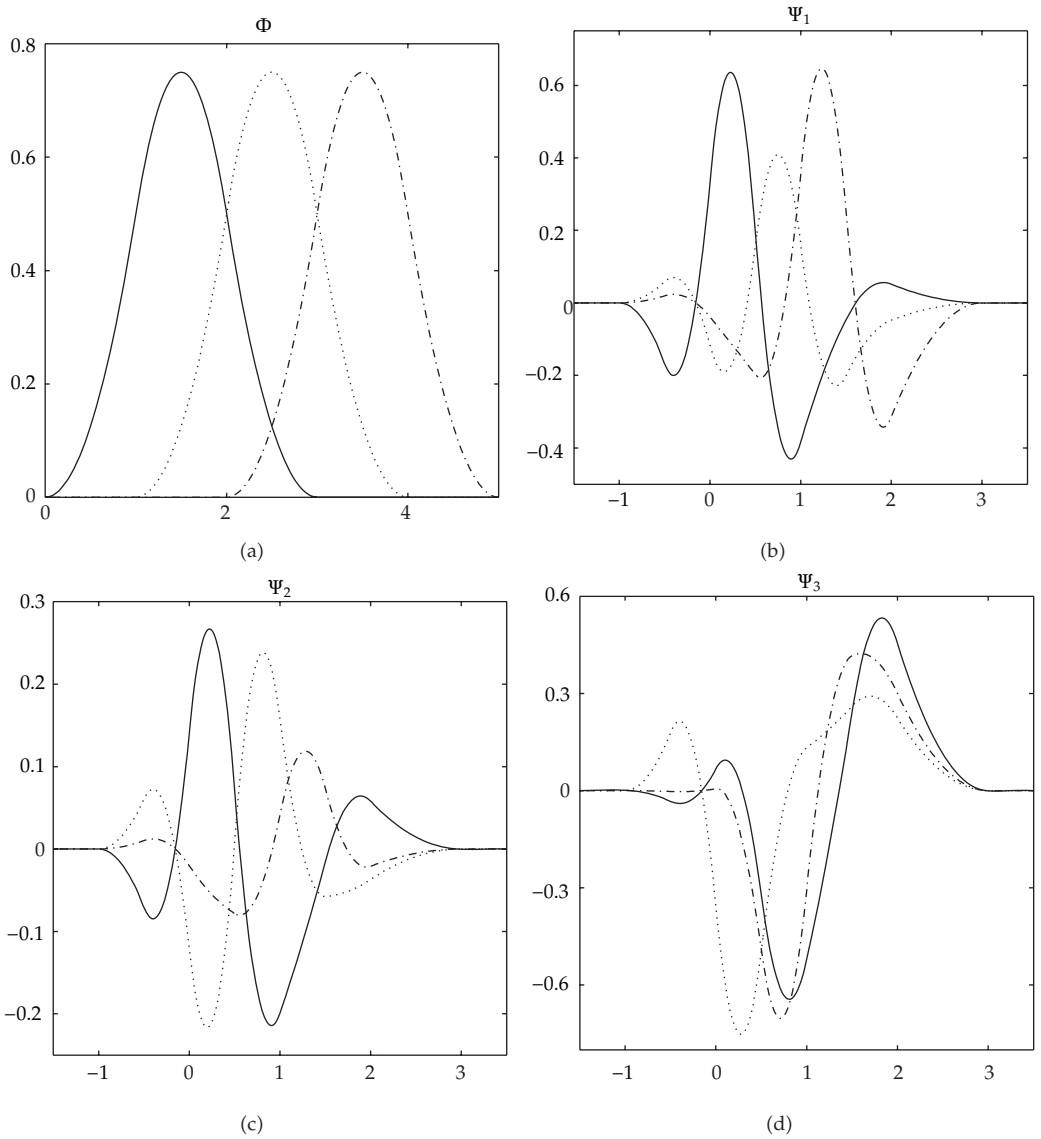

Figure 3

We can discover from Figure 3 that every component of the minimum-energy frames is smooth. When $r = 3$, it is very difficult to construct the minimum-energy multiwavelet frames with symmetry.

5.2. $a = 3$

Example 5.3. With $a = 3$, the symbol of the B-spline $\phi(x) = N_3^3(x)$ is

$$P_3^3(z) = \frac{1 + 3z + 6z^2 + 7z^3 + 6z^4 + 3z^5 + z^6}{27}. \tag{5.20}$$

Take $\phi(x) = N_3^3(x)$, and the support of this function is $[0, 4]$.

(1) Let $\Phi(x) = (\phi(x), \phi(x-1))^T$, and this vector-valued function satisfies

$$\begin{aligned}\Phi(x) = \frac{1}{9}\Bigg(&\begin{pmatrix}1 & \frac{3}{2}\\ 0 & 0\end{pmatrix}\Phi(3x) + \begin{pmatrix}\frac{3}{2} & 3\\ 0 & 0\end{pmatrix}\Phi(3x-1) + \begin{pmatrix}3 & \frac{7}{2}\\ 0 & 0\end{pmatrix}\Phi(3x-2)\\ &+\begin{pmatrix}\frac{7}{2} & 3\\ 1 & \frac{3}{2}\end{pmatrix}\Phi(3x-3) + \begin{pmatrix}3 & \frac{3}{2}\\ \frac{3}{2} & 3\end{pmatrix}\Phi(3x-4) + \begin{pmatrix}\frac{3}{2} & 1\\ 3 & \frac{7}{2}\end{pmatrix}\Phi(3x-5)\\ &+\begin{pmatrix}0 & 0\\ \frac{7}{2} & 3\end{pmatrix}\Phi(3x-6) + \begin{pmatrix}0 & 0\\ 3 & \frac{3}{2}\end{pmatrix}\Phi(3x-7) + \begin{pmatrix}0 & 0\\ \frac{3}{2} & 1\end{pmatrix}\Phi(3x-8)\Bigg).\end{aligned} \tag{5.21}$$

The symbol of $\Phi(x)$ is

$$\begin{aligned}P(z) = \frac{1}{27}\Bigg(&\begin{pmatrix}1 & \frac{3}{2}\\ 0 & 0\end{pmatrix} + z\begin{pmatrix}\frac{3}{2} & 3\\ 0 & 0\end{pmatrix} + z^2\begin{pmatrix}3 & \frac{7}{2}\\ 0 & 0\end{pmatrix} + z^3\begin{pmatrix}\frac{7}{2} & 3\\ 1 & \frac{3}{2}\end{pmatrix} + z^4\begin{pmatrix}3 & \frac{3}{2}\\ \frac{3}{2} & 3\end{pmatrix}\\ &+z^5\begin{pmatrix}\frac{3}{2} & 1\\ 3 & \frac{7}{2}\end{pmatrix} + z^6\begin{pmatrix}0 & 0\\ \frac{7}{2} & 3\end{pmatrix} + z^7\begin{pmatrix}0 & 0\\ 3 & \frac{3}{2}\end{pmatrix} + z^8\begin{pmatrix}0 & 0\\ \frac{3}{2} & 1\end{pmatrix}\Bigg),\end{aligned} \tag{5.22}$$

and its polynomial components are

$$\begin{aligned}P_1(u) &= \frac{\sqrt{3}}{27}\left(\begin{pmatrix}1 & \frac{3}{2}\\ 0 & 0\end{pmatrix} + \begin{pmatrix}\frac{7}{2} & 3\\ 1 & \frac{3}{2}\end{pmatrix}u + \begin{pmatrix}0 & 0\\ \frac{7}{2} & 3\end{pmatrix}u^2\right),\\ P_2(u) &= \frac{\sqrt{3}}{27}\left(\begin{pmatrix}\frac{3}{2} & 3\\ 0 & 0\end{pmatrix} + \begin{pmatrix}3 & \frac{3}{2}\\ \frac{3}{2} & 3\end{pmatrix}u + \begin{pmatrix}0 & 0\\ 3 & \frac{3}{2}\end{pmatrix}u^2\right),\\ P_3(u) &= \frac{\sqrt{3}}{27}\left(\begin{pmatrix}3 & \frac{7}{2}\\ 0 & 0\end{pmatrix} + \begin{pmatrix}\frac{3}{2} & 1\\ 3 & \frac{7}{2}\end{pmatrix}u + \begin{pmatrix}0 & 0\\ \frac{3}{2} & 1\end{pmatrix}u^2\right),\end{aligned} \tag{5.23}$$

then

$$P_1(u)P_1(u)^* + P_2(u)P_2(u)^* + P_3(u)P_3(u)^* = \frac{1}{486}\begin{pmatrix}\frac{50}{u} + 143 + 50u & \frac{50}{u^2} + \frac{143}{u} + 50\\ 50 + 143u + 50u^2 & \frac{50}{u} + 143 + 50u\end{pmatrix}. \tag{5.24}$$

(i) This example satisfies the conditions in Theorem 3.5. Let

$$P_4(u) = \frac{\sqrt{3}}{27}\begin{pmatrix}5 - 5u\\ 5u - 5u^2\end{pmatrix}. \tag{5.25}$$

The sum of l^2-norm for every row in the matrix in (3.34) formed by $P_1(u)$, $P_2(u)$, $P_3(u)$, and $P_4(u)$ is equivalent to 1. Using Theorem 3.5, we can get the symbols of the minimum-energy frames associated with Φ the following:

$$Q_1(z) = \frac{1}{27}\left(\begin{pmatrix} -1 & -\frac{3}{2} \\ 0 & 0 \end{pmatrix} + z\begin{pmatrix} -\frac{3}{2} & -3 \\ 0 & 0 \end{pmatrix} + z^2\begin{pmatrix} -3 & -\frac{7}{2} \\ 0 & 0 \end{pmatrix} + z^3\begin{pmatrix} \frac{7}{2} & 3 \\ -1 & -\frac{3}{2} \end{pmatrix} + z^4\begin{pmatrix} 3 & \frac{3}{2} \\ -\frac{3}{2} & -3 \end{pmatrix} + z^5\begin{pmatrix} \frac{3}{2} & 1 \\ -3 & -\frac{7}{2} \end{pmatrix} + z^6\begin{pmatrix} 0 & 0 \\ \frac{7}{2} & 3 \end{pmatrix} + z^7\begin{pmatrix} 0 & 0 \\ 3 & \frac{3}{2} \end{pmatrix} + z^8\begin{pmatrix} 0 & 0 \\ \frac{3}{2} & 1 \end{pmatrix}\right),$$

$$Q_2(z) = \frac{1}{27}\left(\begin{pmatrix} 0 & -\frac{9\sqrt{3}}{2} \\ 0 & 0 \end{pmatrix} + z\begin{pmatrix} \frac{9\sqrt{3}}{2} & 0 \\ 0 & 0 \end{pmatrix} + z^3\begin{pmatrix} 0 & 0 \\ 0 & -\frac{9\sqrt{3}}{2} \end{pmatrix} + z^4\begin{pmatrix} 0 & 0 \\ \frac{9\sqrt{3}}{2} & 0 \end{pmatrix}\right),$$

$$Q_3(z) = \frac{1}{27}\left(\begin{pmatrix} \frac{9\sqrt{3}}{2} & -3\sqrt{3} \\ 0 & 0 \end{pmatrix} + z\begin{pmatrix} -3\sqrt{3} & \frac{3\sqrt{3}}{2} \\ 0 & 0 \end{pmatrix} + z^3\begin{pmatrix} 0 & 0 \\ \frac{9\sqrt{3}}{2} & -3\sqrt{3} \end{pmatrix} + z^4\begin{pmatrix} 0 & 0 \\ -3\sqrt{3} & \frac{3\sqrt{3}}{2} \end{pmatrix}\right),$$

$$Q_4(z) = \frac{1}{27}\left(\begin{pmatrix} \frac{9}{2}\sqrt{\frac{3}{35}} & -3\sqrt{\frac{3}{35}} \\ 0 & 0 \end{pmatrix} + z\begin{pmatrix} -3\sqrt{\frac{3}{35}} & -\frac{51}{2}\sqrt{\frac{3}{35}} \\ 0 & 0 \end{pmatrix} + z^2\begin{pmatrix} 27\sqrt{\frac{3}{35}} & 0 \\ 0 & 0 \end{pmatrix} + z^3\begin{pmatrix} 0 & 0 \\ \frac{9}{2}\sqrt{\frac{3}{35}} & -3\sqrt{\frac{3}{35}} \end{pmatrix} + z^4\begin{pmatrix} 0 & 0 \\ -3\sqrt{\frac{3}{35}} & -\frac{51}{2}\sqrt{\frac{3}{35}} \end{pmatrix} + z^5\begin{pmatrix} 0 & 0 \\ 27\sqrt{\frac{3}{35}} & 0 \end{pmatrix}\right),$$

$$Q_5(z) = \frac{1}{27}\left(\begin{pmatrix} 45\sqrt{\frac{2}{133}} & \frac{45}{\sqrt{266}} \\ 0 & 0 \end{pmatrix} + z\begin{pmatrix} \frac{45}{\sqrt{266}} & -45\sqrt{\frac{2}{133}} \\ 0 & 0 \end{pmatrix} + z^2\begin{pmatrix} -45\sqrt{\frac{2}{133}} & 0 \\ 0 & 0 \end{pmatrix} + z^3\begin{pmatrix} 0 & 0 \\ 45\sqrt{\frac{2}{133}} & \frac{45}{\sqrt{266}} \end{pmatrix} + z^4\begin{pmatrix} 0 & 0 \\ \frac{45}{\sqrt{266}} & -45\sqrt{\frac{2}{133}} \end{pmatrix} + z^5\begin{pmatrix} 0 & 0 \\ -45\sqrt{\frac{2}{133}} & 0 \end{pmatrix}\right),$$

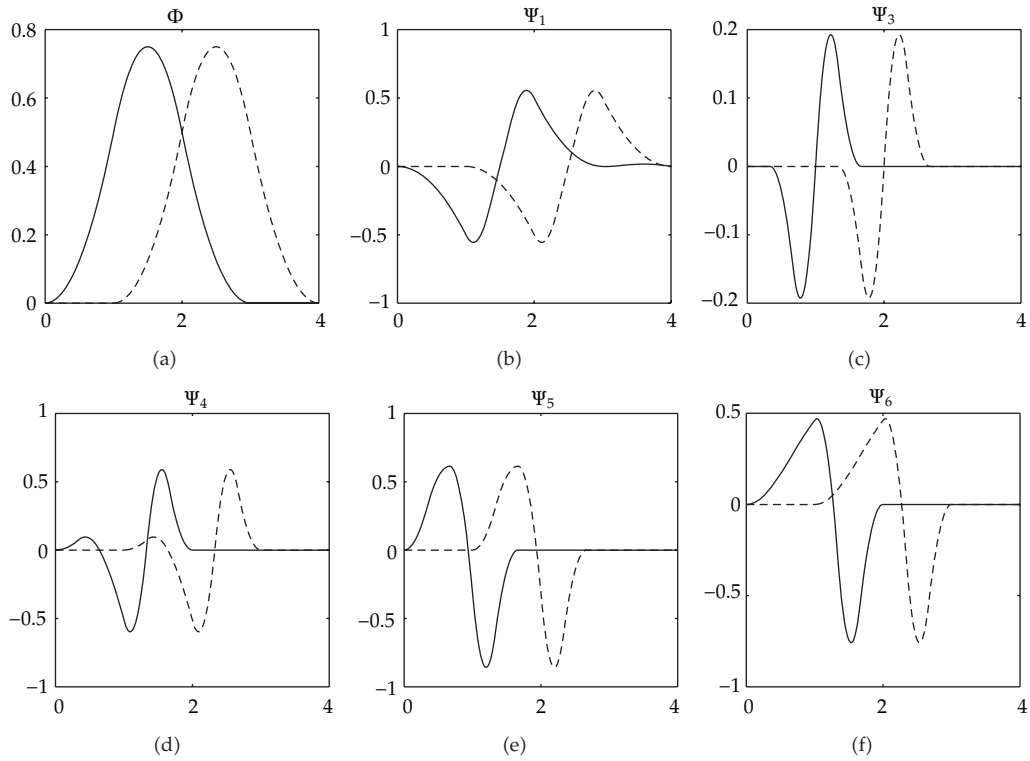

Figure 4

$$Q_6(z) = \frac{1}{27}\left(\begin{pmatrix} \frac{14}{\sqrt{95}} & \frac{33}{2\sqrt{95}} \\ 0 & 0 \end{pmatrix} + z\begin{pmatrix} \frac{33}{2\sqrt{95}} & \frac{24}{\sqrt{95}} \\ 0 & 0 \end{pmatrix} + z^2\begin{pmatrix} \frac{24}{\sqrt{95}} & -\sqrt{95} \\ 0 & 0 \end{pmatrix} + z^3\begin{pmatrix} 0 & 0 \\ \frac{14}{\sqrt{95}} & \frac{33}{2\sqrt{95}} \end{pmatrix} + z^4\begin{pmatrix} 0 & 0 \\ \frac{33}{2\sqrt{95}} & \frac{24}{\sqrt{95}} \end{pmatrix} + z^5\begin{pmatrix} 0 & 0 \\ \frac{24}{\sqrt{95}} & -\sqrt{95} \end{pmatrix}\right). \tag{5.26}$$

The graphs of Φ and the minimum-energy frames associated with it are shown in Figure 4.

From this figure, we can discover that every component of the minimum-energy frames is smooth. The first vector-valued function of frames is antisymmetry and the second function vanishes.

(ii) In fact, this example also satisfies the conditions of Corollary 3.7. Take

$$P_4(u) = \frac{\sqrt{3}}{27}\begin{pmatrix} 5+5u & \sqrt{\frac{43}{2}} & 5\sqrt{2}-5\sqrt{2}u & 0 \\ -5u-5u^2 & -\sqrt{\frac{43}{2}}u & 0 & 5\sqrt{2}u-5\sqrt{2}u^2 \end{pmatrix} \tag{5.27}$$

and with $P_1(u)$, $P_2(u)$, and $P_3(u)$ to form matrix (3.49), which satisfies standard orthogonal by row. By Theorem 3.6, we can get minimum-energy multiwavelet frames associated with Φ.

(2) Let $\Phi(x) = (\phi(x), \phi(x-1), \phi(x-2))^T$. This vector-valued function satisfies

$$\begin{aligned}
\Phi(x) = \frac{1}{9}\Bigg(& \begin{pmatrix} 0 & 0 & \frac{1}{3} \\ 0 & 0 & 0 \\ 0 & 0 & 0 \end{pmatrix}\Phi(3x+2) + \begin{pmatrix} 0 & \frac{1}{3} & 1 \\ 0 & 0 & 0 \\ 0 & 0 & 0 \end{pmatrix}\Phi(3x+1) + \begin{pmatrix} \frac{1}{3} & 1 & 2 \\ 0 & 0 & 0 \\ 0 & 0 & 0 \end{pmatrix}\Phi(3x) \\
& + \begin{pmatrix} 1 & 2 & \frac{7}{3} \\ 0 & 0 & \frac{1}{3} \\ 0 & 0 & 0 \end{pmatrix}\Phi(3x-1) + \begin{pmatrix} 2 & \frac{7}{3} & 2 \\ 0 & \frac{1}{3} & 1 \\ 0 & 0 & 0 \end{pmatrix}\Phi(3x-2) + \begin{pmatrix} \frac{7}{3} & 2 & 1 \\ \frac{1}{3} & 1 & 2 \\ 0 & 0 & 0 \end{pmatrix}\Phi(3x-3) \\
& + \begin{pmatrix} 2 & 1 & \frac{1}{3} \\ 1 & 2 & \frac{7}{3} \\ 0 & 0 & \frac{1}{3} \end{pmatrix}\Phi(3x-4) + \begin{pmatrix} 1 & \frac{1}{3} & 0 \\ 2 & \frac{7}{3} & 2 \\ 0 & \frac{1}{3} & 1 \end{pmatrix}\Phi(3x-5) + \begin{pmatrix} \frac{1}{3} & 0 & 0 \\ \frac{1}{3} & 2 & 1 \\ \frac{1}{3} & 1 & 2 \end{pmatrix}\Phi(3x-6) \\
& + \begin{pmatrix} 0 & 0 & 0 \\ 2 & 1 & \frac{1}{3} \\ 1 & 2 & \frac{7}{3} \end{pmatrix}\Phi(3x-7) + \begin{pmatrix} 0 & 0 & 0 \\ 1 & \frac{1}{3} & 0 \\ 2 & \frac{7}{3} & 2 \end{pmatrix}\Phi(3x-8) + \begin{pmatrix} 0 & 0 & 0 \\ \frac{1}{3} & 0 & 0 \\ \frac{7}{3} & 2 & 1 \end{pmatrix}\Phi(3x-9) \\
& + \begin{pmatrix} 0 & 0 & 0 \\ 0 & 0 & 0 \\ 2 & 1 & \frac{1}{3} \end{pmatrix}\Phi(3x-10) + \begin{pmatrix} 0 & 0 & 0 \\ 0 & 0 & 0 \\ 1 & \frac{1}{3} & 0 \end{pmatrix}\Phi(3x-11) + \begin{pmatrix} 0 & 0 & 0 \\ 0 & 0 & 0 \\ \frac{1}{3} & 0 & 0 \end{pmatrix}\Phi(3x-12)\Bigg),
\end{aligned}$$

$$\begin{aligned}
P_1(u)P_1(u)^* + P_2(u)P_2(u)^* + P_3(u)P_3(u)^* = {} & \frac{1}{729} \\
\times & \begin{pmatrix} \frac{1}{u^2}+\frac{50}{u}+141+50u+u^2 & \frac{1}{u^3}+\frac{50}{u^2}+\frac{141}{u}+50+u & \frac{1}{u^4}+\frac{50}{u^3}+\frac{141}{u^2}+\frac{50}{u}+1 \\ \frac{1}{u}+50+141u+50u^2+u^3 & \frac{1}{u^2}+\frac{50}{u}+141+50u+u^2 & \frac{1}{u^3}+\frac{50}{u^2}+\frac{141}{u}+50+u \\ 1+50u+141u^2+50u^3+u^4 & \frac{1}{u}+50+141u+50u^2+u^3 & \frac{1}{u^2}+\frac{50}{u}+141+50u+u^2 \end{pmatrix}.
\end{aligned} \tag{5.28}$$

Let

$$P_4(u) = \begin{pmatrix} x(u) & 0 & -x(u) & y(u) & 0 & 0 \\ -x(u)u & x(u) & 0 & 0 & y(u)u & 0 \\ 0 & -x(u)u & x(u)u^2 & 0 & 0 & y(u)u^2 \end{pmatrix}, \tag{5.29}$$

where

$$\begin{aligned} x(u) &= 0.4067366251768559 + 0.16724108784847952u + 0.003372556164290336u^2, \\ y(u) &= 0.46250686620877374 - 0.45360921162651374u - 0.008897654582258595u^2, \end{aligned} \tag{5.30}$$

then

$$P_1(u)P_1(u)^* + P_2(u)P_2(u)^* + P_3(u)P_3(u)^* + P_4(u)P_4(u)^* = I_3. \tag{5.31}$$

By Corollary 3.7 and Theorem 3.6, we know that the existence of the minimum-energy multiwavelet frames is associated with Φ.

5.3. $a = 4$

With $a = 4$, the symbol of the B-spline $\phi(x) = N_4^4(x)$ is

$$P_4^4(z) = \frac{1 + 4z + 10z^2 + 20z^3 + 31z^4 + 40z^5 + 44z^6 + 40z^7 + 31z^8 + 20z^9 + 10z^{10} + 4z^{11} + z^{12}}{256}. \tag{5.32}$$

Take $\phi(x) = N_4^4(x)$, and the support of this function is $[0, 5]$, the symbol is

$$\begin{aligned} P(z) = \frac{1}{256}\Bigg(& \begin{pmatrix} 1 & 2 \\ 0 & 0 \end{pmatrix} + z\begin{pmatrix} 2 & 5 \\ 0 & 0 \end{pmatrix} + z^2\begin{pmatrix} 5 & 10 \\ 0 & 0 \end{pmatrix} + z^3\begin{pmatrix} 10 & \frac{31}{2} \\ 0 & 0 \end{pmatrix} \\ & + z^4\begin{pmatrix} \frac{31}{2} & 20 \\ 1 & 2 \end{pmatrix} + z^5\begin{pmatrix} 20 & 22 \\ 2 & 5 \end{pmatrix} + z^6\begin{pmatrix} 22 & 20 \\ 5 & 10 \end{pmatrix} + z^7\begin{pmatrix} 20 & \frac{31}{2} \\ 10 & \frac{31}{2} \end{pmatrix} \\ & + z^8\begin{pmatrix} \frac{31}{2} & 10 \\ \frac{31}{2} & 20 \end{pmatrix} z^9\begin{pmatrix} 10 & 5 \\ 20 & 22 \end{pmatrix} + z^{10}\begin{pmatrix} 5 & 2 \\ 22 & 20 \end{pmatrix} + z^{11}\begin{pmatrix} 2 & 1 \\ 20 & \frac{31}{2} \end{pmatrix} \\ & + z^{12}\begin{pmatrix} 0 & 0 \\ \frac{31}{2} & 10 \end{pmatrix} + z^{13}\begin{pmatrix} 0 & 0 \\ 10 & 5 \end{pmatrix} + z^{14}\begin{pmatrix} 0 & 0 \\ 5 & 2 \end{pmatrix} + z^{15}\begin{pmatrix} 0 & 0 \\ 2 & 1 \end{pmatrix}\Bigg). \end{aligned} \tag{5.33}$$

The polynomial components of $P(z)A = \pi r^2$

$$
\begin{aligned}
P_1(u) &= \frac{1}{128}\left(\begin{pmatrix}1 & 2\\ 0 & 0\end{pmatrix} + u\begin{pmatrix}\frac{31}{2} & 20\\ 1 & 2\end{pmatrix} + u^2\begin{pmatrix}\frac{31}{2} & 10\\ \frac{31}{2} & 20\end{pmatrix} + u^3\begin{pmatrix}0 & 0\\ \frac{31}{2} & 10\end{pmatrix}\right),\\
P_2(u) &= \frac{1}{128}\left(\begin{pmatrix}2 & 5\\ 0 & 0\end{pmatrix} + u\begin{pmatrix}20 & 22\\ 2 & 5\end{pmatrix} + u^2\begin{pmatrix}10 & 5\\ 20 & 22\end{pmatrix} + u^3\begin{pmatrix}0 & 0\\ 10 & 5\end{pmatrix}\right),\\
P_3(u) &= \frac{1}{128}\left(\begin{pmatrix}5 & 10\\ 0 & 0\end{pmatrix} + u\begin{pmatrix}22 & 20\\ 5 & 10\end{pmatrix} + u^2\begin{pmatrix}5 & 2\\ 22 & 20\end{pmatrix} + u^3\begin{pmatrix}0 & 0\\ 5 & 2\end{pmatrix}\right),\\
P_4(u) &= \frac{1}{128}\left(\begin{pmatrix}10 & \frac{31}{2}\\ 0 & 0\end{pmatrix} + u\begin{pmatrix}20 & \frac{31}{2}\\ 10 & \frac{31}{2}\end{pmatrix} + u^2\begin{pmatrix}2 & 1\\ 20 & \frac{31}{2}\end{pmatrix} + u^3\begin{pmatrix}0 & 0\\ 2 & 1\end{pmatrix}\right),
\end{aligned}
\tag{5.34}
$$

and they satisfy the conditions in Theorem 3.5. If we take

$$
P_5(u) = \frac{1}{128}\begin{pmatrix}a + bu + cu^2\\ au + bu^2 + cu^3\end{pmatrix},
\tag{5.35}
$$

where

$$
\begin{aligned}
a &= \frac{\left(-4467 + \sqrt{19539353}\right)\sqrt{4467 + \sqrt{19539353}}}{1288},\\
b &= \frac{\left(-3823 + \sqrt{19539353}\right)\sqrt{4467 + \sqrt{19539353}}}{1288},\\
c &= \frac{\sqrt{4467 + \sqrt{19539353}}}{2},
\end{aligned}
\tag{5.36}
$$

then the sum of l^2-norm for every row of matrix in (3.49) formed by $P_1(u)$, $P_2(u)$, $P_3(u)$, $P_4(u)$, and $P_5(u)$ is equivalent to 1. Using the method in Theorem 3.5, we can get

$$
\begin{aligned}
Q_1(u) = {} & \begin{pmatrix}0.02144655154326434 & 0.04289310308652868\\ 0 & 0\end{pmatrix}\\
& + z\begin{pmatrix}0.04289310308652868 & 0.1072327577163217\\ 0 & 0\end{pmatrix}\\
& + z^2\begin{pmatrix}0.1072327577163217 & 0.2144655154326434\\ 0 & 0\end{pmatrix}
\end{aligned}
$$

$$
\begin{aligned}
&+ z^{3}\begin{pmatrix} 0.2144655154326434 & 0.3324215489205973 \\ 0 & 0 \end{pmatrix} \\
&- z^{4}\begin{pmatrix} 0.19702904865778179 & 0.15557470886671548 \\ -0.02144655154326434 & -0.04289310308652868 \end{pmatrix} \\
&- z^{5}\begin{pmatrix} 0.15557470886671548 & 0.11193838675771434 \\ -0.04289310308652868 & -0.1072327577163217 \end{pmatrix} \\
&- z^{6}\begin{pmatrix} 0.11193838675771434 & 0.07664965153915186 \\ -0.1072327577163217 & -0.2144655154326434 \end{pmatrix} \\
&- z^{7}\begin{pmatrix} 0.07664965153915186 & 0.053977382251572635 \\ -0.2144655154326434 & -0.3324215489205973 \end{pmatrix} \\
&- z^{8}\begin{pmatrix} 0.044111750085627274 & 0.0284591936036305 \\ 0.19702904865778179 & 0.15557470886671548 \end{pmatrix} \\
&- z^{9}\begin{pmatrix} 0.0284591936036305 & 0.01422959680181525 \\ 0.15557470886671548 & 0.11193838675771434 \end{pmatrix} \\
&- z^{10}\begin{pmatrix} 0.01422959680181525 & 0.0056918387207261 \\ 0.11193838675771434 & 0.07664965153915186 \end{pmatrix} \\
&- z^{11}\begin{pmatrix} 0.0056918387207261 & 0.00284591936036305 \\ 0.07664965153915186 & 0.053977382251572635 \end{pmatrix} \\
&- z^{12}\begin{pmatrix} 0 & 0 \\ 0.044111750085627274 & 0.0284591936036305 \end{pmatrix} \\
&- z^{13}\begin{pmatrix} 0 & 0 \\ 0.0284591936036305 & 0.01422959680181525 \end{pmatrix} \\
&- z^{14}\begin{pmatrix} 0 & 0 \\ 0.01422959680181525 & 0.0056918387207261 \end{pmatrix} \\
&- z^{15}\begin{pmatrix} 0 & 0 \\ 0.0056918387207261 & 0.00284591936036305 \end{pmatrix},
\end{aligned}
$$

$$
\begin{aligned}
Q_2(u) = &- \begin{pmatrix} 0.1477957934872654 & 0.10094712082354547 \\ 0 & 0 \end{pmatrix} \\
&- z\begin{pmatrix} -0.6597141432730713 & 0.05159613960533249 \\ 0 & 0 \end{pmatrix} \\
&- z^{2}\begin{pmatrix} 0.05159613960533249 & 0.06585963320155815 \\ 0 & 0 \end{pmatrix} \\
&- z^{3}\begin{pmatrix} 0.06585963320155815 & 0.08467934092975693 \\ 0 & 0 \end{pmatrix}
\end{aligned}
$$

$$
\begin{aligned}
&- z^{4}\begin{pmatrix} 0.028047431831489087 & 0.01809511731063812 \\ 0.1477957934872654 & 0.10094712082354547 \end{pmatrix} \\
&- z^{5}\begin{pmatrix} 0.01809511731063812 & 0.00904755865531906 \\ -0.6597141432730713 & 0.05159613960533249 \end{pmatrix} \\
&- z^{6}\begin{pmatrix} 0.00904755865531906 & 0.003619023462127624 \\ 0.05159613960533249 & 0.06585963320155815 \end{pmatrix} \\
&- z^{7}\begin{pmatrix} 0.003619023462127624 & 0.001809511731063812 \\ 0.06585963320155815 & 0.08467934092975693 \end{pmatrix} \\
&- z^{8}\begin{pmatrix} 0 & 0 \\ 0.028047431831489087 & 0.01809511731063812 \end{pmatrix} \\
&- z^{9}\begin{pmatrix} 0 & 0 \\ 0.01809511731063812 & 0.00904755865531906 \end{pmatrix} \\
&- z^{10}\begin{pmatrix} 0 & 0 \\ 0.00904755865531906 & 0.003619023462127624 \end{pmatrix} \\
&- z^{11}\begin{pmatrix} 0 & 0 \\ 0.003619023462127624 & 0.001809511731063812 \end{pmatrix},
\end{aligned}
$$

$$
\begin{aligned}
Q_3(u) = &- \begin{pmatrix} 0.05761306818263398 & 0.17400836327560223 \\ 0 & 0 \end{pmatrix} \\
&- z\begin{pmatrix} 0.031575865006210874 & -0.6561977852588053 \\ 0 & 0 \end{pmatrix} \\
&- z^{2}\begin{pmatrix} 0.05090899592774225 & 0.0849120583693081 \\ 0 & 0 \end{pmatrix} \\
&- z^{3}\begin{pmatrix} 0.0849120583693081 & 0.12308355988310513 \\ 0 & 0 \end{pmatrix} \\
&- z^{4}\begin{pmatrix} 0.015096022807838986 & 0.009739369553444507 \\ 0.05761306818263398 & 0.17400836327560223 \end{pmatrix} \\
&- z^{5}\begin{pmatrix} 0.009739369553444507 & 0.004869684776722253 \\ 0.031575865006210874 & -0.6561977852588053 \end{pmatrix} \\
&- z^{6}\begin{pmatrix} 0.004869684776722253 & 0.0019478739106889012 \\ 0.05090899592774225 & 0.0849120583693081 \end{pmatrix} \\
&- z^{7}\begin{pmatrix} 0.0019478739106889012 & 0.0009739369553444506 \\ 0.0849120583693081 & 0.12308355988310513 \end{pmatrix} \\
&- z^{8}\begin{pmatrix} 0 & 0 \\ 0.015096022807838986 & 0.009739369553444507 \end{pmatrix}
\end{aligned}
$$

$$
\begin{aligned}
&- z^{9}\begin{pmatrix} 0 & 0 \\ 0.009739369553444507 & 0.004869684776722253 \end{pmatrix} \\
&- z^{10}\begin{pmatrix} 0 & 0 \\ 0.004869684776722253 & 0.0019478739106889012 \end{pmatrix} \\
&- z^{11}\begin{pmatrix} 0 & 0 \\ 0.0019478739106889012 & 0.0009739369553444506 \end{pmatrix},
\end{aligned}
$$

$$
\begin{aligned}
Q_4(u) = &- \begin{pmatrix} 0.05761306818263398 & 0.17400836327560223 \\ 0 & 0 \end{pmatrix} \\
&- z\begin{pmatrix} 0.031575865006210874 & 0.05090899592774225 \\ 0 & 0 \end{pmatrix} \\
&- z^{2}\begin{pmatrix} -0.6561977852588053 & 0.0849120583693081 \\ 0 & 0 \end{pmatrix} \\
&- z^{3}\begin{pmatrix} 0.0849120583693081 & 0.12308355988310513 \\ 0 & 0 \end{pmatrix} \\
&- z^{4}\begin{pmatrix} 0.015096022807838986 & 0.009739369553444507 \\ 0.05761306818263398 & 0.17400836327560223 \end{pmatrix} \\
&- z^{5}\begin{pmatrix} 0.009739369553444507 & 0.004869684776722253 \\ 0.031575865006210874 & 0.05090899592774225 \end{pmatrix} \\
&- z^{6}\begin{pmatrix} 0.004869684776722253 & 0.0019478739106889012 \\ -0.6561977852588053 & 0.0849120583693081 \end{pmatrix} \\
&- z^{7}\begin{pmatrix} 0.0019478739106889012 & 0.0009739369553444506 \\ 0.0849120583693081 & 0.12308355988310513 \end{pmatrix} \\
&- z^{8}\begin{pmatrix} 0 & 0 \\ 0.015096022807838986 & 0.009739369553444507 \end{pmatrix} \\
&- z^{9}\begin{pmatrix} 0 & 0 \\ 0.009739369553444507 & 0.004869684776722253 \end{pmatrix} \\
&- z^{10}\begin{pmatrix} 0 & 0 \\ 0.004869684776722253 & 0.0019478739106889012 \end{pmatrix} \\
&- z^{11}\begin{pmatrix} 0 & 0 \\ 0.0019478739106889012 & 0.0009739369553444506 \end{pmatrix},
\end{aligned}
$$

$$
\begin{aligned}
Q_5(u) = &\begin{pmatrix} 0.026091915441724444 & -0.2968153107875939 \\ 0 & 0 \end{pmatrix} \\
&- z\begin{pmatrix} 0.008531797851123840 & 0.045500780406666190 \\ 0 & 0 \end{pmatrix}
\end{aligned}
$$

$$
\begin{aligned}
&- z^{2}\begin{pmatrix} 0.04550078040666619 & -0.6008203844819463 \\ 0 & 0 \end{pmatrix} \\
&- z^{3}\begin{pmatrix} 0.10628639670460124 & 0.17279291544901831 \\ 0 & 0 \end{pmatrix} \\
&+ z^{4}\begin{pmatrix} 0.014890951803385767 & 0.00960706567960372 \\ 0.02609191544172444 & -0.2968153107875939 \end{pmatrix} \\
&+ z^{5}\begin{pmatrix} 0.00960706567960372 & 0.00480353283980186 \\ -0.00853179785112384 & -0.04550078040666619 \end{pmatrix} \\
&+ z^{6}\begin{pmatrix} 0.00480353283980186 & 0.0019214131359207441 \\ -0.04550078040666619 & 0.6008203844819463 \end{pmatrix} \\
&+ z^{7}\begin{pmatrix} 0.0019214131359207441 & 0.0009607065679603721 \\ -0.10628639670460124 & -0.17279291544901831 \end{pmatrix} \\
&+ z^{8}\begin{pmatrix} 0 & 0 \\ 0.014890951803385767 & 0.00960706567960372 \end{pmatrix} \\
&+ z^{9}\begin{pmatrix} 0 & 0 \\ 0.00960706567960372 & 0.00480353283980186 \end{pmatrix} \\
&+ z^{10}\begin{pmatrix} 0 & 0 \\ 0.00480353283980186 & 0.0019214131359207441 \end{pmatrix} \\
&+ z^{11}\begin{pmatrix} 0 & 0 \\ 0.0019214131359207441 & 0.0009607065679603721 \end{pmatrix},
\end{aligned}
$$

$$
\begin{aligned}
Q_6(u) = &\begin{pmatrix} 0.02609191544172444 & -0.2968153107875939 \\ 0 & 0 \end{pmatrix} \\
&- z\begin{pmatrix} 0.00853179785112384 & 0.04550078040666619 \\ 0 & 0 \end{pmatrix} \\
&- z^{2}\begin{pmatrix} 0.04550078040666619 & 0.10628639670460124 \\ 0 & 0 \end{pmatrix} \\
&- z^{3}\begin{pmatrix} -0.6008203844819463 & 0.17279291544901831 \\ 0 & 0 \end{pmatrix} \\
&+ z^{4}\begin{pmatrix} 0.014890951803385767 & 0.00960706567960372 \\ 0.02609191544172444 & -0.2968153107875939 \end{pmatrix} \\
&+ z^{5}\begin{pmatrix} 0.00960706567960372 & 0.00480353283980186 \\ -0.00853179785112384 & -0.04550078040666619 \end{pmatrix} \\
&+ z^{6}\begin{pmatrix} 0.00480353283980186 & 0.0019214131359207441 \\ -0.04550078040666619 & -0.10628639670460124 \end{pmatrix}
\end{aligned}
$$

$$+ z^{7}\begin{pmatrix} 0.0019214131359207441 & 0.0009607065679603721 \\ 0.6008203844819463 & -0.17279291544901831 \end{pmatrix}$$

$$+ z^{8}\begin{pmatrix} 0 & 0 \\ 0.014890951803385767 & 0.00960706567960372 \end{pmatrix}$$

$$+ z^{9}\begin{pmatrix} 0 & 0 \\ 0.00960706567960372 & 0.00480353283980186 \end{pmatrix}$$

$$+ z^{10}\begin{pmatrix} 0 & 0 \\ 0.00480353283980186 & 0.0019214131359207441 \end{pmatrix}$$

$$+ z^{11}\begin{pmatrix} 0 & 0 \\ 0.0019214131359207441 & 0.0009607065679603721 \end{pmatrix},$$

$$Q_7(u) = \begin{pmatrix} 0.08944633780381946 & -0.43235068115291514 \\ 0 & 0 \end{pmatrix}$$

$$+ z\begin{pmatrix} 0.01538612445300629 & -0.03771333490828642 \\ 0 & 0 \end{pmatrix}$$

$$- z^{2}\begin{pmatrix} 0.03771333490828642 & 0.12532192169119855 \\ 0 & 0 \end{pmatrix}$$

$$+ z^{3}\begin{pmatrix} -0.12532192169119855 & 0.4857994473999439 \\ 0 & 0 \end{pmatrix}$$

$$+ z^{4}\begin{pmatrix} 0.0514996814410752 & 0.033225600929725936 \\ 0.08944633780381946 & -0.43235068115291514 \end{pmatrix}$$

$$+ z^{5}\begin{pmatrix} 0.033225600929725936 & 0.016612800464862968 \\ 0.01538612445300629 & -0.03771333490828642 \end{pmatrix}$$

$$+ z^{6}\begin{pmatrix} 0.016612800464862968 & 0.006645120185945188 \\ -0.03771333490828642 & -0.12532192169119855 \end{pmatrix}$$

$$+ z^{7}\begin{pmatrix} 0.006645120185945188 & 0.003322560092972594 \\ -0.12532192169119855 & 0.4857994473999439 \end{pmatrix}$$

$$+ z^{8}\begin{pmatrix} 0 & 0 \\ 0.0514996814410752 & 0.033225600929725936 \end{pmatrix}$$

$$+ z^{9}\begin{pmatrix} 0 & 0 \\ 0.033225600929725936 & 0.016612800464862968 \end{pmatrix}$$

$$+ z^{10}\begin{pmatrix} 0 & 0 \\ 0.016612800464862968 & 0.006645120185945188 \end{pmatrix}$$

$$+ z^{11}\begin{pmatrix} 0 & 0 \\ 0.006645120185945188 & 0.003322560092972594 \end{pmatrix},$$

$$Q_8(u) = \begin{pmatrix} -0.6202005681344304 & 0.0751156591403543 \\ 0 & 0 \end{pmatrix}$$

$$
\begin{aligned}
&+ z\begin{pmatrix} -0.043785112178583024 & 0.03234387705790018 \\ 0 & 0 \end{pmatrix} \\
&+ z^2\begin{pmatrix} 0.03234387705790018 & 0.1023493218758696 \\ 0 & 0 \end{pmatrix} \\
&+ z^3\begin{pmatrix} 0.1023493218758696 & 0.15482744823966293 \\ 0 & 0 \end{pmatrix} \\
&+ z^4\begin{pmatrix} 0.05053803393098198 & 0.032605183181278696 \\ -0.6202005681344304 & 0.0751156591403543 \end{pmatrix} \\
&+ z^5\begin{pmatrix} 0.032605183181278696 & 0.016302591590639348 \\ -0.043785112178583024 & 0.03234387705790018 \end{pmatrix} \\
&+ z^6\begin{pmatrix} 0.016612800464862968 & 0.006521036636255738 \\ 0.03234387705790018 & 0.1023493218758696 \end{pmatrix} \\
&+ z^7\begin{pmatrix} 0.006521036636255738 & 0.003260518318127869 \\ 0.1023493218758696 & 0.15482744823966293 \end{pmatrix} \\
&+ z^8\begin{pmatrix} 0 & 0 \\ 0.05053803393098198 & 0.032605183181278696 \end{pmatrix} \\
&+ z^9\begin{pmatrix} 0 & 0 \\ 0.032605183181278696 & 0.016302591590639348 \end{pmatrix} \\
&+ z^{10}\begin{pmatrix} 0 & 0 \\ 0.016612800464862968 & 0.006521036636255738 \end{pmatrix} \\
&+ z^{11}\begin{pmatrix} 0 & 0 \\ 0.006521036636255738 & 0.003260518318127869 \end{pmatrix}
\end{aligned}
\tag{5.37}
$$

they are the symbols of the minimum-energy multiwavelet frames associated with Φ. The graphs of the vector-valued functions are shown in Figure 5.

From Figure 5, we can find that every component of the minimum-energy frames is smooth, but not (anti)symmetrical.

6. Conclusions

In this paper, minimum-energy multiwavelet frames with arbitrary integer dilation factor are studied. Firstly, we define the concept of minimum-energy multiwavelet frame with arbitrary dilation factor and present its equivalent characterizations. Secondly, some necessary conditions and sufficient conditions for minimum-energy multiwavelet frame are given, then the decomposition and reconstruction formulas of minimum-energy multiwavelet

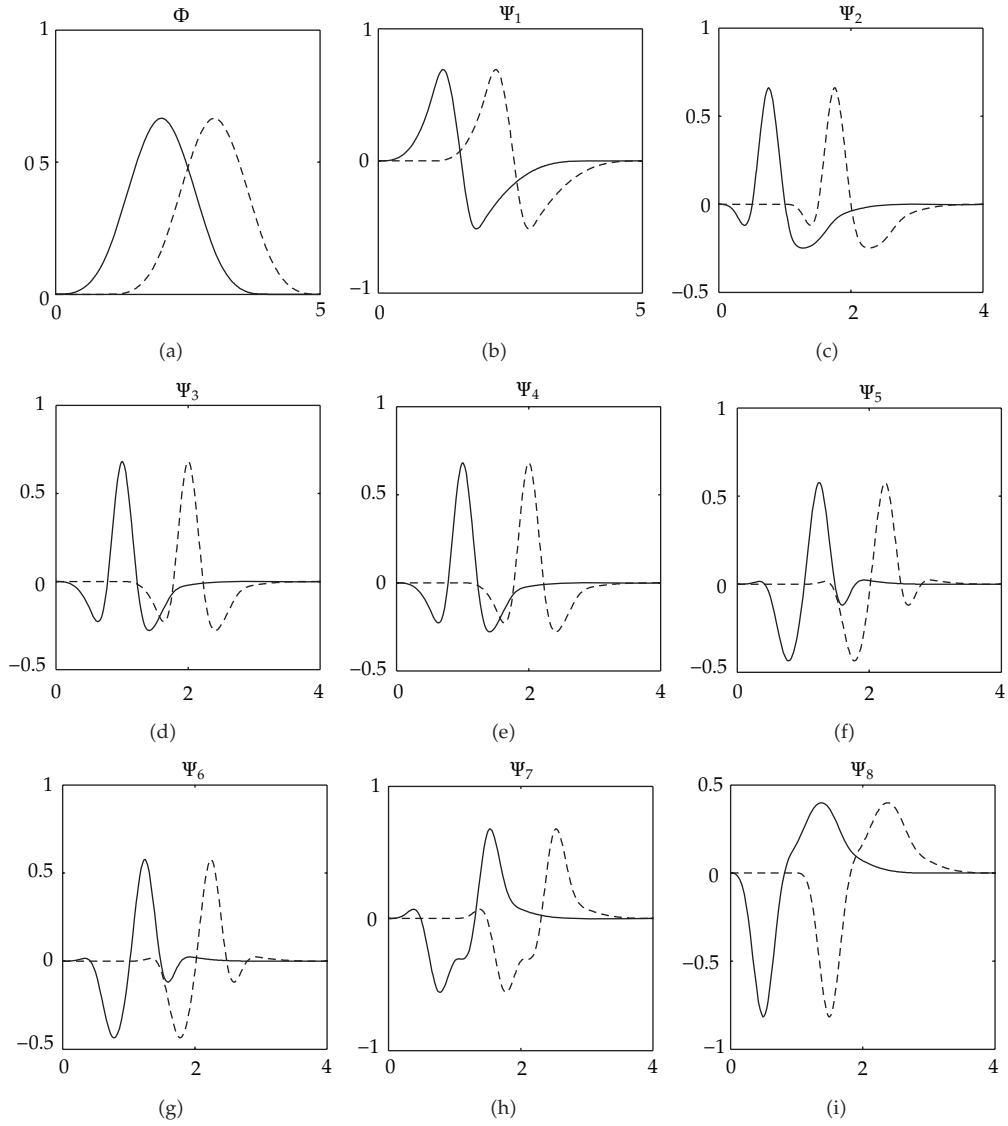

Figure 5

frame with arbitrary integer dilation factor are deduced. Finally, we give several numerical examples based on B-spline.

Acknowledgments

The authors acknowledge the support from the National Natural Science Foundation of China under the Project Grant no. 10961001 and 61261043, the Research Project of Beifang University of Nationalities under the Project no. 2012Y036, and Graduate Students Innovative Project under the Project no. 2011XYC035. M. Li acknowledges the support from the 973 plan under the Project no. 2011CB302800 and the National Natural Science Foundation of China under the Project Grant no.s 61070214 and 60873264.

References

[1] T. N. T. Goodman and S. L. Lee, "Wavelets of multiplicity r," *Transactions of the American Mathematical Society*, vol. 342, no. 1, pp. 307–324, 1994.

[2] J. Geronimo, D. Hardin, and P. Massopust, "Fractal functions and wavelet expansions based on several scaling functions," *Journal of Approximation Theory*, vol. 78, no. 3, pp. 373–401, 1994.

[3] C. K. Chui and J. Lian, "A study of orthonormal multi-wavelets," *Applied Numerical Mathematics*, vol. 20, no. 3, pp. 273–298, 1996.

[4] G. Plonka and V. Strela, "Construction of multiscaling functions with approximation and symmetry," *SIAM Journal on Mathematical Analysis*, vol. 29, no. 2, pp. 481–510, 1998.

[5] W. Lawton, S. L. Lee, and Z. W. Shen, "An algorithm for matrix extension and wavelet construction," *Mathematics of Computation*, vol. 65, no. 214, pp. 723–737, 1996.

[6] Q. T. Jiang, "Symmetric paraunitary matrix extension and parametrization of symmetric orthogonal multifilter banks," *SIAM Journal on Matrix Analysis and Applications*, vol. 23, no. 1, pp. 167–186, 2001.

[7] B. Han and Q. T. Jiang, "Multiwavelets on the interval," *Applied and Computational Harmonic Analysis*, vol. 12, no. 1, pp. 100–127, 2002.

[8] I. Daubechies, A. Grossmann, and Y. Meyer, "Painless nonorthogonal expansions," *Journal of Mathematical Physics*, vol. 27, no. 5, pp. 1271–1283, 1986.

[9] J. J. Benedetto and S. Li, "The theory of multiresolution analysis frames and applications to filter banks," *Applied and Computational Harmonic Analysis*, vol. 5, no. 4, pp. 389–427, 1998.

[10] C. K. Chui and X. L. Shi, "Orthonormal wavelets and tight frames with arbitrary real dilations," *Applied and Computational Harmonic Analysis*, vol. 9, no. 3, pp. 243–264, 2000.

[11] C. K. Chui and W. He, "Compactly supported tight frames associated with refinable functions," *Applied and Computational Harmonic Analysis*, vol. 8, no. 3, pp. 293–319, 2000.

[12] O. Christensen, *An Introduction to Frames and Riesz Bases*, Birkhäuser, Boston, Mass, USA, 2003.

[13] B. Han, S.-G. Kwon, and S. S. Park, "Riesz multiwavelet bases," *Applied and Computational Harmonic Analysis*, vol. 20, no. 2, pp. 161–183, 2006.

[14] H. Wang and L. Peng, "Parameterizations of univariate wavelet tight frames with short support," *Communications in Nonlinear Science and Numerical Simulation*, vol. 11, no. 6, pp. 663–677, 2006.

[15] Y. Huang and Z. Cheng, "Minimum-energy frames associated with refinable function of arbitrary integer dilation factor," *Chaos, Solitons & Fractals*, vol. 32, no. 2, pp. 503–515, 2007.

[16] M. Charina and J. Stöckler, "Tight wavelet frames for irregular multiresolution analysis," *Applied and Computational Harmonic Analysis*, vol. 25, no. 1, pp. 98–113, 2008.

[17] B. Han, "Construction of wavelets and framelets by the projection method," *International Journal of Mathematical Sciences*, vol. 1, no. 1, pp. 1–40, 2008.

[18] X. Gao and C. H. Cao, "Minimum-energy wavelet frame on the interval," *Science in China F*, vol. 51, no. 10, pp. 1547–1562, 2008.

[19] B. Han, "Dual multiwavelet frames with high balancing order and compact fast frame transform," *Applied and Computational Harmonic Analysis*, vol. 26, no. 1, pp. 14–42, 2009.

[20] J.-P. Gabardo, "Weighted irregular Gabor tight frames and dual systems using windows in the Schwartz class," *Journal of Functional Analysis*, vol. 256, no. 3, pp. 635–672, 2009.

[21] Y. Huang and F. Zhu, "Characterizations of tight frame wavelets with special dilation matrices," *Mathematical Problems in Engineering*, vol. 2010, Article ID 128294, 26 pages, 2010.

[22] Y. Huang and N. Sun, "Characterizations of A-Parseval frame wavelet," *Acta Mathematica Sinica*, vol. 54, no. 5, pp. 767–790, 2011.

[23] Q. Liang and P. Zhao, "Minimum-energy multi-wavelets tight frames associated with two scaling functions," in *Proceedings of the International Conference on Wavelet Analysis and Pattern Recognition*, vol. 1, pp. 97–101, 2010.

[24] C. Cattani, "Fractional calculus and Shannon wavelets," *Mathematical Problems in Engineering*, vol. 2012, Article ID 164808, 23 pages, 2012.

[25] C. Cattani, "Shannon wavelets theory," *Mathematical Problems in Engineering*, vol. 2008, Article ID 164808, 24 pages, 2008.

[26] C. Cattani, "Connection coefficients of Shannon wavelets," *Mathematical Modelling and Analysis*, vol. 11, no. 2, pp. 117–132, 2006.

[27] I. Daubechies, *Ten Lectures on Wavelets*, Society for Industrial and Applied Mathematics, Philadelphia, Pa, USA, 1992.

Hindawi Publishing Corporation
Mathematical Problems in Engineering
Volume 2012, Article ID 207381, 15 pages
doi:10.1155/2012/207381

Research Article

An Economic Hybrid J_2 Analytical Orbit Propagator Program Based on SARIMA Models

Juan Félix San-Juan,[1] Montserrat San-Martín,[1] and Iván Pérez[2]

[1] *Departamento de Matemáticas y Computación, Universidad de La Rioja, 26004 Logroño, Spain*
[2] *Departamento de Ingeniería Eléctrica, Universidad de La Rioja, 26004 Logroño, Spain*

Correspondence should be addressed to Juan Félix San-Juan, juanfelix.sanjuan@unirioja.es

Received 28 April 2012; Accepted 8 July 2012

Academic Editor: Carlo Cattani

We present a new economic hybrid analytical orbit propagator program based on SARIMA models, which approximates to a 4×4 tesseral analytical theory for a Quasi-Spot satellite. The J_2 perturbation is described by a first-order closed-form analytical theory, whereas the effects produced by the higher orders of J_2 and the perturbation of the rest of zonal and tesseral harmonic coefficients are modelled by SARIMA models. Time series analysis is a useful statistical prediction tool, which allows building a model for making future predictions based on the study of past observations. The combination of the analytical techniques and time series analysis allows an increase in accuracy without significant loss in efficiency of the new propagators, as a consequence of modelling higher-order terms and other perturbations are not taken into account in the analytical theory.

1. Introduction

An analytical orbit propagator program (AOPP) is an application which collects and arranges all mathematical expressions involved in an approximate analytical solution of the satellite equations of motion. The analytical solutions are known as General Perturbation Theories. It is noteworthy that the perturbation force model used and the order of the analytical approximation are closely related to the accuracy and computational efficiency of an AOPP.

In many situations, in order to improve the accuracy of the solution, it may be necessary to consider a more precise perturbation force model. The solution provided by the General Perturbation Theories may not be the best approach, because the calculating process generates unmanageably large mathematical expressions and, therefore, reduces the computational efficiency of its corresponding AOPP. Other alternatives, although computationally more expensive than an economic analytical approximation, are the Special

Perturbation Theories, which directly integrate the equations of motion using numerical techniques, or by means of semi-analytical theories, which are a combination of General and Special Perturbation Theories.

In this paper we present a new methodology, which we will call *Hybrid Perturbation Theories*, to carry out new families of hybrid orbit propagator programs which combine a simplified analytical orbit propagator [1–4] with statistical time series models [5]. This combination allows an increase in accuracy for predicting the position of a satellite without significant loss in computational efficiency in the new hybrid propagators, as well as modelling higher-order terms and other perturbations not considered in the analytical theory.

Mathematically, the problem consists of estimating the satellite's position and velocity $\mathbf{x}_t$ for which an approximate analytical solution is known:

$$\mathbf{x}_t^{\mathcal{A}} = F(t, \mathbf{x}_{t_0}), \tag{1.1}$$

where $\mathbf{x}_{t_0}$ is the satellite's initial time position and velocity. Moreover, at any moment t_i, a precise observation $\mathbf{x}_{t_i}$ can be obtained. This observation is related to $\mathbf{x}_{t_i}^{\mathcal{A}}$ by the following linear relation:

$$\varepsilon_{t_i} = \mathbf{x}_{t_i} - \mathbf{x}_{t_i}^{\mathcal{A}}, \tag{1.2}$$

where ε_{t_i} represents the errors produced by the perturbation forces not considered in the analytical theory and by the selfsame approximate analytical solution. In order to predict the future values of the ε_{t_i} series, we apply statistical techniques in time series analysis.

The first n values of ε_{t_i} are used to estimate a model by means of these techniques. From this model a forecast of the $\widehat{\varepsilon}_{t_i}$ error can be calculated. Finally these estimations are used to obtain the forecast of the satellite's position and velocity by the relation

$$\widehat{\mathbf{x}}_{t_i} = \mathbf{x}_{t_i}^{\mathcal{A}} + \widehat{\varepsilon}_{t_i}. \tag{1.3}$$

In this paper, the orbit propagator Z2DN1 derived from a first-order closed-form analytical integration of the *main problem* of the artificial satellite theory and the SARIMA time series models are described. Secondly, using the univariate Box-Jenkins time series analysis, a specific Z2DN1-SARIMA model is developed for a Quasi-Spot satellite so as to model the effects of some zonal and tesseral harmonics by means of the statistical part, where these influences have not been taken into consideration in the analytical part. The simulated data are obtained from the numerical integration for an Earth orbiter, which has only taken into account the perturbation due to the nonsymmetrical Earth gravity field up to the fourth degree and order. Finally, we compare the simulation with both the analytical propagator alone and the analytical-statistical hybrid propagator.

2. Z2DN1 Analytical Orbit Propagator Program

This AOPP has been derived from a first-order closed-form analytical theory of the *main problem* of the artificial satellite theory.

The main problem is defined as a Kepler problem perturbed by Earth's oblateness. The Hamiltonian of this dynamical system can be written in a cartesian coordinate system $(\mathbf{x}, \mathbf{X})$ as

$$\mathscr{H} = \frac{1}{2}(\mathbf{X}\cdot\mathbf{X}) - \frac{\mu}{r}\left[1 - J_2\left(\frac{\alpha}{r}\right)^2 P_2\left(\frac{z}{r}\right)\right], \tag{2.1}$$

where $r = \|\mathbf{x}\| = \sqrt{x^2+y^2+z^2}$, μ is the gravitational constant, α the equatorial radius of the Earth, J_2 the oblateness coefficient, and P_2 the second degree Legendre polynomial.

The first step to carry out the analytical theory consists of expressing the Hamiltonian (2.1) in terms of the Delaunay variables (l, g, h, L, G, H). This set of canonical action-angle variables can be defined in terms of the orbital elements such as $l = M$, $g = \omega$, $h = \Omega$, $L = \sqrt{\mu a}$, $G = \sqrt{\mu a(1-e^2)}$, $H = \sqrt{\mu a(1-e^2)}\cos i$, where M, ω, Ω, a, e, i are the mean anomaly, argument of the perigee, longitude of the ascending node, semimajor axis, eccentricity, and inclination, respectively. Then the transformed Hamiltonian is given as

$$\mathscr{H} = -\frac{\mu^2}{2L^2} - \frac{\epsilon}{2}\frac{\mu}{r}\left(\frac{\alpha}{r}\right)^2\left(1 - 3s^2\sin^2(f+g)\right), \tag{2.2}$$

where $\epsilon = J_2$ is a small parameter, $s = \sin i$, and f is the true anomaly.

Next, we normalize the Hamiltonian (2.2) by applying the Lie transform $\varphi : (l, g, h, L, G, H) \to (l', g', h', L', G', H')$, the so-called Delaunay Normalization [6], which up to first order reads

$$\mathscr{K}_0 = \mathscr{H}_0, \tag{2.3}$$

$$\mathscr{K}_1 = \mathscr{H}_1 - \frac{\mu^2}{L'^3}\frac{\partial \mathscr{W}}{\partial l'}. \tag{2.4}$$

The Lie method solves (2.4) by choosing the form of the transformed Hamiltonian; the Delaunay Normalization takes the Hamiltonian as the average over the fastest angle l':

$$\mathscr{K}_1 = \frac{3\alpha^2\mu^4 s'^2}{4L'^6\eta'^3} - \frac{\alpha^2\mu^4}{2L'^6\eta'^3}, \tag{2.5}$$

and then $\mathscr{W}_1$ is computed as

$$\begin{aligned}
\mathscr{W}_1 &= \frac{L'^3}{\mu^2}\int(\mathscr{H}_1 - \mathscr{K}_1)\,dl \\
&= \frac{\mu^2\alpha^2\left(3s'^2-2\right)\phi'}{4L'^3\eta'^3} + \frac{\mu^2\alpha^2 e'^{(3s'^2-2)}}{4L'^3\eta'^3}\sin f' \\
&\quad - \frac{3\mu^2\alpha^2 e' s'^2}{8L'^3\eta'^3}\sin(f'+2g') - \frac{3\mu^2\alpha^2 s'^2}{8L'^3\eta'^3}\sin(2f'+2g') \\
&\quad - \frac{\mu^2\alpha^2 e' s'^2}{8L'^3\eta'^3}\sin(3f'+2g'),
\end{aligned} \tag{2.6}$$

where $\eta' = \sqrt{1-e'^2}$ and $\phi' = f' - l'$.

Hence, up to the first order, the transformed Hamiltonian is given by

$$\mathcal{K} = -\frac{\mu^2}{2L'^2} + \epsilon\left(\frac{3\alpha^2\mu^4 s'^2}{4L'^6\eta'^3} - \frac{\alpha^2\mu^4}{2L'^6\eta'^3}\right). \tag{2.7}$$

We must remark that the Hamiltonian (2.7) is integrable. This Hamiltonian only depends on the momenta L', G', and H', and so therefore the equations of motion are obtained as

$$\begin{aligned}
\frac{\mathrm{d}l'}{\mathrm{d}t} &= \frac{\partial\mathcal{K}}{\partial L'} = \frac{\mu^2}{L'^3} + \epsilon\left(\frac{3\alpha^2\mu^4}{2L'^7\eta'^3} - \frac{9\alpha^2\mu^4 s'^2}{4L'^7\eta'^3}\right),\\
\frac{\mathrm{d}g'}{\mathrm{d}t} &= \frac{\partial\mathcal{K}}{\partial G'} = \epsilon\left(\frac{3\alpha^2\mu^4}{L'^7\eta'^4} - \frac{15\alpha^2\mu^4 s'^2}{4L'^7\eta'^4}\right),\\
\frac{\mathrm{d}h'}{\mathrm{d}t} &= \frac{\partial\mathcal{K}}{\partial G'} = -\epsilon\frac{3\alpha^2\mu^4 c'}{2L'^7\eta'^4},\\
\frac{\mathrm{d}L'}{\mathrm{d}t} &= \frac{\mathrm{d}G'}{\mathrm{d}t} = \frac{\mathrm{d}H'}{\mathrm{d}t} = 0.
\end{aligned} \tag{2.8}$$

By integrating (2.8) we can directly obtain that the values of the momenta L', G', and H' are constants, whereas the variables l', g', and h' yield

$$\begin{aligned}
l' &= \left[\frac{\mu^2}{L'^3} + \epsilon\left(\frac{3\alpha^2\mu^4}{2L'^7\eta'^3} - \frac{9\alpha^2\mu^4 s'^2}{4L'^7\eta'^3}\right)\right](t-t_0) + l'_0,\\
g' &= \left[\epsilon\left(\frac{3\alpha^2\mu^4}{L'^7\eta'^4} - \frac{15\alpha^2\mu^4 s'^2}{4L'^7\eta'^4}\right)\right](t-t_0) + g'_0,\\
h' &= \left[-\epsilon\frac{3\alpha^2\mu^4 c'}{2L'^7\eta'^4}\right](t-t_0) + h'_0,
\end{aligned} \tag{2.9}$$

where l'_0, g'_0, h'_0, L'_0, G'_0, H'_0 are the transformed initial conditions l_0, g_0, h_0, L_0, G_0, H_0 at the epoch t_0.

Finally, from (2.6) the first-order explicit equations of the direct and inverse transformations [7] are calculated.

From the above analytical theory an AOPP was derived, which has to evaluate 93 terms. This AOPP has been called Z2DN1. The algebraic manipulations required to carry out this analytical theory and its corresponding AOPP were built using a set of *Mathematica* packages called MathATESAT [8]. Figure 1 shows the flowchart of the Z2DN1 analytical orbit propagator program.

Z2DN1 begins by initializing the physical parameters and the initial conditions at epoch t_0. Next, it transforms the initial conditions into the Delaunay variables $(l_0, g_0, h_0, L_0, G_0, H_0)$ and transports them across the inverse transformation of the Delaunay normalization $(l'_0, g'_0, h'_0, L'_0, G'_0, H'_0)$. Then, the program provides Delaunay's variables at

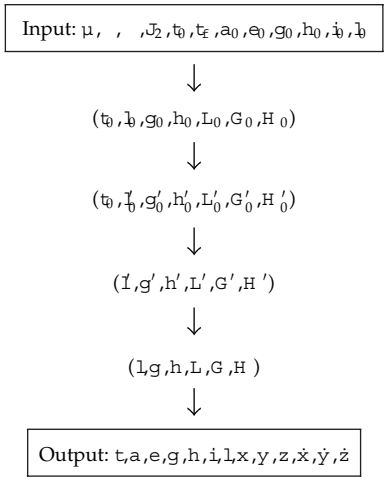

Figure 1: Flowchart of the Z2DN1 orbit propagator program.

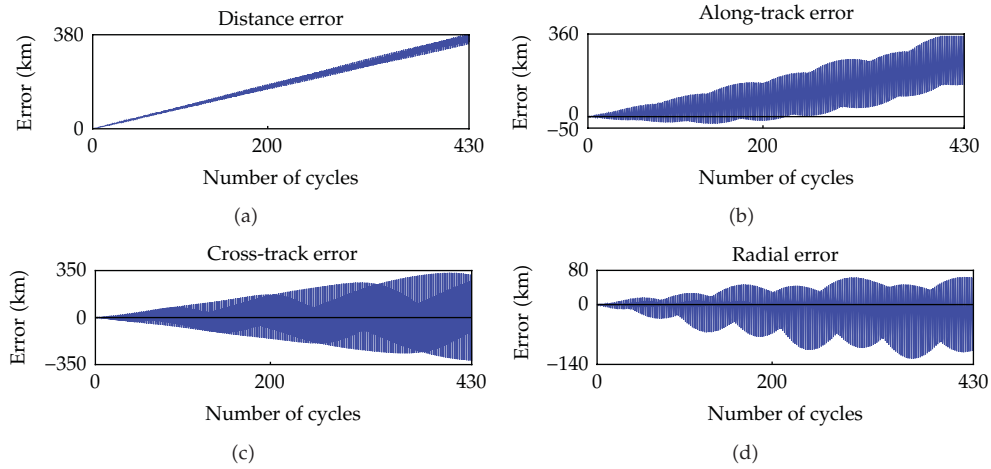

Figure 2: Distance, along-track, cross-track, and radial errors for a Quasi-Spot satellite.

epoch t_f from integrated Hamilton equations (l', g', h', L', G', H'). Finally, the direct transformation of the Delaunay normalization is applied, and therefore the osculating Keplerian elements (a, e, g, h, i, l) and the state vector $(x, y, z, \dot{x}, \dot{y}, \dot{z})$ can be calculated.

This model has been compared with the numerical integration (8th-order Runge-Kutta method) of the equation of motion of a model, which includes the Earth's zonal and tesseral harmonic coefficients of fourth degree and order in the case of a Quasi-Spot satellite ($a = 7148$, $e = 0.001$, $i = 98°$).

Figure 2 shows the distance, along-track, cross-track, and radial errors in a time span interval of 30 days, which is about 430 satellite cycles. As can be observed, the distance error of the first-order J_2 analytical theory when compared with a more complex perturbation model is about 360 km.

Figure 3 shows the relative errors of the orbital elements for a Quasi-Spot satellite. The mean anomaly and argument of the perigee are the variables which present the worst

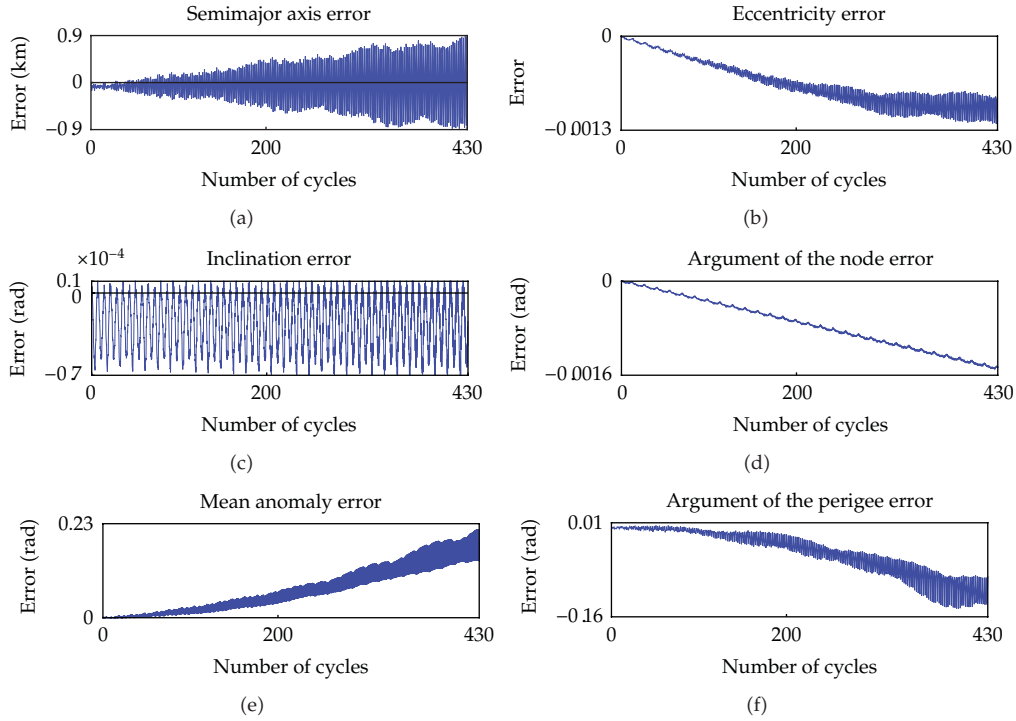

Figure 3: Relative errors of the orbital elements for a Quasi-Spot satellite.

performance. The maximum absolute errors in a time span interval of 30 days are about 12.4° and 9.5°, respectively.

3. Statistical Time Series Analysis: SARIMA Model

Introduced by Box and Jenkins [5], the *autoregressive integrated moving average* (ARIMA) model has been one of the most popular approaches for time series forecasting. Let ε_t be a discrete time series, in an ARIMA(p, d, q) model, in which the future value of a series is assumed to be a linear combination of its own past values and past residuals, expressed as follows:

$$\phi(B)(1-B)^d \widetilde{\varepsilon}_t = \theta(B)\nu_t, \tag{3.1}$$

where $\widetilde{\varepsilon}_t = \varepsilon_t - \mu$, μ is the mean of the original time series, and ν_t is a white noise residual. B is the backward shift, such that $B\widetilde{\varepsilon}_t = \widetilde{\varepsilon}_{t-1}$, whilst d is the number of times that $\widetilde{\varepsilon}_t$ needs to be differentiated to ensure its conversion to a stationary time series, that is, a time series in which the mean, variance, and autocorrelation functions of $\widetilde{\varepsilon}_t$ are time invariants. $\phi(B)$ represents the *autoregressive* (AR) part, where each $\widetilde{\varepsilon}_t$ is made up of a linear combination from prior observations p, which can be expressed as a polynomial in B of degree p in the following form:

$$\phi(B) = 1 - \phi_1 B - \phi_2 B^2 - \cdots - \phi_p B^p, \tag{3.2}$$

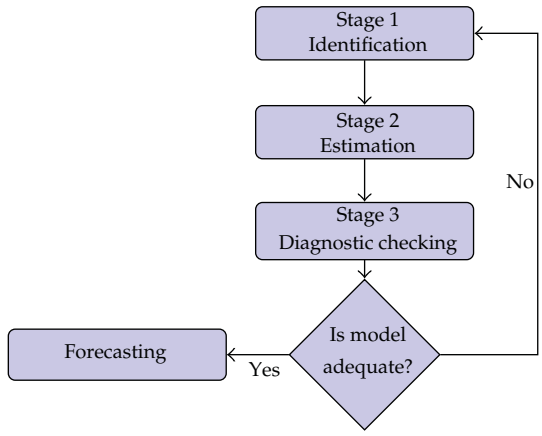

Figure 4: 3-stage Box-Jenkins methodology.

where ϕ_i, $i = 1, \ldots, p$, are the AR parameters. $\theta(B)$ represents the *moving average* (MA) part, which describes the relation of $\widetilde{\varepsilon}_t$ with past residuals and can also be expressed as a polynomial in B of degree q in the following form:

$$\theta(B) = 1 - \theta_1 B - \theta_2 B^2 - \cdots - \theta_q B^q, \tag{3.3}$$

where θ_i, $i = 1, \ldots, p$, are the MA parameters.

In the case that $\widetilde{\varepsilon}_t$ series shows seasonal behaviour, it can be included in (3.1). The extended model is known as a *Seasonal* ARIMA model or SARIMA$(p, d, q)(P, D, Q)_s$ and takes the following form:

$$\Phi(B^s)\phi(B)(1 - B^s)^D (1 - B)^d \widetilde{\varepsilon}_t = \Theta(B^s)\theta(B)\nu_t, \tag{3.4}$$

where

$$\begin{aligned} \Phi(B^s) &= 1 - \Phi_1 B^s - \Phi_2 B^{2s} - \cdots - \Phi_P B^{Ps}, \\ \Theta(B^s) &= 1 - \Theta_1 B^s - \Theta_2 B^{2s} - \cdots - \Theta_q B^{Qs}, \end{aligned} \tag{3.5}$$

represent the seasonal part with periodicity s.

To determine a suitable SARIMA model for a given series, we use the 3-stage Box-Jenkins methodology. This procedure is illustrated in Figure 4. At the identification stage, a preliminary SARIMA model is proposed from the analysis of the estimated autocorrelation function (ACF) and partial autocorrelation function (PACF), allowing us to determine the parameters d, D, p, q, P, and Q. Then, the seasonal and nonseasonal AR and MA parameters are estimated at the second stage. The last stage, diagnostic checking, determines whether the proposed model is adequate or not. If the model is considered adequate, it can be used for forecasting future values; otherwise the process is repeated until a satisfactory model is found.

4. Time Series Analysis

In order to carry out the statistical part of the hybrid propagator, we consider a simulated data set, that is, position and velocity, taken from the numerical integration of the Quasi-Spot equations of motion during 10 satellite cycles. This number of cycles was experimentally calculated; however the models obtained from fewer than 10 cycles were less accurate, but from above 10 cycles the increase in accuracy was not significant either. The force model used to generate the simulated data is a 4×4 EGM-96 gravity field, whereas for the numerical integration a high-order Runge-Kutta method [9] is used.

It is noteworthy to mention that different sets of canonical and noncanonical variables can be used to develop the statistical part, such as cartesian variables, orbital elements, Delaunay variables, and polar-nodal variables. In this work, we will only take into account the Delaunay variables, which allow a direct visualization of the geometry of the orbit.

4.1. Previous Statistical Analysis

The time series analysis begins calculating the linear relations:

$$\varepsilon_t^x = x_t - x_t^{\mathcal{A}}, \tag{4.1}$$

where x represents each of the Delaunay variables (l, g, h, L, G, H), x_t is the simulated data at epoch t, and $x_t^{\mathcal{A}}$ is the data from the analytical theory at the same epoch. Therefore, these six time series $(\varepsilon_t^l, \varepsilon_t^g, \varepsilon_t^h, \varepsilon_t^L, \varepsilon_t^G, \varepsilon_t^H)$ allocate all the information related to the perturbation forces not considered in the analytical theory (tesseral terms of fourth degree and order and the zonal coefficients J_3 and J_4), as well as the higher orders of the analytical solution, that is, the error of the analytical theory $\mathcal{O}(J_2^2)$, during 10 cycles (and 10 data points per cycle).

Then, the periodogram, a mathematical tool for examining cyclical behaviour in time series, and the autocorrelation functions, a measure of how a time series is correlated with itself at different time delays, are used to identify the time series models (see [5], for further details).

The study of the periodogram and autocorrelation functions of each ε_t^x reveals that all variables show cyclical patterns or periodicities and, moreover, there is very similar behaviour between the time series ε_t^l and ε_t^g and ε_t^L and ε_t^G. For example, this study for ε_t^l and ε_t^g can be seen in Figure 5. However ε_t^h and ε_t^H do not show any similar behaviour between them or with the rest of the time series.

On the other hand, the correlation matrix of the ε_t^x series is shown in Table 1. This matrix presents a strong relationship between ε_t^l and ε_t^g, as their correlation coefficient is near -1 (-0.9607), as well as between their respective conjugate momenta time series errors, ε_t^L and ε_t^G, where their correlation coefficient is near 1 (0.9982).

It is noteworthy to mention that although the intrinsic nature of the mean anomaly and the argument of the perigee is different, as mean anomaly is related to short-periodic terms and the argument of the perigee is related to long-periodic terms, the similar behaviours detected in the above statistical studies can be explained, because the Quasi-Spot satellite is near a repeat ground track orbit, in which the argument of the perigee and eccentricity $(e = \sqrt{1 - (G/L)^2})$ are almost constant. Figure 6 shows ε_t^l, ε_t^g and ε_t^L, ε_t^G time series. As can be observed, ε_t^l and ε_t^g are almost symmetric with respect to the x-axis, which explains the negative sign and the near -1 value in the correlation coefficient, whilst ε_t^L and ε_t^G are almost the same, and therefore the sign in the correlation coefficient is positive with a near 1 value.

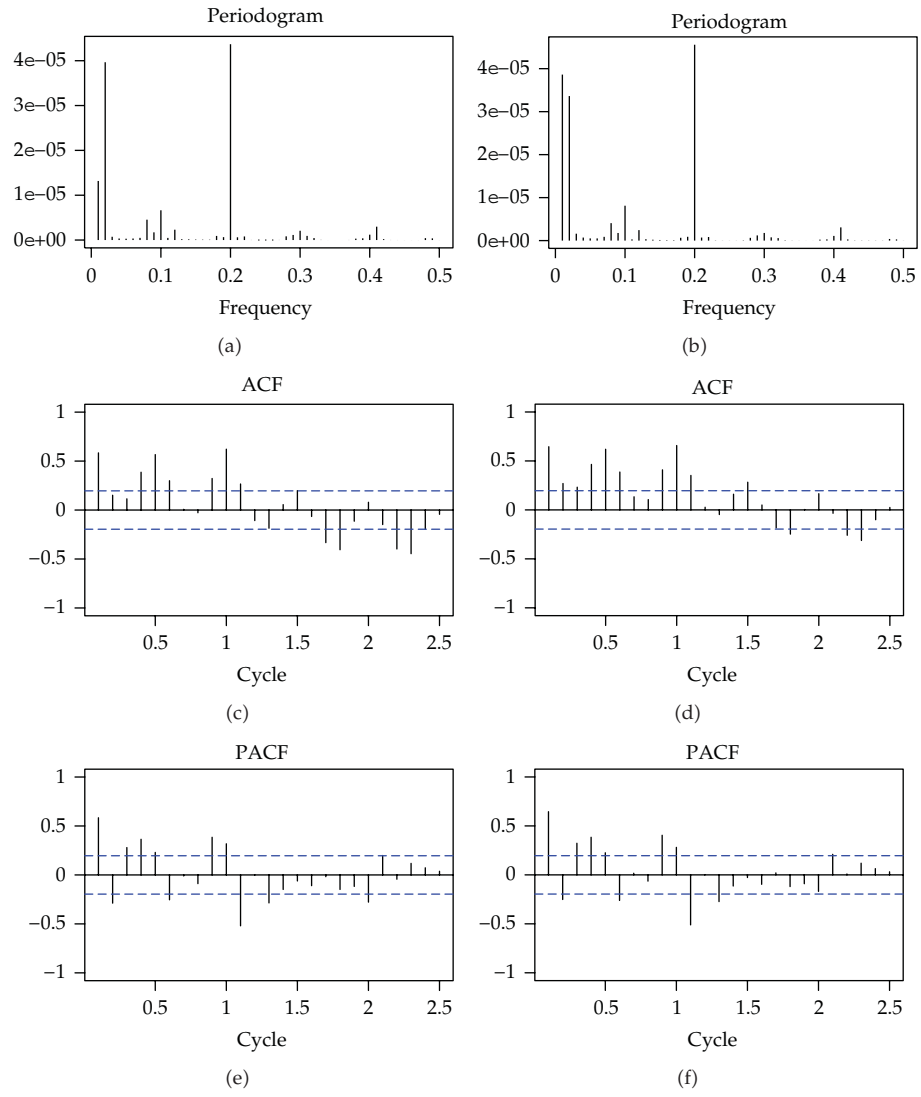

Figure 5: Periodograms and autocorrelation functions of ε_t^l (left) and ε_t^g (right).

Table 1: Correlation matrix of the ε_t^x series.

	ε_t^l	ε_t^g	ε_t^h	ε_t^L	ε_t^G	ε_t^H
ε_t^l	1.0000					
ε_t^g	−0.9607	1.0000				
ε_t^h	−0.0575	−0.1713	1.0000			
ε_t^L	−0.1037	0.0934	0.0451	1.0000		
ε_t^G	−0.1128	0.1168	−0.0070	0.9982	1.0000	
ε_t^H	0.4033	−0.4114	0.0420	0.0066	0.0005	1.0000

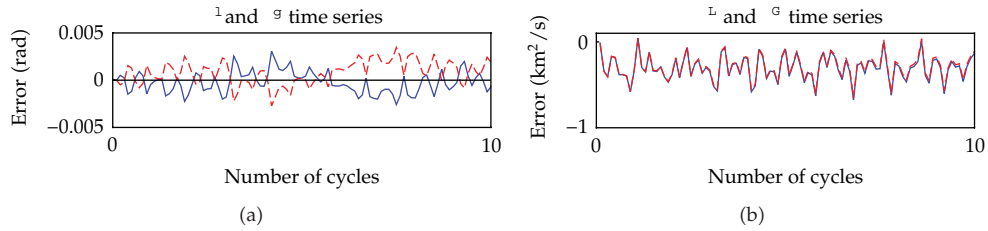

Figure 6: Blue represents ε_t^l, and ε_t^L errors. Dashed red represents ε_t^g and ε_t^G errors.

Finally, this preliminary study can be completed by analyzing the results obtained when the ε_t^x time series are combined with the data obtained from the analytical theory $(l_t^{\mathcal{A}}, g_t^{\mathcal{A}}, h_t^{\mathcal{A}}, L_t^{\mathcal{A}}, G_t^{\mathcal{A}}, H_t^{\mathcal{A}})$ during the first 10 satellite cycles. This test allows us to consider several possibilities. The first consists of considering each series separately, for instance, $(l_t^{\mathcal{A}} + \varepsilon_t^l, g_t^{\mathcal{A}}, h_t^{\mathcal{A}}, L_t^{\mathcal{A}}, G_t^{\mathcal{A}}, H_t^{\mathcal{A}})$. In all these cases the accuracy is not as good as the approach given by the Z2DN1 AOPP. After considering other possibilities we show the relations obtained in previous statistical analyses:

(i) $(l_t^{\mathcal{A}} + \varepsilon_t^l, g_t^{\mathcal{A}} + \varepsilon_t^g, h_t^{\mathcal{A}}, L_t^{\mathcal{A}}, G_t^{\mathcal{A}}, H_t^{\mathcal{A}})$,

(ii) $(l_t^{\mathcal{A}}, g_t^{\mathcal{A}}, h_t^{\mathcal{A}}, L_t^{\mathcal{A}} + \varepsilon_t^L, G_t^{\mathcal{A}} + \varepsilon_t^G, H_t^{\mathcal{A}})$,

(iii) $(l + \varepsilon_t^l, g_t^{\mathcal{A}} + \varepsilon_t^g, h_t^{\mathcal{A}}, L_t^{\mathcal{A}} + \varepsilon_t^L, G_t^{\mathcal{A}} + \varepsilon_t^G, H_t^{\mathcal{A}})$,

(iv) $(l_t^{\mathcal{A}}, g_t^{\mathcal{A}}, h_t^{\mathcal{A}} + \varepsilon_t^h, L_t^{\mathcal{A}}, G_t^{\mathcal{A}}, H_t^{\mathcal{A}} + \varepsilon_t^H)$.

Figure 7 shows the distance errors between the simulated data and analytical theory for the first ten cycles, and the simulated data and the above corrected analytical theories with the exact error added. The strong influence of ε_t^l and ε_t^g can be seen in the first plot; the distance error is reduced to 0.63 km after ten satellite cycles, whereas ε_t^L and ε_t^G only remove part of the short-period variations, as can be seen in the second plot. The third case collects the corrections due to ε_t^l, ε_t^g, ε_t^L, and ε_t^G, which produce a distance error similar to the first case. Finally, the corrections due to ε_t^h and ε_t^H do not have any effect on the distance error, as can be observed in the last plot.

Next we focus our attention on carrying out a hybrid-AOPP from $(l_t^{\mathcal{A}} + \varepsilon_t^l, g_t^{\mathcal{A}} + \varepsilon_t^g, h_t^{\mathcal{A}}, L_t^{\mathcal{A}}, G_t^{\mathcal{A}}, H_t^{\mathcal{A}})$. The following step in the process of looking for the most suitable SARIMA models using the Box-Jenkins methodology is described below.

4.2. Time Series Estimation of ε_t^l and ε_t^g

To estimate the model of the ε_t^g time series, we use the Box-Jenkins methodology. In the first step, the stationary behaviour of the time series is analyzed. Figure 6 suggests that the variance is time-invariant, whereas for the mean value the plot is not conclusive. On the other hand, Figure 5 shows that the autocorrelation function (ACF) decreases slowly and the augmented Dickey-Fuller test [10] allows accepting the null hypothesis that the time series has a unit root (P value 0.6921 $>$ 0.05). Moreover, its periodogram (see Figure 5) shows high peaks at low frequencies (f = 0.01 and 0.02). Therefore, the time series does not seem stationary; thus differentiating the time series data may be necessary.

The second step analyzes the periodicity. The ACF shows a pronounced cyclical fluctuation with a strong correlation at lag 10. Besides, its periodogram shows a peak at

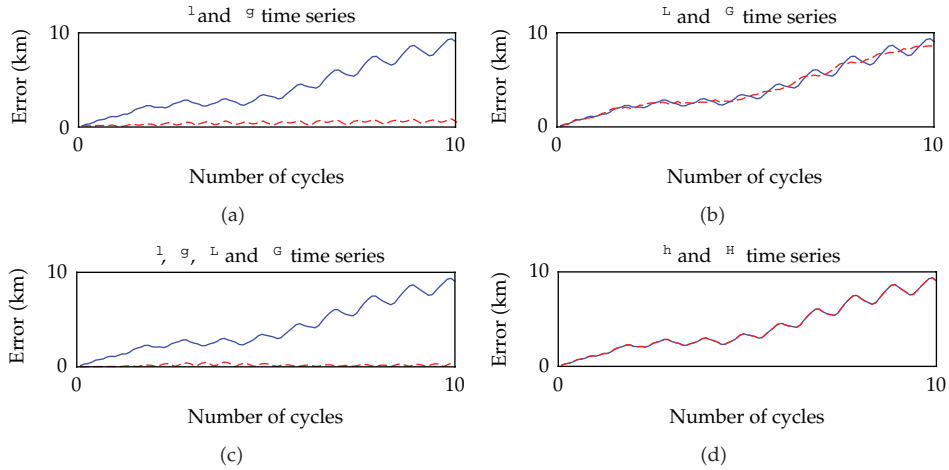

Figure 7: Blue represents the distance error between $\mathbf{x}_{t_i}$ and $\mathbf{x}_{t_i}^{\mathcal{A}}$, whereas dashed red is the distance error between $\mathbf{x}_{t_i}$ and the corrected $\mathbf{x}_{t_i}^{\mathcal{A}}$ from the exact ε_t^x.

the frequency of 0.2, which corresponds to a periodicity of 10. These patterns agree with the satellite cycle. This suggests that a seasonal model might be adequate to estimate ε_t^g. Consequently, the tentative models should incorporate both seasonal and nonseasonal parameters.

We analyzed different SARIMA$(p,d,q)(P,D,Q)_{10}$ models in order to approximate the ε_t^g time series, where the maximum likelihood method was used to estimate model parameters, as can be seen in Table 2. Finally, the diagnostic stage showed a good fit for the SARIMA$(6,1,7)(3,1,3)_{10}$ model, in which the Jarque-Bera and Ljung-Box tests [11, 12] do not reject the null hypothesis of normality nor the no autocorrelation of residuals, with P values 0.182 and 0.993, respectively.

We must note that the model used to approximate the ε_t^l time series is also a SARIMA$(6,1,7)(3,1,3)_{10}$, which confirms the similar behaviour previously detected to ε_t^g, although the model parameters are slightly different, as can be seen in Table 2.

The GNU software R (version 2.14) [13] was the statistical tool used to perform all statistical analyses. In particular, the R packages TSA [14], forecast [15], and tseries [16] were used for all time series analyses.

5. Z2DN1-SARIMA Hybrid-AOPP

Figure 8 shows the flowchart of the Z2DN1-SARIMA hybrid-AOPP. We find the difference to the pure Z2DN1 AOPP (Figure 1) after applying the direct transformation of the Delaunay normalization. At this point, the Delaunay variables are combined with the new forecast $(\hat{\varepsilon}_t^l, \hat{\varepsilon}_t^g)$ and the osculating Keplerian elements (a,e,g,h,i,l) and state vector $(x,y,z,\dot{x},\dot{y},\dot{z})$ are calculated.

At this point, it is noteworthy that a pure analytical theory which takes into account the perturbation of the fourth degree and order harmonic coefficients of the gravity field, considering the dimensionless parameter ω/n, where n is the mean motion of the satellite, and the usual Garfinkel assumptions [17] with a precision of about one kilometer after

Table 2: SARIMA$(6,1,7)(3,1,3)_{10}$ models.

Coefficients	ε_t^l	ε_t^g
ϕ_1	−0.8167142581776827	−0.8312754102958296
ϕ_2	0.5740668630692614	0.5649950239467217
ϕ_3	1.1200190576112987	1.1322145773449677
ϕ_4	−0.3087269639691513	−0.2946598587646277
ϕ_5	−0.8631472597887673	−0.8663595825987899
ϕ_6	−0.4970128310547080	−0.5012076262623468
θ_1	0.8789635328932761	0.8901438163231377
θ_2	−0.9965719584754135	−0.9834775736328421
θ_3	−1.6921042908035564	−1.7044561386678760
θ_4	0.5206249360614155	0.4906661687944900
θ_5	1.5190020299259381	1.5136974115875366
θ_6	0.3606298858846529	0.3820758183271771
θ_7	−0.4721289483358399	−0.4568107050477830
Φ_1	1.4676902604680244	1.4557054355067451
Φ_2	−1.3618276394078148	−1.3525881149216927
Φ_3	0.7076454044934742	0.7023619159769664
Θ_1	0.8412748367694940	0.8370722835862818
Θ_2	−0.8240640881053386	−0.8282527898256336
Θ_3	0.9939014392344844	0.9966285211365780

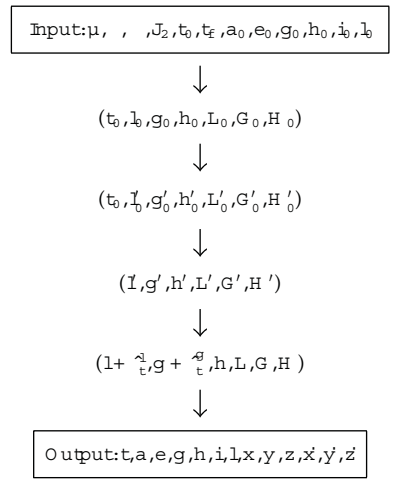

Figure 8: Flowchart of the Z2DN1-SARIMA hybrid orbit propagator program.

30 days, involves several mathematical expressions of more than 10000 terms, whereas the whole Z2DN1 analytical theory only needs to evaluate 93 terms. The technical details of the tesseral analytical theory have been developed in [18, 19].

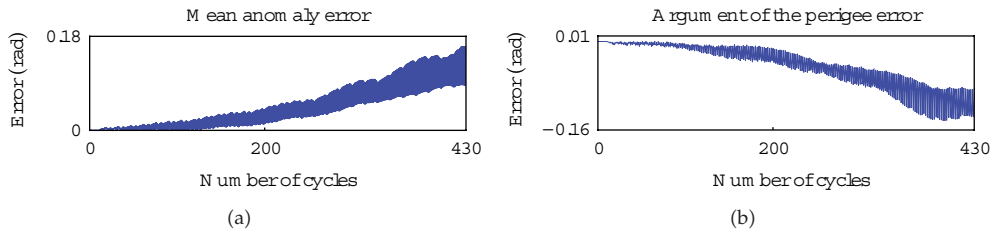

Figure 9: Z2DN1-SARIMA hybrid-AOPP. Relative errors of the mean anomaly and argument of the perigee for a Quasi-Spot satellite.

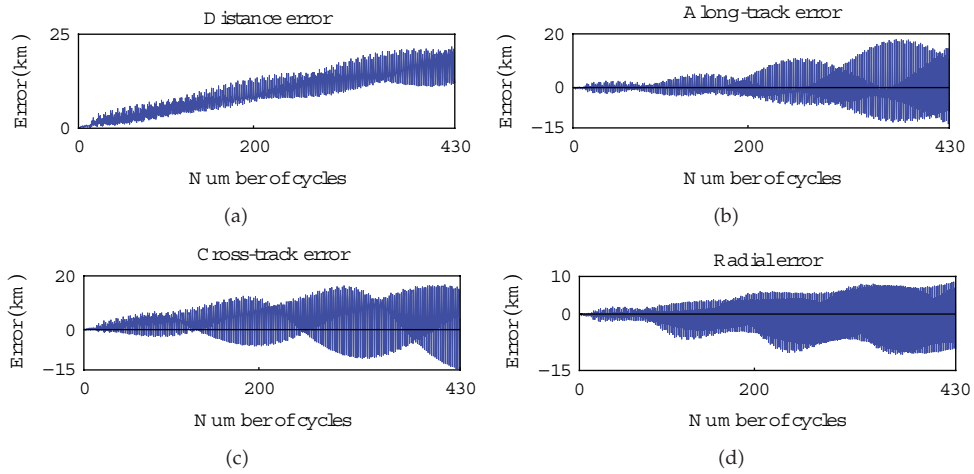

Figure 10: Z2DN1-SARIMA hybrid-AOPP. Distance, along-track, cross-track, and radial errors for a Quasi-Spot satellite.

5.1. Numerical Validations

Finally we analyze the behaviour of Z2DN1-SARIMA hybrid-AOPP designed for a Quasi-Spot satellite versus the numerical integration for an Earth orbiter, which has only taken into account the perturbation due to the nonsymmetrical Earth gravity field up to the fourth degree and order. The first 10 cycles are considered for the estimation stage, whilst from the 10th and up to approximately the 430th cycle, which is about 30 days, are used in the forecasting stage.

Figure 9 shows the relative errors of the mean anomaly and argument of the perigee for a Quasi-Spot satellite. The maximum absolute errors of mean anomaly and argument of the perigee in a time span interval of 30 days are about 9.4° and 8.2°, respectively. These errors have been reduced to 3° in the case of the mean anomaly and to 1.3° in the argument of the perigee, with respect to the Z2DN1 AOPP.

Figure 10 shows the distance, along-track, cross-track, and radial errors. The maximum distance error obtained from Z2DN1 AOPP is 352.076 km while for Z2DN1-SARIMA it is only 23.7489 km. We must remark that the accuracy obtained by the described hybrid-AOPP is only comparable to a higher-order analytical theory, which includes a more precise perturbation model.

6. Conclusions and Future Works

A new methodology to carry out hybrid-AOPP families, based on the combination of an analytical orbit propagator program and statistical time series models, is presented. To illustrate this methodology, a hybrid-AOPP, named Z2DN1-SARIMA, has been developed, which combines an economic first-order closed-form analytical orbit propagator and two SARIMA time series models fitted to the case of the Quasi-Spot satellite. Although the increment in the computational time cost is not significant with respect to the pure analytical theory, the error of our theory is reduced in comparison to the pure Z2DN1 AOPP. The accuracy reached by our new hybrid model is similar to that obtained by a more complex zonal and tesseral analytical theory, but without the inconvenience of losing computational efficiency.

To calculate the SARIMA models, 10 satellite cycles are considered and the univariate Box-Jenkins time series analysis is used to model the ε_t^x time series, using statistical software packages for R. Two of the six components were modelled, whilst, at present, we are working on the study of the bivariate SARIMA models in order to collect the similar behaviour found between the mean anomaly and the argument of the perigee. In the study of the argument of the node and the third component of angular momentum behaviour, we are performing an economic analytical theory, which includes tesseral coefficients.

The behaviour of the Z2DN1-SARIMA hybrid-AOPP with respect to other initial conditions near the Quasi-Spot conditions, as well as the adapted hybrid-AOPP, when other perturbations, like atmospheric drag, third body, and so on, are taken into account, is future works to be investigated.

Acknowledgments

This work has been supported by the Gobierno de La Rioja (Project Fomenta 2010/16). Special thanks are given to the reviewer for constructive advice and thoughtful reviews and comments pointed out and to K. Hatcher for the revision of this paper.

References

[1] D. Brouwer, "Solution of the problem of artificial satellite theory without drag," *The Astronomical Journal*, vol. 64, pp. 378–397, 1959.

[2] K. Aksnes, "A second-order artificial satellite theory based on an intermediate orbit," *Astronomical Journal*, vol. 75, no. 9, pp. 1066–1076, 1970.

[3] H. Kinoshita, "Third-order solution of an artificial satellite theory, Smithsonian Astrophysical Observatory," Special Report No. 379, Cambridge, Mass, USA, 1977.

[4] F. R. Hoots and R. L. Roehrich, *Spacetrack Report No. 3: Models for Propagation of the NORAD Element Sets*, U.S. Air Force Aerospace Defense Command, Colorado Springs, Colo, USA, 1980.

[5] G. E. P. Box and G. M. Jenkins, *Time Series Analysis: Forecasting and Control*, Holden-Day, San Francisco, Calif, USA, 1976.

[6] A. Deprit, "Delaunay normalisations," *Celestial Mechanics and Dynamical Astronomy*, vol. 26, no. 1, pp. 9–21, 1982.

[7] A. A. Kamel, "Peturbation method in the theory of nonlinear oscillations," *Celestial Mechanics*, vol. 3, no. 1, pp. 90–106, 1970.

[8] J. F. San-Juan, L. M. López, and R. López, "MathATESAT: a symbolic-numeric environment in astrodynamics and celestial mechanics," *Lecture Notes in Computer Science*, vol. 6783, no. 2, pp. 436–449, 2011.

[9] J. R. Dormand and P. J. Prince, "Practical runge-kutta processes," *SIAM Journal on Scientific and Statistical Computing*, vol. 10, no. 5, pp. 977–989, 1989.

[10] D. A. Dickey and W. A. Fuller, "Distribution of the estimators for autoregressive time series with a unit root," *Journal of the American Statistical Association*, vol. 74, no. 366, pp. 427–431, 1979.

[11] C. M. Jarque and A. K. Bera, "Efficient tests for normality, homoscedasticity and serial independence of regression residuals," *Economics Letters*, vol. 6, no. 3, pp. 255–259, 1980.

[12] G. M. Ljung and G. E. P. Box, "On a measure of lack of fit in time series models," *Biometrika*, vol. 65, no. 2, pp. 297–303, 1978.

[13] R Development Core Team, *R: A Language and Environment For Statistical Computing*, R Foundation for Statistical Computing, Vienna, Austria, 2011, http://www.Rproject.org/.

[14] K. Chan, "TSA: Time Series Analysis, R package version 0. 98," 2010, http://CRAN.R-project.org/package=TSA/.

[15] R. J. Hyndman, "Forecast: Forecasting functions for time series, R package age version 2.09," 2010, http://CRAN.R-project.org/package=forecast/.

[16] A. Trapletti and K. Hornik, "Tseries: Time Series Analysis and Computational Finance, R package version 0.10-27," 2011, http://CRAN.Rproject.org/package=tseries/.

[17] B. Garfinkel, "Tesseral harmonic perturbations of an artificial satellite," *The Astronomical Journal*, vol. 70, pp. 784–786, 1965.

[18] J. F. San-Juan and S. Serrano, "ATESAT: revisited and improvements. Analytical theory and numerical validation for a SPOT-like satellite," Tech. Rep. No. DTS/MPI/MS/MN/2000-013, Centre National d'Etudes Spatiales, Toulouse, France, 2000.

[19] S. Serrano, *Teoras Analtícas del Movimiento de un Satélite Artificial alrededor de un Planeta. Ordenación Asintótica del Potencial en el Espacio [Fśico Ph.D.]*, Universidad de Zaragoza, 2003.

Hindawi Publishing Corporation
Mathematical Problems in Engineering
Volume 2012, Article ID 817528, 14 pages
doi:10.1155/2012/817528

Research Article

Buffer Management and Hybrid Probability Choice Routing for Packet Delivery in Opportunistic Networks

Daru Pan, Wei Cao, Han Zhang, and Mu Lin

School of Physics and Telecommunication Engineering, South China Normal University, Guangzhou 510006, China

Correspondence should be addressed to Daru Pan, pandaru@126.com

Received 8 April 2012; Accepted 20 May 2012

Academic Editor: Carlo Cattani

Due to the features of long connection delays, frequent network partitions, and topology unsteadiness, the design of opportunistic networks faces the challenge of how to effectively deliver data based only on occasional encountering of nodes, where the conventional routing schemes do not work properly. This paper proposes a hybrid probability choice routing protocol with buffer management for opportunistic networks. A delivery probability function is set up based on continuous encounter duration time, which is used for selecting a better node to relay packets. By combining the buffer management utility and the delivery probability, a total utility is used to decide whether the packet should be kept in the buffer or be directly transmitted to the encountering node. Simulation results show that the proposed routing outperforms the existing one in terms of the delivery rate and the average delay.

1. Introduction

Opportunistic networks [1–4] are one of the most emerging communication paradigms in wireless mobile communications where most of the time the path from a source to a destination is unstable and may break and be discovered from time to time [5, 6]. In this case, how to effectively deliver data based only on occasional encountering of nodes becomes a challenge, since the conventional cannot be adopted straightforwardly. To deal with the unpredictability in connections and network partitions, many routing protocols adopt flooding-based and store-carry-forward routing schemes, such as Epidemic Routing (ER) [7], Spray and Waiting [8–10], PRoPHET [11], and MaxPROP [12], to improve the message delivery, where a node receives packets, stores them in their buffers, carries them while moving, and forwards them to other nodes when they encounter each other.

Epidemic is one of the first routing schemes, adopting the store-carry-forward paradigm. In Epidemic Routing, packets are disseminated in broadcast mode as infectious diseases spread. This packet-spread will continue until all the nodes have a copy of the packet or its TTL (time-to-live) expires. Although, Epidemic Routing achieves eventual delivery of 100% of messages, but it makes no attempt to eliminate replication, and the high delivery rate is at the expense of the network resource consumption, such as storage of buffer space and transmission bandwidth [13, 14]. Performance of ER will get worse when the network traffics congest. Spray and Wait [8, 9, 15] combines the speed of ER with the simplicity and thriftiness and reliability of direct transmission and makes an effort to perform fewer transmissions by controlling the number of packet copies in spray phase and utilizing direct transmission in wait phase. While in scenarios of a high mobility model (like community-based mobility), the direct transmission based wait phase in Spray and Wait routing has low efficiency in delivery delay and probability. ProPHET [11] presents an estimation-based forwarding scheme to direct the messages to the destination node. The basic operation of ProPHET is similar to that of Epidemic. When two nodes meet each other, each node exchanges its summary vectors and delivery predictability to each other. The delivery predictability in the summary vector is used to make a forwarding decision for the packets' delivery. ProPHET is a single-copy forwarding-based scheme, and the limited copy may result in the performance limitation of the initial probability distribution.

Most of the studies on opportunistic networks have been investigated in the design of efficient routing, but few literature focused on buffer management, which is important for the store-carry-forward paradigm, for example, Epidemic Routing has minimum delivery delay under no buffer constrains, but performs worse than other routings when buffer sizes are limited. Most of the routings use the simple drop-tail policy without taking the buffer management into account. However, how to utilize spatial, temporal, and buffer information to make an optimal decision for delivering the packets is an open issue.

In this paper, we propose a hybrid probability choice routing protocol with buffer management. The main work of the proposed method is (1) to set up a delivery probabilities function based on the continuous encounter duration time and buffer information, (2) to let nodes decide how many copies will be transmitted to the encountering nodes according to their delivery probabilities to the destination in the spray phase, and (3) to combine the buffer utility and delivery probability to construct a total utility and to directly deliver the last copy to the encountering node according to the total utility in the wait phase.

The rest of the paper is organized as follows. We give an overview and detailed information of our algorithm in Section 2. We evaluate our scheme through simulation in Section 3 and draw a conclusion in Section 4.

2. Design of Probability Choice Routing Protocol with Buffer Management

2.1. Network Model

This paper considers the probabilistically contacted opportunistic networks where the networks consist of nodes representing portable wireless devices held by moving elements such as people or vehicles in a community. We model an opportunistic network as a dynamic set of mobile nodes. Nodes may join and leave the network at any time. In our opportunistic scenario, there are three groups of moving elements: pedestrian, bicycles, and vehicles. Each

group of moving elements follows the map-based movement model with different speed. We use 30 vehicles following predefined routes, 60 nodes are pedestrians, and 30 nodes are bicycles. The vehicles and bicycles choose random destinations in their reach on the map. The number of different moving elements can be changed, which does not affect the characteristics of basic communication.

Communications are based on pairwise contacts [10, 16, 17]. Through the pairwise encountering of mobile elements, data stored in devices are opportunistically forwarded over the network. Nodes are assumed to have homogeneous capability in terms of computation, communication, and storage. Opportunistic forwarding decisions are made without the help of the localization services. Their communication capacity is limited by specific wireless techniques. For example, through Bluetooth, node can contact with each other when each of two nodes enters the other's communication range. Two nodes in the network are neighbors and can transfer data packets bidirectional if they are within the communication range. Data is forwarded in a store-and-forward manner, which allows nodes to store data temporarily until running into a more competent node to further forward them. We consider a multicopy scenario. The network model can be presented concretely as follows. The topology of the networks is modeled as a graph $G = (V, E)$, V is the set of nodes, and E is the set of hyperarcs. Each node in the network can be a source or destination of traffic.

2.2. Motivation of the Protocol

The core of the processing is how to rank the relay nodes based on the measurement of the delivery predictability and buffer utility. Addressing the above issue, each node records its location and context to a historical information database. Nodes renew their routing passively and share their location and moving information. When a node encounters another node, each node exchanges its location and historical moving information and decides whether it delivers its packets to the encountering node by calculating the delivery predictability, which is based on the historical encounter duration time and buffer situation. Based on this prediction, the node will make a wise decision to deliver the packets or not in both the spray phase and wait phase. In the wait phase of the original Spray and Wait, a node with the last copy has to wait until it encounters the destination, the node will not hand over the last copy to any nodes that might have more chances to encounter the destination, so it might waste some opportunity and keep the buffer out of space. In this scheme, we make an effort to let nodes exchange SV (Summary Vector) once a node with the last one copy encounters a node. We calculate the total utility according to the buffer utility and delivery probability. If the total utility is higher than a given threshold, the node will hand over the last copy to it.

2.3. Delivery Predictability Calculation

In the spray phase of original Spray and Wait routing, for each message originating at a source node, L message copies are initially sprayed and relayed by nodes. An optimal Spray and Wait scheme-Binary Spray and Wait (BSW) is proposed in [8] to speed up the spray phase and improve the routing performance, where any node with $n \geq 1$ copies hands over half copies to the encountered node until $n = 1$. However, if the relay is a very inactive node, which does not contact with other nodes, handing over half the copies to such a node means half of the relay chances will be wasted. In order to overcome this problem, we introduce a novel scheme to the spray phase, where we set up a delivery probability to the destinations for each node as the ProPHET routing [11] does, and nodes exchange different numbers of

copies to each other according to their delivery probabilities $P_{(a,b)} \in [0,1]$, that is, when $P_{(a,b)}$ is larger than a threshold value $P_{\text{threshold}}$, node a will hand over half its copies to node b, otherwise, it will only hand over one copy to node b. The delivery probabilities are updated as follows.

(1) Whenever a node is encountered, the delivery predictability is updated as (2.1), where P_{init} is an initialization constant. It is recommended in [18] that the referential value of P_{init} is 0.75:

$$P(a,b) = P(a,b)_{\text{old}} + (1 - P(a,b)_{\text{old}}) \times P_{\text{init}}. \tag{2.1}$$

(2) The aging equal is shown in (2.2), where $\gamma \in (0,1]$ is the aging constant and k is the number of time units that has elapsed since the last time the metric was aged:

$$P(a,b) = P(a,b)_{\text{old}} \times \gamma^{k}. \tag{2.2}$$

(3) Transitive affection is shown in (2.3), where β is a scaling constant that decides how large impact the transitivity should have on the delivery predictability. It is recommended in [18] that the referential value of β is 0.25:

$$P(a,c) = P(a,c)_{\text{old}} + (1 - P(a,c)_{\text{old}}) \times P(a,b) \times P(b,c) \times \beta. \tag{2.3}$$

In real opportunistic networks, the communication range of nodes, moving speed, and bandwidth may be different. When the network is in an unstable situation, such that the nodes' moving speeds are too fast and have different communication ranges, the links will interrupt frequently. In this case, the nodes encounter each other from time to time according to the link's situation. The number of nodes encountering cannot reflect the real ability of communication between nodes anymore. Based on this observation, we revise (2.1) and (2.2) using the continuous time t to calculate the delivery as that of [19], where τ is a constant, and t is the time that has elapsed since the last encounter time:

$$P_t = P_{\text{old}} \times e^{-\tau t}. \tag{2.4}$$

Compared with (2.2) and (2.4), let

$$t = ku, \quad P_t(a,b) = P(a,b), \tag{2.5}$$

then

$$\begin{gathered} \left(e^{-\tau}\right)^{t} = \left(\gamma^{1/u}\right)^{t} = \left(e^{(1/u)\ln\gamma}\right)^{t} \mid P_{\text{old}} \neq 0, \\ \tau = -\frac{1}{u}\ln\gamma, \end{gathered} \tag{2.6}$$

and then (2.1) can be rewritten as follows:

$$P(a,b) = 1 - e^{-ct_{\text{up}}}(1 - P(a,b)_{\text{old}}), \tag{2.7}$$

$$c = -\frac{1}{u'}\ln(1 - P_{\text{init}}). \tag{2.8}$$

In this way, the discrete-time signal is changed into the continuous-time signal. Therefore, the noise, which is introduced by different encounter communication range and moving speeds, can be removed by certain filter.

2.4. Optimal Node Selection with Buffer Management

In this subsection, we try to maximize the average delivery rate by using a buffer management. In opportunistic networks, nodes have finite buffer space, so they must eventually discard old copies to make room for new requests. Normally, copies will be discarded when the Time to Live (TTL) is elapsed. If the TTL elapsed before the nodes encounter any nodes, the copies will be dropped; otherwise, a decision of which copies should be dropped must be made when the buffer is filled up. Thus, the encountering interval of nodes should be considered. The encountering interval between nodes depends on the value of the mobility model. We assume that there is enough time to exchange their packets. The encountering time (T) between nodes is defined as the time it takes them to first come within transmission rang ($R = \min(r_a, r_b)$). Based on the experimental study, it has been shown that the meeting time of some random-based mobility models like Random Walk, Random Waypoint, and Random Direction is exponentially distributed or has at least an exponential tail, with parameter $\lambda = 1/E(T)$, where $E(T)$ denotes the expectation of a random variable T. We use these mobility models for our test scenarios. And, then, the probability that a copy of a message j will not be delivered is equal to the probability that the next encountering time with the destination node is greater than the remaining Time to Live $R_j(\text{TTL})$ for message j. That is $\exp(-\lambda R_j(\text{TTL}))$. Based on this model, it has been proved that in order to maximize the average delivery rate, the optimal policy of buffer management should drop the message with the lowest probability to delivery [14]. The optimal policy of buffer management uses the Epidemic Routing, whose number of message copies is uncontrolled. Different from that, we employ a fixed number L of copies for messages. The probability that the message will not be delivered can be derived as follows:

$$P_j(\text{undelivered}) = \exp\left(-\lambda n_j R_j(\text{TTL})\right). \tag{2.9}$$

Here, n_j is the total number of copies of message j in network. And the probability of a message being delivered is:

$$P_j(\text{delivered}) = \frac{m_j}{N-1}, \tag{2.10}$$

where N is the number of nodes in the network and m_j is the number of nodes that have ever stored message j. Then, the probability of message that will be delivered can be derived as follows:

$$P_j = P_j(\text{delivered})\left(1 - \exp\left(-\lambda n_j R_j(\text{TTL})\right)\right) + P_j(\text{delivered}), \tag{2.11}$$

$$P_j = \left(1 - \frac{m_j}{N-1}\right)\left(1 - \exp\left(-\lambda n_j R_j(\text{TTL})\right)\right) + \frac{m_j}{N-1}. \tag{2.12}$$

Hence, the maximum of average delivery rate is achieved by maximizing P_j, then we can maximize the average delivery rate. Taking the derivation of (2.12) with respect to n_j:

$$\frac{\partial P_j}{\partial n_j} = \left(1 - \frac{m_j}{N-1}\right)\lambda R_j \exp\left(-\lambda n_j R_j(\text{TTL})\right)\Delta n_j. \tag{2.13}$$

From (2.13), the best drop decision is to drop the message j satisfying:

$$j_{\min} = \arg\min_j \left[\left(1 - \frac{m_j}{N-1}\right)\lambda R_j \exp\left(-\lambda n_j R_j(\text{TTL})\right)\right]. \tag{2.14}$$

Since we are using the fixed number L of the copies, when the proposed routing comes to waiting phase, it means that the nodes have only one copy of the message j. For the worst case, none of them contacts destination node. Replacing n_j with the total number of copies L for (2.14), we get

$$j_{\min} = \arg\min_j \left[\left(1 - \frac{m_j}{N-1}\right)\lambda R_j \exp\left(-\lambda L R_j(\text{TTL})\right)\right]. \tag{2.15}$$

We define the buffer utility as follows:

$$U_j = \left(1 - \frac{m_j}{N-1}\right)\lambda R_j \exp\left(-\lambda L R_j(\text{TTL})\right), \tag{2.16}$$

where value of m_j is a global state of the message in the network. We can calculate it by using the local information. Suppose that

$$m_j = \overline{m}_j = E(M(T)), \tag{2.17}$$

where $M(T)$ is a random variable, which follows the approximated of a Gaussian distribution.

In the fixed number copies' routing, the success delivery rate depends on the threshold of the number of copies and the spray strategy. Multiple-copy routing utilizes multiple paths to transfer packets. Therefore, the node with larger delivery predictability should have more copies of the packet. While the source spray and binary spray strategies used in Spray and Wait routing do not consider the different utilities of the nodes. They spray the packets

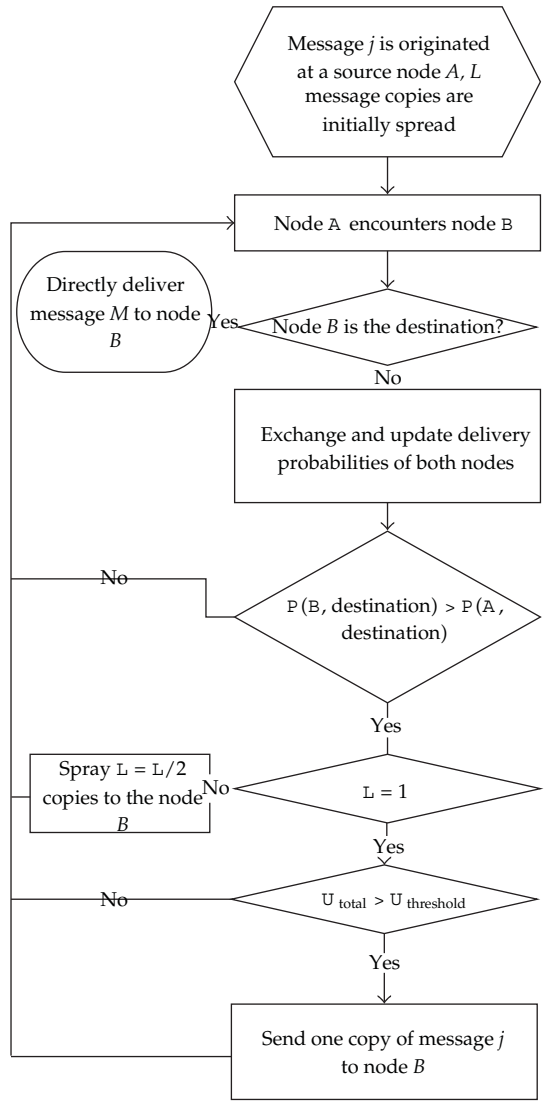

Figure 1: Flow chart of the proposed routing.

equally for each node. According to the analysis in Section 2.3, we apply a simple spray strategy based on mean delivery predictability to the routing. Set B as the sum of average contact and intercontact time between encounters of node pairs. We calculate the mean delivery predictability $\overline{P}$ as follows:

$$\overline{P}_{(a,b)} = \frac{1}{B}\int_0^B P_{\text{init}(a,b)} \times e^{-\lambda t}dt, \tag{2.18}$$

when $P > \overline{P}$, half copies $(L/2)$ will be transferred to the encountering node. When $P < \overline{P}$, only one copy will be transferred to the encountering node.

Table 1: Simulation environment parameters.

Simulation parameters	Simulation values
Map size	4500 m × 3400 m
Packet transmission speed	250 kBps (2 Mbps)
Number of nodes	
Pedestrian	60
Bicycles	30
Vehicles	30
Node movement	Shortest Path Map Based Movement
Speed	
Pedestrian	0.5–1.5 m/s
Bicycles	1.4–4 m/s
Vehicles	2.7–13.9 m/s
Transmission range	10 m
Packet size	500 kB–1 MB
Message generation interval	25 s, 35 s

In the wait phase, the original Spray and Wait store message in the buffer until the destination is reached. Sometimes, however, the encountering node may have more chance to encounter the destination, we consider delivering the last copy to the encountering node with a larger delivery probability. Since this policy may lead to no convergence (none of the nodes reach the destination before TTL), we consider the following process.

By combining (2.7) and (2.16), we construct a total utility of buffer utility and delivery probability as follows:

$$U_{\text{total}} = \delta U_j + \psi P(a,b) = \delta\left[1 - e^{-ct_{\text{up}}}\left(1 - P(a,b)_{\text{old}}\right)\right] + \psi\left(1 - \frac{m_j}{N-1}\right)\lambda R_j \exp\left(-\lambda L R_j(\text{TTL})\right), \tag{2.19}$$

where δ and ψ are the weighted factors that represent the impact of buffer utility and delivery probability on the total utility, respectively.

If the total utility U_{total} is larger than a given threshold $U_{\text{threshold}}$, the last copy will be sent to the encountering node, otherwise it will be kept in the buffer until the TTL expires. The flow of the scheme is shown in Figure 1.

3. Simulation and Analysis

This section evaluates the performance of the proposed routing by modifying and developing the traditional Spray and Wait routing in the ONE [15, 20] simulator. We consider a scenario with three classes of nodes, pedestrians, bicycles, and vehicles. The details of the simulation parameters are listed in Table 1.

In the performance evaluation, we compare the proposed protocol with three representative routing protocols: Epidemic Routing (ER), original Spray and Wait (SNW), and ProPHET routing (PRO), respectively. We run all these routings in the same scenario with the above parameters and compare their performance with regard to the success delivery

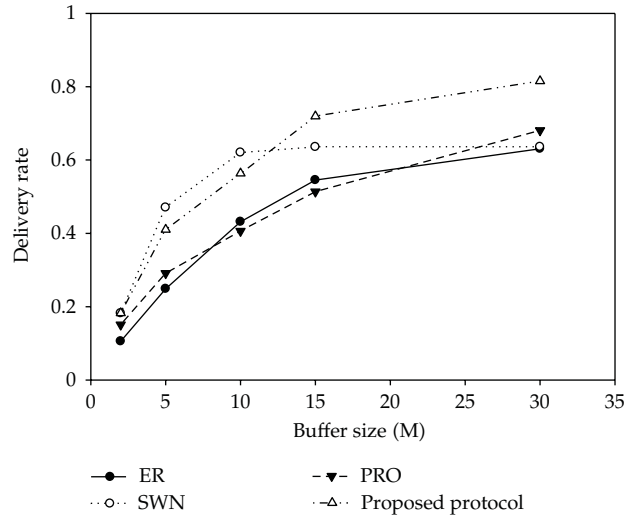

Figure 2: Delivery rate with different buffer size.

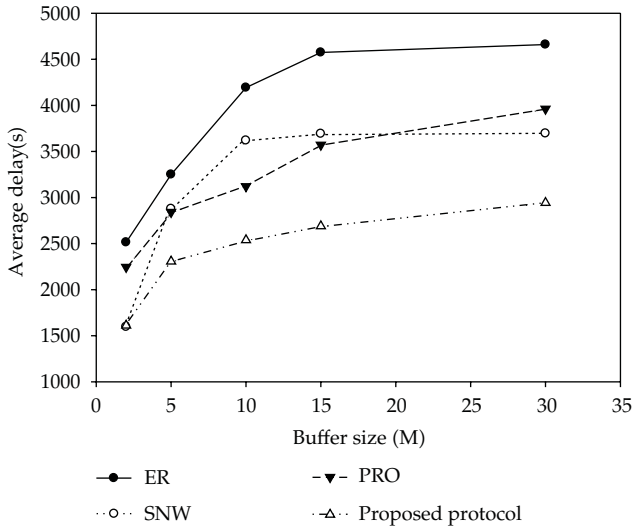

Figure 3: Average delay with different buffer size.

rate and delivery delay under different buffer size, TTL, and total number of messages, respectively.

Figures 2 and 3 show the delivery rate and average delay with variant buffer size for ER, SNW, and PRO in comparison with the proposed optimal probability choice routing protocol with buffer management. Among these routing protocols, the bigger buffer size show the better performance of all protocols, and the performances of SNW and the proposed protocol are better than PRO and ER. This result is due to the use of the limited number of copies among these routings. Note that the proposed protocol provides a higher delivery rate than SNW when the buffer size is larger than 12 M. This result validates the effectiveness of the proposed buffer management policy in Section 2.4.

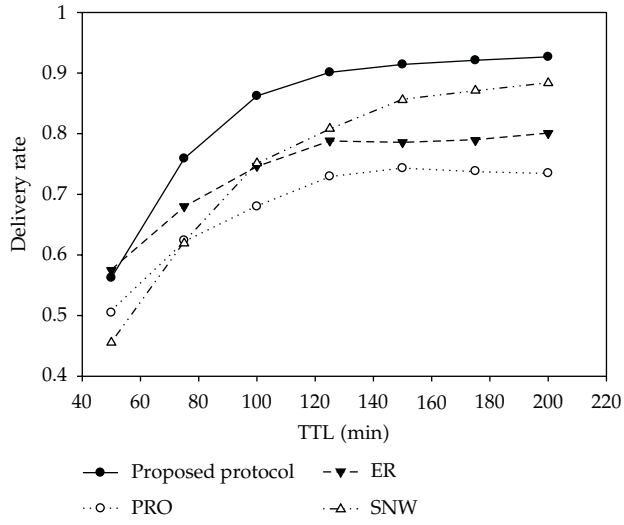

Figure 4: Delivery rate with different TTL.

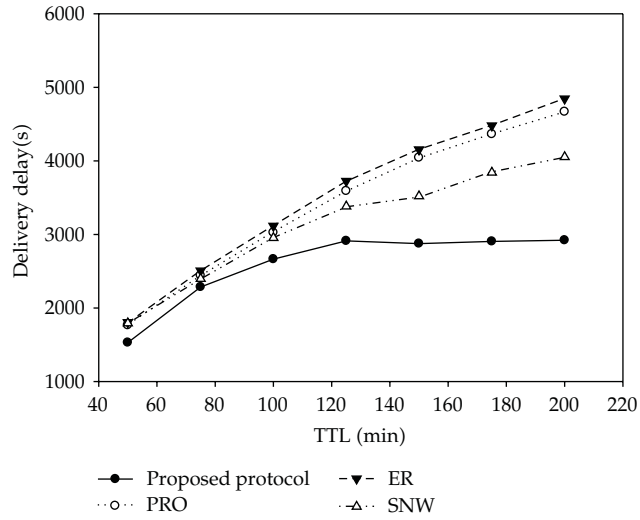

Figure 5: Delay with different TTL.

Figures 4 and 5 show the performance under different TTL. The figures show that the proposed protocol outperforms the other three routing algorithms. Along with the increase of TTL, the delivery rates and the average delivery delays of all the four routings rise gradually. The proposed protocol achieves the largest delivery rate and the shortest delay for all TLL scenarios. This is reasonable because large TTL brings more time for the copies to stay in the relay nodes without discarding, and this helps to increase the success delivery rate, while the long-time staying in nodes will lead to lack of buffer spaces and large average delivery delay, when buffer spaces run out, copies will be discarded again, which will lead to a reduction in success delivery rate. That is, tradeoff is offered in terms of the TTL and buffer space.

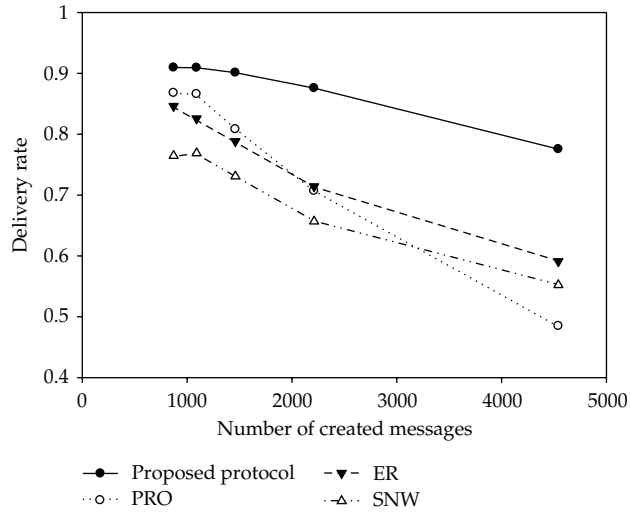

Figure 6: Delivery rate with number of messages.

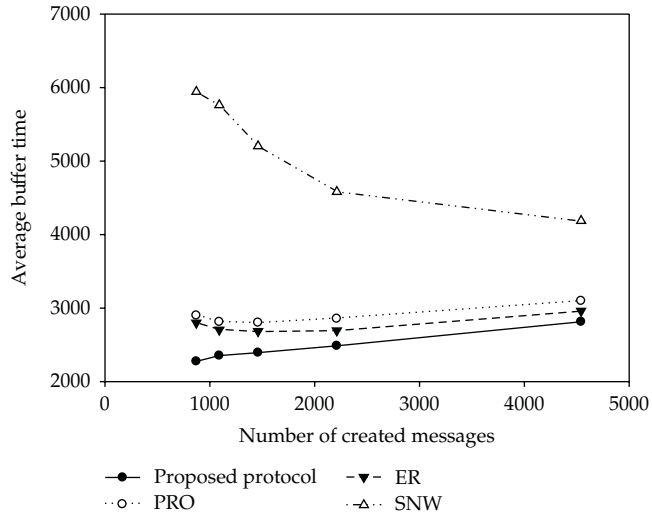

Figure 7: Average buffer time with number of messages.

Although both the proposed protocol and the SNW require more copies than the other schemes, our protocol outperforms the latter as the buffer size is increased. This is because we use directly delivering in the wait phase to transmit the last one copy to the node with a higher delivery probability to destination.

Figures 6, 7, 8, and 9 describe the average delivery rate, average buffer time, the delivery delay, and overhead versus the total number of message. As the traffic increases, the delivery rates and overhead of all the routing protocols decrease, while the average buffer time and delivery delay increase eventually. Overall, the delivery rate of the proposed protocol is the highest one and it is more robust than the other routing protocols, and the average buffer time and overhead of the proposed protocol is kept in a very low level. The

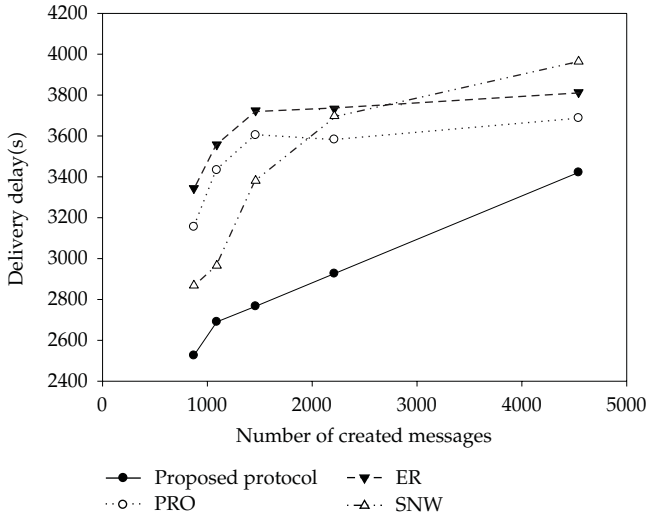

Figure 8: Delivery delay with number of messages.

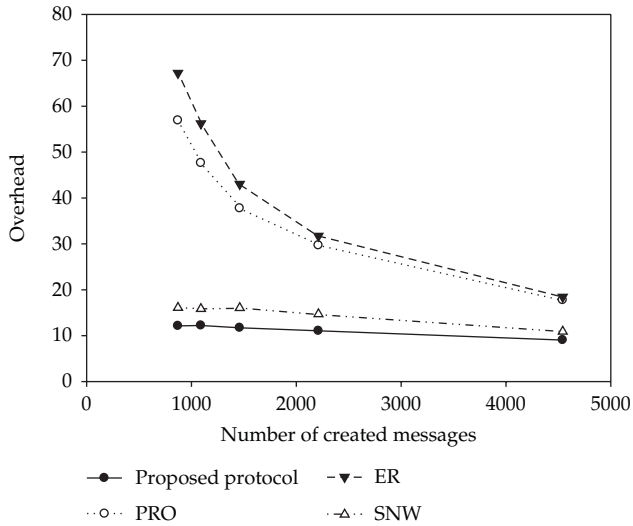

Figure 9: Overhead with number of messages.

reason is as follows. Firstly, we use continuous encounter time to describe the encounter opportunity, which makes it more precisely to describe the encounter opportunity. Secondly, we provide different numbers of exchanging copies to the nodes according to their delivery probabilities to the destination in the spray phase, the node transfers more copies to the node with higher delivery predictability. It takes full advantage of the knowledge about the historical encountering, and the delivery predictability reflects the node's real mobility and transfer ability more precisely and thus yields a faster transfer for the packet to the destination node. Finally, taking the buffer management and the delivery probability into account in final waiting phase will gain more buffer space the buffer and thus reduce the average buffer time and increase the opportunity of finding the destination.

4. Conclusion

Opportunistic networks aim to provide reliable communications in an intermittently connected environment. The major challenge here is to route messages without an end-to-end connection. To deal with the unpredictability in connections and network partitions, we propose the probability choice routing protocol with buffer management for opportunistic networks in this paper. In the proposed protocol, a delivery probability based on continuous encountering duration time is set up such that each node can choose a better node as its relay in spray phase, and a total utility of buffer management utility and delivery probability is taken into consideration for delivering the last copy to the encountering node. Extensive results are provided to evaluate the proposed routing protocol with ONE simulator. Simulation experiments indicate that the proposed routing protocol outperforms the existing routing solutions thanks to its ability to maximize the delivery rate and minimize the delivery delay. Future research topic includes the extension to the real-life mobility.

Acknowledgments

This work is supported by National Natural Science Foundation of China under Grants no. 61172087, no. 61002012, and the Natural Science Foundation of Guangdong Province under Grant no. 06300923.

References

[1] L. Pelusi, A. Passarella, and M. Conti, "Opportunistic networking: data forwarding in disconnected mobile ad hoc networks," *IEEE Communications Magazine*, vol. 44, no. 11, pp. 134–141, 2006.

[2] K. Fall, "A delay-tolerant network architecture for challenged internets," in *Proceedings of the Conference on Applications, Technologies, Architectures, and Protocols for Computer Communication (SIGCOMM '03)*, pp. 27–34, August 2003.

[3] I. F. Akyildiz, B. Akan, C. Chen, J. Fang, and W. Su, "InterPlaNetary Internet: state-of-the-art and research challenges," *Computer Networks*, vol. 43, no. 2, pp. 75–112, 2003.

[4] T. Spyropoulos, K. Psounis, and C. S. Raghavendra, "Multiple-copy routing in intermittently connected mobile networks," Tech. Rep. CENG-2004-12, University of Southern California, Los Angeles, Calif, USA, 2004.

[5] W. Huang and S. Chen, "Epidemic metapopulation model with traffic routing in scale-free networks," *Journal of Statistical Mechanics*, vol. 2011, Article ID P12004, 12 pages, 2011.

[6] S. Chen, W. Huang, C. Cattani, and G. Altieri, "Traffic dynamics on complex networks: a survey," *Mathematical Problems in Engineering*, vol. 2012, Article ID 732698, 23 pages, 2012.

[7] A. Vahdat and D. Becker, "Epidemic routing for partially-connected ad hoc networks," Tech. Rep. CS-2000-06, Duke University Durham, Durham, NC, USA, 2000.

[8] T. Spyropoulos, K. Psounis, and C. S. Raghavendra, "Single-copy routing in intermittently connected mobile networks," in *Proceedings of the 1st Annual IEEE Communications Society Conference on Sensor and Ad Hoc Communications and Networks (SECON '04)*, pp. 235–244, October 2004.

[9] T. Spyropoulos, K. Psounis, and C. S. Raghavendra, "Spray and wait: efficient routing in intermittently connected mobile networks," in *Proceedings of ACMSIGCOMM workshop on Delay Tolerant Networking (WDTN '05)*, 2005.

[10] M. Li, "Approximating ideal filters by systems of fractional order," *Computational and Mathematical Methods in Medicine*, vol. 2012, Article ID 365054, 6 pages, 2012.

[11] H. A. Nguyen, S. GiordanoS, and A. Puiatti, "Probabilistic routing protocol for intermittently connected mobile ad hoc network," in *Proceedings of IEEE International Symposium on a World of Wireless, Mobile and Multimedia Networks*, Espoo, Finland, 2007.

[12] J. Burgess, B. Gallagher, D. Jensen, and B. N. Levine, "MaxProp: routing for vehicle-based disruption-tolerant networks," in *Proceedings of the 25th IEEE International Conference on Computer Communications (INFOCOM '06)*, Barcelona, Spain, April 2006.

[13] T. Anindya, D. Rajkumar, K. Humayun, and C. S. Gholamali, "TTL based routing in opportunistic networks," *Journal of Network and Computer Applications*, vol. 34, no. 5, pp. 1660–1670, 2011.

[14] A. Krifa and C. Barakat, "An optimal joint scheduling and drop policy for delay tolerant networks," in *Proceeding of the International Symposium on World of Wireless, Mobile and Multimedia Networks (WoWMoM '08)*, Newport Beach, Calif, USA, 2008.

[15] S. C. Nelson, M. Bakht, and R. Kravets, "Encounter-based routing in DTNs," in *Proceedings of the 28th Conference on Computer Communications (INFOCOM '09)*, pp. 846–854, Rio de Janeiro, Brazil, April 2009.

[16] R. Santos, J. Orozco, and F. Sergio, "A real-time analysis approach in opportunistic networks," *ACM SIGBED Review*, vol. 8, no. 3, pp. 40–43, 2011.

[17] M. Li, C. Cattani, and S. Y. Chen, "Viewing sea level by a one-dimensional random function with long memory," *Mathematical Problems in Engineering*, vol. 2011, Article ID 654284, 13 pages, 2011.

[18] M. Li and W. Zhao, "Visiting power laws in cyber-physical networking systems," *Mathematical Problems in Engineering*, vol. 2012, Article ID 302786, 13 pages, 2012.

[19] M. Li and W. Zhao, "Representation of a stochastic traffic bound," *IEEE Transactions on Parallel and Distributed Systems*, vol. 21, no. 9, Article ID 5342414, pp. 1368–1372, 2010.

[20] J. Karvo and J. Ott, "Time scales and delay-tolerant routing protocols," in *Proceedings of the 3rd ACM workshop on Challenged networks (CHANTS '08)*, San Francisco, Calif, USA, 2008.

Hindawi Publishing Corporation
Mathematical Problems in Engineering
Volume 2012, Article ID 538342, 11 pages
doi:10.1155/2012/538342

Research Article

Degenerate-Generalized Likelihood Ratio Test for One-Sided Composite Hypotheses

Dongdong Xiang, Xiaolong Pu, Lei Wang, and Yan Li

School of Finance and Statistics, East China Normal University, Shanghai 200241, China

Correspondence should be addressed to Yan Li, yli@stat.ecnu.edu.cn

Received 19 January 2012; Revised 26 March 2012; Accepted 20 April 2012

Academic Editor: Ming Li

We propose the degenerate-generalized likelihood ratio test (DGLRT) for one-sided composite hypotheses in cases of independent and dependent observations. The theoretical results show that the DGLRT has controlled error probabilities and stops sampling with probability 1 under some regularity conditions. Moreover, its stopping boundaries are constants and can be easily determined using the provided searching algorithm. According to the simulation studies, the DGLRT has less overall expected sample sizes and less relative mean index (RMI) values in comparison with the sequential probability ratio test (SPRT) and double sequential probability ratio test (2-SPRT). To illustrate the application of it, a real manufacturing data are analyzed.

1. Introduction

Consider the following hypotheses test problem:

$$H_0 : \theta \le \theta_0 \text{ versus } H_1 : \theta \ge \theta_1 \quad (\theta_0 < \theta_1) \tag{1.1}$$

with the error constraints

$$\begin{aligned} P_\theta\{\text{accept } H_1\} &\le \alpha \quad \text{for } \theta \le \theta_0 \\ P_\theta\{\text{accept } H_0\} &\le \beta \quad \text{for } \theta \ge \theta_1. \end{aligned} \tag{1.2}$$

Here, θ_0, $\theta_1 \in \Theta$, and Θ is the parameter space. Sequential tests for the problem (1.1) with independently and identically distributed (i.i.d.) observations have been widely studied. In cases of the one parameter exponential family with monotone likelihood ratio, the sequential probability ratio test (SPRT) proposed by Wald [1] provided an optimal solution to

the problem (1.1), in the sense of minimizing the expected sample sizes (ESSs) at $\theta = \theta_0$ and $\theta = \theta_1$, among all tests satisfying the constraints (1.2).

However, its ESSs at other parameter points are even larger than that of the test methods with fixed sample sizes. This led Weiss [2], Lai [3], and Lorden [4] to consider the problem (1.1) from the minimax perspective. Subsequently, Huffman [5] extended Lorden's [4] results to show that the 2-SPRT provides an asymptotically optimal solution to the minimax sequential test problem (1.1). Instead of the minimax approach, Wang et al. [6] proposed a test minimizing weighted ESS based on mixture likelihood ratio (MLR). Since the ESSs over $[\theta_0, \theta_1]$ are hard to control and are usually focused on applications, Wang et al. [6] paid much attention to investigate the performance of the ESS over $[\theta_0, \theta_1]$. Many tests for the problem (1.1) under independent observations are developed from other perspectives, including [7–11] and so forth.

It is true that in many practical cases the independence is justified, and hence these tests have been widely used. However, such tests may not be effective in cases when the observations are dependent, for example, Cauchy-class process for sea level (cf. [12]), fractional Gaussian noise with long-range dependence (cf. [13, 14]) and the power law type data in cyber-physical networking systems [15]. Especially for the power law data, the sequential tests for dependent observations are particularly desired. This need is not limited to these cases.

So far, many researchers studied sequential tests for various dependent scenarios. Phatarfod [16] extended the SPRT to test two simple hypotheses $H_0 : \theta = \theta_0$ versus $H_1 : \theta = \theta_1$ when observations constitute a Markov chain. Tartakovsky [17] showed that certain combinations of one-sided SPRT still own the asymptotical optimality in the ESS under fairly general conditions for a finite simple hypotheses. Novikov [18] proposed an optimal sequential test for a general problem of testing two simple hypotheses about the distribution of a discrete-time stochastic process. Niu and Varshney [19] proposed the optimal parametric SPRT with correlated data from a system design point of view. To our best knowledge, however, there are few references available for considering the problem (1.1) with dependent observations from the perspective of minimizing the ESS over $[\theta_0, \theta_1]$. Similar to Wang et al. [6], one can extend the MLR to the dependent case. However, unlike the i.i.d. case, the MLR under the dependent case may not be available because of the complexity of its computation. Besides, its test needs to divide $[\theta_0, \theta_1]$ into two disjoint parts by inserting a point. In i.i.d. cases, this point can be selected following Huffman's [5] suggestion. But, in the dependent case, this suggestion may not be effective. One also can use the generalized likelihood ratio (GLR) instead of the MLR. Unfortunately, as opposite to the MLR, the GLR does not preserve the martingale properties which allow one to choose two constant stopping boundaries in a way to control two types of error. Moreover, the computation of the GLR is hard to be obtained in cases when the maximum likelihood estimator should be searched. This usually happens in the dependent case.

In this paper, we propose a test method for both dependent and independent observations. It has the following features: (1) it has good performances over $[\theta_0, \theta_1]$ in the sense of less overall expected sample sizes; (2) its computation is reasonably simple; (3) its stopping boundaries can be determined conveniently. The rest of the paper is organized as follows. In Section 2, we describe the construction of the proposed test in details and present its basic theoretical properties. Based on these theoretical results, we provide a searching algorithm to compute stopping boundaries for our proposed test. In Section 3, we conduct some simulation studies to show the performance of the proposed test. Some concluding remarks are given in Section 4. Some technical details are provided in the appendix.

2. The Proposed Test

Let $x^i =: (x_1, x_2, \ldots, x_i)$, $i = 1, 2, \ldots$ and suppose that the conditional probability distribution of each $x_i|x^{i-1}$, $f(x_i|x^{i-1}, \theta)$ has an explicit form. Here, $x_1|x^0 =: x_1$ and $f(x_1|x^0, \theta) =: f(x_1, \theta)$. Thus, likelihood ratio can be defined as

$$R_n(\theta, \theta') = \prod_{i=1}^{n} \frac{f(x_i \mid x^{i-1}, \theta)}{f(x_i \mid x^{i-1}, \theta')}, \quad \theta, \theta' \in \Theta. \tag{2.1}$$

Lai [20] introduced this model to construct a sequential test for many simple hypotheses when the observations are dependent. It is very general and also includes the i.i.d. cases.

Example 2.1. Consider, for instance, a simple nonlinear time series model:

$$x_i = \theta x_{i-1}^2 + \varepsilon_i, \quad \varepsilon_i \sim N(0, 1). \tag{2.2}$$

In this case, $R_n(\theta, \theta') = \prod_{i=1}^{n} \phi(x_i - \theta x_{i-1}^2)/\phi(x_i - \theta' x_{i-1}^2)$, $x_0 = 0$, and $\phi(\cdot)$ is the probability density function of the standard normal distribution.

To overcome the difficulty stated in Section 1, we propose a test statistic which minimizes the likelihood ratio with restriction to a finite parameter points in $[\theta_0, \theta_1]$. First, we insert k (≥ 3) points into $[\theta_0, \theta_1]$ uniformly, denoted as $\widetilde{\theta}_i$ with $\widetilde{\theta}_i = \theta_0 + (i-1)(\theta_1 - \theta_0)/(k-1)$, $i = 1, \ldots, k$. Next, we define the test statistic as $\max_{1 \leq i \leq k} R_n(\widetilde{\theta}_i, \theta')$. It can be checked that this test statistic not only preserves the martingale properties, but also inherits the merit of the GLR. As long as k is not very large (e.g., $k > 100$), its computation will be very simple. Thus, it has all the three features stated in Section 1. Since this maximization is restricted to some finite points, we refer to it as degenerate-generalized likelihood ratio (DGLR).

Based on the DGLR, we define a stopping rule T for the problem (1.1) by

$$T = \inf\left\{ n \geq 1, \max_{1 \leq i \leq k} R_n\left(\widetilde{\theta}_i, \theta_0\right) \geq A \text{ or } \max_{1 \leq i \leq k} R_n\left(\widetilde{\theta}_i, \theta_1\right) \geq B \right\}, \tag{2.3}$$

with the terminal decision rule

$$\Delta = \begin{cases} \text{accept } H_1, & \max\limits_{1 \leq i \leq k} R_T\left(\widetilde{\theta}_i, \theta_0\right) \geq A, \\ \text{accept } H_0, & \max\limits_{1 \leq i \leq k} R_T\left(\widetilde{\theta}_i, \theta_1\right) \geq B, \\ \text{continue sampling}, & \text{else}, \end{cases} \tag{2.4}$$

where $0 < A, B < \infty$ are two stopping boundaries. Hereafter, the sequential test method with (2.3) and (2.4) is called the degenerate-generalized likelihood ratio test (DGLRT). It has some theoretical properties which are stated as follows. These theoretical properties provide a guide to the design of the DGLRT, whose proofs are provided in the appendix.

Let

$$\begin{aligned}\alpha'(\theta, A, B) &= P_\theta\left\{\max_{1\le i\le k} R_T\left(\widetilde{\theta}_i, \theta_0\right) \ge A\right\}, \quad \theta \in \Theta_0,\\ \beta'(\theta, A, B) &= P_\theta\left\{\max_{1\le i\le k} R_T\left(\widetilde{\theta}_i, \theta_1\right) \ge B\right\}, \quad \theta \in \Theta_1\end{aligned} \tag{2.5}$$

be the real error probabilities, where Θ_0 and Θ_1 represent the parameter subsets under H_0 and H_1, respectively.

Proposition 2.2. *Suppose*

$$\int \frac{f\left(x_i \mid x^{i-1}, \theta''\right)}{f\left(x_i \mid x^{i-1}, \theta'\right)} f\left(x_i \mid x^{i-1}, \theta\right) dx_i \le 1, \tag{2.6}$$

for any positive integer n and every triple $\theta \le \theta' \le \theta''$. For the DGLRT defined by (2.3) *and* (2.4)*, one has $\alpha'(\theta, A, B) \le k/A$ for all $\theta \in \Theta_0$ and $\beta'(\theta) \le k/B$ for all $\theta \in \Theta_1$.*

Remark 2.3. The assumption (2.6) given in Proposition 2.2 is not restrictive. This holds for the general one parameter exponential family and many others (cf. Robbins and Siegmund [21]).

Proposition 2.4. *Suppose that there exists a constant $\varepsilon > 0$ such that $E_{\theta''}[\log\{f(x_i|x^{i-1};\theta')\} - \log\{f(x_i|x^{i-1};\theta)\}] \ge \varepsilon$ for all i and every triple $\theta \le \theta' \le \theta''$. Under the assumptions stated in Proposition 2.2, one has $P_\theta\{T < \infty\} = 1$ for all $\theta \in \Theta$.*

Remark 2.5. For $\theta'' \ge \theta'$, we have

$$\begin{aligned}&E_{\theta''}\left[\log\left\{f\left(x_i \mid x^{i-1};\theta'\right)\right\} - \log\left\{f\left(x_i \mid x^{i-1};\theta\right)\right\}\right]\\ &\quad= -E_{\theta''}\left[\log\left\{f\left(x_i \mid x^{i-1};\theta\right)\right\} - \log\left\{f\left(x_i \mid x^{i-1};\theta'\right)\right\}\right]\\ &\quad\ge -\log\left\{E_{\theta''}\left[\frac{f\left(x_i \mid x^{i-1};\theta\right)}{f\left(x_i \mid x^{i-1};\theta'\right)}\right]\right\}\\ &\quad\ge 0.\end{aligned} \tag{2.7}$$

The last inequality follows from (2.6). $E_{\theta''}[\log\{f(x_i|x^{i-1};\theta')\} - \log\{f(x_i|x^{i-1};\theta)\}]$ is positive with probability 1 if $\theta \ne \theta'$. Heuristically, the requirement that the difference be greater than the constant $\varepsilon > 0$ for all i amounts to assuming that the sequence of data cumulatively adds information about all the $\theta'' \ge \theta'$, which is generally true in sequential studies.

From Proposition 2.2, we conclude that the DGLRT satisfies the error constraints (1.2) if $A = k/\alpha$ and $B = k/\beta$. From Proposition 2.4, it is easy to find that we absolutely stop sampling after finite observations. These results imply that the DGLRT can be useful in a sequential study for testing the problem (1.1).

In the DGLRT (2.3) and (2.4), the value of the parameter k should be large but finite. In practice, we suggest that $k = 10$ (cf. Section 3). Regarding A and B, we can compute them by simulation. Proposition 2.2 shows $A \le k/\alpha$ and $B \le k/\beta$. Thus, we can search (A, B) over

Table 1: The ESSs at $\theta = -0.8\ (0.1)\ 0$ for $-\theta_0 = \theta_1 = 0.5$ and $\alpha = \beta = 0.01$.

θ	−0.8	−0.7	−0.6	−0.5	−0.4	−0.3	−0.2	−0.1	0
$k = 3$	6.293	7.121	8.181	9.545	11.241	13.156	15.136	16.600	17.141
$k = 5$	6.355	7.173	8.254	9.557	11.172	13.073	14.958	16.396	16.974
$k = 10$	6.380	7.228	8.264	9.577	11.138	13.039	14.897	16.344	16.889
$k = 50$	6.394	7.231	8.265	9.578	11.113	13.070	14.872	16.321	16.862

$[1, k/\alpha] \times [1, k/\beta]$ with the real error probabilities being computed by simulations. One may consider a density grid searching on $[1, k/\alpha] \times [1, k/\beta]$. But this is a time consuming job. To reduce the computation, we introduce an efficient approach as follows. In the first step, we can use bisection searching to find A_1 ($\in [1, k/\alpha]$) such that $\alpha'(\theta_0, A_1, k/\beta) = \alpha$. Then, fix A_1 to find B_1 ($\in [1, k/\beta]$) such that $\beta'(\theta_1, A_1, B_1) = \beta$. Since $\alpha'(\theta_0, x, y)$ and $1 - \beta'(\theta_1, x, y)$ increase in x and decrease in y, we conclude that $(A, B) \in [1, A_1] \times [1, B_1]$. Hence, we repeat the above step over $[1, A_1] \times [1, B_1]$. In this way, we generate a sequence of pairs $(A_1, B_1), (A_2, B_2), \ldots$. Following the above program, we have

$$A_1 \geq A_2 \geq \cdots \geq 1, \qquad B_1 \geq B_2 \geq \cdots \geq 1. \tag{2.8}$$

It can be checked that these pairs converge to the exact stopping boundaries. In practice, we repeat the above process and stop at step l if $|\alpha'(\theta_0, A_l, B_l) - \alpha| \leq \text{tol}_1$ and $|\beta'(\theta_1, A_l, B_l) - \beta| \leq \text{tol}_2$. Here, $\text{tol}_1 = 2\%\alpha$ and $\text{tol}_2 = 2\%\beta$. Computation involved in finding A and B is not difficult partly due to the rapid developments in information technology. For example, in the nonlinear time series model (2.2), setting $-\theta_0 = \theta_1 = 0.25$, $\alpha = 0.01$, $\beta = 0.05$, and $k = 10$, it requires 15 minutes to obtain the stopping boundaries A and B for the DGLRT based on 100,000 simulations, using Intel-Core i7-2.80 GHz CPU. Since this is a one-time computation before testing, it is convenient to accomplish.

3. Numerical Studies

In this section, we present some simulation results regarding the numerical performance of the proposed DGLRT. In the DGLRT, the parameter k needs to be chosen. We first investigate the effect of k on the performance of the DGLRT according to i.i.d. observations from the normal distribution $N(\theta, 1)$. Setting $-\theta_0 = \theta_1 = 0.5$ and $\alpha = \beta = 0.01$, we compare the DGLRTs with $k = 3, 5, 10, 50$. The corresponding stopping boundaries (A, B) are $(69.3, 69.3)$, $(74.3, 74.3)$, $(75.7, 75.7)$, and $(76.7, 76.7)$, respectively. The ESSs at $\theta = -0.8\ (0.1)\ 0.8$ (i.e., θ takes values from -0.8 to 0.8 with step 0.1) are computed based on 100,000 simulated data and are provided in Table 1.

Because of the symmetry, we only include results for $\theta \in [-0.8, 0]$. Table 1 shows that the ESSs under a larger k are smaller than those under a smaller k if $\theta \in (\theta_0, \theta_1)$. Meanwhile, it can be seen that a smaller k has a better performance outside (θ_0, θ_1). In order to assess the overall performance of the tests, we compute their relative mean index (RMI) values.

The RMI is introduced by Han and Tsung [22] for comparing the performance of several control charts. It is defined as

$$\text{RMI} = \frac{1}{N}\sum_{l=1}^{N}\frac{\text{ESS}(\theta_l) - \text{MESS}(\theta_l)}{\text{MESS}(\theta_l)}, \tag{3.1}$$

where N is the total numbers of parameter points (i.e., θ_l's) we considered, $\text{ESS}(\theta_l)$ denotes the ESS at θ_l, and $\text{MESS}(\theta_l)$ is the smallest one among all the three $\text{ESS}(\theta_l)$. So, $(\text{ESS}(\theta_l) - \text{MESS}(\theta_l))/\text{MESS}(\theta_l)$ can be considered as a relative difference of the given test, compared to the best test, at θ_l, and RMI is the average of all such difference values. By this index, a test with smaller RMI value is considered better in its overall performance. Since we focus on the performance over the parameter interval $[\theta_0, \theta_1]$, $\theta_l = -0.5 + 0.1(i-1)$, $i = 1, \ldots, 10$ in this illustration. The resulting RMIs for the DGLRT under $k = 3, 5, 10, 50$ are 0.0116, 0.0042, 0.0017, and 0.0011, respectively, which shows that the DGLRT under a larger k is more efficient than the one under a smaller k. The improvement is minor when k is large enough. Considering the complexity of computation, we select $k = 10$ for practical purposes. From now on, the DGLRT is always the DGLRT under $k = 10$ unless otherwise stated.

Next, we investigate the performance of the DGLRT in controlling the ESSs over $[\theta_0, \theta_1]$. In the i.i.d. case, we know the 2-SPRT has a better performance in controlling the maximum ESS. For the ESSs over the neighborhoods of θ_0 and θ_1, the SPRT provides a closely approximation. Based on extensive simulations, we conclude that these features still preserve in the dependent case. Therefore, the SPRT and the 2-SPRT are compared with the DGLRT in this paper. The following three cases are considered.

Case 1. Observations collected from normal distributions with mean θ and variance 1. Set $-\theta_0 = \theta_1 = 0.5$ and $\alpha = \beta = 0.01$ for the test problem (1.1).

Case 2. Observations collected from exponential distributions with mean $1/\theta$. The problem (1.1) is set with $\theta_0 = 0.5$, $\theta_1 = 2$, and $\alpha = \beta = 0.01$.

Case 3. Consider the test problem (1.1) for the simple nonlinear time series model (2.2) with $\theta_0 = 0$, $\theta_1 = 1$ and $\alpha = \beta = 0.01$.

In each case, the inserted point for the 2-SPRT is searched over $[\theta_0, \theta_1]$. The stopping boundaries are also computed following the searching algorithm stated in Section 2. These stopping boundaries (A, B) are listed in the order of the SPRT, 2-SPRT, and DGLRT: Case 1: (56.4, 56.4), (37.4, 37.4), and (75.7, 75.7); Case 2: (63.8, 25.5), (42.5, 23.5), and (79.5, 39.5); and Case 3: (14.5, 25.5), (8.2, 26.8), and (22.5, 36.5). Figures 1–3 display the ESS curves over $[\theta_0 - 0.5, \theta_1 + 0.5]$ under the three tests for Cases 1–3 with the dashed line for the SPRT, the dotted line for the 2-SPRT, and the solid line for the DGLRT. Figure 1 shows that the DGLRT is comparable to the 2-SPRT in the middle of the parameter range and performs as well as the SPRT in the two tails. It implies that the DGLRT controls both the maximum ESS and the ESSs under H_0 and H_1 very well. The same conclusions can also be obtained from Figures 2 and 3. The RMIs for the SPRT, 2-SPRT, and DGLRT under the three cases are also computed. The results are listed in Table 2. It can be seen that the RMI for the DGLRT is the smallest one among the three tests under all three cases. Thus, the DGLRT performs the best, compared with the SPRT and the 2-SPRT over $[\theta_0, \theta_1]$.

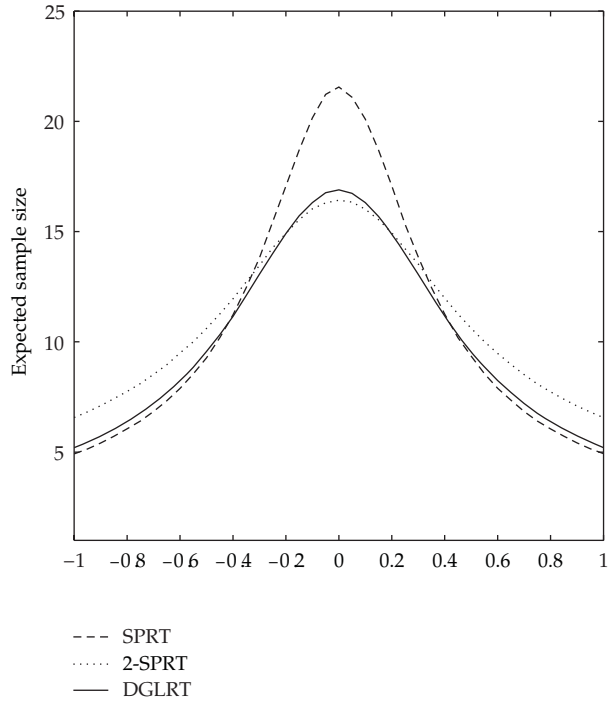

Figure 1: Comparison of ESS curves under the SPRT, the 2-SPRT, and the DGLRT for Case 1: $-\theta_0 = \theta_1 = 0.5$ for the normal distribution with mean θ and variance 1.

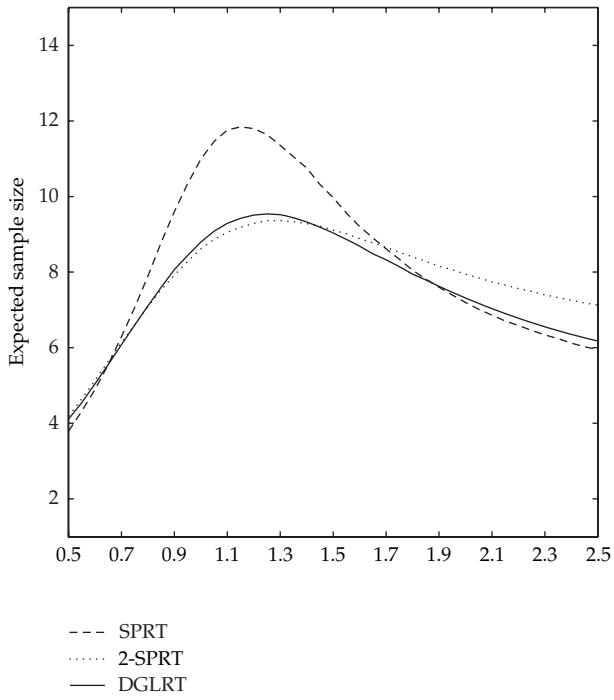

Figure 2: Comparison of ESS curves under the SPRT, the 2-SPRT, and the DGLRT for Case 2: $\theta_0 = 0.5$ and $\theta_1 = 2$ for the exponential distribution with mean $1/\theta$.

Table 2: The RMI for the SPRT, 2-SPRT, and DGLRT under Cases 1–3.

Case	The SPRT	The 2-SPRT	The DGLRT
1	0.1194	0.0402	0.0103
2	0.1148	0.0263	0.0135
3	0.0370	0.0105	0.0059

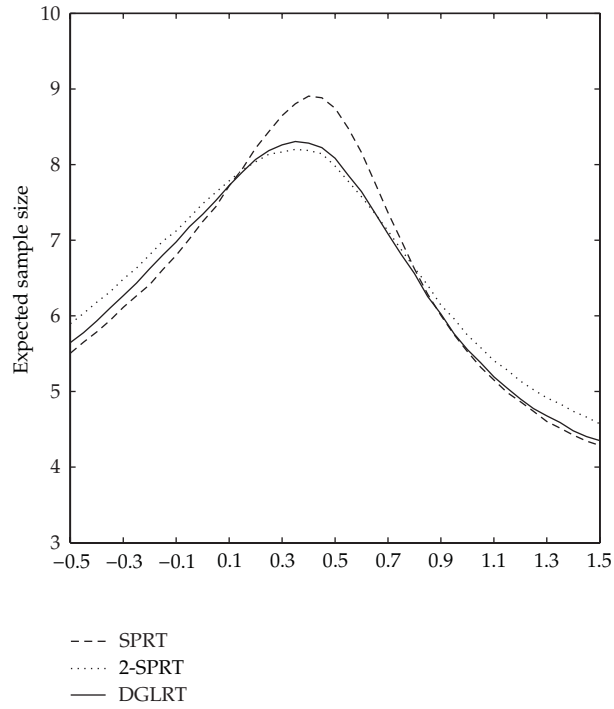

Figure 3: Comparison of ESS curves under the SPRT, the 2-SPRT, and the DGLRT for Case 3: $\theta_0 = 0$ and $\theta_1 = 1$ for the nonlinear time series (2.2).

To illustrate the DGLRT, we apply it to a real manufacturing data (cf. Chou et al. [23]). A customer specifies an average breaking strength of a strapping tape as 200 psi, and the standard deviation is 12 psi. The data are the breaking strength of different strapping tapes, so the random errors mainly stem from the measurement errors. Thus, the observations can be assumed to be independent. The Shapiro and Wilk [24] test shows that the data are taken from a normal distribution. Consider the test problem (1.1) with $\theta_0 = 200$ and $\theta_1 = 212$ and standardize the observations by using a transformation $X_i \to (X_i - 206)/12$, $i = 1, 2, \ldots$. Then the resulting test problem is equivalent to $H_0 : \theta \leq -0.5$ versus $H_1 : \theta \geq 0.5$. Under $\alpha = \beta = 0.01$, the corresponding stopping boundaries for the DGLRT are $(75.7, 75.7)$. Based on the first 20 real observations, we compute the test statistics of the DGLRT, which are displayed in Table 3. In Table 3, standardized X_i indicates $(X_i - 206)/12$. Table 3 shows that $\max_{1\leq j\leq k} R_i(\tilde{\theta}_j, \theta_1)$ increases in i rapidly, while $\max_{1\leq j\leq k} R_i(\tilde{\theta}_j, \theta_0)$ keeps constant for $i = 1, 2, \ldots, 20$ under the real data. Since $\max_{1\leq j\leq k} R_i(\tilde{\theta}_j, \theta_1)$ crosses its stopping boundary at the 11th observation, we should accept the null hypothesis according to the terminal decision rule (2.4).

Table 3: Implementation of the DGLRT with the first 20 observations of breaking strength of a strapping tape.

		Standardized	The DGLRT	
i	X_i	X_i	$\max_{1\le j\le k} R_i(\theta_j, \theta_0)$	$\max_{1\le j\le k} R_i(\theta_j, \theta_1)$
1	191	−1.250	1	3.490
2	193	−1.083	1	10.309
3	204	−0.167	1	12.182
4	215	0.750	1	5.755
5	182	−2.000	1	42.521
6	223	1.417	1	10.309
7	194	−1.000	1	28.022
8	202	−0.333	1	39.095
9	214	0.667	1	20.065
10	210	0.333	1	14.382
11	186	−1.667	1	**76.172**
12	211	0.417	1	50.199
13	202	−0.333	1	70.035
14	201	−0.417	1	106.272
15	191	−1.250	1	370.925
16	193	−1.083	1	1095.537
17	196	−0.833	1	2519.964
18	189	−1.417	1	10394.166
19	194	−1.000	1	28254.274
20	209	0.250	1	22004.450

4. Concluding Remarks

In this paper, we have proposed the DGLRT test in cases where the conditional density function has an explicit form. It has been shown that the properties of the DGLRT can guarantee bounding two error probabilities. To make our method be more applicable, we further discuss the selection of the parameter k and the searching algorithm for its stopping boundaries. From our numerical results, we conclude that the DGLRT has several merits: (1) in contrast to the SPRT, the DGLRT has much smaller ESS for θ in the middle of the parameter range and nearly has the same performance for θ outside the interval (θ_0, θ_1). It is not surprising that the 2-SPRT performs the best in minimizing the maximum ESS because it is designed to be optimal in the minimax sense. However, the relative difference of the maximum ESS between the DGLRT and the 2-SPRT is minor. Moreover, for θ outside (θ_0, θ_1), the ESSs of the DGLRT are much smaller than those of the 2-SPRT. That is to say, the DGLRT controls the maximum ESS and the ESSs under two hypotheses; (2) under the RMI criteria, the DGLRT performs more efficiently than the SPRT and the 2-SPRT over $[\theta_0, \theta_1]$; (3) its implementation is very simple.

While our focus in this paper is on methodological development, there are still some related questions unanswered yet. For instance, at this moment, we do not know how to determine the critical stopping boundaries for the DGLRT in an analytical way instead of the Monte Carlo method. Besides, our method controls the ESS in pointwise, so it can be used to construct control chart for detecting the small shifts. These questions will be addressed in our future research.

Appendix

Proof of Proposition 2.2. Let

$$\begin{aligned} T_1 &= \inf\left\{ n \geq 1,\ \max_{1\leq i\leq k} R_n\left(\widetilde{\theta}_i, \theta_0\right) \geq A \right\}, \\ T_2 &= \inf\left\{ n \geq 1,\ \max_{1\leq i\leq k} R_n\left(\widetilde{\theta}_i, \theta_1\right) \geq B \right\}. \end{aligned} \tag{A.1}$$

So,

$$\begin{aligned} \alpha'(\theta, A, B) &= P_\theta\{\text{accept } H_1\} = P_\theta\left\{ T < \infty, \max_{1\leq i\leq k} R_T\left(\widetilde{\theta}_i, \theta_0\right) \geq A \right\} \\ &= P_\theta\left\{ T_1 \leq T_2, T < \infty, \max_{1\leq i\leq k} R_T\left(\widetilde{\theta}_i, \theta_0\right) \geq A \right\} \\ &\leq P_\theta\{T_1 < \infty\} \leq \int_{\{T_1<\infty\}} \frac{1}{A} \max_{1\leq i\leq k} R_{T_1}\left(\widetilde{\theta}_i, \theta_0\right) dP_\theta \\ &\leq \sum_{i=1}^{k} \frac{1}{A} \int_{\{T_1<\infty\}} R_{T_1}\left(\widetilde{\theta}_i, \theta_0\right) dP_\theta \\ &\leq \frac{k}{A}. \end{aligned} \tag{A.2}$$

The last inequality follows from (2.6). Till now, we prove that the result $\alpha'(\theta, A, \mathrm{B}) \leq k/A$ for all $\theta \in \Theta_0$. The other result can also be proven in a similar way. □

Proof of Proposition 2.4. Since we insert k ($\geq$3) points in $[\theta_0, \theta_1]$, we can find a point θ_2 which belongs to (θ_0, θ_1). Thus, there exists a $\varepsilon > 0$ such that $E_\theta[\log\{f(x_i|x^{i-1}; \theta_2)\} - \log\{f(x_i|x^{i-1}; \theta_0)\}] \geq \varepsilon$. It implies that $E_\theta[R_n(\theta_2, \theta_0)] \to \infty$ for $\theta \geq \theta_2$. So,

$$\lim_{n\to\infty} P_\theta\left\{ \max_{1\leq i\leq k} R_n\left(\widetilde{\theta}_i, \theta_0\right) \geq A \right\} \geq \lim_{n\to\infty} P_\theta\{R_n(\theta_2, \theta_0) \geq A\} = 1. \tag{A.3}$$

Thus, we have the result that $P_\theta\{T < \infty\} = 1$ for all $\theta \geq \theta_2$. In a similar way, we can obtain $P_\theta\{T < \infty\} = 1$ for all $\theta \leq \theta_2$. Combining the two results, we complete this proof. □

Acknowledgments

The authors cordially thank the editor and the anonymous referees for their valuable comments which lead to the improvement of this paper. This research was supported by grants from the National Natural Science Foundation of China (11101156 and 11001083).

References

[1] A. Wald, "Sequential tests of statistical hypotheses," *Annals of Mathematical Statistics*, vol. 16, pp. 117–186, 1945.

[2] L. Weiss, "On sequential tests which minimize the maximum expected sample size. ," *Journal of the American Statistical Association*, vol. 57, pp. 551–566, 1962.

[3] T. L. Lai, "Optimal stopping and sequential tests which minimize the maximum expected sample size," *The Annals of Statistics*, vol. 1, pp. 659–673, 1973.

[4] G. Lorden, "2-SPRT's and the modified Kiefer-Weiss problem of minimizing an expected sample size," *The Annals of Statistics*, vol. 4, no. 2, pp. 281–291, 1976.

[5] M. D. Huffman, "An efficient approximate solution to the Kiefer-Weiss problem," *The Annals of Statistics*, vol. 11, no. 1, pp. 306–316, 1983.

[6] L. Wang, D. Xiang, X. Pu, and Y. Li, "Double sequential weighted probability ratio test for one-sided composite hypotheses," *Communication in Statistics—Theory and Method*. In press.

[7] T. L. Lai, "Nearly optimal sequential tests of composite hypotheses," *The Annals of Statistics*, vol. 16, no. 2, pp. 856–886, 1988.

[8] B. Darkhovsky, "Optimal sequential tests for testing two composite and multiple simple hypotheses," *Sequential Analysis*, vol. 30, no. 4, pp. 479–496, 2011.

[9] H. P. Chan and T. L. Lai, "Importance sampling for generalized likelihood ratio procedures in sequential analysis," *Sequential Analysis*, vol. 24, no. 3, pp. 259–278, 2005.

[10] Y. Li and X. Pu, "Method of sequential mesh on Koopman-Darmois distributions," *Science China A*, vol. 53, no. 4, pp. 917–926, 2010.

[11] Y. Li and X. Pu, "A method for designing three-hypothesis test problems and sequential schemes," *Communications in Statistics—Simulation and Computation*, vol. 39, no. 9, pp. 1690–1708, 2010.

[12] M. Li, "A class of negatively fractal dimensional Gaussian random functions," *Mathematical Problems in Engineering*, Article ID 291028, 18 pages, 2011.

[13] M. Li, C. Cattani, and S. Y. Chen, "Viewing sea level by a one-dimensional random function with long memory," *Mathematical Problems in Engineering*, vol. 2011, Article ID 10.1155/2011/654284, 13 pages, 2011.

[14] M. Li and W. Zhao, "Variance bound of ACF estimation of one block of fGn with LRD," *Mathematical Problems in Engineering*, vol. 2010, Article ID 560429, 14 pages, 2010.

[15] M. Li and W. Zhao, "Visiting power laws in cyber-physical networking systems," *Mathematical Problems in Engineering*, vol. 2012, Article ID 302786, 13 pages, 2012.

[16] R. M. Phatarfod, "Sequential analysis of dependent observations. I," *Biometrika*, vol. 52, pp. 157–165, 1965.

[17] A. Tartakovsky, "Asymptotically optimal sequential tests for nonhomogeneous processes," *Sequential Analysis*, vol. 17, no. 1, pp. 33–61, 1998.

[18] A. Novikov, "Optimal sequential tests for two simple hypotheses," *Sequential Analysis*, vol. 28, no. 2, pp. 188–217, 2009.

[19] R. Niu and P. K. Varshney, "Sampling schemes for sequential detection with dependent observations," *IEEE Transactions on Signal Processing*, vol. 58, no. 3, part 2, pp. 1469–1481, 2010.

[20] T. L. Lai, "Information bounds and quick detection of parameter changes in stochastic systems," *IEEE Transactions on Information Theory*, vol. 44, no. 7, pp. 2917–2929, 1998.

[21] H. Robbins and D. Siegmund, "A class of stopping rules for testing parametric hypotheses," in *Proceedings of the 6th Berkeley Symposium on Mathematical Statistics and Probability*, vol. 4, pp. 37–41, University of California Press, Berkeley, Calif, USA, 1973.

[22] D. Han and F. Tsung, "A reference-free Cuscore chart for dynamic mean change detection and a unified framework for charting performance comparison," *Journal of the American Statistical Association*, vol. 101, no. 473, pp. 368–386, 2006.

[23] Y.-M. Chou, R. L. Mason, and J. C. Young, "The SPRT control chart for standard deviation based on individual observations," *Quality Technology & Quantitative Management*, vol. 3, no. 3, pp. 335–345, 2006.

[24] S. S. Shapiro and M. B. Wilk, "An analysis of variance test for normality: complete samples," *Biometrika*, vol. 52, pp. 591–611, 1965.

Hindawi Publishing Corporation
Mathematical Problems in Engineering
Volume 2012, Article ID 284815, 22 pages
doi:10.1155/2012/284815

Research Article

Nonlinear Blind Identification with Three-Dimensional Tensor Analysis

I. Cherif, S. Abid, and F. Fnaiech

Unit Research SICISI, High School of Sciences and Techniques of Tunis (ESSTT), 5 Avenue Taha Hussein, Montfleury, 1008 Tunis, Tunisia

Correspondence should be addressed to S. Abid, abid2fr@yahoo.fr

Received 15 February 2012; Revised 2 April 2012; Accepted 3 April 2012

Academic Editor: Thomas T. Yang

This paper deals with the analysis of a third-order tensor composed of a fourth-order output cumulants used for blind identification of a second-order Volterra-Hammerstein series. It is demonstrated that this nonlinear identification problem can be converted in a multivariable system with multiequations having the form of $Ax + By = c$. The system may be solved using several methods. Simulation results with the Iterative Alternating Least Squares (IALS) algorithm provide good performances for different signal-to-noise ratio (SNR) levels. Convergence issues using the reversibility analysis of matrices A and B are addressed. Comparison results with other existing algorithms are carried out to show the efficiency of the proposed algorithm.

1. Introduction

Nonlinear system modeling based on real-world input/output measurements is so far used in many applications. The appropriate model and the determination of corresponding parameters using the input/output data are owned to apply a suitable and efficient identification method [1–7].

Hammerstein models are special classes of second-order Volterra systems where the second-order homogenous Volterra kernel is diagonal [8]. These systems have been successfully used to model nonlinear systems in a number of practical applications in several areas such as chemical process, biological process, signal processing, and communications [9–12], where, for example, in digital communication systems, the communication channels are usually impaired by a nonlinear intersymbol interference (ISI). Channel identification allows compensating the ISI effects at the receivers.

In [13], a penalty transformation method is developed. Indeed a penalty function is formed by equations relating the unknown parameters of the model with the autocorrelations

of the signal. This function is then included in the cost function yielding to an augmented Lagrangian function. It has been demonstrated that this approach gives good identification results for a nonlinear systems. However, this approach is still sensitive to additive Gaussian noise because the 2nd-order moment is used as a constraint. Authors, in [7], overcame this sensitivity by using 4th-order cumulants as a constraint instead of 2nd-order moments in order to smooth out the additive Gaussian noise. But the proposed approach which is based on a simplex-genetic algorithm becomes so long and computationally complex.

The main drawback of identification with Volterra series lies on the parametric complexity and the need to estimate a very big number of parameters. In many cases, Volterra series identification problem may be well simplified using the tensor formulation [10–12, 14].

Authors, in [10], used a parallel factor (PARAFAC) decomposition of the kernels to derive Volterra-PARAFAC models yielding an important parametric complexity reduction for Volterra kernels of order higher than two. They proved that these models are equivalent to a set of parallel Wiener models. Consequently, they proposed three adaptive algorithms for identifying these proposed Volterra-PARAFAC models for complex-valued input/output signals, namely, the extended complex Kalman filter, the complex least mean square (CLMS) algorithm, and the normalized CLMS algorithm.

In this paper, the algorithm derived in [14] is extended to be applied to blind identification of a general second-order Volterra-Hammerstein system. The main idea is to develop a general expression for each direction slices of a cubic tensor and then express the tensor slices in an unfolded representation. The three-dimensional tensor elements are formed by the fourth-order output cumulants. This yields to an Iterative Alternating Least Square (IALS) algorithm which has the benefit over the original Volterra filters in terms of implementation and complexity reduction. A convergence analysis based on matrices reversibility study is given showing that the proposed IALS algorithm converges to optimal solutions in the least mean squares sense. Furthermore, some simulation results and comparisons with different existing algorithms are provided.

The present work is organized as follows; in Section 2, a brief study of the three-dimensional tensor is presented. In Section 3, the model under study and the related output cumulants are then proposed, whereas, in Section 4 the decomposition analysis of the cumulant tensor is developed. In Sections 5 to 8, we give, respectively, the proposed blind identification algorithm, the convergence study, some simulation results, and at the end some main conclusions are drawn.

2. Three-Dimensional Tensor and Different Slice Expressions

A three-dimensional tensor $C \in \mathbb{C}^{M\times M\times M}$ can be expressed by

$$C = \sum_{i=1}^{M}\sum_{j=1}^{M}\sum_{k=1}^{M} C_{ijk} e_i^{(M)} \circ e_j^{(M)} \circ e_k^{(M)}, \tag{2.1}$$

where C_{ijk} is the tensor value in the position (i, j, k) of the cube with dimension M, $e_p^{(M)}$ denotes the pth canonical basis vector with dimension M, and the symbol $\circ$ stands for the outer product (Figure 1).

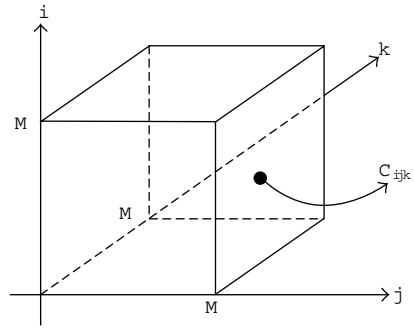

Figure 1: Cubic tensor representation.

A cubic tensor can be always sliced along three possible directions (horizontal, vertical, and frontal) as depicted in Figure 2. This yields, in each case, to M matrices of $M \times M$ dimensions.

The expression of the ith slice in the horizontal direction is given by

$$C_{i\bullet\bullet} = \sum_{j=1}^{M}\sum_{k=1}^{M} C_{ijk} e_j^{(M)} \circ e_k^{(M)} = \sum_{j=1}^{M}\sum_{k=1}^{M} C_{ijk} e_j^{(M)} e_k^{(M)T}. \tag{2.2}$$

In the same manner, the other matrix expressions along with the vertical and frontal directions are expressed, respectively, by

$$C_{\bullet j\bullet} = \sum_{i=1}^{M}\sum_{k=1}^{M} C_{ijk} e_i^{(M)} e_k^{(M)T}; \qquad C_{\bullet\bullet k} = \sum_{i=1}^{M}\sum_{j=1}^{M} C_{ijk} e_i^{(M)} e_j^{(M)T}. \tag{2.3}$$

It is important to express the tensor slices in an unfolded representation, obtained by stacking up the 2D matrices. Hence, three unfolded representations of C are obtained. For the horizontal, the vertical, and the frontal directions, we get, respectively,

$$C_{[1]} = \begin{pmatrix} C_{1..} \\ C_{2..} \\ \vdots \\ C_{M..} \end{pmatrix}; \qquad C_{[2]} = \begin{pmatrix} C_{.1.} \\ C_{.2.} \\ \vdots \\ C_{.M.} \end{pmatrix}; \qquad C_{[3]} = \begin{pmatrix} C_{..1} \\ C_{..2} \\ \vdots \\ C_{..M} \end{pmatrix}. \tag{2.4}$$

We note that each matrix $C_{[p]} : p = 1, 2, 3$ is an $(M \times M, M)$ one.

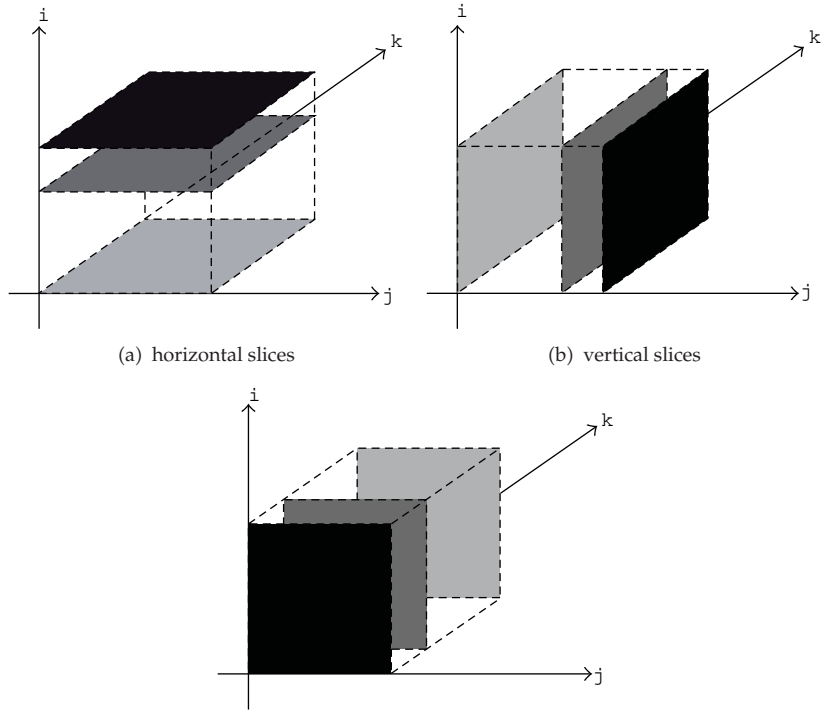

(a) horizontal slices

(b) vertical slices

(c) frontal slices

Figure 2: Different direction slices of a cubic tensor.

3. Nonlinear System Model and Output Cumulants Analysis

We focus on the identification of a second-order Volterra-Hammerstein model with finite memory as it is given in [14]:

$$y(n) = \sum_{k=0}^{M} h_1(k)u(n-k) + \sum_{k=0}^{M} h_2(k)u^2(n-k); \quad h_1(0) = 1;\ h_2(0) = 1,\ h_i(M) \neq 0, \tag{3.1}$$

where $u(n)$ is the input of the system, assumed to be a stationary zero mean Gaussian white random process with $E(u^2(n)) = \gamma_2$. M stands for the model order.

The Hammerstein coefficients vectors $h1$ and $h2$ are defined by

$$hp = \left[h_p(0), h_p(1), \ldots, h_p(M)\right]^T; \quad p = 1; 2. \tag{3.2}$$

As we evoked in the Introduction, identification algorithms based on the computation of 2nd-order output cumulants are sensitive to additive Gaussian noise because 2nd-order cumulants of this latter are in general different to zero. Since the 4th-order cumulants of additive Gaussian noise is null, it will be interesting to use the 4th-order output cumulants to derive identification algorithms. But this will introduce another problem which is the computation complexity. In this paper, we will overcome this shortcoming by using a tensor analysis.

To determine the kernels of this model, we will generate the fourth-order output cumulants. For this purpose, we need to use the standard properties of cumulants and the Leonov-Shiryaev formula for manipulating products of random variables.

The fourth-order output cumulant is given by [15]:

$$\begin{aligned} c_{4y}(i_1,i_2,i_3) &= \operatorname{cum}\left[y(n+i_1),y(n+i_2),y(n+i_3),y(n)\right] \\ &= 8\gamma_2^3\{\phi_0(i_1,i_2,i_3,0)+\phi_0(i_1,i_3,i_2,0) \\ &\quad +\phi_0(i_2,i_3,i_1,0)+\phi_0(i_1,0,i_2,i_3) \\ &\quad +\phi_0(i_2,0,i_1,i_3)+\phi_0(i_3,0,i_1,i_2)\} \\ &\quad +48\gamma_2^4\sum_{l=0}^{M}h_2(l+i_1)h_2(l+i_2)h_2(l+i_3)h_2(l), \end{aligned} \tag{3.3}$$

where

$$\phi_0(i_1,i_2,i_3,i_4)=\sum_{l=0}^{M}h_1(l+i_1)h_1(l+i_2)h_2(l+i_3)h_2(l+i_4). \tag{3.4}$$

It is easy to verify that $c_{4y}(i_1,i_2,i_3)=0$ for all $|i_1|,|i_2|,|i_3|>M$.

All the nonzero terms of $c_{4y}(i_1,i_2,i_3)$ are obtained for $(i_1,i_2,i_3)\in[-M,M]^3$. Such a choice allows us to construct a maximal redundant information, in which the fourth-order cumulants are taken for time lags i_1, i_2, and i_3 within the range $[-M,M]$.

In the sequel we shall present an analysis of a 3rd-order tensor composed of the 4th-order output cumulants.

4. Formulation and Analysis of a Cumulant Cubic Tensor

Let us define the three-dimensional tensor $C^{(4,y)}\in\mathbb{C}^{(2M+1)\times(2M+1)\times(2M+1)}$, in which the element in position (i,j,k) corresponds to $c_{4y}(i_1,i_2,i_3)$, with $i=i_1+M+1$; $j=i_2+M+1$; $k=i_3+M+1$. As $i_1,i_2,i_3\in[-M,M]$, we get $i,j,k\in[1,2M+1]$. Thus,

$$\begin{aligned} C_{ijk} &= c_{4y}(i-M-1,j-M-1,k-M-1) \\ &= 8\gamma_2^3\{\phi_0(i-M-1,j-M-1,k-M-1,0) \\ &\quad +\phi_0(i-M-1,k-M-1,j-M-1,0) \\ &\quad +\phi_0(j-M-1,k-M-1,i-M-1,0) \\ &\quad +\phi_0(i-M-1,0,j-M-1,k-M-1) \\ &\quad +\phi_0(j-M-1,0,i-M-1,k-M-1) \end{aligned}$$

$$+\phi_0\left(k-M-1,0,i-M-1,j-M-1\right)\}$$
$$+48\gamma_2^4\sum_{l=0}^{M}h_2(l+i-M-1)h_2\left(l+j-M-1\right)$$
$$\times h_2(l+k-M-1)h_2(l), \tag{4.1}$$

$\phi_0(\cdot,\cdot,\cdot,\cdot)$ is given by (3.4). It follows that

$$\begin{aligned}C_{ijk}=8\gamma_2^3\Bigg\{&\sum_{l=0}^{M}h_1(l+i-M-1)h_1\left(l+j-M-1\right)h_2(l+k-M-1)h_2(l)\\&+\sum_{l=0}^{M}h_1(l+i-M-1)h_1(l+k-M-1)h_2\left(l+j-M-1\right)h_2(l)\\&+\sum_{l=0}^{M}h_1\left(l+j-M-1\right)h_1(l+k-M-1)h_2(l+i-M-1)h_2(l)\\&+\sum_{l=0}^{M}h_1(l+i-M-1)h_1(l)h_2\left(l+j-M-1\right)h_2(l+k-M-1)\\&+\sum_{l=0}^{M}h_1\left(l+j-M-1\right)h_1(l)h_2(l+i-M-1)h_2(l+k-M-1)\\&+\sum_{l=0}^{M}h_1(l+k-M-1)h_1(l)h_2(l+i-M-1)h_2\left(l+j-M-1\right)\Bigg\}\\&+48\gamma_2^4\sum_{l=0}^{M}h_2(l+i-M-1)h_2\left(l+j-M-1\right)h_2(l+k-M-1)h_2(l).\end{aligned} \tag{4.2}$$

Then, expression of the tensor C will be given by

$$\begin{aligned}C=8\gamma_2^3\sum_{i=1}^{2M+1}\sum_{j=1}^{2M+1}\sum_{k=1}^{2M+1}\Bigg\{&\sum_{l=0}^{M}h_1(l+i-M-1)h_1\left(l+j-M-1\right)h_2(l+k-M-1)h_2(l)\\&+\sum_{l=0}^{M}h_1(l+i-M-1)h_1(l+k-M-1)h_2\left(l+j-M-1\right)h_2(l)\\&+\sum_{l=0}^{M}h_1\left(l+j-M-1\right)h_1(l+k-M-1)h_2(l+i-M-1)h_2(l)\\&+\sum_{l=0}^{M}h_1(l+i-M-1)h_1(l)h_2\left(l+j-M-1\right)h_2(l+k-M-1)\end{aligned}$$

$$+\sum_{l=0}^{M} h_1(l+j-M-1)h_1(l)h_2(l+i-M-1)h_2(l+k-M-1)$$
$$+\sum_{l=0}^{M} h_1(l+k-M-1)h_1(l)h_2(l+i-M-1)h_2(l+j-M-1)\Bigg\}$$
$$\times e_i^{(2M+1)} \circ e_j^{(2M+1)} \circ e_k^{(2M+1)} + 48\gamma_2^4$$
$$\times \sum_{i=1}^{2M+1}\sum_{j=1}^{2M+1}\sum_{k=1}^{2M+1}\sum_{l=0}^{M} h_2(l+i-M-1)\cdot h_2(l+j-M-1)h_2(l+k-M-1)h_2(l)$$
$$\times e_i^{(2M+1)} \circ e_j^{(2M+1)} \circ e_k^{(2M+1)}. \tag{4.3}$$

The mathematical development of the expression (4.3) yields to

$$C = 8\gamma_2^3\Bigg\{\sum_{l=0}^{M} h_2(l)h1_{\bullet l} \circ h1_{\bullet l} \circ h2_{\bullet l} + \sum_{l=0}^{M} h_2(l)h1_{\bullet l} \circ h2_{\bullet l} \circ h1_{\bullet l}$$
$$+\sum_{l=0}^{M} h_2(l)h2_{\bullet l} \circ h1_{\bullet l} \circ h1_{\bullet l} + \sum_{l=0}^{M} h_1(l)h1_{\bullet l} \circ h2_{\bullet l} \circ h2_{\bullet l}$$
$$+\sum_{l=0}^{M} h_1(l)h2_{\bullet l} \circ h1_{\bullet l} \circ h2_{\bullet l} + \sum_{l=0}^{M} h_1(l)h2_{\bullet l} \circ h2_{\bullet l} \circ h1_{\bullet l}\Bigg\}$$
$$+ 48\gamma_2^4\sum_{l=0}^{M} h_2(l)h2_{\bullet l} \circ h2_{\bullet l} \circ h2_{\bullet l}, \tag{4.4}$$

where

$$hp_{\bullet l} = \sum_{m=1}^{2M+1} h_p(l+m-M-1)e_m^{(2M+1)}, \quad p = 1;2. \tag{4.5}$$

This notation leads to define two channel matrices $H_1; H_2 \in \mathbb{C}^{(2M+1)\times(M+1)}$ as follows:

$$H_p \quad \mathscr{H}(h_p) = \left[hp_{\bullet 0}, hp_{\bullet 1}, \ldots, hp_{\bullet M}\right] = \begin{pmatrix} 0 & 0 & \cdots & h_p(0) \\ \vdots & \vdots & \ddots & \vdots \\ 0 & h_p(0) & \cdots & h_p(M-1) \\ h_p(0) & h_p(1) & \cdots & h_p(M) \\ \vdots & \vdots & \ddots & \vdots \\ h_p(M-1) & h_p(M) & \cdots & 0 \\ h_p(M) & 0 & \cdots & 0 \end{pmatrix}, \tag{4.6}$$

with $p = 1;2$, and $\mathscr{H}(\cdot)$ is the operator that builds a special Hankel matrix from the vector argument as shown above.

Let us compute now the different slices of the proposed tensor.

4.1. Horizontal Slices Expressions

From (2.2) and (4.3), we get

$$\begin{aligned}
C_{i\bullet\bullet} = 8\gamma_2^3 \Bigg\{ & \sum_{l=0}^{M} h_2(l) h_1(l+i-M-1) h1_{\bullet l} h2_{\bullet l}^T \\
& + \sum_{l=0}^{M} h_2(l) h_1(l+i-M-1) h2_{\bullet l} h1_{\bullet l}^T \\
& + \sum_{l=0}^{M} h_2(l) h_2(l+i-M-1) h1_{\bullet l} h1_{\bullet l}^T \\
& + \sum_{l=0}^{M} h_1(l) h_1(l+i-M-1) h2_{\bullet l} h2_{\bullet l}^T \\
& + \sum_{l=0}^{M} h_1(l) h_2(l+i-M-1) h1_{\bullet l} h2_{\bullet l}^T \\
& + \sum_{l=0}^{M} h_1(l) h_2(l+i-M-1) h2_{\bullet l} h1_{\bullet l}^T \Bigg\} \\
+ 48\gamma_2^4 & \sum_{l=0}^{M} h_2(l) h_2(l+i-M-1) h2_{\bullet l} h2_{\bullet l}^T,
\end{aligned} \tag{4.7}$$

which can be written as

$$\begin{aligned}
C_{i\bullet\bullet} = 8\gamma_2^3 \Big\{ & H_1 \mathrm{diag}_i(H_1) \Sigma_2^T + \Sigma_2 \mathrm{diag}_i(H_1) H_1 \\
& + H_1 \mathrm{diag}_i(\Sigma_2) H_1^T + H_2 \mathrm{diag}_i(\Sigma_1) H_2^T \\
& + \Sigma_1 \mathrm{diag}_i(H_2) H_2^T + H_2 \mathrm{diag}_i(H_2) \Sigma_1^T \Big\} \\
+ 48\gamma_2^4 & H_2 \mathrm{diag}_i(\Sigma_2) H_2^T,
\end{aligned} \tag{4.8}$$

where $\Sigma_1 = H_1\,\mathrm{diag}(h_1)$; $\Sigma_2 = H_2\,\mathrm{diag}(h_2)$; $\mathrm{diag}_n(\cdot)$ is the diagonal matrix formed by the nth line of its argument.

It can easily be demonstrated that

$$C_{m\bullet\bullet} = C_{\bullet m\bullet} = C_{\bullet\bullet m} = C_m. \tag{4.9}$$

It follows that

$$\begin{aligned} C_m = 8\gamma_2^3 \Big\{ & H_1 \mathrm{diag}_m(H_1)\Sigma_2^T + \Sigma_2 \mathrm{diag}_m(H_1)H_1^T \\ & + H_1 \mathrm{diag}_m(\Sigma_2)\ H_1^T + H_2 \mathrm{diag}_m(\Sigma_1)H_2^T \\ & + \Sigma_1 \mathrm{diag}_m(H_2)H_2^T + H_2 \mathrm{diag}_m(H_2)\Sigma_1^T \Big\} \\ & + 48\gamma_2^4 H_2 \mathrm{diag}_m(\Sigma_2)H_2^T, \end{aligned} \tag{4.10}$$

with $m = 1, \ldots, 2M + 1$.

The expression of the unfolded tensor representation is given by

$$\begin{aligned} C_{[U]} = \begin{pmatrix} C_1 \\ C_2 \\ \vdots \\ C_{2M+1} \end{pmatrix} = 8\gamma_2^3 \underbrace{\left\{ \begin{pmatrix} H_1 \mathrm{diag}_1(H_1)\Sigma_2^T \\ H_1 \mathrm{diag}_2(H_1)\Sigma_2^T \\ \vdots \\ H_1 \mathrm{diag}_{2M+1}(H_1)\Sigma_2^T \end{pmatrix} + \cdots \right\}}_{\text{the 6th terms with respect to } C_m \text{ in (4.10)}} \\ + 48\gamma_2^4 \left\{ \begin{pmatrix} H_2 \mathrm{diag}_1(\Sigma_2)H_2^T \\ H_2 \mathrm{diag}_2(\Sigma_2)H_2^T \\ \vdots \\ H_2 \mathrm{diag}_{2M+1}(\Sigma_2)H_2^T \end{pmatrix} \right\}. \end{aligned} \tag{4.11}$$

To develop this expression, we need the following property.

Property 1. Let A be the matrix with dimensions (M, N) and B the matrix with dimensions (M', N), then

$$\begin{pmatrix} A\mathrm{diag}_1(B) \\ A\mathrm{diag}_2(B) \\ \vdots \\ A\mathrm{diag}_{M'}(B) \end{pmatrix} = B \diamond A, \tag{4.12}$$

where $\diamond$ stands for the Khatri-Rao product.

It becomes that

$$C_{[U]} = 8\gamma_2^3 \left\{ \begin{array}{l} (H_1 \diamond H_1)\,\mathrm{diag}(h_2) H_2^T + (H_1 \diamond H_2)\,\mathrm{diag}(h_2) H_1^T \\ +(H_2 \diamond H_1)\,\mathrm{diag}(h_2) H_1^T + (H_1 \diamond H_2)\,\mathrm{diag}(h_1) H_2^T \\ +(H_2 \diamond H_1)\,\mathrm{diag}(h_1) H_2^T + (H_2 \diamond H_2)\,\mathrm{diag}(h_1) H_1^T \end{array} \right\} + 48\gamma_2^4 \Big((H_2 \diamond H_2)\,\mathrm{diag}(h_2) H_2^T \Big). \tag{4.13}$$

5. Blind Identification System with Cumulant Tensor

To estimate the Volterra-Hammerstein kernels and to avoid the computation of $H_p : p = 1, 2$, we will use the following Khatri-Rao property to propose an Iterative Alternating Least Square (IALS) procedure.

Property 2. If matrices $A \in \mathbb{C}^{m \times n}$ and $B \in \mathbb{C}^{n \times m}$ and vector $d \in \mathbb{C}^n$ are such that $X = A\mathrm{diag}(d)B$, then it holds that $\mathrm{vec}(X) = (B^T \diamond A)d$, where $\mathrm{vec}(\cdot)$ stands for the vectorizing operator.

Applying this property to (4.13), it is straightforward to write

$$\begin{aligned} \mathrm{vec}\big(C_{[U]}\big) &= 8\gamma_2^3 \left\{ \begin{array}{l} (H_2 \diamond H_1 \diamond H_1)h_2 + (H_1 \diamond H_1 \diamond H_2)h_2 \\ +(H_1 \diamond H_2 \diamond H_1)h_2 + (H_2 \diamond H_1 \diamond H_2)h_1 \\ +(H_2 \diamond H_2 \diamond H_1)h_1 + (H_1 \diamond H_2 \diamond H_2)h_1 \end{array} \right\} \\ &\quad + 48\gamma_2^4((H_2 \diamond H_2 \diamond H_2)h_2) \\ &= 8\gamma_2^3\{(H_2 \diamond H_1 \diamond H_2) + (H_2 \diamond H_2 \diamond H_1) + (H_1 \diamond H_2 \diamond H_2)\}h_1 \\ &\quad + \left\{ \begin{array}{l} 8\gamma_2^3((H_2 \diamond H_1 \diamond H_1) + (H_1 \diamond H_1 \diamond H_2) + (H_1 \diamond H_2 \diamond H_1)) \\ +48\gamma_2^4((H_2 \diamond H_2 \diamond H_2)) \end{array} \right\} h_2. \end{aligned} \tag{5.1}$$

Let A and B be

$$\begin{aligned} A &= 8\gamma_2^3\{(H_2 \diamond H_1 \diamond H_2) + (H_2 \diamond H_2 \diamond H_1) + (H_1 \diamond H_2 \diamond H_2)\}, \\ B &= 8\gamma_2^3((H_2 \diamond H_1 \diamond H_1) + (H_1 \diamond H_1 \diamond H_2) + (H_1 \diamond H_2 \diamond H_1)) + 48\gamma_2^4((H_2 \diamond H_2 \diamond H_2)). \end{aligned} \tag{5.2}$$

The problem of the blind nonlinear identification will be expressed as

$$Ah_1 + Bh_2 = \mathrm{vec}(C_U). \tag{5.3}$$

This system can be solved using several methods. We propose to resolve it using the Iterative Alternating Least Square algorithm (IALS).

6. Cost Functions and Iterative Alternating Least Square Algorithm

To apply the IALS algorithm, we suppose alternatively that Ah_1 or Bh_2 is a constant vector. Then, we get two cost functions to be minimized. Assuming that the vector Bh_2 is constant, the first cost function will be expressed by

$$E_1(h_1) = \|(\mathrm{vec}(C_U) - Bh_2) - Ah_1\|^2. \tag{6.1}$$

For the second cost function, we assume that Ah_1 is constant; thus

$$E_2(h_2) = \|(\mathrm{vec}(C_U) - Ah_1) - Bh_2\|^2. \tag{6.2}$$

The application of the least mean squares algorithm to these two functions leads to the following solutions:

$$\begin{aligned} h_1 &= A^{\#}(\mathrm{vec}(C_U) - Bh_2), \\ h_2 &= B^{\#}(\mathrm{vec}(C_U) - Ah_1), \end{aligned} \tag{6.3}$$

where the subscript # denotes the Moore-Penrose pseudoinverse of the corresponding matrix.

Finally, the different steps of the proposed IALS algorithm are summarized in Algorithm 1.

The notation $\widehat{x}$ stands for the estimates of the parameter x.

7. Convergence Analysis

Equation (6.3) shows that the ALS algorithm converges to optimal solutions if and only if the Moore-Penroze pseudoinverse matrices $A^{\#}$ and $B^{\#}$ exist, which implies that matrices A and B must be full rank [14, 16]. To do this, we start by affirming that, due to the Hankel structure and the assumption that $h_i(M) \neq 0$ (3.1), each of the matrices H_1 and H_2 is full rank. Then

$$\mathrm{rank}(H_1) = \mathrm{rank}(H_2) = M + 1. \tag{7.1}$$

Let us now find out the rank of matrices $H_i \diamond H_j \diamond H_k;\ i, j, k \in \{1, 2\}$ obtained from Khatri-Rao product (5.1). We will make use of the following definition and property defining the k-rank of a matrix and the rank of a Khatri-Rao product of two matrices [17].

Definition 7.1. The rank of a matrix $A \in \mathbb{C}^{E\times F}$ (denoted by k_A) is equal to k if and only if every k columns of A are linearly independent. Note that $k_A \leq \min(E, F)$, for all A.

This means that the rank of the matrix A is the largest integer k for which every set containing k columns of A is independent.

Property 3. Consider the Khatri-Rao product $A \diamond B$, where A is $E \times F$ and B is $G \times F$. If neither A nor B contains a zero column (and hence $k_A \geq 1,\ k_B \geq 1$), then $k_{A\diamond B} \geq \min(k_A + k_B - 1, F)$.

Initialize h_1 and h_2 as random variables (estimates $\widehat{h}_1^{(0)}; \widehat{h}_2^{(0)}$).
For $n \geq 1$,

(i) build Hankel matrices using (4.5), for $p = 1; 2$,

$$\widehat{H}_1^{(n)} = \mathscr{H}(\widehat{h}_1^{(n)}), \qquad \widehat{H}_2^{(n)} = \mathscr{H}(\widehat{h}_2^{(n)}),$$

(ii) compute matrices estimate $\widehat{A}$ and $\widehat{B}$ as

$$\widehat{A}^{(n)} = 8\gamma_2^3\{(\widehat{H}_2 \diamond \widehat{H}_1 \diamond \widehat{H}_2) + (\widehat{H}_2 \diamond \widehat{H}_2 \diamond \widehat{H}_1) + (\widehat{H}_1 \diamond \widehat{H}_2 \diamond \widehat{H}_2)\}^{(n)},$$

$$\widehat{B}^{(n)} = \{8\gamma_2{}^3\ ((\widehat{H}_2 \diamond \widehat{H}_1 \diamond \widehat{H}_1) + (\widehat{H}_1 \diamond \widehat{H}_1 \diamond \widehat{H}_2)\ + (\widehat{H}_1 \diamond \widehat{H}_2 \diamond \widehat{H}_1)) + 48\gamma_2^4((\widehat{H}_2 \diamond \widehat{H}_2 \diamond \widehat{H}_2))\}^{(n)},$$

(iii) minimize cost functions (6.1) and (6.2) so that

$$\widehat{h}_1^{(n+1)} = \widehat{A}^{(n)\#}(\mathrm{vec}(C_U) - \widehat{B}^{(n)}\widehat{h}_2^{(n)}),$$
$$\widehat{h}_2^{(n+1)} = \widehat{B}^{(n)\#}(\mathrm{vec}(C_U) - \widehat{A}^{(n)}\widehat{h}_1^{(n)}),$$

(iv) reiterate until parametric error convergence

$$\frac{\|\mathrm{vec}((\widehat{h}_1^{(n+1)} \quad \widehat{h}_2^{(n+1)}) - (\widehat{h}_1^{(n)} \quad \widehat{h}_2^{(n)}))\|}{\|\mathrm{vec}(\widehat{h}_1^{(n+1)} \quad \widehat{h}_2^{(n+1)})\|} \leq \varepsilon.$$

Algorithm 1: Different steps of the new blind identification algorithm-based cumulant tensor analysis.

It follows that

$$k_{H_i \diamond H_j} \geq \min(2M + 1, M + 1), \quad \forall i, j \in \{1, 2\}, \tag{7.2}$$

which is equivalent to

$$k_{H_i \diamond H_j} \geq M + 1. \tag{7.3}$$

Due to the definition of the Khatri-Rao product and the structure of the Hankel matrices $H_i;\ i \in \{1, 2\}$, we conclude that

$$k_{H_i \diamond H_j} = M + 1 = \mathrm{rank}\big(H_i \diamond H_j\big). \tag{7.4}$$

Consequently,

$$k_{(H_i \diamond H_j) \diamond H_k} = M + 1 = \mathrm{rank}\big(H_i \diamond H_j \diamond H_k\big), \quad \forall i, j, k \in \{1, 2\}, \tag{7.5}$$

which means that each matrix $H_i \diamond H_j \diamond H_k$ is full rank whatever the values taken by i and j in the set $\{1, 2\}$.

Let us now find out the rank of matrices A and B. For this purpose, we will study the structure of the matrix $H_i \diamond H_j \diamond H_k$. Recall that H_i is a $(2M + 1, M + 1)$ matrix. Let $\Theta_i = [\ 0\ \ 0\ \ \cdots\ \ 0]^T$ be the zero column vector of dimension $(2M + 1)$; $i = 1, \ldots, M$.

Then, for the matrix $H_i \diamond H_j \diamond H_k$, we will have the following form:

$$H_i \diamond H_j \diamond H_k = \begin{pmatrix} \Theta_1 & \Theta_1 & & \Theta_1 & X_M \\ \Theta_2 & \vdots & & X_{M-1} & \Theta_1 \\ \vdots & \Theta_{M-1} & \cdots & \Theta_2 & \Theta_2 \\ \Theta_M & X_1 & & \vdots & \vdots \\ X_0 & \Theta_M & & \Theta_{M-1} & \Theta_M \end{pmatrix}, \tag{7.6}$$

where X_i stands for the column vector of dimension $(2M+1)^2(M+1)$ which is constituted by products of the kernels model arising from computation of the Khatri-Rao matrix product. We have seen that $H_i \diamond H_j \diamond H_k$ is full rank. The sum of different matrices $H_i \diamond H_j \diamond H_k$ has the same form of $H_i \diamond H_j \diamond H_k$ whatever the system order and the values taken by i, j and k. Consequently, matrices A and B are full rank and then their pseudoinverse exist. We conclude that the IALS converges to an optimal solution in least mean squares sense.

8. Simulation Results

In this section, simulation results will be given to illustrate the performance of the proposed algorithm. Two identification Volterra-Hammerstein systems are considered:

$$\begin{aligned} \text{System 1:} &\begin{cases} z(n) = u(n) - 0.25u(n-1) + 0.9u(n-2) \\ \qquad\quad +u^2(n) + 0.5u^2(n-1) - 0.35u^2(n-2), \\ y(n) = z(n) + e(n), \end{cases} \\ \text{System 2:} &\begin{cases} z(n) = u(n) - 0.4u(n-1) + 0.5u(n-2) + 0.95u(n-3) \\ \qquad\quad +u^2(n) + 0.2u^2(n-1) - 0.7u^2(n-2) + 0.6u^2(n-3), \\ y(n) = z(n) + e(n). \end{cases} \end{aligned} \tag{8.1}$$

The input sequence $u(n)$ is assumed to be stationary, zero mean, white Gaussian noise with variance $\gamma_2 = 1$. The noise signal $e(n)$ is also assumed to be white Gaussian sequence and independent of the input. The parameter estimation was performed for two different signal-to-noise ratio (SNR) levels: 20 dB and 3 dB.

The SNR is computed with the following expression:

$$\text{SNR} = \frac{E\left(z^2(n)\right)}{E(e^2(n))}. \tag{8.2}$$

Fourth-order cumulants were estimated from different lengths of output sequences ($N = 4096$ and $N = 16384$) assuming perfect knowledge of the system model. To reduce the realization dependency, parameters were averaged over 500 Monte-Carlo runs. For each

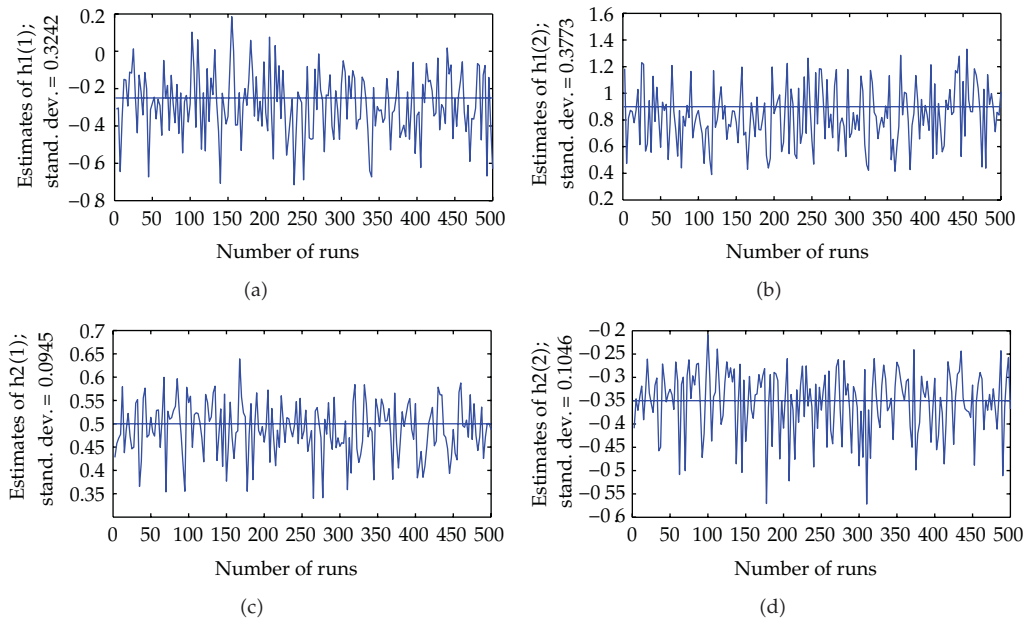

Figure 3: Estimates of the parameters of System 1 with the IALS algorithm for $N = 4096$ and SNR = 3 dB.

simulation, we give the curves representing the variation of the estimates along with the Monte-Carlo runs, and we resume exclusive results in different tables.

System 1

Figures 3 and 4 show the estimates of the different kernels of the proposed model, with the IALS algorithm, for $N = 4096$ and for different SNR levels (3 dB and 20 dB).

The mean and the standard deviation of the estimated kernels against the true ones are shown in Table 1.

Likewise, Figures 5 and 6 show the estimates of the different kernels of System 1 for $N = 16384$ and for SNR levels equal to 3 dB and 20 dB, while, in Table 2, the mean and the standard deviation of the estimated kernels against the true ones are shown.

From these results, we observe that the proposed IALS algorithm performs well generating estimates for a large variation of the SNR (from 20 dB to 3 dB). We also note that the standard deviation is relatively large and decreases with the number of the system observations.

System 2

Figures 7 and 8 show the estimates of the different kernels of the second proposed model for $N = 4096$ and for different SNR (20 dB and 3 dB).

The mean and the standard deviation of the estimated kernels against the true ones are shown in Table 3.

Figures 9 and 10 show the estimates of the different kernels of System 2 for $N = 16384$ and for different SNR (20 dB and 3 dB), while, in Table 4, the mean and the standard deviation of the estimated kernels against the true ones are shown. The mean and the standard

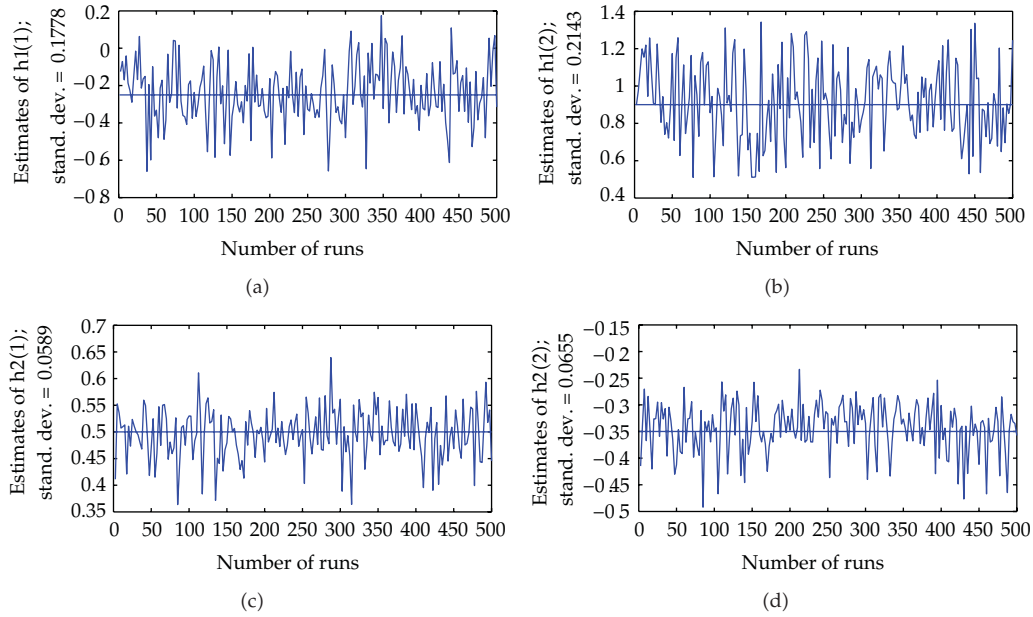

Figure 4: Estimates of the parameters of System 1 with the IALS algorithm for $N = 4096$ and SNR = 20 dB.

Table 1: True and estimated values of the kernels of System 1 for $N = 4096$ (500 Monte-Carlo runs).

True parameters	3 dB		20 dB	
	Mean	St. Dev.	Mean	St. Dev.
−0.25	−0.2401	0.3242	−0.2456	0.1778
0.9	0.9985	0.3773	0.8837	0.2143
0.5	0.5128	0.0945	0.4815	0.0589
−0.35	−0.3411	0.1046	−0.3521	0.0655

Table 2: True and estimated values of the kernels of System 2 for $N = 16384$ (500 Monte-Carlo runs).

True parameters	3 dB		20 dB	
	Mean	St. Dev.	Mean	St. Dev.
−0.25	−0.2464	0.2520	−0.2589	0.1576
0.9	0.9238	0.2947	0.8884	0.1976
0.5	0.4900	0.0679	0.5028	0.0482
−0.35	−0.3665	0.0753	0.3478	0.0508

deviation of the estimated kernels against the true ones, for the second system, are shown in Table 4.

From these results, we note also that the proposed algorithm provides good estimates for the proposed system. The number of observations N affects the range of variation of the standard deviation values. Indeed, for important values of N, this range becomes so small. The method provides good estimates even for low levels of SNR. Furthermore, we note that the larger the Monte-Carlo runs number, the smaller the standard deviations are.

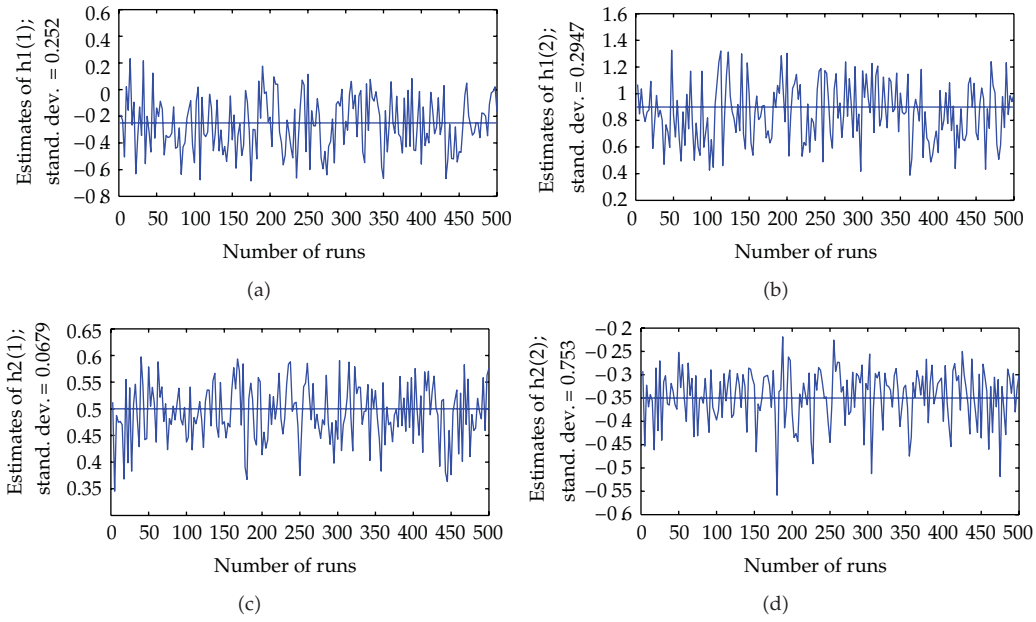

Figure 5: Estimates of the parameters of System 1 with the IALS algorithm for $N = 16384$ and SNR = 3 dB.

Table 3: True and estimated values of the kernels of System 2 for $N = 4096$ (500 Monte-Carlo runs).

True parameters	3 dB		20 dB	
	Mean	St. Dev.	Mean	St. Dev.
−0.4	−0.4512	0.6550	−0.4293	0.1594
0.5	0.5074	0.7632	0.5173	0.1968
0.95	1.1556	0.5329	0.9390	0.1545
0.2	0.2358	0.2525	0.2157	0.0958
−0.7	−0.6794	0.2855	−0.6814	0.1260
0.6	0.5872	0.2268	0.5962	0.0986

8.1. Comparison with Existing Methods

The performance of the previous algorithm was compared with two works: the algorithm proposed in [9] (will be noted as BIL to blind identification with linearization) and the Lagrange Programming Neural Network (LPNN) proposed in [13].

(i) In [14], the problem of blind identification was converted into a linear multivariable form using Kronecker product of the output cumulants. This can be described by the following equations:

$$\overline{C}_y^k(q,\tau) = b(\tau)\left(\overline{\Gamma}_{kw}\right)_{p\times p} b^T(q), \tag{8.3}$$

where $C_y^k(\tau_1,\tau_2,\ldots,\tau_{k-1})$ denotes the output cumulants sequence of order k, Γ_{kw} is the intensity (zero lag cumulant) of order k of the vector W which is formed in its

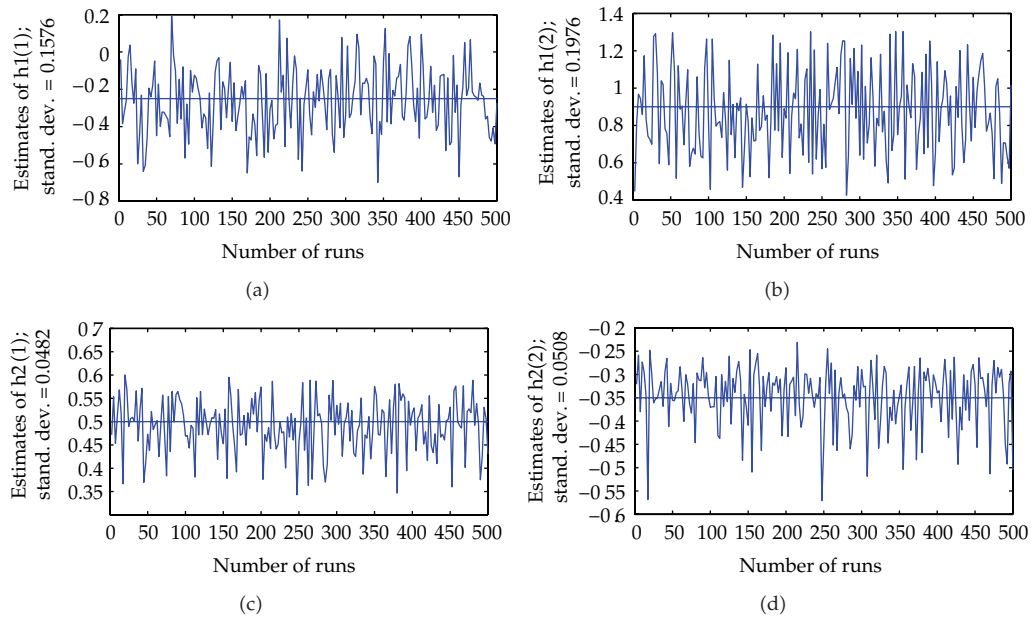

Figure 6: Estimates of the parameters of System 1 with the IALS algorithm for $N = 16384$ and SNR = 20 dB.

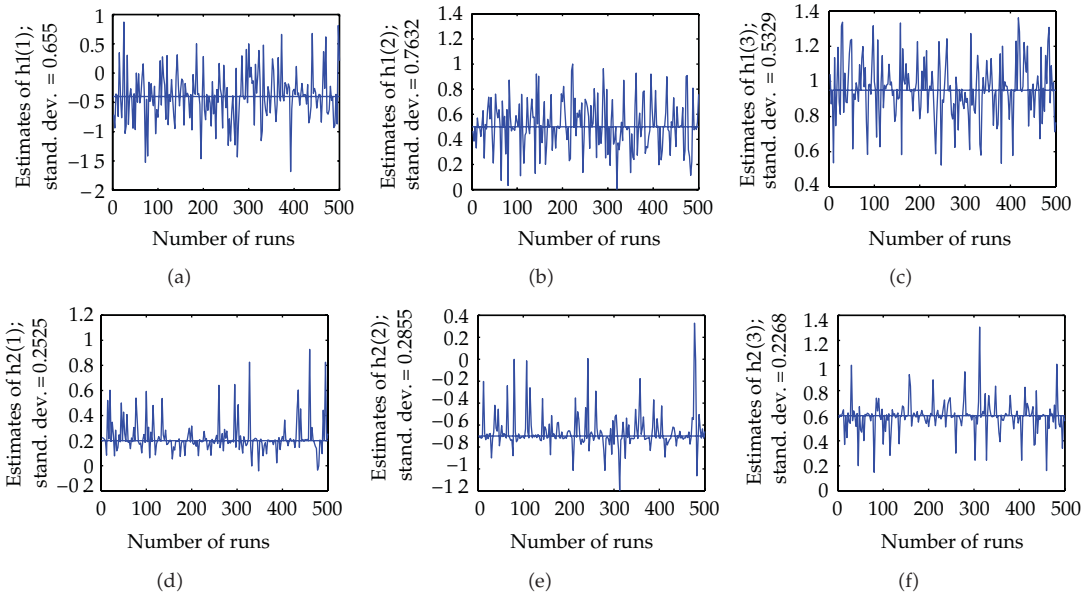

Figure 7: Estimates of the parameters of System 2 with the IALS algorithm for $N = 4096$ and SNR = 3 dB.

turn by the different powers of input, and b is the kernel vector.
For $\tau = 0$, this becomes

$$\overline{C}_y^k(q,0) = b(0)\left(\overline{\Gamma}_{kw}\right)_{p\times p} b^T(q) = \left(\overline{\Gamma}_{kw}\right)_{p\times p} b^T(q). \tag{8.4}$$

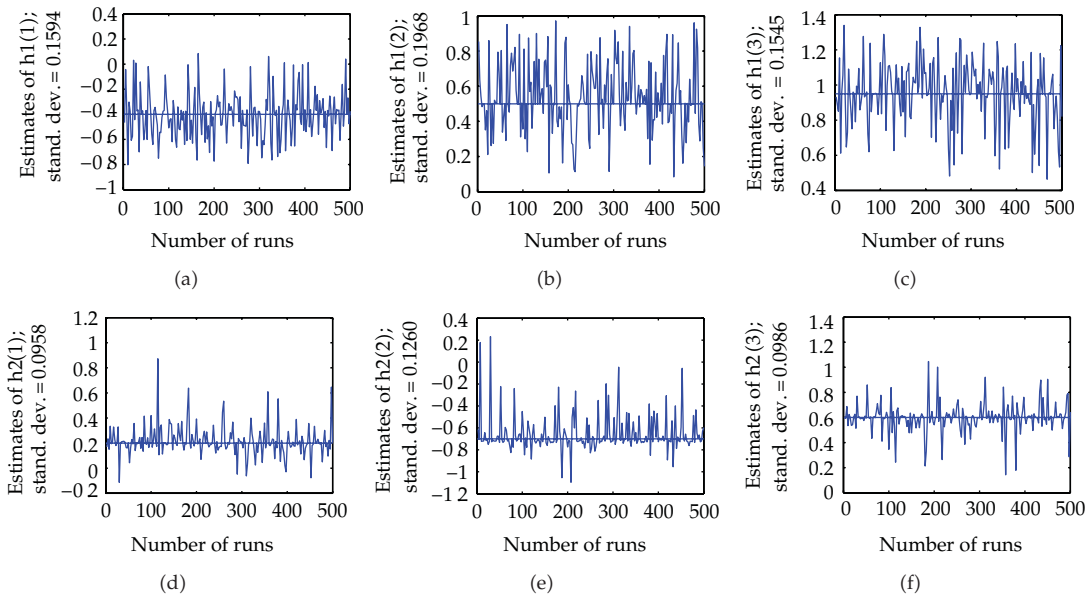

Figure 8: Estimates of the parameters of System 2 with the IALS algorithm for $N = 4096$ and SNR = 20 dB.

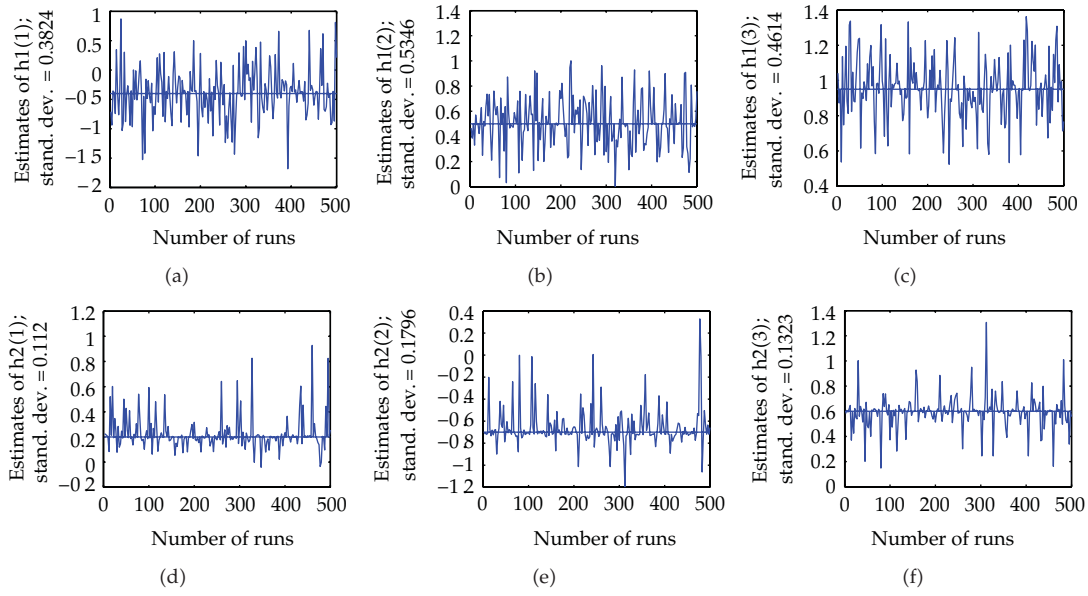

Figure 9: Estimates of the parameters of System 2 with the IALS algorithm for $N = 16384$ and SNR = 3 dB.

Different important scenarios were discussed and successfully resolved. Here, we are interested in the case of Gaussian input when the input statistics are known. Despite the efficiency of the proposed method, the resulting algorithms are in general cumbersome especially for the high series order (As confirmed by authors). For more details, see [14].

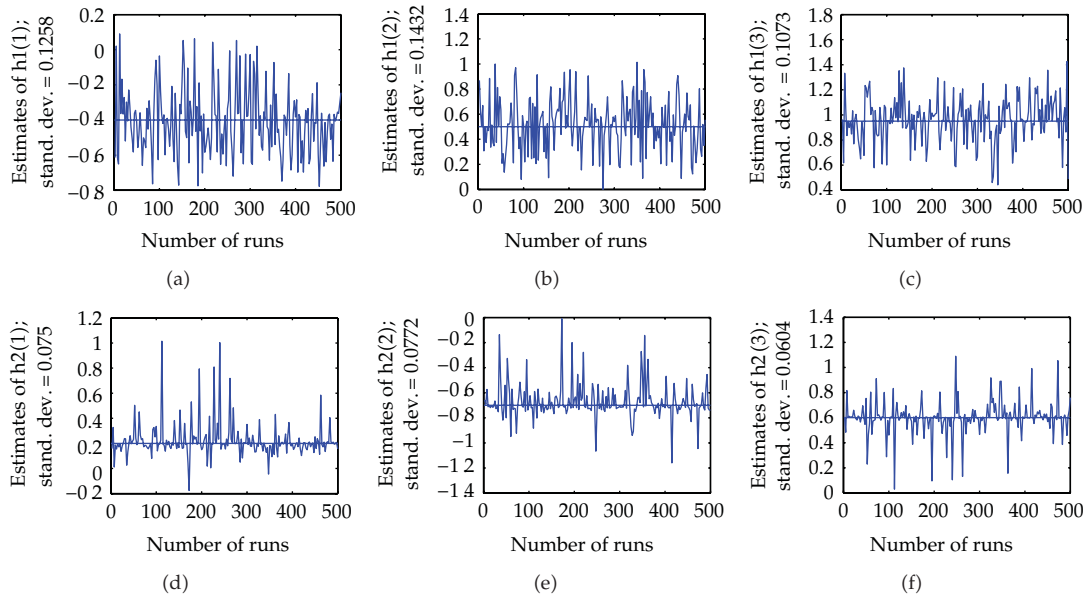

Figure 10: Estimates of the parameters of System 2 with the IALS algorithm for $N = 16384$ and SNR = 20 dB.

Table 4: True and estimated values of the kernels of System 2 for $N = 16384$ (500 Monte-Carlo runs).

True parameters	3 dB		20 dB	
	Mean	St. Dev.	Mean	St. Dev.
−0.4	−0.4378	0.3824	−0.4121	0.1258
0.5	0.5116	0.5346	0.5122	0.1432
0.95	0.9450	0.4614	0.9507	0.1073
0.2	0.1847	0.1120	0.2143	0.0750
−0.7	−0.6877	0.1796	−0.6941	0.0772
0.6	0.6014	0.1323	0.5983	0.0604

(ii) In their work [13], authors tried to determine the different Volterra kernels and the variance of the input from the autocorrelation estimates $\rho[k]$ and the third-order moments estimates $\mu[k,l]$ of the system output, using the Lagrange Programming Neural Network (LPNN). As the LPNN is essentially designed for general nonlinear programming, they expressed the identification problem as follows:

$$\begin{aligned} \text{Minimize:} \quad & L(f) = \sum_i \sum_j \left(\mu[i,j] - M[i,j,f]\right)^2, \\ \text{Subject to:} \quad & \rho[i] \ = R[i,j], \end{aligned} \tag{8.5}$$

where $R[i,j]$ is the autocorrelation function of the real process $y[n]$ and $M[i,j]$ is its third order moment sequence. f is the vector formed by the unknown parameters

of the Volterra model and the unknown variance of the driving noise.
So the Lagrangian function will be written as

$$L(f,\lambda) = L(f) + \sum_i \lambda_i (\rho[i] - R[i,f]). \tag{8.6}$$

To improve the convergence and the precision of the algorithm, authors extended the preceding function by defining the Augmented Lagrangian Function such as

$$L(f,\lambda) = L(f) + \sum_i \lambda_i (\rho[i] - R[i,f]) + \beta \sum_i (\rho[i] - R[i,f])^2, \tag{8.7}$$

where $\{\beta_k\}$ is a penalty parameter sequence satisfying $0 < \beta_k < \beta_{k+1}$ for all k, $\beta_k \to \infty$. So the back-propagation algorithm can be established using the Lagrange multiplier.

The performance of the new proposed algorithm was compared with these two algorithms. Each of these algorithms was used to identify the two models presented above (8.1), for the case of Gaussian excitation, $N = 16384$ samples, and for the tow proposed SNR levels 3 dB and 20 dB.

Figures 11 and 12 show a comparison of the standard deviations given by each algorithm. We note that these results may vary considerably depending on the number of the output observations. These results show that the new proposed algorithm performs well. For a small number of unknown parameters, we note that all algorithms give in general the same STD values and these values decrease by increasing the SNR values. We note furthermore that BIL algorithm is so complex for programming in comparison with the LPNN and the new one. For big number of unknown parameters, the BIL algorithm becomes very computational complex and even the LPNN, while the new algorithm keeps its simplicity and provides good parameters with very competitive STD values.

9. Conclusion

In this paper, a new approach for blind nonlinear identification problem of a second-order Hammerstein-Volterra system is developed. Thanks to a matrix analysis of a cubic tensor composed of the fourth-order output cumulants, the nonlinear identification problem is reduced to a system having the following general form: $Ax + By = c$. This system is solved using the Iterative Alternating Least Square. A convergence analysis shows that matrices A and B are full rank which means that the IALS algorithm converges to optimal solutions in the least mean squares sense. Simulation results on two different systems show good performance of the proposed algorithm. It is noted also that the different values of the estimates improve with the number of the system observation even for small values of SNR. Comparison results with two algorithms show that the new proposed algorithm performs well and especially in the case of great number of unknown parameters. Extending the proposed algorithm for more input classes and for more general Volterra-Hammerstein systems remains an open problem, and it is now the subject matter of current works.

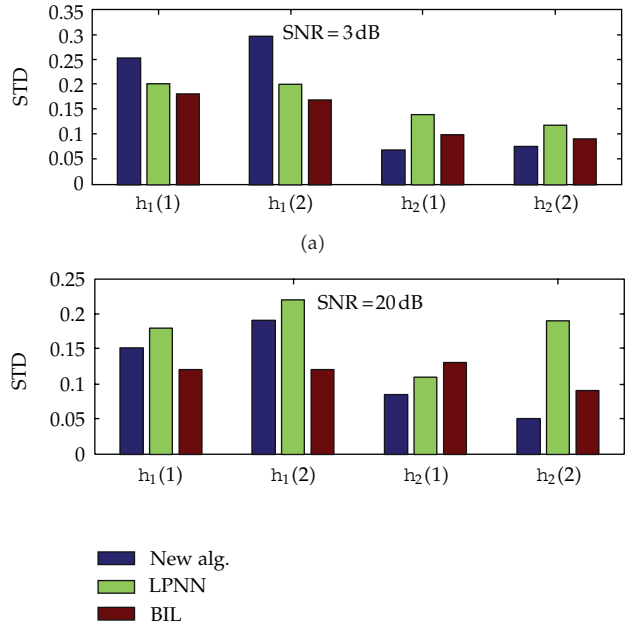

Figure 11: Comparison of the standard deviations (STDs) of the new algorithm against those of the LPNN and the BIL algorithms: System 1.

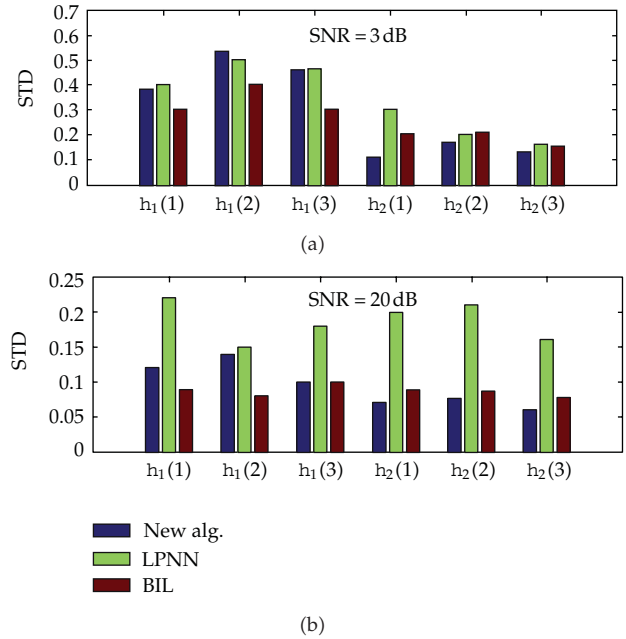

Figure 12: Comparison of the standard deviations (STDs) of the new algorithm against those of the LPNN and the BIL algorithms: System 2.

Acknowledgment

The authors would like to thank Prof. Gerard Favier, Laboratory Director (I3S Laboratory–CNRS, University of Nice Sophia Antipolis, France) for his support, advice, and corrections to carry out this work.

References

[1] M. Li, C. Cattani, and S. Y. Chen, "Viewing sea level by a one-dimensional random function with long memory," *Mathematical Problems in Engineering*, vol. 2011, Article ID 654284, 2011.

[2] S. C. Lim, C. H. Eab, K. H. Mak, M. Li, and S. Y. Chen, "Solving linear coupled fractional differential equations by direct operational method and some applications," *Mathematical Problems in Engineering*, vol. 2012, Article ID 653939, 28 pages, 2012.

[3] S. Y. Chen and Q. Guan, "Parametric shape representation by a deformable NURBS model for cardiac functional measurements," *IEEE Transactions on Biomedical Engineering*, vol. 58, no. 3, pp. 480–487, 2011.

[4] S. Chen, H. Tong, and C. Cattani, "Markov models for image labeling," *Mathematical Problems in Engineering*, vol. 2012, Article ID 814356, 18 pages, 2012.

[5] E. G. Bakhoum and C. Toma, "Specific mathematical aspects of dynamics generated by coherence functions," *Mathematical Problems in Engineering*, vol. 2011, Article ID 436198, 2011.

[6] L. Agarossi, S. Bellini, F. Bregoli, and P. Migliorati, "Simplified nonlinear receivers for the optical disc channel," in *Proceedings of the IEEE International Conference on Communications (ICC '99)*, vol. 3, pp. 1945–1950, June 1999.

[7] K. Watanabe, Y. W. Chen, and K. Yamashita, "Blind nonlinear equalization using 4th –order cumulants," in *Proceedings of the Sice 2002*, pp. 2128–2131, Osaka, Japan, August 2002.

[8] I. Cherif and F. Fnaiech, "Blind identification of a second order Volterra-Hammerstein series using cumulant cubic tensor analysis," in *Proceedings of the 34th Annual Conference of the IEEE Industrial Electronics Society (IECON '08)*, pp. 1851–1856, Orlando, Fla, USA, November 2008.

[9] N. Kalouptsidis and P. Koukoulas, "Blind identification of volterra-hammerstein systems," *IEEE Transactions on Signal Processing*, vol. 53, no. 8, pp. 2777–2787, 2005.

[10] G. Favier, A. Y. Kibangou, and T. Bouilloc, "Nonlinear system modeling and identification using Volterra-PARAFAC models," *International Journal of Adaptive Control and Signal Processing*, vol. 26, pp. 30–53, 2012.

[11] T. Bouilloc and G. Favier, "Nonlinear channel modeling and identification using baseband VolterraParafac models," *Signal Processing*, vol. 92, no. 6, pp. 1492–1498, 2012.

[12] G. Favier, M. N. da Costa, A. L. F. de Almeida, and J. M. T. Romano, "Tensor space–time (TST) coding for MIMO wireless communication systems," *Signal Processing*, vol. 92, pp. 1079–1092, 2012.

[13] T. Stathaki and A. Scohyers, "Constrained optimization approach to the blind estimation of Volterra kernels," in *Proceedings of the IEEE International Conference on Acoustics, Speech, and Signal Processing (ICASSP '97)*, vol. 3, pp. 2373–2376, April 1997.

[14] C. E. R. Fernandes, G. Favier, and J. C. M. Mota, "Tensor-based blind channel identification," in *Proceedings of the IEEE International Conference on Communications (ICC '07)*, pp. 2728–2732, June 2007.

[15] P. Koukoulas and N. Kalouptsidis, "Blind identification of second order Hammerstein series," *Signal Processing*, vol. 83, no. 1, pp. 213–234, 2003.

[16] G. H. Golub and C. F. Van Loan, *Matrix Computations*, Johns Hopkins University Press, Baltimore, Md, USA, 3rd edition, 1996.

[17] Y. Hua, A. B. Gershman, and Q. Cheng, *High Resolution and Robust Signal Processing*, Marcell Dekker, New York, NY, USA, 2004.

Hindawi Publishing Corporation
Mathematical Problems in Engineering
Volume 2012, Article ID 138581, 14 pages
doi:10.1155/2012/138581

Research Article

Reducing Noises and Artifacts Simultaneously of Low-Dosed X-Ray Computed Tomography Using Bilateral Filter Weighted by Gaussian Filtered Sinogram

Shaoxiang Hu,[1] Zhiwu Liao,[2] and Wufan Chen[3]

[1] *School of Automation Engineering, University of Electronic Science and Technology of China, Chengdu 611731, China*
[2] *School of Computer Science, Sichuan Normal University, Chengdu 610101, China*
[3] *Institute of Medical Information and Technology, School of Biomedical Engineering, Southern Medical University, Guangzhou 510515, China*

Correspondence should be addressed to Zhiwu Liao, liaozhiwu@163.com

Received 2 February 2012; Accepted 2 March 2012

Academic Editor: Ming Li

Existing sinogram restoration methods cannot handle noises and nonstationary artifacts simultaneously. Although bilateral filter provides an efficient way to preserve image details while denoising, its performance in sinogram restoration for low-dosed X-ray computed tomography (LDCT) is unsatisfied. The main reason for this situation is that the range filter of the bilateral filter measures similarity by sinogram values, which are polluted seriously by noises and nonstationary artifacts of LDCT. In this paper, we propose a simple method to obtain satisfied restoration results for sinogram of LDCT. That is, the range filter weighs the similarity by Gaussian smoothed sinogram. Since smoothed sinogram can reduce the influence of both noises and nonstationary artifacts for similarity measurement greatly, our new method can provide more satisfied denoising results for sinogram restoration of LDCT. Experimental results show that our method has good visual quality and can preserve anatomy details in sinogram restoration even in both noises and nonstationary artifacts.

1. Introduction

Radiation exposure and associated risk of cancer for patients receiving CT examination have been an increasing concern in recent years. Thus, minimizing the radiation exposure to patients has been one of the major efforts in modern clinical X-ray CT radiology [1–8]. However, the presentation of strong noises and non-stationary artifacts degrades the quality

of low-dose CT images dramatically and decreases the accuracy of diagnosis dose. Many strategies have been proposed to reduce the noise, for example, by nonlinear noise filters [8–19] and statistics-based iterative image reconstructions (SIIRs) [20–28].

The SIIRs utilize the statistical information of the measured data to obtain good denoising results but are limited for their excessive computational demands for the large CT image size. Moreover, the mottled noise and non-stationary artifacts in LDCT images cannot be accurately modeled into one specific distribution, which makes it a difficult task to differentiate between noise/artifact and informative anatomical/pathological features [29].

Although the nonlinear filters show effectiveness in reducing noise both in sinogram space and image space, they cannot handle the noise-induced streak artifacts. Since existing methods cannot handle noises and artifacts simultaneously, designing a method to reduce noise and non-stationary artifacts simultaneously becomes an open problem in sinogram restoration of LDCT.

Recently, many new nonlinear filters are presented and show promising denoising performance on space domain [29–44]. Bilateral filter (BF), which integrates range filter (gray level) and domain filter (space) together, is a well-known one [35, 36]. However, BF cannot obtain satisfied results in sinogram restoration of LDCT because of polluted sinogram values for the range filter. To obtain satisfied denoising results in serious noises, some efforts on image space are proposed [37–41].

Wong suggests that two parameters, σ_s^2 and σ_r^2, the variances of Gaussian functions in domain and range filters, should be modulated according to local phase coherence of the image pixels [37]. But it blurs edges or leaves uncleaned noises.

Ming and Bahadir improve the performance of BF by multiresolution method [38]. That is, filtering LL subband uses BF while smoothing wavelet subbands uses SURE shrinkage. It also leads to blur edges while denoising.

van Boomgaard and van de Weijer argue that the main reason for unsatisfied denoising results is the polluted center pixel of BF [40]. Thus, the satisfied results can be obtained by replacing polluted center pixel with an estimate of its true gray levels.

Following [40], median bilateral filter (MBF) is proposed in [41]. MBF replaces the center pixel with the median of a 3×3 window. However, only replacing the center pixel also cannot obtain satisfied denoising results.

Although BF and its improvements can obtain satisfied results in general image denoising, all these methods cannot handle sinogram restoration with noises and non-stationary artifacts simultaneously. We think that the key to handle noises and artifacts simultaneously is how to reduce the influence of both the noises and artifacts of sinogram of LDCT.

In this paper, we propose a new method to reduce the influence of the noises and artifacts of sinogram simultaneously, named bilateral filter weighted by Gaussian filtered sinogram (BFWGFS), which carried on BF on Gaussian smoothed sinogram. Note that, proposed method is different to the method proposed in [40]. The proposed method in [40] only replaces the gray levels of the center point with the median of a 3×3 square centered at the center point, while our method replaces both the center point and all considering points with their Gaussian smoothed sinogram values.

Since the smoothed sinogram can reduce the influence of both the noises and artifacts of sinogram, the weight of the range filter defined on BFWGFS can measure the similarities more precisely comparing to the original sinogram values in BF. Thus, the proposed method can obtain satisfied results in noises and non-stationary artifacts simultaneously.

In the reminder of this paper, Section 2 will introduce the noise models; then in Section 3, we will discuss the measurement of similarity and discussed the difference between

the proposed method and method in [40]. Section 4 describes the denoising framework. Section 5 is the experimental results and discussion. Section 6 gives conclusions and finally, the acknowledgment part.

2. Noise Models

Based on repeated phantom experiments, low-mA (or low-dose) CT calibrated projection data after logarithm transform were found to follow approximately a Gaussian distribution with an analytical formula between the sample mean and sample variance, that is, the noise is a signal-dependent Gaussian distribution [19].

In this section, we will introduce signal-independent Gaussian noise (SIGN), Poisson noise, and signal-dependent Gaussian noise.

2.1. Signal-Independent Gaussian Noise (SIGN)

SIGN is a common noise for the imaging system. Let the original projection data be $\{x_i\}$, $i = 1, \ldots, m$, where i is the index of the ith bin. The signal has been corrupted by additive noise $\{n_i\}$, $i = 1, \ldots, m$ and one noisy observation

$$y_i = x_i + n_i, \tag{2.1}$$

where y_i, x_i, n_i are observations for the random variables Y_i, X_i, and N_i where the upper-case and letters denote the random variables and the lower-cased letters denote the observations for respective variables. X_i is normal $N(0, \sigma_X^2)$, and N_i is normal $N(0, \sigma_N^2)$ and independent of the Gaussian random variable X_i. Thus, Y_i is normal $N(0, \sigma_X^2 + \sigma_N^2)$.

2.2. Poisson Model and Signal-Dependent Gaussian Model

The photon noise is due to the limited number of photons collected by the detector [30]. For a given attenuating path in the imaged subject, $N_0(i, \alpha)$ and $N(i, \alpha)$ denote the incident and the penetrated photon numbers, respectively. Here, i denotes the index of detector channel or bin, and α is the index of projection angle. In the presence of noises, the sinogram should be considered as a random process, and the attenuating path is given by

$$r_i = -\ln\left[\frac{N(i, \alpha)}{N_0(i, \alpha)}\right], \tag{2.2}$$

where $N_0(i, \alpha)$ is a constant, and $N(i, \alpha)$ is Poisson distribution with mean N.

Thus, we have

$$N(i, \alpha) = N_0(i, \alpha) \exp(-r_i). \tag{2.3}$$

Both its mean value and variance are N.

Gaussian distributions of ployenergetic systems were assumed based on limited theorem for high-flux levels, and following many repeated experiments in [19], we have

$$\sigma_i^2(\mu_i) = f_i \exp\left(\frac{\mu_i}{\gamma}\right), \tag{2.4}$$

where μ_i is the mean, and σ_i^2 is the variance of the projection data at detector channel or bin i, γ is a scaling parameter, and f_i is a parameter adaptive to different detector bins.

The most common conclusion for the relation between Poisson distribution and Gaussian distribution is that the photon count will obey Gaussian distribution for the case with large incident intensity and Poisson distribution with feeble intensity [19]. In addition, in [30], the authors deduce the equivalency between Poisson model and Gaussian model. Therefore, both theories indicate that these two noises have similar statistical properties and can be unified into a whole framework.

3. Measure Similarity

The formula of bilateral filter is

$$B(y_{ij}) = \frac{1}{k(y_{ij})} \iint_{-\infty}^{\infty} y_{st} c\big((s,t),(i,j)\big) s(y_{st}, y_{ij})\, ds\, dt, \tag{3.1}$$

where (s,t) and (i,j) are two pixels of sinogram. Here, sinogram is the observations of projection data, that is, the noisy projection data of LDCT. y_{st} and y_{ij} are sinogram values of (s,t) and (i,j), respectively. $k(y_{ij})$ is a normalized constant for two weighs and is defined as

$$k(y_{ij}) = \iint_{-\infty}^{\infty} c\big((s,t),(i,j)\big) s(y_{st}, y_{ij})\, ds\, dt, \tag{3.2}$$

where $c((s,t),(i,j))$ and $s(y_{st}, y_{ij})$ are measures of the spatial and range similarity between the center pixel y_{ij} and its neighbor y_{st}, respectively. Usually, these two measures are defined as two Gaussian Kernel functions

$$c\big((s,t),(i,j)\big) = e^{(-1/2)(\|(s,t)-(i,j)\|/\sigma_d)^2}, \tag{3.3}$$

$$s(y_{st}, y_{ij}) = e^{(-1/2)(\|y_{st}-y_{ij}\|/\sigma_r)^2}. \tag{3.4}$$

Since the (i,j) value filtered by BF is the weighted average of nearby points weighted by product of spatial distance and gray level difference, it was named by bilateral filter (BF) to distinguish the general filter weighted only by spatial distance.

From (3.1)–(3.4), we can conclude that a pair of pixels y_{st}, y_{ij} with both small spatial distance and small sinogram value difference have high similarity and large-weighed coefficients. It is plausible in slightly noisy projection data. For sinograms with serious noise and non-stationary artifacts, it is unreal! That is, polluted sinogram values lead to incorrect similarity measurement in the range filter of the bilateral filter. Thus, finding a measure of similarity, which can measure similarity correctly in noise and non-stationary artifacts, is a key problem in denoising using BF.

3.1. Gaussian Filter

Gaussian filter is defined as

$$G(y_{ij}) = \frac{1}{\iint_{-\infty}^{\infty} e^{(-1/2)(\|y_{st}-y_{ij}\|/\sigma)^2} ds\, dt} \iint_{-\infty}^{\infty} y_{st} e^{-1/2(\|y_{st}-y_{ij}\|/\sigma)^2} ds\, dt. \tag{3.5}$$

Since $y_{st} \sim N(\mu_{ij}, \sigma_{ij}^2)$ for $s = -\infty, \ldots, \infty$ and $t = -\infty, \ldots, \infty$, noisy sinogram value $Y_{ij} \sim N(\mu_{ij}, \sigma_{ij}^2)$ and the Gaussian-dependent noise (GWN) $N_{ij} \sim N(0, \sigma_{ij}^2)$, the distribution of the pixel (i, j) filtered by the low-passed filter defined in (3.5) is

$$\begin{aligned} & Y_{ij} + e^{1/(-2\sigma^2)}\left(Y_{i-1,j} + Y_{i,j-1} + Y_{i+1,j} + Y_{i,j+1} + \cdots\right) \\ & \sim N\left(\mu_{ij}, \frac{1 + \left(4e^{1/(-2\sigma^2)}\right)^2 + \left(4e^{2/(-2\sigma^2)}\right)^2 + \cdots}{\left(1 + \left(4e^{1/(-2\sigma^2)}\right) + \left(4e^{2/(-2\sigma^2)}\right) + \cdots\right)^2}\sigma_{ij}^2\right) \\ & \sim N\left(\mu_{ij}, \frac{1 + \left(4e^{(-1)/\sigma^2}\right)/\left(1 - e^{(-1)/\sigma^2}\right)}{\left(1 + \left(4e^{(-1)/2\sigma^2}\right)/\left(1 - e^{(-1)/2\sigma^2}\right)\right)^2}\sigma_{ij}^2\right). \end{aligned} \tag{3.6}$$

Thus,

$$G(Y_{ij}) \sim N\left(\mu_{ij}, \frac{\left(e^{1/\sigma^2} + 3\right)\left(e^{1/2\sigma^2} - 1\right)^2}{\left(e^{1/\sigma^2} - 1\right)\left(e^{1/2\sigma^2} + 3\right)^2}\sigma_{ij}^2\right). \tag{3.7}$$

For example, in image denoising, generally, σ is set to 2; thus,

$$G(Y_{ij}) \sim N\left(\mu_{ij}, 0.0157\sigma_{ij}^2\right). \tag{3.8}$$

From the above equation, the variance of the smoothed sinogram value becomes very small (smaller than original variance 0.0157 times). It means that the Gaussian filter makes smoothed sinogram value closer to real projection data than the noisy sinogram value. Since most of non-stationary artifacts in image space are the high-light points in noisy sinogram, most of non-stationary artifacts can be suppressed by Gaussian filter.

In the same way, the distribution of the median in an $s \times s$ window centered at the pixel (i, j) is

$$\text{median}(Y_{ij}) \sim N\left(\mu_{ij}, \frac{\sigma_{ij}^2}{s \times s}\right). \tag{3.9}$$

Just as the above discussion, if the median filter has similar estimate precision to Gaussian filter in image denoising, s should at least be 8, which is estimated by $\sqrt{1/0.0157} = \sqrt{63.6943} \approx 8$. However, so large window of median filter will delete some real lines in sinogram, which will lead to many artifacts in denoising sinogram.

3.2. Similarity Discussion

From the second equation of (3.4), the similarity between the sinogram values of two pixels (i, j) and (s, t) is defined as a Gaussian function of the difference to their sinogram values. Thus, large difference has small similarity, while small difference has large similarity.

Following this conclusion, similarity discussion can be accomplished by discussing the difference for each pair of pixels of sinogram. In this subsection, we will discuss the differences by variances of three denoising schemes for BF.

Assume that Y_{st} and Y_{ij} are iid Gaussian random variables corresponding to a pair of pixels with the same real gray levels, $Y_{ij} \sim N(\mu_{ij}, \sigma_{ij}^2)$, $Y_{st} \sim N(\mu_{ij}, \sigma_{ij}^2)$, and their difference

$$Y_{ij} - Y_{st} \sim N\left(\mu_{ij}, 2\sigma_{ij}^2\right). \tag{3.10}$$

In the same way, since $\text{median}(Y_{ij}) \sim N(\mu_{ij}, \sigma_{ij}^2/s \times s)$, we can conclude that

$$\text{median}(Y_{ij}) - Y_{st} \sim N\left(\mu_{ij}, \frac{1+s^2}{s^2}\sigma_{ij}^2\right). \tag{3.11}$$

Since $G(Y_{ij}) \sim N(\mu_{ij}, (((e^{1/\sigma^2}+3)(e^{1/2\sigma^2}-1)^2)/(e^{1/\sigma^2}-1)(e^{1/2\sigma^2}+3)^2)\sigma_{ij}^2)$, thus

$$G(Y_{ij}) - G(Y_{st}) \sim N\left(\mu_{ij}, 2\frac{\left(e^{1/\sigma^2}+3\right)\left(e^{1/2\sigma^2}-1\right)^2}{\left(e^{1/\sigma^2}-1\right)\left(e^{1/2\sigma^2}+3\right)^2}\sigma_{ij}^2\right). \tag{3.12}$$

Just as discussed in the last subsection, if we set σ to 2,

$$G(Y_{ij}) - G(Y_{st}) \sim N\left(\mu_{ij}, 0.0314\sigma_{ij}^2\right). \tag{3.13}$$

It is obvious that the variance of the first scheme is the biggest in all three schemes, while the variance of the last scheme is the smallest in all three schemes. Since $s \geq 3$, we have

$$2 > \frac{s^2+1}{s^2} > 1 > 0.0314. \tag{3.14}$$

The first scheme corresponds to the bilateral, which measures difference by the sinogram values of (i, j) and (s, t) directly. The second scheme corresponds to the mean bilateral proposed in [41] whose similarity is measured between the median of the center pixel (i, j) and the sinogram value of its neighbor (s, t). The third scheme corresponds to the scheme of measuring the difference on the Gaussian filtered sinogram value.

It is well-known that smallest variance corresponds to the best estimate of real projection data value. According to this rule, our proposed method can provide the best estimate of real projection data value. Thus, BFWGFS can reduce both the influence of noises and non-stationary artifacts.

4. The Algorithm

Just as the above discussion, satisfied denoising results can be got by weighed range filter on Gaussian filtered sinogram. The steps of the algorithm are as follows:

(1) compute the Gaussian filtered sinogram value $G(y_{ij})$ for all sinogram pixels using (3.5),

(2) give σ_d and σ_r,

(3) for each of pixel,

(i) compute $c((s,t),(i,j))$ using the first equation of (3.4) and $s(G(y_{st}),G(y_{ij}))$ using

$$s\left(G\left(y_{st}\right),G\left(y_{ij}\right)\right)=e^{(-1/2)\left(\left\|G\left(y_{st}\right)-G\left(y_{ij}\right)\right\|/\sigma_r\right)^2}, \tag{4.1}$$

(ii) compute $k(y_{ij})$ using

$$k\left(y_{ij}\right)=\iint_{-\infty}^{\infty}c\left((s,t),(i,j)\right)s\left(G\left(y_{st}\right),G\left(y_{ij}\right)\right)ds\,dt, \tag{4.2}$$

(iii) compute $GB(y_{ij})$ using

$$GB\left(y_{ij}\right)=\frac{1}{k\left(y_{ij}\right)}\iint_{-\infty}^{\infty}y_{st}c\left((s,t),(i,j)\right)s\left(G\left(y_{st}\right),G\left(y_{ij}\right)\right)ds\,dt, \tag{4.3}$$

(4) repeat step 3 until all sinogram pixels have been proceeded.

5. Experiments and Discussion

The main objective for smoothing L-CT images is to delete the noise and non-stationary artifacts while to preserve anatomy details for the images. Thus, the image visual quality can be improved, and the denoised image can help doctors make correct medical diagnosis more easily.

5.1. Data

Four groups of CT images with different doses were scanned from a 16 multidetector row CT unit (Somatom Sensation 16; Siemens Medical Solutions) using 120 kVp and 5 mm slice thickness: a 58-year-old man, two groups of 62-year-old women with different reduced dose, and a 60-year-old man. Other remaining scanning parameters are gantry rotation time, 0.5 second; detector configuration (number of detector rows section thickness), 16×1.5 mm; table feed per gantry rotation, 24 mm; pitch, 1 : 1; reconstruction method, filtered back projection (FBP) algorithm with the soft-tissue convolution kernel "B30f." Different CT doses were controlled by using two different fixed tube currents 30 mAs and 150 mAs (60 mA or 300 mAs) for LDCT and standard-dose CT (SDCT) protocols, resp.. The CT dose index volume (CTDIvol) for LDCT images and SDCT images are in positive linear correlation to the tube current and is calculated to be approximately ranged between 15.32 mGy and 3.16 mGy [29]. For additional visually illustration, we also put two groups of abdominal CT images of a same woman with 60 mAs, and two groups of shoulder CT images with low dose 35 mAs and standard dose 135 mAs (see Figure 2).

5.2. Compared Methods

Bilateral filter (BF) is introduced at the beginning of Section 3. The main motivation for BF is that the noisy image should be weighted not only by the position distance (spatial filter) but also by the difference of sinogram values (range filter) [35]. The parameters of BF are Gaussian Kernel for spatial filter $\sigma_s = 1.8$, Gaussian Kernel for range filter $\sigma_r = 20/3$, and iteration time is 3.

Context is a term imported from image coding. The context of a pixel x_{ij} is always defined as a vector used for describing the relationship between this pixels and other image pixels. In this paper, in order to suppress the influence of noises, the context is defined as

$$\widehat{y}_{ij} = \frac{1}{9}\sum_{s=i-1}^{s=i+1}\sum_{t=j-1}^{t=j+1} y_{st}. \tag{5.1}$$

The context filter estimates real sinogram values from the points with similar context value. In this paper, the threshold value for similar context is 10, that is,

$$\begin{aligned} x_{ij} \text{ and } x_{st} \text{ are similar points} \quad &\text{if } \left|\widehat{y}_{ij} - \widehat{y}_{st}\right| \le 10, \\ x_{ij} \text{ and } x_{st} \text{ are not similar points} \quad &\text{otherwise,} \end{aligned} \tag{5.2}$$

where $\widehat{y}_{ij}$ is defined on (5.1). Although context filter can provide more samples for real value estimate, it will produce some artifacts for losing the spatial relationship of sinogram.

Median bilateral filter (MBF) replaces the center pixel with the median of an $s \times s$ window [41]. However, just as analysis in Section 3, only replacing the center pixel also cannot obtain satisfied denoising results. Here, when s set to 5 has the best performance, $\sigma_r = 20/3$ and $\sigma_s = 1.8$.

Multiresolution bilateral filter (MRBF) filtering LL subband uses BF while smoothing wavelet subbands uses SURE shrinkage [38]. The wavelet used in the experiment is 1-level symlets with support 4. The noisy variance $\widehat{\sigma}_N$ is estimated using median of HH band of the wavelet [45] and $\sigma_r = 3\widehat{\sigma}_N$ and $\sigma_s = 2$. Although authors report that MRBF can obtain good denoising results, it also leads to blur some important details.

Weighted intensity averaging over large-scale neighborhoods (WIA-LNs) is a state-of-the-art method for sinogram reconstruction [29]. The motivation for WIA-LN is that the two pixels of the same organ or tissue should have surrounding patches with higher similarities than the two pixels of different organs or tissues. Thus, the real sinogram value of f_i can be estimated as

$$\widehat{f}_i = \sum_{j\in N_i} \frac{\omega_{ij} f_i}{\sum_{j\in N_i}\omega_{ij}}, \tag{5.3}$$

where

$$\omega_{ij} = \exp\left(-\frac{\|n_i - n_j\|_{2,\alpha}^2}{\beta|n_i|}\right). \tag{5.4}$$

Here, f_i denotes the intensities of the neighboring pixels in the search neighborhood N_i centered at pixel index i. The weight of WIA-LN is built by using a similarity criterion between the two comparing patches n_i and n_j. This similarity metrics is calculated using (5.4), in which α denotes the two-dimensional standard deviation of Gaussian kernel. $|n_i|$ is the total pixel number in patch n_i. β is a superparameter. In this paper, β is set to be 0.8, and the sizes n_i are set to 11×11. Although better vision and quantitative performance are reported, the authors also indicate that WIA-LN cannot handle noise and non-stationary artifacts simultaneously (see Figure 3(g)).

Proposed method (BFWGFS) replaces all sinogram values used in range filter of BF by the Gaussian filtered sinogram values. Just as discussed in Section 3, smoothed sinogram values can reduce the influence of both noise and non-stationary artifacts greatly, and BFWGFS can provide good visual results and preserve more anatomy details. The parameters are $\sigma_r = 20/3$, $\sigma_s = 1.8$, iteration number is set to 1, and Gaussian smoothed kernel is set to 1.8.

5.3. Visual Comparison

Three groups of SDCT images, LDCT images, and the processed LDCT images for the clinical abdominal examinations are shown in Figures 1–3. The parameters for compared methods have been given in the last subsection. In Figure 1, the original and processed abdominal CT images of a 58-year-old man are illustrated. Figures 1(a) and 1(b) are one SDCT image and one LDCT image acquired at tube current time product 150 mAs and 30 mAs, respectively. Figures 1(c), 1(d), 1(e), 1(f), 1(g), and 1(h) show BF, context, MBF, MRBF, WIA-LN, and proposed method processed LDCT images, respectively. Figure 2 illustrates the original and processed abdominal CT images of a 62-year-old woman. Figure 2(a) is one SDCT image acquired at tube current time product 150 mAs. Figures 2(b) and 2(c) are two LDCT images acquired at reduced tube current time products 60 mAs and 30 mAs, respectively. Figures 2(d), 2(e), 2(f), 2(j), 2(k), 2(l), 2(g), 2(h), 2(i), 2(m), 2(n), and 2(o) illustrate the two groups of processed LDCT images of Figures 2(b) and 2(c) by using compared methods. Figure 3 illustrates the original and processed images for one shoulder scan of a 60-year-old man, from which we found that WIA-LN tends to smooth both the streak artifacts and informative human tissues, while proposed method can reduce the noise and artifacts with preservation of anatomy details.

Comparing all the original SDCT images and LDCT images in Figures 1–3, we found that the LDCT images were severely degraded by noise and streak artifacts. In Figures 1(c)–1(f), just as the discussion in Section 3, there are so many noises left in processed images using BF, context, MBF, and MRBF. WIA-LN shown in Figure 1(g) also makes some obvious artifacts, while we can observe better noise/artifacts suppression and edge preservation for proposed methods in Figure 1(h). Both WIA-LN and proposed method have good performance in noises. Especially, compared to corresponding original SDCT images, the fine features representing the intrahepatic bile duct dilatation and the hepatic cyst (pointed by the white circles in the images of Figures 1 and 2, resp.) were well restored by using WIA-LN and proposed method. The fine anatomical/pathological features (the exemplary structures pointed by circles in Figures 1 and 2) can be well preserved compared to the original SDCT images (Figures 1(a) and 2(a)) under-standard dose conditions. In Figures 3(g) and 3(h), it indicates that although WIA-LN cannot handle noises and artifacts simultaneously, proposed method can obtain satisfied results in this complex situation. Especially, proposed method not only can suppress noises and artifacts in original LDCT image (Figure 3(a)) but also

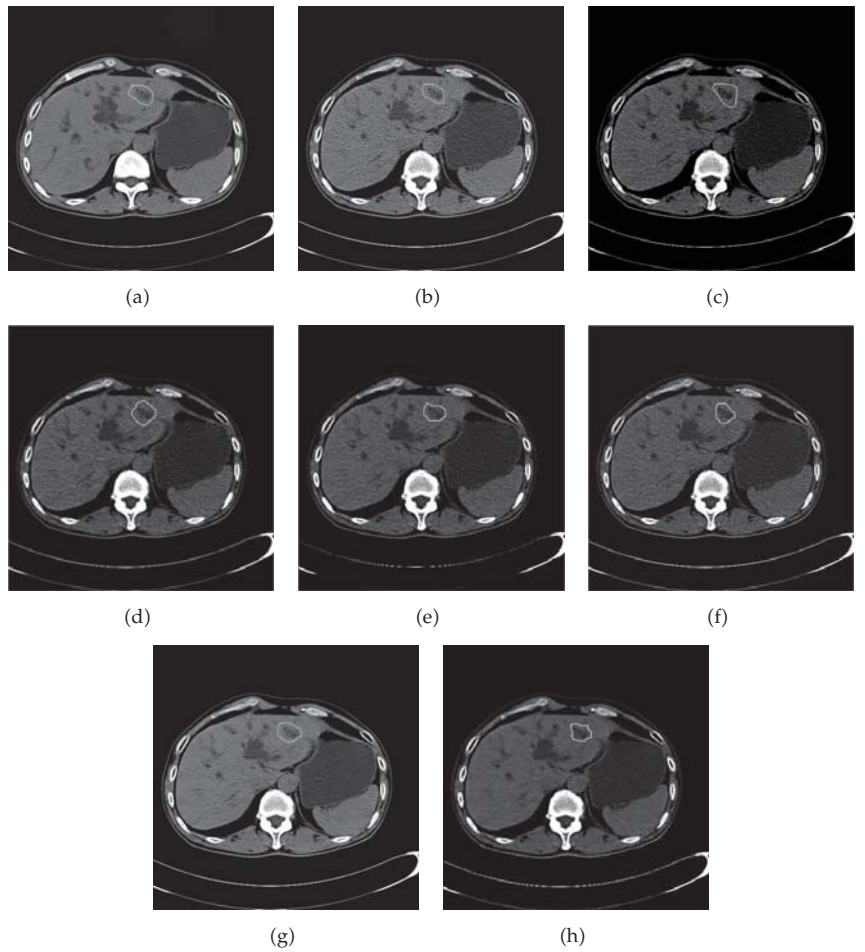

Figure 1: Abdominal CT images of a 58-year-old man. (a) Original SDCT image with tube current time product 150 mAs. (b) Original LDCT image with tube current time product 30 mAs. (c, d, e, f) BF, context, MBF, and MRBF processed LDCT images, respectively. (g) WIA-LN processed LDCT image. (h) Proposed method (BFWGFS) processed LDCT image. Note the obvious improvement of noise suppression and preservation of the intrahepatic bile duct dilatation (white circles) for the WIA-LN and proposed method processed LDCT images (g, h) compared to the original LDCT image in (b).

can preserve tiny anatomy details of subscapular arteries indicated by the white circles in Figure 3(h) compared to the original SDCT image (Figure 3(b)).

6. Conclusions

In this paper, in order to improve the performance of LDCT imaging, we propose a new method, named bilateral filter weighted by Gaussian filtered sinogram (BFWGFS) which replaces the sinogram values of range filter of BF to the Gaussian filtered sinogram values. Since carefully chosen parameters of Gaussian filter can reduce the influence both of noises and non-stationary artifacts greatly, BFWGFS can provide a more reliable estimate sinogram values for the range filter to improve the performance of classical BF in noises. Restoration

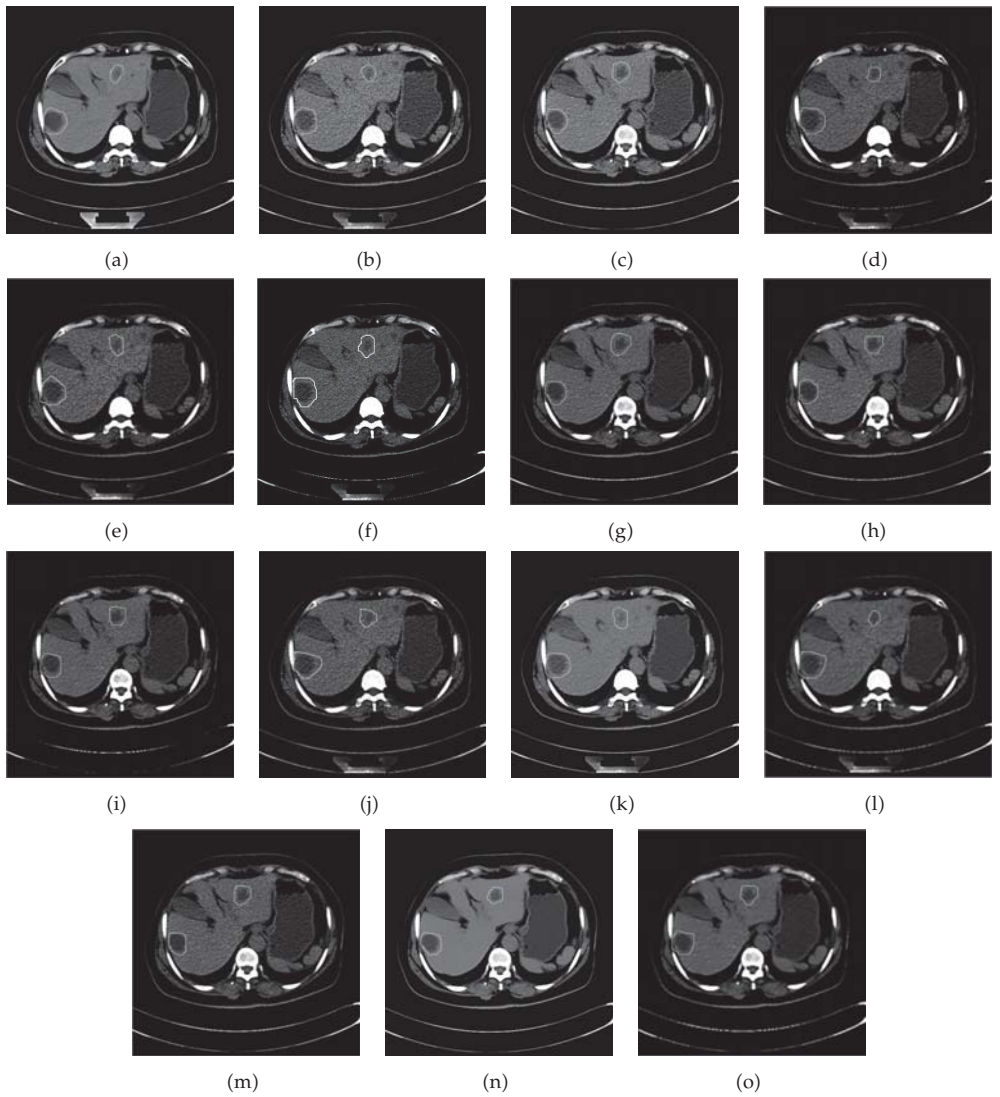

Figure 2: Abdominal CT images of a 62-year-old woman. (a) Original SDCT image with tube current time product 150 mAs. (b) Original LDCT image with tube current time product 60 mAs. (c) Original LDCT image with tube current time product 30 mAs. (d, e, f) LDCT images (60 mAs) processed by BF, context, and MBF, respectively. (g, h, i) LDCT images (30 mAs) processed by BF, context, and MBF, respectively. (j, k, l) LDCT images (60 mAs) processed by MRBF, WIA-LN and proposed method, respectively. (m, n, o) LDCT images (30 mAs) processed by MRBF, WIA-LN, and proposed method, respectively. Compared to the original LDCT images in (b) and (c), the improvement of preservation of the hepatic cyst (white circles) for the WIA-LN, and proposed method in processed LDCT image (k), (l), and (n), (o) can be observed.

results for three real sinograms show that proposed method with suitable parameters can obtain satisfied results even in both the noises and artifacts situation.

Acknowledgments

This paper is supported by the National Natural Science Foundation of China (no. 60873102), Major State Basic Research Development Program (no. 2010CB732501), and Open Foundation

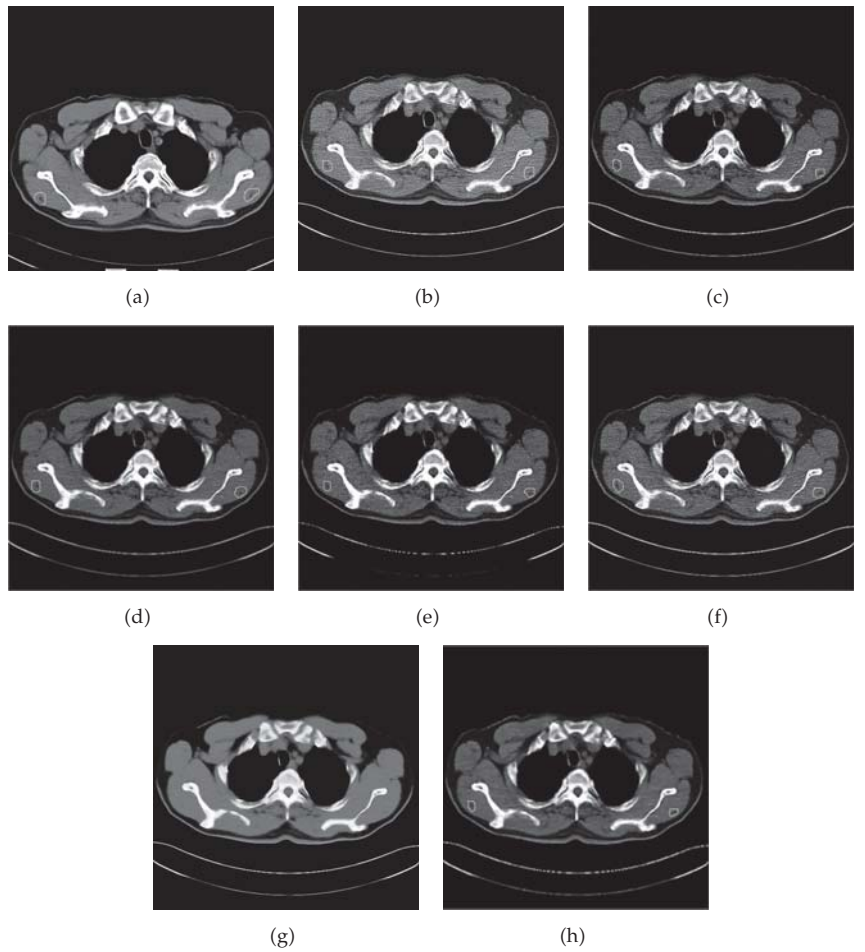

Figure 3: Shoulder CT images of a 60-year-old man. (a) Original SDCT image acquired at a standard tube current-time product 135 mAs. (b) Original LDCT image acquired at a reduced tube current-time product 35 mAs. (c, f, g, h) LDCT images processed by BF, context, MBF, and MRBF, respectively. (d) LDCT image processed by WIA-LN. Note that both the streak artifacts and informative human tissues tend to be smoothed. (e) LDCT image processed by the proposed method. Compared to the original LDCT images in (a), the obvious improvement of noise suppression in the improvement of preservation of the subscapular arteries (white circles) for the proposed method can be observed.

of Visual Computing and Virtual Reality Key Laboratory of Sichuan Province (no. J2010N03). This work was supported by a Grant from the National High Technology Research and Development Program of China (no. 2009AA12Z140).

References

[1] D. J. Brenner and E. J. Hall, "Computed tomography—an increasing source of radiation exposure," *New England Journal of Medicine*, vol. 357, no. 22, pp. 2277–2284, 2007.

[2] J. Hansen and A. G. Jurik, "Survival and radiation risk in patients obtaining more than six CT examinations during one year," *Acta Oncologica*, vol. 48, no. 2, pp. 302–307, 2009.

[3] H. J. Brisse, J. Brenot, N. Pierrat et al., "The relevance of image quality indices for dose optimization in abdominal multi-detector row CT in children: experimental assessment with pediatric phantoms," *Physics in Medicine and Biology*, vol. 54, no. 7, pp. 1871–1892, 2009.

[4] L. Yu, "Radiation dose reduction in computed tomography: techniques and future perspective," *Imaging in Medicine*, vol. 1, no. 1, pp. 65–84, 2009.

[5] J. Weidemann, G. Stamm, M. Galanski, and M. Keberle, "Comparison of the image quality of various fixed and dose modulated protocols for soft tissue neck CT on a GE Lightspeed scanner," *European Journal of Radiology*, vol. 69, no. 3, pp. 473–477, 2009.

[6] W. Qi, J. Li, and X. Du, "Method for automatic tube current selection for obtaining a consistent image quality and dose optimization in a cardiac multidetector CT," *Korean Journal of Radiology*, vol. 10, no. 6, pp. 568–574, 2009.

[7] A. Kuettner, B. Gehann, J. Spolnik et al., "Strategies for dose-optimized imaging in pediatric cardiac dual source CT," *Fortschr. Röntgenstr*, vol. 181, no. 4, pp. 339–348, 2009.

[8] P. Kropil, R. S. Lanzman, C. Walther et al., "Dose reduction and image quality in MDCT of the upper abdomen: potential of an adaptive post-processing filter," *Fortschr. Röntgenstr*, vol. 182, no. 3, pp. 284–253, 2009.

[9] M. K. Kalra, M. M. Maher, M. A. Blake et al., "Detection and characterization of lesions on low-radiation-dose abdominal CT images postprocessed with noise reduction filters," *Radiology*, vol. 232, no. 3, pp. 791–797, 2004.

[10] H. B. Lu, X. Li, L. H. Li et al., "Adaptive noise reduction toward low-dose computed tomography," in *Proceedings of the Medical Imaging 2003: Physics of Medical Imaging*, vol. 5030, parts 1 and 2, pp. 759–766, San Diego, Calif, USA, February 2003.

[11] M. K. Kalra, C. Wittram, M. M. Maher et al., "Can noise reduction filters improve low-radiation-dose chest CT images? Pilot study," *Radiology*, vol. 228, no. 1, pp. 257–264, 2003.

[12] M. K. Kalra, M. M. Maher, D. V. Sahani et al., "Low-dose CT of the abdomen: evaluation of image improvement with use of noise reduction filters pilot study," *Radiology*, vol. 228, no. 1, pp. 251–256, 2003.

[13] J. C. Giraldo, Z. S. Kelm, L. S. Guimaraes et al., "Comparative study of two image space noise reduction methods for computed tomography: bilateral filter and nonlocal means," in *Proceedings of the 31st Annual International Conference of the IEEE Engineering in Medicine and Biology Society: Engineering the Future of Biomedicine (EMBC '09)*, pp. 3529–3532, Minneapolis, Minn, USA, September 2009.

[14] A. Manduca, L. Yu, J. D. Trzasko et al., "Projection space denoising with bilateral filtering and CT noise modeling for dose reduction in CT," *Medical Physics*, vol. 36, no. 11, pp. 4911–4919, 2009.

[15] N. Mail, D. J. Moseley, J. H. Siewerdsen, and D. A. Jaffray, "The influence of bowtie filtration on cone-beam CT image quality," *Medical Physics*, vol. 36, no. 1, pp. 22–32, 2009.

[16] M. Kachelrie, O. Watzke, and W. A. Kalender, "Generalized multi-dimensional adaptive filtering for conventional and spiral single-slice, multi-slice, and cone-beam CT," *Medical Physics*, vol. 28, no. 4, pp. 475–490, 2001.

[17] G. F. Rust, V. Aurich, and M. Reiser, "Noise/dose reduction and image improvements in screening virtual colonoscopy with tube currents of 20 mAs with nonlinear Gaussian filter chains," in *Medical Imaging 2002: Physiology and Function from Multidimensional Images*, vol. 4683 of *Proceedings of SPIE*, pp. 186–197, San Diego, Calif, USA, February 2002.

[18] Z. Liao, S. Hu, and W. Chen, "Determining neighborhoods of image pixels automatically for adaptive image denoising using nonlinear time series analysis," *Mathematical Problems in Engineering*, vol. 2010, Article ID 914564, 14 pages, 2010.

[19] H. Lu, I. T. Hsiao, X. Li, and Z. G. Liang, "Noise properties of low-dose CT projections and noise treatment by scale transformations," in *Proceedings of the IEEE Nuclear Science Symposium Conference Record*, vol. 1–4, pp. 1662–1666, November 2001.

[20] J. Xu and B. M. W. Tsui, "Electronic noise modeling in statistical iterative reconstruction," *IEEE Transactions on Image Processing*, vol. 18, no. 6, pp. 1228–1238, 2009.

[21] I. A. Elbakri and J. A. Fessler, "Statistical image reconstruction for polyenergetic X-ray computed tomography," *IEEE Transactions on Medical Imaging*, vol. 21, no. 2, pp. 89–99, 2002.

[22] P. J. la Rivire and D. M. Billmire, "Reduction of noise-induced streak artifacts in X-ray computed tomography through spline-based penalized-likelihood sinogram smoothing," *IEEE Transactions on Medical Imaging*, vol. 24, no. 1, pp. 105–111, 2005.

[23] P. J. la Rivire, "Penalized-likelihood sinogram smoothing for low-dose CT," *Medical Physics*, vol. 32, no. 6, pp. 1676–1683, 2005.

[24] J. Wang, H. Lu, J. Wen, and Z. G. Liang, "Multiscale penalized weighted least-squares sinogram restoration for low-dose X-ray computed tomography," *IEEE Transactions on Biomedical Engineering*, vol. 55, no. 3, pp. 1022–1031, 2008.
[25] P. Forthmann, T. Kohler, P. G. Begemann, and M. Defrise, "Penalized maximum-likelihood sinogram restoration for dual focal spot computed tomography," *Physics in Medicine and Biology*, vol. 52, no. 15, pp. 4513–4523, 2007.
[26] J. Wang, T. Li, H. Lu, and Z. G. Liang, "Penalized weighted least-squares approach to sinogram noise reduction and image reconstruction for low-dose X-ray computed tomography," *IEEE Transactions on Medical Imaging*, vol. 25, no. 10, pp. 1272–1283, 2006.
[27] Z. Liao, S. Hu, M. Li, and W. Chen, "Noise estimation for single-slice sinogram of low-dose X-ray computed tomography using homogenous patch," *Mathematical Problems in Engineering*, vol. 2012, Article ID 696212, 16 pages, 2012.
[28] H. B. Lu, X. Li, I. T. Hsiao, and Z. G. Liang, "Analytical noise treatment for low-dose CT projection data by penalized weighted least-square smoothing in the K-L domain," in *Proceedings of the Medical Imaging 2002: Physics of Medical Imaging*, vol. 4682, pp. 146–152, May 2002.
[29] C. Yang, C. Wufan, Y. Xindao et al., "Improving low-dose abdominal CT images by weighted intensity averaging over large-scale neighborhoods," *European Journal of Radiology*, vol. 80, no. 2, pp. e42–e49, 2011.
[30] T. Li, X. Li, J. Wang et al., "Nonlinear sinogram smoothing for low-dose X-ray CT," *IEEE Transactions on Nuclear Science*, vol. 51, no. 5, pp. 2505–2513, 2004.
[31] S. Hu, Z. Liao, D. Sun, and W. Chen, "A numerical method for preserving curve edges in nonlinear anisotropic smoothing," *Mathematical Problems in Engineering*, vol. 2011, Article ID 186507, 14 pages, 2011.
[32] M. Li and W. Zhao, "Visiting power laws in cyber-physical networking systems," *Mathematical Problems in Engineering*, vol. 2012, Article ID 302786, 13 pages, 2012.
[33] M. Li, C. Cattani, and S. Y. Chen, "Viewing sea level by a one-dimensional random function with long memory," *Mathematical Problems in Engineering*, vol. 2011, Article ID 654284, 13 pages, 2011.
[34] M. Li, "Fractal time series: a tutorial review," *Mathematical Problems in Engineering*, vol. 2010, Article ID 157264, 26 pages, 2010.
[35] C. Tomasi and R. Manduchi, "Bilateral filtering for gray and color images," in *Proceedings of the IEEE International Conference on Computer Vision*, pp. 836–846, Bombay, India, January 1998.
[36] D. Barash, "A fundamental relationship between bilateral filtering, adaptive smoothing, and the nonlinear diffusion equation," *IEEE Transactions on Pattern Analysis and Machine Intelligence*, vol. 24, no. 6, pp. 844–847, 2002.
[37] A. Wong, "Adaptive bilateral filtering of image signals using local phase characteristics," *Signal Processing*, vol. 88, no. 6, pp. 1615–1619, 2008.
[38] Z. Ming and G. Bahadir, "Multiresolution bilateral filtering for image denoising," *IEEE Transactions on Image Processing*, vol. 17, no. 12, pp. 2324–2333, 2008.
[39] H. Yu, L. Zhao, and H. Wang, "Image denoising using trivariate shrinkage filter in the wavelet domain and joint bilateral filter in the spatial domain," *IEEE Transactions on Image Processing*, vol. 18, no. 10, pp. 2364–2369, 2009.
[40] R. van Boomgaard and J. van de Weijer, "On the equivalence of local-mode finding,robust estimation and mean-shift analysis as used in early vision tasks," in *Proceedings of the 16th International Conference on Pattern Recognition*, vol. 3, pp. 972–930, Quebec, Canada, August 2002.
[41] J. J. Francis and G. de Jager, "The bilateral median filter," *Transactions of the South African Institute of Electrical Engineers*, vol. 96, no. 2, pp. 106–111, 2005.
[42] K. Dabov, A. Foi, V. Katkovnik, and K. Egiazarian, "Image denoising by sparse 3D transform-domain collaborative filtering," *IEEE Transactions on Image Processing*, vol. 16, no. 8, pp. 2080–2095, 2007.
[43] J. Portilla, V. Strela, M. J. Wainwright, and E. P. Simoncelli, "Image denoising using scale mixtures of Gaussians in the wavelet domain," *IEEE Transactions on Image Processing*, vol. 12, no. 11, pp. 1338–1351, 2003.
[44] A. Buades, B. Coll, and J.-M. Morel, "Nonlocal image and movie denoising," *International Journal of Computer Vision*, vol. 76, no. 2, pp. 123–139, 2008, Special section: selection of papers for CVPR 2005, guest editors: C. Schmid, S. Soatto and C. Tomasi.
[45] D. L. Donoho and I. M. Johnstone, "Ideal spatial adaptation by wavelet shrinkage," *Biometrika*, vol. 81, no. 3, pp. 425–455, 1994.

Hindawi Publishing Corporation
Mathematical Problems in Engineering
Volume 2012, Article ID 280869, 14 pages
doi:10.1155/2012/280869

Research Article

Tail Dependence for Regularly Varying Time Series

Ai-Ju Shi[1,2] and Jin-Guan Lin[1]

[1] *Department of Mathematics, Southeast University, Nanjing 210096, China*
[2] *College of Science, Nanjing University of Posts and Telecommunications, Nanjing 210003, China*

Correspondence should be addressed to Jin-Guan Lin, jglin@seu.edu.cn

Received 9 January 2012; Accepted 14 March 2012

Academic Editor: Ming Li

We use tail dependence functions to study tail dependence for regularly varying (RV) time series. First, tail dependence functions about RV time series are deduced through the intensity measure. Then, the relation between the tail dependence function and the intensity measure is established: they are biuniquely determined. Finally, we obtain the expressions of the tail dependence parameters based on the expectation of the RV components of the time series. These expressions are coincided with those obtained by the conditional probability. Some simulation examples are demonstrated to verify the results we established in this paper.

1. Introduction

Copula is a useful tool for handling multivariate distributions with given univariate margins. A copula C is a distribution function, defined on the unit cube $[0,1]^d$, with uniform one-dimensional margins U_i. For any $(u_1,\ldots,u_d) \in [0,1]^d$, $C(u_1,\ldots,u_d) = P\{U_1 \le u_1,\ldots,U_d \le u_d\}$; the survival copula is $\widehat{C}(u_1,\ldots,u_d) = P\{U_1 \ge 1-u_1,\ldots,U_d \ge 1-u_d\}$, the joint survival function of copula C is $\overline{C}(u_1,\ldots,u_d) = \widehat{C}(1-u_1,\ldots,1-u_d)$. Given a copula C, let

$$F(t_1,\ldots,t_d) = C(F_1(t_1),\ldots,F_d(t_d)), \quad \text{where } (t_1,\ldots,t_d) \in \mathbb{R}^d, \tag{1.1}$$

then F is a multivariate distribution with univariate margins $F_1,\ldots,F_d$. On the other hand, given a distribution F with margins $F_1,\ldots,F_d$, there exists a copula C such that (1.1) holds. And copula C is unique if $F_1,\ldots,F_d$ are all continuous (Sklar [1], Nelsen [2]).

In generally, copula forms a natural way to describe the dependence between series when making abstraction of their marginal distributions. Overviews of the probabilistic and statistical properties of copula are to be found in [1–6].

Tail dependence plays an important role among dependence measures due to its ability to describe dependence among extreme values (Frahm et al. [7], Resnick [8, 9], and Nikoloulopoulos et al. [10]) which is introduced by Joe [4]. The issue of tail dependence is mainly for heavy tailed phenomena, heavy tailed phenomenon in fractal time series. It is extensively studied and applied in insurance, risk management, traffic management and engineering management, and so forth. [11–27].

Researchers find various multivariate distributions with heavy tails to describe the extremal or tail dependence, see, Pisarenko and Rodkin [13], Hult and Lindskog [28], and Fang et al. [29]. Many interesting tail quantities have been derived via standard methods: coefficients of tail dependence [30–37] and tail dependence copulas (Charpentier and Segers [38]).

In this paper, we are interested in the tail behavior of the time series $X_1, \ldots, X_t$ which have the form:

$$\mathbf{X} = (X_1, \ldots, X_t) = (RZ_1, \ldots, RZ_t), \tag{1.2}$$

where the scale variable R is independent of random vector $(Z_1, \ldots, Z_t)$. And $\mathbf{X}$ is multivariate regularly varying with distribution function F having copula C.

This distribution is a generalized class, including, for example, multivariate Pareto and multivariate elliptical distribution as special ones. Especially, the multivariate t distribution is included in it. As an example, we will justify the results through multivariate t copula.

In order to analyze the tail dependence behavior of (1.2), we first study the tail dependence functions via intensity measure. Then using the relation between tail dependence parameter and the tail dependence functions, we explore the explicit representations of the tail dependence parameters.

The outline of this paper is as follows. After some preliminaries about multivariate regularly varying series and dependence functions in Section 2, detailed results for the tail dependence functions are discussed in Section 3, the expressions of tail dependence parameters for RV time series are demonstrated in Section 4, and multivariate t distribution is demonstrated as an example in Section 5.

Throughout, $(X_1, \ldots, X_t)$ is a random vector with joint distribution function F and copula C. Minima and maxima will be denoted by $\wedge$ and $\vee$, respectively. The Cartesian product $\prod_{i=1}^{t}[a_i, b_i]$ is denoted by $[\mathbf{a}, \mathbf{b}]$ for any $\mathbf{a}, \mathbf{b} \in \overline{R}^t$.

2. Preliminaries

Definition 2.1. The t-dimensional random vector $\mathbf{X}$ is said to be regularly varying with index $\alpha \geq 0$ if there exists a random vector Θ with values in $\mathbb{S}^{t-1}$ a.s., where $\mathbb{S}^{t-1}$ denotes the unit sphere in R^d with respect to the norm $|\cdot|$, such that, for all $u > 0$,

$$\frac{P\{|\mathbf{X}| > ux, \mathbf{X}/|\mathbf{X}| \in \cdot\}}{P\{|\mathbf{X}| > x\}} \xrightarrow{v} u^{-\alpha} P\{\Theta \in \cdot\}, \tag{2.1}$$

as $x \to \infty$. The symbol $\xrightarrow{v}$ stands for vague convergence on $\mathbb{S}^{t-1}$; vague convergence of measures is treated in detail in Kallenberg [39]. The distribution of Θ is referred to as the

spectral measure of $\mathbf{X}$. For further information on multivariate regular variation we refer to Resnick [8, 9].

In fact, (2.1) is equivalent to the following expression

$$nP\left\{a_n^{-1}\mathbf{X}\in\cdot\right\}\xrightarrow{v}\mu(\cdot), \tag{2.2}$$

where μ is an intensity measure or Radon measure on $R/\{0\}$ and a_n is a sequence an of nonnegative numbers.

From the Definition 2.1, we can see that the regularly varying distribution is connected with intensity measure μ. The following lemma yields the explicit relation between them which can be found in [8].

Lemma 2.2. *Let random vector $\mathbf{X}$ be regularly varying with index $\alpha\geq 0$ and distribution function F, then it is equivalent to the following.*

(1) *There exists an intensity measure μ on $R^t/\{0\}$, such that for every Borel set $B\subset R^t/\{0\}$ bounded away from the origin that satisfies $\mu(\partial B)=0$,*

$$\lim_{u\to\infty}\frac{P\{\mathbf{X}\in uB\}}{P\{|\mathbf{X}|>u\}}=\mu(B), \tag{2.3}$$

with the homogeneous condition $\mu(uB)=u^{-\alpha}\mu(B)$.

(2) *There exists an intensity measure μ on $R^t/\{0\}$, such that*

$$\lim_{u\to\infty}\frac{1-F(ux_1,ux_2,\ldots,ux_t)}{1-F(u,u,\ldots,u)}=\frac{P\{\mathbf{X}/u\in[0,\mathbf{x}]^c\}}{P\{\mathbf{X}/u\in[0,1]^c\}}=\mu\left([0,\mathbf{x}]^c\right), \tag{2.4}$$

for all continuous points $\mathbf{x}$ of μ. According to Lemma 2.2, one notices that for any nonnegative multivariate regularly varying random vector $\mathbf{X}$, its nondegenerate univariate margins X_i have regularly varying right tails and with the same index of $\mathbf{X}$ also, that is,

$$\overline{F}_i(x)=P\{\mathbf{X}_i>x\}=x^{-\alpha}L_i(x),\quad x>0, \tag{2.5}$$

where $L_i(x)$ is a slowly varying function.

Lemma 2.3 (Breiman [40]). *Let ξ and η be two independent nonnegative random variables, η be regularly varying with index α. If there exists a $\gamma>\alpha$, such that $E\xi^{\gamma}<\infty$, then*

$$P\{\xi\eta>x\}\sim E(\xi^{\alpha})P\{\eta>x\}. \tag{2.6}$$

The multivariate version of the Lemma belongs to Basrak et al. [41]. It is said that, if $\mathbf{X}$ *is regularly varying in the sense of* (2.2), $\mathbf{A}$ *is a random* $t \times t$ *matrix, independent of* $\mathbf{X}$, *with* $0 < E\|\mathbf{A}\|^{\gamma} < \infty$ *for some* $\gamma > \alpha$, *then*

$$nP\left\{a_n^{-1}\mathbf{A}X \in \cdot\right\} \xrightarrow{v} \tilde{\mu}(\cdot) := E\left(\mu \circ \mathbf{A}^{-1}(\cdot)\right), \tag{2.7}$$

where $\xrightarrow{v}$ *denotes vague convergence on* $\mathbb{R}^t/\{0\}$.

Definition 2.4 (Kluppelberg et al. [42]). Let F be the distribution function of random vector $\mathbf{X}$ with continuous margins $F_i, 1 \le i \le t$ and copula C. For any $\mathbf{w} = (w_1, w_2, \ldots, w_t) \in R_+^t$, the lower dependence function is defined as

$$l(\mathbf{w}; C) = \lim_{x \to 0^+} \frac{C(xw_1, xw_2, \ldots, xw_t)}{x}, \tag{2.8}$$

and the upper dependence function is defined as

$$u(\mathbf{w}; C) = \lim_{x \to 0^+} \frac{\overline{C}(1 - xw_1, 1 - xw_2, \ldots, 1 - xw_t)}{x}. \tag{2.9}$$

The upper exponent function is defined as

$$u^*(\mathbf{w}; C) = \sum_{\emptyset \neq S \subset I} (-1)^{|S|-1} u_S(w_S; C_S), \tag{2.10}$$

where $u_S(w_S; C_S) = \lim_{x \to 0^+} \overline{C}(1 - xw_j, \forall j \in S)/x$.

From the definition, we can verify the elementary properties listed in Proposition 2.5 of the tail dependence function. We denote $\tau_J = \lim_{x \to 1^-} P\{F_j(X_j) > x, \forall j \notin \mathbf{J} \mid F_i(X_i) > x, \forall i \in \mathbf{J}\}$ and $\xi_J = \lim_{x \to 0^+} P\{F_j(X_j) < x, \forall j \notin \mathbf{J} \mid F_i(X_i) < x, \forall i \in \mathbf{J}\}$ are the upper tail and lower dependence parameters of $\mathbf{X}$, respectively, where J is a nonempty subset of $I = \{1, \ldots, t\}$. C_J is the margin of C with component indexes in J.

Proposition 2.5. (1) *For any* $1 \le i, j \le t$,

$$\tau_{ij} = u(1, 1; C_{ij}); \qquad \xi_{ij} = l(1, 1; C_{ij}), \tag{2.11}$$

where C_{ij} *is the margin copula of* X_i, X_j.

(2) *For any nonempty* $J \subset I$,

$$\tau_J = \frac{u(1, 1, \ldots, 1; C)}{u(1, 1, \ldots, 1; C_J)}; \qquad \xi_J = \frac{l(1, 1, \ldots, 1; C)}{l(1, 1, \ldots, 1; C_J)}, \tag{2.12}$$

(3)

$$u(\mathbf{w};C)=\lim_{x\to 0^+}\frac{\widehat{C}(xw_1,xw_2,\ldots,xw_t)}{x}=l\left(\mathbf{w};\widehat{C}\right). \tag{2.13}$$

Proof. (1) According to the definition of τ_{ij}, we get

$$\begin{aligned}\tau_{ij}&=\lim_{x\to 1^-}P\{F_j(X_j)>x\mid F_i(X_i)>x\}=\lim_{x\to 0^+}\frac{P\{F_j(X_j)>1-x,F_i(X_i)>1-x\}}{P\{F_i(X_i)>1-x\}}\\&=\lim_{x\to 0^+}\frac{\overline{C}_{ij}(1-x,1-x)}{x}=u\left(1,1;C_{ij}\right);\end{aligned} \tag{2.14}$$

similarly,

$$\begin{aligned}\xi_{ij}&=\lim_{x\to 0^+}P\{F_j(X_j)<x\mid F_i(X_i)<x\}=\lim_{x\to 0^+}\frac{P\{F_j(X_j)<x,F_i(X_i)<x\}}{P\{F_i(X_i)<x\}}\\&=\lim_{x\to 0^+}\frac{C_{ij}(x,x)}{x}=l\left(1,1;C_{ij}\right).\end{aligned} \tag{2.15}$$

(2) Note that

$$\tau_J=\lim_{x\to 1^-}\frac{P\{F_j(X_j)>x,\forall j\in I\}}{P\{F_i(X_i)>x,\forall i\in \mathbf{J}\}}=\lim_{x\to 0^+}\frac{\overline{C}(1-x,\ldots,1-x)/x}{\overline{C_J}(1-x,\ldots,1-x)/x} \tag{2.16}$$

combined with (2.9), the first part is determined. The second part can be verified similarly.

(3) We can obtained the proof only paying attention to $\overline{C}(u_1,\ldots,u_t)=\widehat{C}(1-u_1,\ldots,1-u_t)$.

From the proposition, the upper tail dependence function of copula C is the lower one of its survival copula $\widehat{C}$. And in most fractal time series, from the point of view of either theory or applications, people only need to understand the right tail of the data, so we focus on the upper tail function $u(\mathbf{w};C)$ and coefficient τ_J in the following.

We first study the upper tail dependence function of multivariate regularly varying time series in (1.2) using the intensity measure. □

3. The Upper Tail Dependence Function for RV Time Series

Theorem 3.1. *Let $\mathbf{X}_1,\ldots,X_t$ be RV time series with regularly varying index α, distribution function F, copula C, and the stochastic representation as* (1.2). *If the margins are tail equivalent as $x\to\infty$, then the upper tail dependence function can be written as*

$$u(\mathbf{w};C)=\frac{\mu\left(\prod_{i=1}^{t}\left[w_i^{-1/\alpha},\infty\right]\right)}{\mu\left([1,\infty]\times\overline{R}^{t-1}\right)}, \tag{3.1}$$

and the upper exponent function can be written as

$$u^*(\mathbf{w};C)=\frac{\mu\left(\left(\prod_{i=1}^{t}\left[0,w_i^{-1/\alpha}\right]\right)^{c}\right)}{\mu\left(\left([0,1]\times\overline{R}^{t-1}\right)^{c}\right)}. \tag{3.2}$$

Proof. For any $\mathbf{w}=(w_1,\ldots,w_t)\in R_+^t$,

$$u(\mathbf{w};C)=\lim_{x\to 0^+}\frac{P\left\{\overline{F}_i(X_i)\le xw_i,\forall i\in I\right\}}{P\left\{\overline{F}_1(X_1)\le x\right\}}=\lim_{x\to 0^+}\frac{P\left\{X_i>\overline{\mathbf{F}}_i^{-1}(xw_i),\forall i\in I\right\}}{P\left\{X_1>\overline{\mathbf{F}}_1^{-1}(x)\right\}}. \tag{3.3}$$

Since every margin F_i is regularly varying with the same index α, we obtain that

$$\overline{F}_i(y)=\frac{L_i(y)}{y^{\alpha}},\quad y>0, \tag{3.4}$$

where $L_i(y)$ is slowing varying function. So for any $w_i>0$, as $x\to 0^+$,

$$\overline{F}_i\left(w_i^{1/\alpha}y\right)=\frac{L_i\left(w_i^{1/\alpha}y\right)}{w_iy^{\alpha}}=\frac{1}{w_i}\cdot\frac{L_i\left(w_i^{1/\alpha}y\right)}{L_i(y)}\cdot\frac{L_i(y)}{y^{\alpha}}=\frac{1}{w_i}\cdot h_i(w_i,y)\cdot\overline{F}_i(y), \tag{3.5}$$

where $h_i(w_i,y)=L_i(w_i^{1/\alpha}y)/L_i(y)\to 1$ as $y\to\infty$. So the equation becomes

$$\overline{F}_i\left(w_i^{1/\alpha}y\right)=\frac{1}{w_i}\cdot h_i(w_i,y)\cdot\overline{F}_i(y), \tag{3.6}$$

in other words,

$$w_i^{1/\alpha}y=\overline{\mathbf{F}}_i^{-1}\left(\frac{1}{w_i}\overline{F}_i(y)h_i(w_i,y)\right). \tag{3.7}$$

Now we let $\overline{F}_i(y)=xw_i$, then

$$w_i^{1/\alpha}\overline{\mathbf{F}}_i^{-1}(xw_i)=\overline{\mathbf{F}}_i^{-1}\left(xh_i\left(w_i,\overline{\mathbf{F}}_i^{-1}(xw_i)\right)\right), \tag{3.8}$$

so, $\overline{\mathbf{F}}_i^{-1}(xw_i)=w_i^{-1/\alpha}\overline{\mathbf{F}}_i^{-1}(xh_i(w_i,\overline{\mathbf{F}}_i^{-1}(xw_i)))$.

As $x\to 0^+$, $h_i(w_i,\overline{\mathbf{F}}_i^{-1}(xw_i))\to 1$, so we get that

$$\overline{\mathbf{F}}_i^{-1}(xw_i)\approx w_i^{-1/\alpha}\overline{\mathbf{F}}_i^{-1}(x). \tag{3.9}$$

And since the margins are equivalent, that is, $\overline{F}_i(y)/\overline{F}_1(y) \to 1$ as $y \to \infty$. We have $\overline{\mathbf{F}}_i^{-1}(x)/\overline{\mathbf{F}}_1^{-1}(x) \to 1$ as $x \to 0^+$ (Resnick [8]). So for sufficient small x, $\overline{\mathbf{F}}_i^{-1}(x) \approx \overline{\mathbf{F}}_1^{-1}(x)$, and $z = \overline{\mathbf{F}}_1^{-1}(x)$, combining (3.3) and (2.3), we obtain that

$$\begin{aligned} u(\mathbf{w};C) &= \lim_{x\to 0^+} \frac{P\left\{X_i > w_i^{-1/\alpha}\overline{\mathbf{F}}_i^{-1}(x), \forall i \in I\right\}}{P\left\{X_1 > \overline{\mathbf{F}}_1^{-1}(x)\right\}} = \lim_{z\to\infty} \frac{P\left\{X_i > w_i^{-1/\alpha} z, \forall i \in I\right\}}{P\{X_1 > z\}} \\ &= \frac{\mu\left(\prod_{i=1}^{t}\left[w_i^{-1/\alpha}, \infty\right]\right)}{\mu\left([1,\infty]\times \overline{R}^{t-1}\right)}. \end{aligned} \tag{3.10}$$

In order to calculate $u^*(\mathbf{w};C)$, we recall *the inclusion-exclusion formula*, it says that

$$P\{\cap_{i\in I} A_i\} = \sum_{\emptyset \neq S\subset I} (-1)^{|S|-1} P\{\cup_{j\in S} A_j\} \tag{3.11}$$

is valid for any finite set I and arbitrary events A_i, where $i \in I$.

Using this formula, (2.10) becomes

$$\begin{aligned} u^*(\mathbf{w};C) &= \lim_{x\to 0^+} \frac{P\{F_j(X_j) \ > 1 - x w_j, \exists j \in I\}}{x} = \lim_{x\to 0^+} \frac{P\left\{\overline{F}_j(X_j) \le x w_j, \exists j \in I\right\}}{P\left\{\overline{F}_1(X_1) \le x\right\}} \\ &= \lim_{x\to 0^+} \frac{P\left\{X_j > \overline{\mathbf{F}}_j^{-1}(x w_j), \exists j \in I\right\}}{P\left\{X_1 > \overline{\mathbf{F}}_1^{-1}(x)\right\}}. \end{aligned} \tag{3.12}$$

By using the same method of (3.3), the following equation holds:

$$u^*(\mathbf{w};C) = \lim_{z\to\infty} \frac{P\left\{X_i > w_i^{-1/\alpha} z, \exists i \in I\right\}}{P\{X_1 > z\}} = \frac{\mu\left(\left(\prod_{i=1}^{t}\left[0, w_i^{-1/\alpha}\right]\right)^c\right)}{\mu\left([1,\infty]\times \overline{R}^{t-1}\right)}. \tag{3.13}$$

□

Corollary 3.2. *Under the same conditions as Theorem 3.1, the following result holds*

$$\mu\left([1,\infty]\times \overline{R}^{t-1}\right) = \frac{1}{u^*(1,\ldots,1;C)}. \tag{3.14}$$

Proof. By (2.4), one can see that $\mu([0,1]^c) = 1$. So we can get the result immediately by letting all $w_i = 1$, $1 \le i \le t$ in (3.2).

According to Theorem 3.1 and Corollary 3.2, we can represent the intensity measure through the tail dependence function as the following Corollary. □

Corollary 3.3. *Under the same conditions as Theorem 3.1, one has*

$$\mu([\mathbf{w},\infty]) = \frac{u\left(w_1^{-\alpha},\ldots,w_t^{-\alpha};C\right)}{u^*(1,\ldots,1;C)},$$
$$\mu\left([0,\mathbf{w}]^c\right) = \frac{u^*\left(w_1^{-\alpha},\ldots,w_t^{-\alpha};C\right)}{u^*(1,\ldots,1;C)}. \tag{3.15}$$

4. The Upper Tail Dependence Parameters for Regularly Varying Time Series

According to Proposition 2.5 and Theorem 3.1, we can express the tail dependence parameters by their tail dependence functions. In this section, we will deduce the upper tail dependence parameters of time series with multivariate varying distribution in (1.2) by this method. Hereafter, we let μ be the intensity measure of $\mathbf{R} = (R, R, \ldots, R)$ with copula C^R. Where R is regularly varying at ∞ with index α, with survival function $\overline{F}_R(r) = L(r)/r^\alpha$, and $L(\cdot)$ is a slowly varying function. So for any nonnegative vector $\mathbf{w} = (w_1,\ldots,w_t)$, we have

$$\mu\left([\mathbf{0},\mathbf{w}]^c;C^R\right) = \lim_{r\to\infty}\frac{P\{R > r\wedge_{i=1}^t w_i\}}{P\{R>r\}} = \lim_{r\to\infty}\frac{\overline{F}_R\left(r\bigwedge_{i=1}^t w_i\right)}{\overline{F}_R(r)}, \tag{4.1}$$

by inserting $\overline{F}_R(r\wedge_{i=1}^t w_i) = L(r\bigwedge_{i=1}^t w_i)/(r\bigwedge_{i=1}^t w_i)^\alpha$ and $\overline{F}_R(r) = L(r)/r^\alpha$ into the representation, then,

$$\mu\left([\mathbf{0},\mathbf{w}]^c;C^R\right) = \frac{1}{\left(\bigwedge_{i=1}^t w_i\right)^\alpha} = \left(\bigvee_{i=1}^t w_i\right)^{-\alpha}. \tag{4.2}$$

Similarly, we have,

$$\mu\left([\mathbf{w},\infty];C^R\right) = \bigwedge_{i=1}^t w_i^{-\alpha}. \tag{4.3}$$

Consequently, we get the main result as follows.

Theorem 4.1. *Let $X_1,\ldots,X_t$ be regularly varying time series with the same regularly varying index α and the stochastic representation given in (1.2), the margins are tail equivalent as $x\to\infty$. If there exists a $\gamma > \alpha$ holds for $0 < E(Z_{i+}^\gamma) < \infty$, then the upper tail dependence parameter of $X_1,\ldots,X_t$ is*

$$\tau_J = \frac{E\left(\bigwedge_{i=1}^t\left(Z_{i+}^\alpha/E(Z_{i+}^\alpha)\right)\right)}{E\left(\bigwedge_{i\in J}\left(Z_{i+}^\alpha/E(Z_{i+}^\alpha)\right)\right)}. \tag{4.4}$$

Proof. We first calculate the tail dependence function of $\mathbf{X} = (RZ_1, \ldots, RZ_t)$. In the following, let C^X and C^Y be the copula of $\mathbf{X}$ and $\mathbf{Y}$, respectively. Denote

$$(Y_1, \ldots, Y_t)^T = \mathbf{A}(R, \ldots, R)^T, \tag{4.5}$$

where

$$\mathbf{A} = \operatorname{diag}\left(\frac{Z_{1+}}{(E(Z_{1+}^{\alpha}))^{1/\alpha}}, \ldots, \frac{Z_{t+}}{(E(Z_{1+}^{\alpha}))^{1/\alpha}} \right). \tag{4.6}$$

Note that $Y_i = (Z_{i+}/(E(Z_{i+}^{\alpha}))^{1/\alpha})R$ is strictly increasing transformation of $X_i > 0$, for all $i \in I$, and the tail dependence function and the parameter are all copula properties. Hence $\mathbf{Y}$ and $\mathbf{X}$ have the same tail dependence functions. By Lemma 2.3, one can see that the marginal variables Y_i of vector $\mathbf{Y}$ are tail equivalent and regularly varying with the same index as $\mathbf{X}$ as $x \to \infty$. Denote the intensity measures of $\mathbf{Y}$ and $\mathbf{R}$ by $\widetilde{\mu}(\cdot)$ and $\mu(\cdot)$, respectively. According to (2.7),

$$\widetilde{\mu}(\cdot) = E\Big(\mu\Big(\mathbf{A}^{-1}\cdot\Big)\Big). \tag{4.7}$$

Now by (4.6), we see that,

$$\mathbf{A}^{-1} = \operatorname{diag}\left(\frac{(E(Z_{1+}^{\alpha}))^{1/\alpha}}{Z_{1+}}, \ldots, \frac{(E(Z_{t+}^{\alpha}))^{1/\alpha}}{Z_{t+}} \right), \tag{4.8}$$

combining this with (4.3), for any nonnegative $\mathbf{w}$, we obtain the intensity measure given by

$$\begin{aligned} \widetilde{\mu}([\mathbf{w}, \infty]) = E\Big(\mu\Big(\mathbf{A}^{-1}[\mathbf{w}, \infty]\Big)\Big) &= E\left(\mu\left(\prod_{i=1}^{t} \left[\frac{(E(Z_{i+}^{\alpha}))^{1/\alpha}}{Z_{i+}} w_i, \infty \right]; C^R \right) \right) \\ &= E\left(\bigwedge_{i=1}^{t} \frac{Z_{i+}^{\alpha}}{E(Z_{i+}^{\alpha})} w_i^{-\alpha} \right). \end{aligned} \tag{4.9}$$

Hence, we have

$$\widetilde{\mu}\left(\prod_{i=1}^{t} [\mathbf{w}_i^{-\alpha}, \infty] \right) = E\left(\bigwedge_{i=1}^{t} \frac{Z_{i+}^{\alpha}}{E(Z_{i+}^{\alpha})} w_i \right). \tag{4.10}$$

Substituting this measure into (3.1), we get the upper tail dependence function of vector $\mathbf{Y}$ as follows:

$$u\Big(\mathbf{w}; C^Y\Big) = E\left(\bigwedge_{i=1}^{t} \frac{Z_{i+}^{\alpha}}{E(Z_{i+}^{\alpha})} w_i \right). \tag{4.11}$$

Since $\mathbf{Y}$ and $\mathbf{X}$ have the same tail dependence functions, we have

$$u\left(\mathbf{w}; C^X\right) = E\left(\bigwedge_{i=1}^{t} \frac{Z_{i+}^{\alpha}}{E(Z_{i+}^{\alpha})} w_i\right). \tag{4.12}$$

By (2) in Proposition 2.5, we obtain the upper tail dependence parameters of vector $\mathbf{X}$. □

5. Examples

Let $\mathbf{Z}$ in (1.2) be $\mathbf{Z} = A(U_1, \ldots, U_n)$, where A is a $t \times n$ matrix with $AA^T = \Sigma$, and Σ is a $t \times t$ semidefinite matrix, $U = (U_1, \ldots, U_n)$ is uniformly distributed on the unit sphere (with respect to Euclidean distance) in R^n. We know that $\mathbf{X}$ conforms to an elliptical contoured distribution (Fang et al. [43]). The tail dependence of the elliptical contoured distribution has been discussed in Schmidt [33]. Here we select the t distribution to display our results in Theorem 4.1 as a special case.

If $\mathbf{X} \sim \mathfrak{t}_n(\boldsymbol{\mu}, \boldsymbol{\Sigma}, \nu)$, then $\mathbf{X}$ has the stochastic representation ([43]):

$$\mathbf{X} = \boldsymbol{\mu} + \frac{\sqrt{\nu}}{\sqrt{S}} \mathbf{Z}, \tag{5.1}$$

where $S \sim \chi_{\nu}^2$ and $\mathbf{Z} \sim \mathbb{N}_n(\mathbf{0}, \boldsymbol{\Sigma})$ are independent, $\boldsymbol{\mu} \in R^n$.

Let $R = \sqrt{\nu/S}$. Then $R^2 \sim IG(\nu/2, \nu/2)$ and R is regularly varying with index ν at ∞. So the vector $(X_1, \ldots, X_n)$ is regularly varying according to Schmidt [33].

For the upper tail dependence that only relies on the tail behavior of the random vector, we can focus, without loss of generality, on the random vector $\mathbf{X}$ with zero mean vector. Furthermore, since the strictly increasing transformation of $(X_1, \ldots, X_n)$ does not change the copula, $\Delta^{-1/2}\mathbf{X}$ has the same copula as $\mathbf{X}$, where $\boldsymbol{\Sigma} = (\sigma_{ij})$ and $\Delta = \operatorname{diag}(\sigma_{11}, \sigma_{22}, \ldots, \sigma_{nn})$. Thus $\Delta^{-1/2}\mathbf{X} \sim \mathfrak{t}_n(0, \Delta^{-1/2}\boldsymbol{\Sigma}\Delta^{-1/2}, \nu)$. It is evident that $\Delta^{-1/2}\boldsymbol{\Sigma}\Delta^{-1/2}$ becomes the correlation matrix of the random vector. Consequently, we may assume that the covariance matrix $\boldsymbol{\Sigma}$ is the correlation matrix. In this situation, all $Z_i's$ have the same margins as $N(0,1)$. So $E(Z_{i+}^{\nu})$ are all equal for any $1 \le i \le n$. Under these assumptions, using (4.4), we get the upper tail dependence parameter of $\mathbf{t}_n(0, \boldsymbol{\Sigma}, \nu)$ as

$$\tau_J = \frac{E\left(\bigwedge_{i=1}^{n} Z_{i+}^{\nu}\right)}{E\left(\bigwedge_{i \in J} Z_{i+}^{\nu}\right)}. \tag{5.2}$$

This is coincided to the one obtained in Shi and Lin [34].

6. Simulations

In Section 4, we obtain the expressions of the tail dependence indexes about RV time series in (1.2). In Section 5, we display our result in the multivariate t distribution as example. In this Section, we will illustrate these results by some Monte Carlo simulated numerical examples.

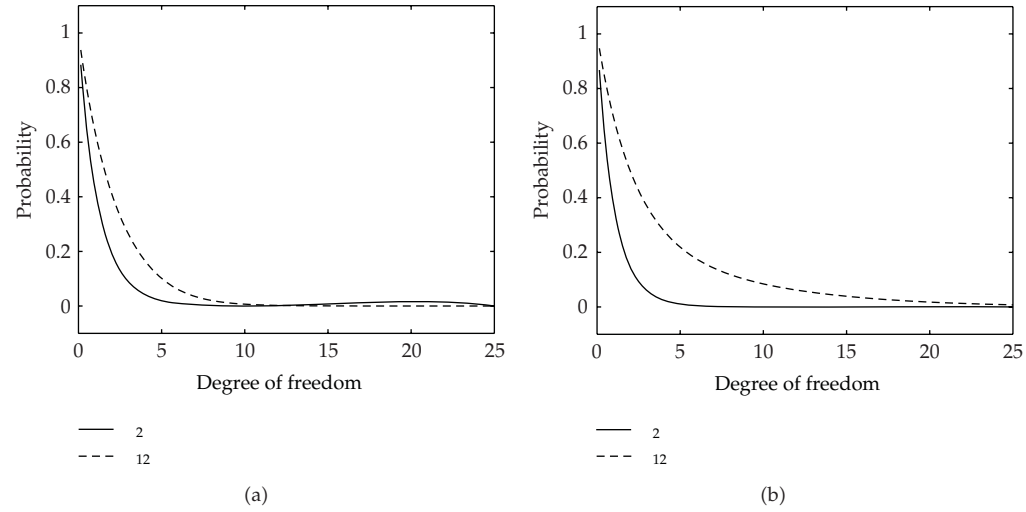

Figure 1: The estimation of τ_2, τ_{12} under AR(1) (the left one) and EX (the right one) correlation structure.

Given that $y^{(1)}, y^{(2)}, \ldots, y^{(m)}$ be generated from the multivariate normal distribution $\mathbf{N}_n(\mathbf{0}, \boldsymbol{\rho})$, then the upper tail dependence indices of $\mathbf{t}_n(\boldsymbol{\mu}, \boldsymbol{\Sigma}, \nu)$ can be estimated by

$$\widehat{\tau}_J = \frac{\sum_{k=1}^{m} \left(\bigwedge_{j=1}^{n} \left| y_j^{(k)} \right| \right)^{\nu} I\{ y^{(k)} > 0 \text{ or } y^{(k)} < 0 \}}{\sum_{k=1}^{m} \left(\bigwedge_{i \in J} \left| y_i^{(k)} \right| \right)^{\nu} I\{ y^{(k)} > 0 \text{ or } y^{(k)} < 0 \}}. \tag{6.1}$$

We estimate the upper tail dependence parameter of 3-dimensional t distribution under autoregressive of order 1 (AR(1)), exchangeable(EX), Toeplitz(TOEP), and unstructured(UN) correlation structure, respectively. For each correlation matrix, we first generate 80,000 pseudorandom vectors, then use (5.2) to estimate tail dependence parameter for different ν. Specifically, we do the following simulations.

$$\sum_1 = \begin{pmatrix} 1 & -0.3 & 0.09 \\ -0.3 & 1 & -0.3 \\ 0.09 & -0.3 & 1 \end{pmatrix}, \qquad \sum_2 = \begin{pmatrix} 1 & -0.3 & -0.3 \\ -0.3 & 1 & -0.3 \\ -0.3 & -0.3 & 1 \end{pmatrix}. \tag{6.2}$$

Let $\mathbf{J} = \{2\}$ and $\{1, 2\}$, respectively. The corresponding upper tail dependence parameters are denoted by τ_2 and τ_{12}. $\boldsymbol{\Sigma}_1$ and $\boldsymbol{\Sigma}_2$ are under AR(1) and EX correlation structure, respectively, the simulated values of τ_2, τ_{12} about different ν are computed and plotted in Figure 1. $\boldsymbol{\Sigma}_3$ and $\boldsymbol{\Sigma}_4$ are under TOEP and UN correlation structure, the corresponding results are demonstrated in Figure 2.

From the two figures, in spite of the correlation structure, τ_J decreased and approached 0 quickly as ν increased to ∞, which is the tail dependence index for multivariate normal copula.

Many researchers try to discuss the monotonicity of the tail dependence parameter about the regular varying index. Embrechts et al. [11] proved that the tail dependence of the bivariate t distribution is decreasing about the regular varying index ν, and demonstrated

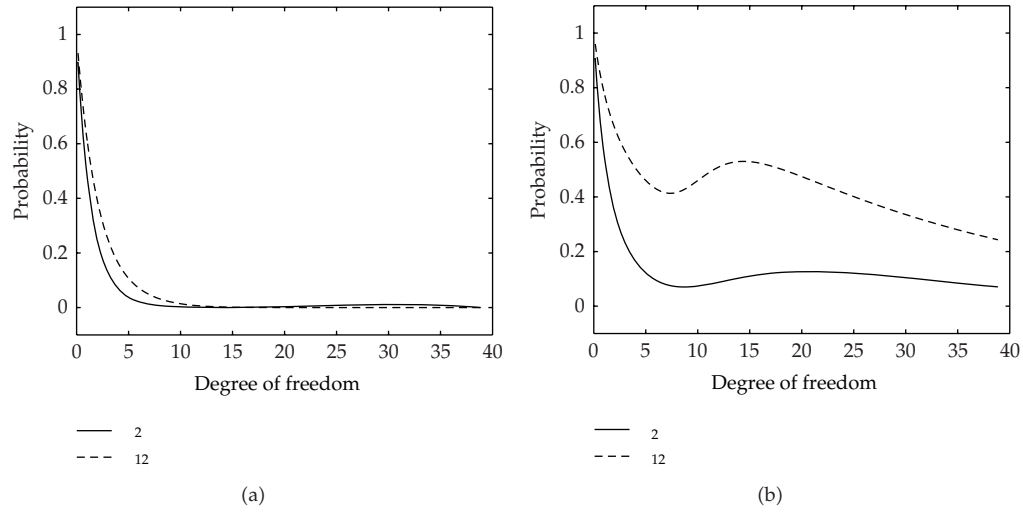

Figure 2: The estimation of τ_2, τ_{12} under TOEP (the left one) and UN (the right one) correlation structure.

that the tail dependence parameter τ_1 is decreasing in ν by numerical results. But From the right graph in Figure 2., these conclusions are not always correct when $t \geq 3$.

$$\sum_3 = \begin{pmatrix} 1 & -0.3 & 0.5 \\ -0.3 & 1 & -0.3 \\ 0.5 & -0.3 & 1 \end{pmatrix}, \qquad \sum_4 = \begin{pmatrix} 1 & 0.3 & 0.5 \\ 0.3 & 1 & 0.7 \\ 0.5 & 0.7 & 1 \end{pmatrix}. \tag{6.3}$$

7. Conclusion

In the paper, we mainly study tail dependence of RV time series in (1.2). We use tail dependence function and intensity measure to express tail dependence parameters. Using tail dependence function, we do not need to consider the explicit representation of the copula. We first discuss the tail dependence function of the RV time series due to the propositions of the regularly varying function, connecting the biuniquely determined property between the tail dependence function and the intensity measure. Then we calculate the explicit formula of the upper tail dependence parameter about the RV time series under some conditions. In fact, we can obtain the extreme upper tail dependence index (Shi and Lin [34]) very similarly to Theorem 4.1, for concise, we omit it here.

Copula of continuous variables is invariant under strictly increasing transformation (Nelsen [2]). In order to obtain the tail dependence function of random vector $\mathbf{X}$, we shift to solve that of $\mathbf{Y}$ in (4.5), which is just a strictly increasing transformation of $\mathbf{X}$.

At last, we select the t distribution as a special case to display our result, they are coincided to the one given in [34]. The monotonicity of the tail dependence parameters about the regular varying index is still an open problem. Under what constraints the tail dependence parameters will be deceasing in the variation index? We are still interested in the problem. We will discuss it in the following work in details. In engineering application, when we confront fractal time series and seasonal data, we can model the tail dependence property via the tail dependence function if the data is consistent with the constraint conditions in our work.

Acknowledgment

The authors are very grateful to the referees for their comments and suggestions on the earlier version of the paper, which led to a much improved paper. This project is supported by MSRFSEU 3207011102, NSFC 11171065, and NSFJS BK2011058.

References

[1] M. Sklar, "Fonctions de répartition à n dimensions et leurs marges," vol. 8, pp. 229–231, 1959.

[2] R. B. Nelsen, *An introduction to Copulas*, Springer Series in Statistics, Springer, New York, NY, USA, 2nd edition, 2006.

[3] B. Schweizer and A. Sklar, *Probabilistic Metric Spaces*, North-Holland Series in Probability and Applied Mathematics, North-Holland Publishing, New York, NY, USA, 1983.

[4] H. Joe, *Multivariate Models and dependence concepts*, vol. 73 of *Monographs on Statistics and Applied Probability*, Chapman & Hall, London, 1997.

[5] C. Genest and A. C Favre, "Everything you always wanted to know about copula modeling but were afraid to ask," *Journal of Hydrological Engineering*, vol. 12, pp. 347–368, 2007.

[6] C. Klüppelberg and G. Kuhn, "Copula structure analysis," *Journal of the Royal Statistical Society. Series B. Statistical Methodology*, vol. 71, no. 3, pp. 737–753, 2009.

[7] G. Frahm, M. Junker, and R. Schmidt, "Estimating the tail-dependence coefficient: properties and pitfalls," *Insurance: Mathematics & Economics*, vol. 37, no. 1, pp. 80–100, 2005.

[8] S. I. Resnick, *Extreme Values, Regular Variation, and Point Processes*, vol. 4 of *Applied Probability. A Series of the Applied Probability Trust*, Springer, New York, NY, USA, 1987.

[9] S. I. Resnick, *Heavy-Tail Phenomena: Probabilistic and Statistical Modeling*, Springer Series in Operations Research and Financial Engineering, Springer, New York, NY, USA, 2007.

[10] A. K. Nikoloulopoulos, H. Joe, and H. Li, "Extreme value properties of multivariate t copulas," *Extremes. Statistical Theory and Applications in Science, Engineering and Economics*, vol. 12, no. 2, pp. 129–148, 2009.

[11] P. Embrechts, F. Lindskog, and A. McNeil, "Modelling dependence with copulas and applications to risk management," in *Handbook of Heavy Tailed Distributions in Finance*, S. Rachev, Ed., Elsevier, New York, NY, USA, 2003.

[12] P. Embrechts, A. J. McNeil, and D. Straumann, "Correlation and dependence in risk management: properties and pitfalls," in *Risk Management: Value at Risk and Beyond*, M. A. H. Dempster, Ed., pp. 176–223, Cambridge University Press, Cambridge, UK, 1999.

[13] V. Pisarenko and M. Rodkin, *Heavy-Tailed Distributions in Disaster Analysis*, Springer, 2010.

[14] E. Kole, K. Koedijk, and M. Verbeek, "Selecting copulas for risk management," Tech. Rep., Erasmus School of Economics and Business Economics, Erasmus University Rotterdam, Rotterdam, The Netherlands, 2006.

[15] S. Ghosh, "Modelling bivariate rainfall distribution and generating bivariate correlated rainfall data in neighbouring meteorological subdivisions using copula," *Hydrological Processes*, vol. 24, pp. 3558–3567, 2010.

[16] V. Ganti, K. M. Straub, E. Foufoula-Georgiou, and C. Paola, "Space-time dynamics of depositional systems: experimental evidence and theoretical modeling of heavy-tailed statistics," *Journal of Geophysical Research*, vol. 116, no. F2, Article ID F02011, 17 pages, 2011.

[17] V. Fasen, "Modeling network traffic by a cluster Poisson input process with heavy and light-tailed file sizes," *Queueing Systems*, vol. 66, no. 4, pp. 313–350, 2010.

[18] P. Loiseau, P. Goncalves, G. Dewaele, P. Borgnat, P. Abry, and P. Vicat-Blanc, "Investigating self-similarity and heavy-tailed distributions on a large-scale experimental facility," *IEEE/ACM Transactions on Networking*, vol. 18, no. 4, pp. 1261–1274, 2010.

[19] M. Li and W. Zhao, "Representation of a stochastic traffic bound," *IEEE Transactions on Parallel and Distributed Systems*, vol. 21, no. 9, pp. 1368–1372, 2010.

[20] P. Abry, P. Borgnat, F. Ricciato, A. Scherrer, and D. Veitch, "Revisiting an old friend: on the observability of the relation between long range dependence and heavy tail," *Telecommunication Systems*, vol. 43, no. 3-4, pp. 147–165, 2010.

[21] J. A. Hernádez, I. W. Phillips, and J. Aracil, "Discrete-time heavy-tailed chains, and their properties in modeling network traffic," *ACM Transactions on Modeling and Computer Simulation*, vol. 17, no. 4, 11 pages, 2007.

[22] C. Cattani and G. Pierro, "Complexity on acute myeloid leukemia mRNA transcript variant," *Mathematical Problems in Engineering*, Article ID 379873, 16 pages, 2011.

[23] M. Li, C. Cattani, and S. Y. Chen, "Viewing sea level by a one-dimensional random function with long memory," *Mathematical Problems in Engineering*, vol. 2011, Article ID 654284, 13 pages, 2011.

[24] M. Li and W. Zhao, "Visiting power laws in cyber-physical networking systems," *Mathematical Problems in Engineering*, vol. 2012, Article ID 302786, 13 pages, 2012.

[25] S. Y. Chen, H. Tong, Z. Wang, S. Liu, M. Li, and B. Zhang, "Improved generalized belief propagation for vision processing," *Mathematical Problems in Engineering*, Article ID 416963, 12 pages, 2011.

[26] M. Li, "Fractal time series—a tutorial review," *Mathematical Problems in Engineering*, Article ID 157264, 26 pages, 2010.

[27] H. Sheng, Y. Chen, and T. Qiu, *Fractional Processes and Fractional-Order Signal Processing*, Signals and Communication Technology, Springer, London, UK, 2012, http://www.springer.com/engineering/signals/book/978-1-4471-2232-6.

[28] H. Hult and F. Lindskog, "Multivariate extremes, aggregation and dependence in elliptical distributions," *Advances in Applied Probability*, vol. 34, no. 3, pp. 587–608, 2002.

[29] H.-B. Fang, K.-T. Fang, and S. Kotz, "The meta-elliptical distributions with given marginals," *Journal of Multivariate Analysis*, vol. 82, no. 1, pp. 1–16, 2002.

[30] S. G. Coles, J. Heffernan, and J. A. Tawn, "Dependence measures for multivariate extremes," *Extremes*, vol. 2, pp. 339–365, 1999.

[31] A. W. Ledford and J. A. Tawn, "Statistics for near independence in multivariate extreme values," *Biometrika*, vol. 83, no. 1, pp. 169–187, 1996.

[32] M. Mesfioui and J.-F. Quessy, "Dependence structure of conditional Archimedean copulas," *Journal of Multivariate Analysis*, vol. 99, no. 3, pp. 372–385, 2008.

[33] R. Schmidt, "Tail dependence for elliptically contoured distributions," *Mathematical Methods of Operations Research*, vol. 55, no. 2, pp. 301–327, 2002.

[34] A. J. Shi and J. G. Lin, "Monotonicity of the tail dependence for multivariate t-copula," *Journal of Southeast University*, vol. 27, no. 4, pp. 466–470, 2011.

[35] H. Li, "Orthant tail dependence of multivariate extreme value distributions," *Journal of Multivariate Analysis*, vol. 100, no. 1, pp. 243–256, 2009.

[36] C. Arthur and S. Johan, "Tails of multivariate Archimedean copulas," *Journal of Multivariate Analysis*, vol. 100, no. 7, pp. 1521–1537, 2009.

[37] G. Frahm, "On the extremal dependence coefficient of multivariate distributions," *Statistics & Probability Letters*, vol. 76, no. 14, pp. 1470–1481, 2006.

[38] A. Charpentier and J. Segers, "Lower tail dependence for Archimedean copulas: characterizations and pitfalls," *Insurance: Mathematics & Economics*, vol. 40, no. 3, pp. 525–532, 2007.

[39] O. Kallenberg, *Random Measures*, Academic Press, Berlin, Germany, 3rd edition, 1983.

[40] L. Breiman, "On some limit theorems similar to the arc-sin law," *Theory of Probability and Its Applications*, vol. 10, pp. 323–331, 1965.

[41] B. Basrak, R. A. Davis, and T. Mikosch, "Regular variation of GARCH processes," *Stochastic Processes and their Applications*, vol. 99, no. 1, pp. 95–116, 2002.

[42] C. Kluppelberg, G. Kuhn, and L. Peng, "Multivariate tail copula: modeling and estimation," Tech. Rep. number 468, Center for Mathematical Sciences, Munich University of Technology, 2006, http://epub.ub.uni-muenchen.de/.

[43] K. T. Fang, S. Kotz, and K. W. Ng, *Symmetric Multivariate and Related Distributions*, vol. 36 of *Monographs on Statistics and Applied Probability*, Chapman & Hall, London, UK, 1990.

Hindawi Publishing Corporation
Mathematical Problems in Engineering
Volume 2012, Article ID 820190, 18 pages
doi:10.1155/2012/820190

Research Article

An Adaptive Test Sheet Generation Mechanism Using Genetic Algorithm

Huan-Yu Lin,[1] Jun-Ming Su,[2] and Shian-Shyong Tseng[3]

[1] *Department of Computer Science, National Chiao Tung University, 1001 University Road, Hsinchu 300, Taiwan*
[2] *Department of Information and Learning Technology, National University of Tainan, 33, Section 2, Shu-Lin Street, Tainan 700, Taiwan*
[3] *Department of Information Science and Applications, Asia University, 500 Lioufeng Road, Wufeng, Taichung 41354, Taiwan*

Correspondence should be addressed to Jun-Ming Su, junming.su@gmail.com

Received 7 February 2012; Revised 26 March 2012; Accepted 27 March 2012

Academic Editor: Ming Li

For test-sheet composition systems, it is important to adaptively compose test sheets with diverse conceptual scopes, discrimination and difficulty degrees to meet various assessment requirements during real learning situations. Computation time and item exposure rate also influence performance and item bank security. Therefore, this study proposes an Adaptive Test Sheet Generation (ATSG) mechanism, where a Candidate Item Selection Strategy adaptively determines candidate test items and conceptual granularities according to desired conceptual scopes, and an Aggregate Objective Function applies Genetic Algorithm (GA) to figure out the approximate solution of mixed integer programming problem for the test-sheet composition. Experimental results show that the ATSG mechanism can efficiently, precisely generate test sheets to meet the various assessment requirements than existing ones. Furthermore, according to experimental finding, Fractal Time Series approach can be applied to analyze the self-similarity characteristics of GA's fitness scores for improving the quality of the test-sheet composition in the near future.

1. Introduction

With the rapid developments of information and assessment technology, the computerized testing is generally used to assess, predict, and diagnose learners' learning statuses because it is able to effectively analyze examinees' abilities and learning barriers. The test quality offered by a computerized testing system depends on not only the quality of test items but also the satisfied test sheets to meet the various requirements of assessment parameters, such as the

difficulty degree, the discrimination degree, the associated concepts, and the expected testing time. Thus, how to efficiently assist teachers in composing and generating an appropriate test sheet to meet the diverse assessment requirements has become an important research issue.

Hwang [1] applied the dynamic programming technique to solve this issue, but the solution is inefficient for a large-item bank because of the exponential growth of time and space complexity. Su and Wang [2] developed an assistance system to provide teachers with statistic information for assisting teachers in manually composing the desired test sheets, but manually selecting appropriate test items in a large item bank is still inefficient and difficult to ensure the qualities of test sheets. Therefore, the pressing problem of automatic test item allocation is emerging and it can be regarded as a combinatorial optimization problem, which is proven an NP-hard problem [3]. Therefore, Hwang et al. [4] formulated this problem as a mixed integer programming model and proposed approximate solutions by using the Genetic Algorithm (GA) approach [5]. The experimental results show that their proposed approach can efficiently automatically compose a good enough test sheet for a large-scale test.

However, the aforementioned studies mainly aim to automatically generate a test sheet with a highest discrimination degree and to meet the constraints in terms of expected testing time and concept relevance. These mechanisms are suitable for the large-scale test only, but their natures are difficult to satisfy various purposes of assessments during the real learning situation. In order to efficiently understand the students' learning problems, it is important to compose the test sheets with diverse conceptual scopes ($\mathbb{C}$), discrimination ($\mathbb{D}$) and difficulty ($\mathbb{P}$) degrees, such as displacement and summative assessments (with normal distribution $\mathbb{C}$ and $\mathbb{P}$), and formative and diagnostic assessments (with various or specific $\mathbb{C}$ and $\mathbb{P}$) [6–9]. Moreover, the computation time of the test-sheet composition process and the Item Exposure Rate are our concerns as well. A long computation time will decrease the performance of test-sheet composition system and a high-item exposure rate will decrease the qualities of test items and Item Bank Security [10, 11]. Accordingly, to consider not only the various assessment requirements but also the computation time and item exposure rate, this study defines a new problem of automatic test item allocation, called an Adaptive Test Sheet Generation problem. To solve it, this research proposes Adaptive Test Sheet Generation (ATSG) mechanism, consisting of a Candidate Item Selection Strategy (CISS) and an Aggregate Objective Function (AOF). CISS process can adaptively determine candidate test items set and the conceptual granularities according to the desired concept scope, and AOF applies GA algorithms to solve the mixed integer programming problem. The evaluation results show that the proposed approach can generate test sheets to meet the various assessment requirements.

2. Related Work

The original issue of the test sheet generation problem is identified for the large-scale tests, where these test items covering all required concepts and having the highest degree of discrimination are selected from a test item bank. Hwang [1] proposed an algorithm based on dynamic programming technique to find optimal test sheets, but the exponential time complexity causes the efficiency issue for a large number of candidate test items. Therefore, the researchers formulated this problem as a mixed integer programming model and applied a genetic algorithm [4] to figure out the approximate solution. In this paper, assume that a

set of test items, which are related to m concepts, should be selected from n items in the item bank. Each test item Q_i is defined as

$$Q_i = (t_i, d_i, r_{ij}), \tag{2.1}$$

where Q_i is a test item in the item bank (IB) and has a set of parameters including the expected time t_i needed for answering, the degree of discrimination d_i, and the degree of association r_{ij} between Q_i and a concept C_j.

The assessment requirement of a Test Sheet (TS) includes the lower bound l and upper bound u of the totally expected answering time, and the lower bound h_j of the total relevance of each concept C_j. To formulate the problem, a decision variable x_i is defined as a *Kronecker delta*, that is,

$$x_i = \begin{cases} 1, & \text{if } Q_i \in \text{TS}, \\ 0, & \text{if } Q_i \notin \text{TS}. \end{cases} \tag{2.2}$$

The goal of this problem is to maximize $Z = (\sum_{i=1}^{n} d_i x_i)/(\sum_{i=1}^{n} x_i)$.

Subject to the concept range $\sum_{i=1}^{n} r_{ij} x_i \geq h_j$ for $j = 1$ to n and the testing time limitation $l \leq \sum_{i=1}^{n} t_i x_i \leq u$.

A Genetic Algorithm (GA) approach [5] is used to solve this problem, where a chromosome is represented as an n-bit binary string $[x_1, x_2, \ldots, x_n]$ and the fitness rank is the summation of selected items' discrimination degrees subtracted by the penalty scores. The penalty scores are the degrees about the violation of expected time and concept ranges constraints. The genetic algorithm iteratively generates new generation of chromosomes by the Crossover and Mutation processes, as Random Functions, and finds the best chromosomes according to their fitness ranks. In the Crossover, chromosomes of the next iteration are generated by combining halves of two chromosomes, which are randomly selected from the chromosomes in the current iteration. A chromosome can be more probably selected because it has a higher fitness rank. Mutation is the other operation of changing a chromosome, where the change of an arbitrary bit is randomly raised to a chromosome. This kind of evolutionary algorithm can iteratively approach to the optimal solution and use some random operations, such as the operations of Crossover and Mutation, to prevent falling into the local optimal solutions. According to the evaluation, the test sheet generation approach based on a GA can really provide good solutions among more than ten thousand test items in an acceptable response time. Furthermore, the greedy algorithm approach [12], the tabu search algorithm [13], and the discrete particle swarm optimization algorithm [14] were subsequently applied to enhance the computation efficiency of test sheet generation based on the aforementioned problem formulation.

Besides, the test sheet composition problem was extended to a parallel test sheets composition problem, where multiple test sheets are generated at one time. These sheets must have similar concept relevance, discrimination, and difficulty degrees but contain no common test items. The problem was solved by extending the existing tabu search algorithm [15] and the particle swarm optimization algorithm [16].

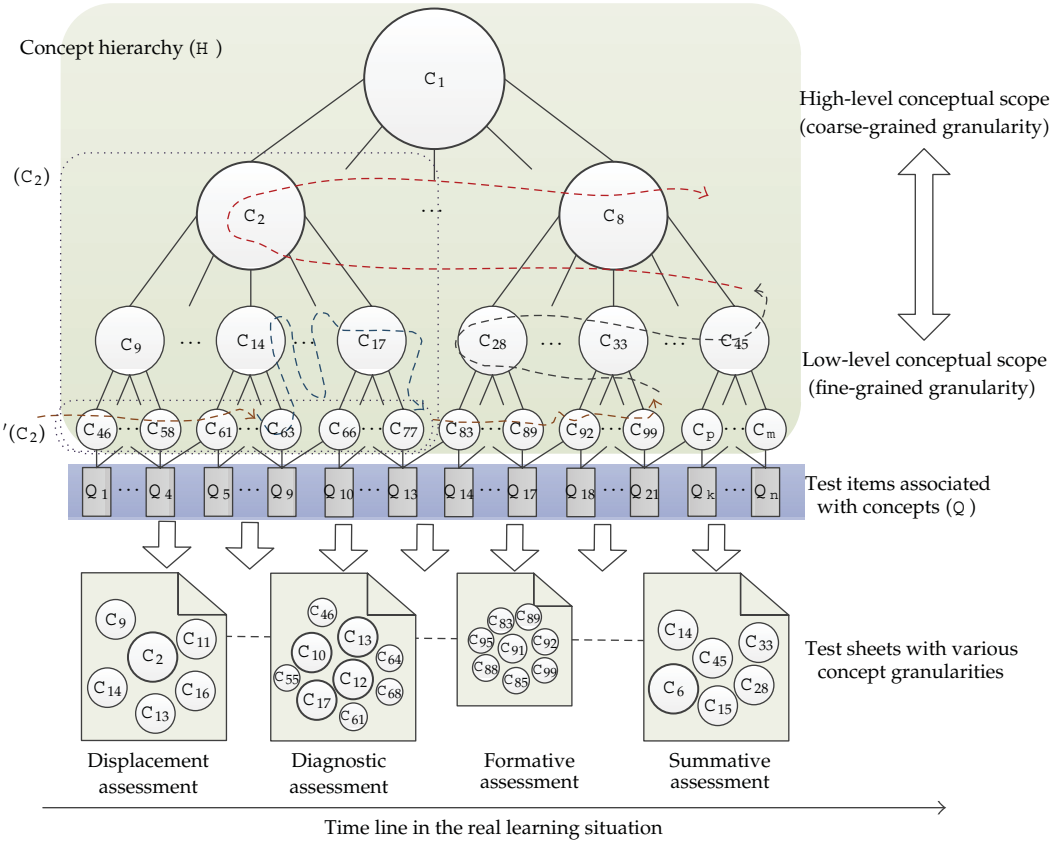

Figure 1: Test sheet types to meet various assessment requirements.

3. Adaptive Test Sheet Generation Problem

In order to efficiently understand the students' learning problems, the parameters of a test sheet including conceptual scopes ($\mathbb{C}$), discrimination ($\mathbb{D}$), and difficulty ($\mathbb{P}$) degrees should be adaptively composed according to the various assessment purposes, such as displacement and summative assessments (with normal distribution $\mathbb{C}$ and $\mathbb{P}$), and formative and diagnostic assessments (with various or specific $\mathbb{C}$ and $\mathbb{P}$). As illustrated in Figure 1, for the formative assessment, like a small-scale test, a test sheet with the specific and detailed concepts, that is, low-level conceptual scope/fine-grained granularity, is required to evaluate the students' specific conceptual capabilities during the learning; for the diagnostic assessment, like a specific-scale test, a test sheet with the diverse conceptual scopes and granularities is used to diagnose the students' learning problems; for the displacement and summative assessments, like a large-scale test, a test sheet with the high-level conceptual granularities is required to evaluate the students' learning performance before and after the learning, respectively.

However, as seen in Figure 2, the existing approaches did not take the adaptive requirements, that is, $\mathbb{C}$, $\mathbb{P}$, and $\mathbb{D}$ into account, and only focus on the highest $\mathbb{D}$. Consequently, their composed test sheets may contain the *miss-* and *error-included concept* nodes and cannot meet the adaptive requirements. Moreover, they also need to spend much more computation

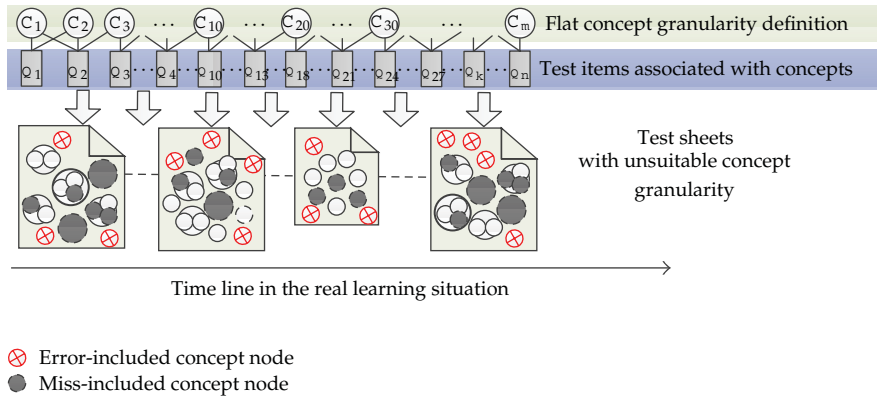

Figure 2: Issues for existing test sheet generation mechanisms.

time to select candidate test items in the item bank because they have no item selection strategy to filter the irrelevant ones in advance. Besides, item exposure rate, which denotes the number of a test item used in the test sheets, also needs to consider for enhancing the Item Bank Security.

Therefore, three issues are required to be solved for satisfying the adaptive requirements of a test sheet:

(i) how to generate a test sheet to precisely meet the adaptive requirements in terms of conceptual granularities, discrimination, difficulty, and expected test time parameters;

(ii) how to speed up the test sheet generation process for reducing the computation time;

(iii) how to consider the item exposure rate issue to enhance the Item Bank Security.

An Adaptive Test Sheet Generation Problem Is Defined as Follows

Assume that a set of test items should be selected from n items in the item bank $Q = \{Q_1, Q_2, \ldots, Q_n\}$. All items should be related to the concepts in a concept hierarchy H, a tree of concepts as shown in Figure 1. The tree H contains m concepts as the tree nodes C, namely, $C = \{C_1, C_2, \ldots, C_m\}$. δ is a descendent function, where $\delta(C_i) \subset C$ is a set of descendent nodes of C_i, and $\delta'(C_i) \subset C$ is a descendent leaf function, whereC_j belongs to $\delta'(C_i)$ if and only if C_j is a leaf concept of H and the descendent of C_i.

$$C_j \in \delta'(C_i) \quad \text{iff } \left(C_j \in \delta(C_i)\right) \wedge \left(\delta\left(C_j\right) = \{\emptyset\}\right). \tag{3.1}$$

Based on the Q_i definition in Section 2, the item exposure times e_i and the degree of difficulty p_i are taken in account in this study. Thus, each test item Q_i is defined as follows.

$$Q_i = \left(p_i, t_i, d_i, r_{ij}, e_i\right), \quad \text{where } 0 \le d_i, p_i, r_i \le 1, \quad t_i,\ e_i \in \mathbb{N} \text{ (Natural Number)}. \tag{3.2}$$

An example is provided in Figure 3, where the concept hierarchy H is a tree of concept C_j and the test item set Q is a set of test items Q_i. A weight r_{ij} denotes relevance degree between

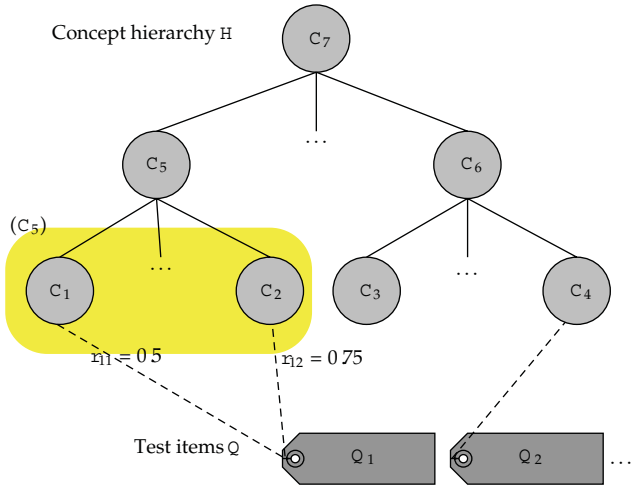

Figure 3: Concept hierarchy H and its related test items Q.

the concept C_j test item Q_i, for example, the relevance of C_2 and Q_1 is $r_{12} = 0.75$. The $\delta(C_j)$ denotes the subtree of the concept C_j, for example, C_1 and C_2 belong to the $\delta(C_5)$.

Therefore, in this study, a test sheet (TS) can be defined as follows:

$$\text{TS} = (Qs, t', p', C', r'), \tag{3.3}$$

where TS includes the expected test time t' of the test sheet, target difficulty degree p', target concepts $C' \subset C$, and the lower bound of average concept relevance r'. Based on the definitions of existing studies mentioned in Section 2, a decision variable $X = [x_1, x_2, \ldots, x_n]$ is defined where x_i is 1 if the test item Q_i is selected to the test sheet; 0, otherwise.

The goal of the adaptive test sheet generation problem is to generate a test sheet to

(i) approach all the target parameters p' and t',

(ii) have the highest average discrimination degree,

(iii) have the balanced concept relevance weight sum of each required conceptual granularity and its descents among the required concept range C' and the average relevance to be higher than r',

(iv) have the lowest average item exposure rate.

This is a multiobjective optimization problem, and the objective functions are defined as follows.

The objective function of the discrimination degree is inversed to the average discrimination degree of the test sheet:

$$D(X) = 1 - \left(\frac{\sum_{i=1}^{n} d_i x_i}{\sum_{i=1}^{n} x_i} \right). \tag{3.4}$$

The objective function of the expected test time is the distance between the sum of expected test time and the target expected time:

$$T(X) = \left| \left(\sum_{i=1}^{n} t_i x_i \right) - t' \right|. \tag{3.5}$$

The objective function of the difficulty degree is the distance between the average difficulty degree and the target difficulty degree:

$$P(X) = \left| \frac{\sum_{i=1}^{n} p_i x_i}{\sum_{i=1}^{n} x_i} - p' \right|. \tag{3.6}$$

Let $\overline{r}(X)$ be the average sum of relevance degree of each concept in the test sheet:

$$\overline{r}(X) = \frac{\sum_{j=1}^{m} \sum_{i=1}^{n} r_{ij} x_i}{|C'|}. \tag{3.7}$$

Let the generalized concept relevance $\Re_{ij}$ denote the maximum concept relevance of a test item toward the concept C_j or its descendent concepts:

$$\Re_{ij} = \mathrm{Max}(r_{ik}) \mid C_k \in \delta(C_j). \tag{3.8}$$

The objective function of concept relevance is the distance between the sum of generalized concept relevance degrees and the average sum $\overline{r}(X)$. This objective function shows the imbalance degree of the concept relevance:

$$R(X) = \sum_{j=1}^{m} \left| \sum_{i=1}^{n} \Re_{ij} x_i - \overline{r}(X) \right|. \tag{3.9}$$

The objective function of the item exposure rate is the average exposure times:

$$E(X) = \frac{\sum_{i=1}^{n} e_i x_i}{\sum_{i=1}^{n} x_i}. \tag{3.10}$$

The multiobjective optimization problem is to find a test sheet X to minimize all the values of objective functions and subject to the lower bound of average concept relevance r', as shown in the following:

$$\begin{aligned} \min_{X} \quad & [D(X), T(X), P(X), R(X), E(X)]^T \\ \text{Subject to} \quad & \overline{r}(X) \geq r'. \end{aligned} \tag{3.11}$$

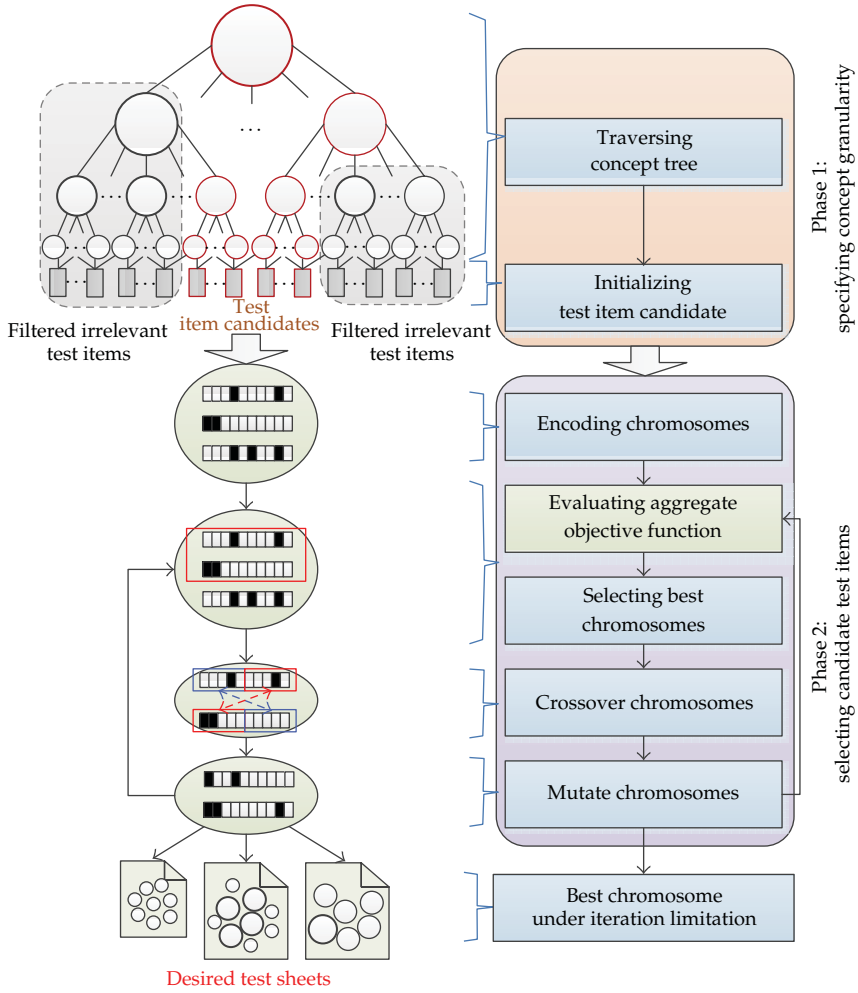

Figure 4: The flowchart of the CISS process.

4. Methodology

To solve the Adaptive Test Sheet Generation Problem, an Adaptive Test Sheet Generation (ATSG) mechanism has been proposed. ASTG mechanism consists of a Candidate Item Selection Strategy (CISS) to adaptively determine candidate test items set and the conceptual granularities according to the desired concept scope, and an Aggregate Objective Function (AOF) to apply Genetic Algorithm (GA) to figure out the approximate solution of mixed integer programming problem for the test-sheet composition. CISS process is illustrated in Figure 4.

4.1. Candidate Item Selection Strategy (CISS)

CISS process includes two phases: (1) specifying Concept Granularity and (2) selecting Candidate Test Item Set.

Phase 1: Specifying Concept Granularity

Concepts associated with a test sheet might be in various granularities for specific educational situations, so the conceptual granularities should be determined before generating a test sheet. Because the required concepts $C_i \in C'$ might be in various granularities, the most specific required concepts should be selected as the target concept set to precisely express the requirements. Let $\overline{C}'$ denote the target concept set, where no concepts in the set are the other concepts' ancestors, and the goal of the first phase is determining the concepts in $\overline{C}'$:

Phase 2: Selecting Candidate Test Item Set

Let θ be the candidate test item set, where the inner test items should be related to the target concept set. In Phase 2, test items whose related concepts are out of $\overline{C}'$ are filtered:

$$C_i \in \overline{C}' \quad \text{iff } (C_i \in C') \wedge (\neg\exists j, C_i \in \delta(C_j)). \tag{4.1}$$

Besides, the generalized concept relevance degrees $\Re$ of all test items toward all concepts in $\overline{C}'$ are calculated.

$$Q_i \in \theta \quad \text{iff } \exists j, \left(\left(C_j \in \overline{C}'\right) \wedge (\Re_{ij} > 0)\right) \wedge \neg\exists k, \left(\left(C_k \notin \overline{C}'\right) \wedge (\Re_{ik} > 0)\right). \tag{4.2}$$

After this phase, the search space can be reduced from Q to θ.

An example of CISS process is provided in Figure 5, where assume the required concepts set $C' = \{C_4, C_5, C_9, C_{10}\}$. In Phase 1, C_4, C_9, and C_{10} are selected into $\overline{C}'$ for expressing the most specific required concepts. In Phase 2, only the test items which are associated with the subtrees of concepts in $\overline{C}'$ can be selected to the candidate item set θ, so Q_3 and Q_4 are filtered before solving the optimization problem.

4.2. Aggregate Objective Function

An aggregate objective function $F(X)$ is defined to solve the multiobjective optimization problem:

$$F(X) = S_D + (1 - P_t) + \left(1 - P_p\right) + (1 - P_r) + (1 - P_e) + \left(1 - P_r'\right). \tag{4.3}$$

The aggregate objective function includes the discrimination score S_D and the penalty scores of the expected time P_t, the difficulty degree P_p, the concept relevance P_r, the concept relevance lower bound P_r', and the exposure times P_e. All score and penalty score are normalized to the range from 0 to 1.

The discrimination score S_D is inversed to the objective function $D(X)$:

$$S_D = 1 - D(X). \tag{4.4}$$

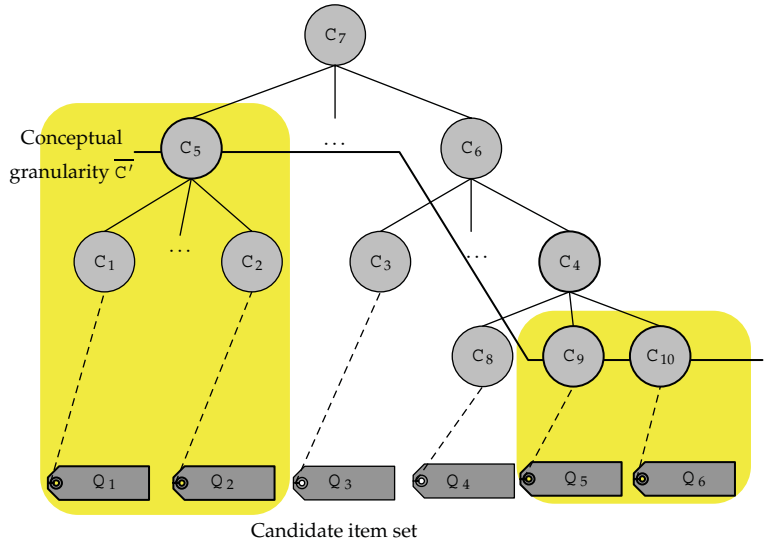

Figure 5: An example of the candidate item selection strategy (CISS) process.

The penalty score of the expected time is the percentage of the distance between the sum of expected test time and the target expected time over the target expected time. If the penalty score is greater than 1, 1 is assigned the penalty score:

$$P_t = \min\left(\frac{T(X)}{t'}, 1\right). \tag{4.5}$$

The penalty score of the difficulty degree is the value generated by the objective function of the difficulty degree:

$$P_p = P(X). \tag{4.6}$$

The penalty score of the concept relevance balance degree is the average distance between the sum of relevance degrees and the average sum of a concept:

$$P_r = \frac{R(X)}{|C'|}. \tag{4.7}$$

The penalty score of the concept relevance lower bound is greater than 0 if the average concept relevance is lower than the concept relevance lower bound and the value the percentage of the distance over the concept relevance lower bound. If the penalty score is greater than 1, the penalty score will be set as 1:

$$P'_r = \min\left(\frac{|\mathrm{Max}(r'(X) - \overline{r}, 0)|}{r'}, 1\right). \tag{4.8}$$

The penalty score of the exposure times is the percentage of the average of exposure times over the exposure times parameter e', which denotes the maximum exposure times to be considered. If the average of the exposure times is greater than e', the penalty score will be set as 1:

$$P_e = \min\left(\frac{E(X)}{e'}, 1\right). \tag{4.9}$$

Thus, a single aggregate objective function $F(X)$ can be defined to integrate all the score and penalty scores to a single objective score as (5.1).

The genetic algorithm (GA) can be applied to solve the Adaptive Test Sheet Generation Problem by maximizing the aggregate objective function $F(X)$. The overall process of the GA algorithm is shown in Figure 4. The CISS process can adaptively determine the desired concept scopes and granularities, and the out-of-scope test items, that is, *error-included concept nodes* in Figure 2, can be adaptively filtered to reduce the problem space of the test sheet generation. The candidate test items can be encoded into chromosomes, which is an N-bit binary string $[x_1,x_2,\ldots,x_N]$, where N is the amount of candidate test items and $x_i = 1$ denotes the test item i selected into the test sheet. In the beginning, a set of chromosomes, each whose bit value is randomly set, are generated as the initial selection states. Then, each chromosome is evaluated by the aggregate objective function $F(X)$. The higher score the chromosome gets, the more probability the chromosome can be reserved to generate the next generation. In the Crossover step, the chromosomes with higher score of $F(X)$ are selected to generate new chromosomes. Two chromosomes are both broken into two segments in the randomly selected segment lengths and the new chromosomes are generated by exchanging a segment with each other. Further, in the Mutation step, a random bit of a random chromosome in the new generation is inversed in order to prevent falling into the local optimal solutions. Then, return to the Crossover step to further generate next generation until the iteration limitation is achieved. Finally, the chromosome having the highest score of $F(X)$ among the whole process is the approximate solution.

5. Experiment and Evaluation

In order to evaluate the effectiveness of the proposed methodology in support of various purposes of assessments during the real learning situation, three experiments have been conducted. Firstly, various sizes of item banks are used to evaluate the efficiency and fitness scores of the proposed ATSG mechanism. Secondly, various levels of target concepts C' are used to evaluate the performance and the satisfaction degree of concepts in ATSG mechanism. Thirdly, exposure times of selected test items are measured during the 50 times of use. The exposure times of test items are accumulated and the experiment can evaluate whether ATSG mechanism can prevent the generation of the test sheets with high exposure times. In the three experiments, a system of the control group has also been developed based on Hwang's methodology [4], where the objective function shown in (5.1) was modified to meet the experimental requirements:

$$F(X) = S_D + (1 - P_t) + (1 - P_p) + (1 - P_r) + (1 - P_r'). \tag{5.1}$$

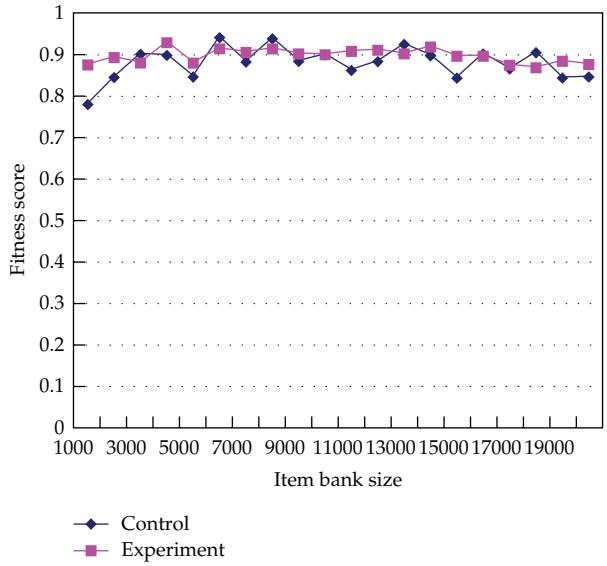

Figure 6: Fitness scores in various sizes of item banks.

Some differences in the system of control group are listed as follows:

(1) It does not run the CISS; all test items are considered in the GA algorithm.

(2) It does not consider the exposure times of test items.

(3) It does not calculate the generalized concept relevance, so the required concepts for control group are expended to all their descendent concepts.

The parameters of the GA algorithms used by the experimental and control systems were determined to balance the effectiveness and efficiency. In the three experiments, the GA algorithms were limited to 1,000 iterations and the mutation rate was 0.1. The population size was 30 and all initial bits of chromosomes were assigned to 0 because the amount of all test items was much larger than the amount of the selected test items.

5.1. Various Size of the Item Bank

The item banks having 1,000 to 20,000 test items are used to evaluate the systems' efficiency and effectiveness. In each item bank, 10 test sheets with randomly chosen parameters are generated by the control and experimental systems. The effectiveness is measured by the fitness score of the aggregate objective function $F(X)$. The result of effectiveness is shown in Figure 6, where the experimental system has more stable and generally higher fitness scores than those of the control system.

The experimental result of efficiency is shown in Figure 7, where the response time of the GA algorithm becomes higher if the size of item bank grows gradually. The reason is that if there are more candidate test items, much longer chromosomes will be used and the computing time dealing with all bits in chromosomes becomes much longer as well. Among the two systems, experimental system, which applies CISS process to dramatically reduce the size of candidate test items, can have much more efficient response time.

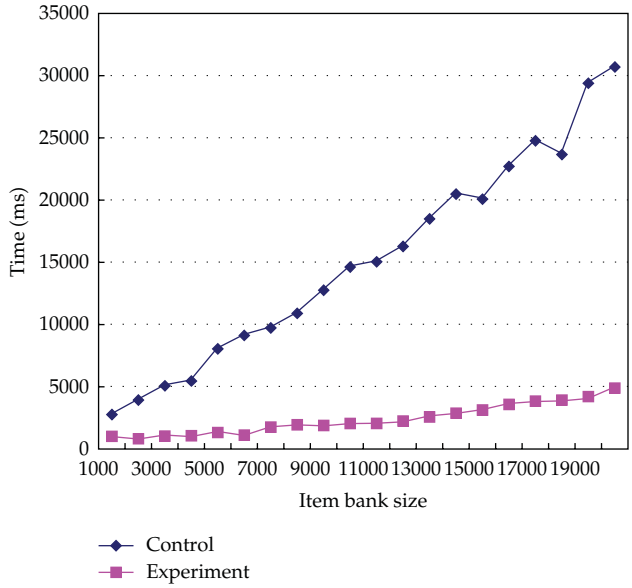

Figure 7: Response time in various sizes of item banks.

5.2. Various Levels of Target Concepts

This experiment demonstrates the systems' effectiveness of generating a test sheet for specific level of target concepts. Target concepts in the most coarse-grained level, level 1, to the most fine-grained level, level 6, are randomly chosen for the two systems. As shown in Figure 8, the concept relevance scores of the control system are much lower than those of the experimental system, especially when the concept level is fine grained. The reason is that without filtering out-of-scope test items, the GA algorithm of the control system is difficult to precisely choose the test items with accurate concepts. Figure 9 also shows that the test sheet generated by the control system contains many out-of-scope test items, which will seriously affect the test quality.

The result of response time in Figure 10 also reveals that the control system needs more computation times to generate a test sheet because many out-of-scope test items are also computed.

5.3. Exposure Times Measurement of Test Items

In the last experiment, 50 test sheets with similar target concept ranges are generated from the item bank containing 2,000 test items and the used test items are recorded to calculate the exposure times of each test item. Results of the average exposure times of test items are shown in Figure 11, where the control system and the experimental system have no noticeable difference. According to the analysis of each test sheet, although the experimental system can prevent the test items with high exposure times, the average exposure times are still accumulated due to the small range of target concepts. However, the out-of-scope test items are usually used in the test sheet generated by the control system, so the exposure times of a

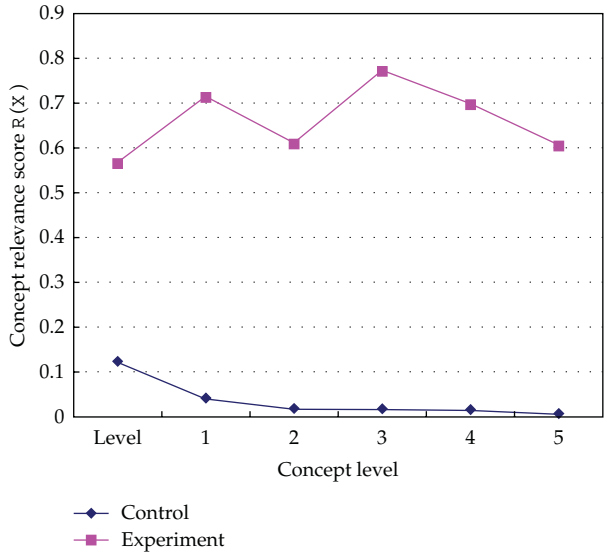

Figure 8: Concept relevance scores for various level of target concepts.

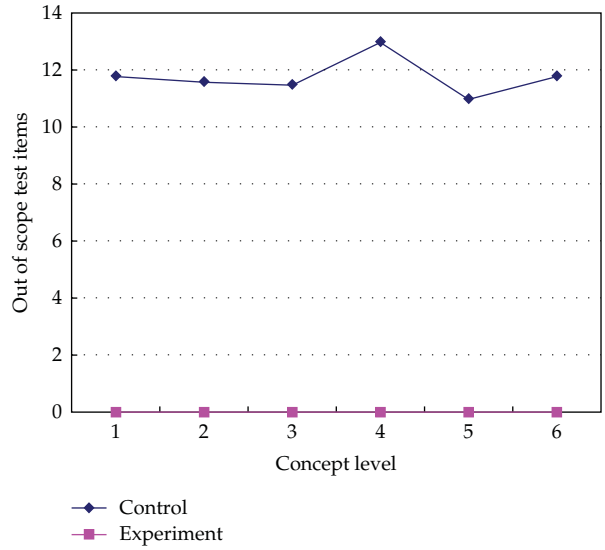

Figure 9: Amount of out-of-scope test items for various levels of target concepts.

single test item are accumulated slowly. That makes the exposure times of the experimental system are not better than those of the control system.

6. Discussion

The proposed ATSG mechanism is able to solve Adaptive Test Sheet Generation Problem in terms of the following aspects.

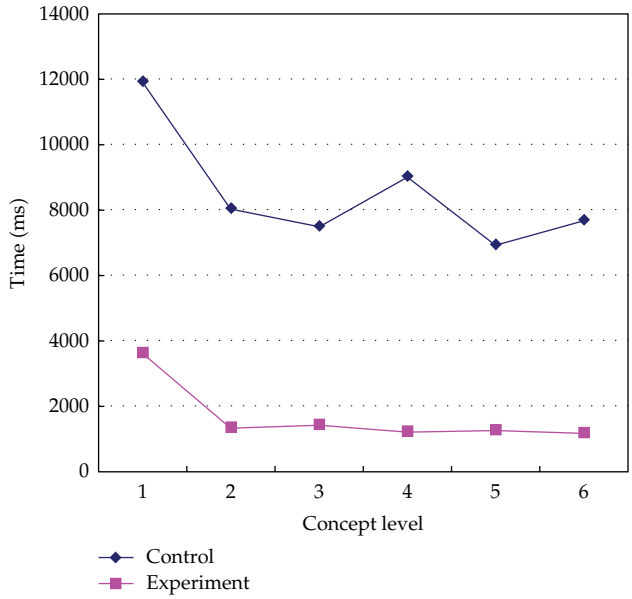

Figure 10: Response time for various level of target concepts.

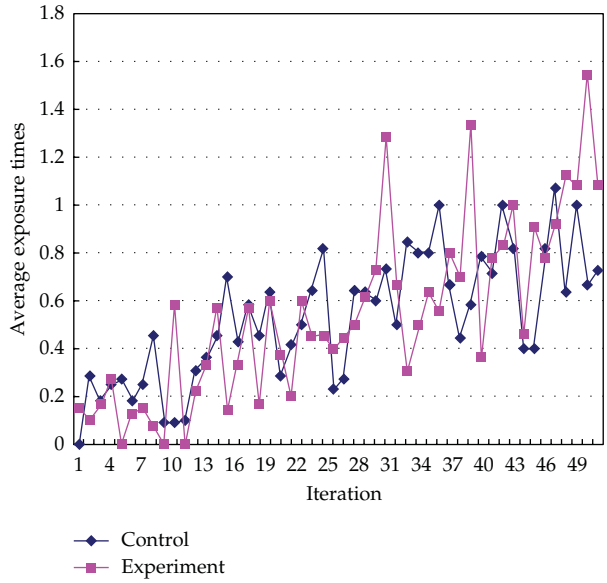

Figure 11: Average exposure times during 50 times of usage.

6.1. The Control of the Concept Granularity of the Test Sheets and the Prevention of the Irrelevant Problem Space

To simplify the discussion of this problem, assume that the concept tree is an L-level balanced tree, and the amount of branches in each level is B. Let an adaptive requirement of the test sheet contain n target concepts in level X. By applying the CISS mechanism, the problem

space of the test sheet generation problem can be reduced to n/B^{X-1} of the original problem space.

Proof. Assume that m items are related to a concept. The amount of candidate test items in the previous research is mB^{L-1}. By using the candidate item selection strategy, the amount of the candidate test items $\overline{C}'$ is mnB^{L-X}. Thus, the percentage of the new problem space over the previous problem space is $mnB^{L-X}/mB^{L-1} = n/B^{X-1}$. □

6.2. The Generation of a Test Sheet to Precisely Fit the Target Concept Range, Difficulty, and Expected Test Time

In the new objective functions, the distances toward the target thresholds are used instead of the lower bound and upper bound in the previous studies. Thus, the difficulty and expected test item can be precisely fitted. Moreover, the candidate item selection strategy and the penalty score of the concept relevance balance degree can ensure that the test sheet contains balanced target concepts. As shown in Section 5.2, the concept relevance scores of the test sheets generated by the experimental system are also much higher than those of the control system.

6.3. The Consideration of the Item Exposure Rate

The penalty score of the exposure times P_e can prevent the high-exposure-rate items selected to the test sheet.

6.4. The Extensibility of the ATSG Mechanism

Most approaches mentioned in the related work section applied more efficient evolutionary algorithms, for example, the greedy algorithm approach [12], the tabu search algorithm [13], and the discrete particle swarm optimization algorithm [14] to enhance the computation efficiency of test sheet generation. However, these approaches did not yet take the conceptual granularity, exposure rates, and test item filtering into account. Therefore, these enhanced evolutionary approaches can thus be expected to replace the Hwang's methodology [4] for improving the efficiency of the Selecting Candidate Test Item Set phase (Figure 4) in the CISS process of ATSG mechanism.

6.5. The Future Work of the ATSG Mechanism

According to our observation and finding of experimental results, the degree of fitness score changes with the item bank sizes and the computation time (see Figure 6). Because the fitness scores directly affect the quality of the generated test sheet, a new important issue will be how to analyze the characteristics and predict the trends of fitness scores over times and item bank sizes for improving the quality of test sheet composition. However, this kind of time series problem may not be modeled by the conventional distribution model because the quality of the GA selection strategy seems to have the characteristics of self-similarity. Therefore, according to the study of Li [17], Fractal Time Series, which has the features of Long-Range Dependence (LRD) and obeys the Power Law, are a suitable mathematical approach to model

and analyze the features and phenomenon of self-similar series [18], for example, the data series in the cyber-physical networking systems [19], the time series of sea level [20] and molecular motion on the cell membrane [21], the DNA series [22], and the fractal lattice geometry using Iterated Function System (IFS) on simplexes [23]. Accordingly, in the near future, we are going to try to apply the fractal time series approach to analyze and model the series of fitness score for figuring out the characteristics of self-similarity.

7. Conclusion

In this paper, an Adaptive Test Sheet Generation (ATSG) mechanism is proposed, where the Candidate Item Selection Strategy (CISS) is come up to reduce the problem space of test sheet composition and an Aggregate Objective Function (AOF) based on the Genetic Algorithm (GA) is modeled to figure out the approximate solution. In this approach, the adaptive conceptual scope and granularity and item exposure rates have been considered to meet the various purposes of assessments during the real learning situation. Experimental results show that ATSG mechanism is able to more efficiently, precisely, adaptively generate the various test sheets than the existing approaches in terms of various conceptual scopes, computation time, and item exposure rates. Furthermore, in the near future, the fractal time series approach can be expected to be applied to analyze and model the series of GA's fitness score for figuring out the characteristics of self-similarity and improving the quality of test sheet composition according to the experimental finding.

Acknowledgment

This paper was partially supported by the National Science Council of Republic of China under the number of NSC 101-2511-S-024-004-MY3 and NSC 100-2511-S-468-002.

References

[1] G. J. Hwang, "A test-sheet generating algorithm for multiple assessment requirements," *IEEE Transactions on Education*, vol. 46, no. 3, pp. 329–337, 2003.

[2] C. Y. Su and T. I. Wang, "Construction and analysis of educational assessments using knowledge maps with weight appraisal of concepts," *Computers & Education*, vol. 55, pp. 1300–1311, 2010.

[3] T. H. Cormen, C. E. Leiserson, R. L. Rivest, and C. Stein, *Introduction to Algorithms*, The MIT Press, Cambridge, Mass, USA, 3rd edition, 2009.

[4] G. J. Hwang, B. M. T. Lin, H. H. Tseng, and T. L. Lin, "On the development of a computer-assisted testing system with genetic test sheet-generating approach," *IEEE Transactions on Systems, Man, and Cybernetics C*, vol. 35, no. 4, pp. 590–594, 2005.

[5] W. Banzhaf, P. Nordin, R. E. Keller, and F. D. Francone, *Genetic Programming: An Introduction*, Morgan Kaufmann, San Francisco, Calif, USA, 1997.

[6] D. Fisher and N. Frey, *Checking for Understanding: Formative Assessment Techniques for Your Classroom*, Association for Supervision & Curriculum Deve, Alexandria, Va, USA, 2007.

[7] J. Leighton and M. Gierl, *Cognitive Diagnostic Assessment for Education: Theory and Applications*, Cambridge University Press, Cambridge, UK, 2007.

[8] K. Burke, *Balanced Assessment: From Formative to Summative*, Solution Tree, Bloomington, Ind, USA, 2010.

[9] C. Tovani, *So What Do They Really Know?: Assessment That Informs Teaching and Learning*, Stenhouse, Portland, Me, USA, 2011.

[10] S. W. Chang and B. Y. Twu, "A comparative study of item exposure control methods in computerized adaptive testing," Tech. Rep. 99-3, ACT Research Report Series, 1998.

[11] S. Y. Chen, R. D. Ankenmann, and J. A. Spray, "Exploring the relationship between item exposure rate and test overlap rate in computerized adaptive testing," Tech. Rep. 99-5, ACT Research Report Series, 1999.
[12] G. J. Hwang, B. M. T. Lin, and T. L. Lin, "An effective approach for test-sheet composition with large-scale item banks," *Computers & Education*, vol. 46, pp. 122–139, 2006.
[13] G. J. Hwang, P. Y. Yin, and S. H. Yeh, "A tabu search approach to generating test sheets for multiple assessment criteria," *IEEE Transactions on Education*, vol. 49, no. 1, pp. 88–97, 2006.
[14] K. H. Tsai, T. I. Wang, T. C. Hsieh, T. K. Chiu, and M. C. Lee, "Dynamic computerized testlet-based test generation system by discrete PSO with partial course ontology," *Expert Systems with Applications*, vol. 37, pp. 774–786, 2010.
[15] G. J. Hwang, H. C. Chu, P. Y. Yin, and J. Y. Lin, "An innovative parallel test sheet composition approach to meet multiple assessment criteria for national tests," *Computers $#38; Education*, vol. 51, pp. 1058–1072, 2008.
[16] T. F. Ho, P. Y. Yin, G. J. Hwang, S. J. Shyu, and Y. N. Yean, "Multi-objective parallel test-sheet composition using enhanced particle swarm optimization," *Educational Technology & Society*, vol. 12, no. 4, pp. 193–206, 2009.
[17] M. Li, "Fractal time series—a tutorial review," *Mathematical Problems in Engineering*, vol. 2010, Article ID 157264, 26 pages, 2010.
[18] H. Sheng, Y. Q. Chen, and T. S. Qiu, *Fractional Processes and Fractional-Order Signal Processing*, Springer, New York, NY, USA, 2011.
[19] M. Li and W. Zhao, "Visiting power laws in cyber-physical networking systems," *Mathematical Problems in Engineering*, vol. 2012, Article ID 302786, 13 pages, 2012.
[20] M. Li, C. Cattani, and S. Y. Chen, "Viewing sea level by a one-dimensional random function with long memory," *Mathematical Problems in Engineering*, vol. 2011, Article ID 654284, 13 pages, 2011.
[21] H. Sheng, Y. Q. Chen, and T. S. Qiu, "Heavy-tailed distribution and local long memory in time series of molecular motion on the cell membrane," *Fluctuation and Noise Letters*, vol. 10, no. 1, pp. 93–119, 2011.
[22] C. Cattani, G. Pierro, and G. Altieri, "Entropy and multifractality for the myeloma multiple TET 2 gene," *Mathematical Problems in Engineering*, vol. 2012, Article ID 193761, 14 pages, 2012.
[23] C. Cattani, E. Laserra, and I. Bochicchio, "Simplicial approach to fractal structures," *Mathematical Problems in Engineering*, vol. 2012, Article ID 958101, 21 pages, 2012.

Hindawi Publishing Corporation
Mathematical Problems in Engineering
Volume 2012, Article ID 615152, 20 pages
doi:10.1155/2012/615152

Research Article

A Trend-Based Segmentation Method and the Support Vector Regression for Financial Time Series Forecasting

Jheng-Long Wu and Pei-Chann Chang

Department of Information Management, Yuan Ze University, Taoyuan 32026, Taiwan

Correspondence should be addressed to Pei-Chann Chang, iepchang@saturn.yzu.edu.tw

Received 10 February 2012; Accepted 28 March 2012

Academic Editor: Ming Li

This paper presents a novel trend-based segmentation method (TBSM) and the support vector regression (SVR) for financial time series forecasting. The model is named as TBSM-SVR. Over the last decade, SVR has been a popular forecasting model for nonlinear time series problem. The general segmentation method, that is, the piecewise linear representation (PLR), has been applied to locate a set of trading points within a financial time series data. However, owing to the dynamics in stock trading, PLR cannot reflect the trend changes within a specific time period. Therefore, a trend based segmentation method is developed in this research to overcome this issue. The model is tested using various stocks from America stock market with different trend tendencies. The experimental results show that the proposed model can generate more profits than other models. The model is very practical for real-world application, and it can be implemented in a real-time environment.

1. Introduction

Support vector machines (SVMs) have outperformed other forecasting models of machine learning or soft computing (SC) tools such as decision tree, neural network (NN), bayes classifier, fuzzy systems (FSs), evolutionary computation (EC), and chaos theory by many researchers from historical nonlinear time series data applications in the last decade [1–5]. In these techniques, many researchers presented different forecasting models in dealing with characteristics such as imprecision, uncertainty, partial truth, and approximation to achieve practicability, robustness, and low solution cost in real applications [6–8]. However, the most important issue in resolving the nonlinear time series problem is error revision. ANNs use the empirical risk minimization principle to minimize the generalization errors but SVRs use the structural risk minimization principle because SVR is able to analyze with small

samples and to overcome the local optimal solution problem, which surpasses to ANNs [9–11]. Therefore, the SVRs forecasting model is applied to accomplish the forecasting task in this research. Presently, support vector regression (SVR), which was evolved from support vector machine (SVM) based on the statistical learning theory, is a powerful forecasting and machine learning approach for numerical prediction [12–15]. Also, SVR has high toleration error rate and high accuracy for learning solution knowledge in complex problems [16]. Although SVR can be applied well in time series data, the input vector is a key successful factor. Despite the volatile nature of the stock markets, researchers still can find certain correlations between these factors and stock prices. An investor's primary goal is to make profits. In order to help investors achieve their financial objectives, researchers have studied the relationship between financial markets and price variations over time from [17–20].

In the last few years, several representations of time series data have been proposed; the most often used representation is piecewise linear representation (PLR) [21–23]. It can decompose a time series data into a series of bottom and peak points [24, 25] in financial market. But the traditional PLR does not consider the multiple trending characteristics in time series. Moreover, the price movements of stocks are affected by many factors such as government policies, economic environments, interest rates, and inflation rates. The share prices of most listed companies also move up and down with other changing factors like market capitalization, earnings per share (EPS), price- to -earnings ratio, demand and supply, and market news. Moreover, there are more fractal properties of financial data, such as self-similarity, heavy-tailed distributions, long memory, as well as power laws [26–29]. One of fractal properties is long memory which is a common characteristic in financial data or other fields [30–32]. The daily stock trading is a short-term return so in this paper these fractal properties were not considered in our framework, just focusing on the real stock price's trends.

Therefore, there is a need to develop a new segmentation method which takes the price moving trends into consideration. As a result, this research will consider the multiple trends of stock price's movements in TBSM segmentation approach to capture the embedded knowledge of nonlinear time series. This research intends to improve the SVR forecasting performance using a trend based decomposition method. The TBSM approach has captured the tendency of stock price's movement which can be inputted into SVR in learning the historical knowledge of the time series data. Moreover, a more accurate forecasting result can be achieved when applied in real-time stock trading decision.

The rest of this paper is organized as follows. In Section 2, we describe TBSM segmentation principle. Forecasting model is discussed in Section 3. Section 4 explains modeling for trading decisions including using historical data to make trading decisions by the TBSM approach, selecting highly correlated technical indices by stepwise regression analysis (SRA), forecasting trading signals by SVR, and evaluating trading strategies. Section 5 explains how the TBSM with SVR for stock trading decisions and compares the profits obtained from various forecasting approaches. Finally, conclusions and directions for further research are discussed in Section 6.

2. A Trend Based Segmentation Method (TBSM)

In the time series database there are many approaches such as Fourier transform, wavelets, and piecewise linear representation which can be applied to find the turning point on time series data. According to the characteristics of sequential data, a piecewise linear representation of the data is more appropriate. A variety of algorithms to obtain a proper linear

```
Define: Threshold // cutting threshold
        X_Thld // horizontal area
        Y_Thld // vertical area
        X // a time series
        Y // stock price
1:  Procedure TBSM(T)
2:  Let T be represented as X[1, 2,..., n], Y[1, 2,..., n]
3:  n = 0
4:  Draw a line between (X1, Y1) and (Xn, Yn)
5:  Max d = maximum distance of (Xi, Yi) to the line
6:  If (Max d > Threshold)
7:     Let (Xi, Yi) be the point with maximum distance
8:     For j = X1 : Xn
9:        If (|Xj − Xi| < X_Thld) and (|Yj − Yi| < Y_Thld)
10:          Then Point[n] = [Xj, Yj], n = n + 1
11:       End If
12:    End For
13:    Select from Point[n ] : Xt1 = Min(X0), Xt2 = Max(Xn)
14:    Return:  S1 = T [X1, Xt1]
15:             S2 = T [Xt2, Xn]
16: End If
```

Algorithm 1: A pseudocode for TBSM in time series data.

representation of segment data have been presented. As reported in [33–36], PLR is used to support more tasks and provides an efficient and effective solution. In this paper we intend to enhance the segmentation accuracy based on different trends in stock price's movements. The basic idea of TBSM is to modify the PLR segmentation using the trend tendency in a specific time period. Three different trends such as uptrend, downtrend, and hold trend will be considered when making the segmentation. Detailed procedures of TBSM include the following. (1) PLR is applied to locate the turning points from the time series including up or downtrends. (2) The points around each turning point will be double-checked if the variations of the points are within the threshold. If yes, these points will have the same buy/sell trading in this period. (3) These points are set to be in the same trend. The pseudocode of the TBSM is shown in Algorithm 1.

For example, a time series $T = \{t_1, t_2, \ldots, t_{191}\}$ with 191 data is given to explain the basic idea of the TBSM procedure. As shown in Figure 1(a), several trading points are represented as buy (four red points) or sell (six green points) in this case. According to the TBSM procedure, we can draw a line S_1 form the first point to the last point as shown in Figure 1(b) and find the max distance to line S_1 which is point t_{26}. Then line S_1 is decomposed into two segments including line S_2 from t_1 to t_{26} and line S_3 from t_{26} to t_{191}. Based on point t_{26}, we can locate point t_{16} to t_{56} which are varied within the threshold. These points are set as hold trend and with the same state of point t_{26}. Therefore line S_2 and line S_3 will be changed to three different lines including line S_4 from point t_1 to point t_{16}, line S_5 from point t_{16} to point t_{56}, and line S_6 is from point t_{56} to point t_{191} as shown in Figure 1(c). Next step is repeating the same process for the rest of segments as t_{56} to t_{191}. The final results are shown in Figure 1(d) including two hold trend segments (dotted line), one uptrend segment, and two downtrend segments (solid line) in this time series.

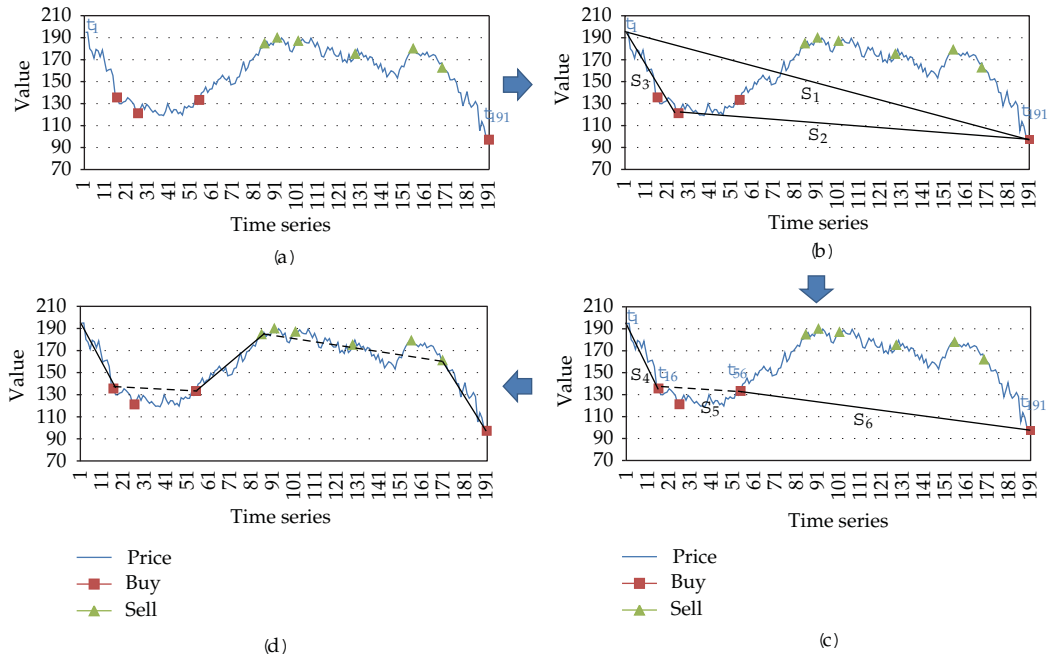

Figure 1: An example for TBSM in time series data.

3. Support Vector Regressions (SVRs)

Support vector regression is a modification of machine-learning-theory-based classification called support vector machine. Machine learning techniques have been applied for assigning trading signal. Many studies used support vector machine for determining whether a case contains particular class [37, 38]. But the shortcoming only deal with discrete class labels, whereas trading signal continuum data type because a weight of signal can take a buy or sell power. Grounded in statistical learning theory [1, 2], support vector regression is capable to predict the continuous trading signal while still benefiting from the robustness of SVM. SVM has been successfully employed to solve forecasting problems in many fields, such as financial time series forecasting [39] and emotion computation [40]. For explaining the concept of SVR, we have considered a standard regression problem. Let $S = \{X_i, Y_i\}_{i=1\ldots n}$ be the set of data where X_i is input vector (selected technical index in this research), Y_i (trading signal ts) is an output vector, and n is the number of data points. In regression analysis, we find a function $f(X_i)$ such that $Y_i = f(X_i)$. This function can be used to find the output value Y of any X. The standard regression function is as follows:

$$q_i = f(x_i) + \delta, \tag{3.1}$$

where δ denotes the random error and q_i denotes the estimated output. There are two types of regression problems, namely, linear and nonlinear. SVR is developed to tackle the nonlinear regression problems because the nonlinear regression problems have high complexity as well

as stock market trade. In SVR, at first the input vectors are nonlinearly mapped into a high-dimensional feature space (F), where they are linearly correlated with the respective output values.

SVR uses the following linear estimation function:

$$f(x) = (\omega \cdot \phi(x)) + b, \tag{3.2}$$

where ω denotes the weight vector, b denotes a constant, $\phi(x)$ denotes the mapping function in the feature space, and $(\omega \cdot \phi(x))$ denotes the dot product in the feature space F. SVR transfers the nonlinear regression problem of the lower dimension input space (x) into a linear regression problem of a high-dimension feature space. In other words, the optimization problem involving a nonlinear regression is converted into finding the flattest function in the feature space instead of input space.

Various cost functions like Laplacian, Huber's Gaussian, and ε-insensitive can be used in the formulation of SVR. The cost function should be suitable for the problem and should not be very complicated because a complicated cost function could lead to difficult optimization problems. Thus, we have used robust ε-sensitive cost function which is shown below:

$$L_\varepsilon(f(x), q) = \begin{cases} |f(x) - q| - \varepsilon, & \text{if } |f(x) - q| \geq 0 \\ 0, & \text{otherwise,} \end{cases} \tag{3.3}$$

where ε denotes a precision parameter which represents the radius of the tube located around the regression function $f(x)$.

The $\{+\varepsilon, -\varepsilon\}$ region is called ε-insensitive zone. ε is determined by the user. If the actual output value lies in this region, the forecasting error is considered to be zero.

The weight vector, ω, and constant, b, in (3.2) are calculated by minimizing regularized risk function which is shown in (3.4):

$$R(C) = \frac{C}{n}\sum_{i=1}^{n} L_\varepsilon(f(x_i), q_i) + \frac{1}{2}|\omega|^2, \tag{3.4}$$

where $L_\varepsilon(f(x_i), q_i)$ denotes the ε-insensitive loss function, $|\omega|^2/2$ denotes the regularization term, and C denotes the regularization constant. ω decides the complexity and approximate accuracy of the regression model. Value of C is selected by the user to ensure appropriate value of w and low empirical risk.

The two positive slack variables ξ_i and ξ_i^* are used to replace the ε-insensitive loss function of (3.3). ξ_i is defined as the distance between the q_i and higher boundary of the ε-insensitive zone, and ξ_i^* is defined as the distance between the q_i and lower boundary of the ε-insensitive zone. Equation (3.4) is transformed into (3.5) by using the slack variables:

$$\text{Minimize} : R_{\text{reg}}(f) = \frac{1}{2}|\omega|^2 + C\sum_{i=1}^{n}(\xi_i + \xi_i^*) \tag{3.5}$$

$$\text{Subject to} \begin{cases} q_i - (\omega \cdot \phi(x_i)) - b \leq \varepsilon + \xi_i \\ (\omega \cdot \phi(x_i)) + b - q_i \leq \varepsilon + \xi_i^* \\ \xi_i, \xi_i^* \geq 0, \quad \text{for } i = 1, \ldots, n. \end{cases} \tag{3.6}$$

Lagrange function method is used to find the solution which minimizes the regression risk of (3.4) with the cost function in (3.3) which results in the following quadratic programming problem (QP):

$$\begin{aligned}\text{Minimize}: \frac{1}{2}\sum_{i=1}^{N}\sum_{j=1}^{N}(\alpha_i-\alpha_i^*)\left(\alpha_j-\alpha_j^*\right)(\phi(x_i)\cdot\phi(x_j))\\ +\sum_{i=1}^{N}\left(\varepsilon_i^{\text{up}}-y_i\right)\alpha_i+\sum_{i=1}^{N}\left(\varepsilon_i^{\text{down}}-y_i\right)\alpha_i^*,\end{aligned} \tag{3.7}$$

$$\text{Subject to}: \sum_{i=1}^{N}(\alpha_i-\alpha_i^*)=0, \quad \text{where } \alpha_i,\alpha_i^*\in[0,C], \tag{3.8}$$

where α_i and α_i^* denote Lagrange multipliers. $\varepsilon_i^{\text{up}}$ and $\varepsilon_i^{\text{down}}$ represent the ith up- and downmargin, respectively. The value of $\varepsilon_i^{\text{up}}$ and $\varepsilon_i^{\text{down}}$ is equal to ε. The QP problem of (3.7) is solved under the constraints of (3.8). After solving the QP problem, we obtained Lagrange multiplier from (3.9), and (3.2) is transformed into the following equation (3.10):

$$\omega=\sum_{i=1}^{N}(\alpha_i-\alpha_i^*)\cdot\phi(x_i), \tag{3.9}$$

$$f(x)=(\alpha_i-\alpha_i^*)(\phi(x_i)\cdot\phi(x))+b. \tag{3.10}$$

The Karush-Kuhn-Tucker (KKT) conditions are used to find the value of b. KKT conditions state that at the optimal solution, the product between the Lagrange multipliers and the constraints is equal to zero. The value of b can be calculated as follows:

$$b=\begin{cases}y_i-(\omega\cdot\phi(x_i))-\varepsilon_i^{\text{up}}, & \text{for } \alpha_i\in(0,C),\\ y_i-(\omega\cdot\phi(x_i))+\varepsilon_i^{\text{down}}, & \text{for } \alpha_i^*\in(0,C).\end{cases} \tag{3.11}$$

Using the trick of the kernel function, (3.10) can be written as (3.12):

$$f(x)=\sum_{i=1}^{n}(\alpha_i-\alpha_i^*)K(x,x_i)+b, \tag{3.12}$$

where $K(x,x_i)=(\phi(x)\cdot\phi(x_i))$ denotes the kernel function which is symmetric and satisfies the Mercer's condition. SVR was able to predict the nonlinear relationship between technical indices and trading signal *ts* better than other soft computing (SC) techniques.

4. Application in Financial Time Series Data

This paper proposes a forecasting framework using a TBSM combined with SVR model which is called TBSM-SVR trading model for stock trading. The framework of TBSM-SVR trading model has five stages: the first is generating nonlinear trading segments by TBSM approach

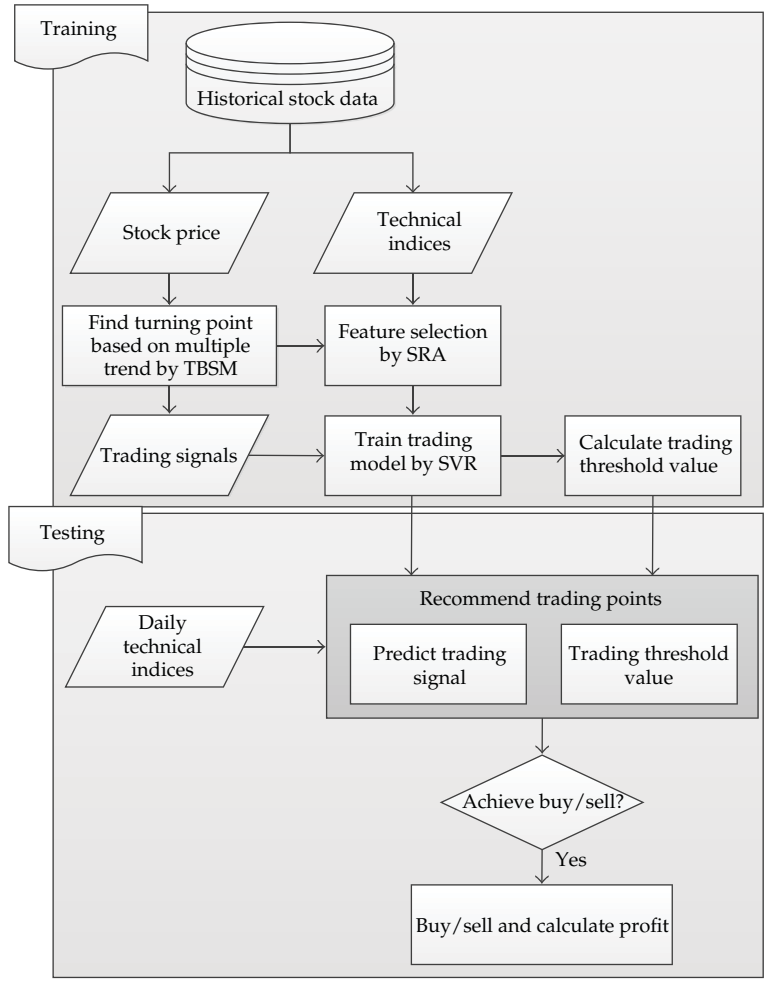

Figure 2: The framework of TBSM-SVR model for stock trading.

from historical stock price; the second is trading signal transformation from trading segments; the third is feature selection from technical indices by SRA approach; the fourth is learning the trading forecasting model by SVRs approach. The framework of TBSM-SVR model is shown in Figure 2. The five stages of TBSM-SVR model are explained as follows.

4.1. Find Turning Points Based on Multiple Trend by TBSM

According to TBSM procedure to find turning point based on trend of stock price, we selected a time series of historical stock price in a period to segment into several segments based on three trends including uptrend, downtrend, and hold trend. For example, a time series is given to segment trend segments from the date 2008/1/2 to 2008/12/30. Figure 3 shows the segmentation result by our proposed TBSM approach. The blue line is original historical stock price. The dashed lines are up/down trends which if the segment trend goes up is belonging to uptrend and if the segment trend goes down is belonging to downtrend. The dot line is

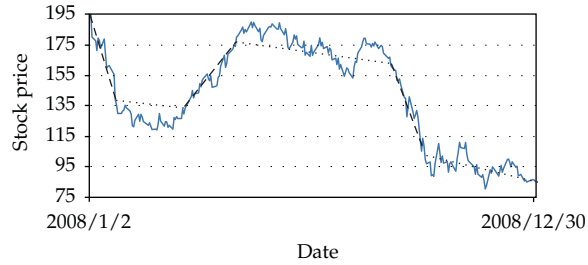

Figure 3: An example of segmentation result by TBSM.

belonging to hold trend. In our experiment, each stock price can split to multiple trend segments for trading signal transformation.

4.2. Trading Signal Transformation

In this stage, the aim is calculating the trading signal for a nonlinear time series of segmentation result which are a lot of segments based on trends. We suppose a segment S_k is uptrend; then we assume the real value into the vector S'_k like to $S_k = [0, 0.1, \ldots, 1]$; if S_k is hold trend but locates in buy point, then the vector like to $S'_k = [0.5, 0, 0.5]$; if S_k is hold trend but locates in sell point; then the vector like to $S'_k = [0.5, 1, 0.5]$; if S_k is downtrend, then the vector S'_k like to $[1, 0.9, \ldots, 0]$. Finally we combine these S'_k to a full time series of trading signal ts. If the segment belongs to uptrend or downtrend, then the formula equation (4.1) is used to calculate trading signal value:

$$S'_{k,i} = \begin{cases} \dfrac{i}{L} & \text{if } S_k \text{ is uptrend segment,} \\ \dfrac{(L-i)}{L} & \text{if } S_k \text{ is downtrend segment,} \end{cases} \tag{4.1}$$

where L denotes the length of segment S_k, whereas segment belonging to hold trend is using (4.2) to calculation:

$$S'_{k,i} = \begin{cases} 1 & \text{if } i\text{th is higherpoint in time series,} \\ 0 & \text{if } i\text{th is lower point in time series,} \\ 0.5 & \text{otherwise.} \end{cases} \tag{4.2}$$

For example, the S_1, and S_3 are hold trend; the S_1 is down-trend; the S_4 is up-trend. The result of trading signal ts is shown in Figure 4. The red dotted line is the hold trend which is a special signal for increasing reflects on the original turning points, so the hold trend is not a horizontal line. The purple dotted line is downtrend signal, and the orange dotted line is uptrend signal. For example, in the time series T the T_1 to T_5 and T_{10} to T_{14} are hold trend signal representation, T_6 to T_9 is downtrend signal representation, and finally T_{15} to T_{18} is uptrend signal representation. Finally the trading signal ts which is like to $ts = \{S_1, S_2, S_3, S_4\} = \{\langle 0.5, 0.5, 1, 0.5, 0.5\rangle, \langle 1, 0.66, 0.333, 0\rangle, \langle 0.5, 0.5, 0, 0.5, 0.5\rangle, \langle 0, 0.33, 0.66, 1\rangle\}$. For the detail process see the pseudocode in Algorithm 2.

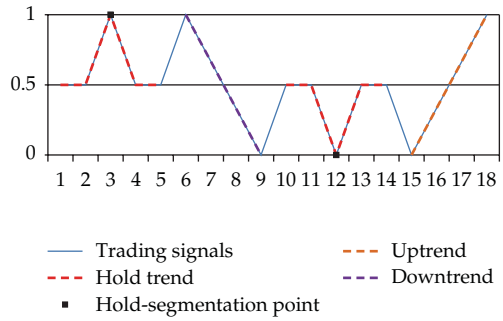

Figure 4: A sample of trading signal.

Input: *length*, *oldTs* // input data length and vector.
Output: *newTs* // a new time series vector of trading signal.
Method:

```
1:  Start = oldTs [1]
2:  End = oldTs[length]
3:  If Start = = −1 and End = = 1
4:        newTs [1] = 0
5:        For i = 1: length−1
6:              newTs[i+1] = 1/(lenghth−1)*i
7:        End For
8:  Else If Start = = 1 and End = = −1
9:        newTs[length] = 0
10:       For i = 1 : length−1
11:             newTs[i+1] = 1/(lenghth−1)*(length−i)
12:       End For
13:  Else
14:       For i = 2 : length−1
15:           newTs[i] = 0.5
16:       End For
17:  End If
```

Algorithm 2: A pseudocode for trend segments by TBSM in time series.

4.3. Feature Selection for Technical Indices by SRA

In this paper, we have considered 28 variables (technical indices) as listed in Table 1. These variables are correlated with variations in stock prices to some degree. The quantity of correlation varies for different variables. Rather than using all the 28 variables, we select the variables with a greater correlation than a user-defined threshold. The variable selection is done by stepwise regression analysis. We apply the SRA approach to determine which technical indices affecting the stock price. This is accomplished by selecting the variables repeatedly.

In the feature selection part input factors will be further selected using stepwise regression analysis (SRA). The SRA has been applied to determine the set of independent variables which is most closely affecting the dependent variable. The SRA is step by step to

Table 1: Technical indices used as input variables.

Technical	Technical index	Explanation
Moving average (Ma)	5 MA, 6 MA, 10 MA, 20 MA	Moving averages are used to emphasize the direction of a trend and smooth out price and volume fluctuations that can confuse interpretation.
Bias (BIAS)	5 BIAS, 10 BIAS	The difference between the closing value and moving average line, which uses the stock price nature of returning back to average price to analyze the stock market.
Relative strength index (RSI)	6 RSI, 12 RSI	RSI compares the magnitude of recent gains to recent losses in an attempt to determine overbought and oversold conditions of an asset.
Nine days stochastic line (K, D)	9 K, 9 D	The stochastic line K and line D are used to determine the signals of overpurchasing, overselling, or deviation.
Moving average convergence and divergence (MACD)	9 MACD	MACD shows the difference between a fast and slow exponential moving average (EMA) of closing prices. Fast means a short-period average, and slow means a long period one.
Williams %R (pronounced "percent R")	12 W%R	Williams %R is usually plotted using negative values. For the purpose of analysis and discussion, simply ignore the negative symbols. It is best to wait for the security's price to change direction before placing your trades.
Moving average convergence and divergence (MACD)	9 MACD	MACD shows the difference between a fast and slow exponential moving average (EMA) of closing prices. Fast means a short-period average, and slow means a long period one.
Williams %R (pronounced "percent R")	12 W%R	Williams %R is usually plotted using negative values. For the purpose of analysis and discussion, simply ignore the negative symbols. It is best to wait for the security's price to change direction before placing your trades.
Transaction volume (TV)	5 TV, 10 TV, 15 TV	Transaction volume is a basic yet very important element of market timing strategy. Volume provides clues as to the intensity of a given price move.
Differences of technical index (Δ)	Δ5 MA, Δ6 MA, Δ10 MA, Δ5 BIAS, Δ10 BIAS, Δ6 RSI, Δ12 RSI, Δ12 W%R, Δ9 K, Δ9 D, Δ9 MACD	Differences of technical index between the day and next day.

select factor into regression model which if factor has the significance level, then it is selected. We can follow (4.4) to calculate the F value of SRA:

$$\begin{aligned} \mathrm{SSR} &= \sum \left(\widehat{Y} - \overline{Y}\right)^2, \\ \mathrm{SSE} &= \sum \left(\widehat{Y}_i - Y_i\right)^2, \end{aligned} \tag{4.3}$$

$$F_j^* = \frac{\mathrm{MSR}(x_j \mid x_i)}{\mathrm{MSE}(x_j \mid x_i)} = \frac{\mathrm{SSR}(x_j \mid x_i)}{\mathrm{SSE}/(n-2)\ (x_j \mid x_i)} \quad i \in I, \tag{4.4}$$

where SSR denotes a regression sum of square. SSE denotes residual sum of squares. x is the value of technical index. y is the value of stock price. n is the total number of training data. $\widehat{Y}$ is the forecasting value of regression. $\overline{Y}$ is the average stock price of training data. After the feature selection by SRA, we can provide a set of features to form an input vector for the next step to learning the forecasting model.

The steps of the SRA approach are described as follows.

Step 1. Find the correlation coefficient $r$for each technical index $v_1, v_2, \ldots, v_n$ with the stock price y in a stock. These correlation coefficients are stored in a matrix called correlation matrix.

Step 2. The technical index with largest R^2 value is selected from the correlation matrix. Let the technical index be v_i. Derive a regression model between the stock price and technical index, that is, $\widehat{y} = f(v_i)$.

Step 3. Calculate the partial F value of other technical indices. Compare the R^2 value of the remaining technical indices and select the technical index with the highest correlation coefficient. Let the technical index be v_j. Derive another regression model, that is, $\widehat{y} = f(v_i, v_j)$.

Step 4. Calculate the partial F value of the original data for the technical index v_j. If the F-value is smaller than the user-defined threshold, v_j is removed from the regression model since it does not affect the stock price significantly.

Step 5. Repeat Step 3 to Step 4. If the F-value of variable is more than the user-defined threshold, the variable should be added to the model, otherwise it should be removed.

In addition, the range of the input variables of SVR model should be between 0 and 1. Hence, the selected technical indices are normalized as follows:

$$\mathrm{Normal}(x_{ij}) = \frac{x_{ij} - \mathrm{Min}(x_i)}{\mathrm{Max}(x_i) - \mathrm{Min}(x_i)} \quad i = 1, \ldots, n;\ j = 1, \ldots, m;\ n,\ \ m \in \Re, \tag{4.5}$$

where $\mathrm{Normal}(x_{ij})$ denotes the normalized value of jth data point of ith technical index. $\mathrm{Max}(x_i)$ denotes the maximum value of ith technical index. $\mathrm{Min}(x_i)$ denotes the minimum value of ith technical index. x_{ij} denotes original value of jth data point of ith technical index. n and m denote the total number of technical indices and data points, respectively.

4.4. Learning the Trading Forecasting Model by SVR

Support vector regression will be applied as a machine learning model to extract the hidden knowledge in the historic stock database. The single output is the trading signal ts from TSBM process, and the multiple input features are technical indices from SRA selection. SVR learning model transforms multiple features into high multidimensional feature space, and the transformed feature space can be mapped into a hyperplane space to determine correct signals based on those support vector points. On the kernel function selection, we try to use linear, RBF, polynomial, and sigmoid functions to generate better performance for the SVR model because the stock market is a very complicated nonlinear environment. Since the SVR approach possesses high learning capability and accuracy in predicting continuous signals for building hidden knowledge among trading signals and technical indices, it is a widely used tool for predicting the trading signals.

4.5. Trading Points Decision from Forecasted Trading Signal

In the daily forecasting, if the forecasted trading signals by SVR satisfied buy threshold, then this means it is needed to buy stock quickly because it is very close to turning point; otherwise if the state satisfied a sell threshold, then there is need to sell stock. These satisfied points are recommended to transaction in stock market. Before determining the trading point, we will calculate the buy/sell threshold values for two trading types. The trading thresholds of two types are as follows:

$$\begin{aligned} \text{Buy}_{\text{threshold}} &= \mu + \sigma, \\ \text{Sell}_{\text{threshold}} &= 1 - \mu + \sigma, \\ \mu &= \frac{1}{N}\sum_{i=1}^{N} x_i', \\ \sigma &= \sqrt{\frac{1}{N}\sum_{i=1}^{N}(x_i' - \mu)}, \end{aligned} \tag{4.6}$$

where μ denotes the average of trading signal in training data. σ denotes the standard deviation of trading signal in training data. Buy_threshold denotes the buy trading threshold. Sell_threshold denotes the sell trading threshold. If forecasted trading signals form SVR model in testing data are more than buy_threshold, then this suggests trading point for buy stocks else if forecasting signal in testing data is smaller than sell_threshold, then this suggests trading for sell stock.

In the trading decision step, the TBSM-SVR model is employed to calculate daily trading signals. The detailed principles for making trading decisions include the following.

(1) If the time series prediction of trading signals by TBSM-SVR model is going up and intersects with buy trading threshold Buy_threshold, then it is a "buy" trading decision.

(2) If the time series prediction of trading signals by TBSM-SVR model is going down and intersects with sell trading threshold sell_threshold, then it is a "sell" trading decision.

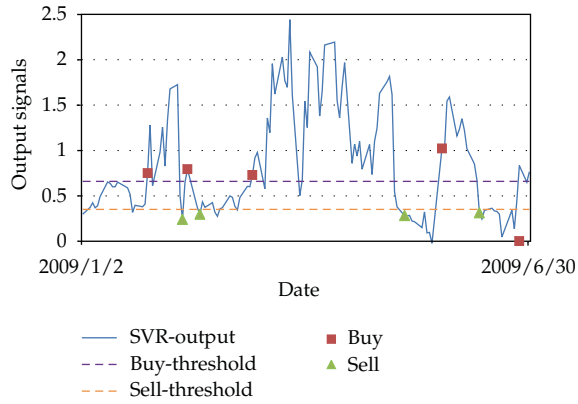

Figure 5: An example of result for detecting trading points of Apple.

(3) A "hold" trading decision is made (or do not make any trading decision) when the forecasting trading signal does not intersect with buy and sell thresholds.

For example, Figure 5 shows trading points decision for Apple stock. How to suggest the buy/sell points for stock in a time series in which the red square points are buy points and green triangle points are the sell points? Both are satisfied two thresholds in which the orange dotted line is sell threshold and the purple dotted line is buy threshold, so we can forecast the trading points daily by an automatically trading system.

5. Experimental Results

5.1. Profit Evaluation and Parameters Setting

In this research, the trading point (buy and sell timing) is decided by the TBSM-SVR model based on the forecasting trading signal of SVR and TBSM segmentation. In the experimental section, we also use various forecasting models to the generated profiting trading points and compare their performances. The profits in each different forecasting model are calculated as follows:

$$\text{profits} = C\prod_{i=1}^{k}\left\{\frac{(1-a-b)\times p_{S_i} - (1+a)\times p_{B_i}}{(1+a)\times p_{B_i}}\right\}, \tag{5.1}$$

where C is the total amount of money to be invested at the beginning as well as the capital of money, a refers to the tax rate of ith transaction, b refers to the handling charge of ith transaction, k is the total number of transaction, p_{S_i} is the selling price of the ith transaction and p_{B_i} is the buying price of ith transaction.

This study uses minimal root mean square error (RMSE) to measure the model performance in SVR train stage. In the model selection strategy that the dataset uses the last one trading period of training data contains (buy/sell and sell/buy states). The RMSE of an

Table 2: The parameter setup for TBSM and SVR by DOEs (design of experiments).

Approach	Parameter	Value	Explanation
TBSM	*Threshold*	0.1σ to 1σ	The difference of price at uptrend or downtrend
TBSM	*X_Thld*	0.1σ to 1σ	The difference of days at hold trend
TBSM	*Y_Thld*	0.1σ to 1σ	The difference of price at hold trend
SVR	C	10^{-3} to 10^{3}	Cost
SVR	ε	10^{-4} to 10^{-1}	Epsilon
SVR	d	2^{-9} to 2^{-1}	Degree
SVR	g	2^{1} to 2^{4}	Gamma

estimator $\widehat{ts}$ with respect to the estimated parameter ts is defined as the square root of the mean square error:

$$\text{RMSE} = \sqrt{\frac{\sum_{i=1}^{n} ts_i - \widehat{ts_i}}{N}}. \tag{5.2}$$

ts denotes the trading signal by trading signal transformation from TBSM segmentation in Section 4.2. $\widehat{ts}$ denotes the estimated trading signal by SVR forecasting model. N denotes total number in each training data (Table 2).

In parameter section we use design of experiments (DOEs) approach to set each parameter for capture optimal parameter combination for trading system in financial data. The parameters of the TBSM are based on standard deviation σ from stock price in each stock which is the range from 0.1σ to 1σ for testing in each parameters. In SVR model, the kernels chosen for testing are "radial basis function (RBF)" and "polynomial" function. The common combination includes cost C; epsilon ε and γ are selected by the grid search with exponentially growing sequences. C ranges from 10^{-3} to 10^{3}. ε from 10^{-4} to 10^{-1} and γ is fixed as 0. In "polynomial" function, the degree d ranges from 2^{-9} to 2^{-1}. The gamma g ranges from 2^{1} to 2^{4} in RBF kernel.

5.2. Profit Comparison in the US Stock Market

In this research, we have selected 7 stocks from the US stock market to compare the profit achieved by various trading models, including Apple, BOENING CO. (BA), Caterpillar Inc. (CAT), Johnson and Johnson (JNJ), Exxon Mobil Corp. (XOM), Verizon Communication Inc. (VZ), and S&P 500. Among all the stocks, 253 data points were collected for the training period from 1/2/2008 (mm/dd/yy) to 12/31/2008 while 124 data points were used for the testing period from 1/2/2009 to 6/30/2009. In this research, we have compared our forecasting model of TBMS-SVR approach with two other identification models developed in the past. The PLR-BPN model proposed by Chang et al. [26] used neural networks in combination with PLR and exponential smoothing to determine the trading points. Kwon and Kish [41] used statistical model such as moving average, rate of change and trading volumes to determine the buy-sell points and generated profit.

Table 3: Feature selection result in each stock for technical indices by SRA.

Stock	Technical index
Apple	5 MA, 6 MA, 9 K, 9 MACD, 12 W%R
BA	5 MA, 6 MA, 9 K, 10 TV, 12 W%R
CAT	5 MA, 6 MA, 9 K, 10 TV, Δ5 MA
JNJ	5 MA, 6 MA, 6 RSI, 9 MACD, Δ5 MA
S&P 500	5 MA, 5 BIAS, 10 TV, 26 BR, TAPI
VZ	5 MA, 6 MA, Δ5 MA, 10 TV, 26 VR
XOM	5 MA,6 MA, Δ5 MA

Table 4: Model selection results from TSBM-SVR model for each stock.

Stock	Kernel									
	Radial basis function (RBF)					Polynomial				
	g	C	ε	SVs	RMSE	d	C	ε	SVs	RMSE
Apple	2^{-1}	10^3	10^{-4}	253	0.0819	2	[0.001 : 1000]	[0.0001 : 0.1]	71	0.266
BA	2^{-1}	10^3	10^{-1}	107	0.0955	2	[0.001 : 1000]	[0.0001 : 0.1]	76	0.269
CAT	2^{-1}	10^3	10^{-3}	254	0.0898	2	[0.001 : 1000]	[0.0001 : 0.1]	156	0.233
JNJ	2^{-1}	10^2	10^{-1}	137	0.2617	1	[0.001 : 1000]	[0.0001 : 0.1]	116	0.426
S&P 500	2^{-1}	10^3	10^{-4}	254	0.0004	1	[0.001 : 1000]	[0.0001 : 0.1]	112	0.379
VZ	2^{-1}	10^3	10^{-3}	251	0.0031	1	[0.001 : 1000]	[0.0001 : 0.1]	125	0.269
XOM	2^{-1}	10^3	10^{-4}	253	0.0001	2	[0.001 : 1000]	[0.0001 : 0.1]	182	0.18

Table 5: Comparison of profit obtained by various forecasting models.

Stock no.	Stock name	TBSN-SVR model (RBF)	PLR-SVR model (RBF)	PLR-BPN model	Statistical model
1	Apple	92.35%	35.84%	12.97%	20.50%
2	BA	59.49%	35.69%	17.50%	20.03%
3	CAT	43.39%	36.09%	9.36%	24.83%
4	JNJ	13.95%	9.47%	16.88%	0%
5	S&P 500	22.78%	4.19%	3.77%	9.81%
6	VZ	28.60%	2.60%	27.72%	0%
7	XOM	22.40%	12.34%	–1.99%	–7.65%
Average		40.42%	19.46%	12.32%	9.65%

The technical indices selected result by SRA as shown in Table 3. Apple, Ba, CAT, JNJ, S&P 500, and VZ used 5 features (technical indices) for training forecasting model; XOM used 3 features for training forecasting model. From this result we can know that a few features can capture more trading knowledge.

From model selection results the RBF kernel has better low error in each stock by RMSE. Moreover, the gamma, degree, cost, epsilon, support vectors, and RMSE as shown in Table 4 are necessary parameters and measures. The models of TBSM-SVR in each stock are selecting optimal parameter combination by RMSE consideration.

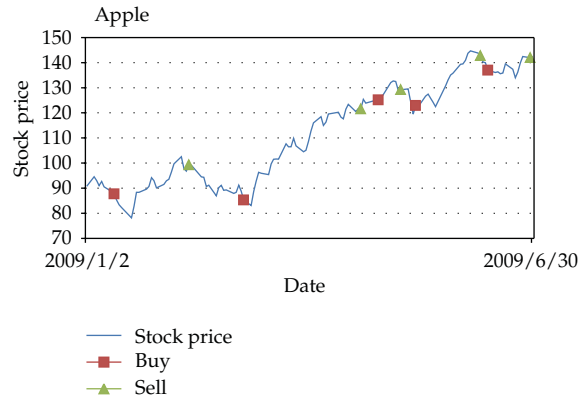

Figure 6: The forecasted trading points of Apple (an uptrend stock).

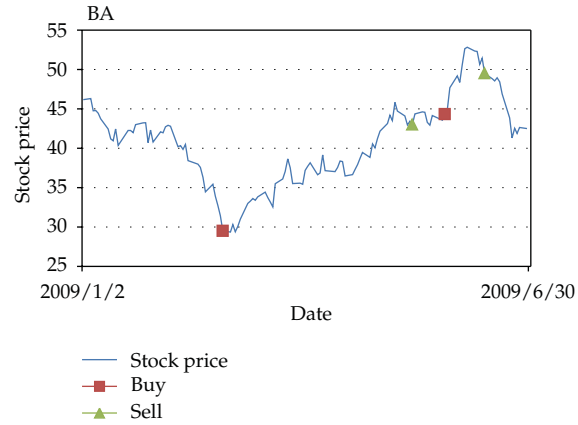

Figure 7: The forecasted trading points of BA (a steady-trend stock).

Each forecasting model provides trading points for each stock, so the best profits of the 3 forecasting models are shown in Table 5. The results turn out that our proposed TBSM with SVR model generates the greatest returns for the seven stocks, that is, number 1, 2, 3, 4, 5, 6, and 7 outperform other models. The average profit rate of these seven stocks is 40.42% using the TBSM-SVR model whereas the average profit rate generated by other models like PLR-SVR, PLR-BPN, and Statistical is 19.46%, 12.32%, and 9.65%, respectively. Therefore, our TBSM approach is better than PLR approach which is only considered linear representation.

The buy and sell points obtained from the TBSM forecasting model in each stock are shown in Figures 6, 7, 8, 9, 10, 11, and 12. The red square represents the buy point, and the black triangle represents the sell point using a trading strategy to determine turning points. Furthermore, our proposed approach TBSM is better than PLR segmentation which denotes that TBSM approach captures better trading knowledge for SVR forecasting model. Due to PLR only the linear representation is considering, so it loses important trend. Therefore, TBSM is an effective segmentation method for nonlinear time series data in stock market.

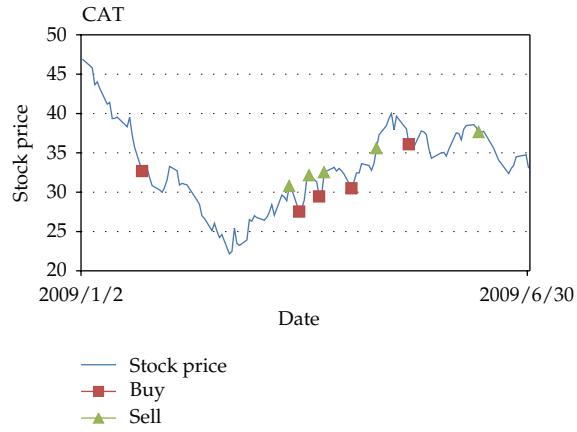

Figure 8: The forecasted trading points of CAT (a downtrend stock).

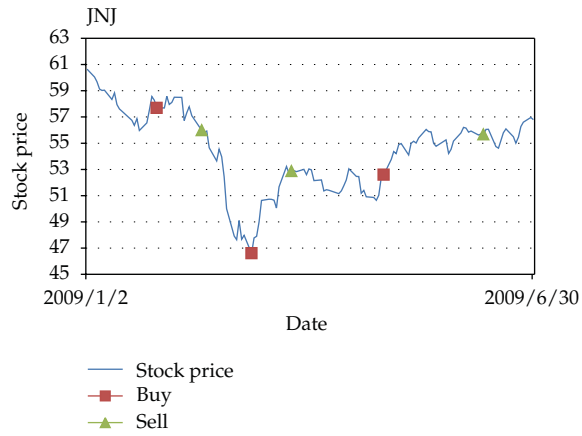

Figure 9: The forecasted trading points of JNJ (a steady-trend stock).

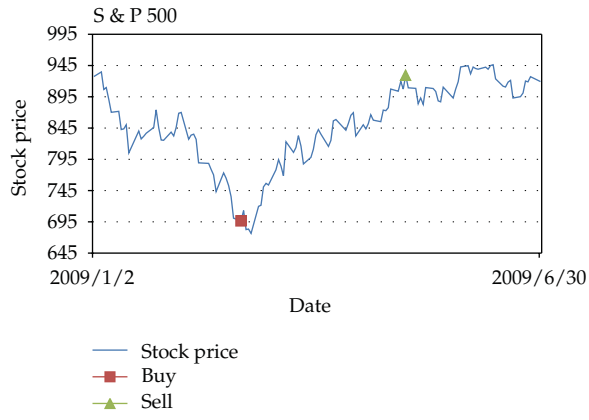

Figure 10: The forecasted trading points of S&P 500 (a steady-trend stock).

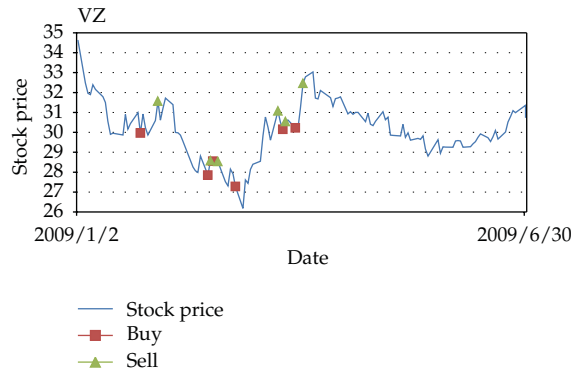

Figure 11: The forecasted trading points of VZ (a downtrend stock).

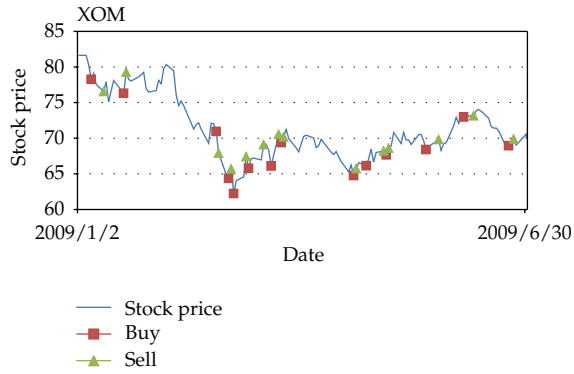

Figure 12: The forecasted trading points of XOM (a downtrend stock).

6. Conclusions

In this paper we proposed a trading system combining TBSM with SVR, and it is called TBSM-SVR-based stock trading system. This new trading system has been very effective in earning high profit while with the greatest ability. Experimental results showed that the TSBM can segment the stock price's variation into different trading trends. The trading signal in each trading trend will be assumed to be the same. The nonlinear time series can be better represented using these trading trends. Additionally, SVR is applied to capture the trading knowledge using the trading signals derived from these trading trends. The captured knowledge is more effective using TBSM-SVR when compared to PLR segmentation method. As a result, the primary goal of the investor could be easily achieved by providing him with simple trading decisions. However, the limitation of the TBSM-SVR trading system is the machine learning tool; that is, SVR is still not that mature yet. There are still rooms for the improvement of a better machine learning mechanism to be developed. Therefore, the trading system may make a wrong trading and lose money. In the future works, we can extend the segmentation method by considering a more detailed trend by investigating different buy-hold strategy or better trading strategy. In addition, the trend based segmentation method can further consider the fractal properties such as long memory, which can be accommodated to improve the segmentation performances.

References

[1] V. N. Vapnik, *The Nature of Statistical Learning Theory*, Springer, New York, NY, USA, 1995.

[2] V. N. Vapnik, *Statistical Learning Theory*, Adaptive and Learning Systems for Signal Processing, Communications, and Control, John Wiley & Sons, New York, NY, USA, 1998.

[3] Z. Liu, "Chaotic time series analysis," *Mathematical Problems in Engineering*, vol. 2010, Article ID 720190, 31 pages, 2010.

[4] B. J. Chen, M. W. Chang, and C. J. Lin, "Load forecasting using support vector machines: a study on EUNITE Competition 2001," *IEEE Transactions on Power Systems*, vol. 19, no. 4, pp. 1821–1830, 2004.

[5] F. Girosi, M. Jones, and T. Poggio, "Regularization theory and neural networks architectures," *Neural Computation*, vol. 7, pp. 219–269, 1995.

[6] X. H. Yang, D. X. She, Z. F. Yang, Q. H. Tang, and J. Q. Li, "Chaotic bayesian method based on multiple criteria decision making (MCDM) for forecasting nonlinear hydrological time series," *International Journal of Nonlinear Sciences and Numerical Simulation*, vol. 10, no. 11-12, pp. 1595–1610, 2009.

[7] D. She and X. Yang, "A new adaptive local linear prediction method and its application in hydrological time series," *Mathematical Problems in Engineering*, vol. 2010, Article ID 205438, 15 pages, 2010.

[8] N. Muttil and K. W. Chau, "Neural network and genetic programming for modelling coastal algal blooms," *International Journal of Environment and Pollution*, vol. 28, no. 3-4, pp. 223–238, 2006.

[9] D. Niu, Y. Wang, and D. D. Wu, "Power load forecasting using support vector machine and ant colony optimization," *Expert Systems with Applications*, vol. 37, no. 3, pp. 2531–2539, 2010.

[10] P. F. Pai and W. C. Hong, "Forecasting regional electricity load based on recurrent support vector machines with genetic algorithms," *Electric Power Systems Research*, vol. 74, no. 3, pp. 417–425, 2005.

[11] W. C. Hong, "Chaotic particle swarm optimization algorithm in a support vector regression electric load forecasting model," *Energy Conversion and Management*, vol. 50, no. 1, pp. 105–117, 2009.

[12] T. Farooq, A. Guergachi, and S. Krishnan, "Knowledge-based Green's Kernel for support vector regression," *Mathematical Problems in Engineering*, vol. 2010, Article ID 378652, 16 pages, 2010.

[13] S. O. Lozza, E. Angelelli, and A. Bianchi, "Financial applications of bivariate Markov processes," *Mathematical Problems in Engineering*, vol. 2011, Article ID 347604, 15 pages, 2011.

[14] A. Swishchuk and R. Manca, "Modeling and pricing of variance and volatility swaps for local semi-markov volatilities in financial engineering," *Mathematical Problems in Engineering*, vol. 2010, Article ID 537571, 17 pages, 2010.

[15] M. S. Abd-Elouahab, N. E. Hamri, and J. Wang, "Chaos control of a fractional-order financial system," *Mathematical Problems in Engineering*, vol. 2010, Article ID 270646, 18 pages, 2010.

[16] A. J. Smola and B. Schölkopf, "A tutorial on support vector regression," *Statistics and Computing*, vol. 14, no. 3, pp. 199–222, 2004.

[17] P. C. Chang and C. H. Liu, "A TSK type fuzzy rule based system for stock price prediction," *Expert Systems with Applications*, vol. 34, no. 1, pp. 135–144, 2008.

[18] P. F. Pai and C. S. Lin, "A hybrid ARIMA and support vector machines model in stock price forecasting," *Omega*, vol. 33, no. 6, pp. 497–505, 2005.

[19] F. X. Diebold and R. S. Mariano, "Comparing predictive accuracy," *Journal of Business and Economic Statistics*, vol. 20, no. 1, pp. 134–144, 2002.

[20] H. Liu and J. Wang, "Integrating independent component analysis and principal component analysis with neural network to predict Chinese stock market," *Mathematical Problems in Engineering*, vol. 2011, Article ID 382659, 15 pages, 2011.

[21] X. P. Ge, "Pattern matching in financial time series data," *Computer Communications*, vol. 27, pp. 935–945, 1998.

[22] E. Keogh and M. Pazzani, "An enhanced representation of time series which allows fast and accurate classification, clustering and relevance feedback," in *Proceedings of the 4th International Conference on Knowledge Discovery and Data Mining (KDD '98)*, pp. 239–241, August 1998.

[23] V. Lavrenko, M. Schmill, D. Lawrie, P. Ogilvie, D. Jensen, and J. Allan, "Mining of concurrent text and time series," in *Proceedings of the 6th International Conference on Knowledge Discovery and Data Mining (KDD '00)*, pp. 37–44, August 2000.

[24] S. Ghosh, P. Manimaran, and P. K. Panigrahi, "Characterizing multi-scale self-similar behavior and non-statistical properties of fluctuations in financial time series," *Physica A*, vol. 390, no. 23-24, pp. 4304–4316, 2011.

[25] P. C. Chang, C. Y. Tsai, C. H. Huang, and C. Y. Fan, "Application of a case base reasoning based support vector machine for financial time series data forecasting," in *Proceedings of the International Conference on Intelligent Computing (ICIC '09)*, vol. 5755, pp. 294–304, September 2009.

[26] P. C. Chang, C. Y. Fan, and C. H. Liu, "Integrating a piecewise linear representation method and a neural network model for stock trading points prediction," *IEEE Transactions on Systems, Man and Cybernetics Part C*, vol. 39, no. 1, pp. 80–92, 2009.

[27] L. Todorova and B. Vogt, "Power law distribution in high frequency financial data? An econometric analysis," *Physica A*, vol. 390, no. 23-24, pp. 4433–4444, 2011.

[28] M. K. P. So, C. W. S. Chen, J. Y. Lee, and Y. P. Chang, "An empirical evaluation of fat-tailed distributions in modeling financial time series," *Mathematics and Computers in Simulation*, vol. 77, no. 1, pp. 96–108, 2008.

[29] M. Li and W. Zhao, "Visiting power laws in cyber-physical networking systems," *Mathematical Problems in Engineering*, vol. 2012, Article ID 302786, 13 pages, 2012.

[30] L. Muchnik, A. Bunde, and S. Havlin, "Long term memory in extreme returns of financial time series," *Physica A*, vol. 388, no. 19, pp. 4145–4150, 2009.

[31] M. Li, C. Cattani, and S. Y. Chen, "Viewing sea level by a one-dimensional random function with long memory," *Mathematical Problems in Engineering*, vol. 2011, Article ID 654284, 13 pages, 2011.

[32] M. Li, "Fractal time series—a tutorial review," *Mathematical Problems in Engineering*, vol. 2010, Article ID 157264, 26 pages, 2010.

[33] J. O. Lachaud, A. Vialard, and F. De Vieilleville, "Analysis and comparative evaluation of discrete tangent estimators," in *Proceedings of the 12th International Conference on Discrete Geometry for Computer Imagery (DGCI '05)*, E. Andres, G. Damiand, and P. Lienhardt, Eds., vol. 3429,, pp. 240–251, Springer, April 2005.

[34] Y. Zhu, D. Wu, and S. Li, "A piecewise linear representation method of time series based on feature pints," in *Proceedings of the11th International Conference on Knowledge-Based Intelligent Information and Engineering Systems (KES '07), 17th Italian Workshop on Neural Networks (WIRN '07)*, pp. 1066–1072, January 2007.

[35] H. Wu, B. Salzberg, and D. Zhang, "Online event-driven subsequence matching over financial data streams," in *Proceedings of the ACM SIGMOD International Conference on Management of Data (SIGMOD '04)*, pp. 23–34, June 2004.

[36] Z. Zhang, J. Jiang, X. Liu et al., "Pattern recognition in stock data based on a new segmentation algorithm," in *Proceedings of the 2nd International Conference on Knowledge Science, Engineering and Management (KSEM '07)*, vol. 4798 of *Lecture Notes in Computer Science*, pp. 520–525, 2007.

[37] Y. W. Wang, P. C. Chang, C. Y. Fan, and C. H. Huang, "Database classification by integrating a case-based reasoning and support vector machine for induction," *Journal of Circuits, Systems and Computers*, vol. 19, no. 1, pp. 31–44, 2010.

[38] L. Zhang, W. D. Zhou, and P. C. Chang, "Generalized nonlinear discriminant analysis and its small sample size problems," *Neurocomputing*, vol. 74, no. 4, pp. 568–574, 2011.

[39] N. Sapankevych and R. Sankar, "Time series prediction using support vector machines: a survey," *IEEE Computational Intelligence Magazine*, vol. 4, no. 2, pp. 24–38, 2009.

[40] J. L. Wu, L. C. Yu, and P. C. Chang, "Emotion classification by removal of the overlap from incremental association language features," *Journal of the Chinese Institute of Engineers*, vol. 34, no. 7, pp. 947–955, 2011.

[41] K. Y. Kwon and R. J. Kish, "Technical trading strategies and return predictability: NYSE," *Applied Financial Economics*, vol. 12, no. 9, pp. 639–653, 2002.

Hindawi Publishing Corporation
Mathematical Problems in Engineering
Volume 2012, Article ID 376010, 13 pages
doi:10.1155/2012/376010

Research Article

New Optimal Weight Combination Model for Forecasting Precipitation

Song-shan Yang,[1] Xiao-hua Yang,[2] Rong Jiang,[2] and Yi-che Zhang[1]

[1] *School of Mathematical Sciences, Beijing Normal University, Beijing 100875, China*
[2] *The Key Laboratory of Water and Sediment Sciences, State Key Laboratory of Water Environment Simulation, School of Environment, Beijing Normal University, Beijing 100875, China*

Correspondence should be addressed to Xiao-hua Yang, xiaohuayang@bnu.edu.cn

Received 9 February 2012; Accepted 21 March 2012

Academic Editor: Ming Li

In order to overcome the inaccuracy of the forecast of a single model, a new optimal weight combination model is established to increase accuracies in precipitation forecasting, in which three forecast submodels based on rank set pair analysis (R-SPA) model, radical basis function (RBF) model and autoregressive model (AR) and one weight optimization model based on improved real-code genetic algorithm (IRGA) are introduced. The new model for forecasting precipitation time series is tested using the annual precipitation data of Beijing, China, from 1978 to 2008. Results indicate the optimal weights were obtained by using genetic algorithm in the new optimal weight combination model. Compared with the results of R-SPA, RBF, and AR models, the new model can improve the forecast accuracy of precipitation in terms of the error sum of squares. The amount of improved precision is 22.6%, 47.4%, 40.6%, respectively. This new forecast method is an extension to the combination prediction method.

1. Introduction

Precipitation time series forecast has received tremendous attention in the world because of the uncertainty of climate change which increases the difficulty of accurately forecasting such time series. The forecast of the nonlinear and uncertain time series is very difficult with the traditional deterministic mathematic models, which cause new challenges to increase forecast accuracies [1, 2]. There are many methods for predicting complex time series [3–13].

Rank set pair analysis (R-SPA) model is based on the principle of set pair analysis, and, in this model, we take rank as the particular characteristic of the time series which could be regarded as the standard of the similarity analysis. Radical basis function (RBF) neural

network was firstly introduced by Broomhead and Lowe [7]. The RBF network model is motivated by the locally tuned response observed in biological neurons. Neurons with a locally tuned response characteristic can be found in several parts of the nervous system. The theoretical basis of the RBF approach lies in the field of interpolation of multivariate functions [8]. Chau applied particle swarm optimization training algorithm for artificial neural network system (ANN) in prediction [3, 4]. The content of autoregressive (AR) model is a random process, which is often used to model and forecast various types of natural phenomena.

The combination model techniques provide consensus forecast by linear combination of individual model predictions according to different weighting strategies. The weights can be equal for all models in the simplest case or be determined through certain regression based methods [9]. The concept of combining the forecast model obtained from different models has been discussed and used previously [10–19]. The sensible combination of the outputs of different models has the additional merit that it may assist in the understanding of the underlying physical processes. Genetic algorithms (GAs) encode a potential solution to a specific problem on a simple chromosome-like data structure and apply recombination operators to these structures so as to preserve critical information. GAs are chosen to calculate the weights of three submodels because of its outstanding performance in optimization analysis, especially regarding the process of finding optimal parameters.

This study first combines the three submodels which are introduced as previous, and the improved real-code genetic algorithm (IRGA) [19] is used to calculate the weights of the combination model. The three submodels and the new optimal weight combination model are used to forecast the annual precipitation for Beijing from 2004 to 2008. In the next section, optimal weight combination model is presented. In Section 3, we discuss the application of the optimal weight combination model. In Section 4, we give the conclusions.

2. The Optimal Weight Combination Model

In this paper, the procedure of establishing the new optimal weight combination model can be divided into three steps as follows.

(1) Construct the weight combination model.

(2) Establish three submodels.

(3) Calculate the weights of the three submodels by using IRGA.

The flow chart of this procedure is shown in Figure 1.

2.1. Construction of the Weight Combination Model

In the case of N forecast models, the weight combination forecast model [20] may be expressed as

$$x_i = \sum_{j=1}^{N} w_j x_{ji} + e_i, \tag{2.1}$$

where x_i is the observed discharge of the ith time period, w_j is the weight assigned to the jth model, and estimated discharge x_{ji} and e_i are the combination error term.

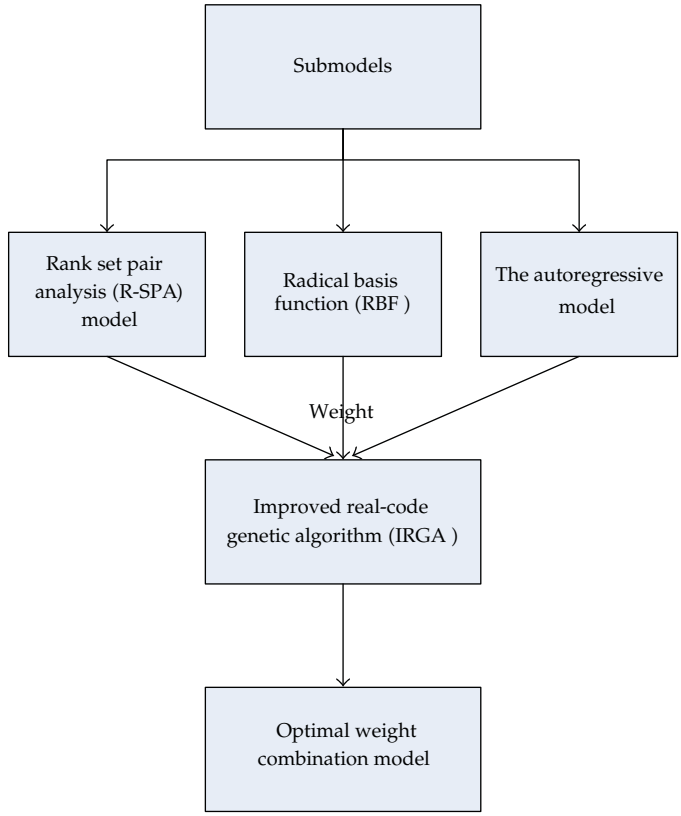

Figure 1: The flow chart of the procedure of establishing the new optimal weight combination model.

Equation (2.1) can be represented in matrix notation as

$$X = YW + E, \tag{2.2}$$

where Y is the input matrix defined by

$$\begin{bmatrix} x_{11} & x_{21} & \dots & x_{N1} \\ x_{12} & x_{22} & \dots & x_{N2} \\ \vdots & \vdots & \ddots & \vdots \\ x_{1n} & x_{2n} & \dots & x_{Nn} \end{bmatrix}, \tag{2.3}$$

$X = (x_1, x_2, \dots, x_n)^T$ is the output vector, $W = (w_1, w_2, \dots, w_N)^T$ is the weight vector, $E = (e_1, e_2, \dots, e_n)^T$ is the combination error vector, T denotes the transpose of the vector, and n is the total number of observations.

Table 1: History set A_t and current set B.

History set	Elements	Subsequent value
A_1	$x_1, x_2, \ldots, x_T$	x_{T+1}
A_2	$x_2, x_3, \ldots, x_{T+1}$	x_{T+2}
$\vdots$	$\cdots$	$\cdots$
A_i	$x_{i+1}, x_{i+2}, \ldots, x_{i+T}$	x_{i+T+1}
$\vdots$	$\cdots$	$\cdots$
A_{n-T}	$x_{n-T}, x_{n-T+1}, \ldots, x_{n-1}$	x_n
Current set	Elements	Subsequent value
B	$x_{n-T+1}, x_{n-T+2}, \ldots, x_n$	x_{n+1}

In the weight combination forecasting model, the sum of the weights w is normally constrained to be equal to unity, that is

$$\sum_{j=1}^{N} w_j = 1. \tag{2.4}$$

The value of the weight w cannot be less than zero, that is

$$w_j \geq 0 \quad (j = 1, 2, \ldots, N). \tag{2.5}$$

2.2. Establishment of the Three Submodels

2.2.1. Rank Set Pair Analysis (R-SPA) Model

The procedure of the establishment of this model is shown as follows.

(1) Consider an annual precipitation series $x_1, x_2, \ldots, x_n$, we constructed the history sets $A_1, A_2, \ldots A_{n-T}$, current set B and the subsequent value of these sets are represented in Table 1.

Because of the weak dependence in the annual precipitation series, we assume that the number of history set and current set T to be an integer from 4 to 6.

(2) Rank transformation. We mark the elements in $A_1, A_2, \ldots, A_{n-T}$, B from 1 to T according to the rank of elements in the sets they belong to. If some elements have the same rank, we mark them according to their average rank and round off the value. Then, we could obtain the rank set $A'_1, A'_2, \ldots, A'_{n-T}, B'$.

(3) Construct $n-T$ rank set pairs (A'_i, B') $(i = 1, 2, \ldots, n-T)$ and calculate the difference d between the corresponding elements of A'_i and B'. If the absolute value of d is equal to zero, we mark them "identical"; if the absolute value of d is greater than $T-2$, we mark them "contrary"; if the absolute value of d is between zero and $T-2$, we mark them "discrepant." Respectively, count the total number of "identical," "contrary," and "discrepant" of each rank set pair. According to the value of the

coefficient of the discrepancy degree i and the coefficient of the contrary degree j, the connection degree formula as follows:

$$\mu_{A-B} = \frac{S}{N} + \frac{F}{N}i + \frac{P}{N}j, \tag{2.6}$$

where μ is the connection degree of the set pair, N denotes the total number of characteristics of the set pair, S represents the number of identity characteristics, P is the number of contrary characteristics, F is the number of the characteristics if the set pair is neither identity nor contrary. According to (2.6), we calculate the value of the connection degree of each rank set pair.

(4) In accordance with the maximum principle, we can find a similar set A_i' of B, and also we can find several similar sets of B under certain circumstances. A_i' is the counterpart of A_i, and the subsequent value of A_i is x_{T+1}. We can obtain the value of x_{n+1} through the formula as follows:

$$x_{n+1} = \frac{1}{m}\sum_{k=1}^{m} w_k x_{T+k}, \tag{2.7}$$

where w_k is the ratio of the average of the elements in B and the average of the elements in A_k, m is the number of the similar sets of B.

2.2.2. Radical Basis Function (RBF) Model

The interpretation of the RBF method as an artificial neural network consists of three layers: one layer is the input layer neurons feeding the feature vectors into the network; another layer is a hidden layer of RBF neurons calculating the outcome of the bas functions; the last layer is the output layer neurons calculating a linear combination of the basis functions [21, 22]. The different numbers of hidden layer neurons and spread constant are tried in the study. Its topological structure is shown in Figure 2.

The procedure of the establishment of this model is shown as follows.

(1) Normalization of the time series. Consider an annual precipitation series $\{x_1, x_2, \ldots, x_n\}$, we can transform the series to $\{x_1', x_2', \ldots, x_n'\}$ by the normalization formula as follows.

$$x_t' = \frac{x_t - x_{\min}}{x_{\max} - x_{\min}} \quad (t = 1, 2, \ldots, n), \tag{2.8}$$

where $x_{\min}$ and $x_{\max}$ denote the minimum and the maximum of the time series $\{x_1, x_2, \ldots, x_n\}$.

(2) Forecast of the data. The application of the RBF neural networks to time series data consists of two steps. The first step is the training of the neural networks. Choose the first N value of the new series $\{x_1', x_2', \ldots, x_n'\}$ as the training sample, and set up the RBF neural networks. Once the training stage is completed, the RBF neural networks will be applied to the forecasting data. Based upon the RBF

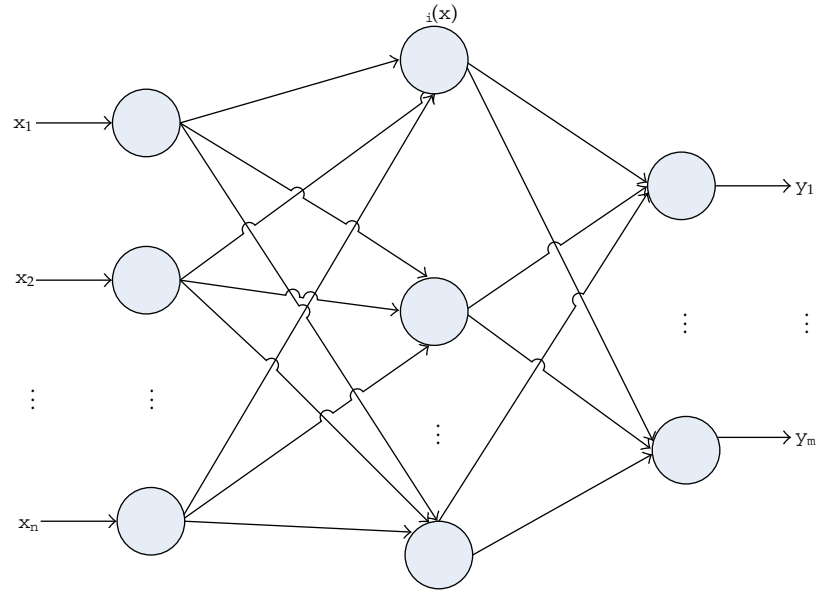

Figure 2: The topological structure of RBF.

neural networks established by the training sample, we forecast the value of the last $n - N$ elements of the series $\{x'_1, x'_2, \ldots, x'_n\}$ and the forecasting series can be represented as $\{y'_{N+1}, y'_{N+2}, \ldots, y'_n\}$. In this study, we take that the value of the mean-square error is 0.0001 and the width of the radical primary function is 1.

(3) Denormalization of the forecasting series. Since the value of the elements in forecasting series is between zero and one, that is $y'_j \in [0, 1]$, we should denormalize the forecasting series $\{y'_{N+1}, y'_{N+2}, \ldots, y'_n\}$ to final forecasting $\{y_{N+1}, y_{N+2}, \ldots, y_n\}$ through the denormalization formula as follows:

$$y_j = y'_j \times (x_{\max} - x_{\min}) + x_{\min} \quad (j = N + 1, N + 2, \ldots, n). \tag{2.9}$$

2.2.3. Autoregressive (AR) Model

In this paper, we regard the data of the annual precipitation as a time series and the trend term, seasonal term, and random term can be extracted from the time series in sequence. Then, we superpose the trend term, seasonal term and random term, and obtain the equation as follows [23–25]:

$$x_t = A_t + B_t + C_t, \tag{2.10}$$

where x_t is the precipitation time series, A_t is the trend term, B_t is the seasonal term, and C_t is the random term.

The procedure of establishing the autoregressive model is shown as follows.

(1) The extraction of the trend term. In this paper, the data performs a clear quadratic algorithms component, so a polynomial function is used to fit the precipitation data. The trend term A_t can be described as follows:

$$A_t = P_2 t^2 + P_1 t + P_0, \tag{2.11}$$

where P_i $(i = 0, 1, 2)$ is the coefficient of the quadratic polynomial (2.11).

(2) The extraction of the seasonal term. The analysis of precipitation seasonality can be accomplished with the aid of modeling via spectral analysis. The precipitation seasonality can be indicated with L waves. BB_t is the output of P_t subtract A_t, and the estimated value of BB_t can be defined as BB'_t:

$$BB'_t = \frac{a_0}{2} + \sum_{k=1}^{L} \left[a_k \cos \frac{2pkt}{n} + b_k \sin \frac{2pkt}{n} \right], \tag{2.12}$$

where $L = [n/2]$ is the number of harmonicwave, a_k and b_k are the coefficient of the Fourier series (2.12):

$$\begin{aligned} a_0 &= \frac{1}{n} \sum_{t=1}^{n} BB_t, \\ a_k &= \frac{2}{n} \sum_{i=1}^{n} BB_t \cos \frac{2\pi ki}{n} \quad (k = 1, 2, \ldots, L), \\ b_k &= \frac{2}{n} \sum_{i=1}^{n} BB_t \sin \frac{2\pi ki}{n}. \end{aligned} \tag{2.13}$$

Taking the working capacity into consideration, we choose the significant wave to forecast. And we define the kth wave as the significant wave when the following inequality is satisfied:

$$s_k{}^2 = a_k{}^2 + b_k{}^2 > \frac{0.5 s^2 \ln(k/a)}{n}, \tag{2.14}$$

where a is the level of significance ($a = 5\%$); s^2 is the variance of the series:

$$s^2 = \frac{1}{n-1} \sum_{t=1}^{n} \left(P_t - \overline{P}_t \right)^2. \tag{2.15}$$

(3) The extraction of the random term. The random term C_t is defined as a linear combination of $C_{t-1}, C_{t-2}, \ldots, C_{t-p}$:

$$C_t = \alpha_0 + \alpha_1 C_{t-1} + \alpha_2 C_{t-2} + \cdots + \alpha_p C_{t-p}, \tag{2.16}$$

where p is the order number of the model; α_i $(i = 0, 1, \ldots, p)$ denotes the coefficient of the regression model, which can be confirmed by AIC (Akaike's Information Criterion) formula:

$$\mathrm{AIC}(p) = n \ln {\sigma_p}^2 + 2p, \tag{2.17}$$

where n is the number of series, ${\sigma_p}^2$ represents the variance of AR(p) and the appropriative of p can be chosen among 1, 2, 3, and 4.

2.3. Calculation of the Weights of the Submodels

The key of setting up the optimal weight combination model is to ascertain the weight of each forecasting model. In this study, we choose the weight which satisfies that the error sum of squares of the combination model is the minimum among all weight combination forecasting models, that is

$$\min f = \min \sum_{i=1}^{n} e_i^2 = \min \sum_{i=1}^{n} \left(x_i - \sum_{j=1}^{N} w_j x_{ji} \right)^2, \tag{2.18}$$

where f is the error sum of squares of the combination model.

Two matrices S and E' are defined as

$$S = \begin{bmatrix} e_{11} & e_{12} & \cdots & e_{1n} \\ e_{21} & e_{22} & \cdots & e_{2n} \\ \vdots & \vdots & \ddots & \vdots \\ e_{N1} & e_{N2} & \cdots & e_{Nn} \end{bmatrix}, \quad e_{ij}(i = 1, 2, \ldots, N, j = 1, 2, \ldots, n), \tag{2.19}$$

e_{ij} is the error of the jth forecasting value of the ith model,

$$E' = SS^T = \begin{bmatrix} e'_{11} & e'_{12} & \cdots & e'_{1N} \\ e'_{21} & e'_{22} & \cdots & e'_{2N} \\ \vdots & \vdots & \ddots & \vdots \\ e'_{N1} & e'_{N2} & \cdots & e'_{NN} \end{bmatrix}. \tag{2.20}$$

And, the formula (2.13) can be represented as follows:

$$\min f = \min \sum_{i=1}^{n} e_i^2 = \min \sum_{i=1}^{n} \left(x_i - \sum_{j=1}^{N} w_j x_{ji} \right)^2 = \sum_{i=1}^{N} \sum_{j=1}^{N} w_i w_j e'_{ij}. \tag{2.21}$$

If we obtain the value of w_j $(j = 1, 2, \ldots, N)$ with the aid of formula (2.4), (2.5), and (2.21), then we can ascertain optimal weight combination model.

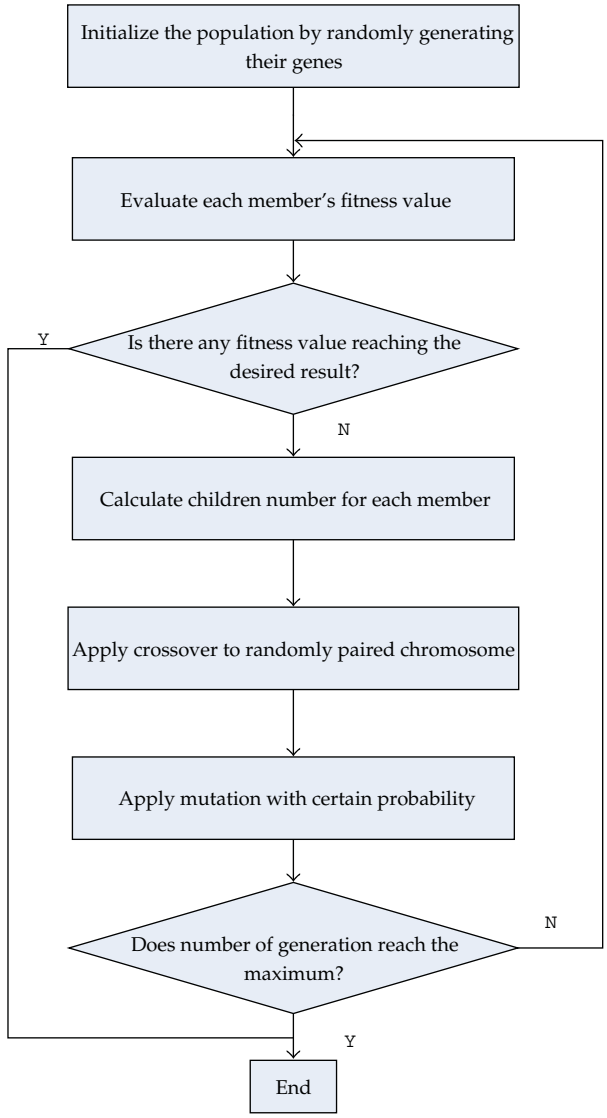

Figure 3: The flow chart of genetic algorithm.

Genetic algorithm is an adaptive heuristic search algorithm premised on the evolutionary ideas of natural selection and genetic mutation, and it has always been regarded as a function optimizer [26–28]. The flow chart of genetic algorithm is shown in Figure 3.

In this paper, we use the improved real-code genetic algorithm (IRGA) to solve this optimization problem. The population size is 20; the crossover fraction is 0.8, and the generation is 100.

3. Application of the Optimal Weight Combination Model

In this study, the data of the annual precipitation from 1978 to 2008 for Beijing are collected and shown in Figure 4.

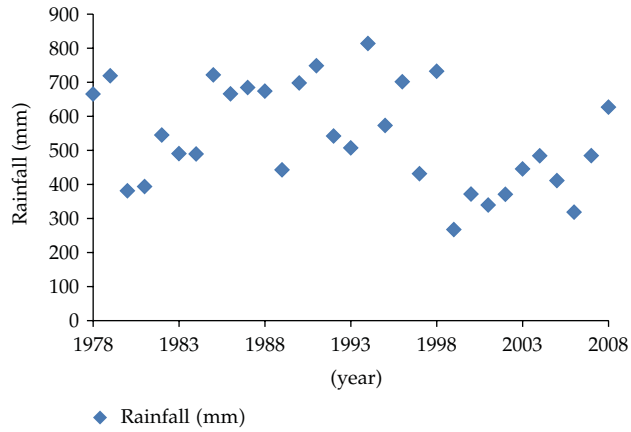

Figure 4: An annual precipitation from 1978 to 2008 for Beijing.

Table 2: The forecasted data of three submodels.

Year	Measured value (mm)	Model					
		R-SPA		RBF		The autoregressive model	
		Forecasted value (mm)	Error (%)	Forecasted value (mm)	Error (%)	Forecasted value (mm)	Error (%)
2004	483.5	379.0	104.5	178.8	304.7	520.2	−36.7
2005	410.7	358.8	51.9	317.8	92.9	429.1	−18.4
2006	318.0	369.1	−51.1	407.5	−89.5	541.9	−223.9
2007	483.9	382.5	101.4	531.0	−47.1	445.1	38.8
2008	626.3	400.1	226.2	576.0	50.3	407.8	218.5

Table 3: The weights of the three submodels.

Model	Weight
R-SPA model	22.9%
RBF neural networks model	37.2%
Autoregressive model	39.9%

Firstly, we use R-SPA, RBF, and AR models to forecast the annual precipitation from 2004 to 2008 of Beijing, respectively. And the outputs of the three models are shown in Table 2.

Based on the forecasted data of the three submodels, the weights of the three submodels in the combination model are obtained by using IRGA [19] and the weights of the three models are 22.9%, 37.2%, and 39.9%, respectively, and are given in Table 3.

Based on the obtained weights, we calculate the forecasted data of optimal weight combination model, and the output is represented in Table 4.

By comparing the output of the combination model with the output of the three submodels, we find that the error sum of squares of the combination model is apparently lower than that obtained for any other submodel. In this study, the value of the error sum of squares is regarded as the standard for judging the precision of the forecast of the annual precipitation of Beijing, and the improvement of the precision of the new weight combination model compared with three submodels is shown in Table 5.

Table 4: The forecasted data of the combination model.

Year	Measured value (mm)	Forecasted value (mm)
2004	483.5	360.6
2005	410.7	371.3
2006	318.0	451.9
2007	483.9	462.2
2008	626.3	468.1

Table 5: The improvement of the precision of the new weight combination model.

Compared models	The improved precision of new weight combination model
R-SPA model	22.6%
RBF model	47.4%
Autoregressive model	40.6%

So we conclude that the precision of the combination model is higher than that of three models in terms of the error sum of squares.

4. Conclusions

A new optimal weight combination model, based on the R-SPA, RBF, and AR models and one weight optimization model based on improved real-code genetic algorithm (IRGA), is proposed in this paper. The annual precipitation time series of Beijing from 1978 to 2008 are studied by using the new model. The main conclusions are given as follows.

(1) Three submodels, that is, R-SPA model, RBF model, and AR model, are tested to forecast the annual precipitation of Beijing, and the results suggest that R-SPA is better and RBF worst in the three models in terms of the error sum of squares. Different models have different precision for forecasting annual precipitation.

(2) The optimal weights can be obtained by use of IRGA in new optimal weight combination model. Application results of the combination model indicate the weights of the submodels can be appropriately confirmed and such method provides a new way to improve the prediction precision for forecasting complex precipitation time series.

(3) Compared with the results of R-SPA, RBF, and AR models, the proposed model can improve the forecast accuracy of precipitation in terms of the error sum of squares, and its improved precision is 22.6%, 47.4%, 40.6%, respectively. So the precision of the three submodels can be improved by establishing the new model in precipitation forecast.

(4) Because of the fail to avoid the drawbacks of three submodels completely, the accuracy of the combination model is inevitably affected. In the future, the accuracy of the combination model may be improved by applying some more advanced submodels.

Acknowledgments

The present work is supported by the Program for the National Basic Research Program of China (no. 2010CB951104), the Project of National Natural Science Foundation of China (nos. 50939001 and 51079004), the Specialized Research Fund for the Doctoral Tutor Program of Higher Education (no. 20100003110024), and the Program for Changjiang Scholars and Innovative Research Team in University (no. IRT0809).

References

[1] X. H. Yang, D. X. She, Z. F. Yang, Q. H. Tang, and J. Q. Li, "Chaotic bayesian method based on multiple criteria decision making (MCDM) for forecasting nonlinear hydrological time series," *International Journal of Nonlinear Sciences and Numerical Simulation*, vol. 10, no. 11-12, pp. 1595–1610, 2009.

[2] M. Li, C. Cattani, and S. Y. Chen, "Viewing sea level by a one-dimensional random function with long memory," *Mathematical Problems in Engineering*, vol. 2011, Article ID 654284, 13 pages, 2011.

[3] K. W. Chau, "Particle swarm optimization training algorithm for ANNs in stage prediction of Shing Mun River," *Journal of Hydrology*, vol. 329, no. 3-4, pp. 363–367, 2006.

[4] X. H. Yang, X. J. Zhang, X. X. Hu, Z. F. Yang, and J. Q. Li, "Nonlinear optimization set pair analysis model (NOSPAM) for assessing water resource renewability," *Nonlinear Processes in Geophysics*, vol. 18, no. 5, pp. 599–607, 2011.

[5] K. W. Chau, C. L. Wu, and Y. S. Li, "Comparison of several flood forecasting models in Yangtze River," *Journal of Hydrologic Engineering*, vol. 10, no. 6, pp. 485–491, 2005.

[6] J. X. Xu, Y. D. Liu, Z. Z. Zhang, and Y. B. Li, "Ordinal-set pair prediction model and application in Liao river basin," in *Computer Informatics Cybernetics and Applications*, vol. 1 of *Lecture Notes in Electrical Engineering 107*, chapter 42, pp. 395–402, 2012.

[7] D. Broomhead and D. Lowe, "Multivariable functional interpolation and adaptive networks," *Complex Systems*, vol. 2, pp. 321–355, 1988.

[8] M. Alp and H. K. Cigizoglu, "Suspended sediment load simulation by two artificial neural network methods using hydro meteorological data," *Environmental Modelling & Software*, vol. 22, no. 1, pp. 2–13, 2007.

[9] Q. Duan, N. K. Ajami, X. Gao, and S. Sorooshian, "Multi-model ensemble hydrologic prediction using Bayesian model averaging," *Advances in Water Resources*, vol. 30, no. 5, pp. 1371–1386, 2007.

[10] J. M. Bates and C. W. J. Granger, "The combination of forecasts," *Operational Research Quarterly*, vol. 20, no. 4, pp. 451–468, 1969.

[11] J. P. Dickinson, "Some statistical results in the combination of forecasts," *Operational Research Quarterly*, vol. 24, no. 2, pp. 253–260, 1973.

[12] J. P. Dickinson, "Some comments on the combination of forecasts," *Operational Research Quarterly*, vol. 26, no. 1, pp. 205–210, 1975.

[13] P. Newbold and C. W. J. Granger, "Experience with forecasting univariate time series and the combination of forecasts," *Journal of the Royal Statistical Society A*, vol. 137, no. 2, pp. 131–146, 1974.

[14] M. Li and W. Zhao, "Visiting power laws in cyber-physical networking systems," *Mathematical Problems in Engineering*, vol. 2012, Article ID 302786, 13 pages, 2012.

[15] A. Y. Shamseldin and K. M. O'Connor, "A real-time combination method for the outputs of different rainfall-runoff models," *Hydrological Sciences Journal*, vol. 44, no. 6, pp. 895–912, 1999.

[16] A. E. Raftery, F. Balabdaoui, T. Gneiting, and M. Polakowski, "Using Bayesian model averaging to calibrate forecast ensembles," *Monthly Weather Review*, vol. 133, no. 5, pp. 1155–1174, 2005.

[17] C. T. Cheng, C. P. Ou, and K. W. Chau, "Combining a fuzzy optimal model with a genetic algorithm to solve multi-objective rainfall-runoff model calibration," *Journal of Hydrology*, vol. 268, no. 1–4, pp. 72–86, 2002.

[18] N. K. Ajami, Q. Duan, X. Gao, and S. Sorooshian, "Multi-model combination techniques for hydrological forecasting: application to distributed model intercomparison project results," *Journal of Hydrometeorology*, vol. 7, no. 8, pp. 755–768, 2006.

[19] X. H. Yang, Y. N. Guo, Y. Q. Li, and L. H. Geng, "Projection pursuit hierarchy model based on chaos real-code genetic algorithm for river health assessment," *Nonlinear Science Letters C*, vol. 1, no. 1, pp. 1–13, 2011.

[20] A. Y. Shamseldin, K. M. O'Connor, and G. C. Liang, "Methods for combining the outputs of different rainfall-runoff models," *Journal of Hydrology*, vol. 197, no. 1–4, pp. 203–229, 1997.
[21] N. Muttil and K. W. Chau, "Neural network and genetic programming for modelling coastal algal blooms," *International Journal of Environment and Pollution*, vol. 28, no. 3-4, pp. 223–238, 2006.
[22] A. M. Taurino, C. Distante, P. Siciliano, and L. Vasanelli, "Quantitative and qualitative analysis of VOCs mixtures by means of a microsensors array and different evaluation methods," *Sensors and Actuators B*, vol. 93, no. 1–3, pp. 117–125, 2003.
[23] I. Vilibic and N. Leder, "Long-term variations in the Mediterranean sea level calculated by spectral analysis," *Oceanologica Acta*, vol. 19, no. 6, pp. 599–607, 1996.
[24] D. H. Fitzpatrick and S. B. Caroline, "Spectral analysis of pressure variations during combined air and water backwash of rapid gravity filters," *Water Research*, vol. 33, no. 17, pp. 3666–3672, 1999.
[25] P. J. Brockwell and A. D. Richard, *Time Series Theory and Methods*, Springer; Chep, Berlin, Germany, 2001.
[26] G. M. Morris, D. S. Goodsell, R. S. Halliday et al., "Automated docking using a Lamarckian genetic algorithm and an empirical binding free energy function," *Journal of Computational Chemistry*, vol. 19, no. 14, pp. 1639–1662, 1998.
[27] K. Deb, "An efficient constraint handling method for genetic algorithms," *Computer Methods in Applied Mechanics and Engineering*, vol. 186, no. 2–4, pp. 311–338, 2000.
[28] X. B. Hu, M. S. Leeson, and E. L. Hines, "An effective genetic algorithm for network coding," *Computers and Operations Research*, vol. 39, no. 5, pp. 952–963, 2012.

Hindawi Publishing Corporation
Mathematical Problems in Engineering
Volume 2012, Article ID 242043, 14 pages
doi:10.1155/2012/242043

Research Article

A Multiplicative Noise Removal Approach Based on Partial Differential Equation Model

Bo Chen, Jin-Lin Cai, Wen-Sheng Chen, and Yan Li

College of Mathematics and Computational Science, Shenzhen University, Shenzhen 518060, China

Correspondence should be addressed to Wen-Sheng Chen, chenws@szu.edu.cn

Received 26 February 2012; Accepted 23 March 2012

Academic Editor: Ming Li

Multiplicative noise, also known as speckle noise, is signal dependent and difficult to remove. Based on a fourth-order PDE model, this paper proposes a novel approach to remove the multiplicative noise on images. In practice, Fourier transform and logarithm strategy are utilized on the noisy image to convert the convolutional noise into additive noise, so that the noise can be removed by using the traditional additive noise removal algorithm in frequency domain. For noise removal, a new fourth-order PDE model is developed, which avoids the blocky effects produced by second-order PDE model and attains better edge-preserve ability. The performance of the proposed method has been evaluated on the images with both additive and multiplicative noise. Compared with some traditional methods, experimental results show that the proposed method obtains superior performance on different PSNR values and visual quality.

1. Introduction

Image denoising plays an important role in the areas of image processing. A real recorded image may be distorted by many expected or unexpected random factors, of which random noise is an unavoidable one [1, 2]. The objective of image denoising or filtering is to recover the true image from the noisy one. One of the challenges during the denoising process is to preserve and enhance the important features. For images, edge is one of the most universal and crucial features. Denoising via linear filters normally does not give satisfactory performance since both noises and edges contain high frequencies. Therefore, some nonlinear filters [3–18] have been proposed. Median filter [1] is one of the classical examples. Wavelet-based image filters [19–22] are developing quickly. PDE-based nonlinear diffusion filters [23–26] also make a hit on image denoising. One of PDE-based methods is the famous total variation model (TVM) [27–35]. TVM has been improved in theory and algorithm continuously.

Recently, Kim [23] proposed a model called $\alpha\beta\omega$(ABO)-model by hybridizing a nonconvex variant of the TVM, the motion by mean curvature (MMC) [29], and Perona-Malik model [4] to deal with the mixture of the impulse and Gaussian noises reliably. In [23], they apply the essentially nondissipative difference (ENoD) schemes [5, 6] for the MMC component to eliminate the impulse noise with a minimum (ideally no) introduction of dissipation. Many denoising methods are also employed in medical image processing [36–39].

Due to the coherent nature of some complicated image acquisition processes, such as ultrasound imaging, synthetic aperture radar (SAR) and sonar (SAS), and laser imaging, the standard additive noise model, so prevalent in image processing, is inadequate. Instead, multiplicative noise models, that is, in which the noise field is multiplied by (not added to) the original image, provide an accurate description of coherent imaging systems [40–42]. Multiplicative noise is naturally dependent on the image data. Various adaptive filters [43, 44] for multiplicative noise removal have been proposed. Experiments have shown that filtering methods work well when the multiplicative noise is weak.

In this paper, a new fourth-order PDE model is introduced by improving the original fourth-order PDE model [24] in order to get high fidelity of the denoised images. To solve the model efficiently and reliably, we suggest a simple and symmetrical difference schemes. Median filter is exploited to alleviate the speckle effects in the processed image. At the same time, a new multiplicative noise removal algorithm based on fourth-order PDE model is proposed for the restoration of noisy image. To apply the proposed model for removal of multiplicative noise, the Fourier transform is used to change convolution into product; meanwhile, the logarithmic transformation is used to convert multiplicative noise into additive one. Experimental results show that the proposed method gets nice result in restoring images, especially in edge preservation and enhancement.

The rest of this paper is organized as follows. In Section 2 we investigate a general model of multiplicative noise. Total variation model and its discretization are introduced in Section 3. In order to avoid the blocky effects of second-order PDE model and preserve edges, a new fourth-order PDE denoising model is proposed in Section 4. Section 5 is devoted to a study of multiplicative noise removal method, and an algorithm based on fourth-order PDE model is developed. Numerical results are presented in Section 6. We summarize our conclusions in Section 7.

2. Multiplicative Noise Model

Noise removal or reduction is very important in image processing community. The objection of image denoising or filtering is to recover the true image from a noisy one. There are different noise types in real world. Multiplicative noise is common beside additive noise. Quality of images may degenerate while images' obtaining, transferring, and storage. The movement of objects, the defects of the imaging system, the noise of the inherent record equipment, and external disturbance also cause the image noise. Under the assumption that imaging system is linear translation invariance system, we can use the following degradation model to describe the multiplicative noise images:

$$u_0(x,y) = h_d(x,y) * f(x,y) + n(x,y), \tag{2.1}$$

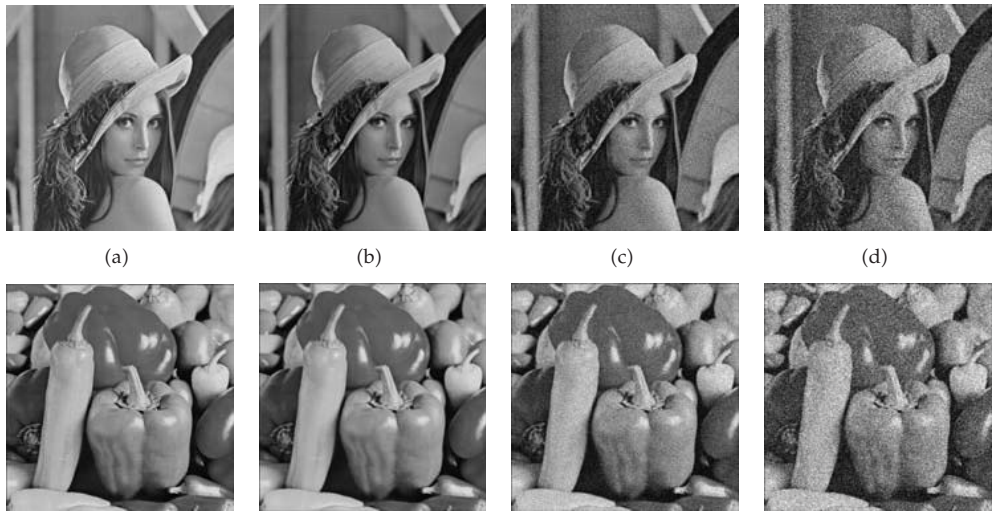

Figure 1: Multiplicative noise images. (a) Original "Lena" image; (b) image convolution with template 3 × 3 of (a); (c) image with Gaussian white noise of mean 0 and variance 0.01; (d) image with Gaussian white noise of mean 0 and variance 0.05; (e) original "vegetables" image; (f) image convolution with template 3 × 3 of (a); (g) image with Gaussian white noise of mean 0 and variance 0.01; (h) image with Gaussian white noise of mean 0 and variance 0.05.

where f is the ideal image, u_0 is the noised image, n denotes the additive noise with mean 0 and variance σ^2, $*$ denotes convolution operation, h_d denotes the point spread function (PSF), andGaussian function can be considered as one of the classical PSF:

$$G_d(x,y) = \exp\left\{\frac{-(x^2+y^2)}{2\sigma^2}\right\}, \tag{2.2}$$

Therefore, the synthesized images with multiplicative noise in this paper are generated for ideal images convolution with 2D Gaussian kernels and then noised with additive Gaussian white noise. An example is shown in Figure 1. h_d in (2.1) is chosen as (2.2), namely Gaussian function templates. 3 × 3 Gaussian function template $T_3 = (1/16) \times \begin{bmatrix} 1 & 2 & 1 \\ 2 & 4 & 2 \\ 1 & 2 & 1 \end{bmatrix}$ is employed here.

3. Total Variation Model

In order to recover the true image f as much as possible and/or to find a new image u in which the information of interest such as object boundary in the image is more obvious and/or more easily extracted, we will discuss PDE-based image denoising in this section. Second-order PDE models have been studied as a useful tool for image denoising. The classical model of them is total variation model (TVM) [27], and we will introduce it.

TVM was first proposed by Rudin et al. [27]. It is now one of the most successful tools in image restoration. TVM has a simple fixed filter structure. In terms of the mathematical foundation, unlike most statistical filters, TVM is based on functional analysis and geometry.

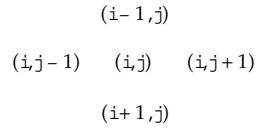

Figure 2: Four neighboring image structure.

The additive noise removal problem is converted to energy function minimization problem as below:

$$\begin{aligned} u &= \operatorname{argmin}\{E_{\mathrm{TV}}(u)\} \\ E_{\mathrm{TV}}(u) &= \iint_{\Omega} |\nabla u| dxdy + \frac{\lambda}{2} \iint_{\Omega} (u_0 - u)^2 dxdy, \end{aligned} \tag{3.1}$$

where Ω denotes image domain, and λ is Lagrange multiplier. The selection of the parameter λ is very important for the smoothing result. The corresponding Euler-Lagrange equation is

$$-\nabla \cdot \left(\frac{\nabla u}{|\nabla u|} \right) + \lambda (u - u_0) = 0, \tag{3.2}$$

and the steepest descent marching gives

$$\frac{\partial u}{\partial t} = \nabla \cdot \left(\frac{\nabla u}{|\nabla u|} \right) - \lambda (u - u_0). \tag{3.3}$$

To avoid singularities in flat regions or at local extreme, $|\nabla u|$ in (3.2) is regularized to $|\nabla u|_{\varepsilon} = \sqrt{|\nabla u|^2 + \varepsilon^2}$ for a small positive parameter ε. Chan et al. [30] deduce discrete iterative equation of TV model as follows:

$$u_{\alpha}^{n+1} = \sum_{\beta \in N(\alpha)} h_{\alpha\beta} u_{\beta}^{n} + h_{\alpha\alpha} u_{\alpha}^{0}, \tag{3.4}$$

where u_{α}^{0} denotes the pixel value at node α in the noisy image, n denotes iteration times, u_{α}^{n} denotes the image pixel value after n+1 iterations, $N(\alpha)$ denotes field of node α (see Figure 2). The filter coefficients $h_{\alpha\alpha}$ and $h_{\alpha\beta}$ are given by

$$\begin{aligned} h_{\alpha\alpha} &= \frac{\lambda}{\lambda + \sum_{\beta \in N(\alpha)} w_{\alpha\beta}}, \\ h_{\alpha\beta} &= \frac{w_{\alpha\beta}}{\lambda + \sum_{\beta \in N(\alpha)} w_{\alpha\beta}}, \end{aligned} \tag{3.5}$$

$$w_{\alpha\beta} = \frac{g_\alpha^n + g_\beta^n}{2h^2},$$
$$g_\alpha^n = \frac{1}{|\nabla u_\alpha^n|}, \tag{3.6}$$

$$|\nabla u_\alpha^n| \approx \sqrt{\frac{1}{2h^2} \sum_{\beta \in N(\alpha)} \left(u_\beta^n - u_\alpha^n\right)^2}. \tag{3.7}$$

Here, for any node $\alpha h_{\alpha\alpha} + \sum_{\beta \in N(\alpha)} h_{\alpha\beta} = 1$.

In conclusion, TV denoising algorithm steps can be summarized as follows:

(1) to assign parameter λ and a;

(2) compute the local variation $|\nabla u_\alpha^n|$ by (3.7);

(3) compute respectively g_α^n and $w_{\alpha\beta}^n$ (3.6);

(4) compute the filter coefficients $h_{\alpha\alpha}$ and $h_{\alpha\beta}$ by (3.5);

(5) calculate iterative equation (3.4).

For TV filtering process, the computational cost can be reduced by the algorithm. TVM not only can remove noise but also can keep the image edge information. Some experimental results are shown in Figure 3. TVM is better than the traditional denoising methods not only in PSNR values but also in visual quality.

4. A New Fourth-Order PDE Denoising Model

In order to avoid the blocky effects (seen in Figure 3(f) and Figure 4(f)) widely seen in images processed by anisotropic diffusion while preserve edges, You and Kaveh [24] proposed a fourth-order PDE for noise removal. Motivated by [24] and TVM, we proposed a novel model in [25, 26]. The new approach combines the advantages of the famous TVM and original fourth-order PDE model. It can avoid the blocky effects and get high fidelity (improve the quality of the processed image), which is important for image filter application (see Figure 4).

Consider the energy function as follows:

$$E(u) = \iint_\Omega \left(f\left(\left|\nabla^2 u\right|\right) + \frac{\lambda}{2}\left|u - u^0\right|^2 \right) dxdy, \tag{4.1}$$

where Ω is the image domain and $\lambda > 0$ is a parameter similar as in TVM. u^0 is the noisy image. ∇^2 denotes Laplacian operator and we require f is an increasing function and bigger than zero. Therefore, the minimization of the functional is equivalent to smoothing the image as measured by $|\nabla^2 u|$.

The corresponding Euler-Lagrange equation is

$$\nabla^2\left(f'\left(\left|\nabla^2 u\right|\right) \operatorname{sign}\left(\nabla^2 u\right)\right) + \lambda \cdot \left(u - u^0\right) = 0, \tag{4.2}$$

Figure 3: Detail of restoring noisy Elaine image (512 × 512) with different filters. (a) Original image; (b) noisy image, PSNR = 20.0742; (c) median, PSNR = 26.4554; (d) averaging, PSNR = 27.6876; (e) wiener, PSNR = 26.7866; (f) TVM, PSNR = 30.0919.

where sign is the signed distance function, so (4.2) can be written as

$$\nabla^2\left(f'\left(\left|\nabla^2 u\right|\right)\frac{\nabla^2 u}{|\nabla^2 u|}\right) + \lambda\cdot\left(u-u^0\right)=0. \tag{4.3}$$

If we define $c(s)=f'(s)/s$, which is

$$\nabla^2\left(c\left(\left|\nabla^2 u\right|\right)\nabla^2 u\right)+\lambda\cdot\left(u-u^0\right)=0, \tag{4.4}$$

therefore, the Euler equation may be solved through the following gradient descent procedure:

$$\frac{\partial u}{\partial t}=-\nabla^2\left(c\left(\left|\nabla^2 u\right|\right)\nabla^2 u\right)-\lambda\cdot\left(u-u^0\right). \tag{4.5}$$

So we can discretize and iterate to solve the equation.

To solve the model in (4.5) efficiently and reliably, we propose a simple symmetric difference algorithm based on four neighboring systems (seen in Figure 2).

We calculate Laplacian of the image intensity function as

$$\nabla^2 u|_{i,j} = \frac{u_{i+1,j} + u_{i-1,j} + u_{i,j+1} + u_{i,j-1} - 4u_{i,j}}{h^2}, \tag{4.6}$$

where h is space grid size. Given a time step Δt, (4.5) can be discretized as

$$u^{n+1} = u^n - \Delta t\left(\nabla^2\left(c\left(\left|\nabla^2 u^n\right|\right)\nabla^2 u^n\right) + \lambda\left(u^n - u^0\right)\right). \tag{4.7}$$

Similar as [24], we define

$$c(s) = \frac{1}{1 + (s/k)^2}, \tag{4.8}$$

where k is a parameter.

So the symmetric fourth-order PDE denoising algorithm is as follows.

Step 1. Initialization: select the constants λ, k, h, Δt and choose an initial function (image) u.

Step 2. Compute $\nabla^2 u$ and $|\nabla^2 u|$ using (4.6).

Step 3. Compute $c(|\nabla^2 u^n|)$ using (4.8).

Step 4. Update u using (4.7).

Step 5. Repeat Steps 2 and 4 until convergence.

Figure 4 shows the results for a medical image with Gaussian white noise of mean 0 and variance 0.01. Median filter is applied to alleviating the speckle effects in the processed image. We can see from Figure 4 that the new fourth-order PDE method obtains the biggest PSNR values in all filter method and can avoid the block effect in Figure 4(f). At the same time, the last result of the new method (Figure 4(j), PSNR = 28.4746 dB) is better than the original fourth-order PDE method (Figure 4(b), PSNR = 27.7743 dB) not only in PSNR values but also in visual quality.

5. Multiplicative Noise Removal Algorithm Based on Fourth-Order PDE Model

Objective of most traditional algorithms is to deal with additive noise, but the result is not ideal for the big multiplicative noise. This paper proposes a new multiplicative noise removal algorithm and combines the denoising algorithm with image frequency domain. The whole process is as follows.

Firstly, remove the additive noise n in model (2.1) by denoising algorithm, then the model is simplified as

$$u_0(x, y) = h_d(x, y) * f(x, y). \tag{5.1}$$

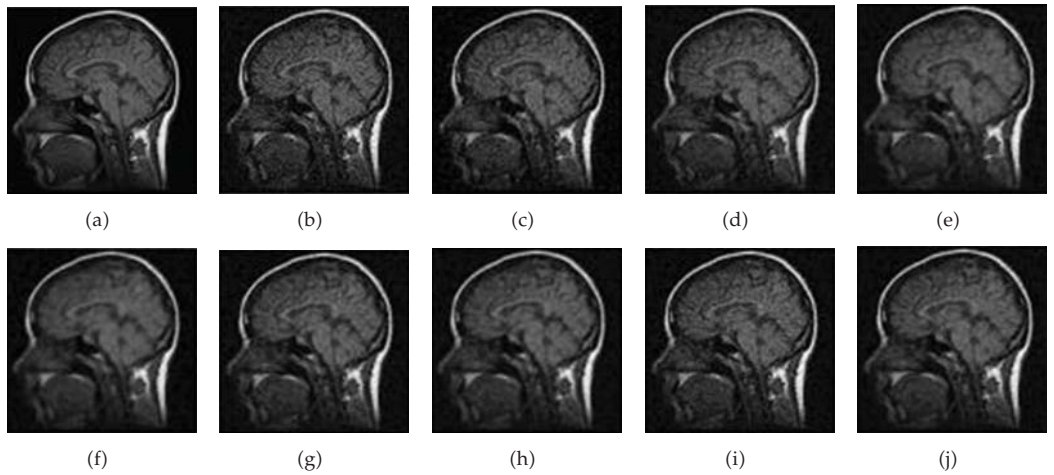

Figure 4: Detail of the denoising medical image with different methods. (a) A slice of an MRI brain image; (b) image with Gaussian white noise of mean 0 and variance 0.01, PSNR = 21.0980; (c) denoised with median filter (template: 3 × 3), PSNR = 27.3774; (d) denoised with averaging filter (template: 3 × 3), PSNR = 27.7701; (e) denoised with Wiener filter (template: 5 × 5), PSNR = 27.8061; (f) denoised with TVM (λ = 0.01, 10 iterations), PSNR = 24.9200; (g) results with the original fourth-order PDE model, PSNR = 27.6730; (h) denoised (g) with Median filter, PSNR = 27.7743; (i) results with the new fourth-order PDE model, PSNR = 26.9902; (j) denoised (i) with median filter, PSNR = 28.4746.

Secondly, convolution in (5.1) changes to product according to fast Fourier transform (FFT):

$$U(u,v) = H_d(u,v) \cdot F(u,v), \tag{5.2}$$

where $U(u,v)$, $H_d(u,v)$, and $F(u,v)$ denote FFT of $u_0(x,y)$, $h_d(x,y)$, and $f(x,y)$, respectively.

Thirdly, (5.2) can be rewritten by logarithmic transformation (LN) as follows:

$$\ln U(u,v) = \ln F(u,v) + \ln H_d(u,v). \tag{5.3}$$

Fourthly, $\ln H_d(u,v)$ in (5.3) can be regarded as additive noise in image frequency domain, and we can remove it by some additive denoising algorithms, such as TVM and fourth-order PDE model. Therefore,

$$\ln U(u,v) = \ln F(u,v). \tag{5.4}$$

Fifthly, by exponential transform (EXP), (5.4) is rewritten as

$$U(u,v) = F(u,v). \tag{5.5}$$

Sixthly, by inverse fast Fourier transform for (5.5), we can get

$$u = f, \tag{5.6}$$

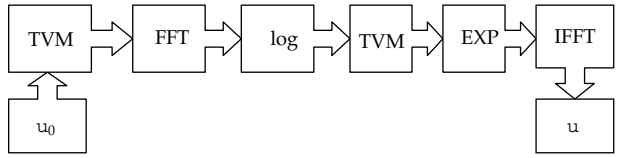

Figure 5: Structure of multiplicative noise removal algorithm based on the total variational model.

Table 1: PSNR values obtained with difference filters (template 3 × 3).

Noise level	PSNR(dB) for Lena/vegetables image				
	Noisy image	Average filter	Median filter	TV filter	MNRATV
0.05	13.73/13.67	22.08/22.15	23.66/23.56	25.06/25.26	**25.47/26.04**
0.10	11.40/11.39	19.71/19.74	21.32/21.25	22.48/22.48	**23.81/24.14**
0.15	10.25/1024	18.36/18.46	19.85/19.80	20.64/20.74	**22.64/22.92**
0.20	9.54/9.52	17.46/17.50	18.78/18.66	19.44/19.40	**21.74/21.78**
0.25	9.05/9.05	16.84/16.87	17.96/17.83	18.54/18.56	**21.05/21.12**
0.30	8.69/8.68	16.40/16.49	17.29/17.16	17.86/17.85	**20.46/20.51**
0.35	8.42/8.40	16.02/15.98	16.67/16.62	17.29/17.33	**19.93/20.02**
0.40	8.19/8.20	15.68/15.71	16.24/16.40	16.86/16.90	**19.56/19.62**

where u in (5.6) is considered as the denoised image got by our algorithm. There are two denoising processes in the multiplicative noise removal framework, that is, the first step and the fourth step, if we select the denoising methods all as TVM removal framework of all as TVM, structure of multiplicative noise removal algorithm can be seen below.

In Figure 5, multiplicative noise removal algorithm considers the natural image noise as two parts, convolution changes to product by Fourier transform and product changes to summation by logarithm, then noise can be removal according to total variation model and the image is rebuilt.

6. Experimental Results

We use MATLAB 7.10 (R2010a) as the tool to carry out all algorithms a PC equipped with an Intel Core i3-2330 M CPU at 2.20 GHz and 4G RAM memory and Windows 7 operating system. Denoising performance is evaluated using the PSNR (peak signal-to-noise ratio) in dB which defined by

$$\mathrm{PSNR} = 10 \cdot \log_{10} \frac{R^2 M \cdot N}{\left[f(x,y) - u(x,y)\right]^2}, \tag{6.1}$$

where $u(x,y)$ denotes the restored image with respect to the original image $f(x,y)$, $R = 255$, and M and N are the wide and high of image.

The effectiveness of the new multiplicative noise removal algorithm is based on the total variation model (MNRATV) shown in Table 1, Figures 6 and 7. The sizes of the noisy "Lena" and "vegetables" images is all 512 × 512. The numerical results are listed in Table 1 and compared in Figure 6. Visual quality is shown in Figure 7. Experimental results show that

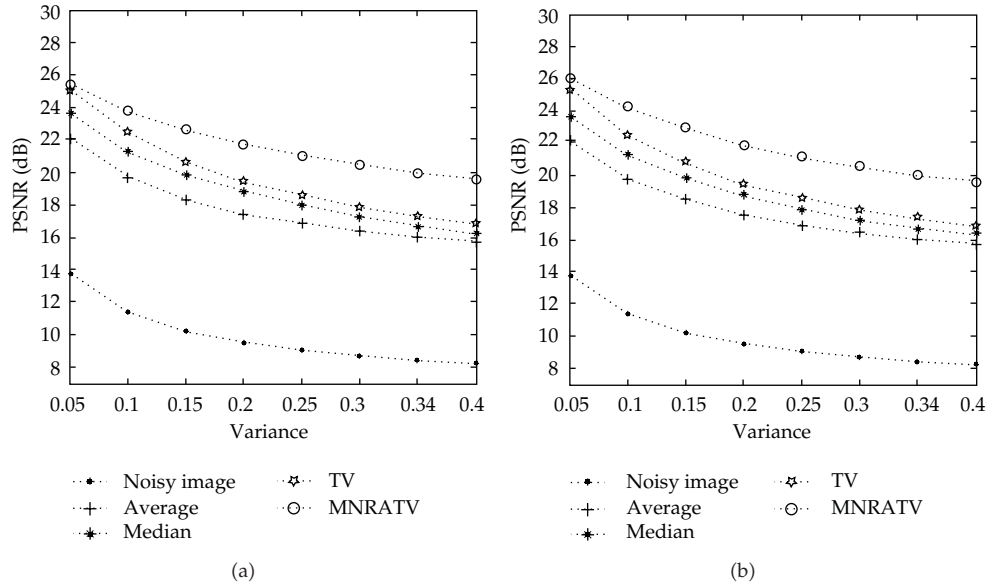

Figure 6: PSNR values in Table 1 plotted together. (a) Lena image; (b) vegetables image.

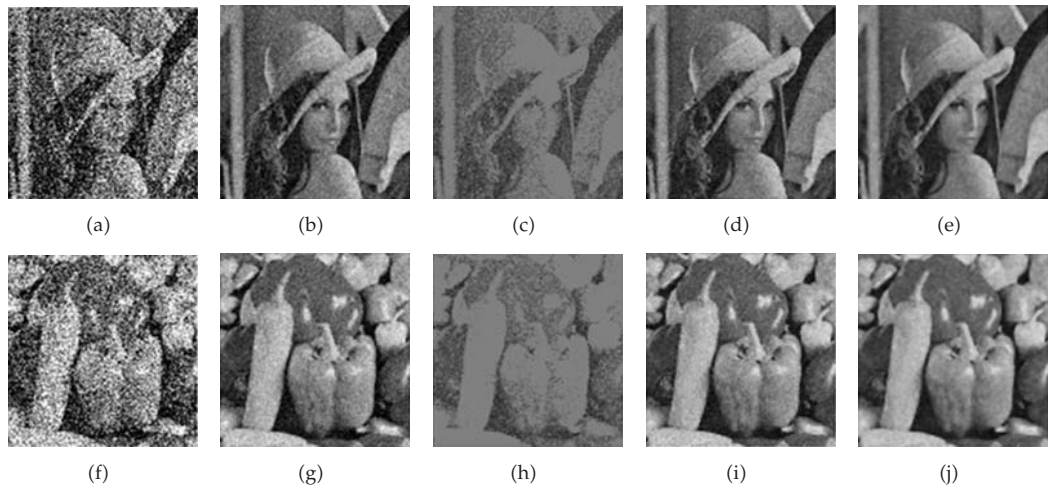

Figure 7: Results of difference noise removal algorithms for noisy "Lena" and "vegetables" images. (a) The multiplicative noisy image; (b) results of Median filter algorithm; (c) results of Averaging filter algorithm; (d) results of TVM; (e) results of MNRATV.

the new method is available. It is better than the traditional denoising algorithm not only in PSNR values but also in visual quality.

We can see from Table 1 and Figure 6 that the PSNR values of the restored images by MNRATV are higher than restored images by all the other methods. It is little bigger than those by TVM when the noise level is lower. The results of MNRATV and TVM are shown in Figure 8.

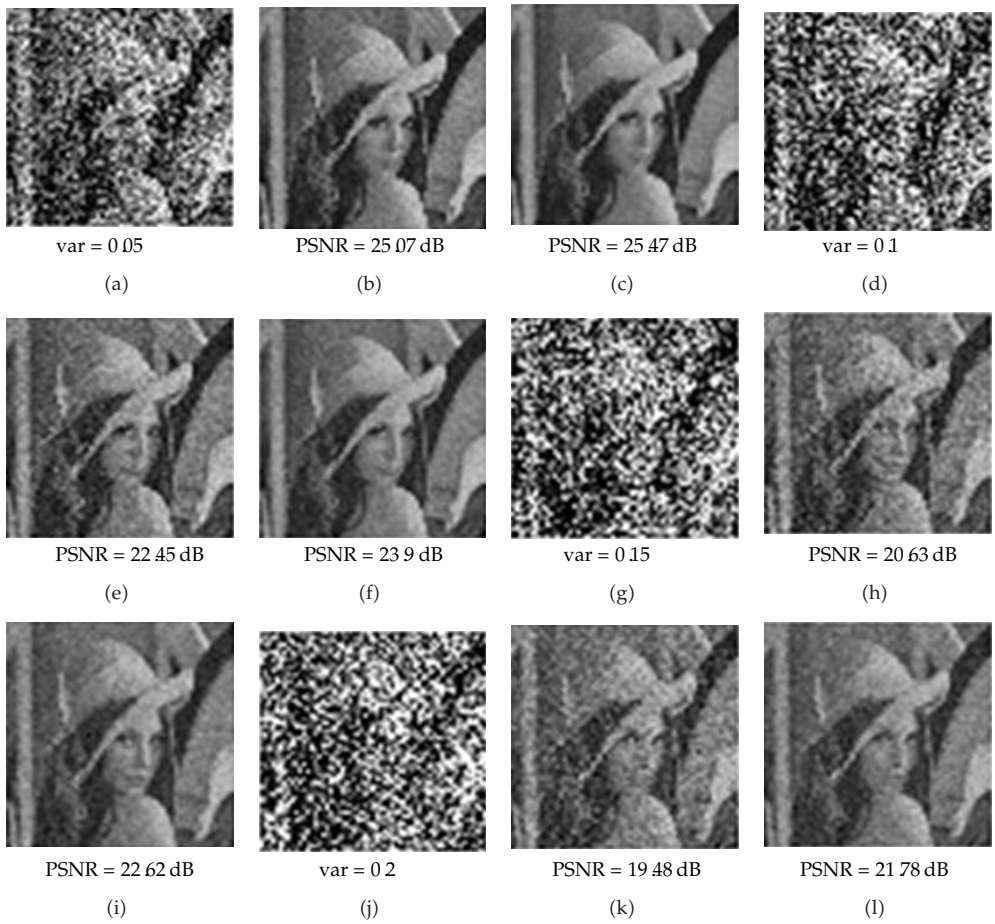

Figure 8: Results of MNRATV and TVM. Column 1 is the multiplicative noise with variance 0.05, 0.10, 0.15, and 0.20; respectively, Column 2 is the corresponding results with TVM, and Column 3 is the corresponding results with MNRATV.

Table 2: Different multiplicative noise removal method constructed with exist model.

Denoising method 1	Denoising method 2	New method
TVM	TVM	MNRA1(MNRATV)
FPDE	TVM	MNRA2
TVM	FPDE	MNRA3
FPDE	FPDE	MNRA4

There are two denoising methods in the first step and fourth step of the multiplicative noise removal framework; we can call it denoising method 1 and denoising method 2. If they are all chosen as TVM, then the whole framework in Figure 5 is called MNRA1 method, which is called MNRATV before. TVM and fourth-order PDE (FPDE) model which we introduced in Section 4 constitutes four methods. Details are shown in Table 2.

Different methods are employed to remove the noisy Lena image with different variance. PSNR values are shown in Table 3. Seen from Table 3, TVM or FPDE directly is not

Table 3: PSNR values obtained with difference algorithm for Lena image.

variance	PSNR(dB)						
	Noisy image	TVM	FPDE	MNRA1	MNRA2	MNRA3	MNRA4
0.05	13.6935	25.0739	24.0739	25.4833	25.6347	**25.8190**	25.7443
0.10	11.4336	22.4860	22.3232	23.9355	**24.2382**	23.8612	23.9770
0.15	10.2712	20.7197	20.7700	22.7277	**23.2101**	22.4985	22.7830
0.20	9.5307	19.4144	19.6830	21.6790	**22.4667**	21.3851	21.7750
0.25	9.0769	18.6046	18.8871	21.0824	**21.8927**	20.6409	21.0582
0.30	8.6769	17.7913	18.0713	20.3577	**21.2616**	19.9417	20.3536
0.35	8.4000	17.2305	17.4785	19.8687	**20.7377**	19.3328	19.7712
0.40	8.1948	16.8051	16.9839	19.5339	**20.3135**	19.1239	19.4284

good because of the multiplicative noise type. Median filter cannot be exploited as denoising method 2 since complex number is generated by the Fourier transform. Denoising method 1 is selected as FPDE in MNRA2, and it gets better results.

7. Conclusion

PDE models have been widely applied in image processing community especially in image denoising. However, traditional PDE-based methods have some drawbacks unless the governing equations are both incorporating appropriate parameters and discretized by suitable numerical schemes. In this paper, a new fourth-order PDE model is introduced by improving the original fourth-order one [24] in order to avoid the blocky effect. To solve the model efficiently and reliably, we suggest a symmetrically difference schemes. Median filtering is exploited to alleviate the speckle effects in the processed image in succession. Accordingly, a new multiplicative noise removal algorithm based on the proposed fourth-order PDE model is presented. To remove the multiplicative noise, the convolution is changed into a product by applying the Fourier transform. Furthermore, the multiplicative noise is converted into the additive one by using a logarithmic transformation. Then the noise can be removed by applying the proposed PDE model. Experimental results have shown the effectiveness of the proposal.

Acknowledgments

This paper is partially supported by NSFC (61070087, 61105130), the Natural Science Foundation of Guangdong Province (S2011040000433, S2011040004017), the Science & Technology Planning Project of Shenzhen City (JC200903130300A, JYC200903250175A), and the Opening Project of Guangdong Province Key Laboratory of Computational Science of Sun Yat-Sen University (201106002) and Teaching Reform and Research Project for Young Teachers of Shenzhen University (JG2010118). The authors would like to thank the Key Laboratory of Medical Image Processing in Southern Medical University for providing original medical images.

References

[1] Q. Y. Ruan and Y. Z. Ruan, *Digital Image Processing*, Publishing House of Electronics Industry, Beijing, China, 2nd edition, 2004.

[2] Q. H. Chang and T. Yang, "A lattice Boltzmann method for image denoising," *IEEE Transactions on Image Processing*, vol. 18, no. 12, pp. 2797–2802, 2009.

[3] C. Chaux, L. Duval, A. Benazza-Benyahia, and J.-C. Pesquet, "A nonlinear Stein-based estimator for multichannel image denoising," *IEEE Transactions on Signal Processing*, vol. 56, no. 8, part 2, pp. 3855–3870, 2008.

[4] P. Perona and J. Malik, "Scale-space and edge detection using anisotropic diffusion," *IEEE Transactions on Pattern Analysis and Machine Intelligence*, vol. 12, no. 7, pp. 629–639, 1990.

[5] S. Osher and J. A. Sethian, "Fronts propagating with curvature-dependent speed: algorithms based on Hamilton-Jacobi formulations," *Journal of Computational Physics*, vol. 79, no. 1, pp. 12–49, 1988.

[6] S. Osher and C. W. Shu, "High-order essentially nonoscillatory schemes for Hamilton-Jacobi equations," *SIAM Journal on Numerical Analysis*, vol. 28, no. 4, pp. 907–922, 1991.

[7] B. Chen, Y. Li, and J.-L. Cai, "Noisy image segmentation based on nonlinear diffusion equation model," *Applied Mathematical Modelling*, vol. 36, no. 3, pp. 1197–1208, 2012.

[8] Z. Liao, S. Hu, and W. Chen, "Determining neighborhoods of image pixels automatically for adaptive image denoising using nonlinear time series analysis," *Mathematical Problems in Engineering*, vol. 2010, Article ID 914564, 14 pages, 2010.

[9] S. Hu, Z. Liao, D. Sun, and W. Chen, "A numerical method for preserving curve edges in nonlinear anisotropic smoothing," *Mathematical Problems in Engineering*, vol. 2011, Article ID 186507, 14 pages, 2011.

[10] M. Li, "Fractal time series—a tutorial review," *Mathematical Problems in Engineering*, vol. 2010, Article ID 157264, 26 pages, 2010.

[11] Z. Shang, L. Zhang, S. Ma, B. Fang, and T. Zhang, "Incomplete time series prediction using max-margin classification of data with absent features," *Mathematical Problems in Engineering*, vol. 2010, 14 pages, 2010.

[12] M. Freiberger, H. Egger, and H. Scharfetter, "Nonlinear inversion schemes for fluorescence optical tomography," *IEEE Transactions on Biomedical Engineering*, vol. 57, no. 11, pp. 2723–2729, 2010.

[13] Z. Liao, S. Hu, D. Sun, and W. Chen, "Enclosed Laplacian operator of nonlinear anisotropic diffusion to preserve singularities and delete isolated points in image smoothing," *Mathematical Problems in Engineering*, vol. 2011, Article ID 749456, 15 pages, 2011.

[14] M. Li and W. Zhao, "Visiting power laws in cyber-physical networking systems," *Mathematical Problems in Engineering*, vol. 2012, Article ID 302786, 13 pages, 2012.

[15] M. Li, C. Cattani, and S. Chen, "Viewing sea level by a one-dimensional random function with long memory," *Mathematical Problems in Engineering*, vol. 2011, Article ID 654284, 13 pages, 2011.

[16] F. Zhang, Y. M. Yoo, L. M. Koh, and Y. Kim, "Nonlinear diffusion in laplacian pyramid domain for ultrasonic speckle reduction," *IEEE Transactions on Medical Imaging*, vol. 26, no. 2, pp. 200–211, 2007.

[17] M. Ceccarelli, V. De Simone, and A. Murli, "Well-posed anisotropic diffusion for image denoising," *IEE Proceedings: Vision, Image and Signal Processing*, vol. 149, no. 4, pp. 244–252, 2002.

[18] M. Li, M. Scalia, and C. Toma, "Nonlinear time series: computations and applications," *Mathematical Problems in Engineering*, vol. 2010, Article ID 101523, 5 pages, 2010.

[19] L. X. Shen, M. Papadakis, I. A. Kakadiaris et al., "Image denoising using a tight frame," *IEEE Transaction on Image Processing*, vol. 15, no. 5, pp. 1254–1263, 2006.

[20] B. Chen and W.-S. Chen, "Noisy image segmentation based on wavelet transform and active contour model," *Applicable Analysis*, vol. 90, no. 8, pp. 1243–1255, 2011.

[21] T. Celik and K. Ma, "multitemporal image change detection using undecimated discrete wavelet transform and active contours," *IEEE Transactions on Geoscience and Remote Sensing*, vol. 49, no. 2, pp. 706–716, 2011.

[22] T. Celik and K. Ma, "Unsupervised change detection for satellite images using dual-tree complex wavelet transform," *IEEE Transactions on Geoscience and Remote Sensing*, vol. 48, no. 3, pp. 1199–1210, 2010.

[23] S. Kim, "PDE-based image restoration: a hybrid model and color image denoising," *IEEE Transaction on Image Processing*, vol. 15, no. 5, pp. 1163–1170, 2006.

[24] Y.-L. You and M. Kaveh, "Fourth-order partial differential equations for noise removal," *IEEE Transactions on Image Processing*, vol. 9, no. 10, pp. 1723–1730, 2000.

[25] B. Chen, W.-S. Chen, L.-W. Zhang et al., "Image restoration based on fourth-order PDE model," in *Proceedings of the IEEE International Conference on Natural Computation*, vol. 5, pp. 549–554, Jinan, China, 2008.

[26] B. Chen, P.-C. Yuen, J.-H. Lai, and W.-S. Chen, "Image segmentation and selective smoothing based on variational framework," *Journal of Signal Processing Systems*, vol. 54, pp. 145–158, 2009.

[27] L. Rudin, S. Osher, and E. Fatemi, "Nonlinear total variation based noise removel algorithms," *Physica D*, vol. 60, pp. 259–268, 1992.

[28] S. D. Babacan, R. Molina, and A. Katsaggelos, "Variational bayesian blind deconvolution using a total variation prior," *IEEE Transactions on Image Processing*, vol. 18, no. 1, pp. 12–26, 2009.

[29] L. Rudin and S. Osher, "Total variation based image restoration with free local constraints," in *Proceedings of the 1st IEEE International Conference on Image Processing*, vol. 1, pp. 31–35, 1994.

[30] T. F. Chan, S. Osher, and J. H. Shen, "The digital TV filter and Nonlinear Denoising," *IEEE Transaction on Image Processing*, vol. 10, no. 2, pp. 231–241, 2001.

[31] A. Beck and M. Teboulle, "Fast gradient-based algorithms for constrained total variation image denoising and deblurring problems," *IEEE Transactions on Image Processing*, vol. 18, no. 11, pp. 2419–2434, 2009.

[32] C. Drapaca, "A nonlinear total variation-based denoising method with two regularization parameters," *IEEE Transactions on Biomedical Engineering*, vol. 56, no. 3, pp. 582–586, 2009.

[33] M. Kumar and S. Dass, "A total variation-based algorithm for pixel-level image fusion," *IEEE Transactions on Image Processing*, vol. 18, no. 9, pp. 2137–2143, 2009.

[34] P. Rodríguez and B. Wohlberg, "Efficient minimization method for a generalized total variation functional," *IEEE Transactions on Image Processing*, vol. 18, no. 2, pp. 322–332, 2009.

[35] T. Zeng and M. Ng, "On the total variation dictionary model," *IEEE Transactions on Image Processing*, vol. 19, no. 3, pp. 821–825, 2010.

[36] B. C. Vemuri, M. Liu, S. Amari et al., "Total bregman divergence and its applications to DTI analysis," *IEEE Transactions on Medical Imaging*, vol. 30, no. 2, pp. 475–483, 2011.

[37] S. Ramani, P. Thevenaz, and M. Unser, "Regularized interpolation for noisy images," *IEEE Transactions on Medical Imaging*, vol. 29, no. 2, pp. 543–558, 2010.

[38] J. Yao, J. Chen, and C. Chow, "Breast tumor analysis in dynamic contrast enhanced MRI using texture features and wavelet transform," *IEEE Journal of Selected Topics in Signal Processing*, vol. 3, no. 1, pp. 94–100, 2009.

[39] M. Zibetti and A. R. De Pierro, "A new distortion model for strong inhomogeneity problems in Echo-Planar MRI," *IEEE Transactions on Medical Imaging*, vol. 28, no. 11, pp. 1736–1753, 2009.

[40] J. M. Bioucas-Dias and M. A. T. Figueiredo, "Multiplicative noise removal using variable splitting and constrained optimization," *IEEE Transactions on Image Processing*, vol. 19, no. 7, pp. 1720–1730, 2010.

[41] L. Rudin, P. Lions, and S. Osher, "Multiplicative denoising and deblurring: theory and algorithms," in *Geometric Level Set Methods in Imaging, Vision, and Graphics*, S. Osher and N. Paragios, Eds., pp. 103–120, Springer, New York, NY, USA, 2003.

[42] J. Goodman, "Some fundamental properties of speckle," *Journal of the Optical Society of America*, vol. 66, pp. 1145–1150, 1976.

[43] Y. Yu and S. T. Acton, "Speckle reducing anisotropic diffusion," *IEEE Transactions on Image Processing*, vol. 11, no. 11, pp. 1260–1270, 2002.

[44] K. Krissian, C.-F. Westin, R. Kikinis, and K. G. Vosburgh, "Oriented speckle reducing anisotropic diffusion," *IEEE Transactions on Image Processing*, vol. 16, no. 5, pp. 1412–1424, 2007.

Hindawi Publishing Corporation
Mathematical Problems in Engineering
Volume 2012, Article ID 862398, 19 pages
doi:10.1155/2012/862398

Research Article

Hypothesis Testing in Generalized Linear Models with Functional Coefficient Autoregressive Processes

Lei Song,[1] Hongchang Hu,[1] and Xiaosheng Cheng[2]

[1] *School of Mathematics and Statistics, Hubei Normal University, Huangshi 435002, China*
[2] *Department of Mathematics, Huizhou University, Huizhou 516007, China*

Correspondence should be addressed to Hongchang Hu, retutome@163.com

Received 28 January 2012; Accepted 25 March 2012

Academic Editor: Ming Li

The paper studies the hypothesis testing in generalized linear models with functional coefficient autoregressive (FCA) processes. The quasi-maximum likelihood (QML) estimators are given, which extend those estimators of Hu (2010) and Maller (2003). Asymptotic chi-squares distributions of pseudo likelihood ratio (LR) statistics are investigated.

1. Introduction

Consider the following generalized linear model:

$$y_t = g\left(x_t^T \beta\right) + \varepsilon_t, \quad t = 1, 2, \ldots, n, \tag{1.1}$$

where β is d-dimensional unknown parameter, $\{\varepsilon_t, t = 1, 2, \ldots, n\}$ are functional coefficient autoregressive processes given by

$$\varepsilon_1 = \eta_1, \qquad \varepsilon_t = f_t(\theta)\varepsilon_{t-1} + \eta_t, \quad t = 2, 3, \ldots, n, \tag{1.2}$$

where $\{\eta_t, t = 1, 2, \ldots, n\}$ are independent and identically distributed random variable errors with zero mean and finite variance σ^2, θ is a one-dimensional unknown parameter, and $f_t(\theta)$ is a real valued function defined on a compact set Θ which contains the true value θ_0 as

an inner point and is a subset of R^1. The values of θ_0 and σ^2 are unknown. $g(\cdot)$ is a known continuous differentiable function.

Model (1.1) includes many special cases, such as an ordinary regression model (when $f_t(\theta) \equiv 0$, $g(\tau) = \tau$; see [1–7]), an ordinary generalized regression model (when $f_t(\theta) \equiv 0$; see [8–13]), a linear regression model with constant coefficient autoregressive processes (when $f_t(\theta) = \theta$, $g(\tau) = \tau$; see [14–16]), time-dependent and function coefficient autoregressive processes (when $g(\tau) = 0$; see [17]), constant coefficient autoregressive processes (when $f_t(\theta) = \theta$, $g(\tau) = 0$; see [18–20]), time-dependent or time-varying autoregressive processes (when $f_t(\theta) = a_t$, $g(\tau) = 0$; see [21–23]), and a linear regression model with functional coefficient autoregressive processes (when $g(\tau) = \tau$; see [24]). Many authors have discussed some special cases of models (1.1) and (1.2) (see [1–24]). However, few people investigate the model (1.1) with (1.2). This paper studies the model (1.1) with (1.2). The organization of this paper is as follows. In Section 2, some estimators are given by the quasi-maximum likelihood method. In Section 3, the main results are investigated. The proofs of the main results are presented in Section 4, with the conclusions and some open problems in Section 5.

2. The Quasi-Maximum Likelihood Estimate

Write the "true" model as

$$y_t = g\left(x_t^T \beta_0\right) + e_t, \quad t = 1, 2, \ldots, n, \tag{2.1}$$

$$e_1 = \eta_1, \qquad e_t = f_t(\theta_0) e_{t-1} + \eta_t, \quad t = 2, 3, \ldots, n, \tag{2.2}$$

where $g'(\tau) = (dg(\tau)/d\tau) \neq 0$, $f_t'(\theta) = (df_t(\theta)/d\theta) \neq 0$. Define $\prod_{i=0}^{-1} f_{t-i}(\theta_0) = 1$, and by (2.2), we have

$$e_t = \sum_{j=0}^{t-1} \left(\prod_{i=0}^{j-1} f_{t-i}(\theta_0) \right) \eta_{t-j}. \tag{2.3}$$

Thus e_t is measurable with respect to the $\sigma-$field H generated by $\eta_1, \eta_2, \ldots, \eta_t$, and

$$Ee_t = 0, \qquad \operatorname{Var}(e_t) = \sigma_0^2 \sum_{j=0}^{t-1} \left(\prod_{i=0}^{j-1} f_{t-i}^2(\theta_0) \right). \tag{2.4}$$

Assume at first that the η_t are i.i.d. $N(0, \sigma^2)$, we get the log-likelihood of $y_2, \ldots, y_n$ conditional on y_1 given by

$$\Phi_n = \ln L_n = -\frac{(n-1)\ln \sigma^2}{2} - \frac{\sum_{t=2}^{n} \left(\varepsilon_t - f_t(\theta)\varepsilon_{t-1}\right)^2}{2\sigma^2} - \frac{(n-1)\ln 2\pi}{2}. \tag{2.5}$$

At this stage we drop the normality assumption, but still maximize (2.5) to obtain QML estimators, denoted by $\widehat{\sigma}_n^2, \widehat{\beta}_n, \widehat{\theta}_n$. The estimating equations for unknown parameters in (2.5) may be written as

$$\frac{\partial \Phi_n}{\partial \sigma^2} = -\frac{n-1}{2\sigma^2} + \frac{1}{2\sigma^4}\sum_{t=2}^{n}\left(\varepsilon_t - f_t(\theta)\varepsilon_{t-1}\right)^2, \tag{2.6}$$

$$\begin{aligned} \frac{\partial \Phi_n}{\partial \theta} &= \frac{1}{\sigma^2}\sum_{t=2}^{n} f_t'(\theta)\left(\varepsilon_t - f_t(\theta)\varepsilon_{t-1}\right)\varepsilon_{t-1}, \\ \frac{\partial \Phi_n}{\partial \beta_{d\times 1}} &= \frac{1}{\sigma^2}\sum_{t=2}^{n}\left(\varepsilon_t - f_t(\theta)\varepsilon_{t-1}\right)\cdot\left(g'\left(x_t^T\beta\right)x_t - f_t(\theta)g'\left(x_{t-1}^T\beta\right)x_{t-1}\right). \end{aligned} \tag{2.7}$$

Thus, $\widehat{\sigma}_n^2, \widehat{\beta}_n, \widehat{\theta}_n$ satisfy the following estimation equations

$$\widehat{\sigma}_n^2 = \frac{1}{n-1}\sum_{t=2}^{n}\left(\widehat{\varepsilon}_t - f_t\left(\widehat{\theta}_n\right)\widehat{\varepsilon}_{t-1}\right)^2, \tag{2.8}$$

$$\sum_{t=2}^{n}\left(\widehat{\varepsilon}_t - f_t\left(\widehat{\theta}_n\right)\widehat{\varepsilon}_{t-1}\right)f_t'\left(\widehat{\theta}_n\right)\widehat{\varepsilon}_{t-1} = 0, \tag{2.9}$$

$$\sum_{t=2}^{n}\left(\widehat{\varepsilon}_t - f_t\left(\widehat{\theta}_n\right)\widehat{\varepsilon}_{t-1}\right)\left(g'\left(x_t^T\widehat{\beta}_n\right)x_t - f_t\left(\widehat{\theta}_n\right)g'\left(x_{t-1}^T\widehat{\beta}_n\right)x_{t-1}\right) = 0, \tag{2.10}$$

where

$$\widehat{\varepsilon}_t = y_t - g\left(x_t^T\widehat{\beta}_n\right). \tag{2.11}$$

Remark 2.1. If $g(x_t^T\beta) = x_t^T\beta$, then the above equations become the same as Hu's (see [24]). If $f_t(\theta) = \theta$, $g(x_t^T\beta) = x_t^T\beta$, then the above equations become the same as Maller's (see [15]). Thus we extend those QML estimators of Hu [24] and Maller [15].

For ease of exposition, we will introduce the following notations, which will be used later in the paper. Let $(d+1)\times 1-$ vector $\varphi = (\beta^T, \theta)^T$. Define

$$S_n(\varphi) = \sigma^2\frac{\partial \Phi_n}{\partial \varphi} = \sigma^2\left(\frac{\partial \Phi_n}{\partial \beta}, \frac{\partial \Phi_n}{\partial \theta}\right), \qquad F_n(\varphi) = -\sigma^2\frac{\partial^2 \Phi_n}{\partial \varphi \partial \varphi^T}. \tag{2.12}$$

By (2.7), we have

$$F_n(\varphi) = \begin{pmatrix} X_n(\varphi,\omega) & U \\ * & \sum_{t=2}^{n}\left(\left(f_t'^2(\theta) + f_t(\theta)f_t''(\theta)\right)\varepsilon_{t-1}^2 - f_t''(\theta)\varepsilon_t\varepsilon_{t-1}\right) \end{pmatrix}, \tag{2.13}$$

where the * indicates that the elements are filled in by symmetry,

$$X_n(\varphi,\omega) = -\sigma^2\left(\frac{\partial^2\Phi_n}{\partial\beta\partial\beta^T}\right),$$

$$U = \sum_{t=2}^{n}\left(f_t'(\theta)\varepsilon_{t-1}g'\left(x_t^T\beta\right)x_t + f_t'(\theta)\varepsilon_t g'\left(x_{t-1}^T\beta\right)x_{t-1} - 2f_t(\theta)f_t'(\theta)\varepsilon_{t-1}g'\left(x_{t-1}^T\beta\right)x_{t-1}\right),$$

$$\frac{\partial^2\Phi_n}{\partial\beta\partial\beta^T} = -\frac{1}{\sigma^2}\sum_{t=2}^{n}\left(g'\left(x_t^T\beta\right)x_t - f_t(\theta)g'\left(x_{t-1}^T\beta\right)x_{t-1}\right)\left(g'\left(x_t^T\beta\right)x_t - f_t(\theta)g'\left(x_{t-1}^T\beta\right)x_{t-1}\right)^T$$

$$+\frac{1}{\sigma^2}\sum_{t=2}^{n}\left(\varepsilon_t - f_t(\theta)\varepsilon_{t-1}\right)\left(g''\left(x_t^T\beta\right)x_t x_t^T - f_t(\theta)g''\left(x_{t-1}^T\beta\right)x_{t-1}x_{t-1}^T\right). \tag{2.14}$$

Because $\{e_{t-1}\}$ and $\{\eta_t\}$ are mutually independent, we have

$$D_n = E(F_n(\varphi_0)) = \begin{pmatrix} X_n(\varphi_0) & 0 \\ 0 & \sum_{t=2}^{n} f_t'^2(\theta_0)Ee_{t-1}^2 \end{pmatrix} = \begin{pmatrix} X_n(\varphi_0) & 0 \\ 0 & \Delta(\theta_0,\sigma_0) \end{pmatrix}, \tag{2.15}$$

where

$$X_n(\varphi_0) = \sum_{t=2}^{n}\left(g'\left(x_t^T\beta_0\right)x_t - f_t(\theta_0)g'\left(x_{t-1}^T\beta_0\right)x_{t-1}\right)\left(g'\left(x_t^T\beta_0\right)x_t - f_t(\theta_0)g'\left(x_{t-1}^T\beta_0\right)x_{t-1}\right)^T,$$

$$\Delta(\theta_0,\sigma_0) = \sum_{t=2}^{n} f_t'^2(\theta_0)Ee_{t-1}^2 = \sigma_0^2\sum_{t=2}^{n} f_t'^2(\theta_0)\sum_{j=0}^{t-2}\left(\prod_{i=0}^{j-1} f_{t-i}^2(\theta)\right) = O(n). \tag{2.16}$$

By (2.8) (2.7) and $E\eta_t = 0$, we have

$$\sigma_0^2 E\left(\frac{\partial\Phi_n}{\partial\beta}\bigg|_{\beta=\beta_0}\right) = \sum_{t=2}^{n} E\eta_t\left(g'(x_t^T\beta_0)x_t - f_t(\theta_0)g'(x_{t-1}^T\beta_0)x_{t-1}\right) = 0,$$

$$\sigma_0^2 E\left(\frac{\partial\Phi_n}{\partial\theta}\bigg|_{\theta=\theta_0}\right) = \sum_{t=2}^{n} f_t'(\theta_0)E\left(\eta_t e_{t-1}\right) = 0. \tag{2.17}$$

3. Statement of Main Results

In the section pseudo likelihood ratio (LR) statistics for various hypothesis tests of interest are derived. We consider the following hypothesis:

$$H_1 : g(\cdot), f(\cdot) \text{ are continuous functions, and } f^{'(\cdot)} \neq 0,\ \sigma_0^2 > 0. \tag{3.1}$$

When the parameter space is restricted by a hypothesis H_{0j}, $j = 1, 2, \ldots$, let $\widehat{\beta}_{jn}, \widehat{\theta}_{jn}, \widehat{\sigma}^2_{jn}$ be the corresponding QML estimators of β, θ, σ^2, and let

$$\widehat{L}_{jn} = -2\Phi_n\left(\widehat{\beta}_{jn}, \widehat{\theta}_{jn}, \widehat{\sigma}^2_{jn}\right) \tag{3.2}$$

be minus twice the log-likelihood, evaluated at the fitted parameters. Also let

$$\begin{aligned} \widehat{L}_n &= -2\Phi_n\left(\widehat{\beta}_n, \widehat{\theta}_n, \widehat{\sigma}^2_n\right), \\ d_{jn} &= \widehat{L}_{jn} - \widehat{L}_n \end{aligned} \tag{3.3}$$

be the "deviance" statistic for testing H_{0j} against H_1. From (2.5) and (2.8),

$$\widehat{L}_n = (n-1)\ln\widehat{\sigma}^2_n + (n-1)(1 + \ln 2\pi) \tag{3.4}$$

and similarly

$$\widehat{L}_{jn} = (n-1)\ln\widehat{\sigma}^2_{jn} + (n-1)(1 + \ln 2\pi). \tag{3.5}$$

In order to obtain our results, we give some sufficient conditions as follows.

(A1) $X_n = \sum_{t=2}^{n} x_t x_t^T$ is positive definite for sufficiently large n and

$$\lim_{n\to\infty} \max_{1\le t\le n} x_t^T X_n^{-1} x_t = O\left(n^{-\alpha}\right), \quad \forall \alpha \in \left(\frac{1}{2}, 1\right], \qquad \lim_{n\to\infty} \sup |\lambda|_{\max}\left(X_n^{-1/2} Z_n X_n^{-T/2}\right) < 1, \tag{3.6}$$

where $Z_n = (1/2)\sum_{t=2}^{n}(x_t x_{t-1}^T + x_{t-1}x_t^T)$ and $|\lambda|_{\max}(\cdot)$ denotes the maximum in absolute value of the eigenvalues of a symmetric matrix.

(A2) There is a constant $\alpha > 0$ such that

$$\sum_{j=1}^{t}\left(\prod_{i=0}^{j-1} f^2_{t-i}(\theta)\right) \le \alpha, \qquad \max_{1\le j\le n}\left|\sum_{t=j+1}^{n}\left(\prod_{i=0}^{t-j-1} f_{t-i}(\theta_0)\right)\right| \le \gamma. \tag{3.7}$$

(A3) $f_t'(\theta) = df_t(\theta)/d\theta \neq 0$ and $f_t''(\theta) = df_t'(\theta)/d\theta$ exist and are bounded, and $g(\cdot)$ is twice continuously differentiable, $0 < m \le \max_u |g'(u)| \le M < \infty$, $0 < \widetilde{m} \le \max_u |g''(u)| \le \widetilde{M} < \infty$.

Theorem 3.1. *Assume* (2.1), (2.2) *and (A1)–(A3).*

(1) *Suppose* $H_{01} : f_t(\theta) = \theta$ *and* $g(u)$ *is a continuous function,* $\sigma_0^2 > 0$ *holds. Then*

$$d_{1n} \xrightarrow{D} \chi^2_1, \quad n \longrightarrow \infty. \tag{3.8}$$

(2) *Suppose* $H_{02}: f_t(\theta) = \theta, g(u) = u, \sigma_0^2 > 0$ *holds. Then*

$$d_{2n} \xrightarrow{D} \chi_1^2, \quad n \longrightarrow \infty. \tag{3.9}$$

(3) *Suppose* $H_{03}: f_t(\theta) = \theta, g(u) = e^u/(1+e^u), \sigma_0^2 > 0$ *holds. Then*

$$d_{3n} \xrightarrow{D} \chi_1^2, \quad n \longrightarrow \infty. \tag{3.10}$$

4. Proof of Theorem

To prove Theorem 3.1, we first introduce the following lemmas.

Lemma 4.1. *Suppose that (A1)–(A3) hold. Then, for all* $A > 0$,

$$\sup_{\varphi \in N_n(A)} \left\| D_n^{-1/2} F_n(\varphi) D_n^{-T/2} - \Phi_n \right\| \xrightarrow{P} 0, \quad n \to \infty, \tag{4.1}$$

where

$$\Phi_n = \operatorname{diag}\left(I_d, \frac{\sum_{t=2}^{n} f_t'^2(\theta_0) e_{t-1}^2}{\Delta_n(\theta_0, \sigma_0)} \right), \tag{4.2}$$

$$N_n(A) = \left\{ \varphi \in R^{d+1} : (\varphi - \varphi_0)^T D_n (\varphi - \varphi_0) \le A^2 \right\}. \tag{4.3}$$

Proof. Similar to proof of Lemma 4.1 in Hu [24], here we omit. □

Lemma 4.2. *Suppose that (A1)–(A3) hold. Then* $\widehat{\varphi}_n \to \varphi_0$, $\widehat{\sigma}_n^2 \to \sigma_0^2$ *and*

$$X_n\left(\beta^*, \beta^{**}, \widehat{\theta}_n\right) \longrightarrow X_n(\varphi_0), \tag{4.4}$$

where β^*, β^{**} *are on the line of* β_0 *and* $\widehat{\beta}_n$.

Proof. Similar to proof of Theorem 3.1 in Hu [24], we easily prove that $\widehat{\varphi}_n \to \varphi_0$, and $\widehat{\sigma}_n^2 \to \sigma_0^2$. Since (4.4) is easily proved, here we omit the proof (4.4). □

Proof of Theorem 3.1. Note that $S_n(\widehat{\varphi}_n) = 0$ and $F_n(\widehat{\varphi}_n)$ are nonsingular. By Taylor's expansion, we have

$$0 = S_n(\widehat{\varphi}_n) = S_n(\varphi_0) - F_n(\widetilde{\varphi}_n)(\widehat{\varphi}_n - \varphi_0), \tag{4.5}$$

where $\widetilde{\varphi}_n = a\widehat{\varphi}_n + (1-a)\varphi_0$ for some $0 \le a \le 1$. Since $\widehat{\varphi}_n \in N_n(A)$, also $\widetilde{\varphi}_n \in N_n(A)$. By (4.1), we have

$$F_n(\widetilde{\varphi}_n) = D_n^{1/2}\left(\Phi_n + \widetilde{A}_n\right)D_n^{T/2}. \tag{4.6}$$

Thus $\widetilde{A}_n$ is a symmetric matrix with $\widetilde{A}_n \xrightarrow{P} 0$. By (4.5) and (4.6), we have

$$D_n^{T/2}(\widehat{\varphi}_n - \varphi_0) = D_n^{T/2}F_n^{-1}(\widetilde{\varphi}_n)S_n(\varphi_0) = \left(\Phi_n + \widetilde{A}_n\right)^{-1}D_n^{-1/2}S_n(\varphi_0). \tag{4.7}$$

Let $S_n(\varphi), F_n(\varphi)$ denote $S_n^{(\beta)}(\varphi), S_n^{(\theta)}(\varphi)$, and $F_n^{(\beta)}(\varphi), F_n^{(\theta)}(\varphi)$, respectively. By (4.7), we have

$$\Phi_n D_n^{T/2}\left(\widehat{\beta}_n - \beta_0, \widehat{\theta}_n - \theta_0\right) = D_n^{-1/2}\left(S_n^{(\beta)}(\varphi_0), S_n^{(\theta)}(\varphi_0)\right) + o_P(1). \tag{4.8}$$

Note that

$$\begin{aligned}
\Phi_n D_n^{T/2} &= \begin{pmatrix} X_n^{T/2}(\varphi_0) & 0 \\ 0 & \dfrac{\left(\sum_{t=2}^n f_t'^2(\theta_0)e_{t-1}^2\right)}{\sqrt{\Delta_n(\theta_0,\sigma_0)}} \end{pmatrix}, \\
D_n^{-1/2} &= \begin{pmatrix} X_n^{-1/2}(\varphi_0) & 0 \\ 0 & \dfrac{1}{\sqrt{\Delta_n(\theta_0,\sigma_0)}} \end{pmatrix}.
\end{aligned} \tag{4.9}$$

By (2.15), (4.2) and (4.8), we get

$$\begin{aligned}
X_n^{T/2}(\varphi_0)\left(\widehat{\beta}_n - \beta_0\right) &= X_n^{-1/2}(\varphi_0)S_n^{(\beta)}(\varphi_0) + o_P(1) \\
&= X_n^{-1/2}(\varphi_0)\sum_{t=2}^n \eta_t\left(g'\left(x_t^T\beta_0\right)x_t - f_t(\theta_0)g'\left(x_{t-1}^T\beta_0\right)x_{t-1}\right) + o_P(1),
\end{aligned} \tag{4.10}$$

$$\begin{aligned}
\sum_{t=2}^n f_t'^2(\theta_0)e_{t-1}^2\left(\widehat{\theta}_n - \theta_0\right) &= S_n^{(\theta)}(\varphi_0) + o_P\left(\sqrt{\Delta_n(\theta_0,\sigma_0)}\right) \\
&= \sum_{t=2}^n f_t'(\theta_0)\eta_t e_{t-1} + o_P\left(\sqrt{\Delta_n(\theta_0,\sigma_0)}\right).
\end{aligned} \tag{4.11}$$

Note that

$$\varepsilon_t = y_t - g\left(x_t^T\beta\right) = g'\left(x_t^T\beta^*\right)x_t^T(\beta_0 - \beta) + e_t \tag{4.12}$$

By (2.1), (2.11) and (4.12), we have

$$\widehat{\varepsilon}_t - f_t\left(\widehat{\theta}_n\right)\widehat{\varepsilon}_{t-1} = \left(g'\left(x_t^T\beta^*\right)x_t^T - f_t\left(\widehat{\theta}_n\right)g'\left(x_{t-1}^T\beta^{**}\right)x_{t-1}^T\right)\left(\beta_0 - \widehat{\beta}_n\right) + \left(e_t - f_t\left(\widehat{\theta}_n\right)e_{t-1}\right). \tag{4.13}$$

By (4.13) and (2.10), we have

$$\begin{aligned}\sum_{t=2}^{n}\left(\widehat{\varepsilon}_t - f_t\left(\widehat{\theta}_n\right)\widehat{\varepsilon}_{t-1}\right)^2 &= \sum_{t=2}^{n}\left(\widehat{\varepsilon}_t - f_t\left(\widehat{\theta}_n\right)\widehat{\varepsilon}_{t-1}\right)\left(\left(g'\left(x_t^T\beta^*\right)x_t^T - f_t\left(\widehat{\theta}_n\right)g'\left(x_{t-1}^T\beta^{**}\right)x_{t-1}^T\right)\right.\\ &\quad\left.\times\left(\beta_0 - \widehat{\beta}_n\right) + \left(e_t - f_t\left(\widehat{\theta}_n\right)e_{t-1}\right)\right)\\ &= \sum_{t=2}^{n}\left(\widehat{\varepsilon}_t - f_t\left(\widehat{\theta}_n\right)\widehat{\varepsilon}_{t-1}\right)\left(g'\left(x_t^T\beta^*\right)x_t^T - f_t\left(\widehat{\theta}_n\right)g'\left(x_{t-1}^T\beta^{**}\right)x_{t-1}^T\right)\left(\beta_0 - \widehat{\beta}_n\right)\\ &\quad + \sum_{t=2}^{n}\left(\widehat{\varepsilon}_t - f_t\left(\widehat{\theta}_n\right)\widehat{\varepsilon}_{t-1}\right)\left(e_t - f_t\left(\widehat{\theta}_n\right)e_{t-1}\right)\\ &= \sum_{t=2}^{n}\left(\widehat{\varepsilon}_t - f_t\left(\widehat{\theta}_n\right)\widehat{\varepsilon}_{t-1}\right)\left(e_t - f_t\left(\widehat{\theta}_n\right)e_{t-1}\right).\end{aligned} \tag{4.14}$$

By (4.13), we have

$$\left(g'\left(x_t^T\beta^*\right)x_t^T - f_t\left(\widehat{\theta}_n\right)g'\left(x_{t-1}^T\beta^{**}\right)x_{t-1}^T\right)\left(\beta_0 - \widehat{\beta}_n\right) = \left(\widehat{\varepsilon}_t - f_t\left(\widehat{\theta}_n\right)\widehat{\varepsilon}_{t-1}\right) - \left(e_t - f_t\left(\widehat{\theta}_n\right)e_{t-1}\right). \tag{4.15}$$

By (4.15), we have

$$\begin{aligned}&\sum_{t=2}^{n}\left(\left(g'\left(x_t^T\beta^*\right)x_t^T - f_t\left(\widehat{\theta}_n\right)g'\left(x_{t-1}^T\beta^{**}\right)x_{t-1}^T\right)\left(\beta_0 - \widehat{\beta}_n\right)\right)^2\\ &\quad= \sum_{t=2}^{n}\left(\widehat{\varepsilon}_t - f_t\left(\widehat{\theta}_n\right)\widehat{\varepsilon}_{t-1}\right)^2 + \sum_{t=2}^{n}\left(e_t - f_t\left(\widehat{\theta}_n\right)e_{t-1}\right)^2\\ &\qquad- 2\sum_{t=2}^{n}\left(\widehat{\varepsilon}_t - f_t\left(\widehat{\theta}_n\right)\widehat{\varepsilon}_{t-1}\right)\left(e_t - f_t\left(\widehat{\theta}_n\right)e_{t-1}\right)\\ &\quad= \sum_{t=2}^{n}\left(e_t - f_t\left(\widehat{\theta}_n\right)e_{t-1}\right)^2 - \sum_{t=2}^{n}\left(\widehat{\varepsilon}_t - f_t\left(\widehat{\theta}_n\right)\widehat{\varepsilon}_{t-1}\right)^2.\end{aligned} \tag{4.16}$$

By (4.14) and (4.16), we have

$$\sum_{t=2}^{n}\left(\widehat{\varepsilon}_t - f_t\left(\widehat{\theta}_n\right)\widehat{\varepsilon}_{t-1}\right)^2 = \sum_{t=2}^{n}\left(e_t - f_t\left(\widehat{\theta}_n\right)e_{t-1}\right)^2 - \sum_{t=2}^{n}\left(\left(g'\left(x_t^T\beta^*\right)x_t^T - f_t\left(\widehat{\theta}_n\right)g'\left(x_{t-1}^T\beta^{**}\right)x_{t-1}^T\right)\left(\beta_0 - \widehat{\beta}_n\right)\right)^2. \tag{4.17}$$

By (4.15), we have

$$\begin{aligned}&\sum_{t=2}^{n}\left(\widehat{\varepsilon}_t - f_t\left(\widehat{\theta}_n\right)\widehat{\varepsilon}_{t-1}\right)^2 \\ &\quad= \sum_{t=2}^{n}\left(e_t - f_t\left(\widehat{\theta}_n\right)e_{t-1}\right)^2 + \sum_{t=2}^{n}\left(\left(g'\left(x_t^T\beta^*\right)x_t^T - f_t\left(\widehat{\theta}_n\right)g'\left(x_{t-1}^T\beta^{**}\right)x_{t-1}^T\right)\left(\beta_0 - \widehat{\beta}_n\right)\right)^2 \\ &\qquad+ 2\sum_{t=2}^{n}\left(e_t - f_t\left(\widehat{\theta}_n\right)e_{t-1}\right)\left(\left(g'\left(x_t^T\beta^*\right)x_t^T - f_t\left(\widehat{\theta}_n\right)g'\left(x_{t-1}^T\beta^{**}\right)x_{t-1}^T\right)\left(\beta_0 - \widehat{\beta}_n\right)\right).\end{aligned} \tag{4.18}$$

Thus, by (4.17) and (4.18), we have

$$\begin{aligned}&\sum_{t=2}^{n}\left(\left(g'\left(x_t^T\beta^*\right)x_t^T - f_t\left(\widehat{\theta}_n\right)g'\left(x_{t-1}^T\beta^{**}\right)x_{t-1}^T\right)\left(\beta_0 - \widehat{\beta}_n\right)\right)^2 \\ &\qquad+ \sum_{t=2}^{n}\left(e_t - f_t\left(\widehat{\theta}_n\right)e_{t-1}\right)\left(\left(g'\left(x_t^T\beta^*\right)x_t^T - f_t\left(\widehat{\theta}_n\right)g'\left(x_{t-1}^T\beta^{**}\right)x_{t-1}^T\right)\left(\beta_0 - \widehat{\beta}_n\right)\right) = 0.\end{aligned} \tag{4.19}$$

Since $\eta_t = e_t - f_t(\theta_0)e_{t-1}$, we have

$$\begin{aligned}\sum_{t=2}^{n}\left(e_t - f_t\left(\widehat{\theta}_n\right)e_{t-1}\right)^2 &= \sum_{t=2}^{n}\left(\eta_t + f_t(\theta_0)e_{t-1} - f_t\left(\widehat{\theta}_n\right)e_{t-1}\right)^2 \\ &= \sum_{t=1}^{n}\eta_t^2 + \sum_{t=2}^{n}\left(f_t(\theta_0) - f_t\left(\widehat{\theta}_n\right)\right)^2 e_{t-1}^2 + 2\left(f_t(\theta_0) - f_t\left(\widehat{\theta}_n\right)\right)\eta_t e_{t-1}.\end{aligned} \tag{4.20}$$

Thus, by (4.17), (4.20) and mean value theorem, we have

$$\begin{aligned}(n-1)\widehat{\sigma}_n^2 &= \sum_{t=2}^{n}\left(\widehat{\varepsilon}_t - f_t\left(\widehat{\theta}_n\right)\widehat{\varepsilon}_{t-1}\right)^2 \\ &= \sum_{t=1}^{n}\eta_t^2 + \sum_{t=2}^{n}\left(f_t(\theta_0) - f_t\left(\widehat{\theta}_n\right)\right)^2 e_{t-1}^2 + 2\left(f_t(\theta_0) - f_t\left(\widehat{\theta}_n\right)\right)\eta_t e_{t-1}\end{aligned}$$

$$
\begin{aligned}
&- \sum_{t=2}^{n} \left(\left(g'\left(x_t^T \beta^*\right) x_t^T - f_t\left(\widehat{\theta}_n\right) g'\left(x_{t-1}^T \beta^{**}\right) x_{t-1}^T \right) \left(\beta_0 - \widehat{\beta}_n\right) \right)^2 \\
&= \sum_{t=1}^{n} \eta_t^2 + \left(\theta_0 - \widehat{\theta}_n\right)^2 \sum_{t=2}^{n} f_t'^2\left(\widetilde{\theta}\right) e_{t-1}^2 + 2\left(\theta_0 - \widehat{\theta}_n\right) \sum_{t=2}^{n} f_t'\left(\widetilde{\theta}\right) e_{t-1} \eta_t \\
&- \sum_{t=2}^{n} \left(\left(g'\left(x_t^T \beta^*\right) x_t^T - f_t\left(\widehat{\theta}_n\right) g'\left(x_{t-1}^T \beta^{**}\right) x_{t-1}^T \right) \left(\beta_0 - \widehat{\beta}_n\right) \right)^2,
\end{aligned}
\tag{4.21}
$$

where $\widetilde{\theta} = a\theta_0 + (1-a)\widehat{\theta}_n$ for some $0 \le a \le 1$.

It is easy to know that

$$
\begin{aligned}
&\left(\widehat{\beta}_n - \beta_0\right)^T X_n(\varphi_0) \left(\widehat{\beta}_n - \beta_0\right) \\
&\quad = \left(\sum_{t=2}^{n} \eta_t X_n^{-1/2}(\varphi_0) \left(g'\left(x_t^T \beta_0\right) x_t - f_t(\theta_0) g'\left(x_{t-1}^T \beta_0\right) x_{t-1} \right) \right)^2 + o_p(1).
\end{aligned}
\tag{4.22}
$$

By Lemma 4.2 and (4.22), we have

$$
\begin{aligned}
(n-1)\widehat{\sigma}_n^2 &= \sum_{t=1}^{n} \eta_t^2 + \left(\theta_0 - \widehat{\theta}_n\right)^2 \sum_{t=2}^{n} f_t'^2\left(\widetilde{\theta}\right) e_{t-1}^2 + 2\left(\theta_0 - \widehat{\theta}_n\right) \sum_{t=2}^{n} f_t'\left(\widetilde{\theta}\right) e_{t-1} \eta_t \\
&\quad - \left(\sum_{t=2}^{n} \eta_t X_n^{-1/2}\left(\beta^*, \beta^{**}, \widehat{\theta}_n\right) \left(g'\left(x_t^T \beta_0\right) x_t - f_t(\theta_0) g'\left(x_{t-1}^T \beta_0\right) x_{t-1} \right) \right)^2 + o_P(1) \\
&= \sum_{t=1}^{n} \eta_t^2 + \left(\theta_0 - \widehat{\theta}_n\right)^2 \sum_{t=2}^{n} f_t'^2\left(\widetilde{\theta}\right) e_{t-1}^2 + 2\left(\theta_0 - \widehat{\theta}_n\right) \sum_{t=2}^{n} f_t'\left(\widetilde{\theta}\right) e_{t-1} \eta_t \\
&\quad - \left(\sum_{t=2}^{n} \eta_t X_n^{-1/2}(\varphi_0) \left(g'\left(x_t^T \beta_0\right) x_t - f_t(\theta_0) g'\left(x_{t-1}^T \beta_0\right) x_{t-1} \right) \right)^2 + o_P(1).
\end{aligned}
\tag{4.23}
$$

Hence, by (4.11), we have

$$
\begin{aligned}
\widehat{\theta}_n - \theta_0 &= \frac{\sum_{t=2}^{n} f_t'(\theta_0) \eta_t e_{t-1}}{\sum_{t=2}^{n} f_t'^2(\theta_0) e_{t-1}^2} + o_P\left(\frac{\sqrt{\Delta_n(\theta_0, \sigma_0)}}{\sum_{t=2}^{n} f_t'^2(\theta_0) e_{t-1}^2} \right) \\
&= \frac{\sum_{t=2}^{n} f_t'(\theta_0) \eta_t e_{t-1}}{\sum_{t=2}^{n} f_t'^2(\theta_0) e_{t-1}^2} + o_P\left(\frac{1}{\sqrt{\sum_{t=2}^{n} f_t'^2(\theta_0) e_{t-1}^2}} \right).
\end{aligned}
\tag{4.24}
$$

By (4.24), we have

$$\begin{aligned}
&\left(\theta_0-\widehat{\theta}_n\right)^2\sum_{t=2}^{n}f_t'^2\left(\widetilde{\theta}\right)e_{t-1}^2+2\left(\theta_0-\widehat{\theta}_n\right)\sum_{t=2}^{n}f_t'\left(\widetilde{\theta}\right)e_{t-1}\eta_t\\
&\quad=\left(\frac{\sum_{t=2}^{n}f_t'(\theta_0)\eta_te_{t-1}}{\sum_{t=2}^{n}f_t'^2(\theta_0)e_{t-1}^2}+o_P\left(\frac{1}{\sqrt{\sum_{t=2}^{n}f_t'^2(\theta_0)e_{t-1}^2}}\right)\right)^2\sum_{t=2}^{n}f_t'^2\left(\widetilde{\theta}\right)e_{t-1}^2\\
&\qquad+2\left(\frac{\sum_{t=2}^{n}f_t'(\theta_0)\eta_te_{t-1}}{\sum_{t=2}^{n}f_t'^2(\theta_0)e_{t-1}^2}+o_P\left(\frac{1}{\sqrt{\sum_{t=2}^{n}f_t'^2(\theta_0)e_{t-1}^2}}\right)\right)\sum_{t=2}^{n}f_t'\left(\widetilde{\theta}\right)e_{t-1}\eta_t+o_P(1)\\
&\quad=\left(\frac{\sum_{t=2}^{n}f_t'(\theta_0)\eta_te_{t-1}}{\sum_{t=2}^{n}f_t'^2(\theta_0)e_{t-1}^2}+o_P\left(\frac{1}{\sqrt{\sum_{t=2}^{n}f_t'^2(\theta_0)e_{t-1}^2}}\right)\right)^2\sum_{t=2}^{n}\left(f_t'(\theta_0)+o(1)\right)^2e_{t-1}^2\\
&\qquad+2\left(\frac{\sum_{t=2}^{n}f_t'(\theta_0)\eta_te_{t-1}}{\sum_{t=2}^{n}f_t'^2(\theta_0)e_{t-1}^2}+o_P\left(\frac{1}{\sqrt{\sum_{t=2}^{n}f_t'^2(\theta_0)e_{t-1}^2}}\right)\right)\\
&\qquad\cdot\sum_{t=2}^{n}\left(f_t''(\theta_0)+o(1)\right)e_{t-1}\eta_t+o_P(1)\\
&\quad=\frac{\left(\sum_{t=2}^{n}f_t'(\theta_0)\eta_te_{t-1}\right)^2}{\sum_{t=2}^{n}f_t'^2(\theta_0)e_{t-1}^2}-\frac{2\left(\sum_{t=2}^{n}f_t'(\theta_0)\eta_te_{t-1}\right)^2}{\sum_{t=2}^{n}f_t'^2(\theta_0)e_{t-1}^2}+o_P(1)\\
&\quad=-\frac{\left(\sum_{t=2}^{n}f_t'(\theta_0)\eta_te_{t-1}\right)^2}{\sum_{t=2}^{n}f_t'^2(\theta_0)e_{t-1}^2}+o_P(1).
\end{aligned}\tag{4.25}$$

By Lemma 4.2, we have

$$\begin{aligned}
(n-1)\widehat{\sigma}_n^2&=\sum_{t=1}^{n}\eta_t^2-\frac{\left(\sum_{t=2}^{n}f_t'(\theta_0)\eta_te_{t-1}\right)^2}{\sum_{t=2}^{n}f_t'^2(\theta_0)e_{t-1}^2}\\
&\quad-\left(\sum_{t=2}^{n}\eta_tX_n^{-1/2}\left(\beta^*,\beta^{**},\widehat{\theta}_n\right)\left(g'\left(x_t^T\beta_0\right)x_t-f_t(\theta_0)g'\left(x_{t-1}^T\beta_0\right)x_{t-1}\right)\right)^2+o_P(1)\\
&=\sum_{t=1}^{n}\eta_t^2-\frac{\left(\sum_{t=2}^{n}f_t'(\theta_0)\eta_te_{t-1}\right)^2}{\sum_{t=2}^{n}f_t'^2(\theta_0)e_{t-1}^2}\\
&\quad-\left(\sum_{t=2}^{n}\eta_tX_n^{-1/2}(\varphi_0)\left(g'\left(x_t^T\beta_0\right)x_t-f_t(\theta_0)g'\left(x_{t-1}^T\beta_0\right)x_{t-1}\right)\right)^2+o_P(1).
\end{aligned}\tag{4.26}$$

Now, we prove (3.8). By (4.12), we have

$$\widehat{\varepsilon}_t(1) = y_t - g\left(x_t^T\widehat{\beta}_{1n}\right) = g'\left(x_t^T\widehat{\beta}_{1n}^*\right)x_t^T\left(\beta_0 - \widehat{\beta}_{1n}\right) + e_t. \tag{4.27}$$

Note that

$$\varepsilon_t - f_t(\theta_0)\varepsilon_{t-1} = \left(g'\left(x_t^T\beta^*\right)x_t^T - f_t(\theta_0)g'\left(x_{t-1}^T\beta^{**}\right)x_{t-1}^T\right)(\beta_0 - \beta) + \eta_t. \tag{4.28}$$

From (4.28), we have

$$\widehat{\varepsilon}_t(1) - \widehat{\theta}_{1n}\widehat{\varepsilon}_{t-1}(1) = \left(g'\left(x_t^T\widehat{\beta}_{1n}^*\right)x_t^T - \widehat{\theta}_{1n}g'\left(x_{t-1}^T\widehat{\beta}_{1n}^{**}\right)x_{t-1}^T\right)\left(\beta_0 - \widehat{\beta}_{1n}\right) + \eta_t. \tag{4.29}$$

By (2.8) and (2.10), we have

$$\begin{aligned}
0 &= \sum_{t=2}^{n}\left(\widehat{\varepsilon}_t(1) - \widehat{\theta}_{1n}\widehat{\varepsilon}_{t-1}(1)\right)\left(g'\left(x_t^T\widehat{\beta}_{1n}^*\right)x_t - \widehat{\theta}_{1n}g'\left(x_{t-1}^T\widehat{\beta}_{1n}^{**}\right)x_{t-1}\right) \\
&= \sum_{t=2}^{n}\left(g'\left(x_t^T\widehat{\beta}_{1n}^*\right)x_t^T - \widehat{\theta}_{1n}g'\left(x_{t-1}^T\widehat{\beta}_{1n}^{**}\right)x_{t-1}^T\right)\left(\beta_0 - \widehat{\beta}_{1n}\right)\left(g'\left(x_t^T\widehat{\beta}_{1n}^*\right)x_t - \widehat{\theta}_{1n}g'\left(x_{t-1}^T\widehat{\beta}_{1n}^{**}\right)x_{t-1}\right) \\
&\quad + \sum_{t=2}^{n}\eta_t\left(g'\left(x_t^T\widehat{\beta}_{1n}^*\right)x_t - \widehat{\theta}_{1n}g'\left(x_{t-1}^T\widehat{\beta}_{1n}^{**}\right)x_{t-1}\right) \\
&= \left(\beta_0 - \widehat{\beta}_{1n}\right)^T X_{1n}\left(\widehat{\beta}_{1n}^*, \widehat{\beta}_{1n}^{**}, \widehat{\theta}_{1n}\right) + \sum_{t=2}^{n}\eta_t\left(g'\left(x_t^T\widehat{\beta}_{1n}^*\right)x_t - \widehat{\theta}_{1n}g'\left(x_{t-1}^T\widehat{\beta}_{1n}^{**}\right)x_{t-1}\right).
\end{aligned} \tag{4.30}$$

From (4.30), we obtain that

$$\widehat{\beta}_{1n} - \beta_0 = X_{1n}^{-1}\left(\widehat{\beta}_{1n}^*, \widehat{\beta}_{1n}^{**}, \widehat{\theta}_{1n}\right)\sum_{t=2}^{n}\eta_t\left(g'\left(x_t^T\widehat{\beta}_{1n}\right)x_t - \widehat{\theta}_{1n}g'\left(x_{t-1}^T\widehat{\beta}_{1n}\right)x_{t-1}\right). \tag{4.31}$$

By (4.29), (4.31) and Lemma 4.2, we have

$$\begin{aligned}
(n-1)\widehat{\sigma}_{1n}^2 &= \sum_{t=2}^{n}\left(\widehat{\varepsilon}_t(1) - \widehat{\theta}_{1n}\widehat{\varepsilon}_{t-1}(1)\right)^2 \\
&= \sum_{t=1}^{n}\eta_t^2 + \left(\beta_0 - \widehat{\beta}_{1n}\right)^T X_{1n}\left(\widehat{\beta}_{1n}^*, \widehat{\beta}_{1n}^{**}, \widehat{\theta}_{1n}\right)\left(\beta_0 - \widehat{\beta}_{1n}\right) \\
&\quad + 2\left(\beta_0 - \widehat{\beta}_{1n}\right)^T\sum_{t=2}^{n}\eta_t\left(g'\left(x_t^T\widehat{\beta}_{1n}^*\right)x_t - \widehat{\theta}_{1n}g'\left(x_{t-1}^T\widehat{\beta}_{1n}^{**}\right)x_{t-1}\right)
\end{aligned}$$

$$
\begin{aligned}
&= \sum_{t=1}^{n} \eta_t^2 - \left(\sum_{t=2}^{n} \eta_t X_{1n}^{-1/2} \left(\widehat{\beta}_{1n}^{*}, \widehat{\beta}_{1n}^{**}, \widehat{\theta}_{1n} \right) \left(g' \left(x_t^T \widehat{\beta}_{1n}^{*} \right) x_t - \widehat{\theta}_{1n} g' \left(x_{t-1}^T \widehat{\beta}_{1n}^{**} \right) x_{t-1} \right) \right)^2 + o_p(1) \\
&= \sum_{t=1}^{n} \eta_t^2 - \left(\sum_{t=2}^{n} \eta_t X_{1n}^{-1/2} (\varphi_0) \left(g' \left(x_t^T \beta_0 \right) x_t - \theta_0 g' \left(x_{t-1}^T \beta_0 \right) x_{t-1} \right) \right)^2 + o_p.
\end{aligned}
\tag{4.32}
$$

By (3.3)–(3.5), we have

$$
d_{1n} = \widehat{L}_{1n} - \widehat{L}_n = (n-1) \ln \left(\frac{\widehat{\sigma}_{1n}^2}{\widehat{\sigma}_n^2} \right) = (n-1) \left(\left(\frac{\widehat{\sigma}_{1n}^2}{\widehat{\sigma}_n^2} \right) - 1 \right) + o_P(1). \tag{4.33}
$$

Under the H_{01}, and by (4.26), (4.32) and (4.33), we have

$$
\begin{aligned}
\frac{(n-1)\left(\widehat{\sigma}_{1n}^2 - \widehat{\sigma}_n^2\right)}{\widehat{\sigma}_n^2} &= \frac{\left(\sum_{t=2}^{n} \eta_t e_{t-1}\right)^2}{\widehat{\sigma}_n^2 \sum_{t=2}^{n} e_{t-1}^2} + o_P(1) \\
&= \frac{\left(\sum_{t=2}^{n} \eta_t e_{t-1}\right)^2}{\sigma_0^2 \sum_{t=2}^{n} e_{t-1}^2} + o_P(1).
\end{aligned}
\tag{4.34}
$$

It is easily proven that

$$
\frac{\sum_{t=2}^{n} \eta_t e_{t-1}}{\sigma_0 \sqrt{\sum_{t=2}^{n} e_{t-1}^2}} \longrightarrow N(0,1). \tag{4.35}
$$

Thus, by (4.33)–(4.35), we finish the proof of (3.8).

Next we prove (3.9). Under H_{02} : $f_t(\theta) = \theta$, $g(u) = u$, and $y_t = x_t^T \beta_0 + e_t$, we have

$$
\widehat{\varepsilon}_t(2) = y_t - x_t^T \widehat{\beta}_{2n} = x_t^T \beta_0 - x_t^T \widehat{\beta}_{2n} + e_t = x_t^T \left(\beta_0 - \widehat{\beta}_{2n} \right) + e_t. \tag{4.36}
$$

Hence

$$
\begin{aligned}
\widehat{\varepsilon}_t(2) - \widehat{\theta}_{2n} \widehat{\varepsilon}_{t-1}(2) &= x_t^T \left(\beta_0 - \widehat{\beta}_{2n} \right) + e_t - \widehat{\theta}_{2n} \left(x_{t-1}^T \left(\beta_0 - \widehat{\beta}_{2n} \right) + e_{t-1} \right) \\
&= \left(x_t^T - \widehat{\theta}_{2n} x_{t-1}^T \right) \left(\beta_0 - \widehat{\beta}_{2n} \right) + \eta_t.
\end{aligned}
\tag{4.37}
$$

By (2.8), (2.10), we have

$$
\begin{aligned}
0 &= \sum_{t=2}^{n} \left(\widehat{\varepsilon}_t(2) - \widehat{\theta}_{2n} \widehat{\varepsilon}_{t-1}(2) \right) \left(x_t - \widehat{\theta}_{2n} x_{t-1} \right) \\
&= \sum_{t=2}^{n} \left(x_t^T - \widehat{\theta}_{2n} x_{t-1}^T \right) \left(\beta_0 - \widehat{\beta}_{2n} \right) \left(x_t - \widehat{\theta}_{2n} x_{t-1} \right) + \sum_{t=2}^{n} \eta_t \left(x_t - \widehat{\theta}_{2n} x_{t-1} \right).
\end{aligned}
\tag{4.38}
$$

From (4.38), we obtain,

$$\widehat{\beta}_{2n} - \beta_0 = X_{2n}^{-1}\left(\widehat{\theta}_{2n}\right)\sum_{t=2}^{n}\eta_t\left(x_t - \widehat{\theta}_{2n}x_{t-1}\right). \tag{4.39}$$

Thus, by (4.37), (4.39) and Lemma 4.2, we have

$$\begin{aligned}
(n-1)\widehat{\sigma}_{2n}^2 &= \sum_{t=2}^{n}\left(\widehat{\varepsilon}_t(2) - \widehat{\theta}_{2n}\widehat{\varepsilon}_{t-1}(2)\right)^2 \\
&= \sum_{t=1}^{n}\eta_t^2 + \left(\beta_0 - \widehat{\beta}_{2n}\right)^T X_{2n}\left(\widehat{\theta}_{2n}\right)\left(\beta_0 - \widehat{\beta}_{2n}\right) + 2\left(\beta_0 - \widehat{\beta}_{2n}\right)^T\sum_{t=2}^{n}\eta_t\left(x_t - \widehat{\theta}_{2n}x_{t-1}\right) \\
&= \sum_{t=1}^{n}\eta_t^2 - \left(\sum_{t=2}^{n}\eta_t\left(x_t - \widehat{\theta}_{2n}x_{t-1}\right)^T\right)X_{2n}^{-1}\left(\widehat{\theta}_{2n}\right)\left(\sum_{t=2}^{n}\eta_t\left(x_t - \widehat{\theta}_{2n}x_{t-1}\right)\right) \\
&= \sum_{t=1}^{n}\eta_t^2 - \left(\sum_{t=2}^{n}\eta_t X_{2n}^{-1/2}(\theta_0)(x_t - \theta_0 x_{t-1})\right)^2 + o_p(1).
\end{aligned} \tag{4.40}$$

By (3.3)–(3.5), we have

$$d_{2n} = \widehat{L}_{2n} - \widehat{L}_n = (n-1)\ln\left(\frac{\widehat{\sigma}_{2n}^2}{\widehat{\sigma}_n^2}\right) = (n-1)\left(\left(\frac{\widehat{\sigma}_{2n}^2}{\widehat{\sigma}_n^2}\right) - 1\right) + o_P(1). \tag{4.41}$$

Under the H_{02}, by (4.26), (4.40), and (4.41), we obtain

$$\begin{aligned}
\frac{(n-1)\left(\widehat{\sigma}_{2n}^2 - \widehat{\sigma}_n^2\right)}{\widehat{\sigma}_n^2} &= \frac{\left(\sum_{t=2}^{n}\eta_t e_{t-1}\right)^2}{\widehat{\sigma}_n^2\sum_{t=2}^{n}e_{t-1}^2} + o_P(1) \\
&= \frac{\left(\sum_{t=2}^{n}\eta_t e_{t-1}\right)^2}{\sigma_0^2\sum_{t=2}^{n}e_{t-1}^2} + o_P(1).
\end{aligned} \tag{4.42}$$

Thus, by (4.35), (4.42), (3.9) holds.

Finally, we prove (3.10). Under H_{03}, we have

$$\widehat{\varepsilon}_t(3) = y_t - \frac{e^{x_t^T\widehat{\beta}_{3n}^*}}{1 + e^{x_t^T\widehat{\beta}_{3n}^*}} = \frac{e^{x_t^T\widehat{\beta}_{3n}^*}}{\left(1 + e^{x_t^T\widehat{\beta}_{3n}^*}\right)^2}x_t^T\left(\beta_0 - \widehat{\beta}_{3n}\right) + e_t. \tag{4.43}$$

Thus

$$\begin{aligned}\widehat{\varepsilon}_t(3)-\widehat{\theta}_{3n}\widehat{\varepsilon}_{t-1}(3) &= \frac{e^{x_t^T\widehat{\beta}_{3n}^*}}{\left(1+e^{x_t^T\widehat{\beta}_{3n}^*}\right)^2}x_t^T\left(\beta_0-\widehat{\beta}_{3n}\right)+e_t\\ &\quad-\widehat{\theta}_{3n}\frac{e^{x_{t-1}^T\widehat{\beta}_{3n}^{**}}}{\left(1+e^{x_{t-1}^T\widehat{\beta}_{3n}^{**}}\right)^2}x_{t-1}^T\left(\beta_0-\widehat{\beta}_{3n}\right)-\widehat{\theta}_{3n}e_{t-1}\\ &= \left(\frac{e^{x_t^T\widehat{\beta}_{3n}^*}}{\left(1+e^{x_t^T\widehat{\beta}_{3n}^*}\right)^2}x_t^T-\widehat{\theta}_{3n}\frac{e^{x_{t-1}^T\widehat{\beta}_{3n}^{**}}}{\left(1+e^{x_{t-1}^T\widehat{\beta}_{3n}^{**}}\right)^2}x_{t-1}^T\right)\left(\beta_0-\widehat{\beta}_{3n}\right)+\eta_t.\end{aligned} \tag{4.44}$$

By (2.8) and (2.10), we have

$$\begin{aligned}0 &= \sum_{t=2}^{n}\left(\widehat{\varepsilon}_t(3)-\widehat{\theta}_{3n}\widehat{\varepsilon}_{t-1}(3)\right)\left(\frac{e^{x_t^T\widehat{\beta}_{3n}^*}}{\left(1+e^{x_t^T\widehat{\beta}_{3n}^*}\right)^2}x_t-\widehat{\theta}_{3n}\frac{e^{x_{t-1}^T\widehat{\beta}_{3n}^{**}}}{\left(1+e^{x_{t-1}^T\widehat{\beta}_{3n}^{**}}\right)^2}x_{t-1}\right)\\ &= \sum_{t=2}^{n}\left(\frac{e^{x_t^T\widehat{\beta}_{3n}^*}}{\left(1+e^{x_t^T\widehat{\beta}_{3n}^*}\right)^2}x_t^T-\widehat{\theta}_{3n}\frac{e^{x_{t-1}^T\widehat{\beta}_{3n}^{**}}}{\left(1+e^{x_{t-1}^T\widehat{\beta}_{3n}^{**}}\right)^2}x_{t-1}^T\right)\left(\beta_0-\widehat{\beta}_{3n}\right)\\ &\quad\times\left(\frac{e^{x_t^T\widehat{\beta}_{3n}^*}}{\left(1+e^{x_t^T\widehat{\beta}_{3n}^*}\right)^2}x_t-\widehat{\theta}_{3n}\frac{e^{x_{t-1}^T\widehat{\beta}_{3n}^{**}}}{\left(1+e^{x_{t-1}^T\widehat{\beta}_{3n}^{**}}\right)^2}x_{t-1}\right)\\ &\quad+\sum_{t=2}^{n}\eta_t\left(\frac{e^{x_t^T\widehat{\beta}_{3n}^*}}{\left(1+e^{x_t^T\widehat{\beta}_{3n}^*}\right)^2}x_t-\widehat{\theta}_{3n}\frac{e^{x_{t-1}^T\widehat{\beta}_{3n}^{**}}}{\left(1+e^{x_{t-1}^T\widehat{\beta}_{3n}^{**}}\right)^2}x_{t-1}\right)\\ &= \left(\beta_0-\widehat{\beta}_{3n}\right)^T X_{3n}\left(\widehat{\beta}_{3n}^*,\widehat{\beta}_{3n}^{**},\widehat{\theta}_{3n}\right)+\sum_{t=2}^{n}\eta_t\left(\frac{e^{x_t^T\widehat{\beta}_{3n}^*}}{\left(1+e^{x_t^T\widehat{\beta}_{3n}^*}\right)^2}x_t-\widehat{\theta}_{3n}\frac{e^{x_{t-1}^T\widehat{\beta}_{3n}^{**}}}{\left(1+e^{x_{t-1}^T\widehat{\beta}_{3n}^{**}}\right)^2}x_{t-1}\right).\end{aligned} \tag{4.45}$$

From (4.45), we obtain

$$\widehat{\beta}_{3n}-\beta_0 = X_{3n}^{-1}\left(\widehat{\beta}_{3n}^*,\widehat{\beta}_{3n}^{**},\widehat{\theta}_{3n}\right)\sum_{t=2}^{n}\eta_t\left(\frac{e^{x_t^T\widehat{\beta}_{3n}^*}}{\left(1+e^{x_t^T\widehat{\beta}_{3n}^*}\right)^2}x_t-\widehat{\theta}_{3n}\frac{e^{x_{t-1}^T\widehat{\beta}_{3n}^{**}}}{\left(1+e^{x_{t-1}^T\widehat{\beta}_{3n}^{**}}\right)^2}x_{t-1}\right). \tag{4.46}$$

By (4.44), (4.46) and Lemma 4.2, we have

$$\begin{aligned}
(n-1)\widehat{\sigma}_{3n}^2 &= \sum_{t=2}^{n}\left(\widehat{\varepsilon}_t(3)-\widehat{\theta}_{3n}\widehat{\varepsilon}_{t-1}(3)\right)^2 \\
&= \sum_{t=1}^{n}\eta_t^2+\left(\beta_0-\widehat{\beta}_{3n}\right)^T X_{3n}\left(\widehat{\beta}_{3n}^*,\widehat{\beta}_{3n}^{**},\widehat{\theta}_{3n}\right)\left(\beta_0-\widehat{\beta}_{3n}\right) \\
&\quad +2\left(\beta_0-\widehat{\beta}_{3n}\right)^T\sum_{t=2}^{n}\eta_t\left(\frac{e^{x_t^T\widehat{\beta}_{3n}^*}}{\left(1+e^{x_t^T\widehat{\beta}_{3n}^*}\right)^2}x_t-\widehat{\theta}_{3n}\frac{e^{x_{t-1}^T\widehat{\beta}_{3n}^{**}}}{\left(1+e^{x_{t-1}^T\widehat{\beta}_{3n}^{**}}\right)^2}x_{t-1}\right) \\
&= \sum_{t=1}^{n}\eta_t^2-\left(\sum_{t=2}^{n}\eta_t X_{3n}^{-1/2}\left(\widehat{\beta}_{3n}^*,\widehat{\beta}_{3n}^{**},\widehat{\theta}_{3n}\right)\right. \\
&\qquad \left.\times\left(\frac{e^{x_t^T\widehat{\beta}_{3n}^*}}{\left(1+e^{x_t^T\widehat{\beta}_{3n}^*}\right)^2}x_t^T-\widehat{\theta}_{3n}\frac{e^{x_{t-1}^T\widehat{\beta}_{3n}^{**}}}{\left(1+e^{x_{t-1}^T\widehat{\beta}_{3n}^{**}}\right)^2}x_{t-1}^T\right)\right)^2 \\
&= \sum_{t=1}^{n}\eta_t^2-\left(\sum_{t=2}^{n}\eta_t X_{3n}^{-1/2}(\varphi_0)\left(\frac{e^{x_t^T\beta_0}}{\left(1+e^{x_t^T\beta_0}\right)^2}x_t-\theta_0\frac{e^{x_{t-1}^T\beta_0}}{\left(1+e^{x_{t-1}^T\beta_0}\right)^2}x_{t-1}\right)\right)^2+o_p(1).
\end{aligned} \tag{4.47}$$

By (3.3)–(3.5), we know that

$$d_{3n}=\widehat{L}_{3n}-\widehat{L}_n=(n-1)\ln\left(\frac{\widehat{\sigma}_{3n}^2}{\widehat{\sigma}_n^2}\right)=(n-1)\left(\left(\frac{\widehat{\sigma}_{3n}^2}{\widehat{\sigma}_n^2}\right)-1\right)+o_P(1). \tag{4.48}$$

Under the H_{03}, by (4.26), (4.47) and (4.48), we have

$$\frac{(n-1)\left(\widehat{\sigma}_{3n}^2-\widehat{\sigma}_n^2\right)}{\widehat{\sigma}_n^2}=\frac{\left(\sum_{t=2}^{n}\eta_t e_{t-1}\right)^2}{\sigma_0^2\sum_{t=2}^{n}e_{t-1}^2}+o_P(1). \tag{4.49}$$

Thus, (3.10) follows from (4.48), (4.49), and (4.35). Therefore, we complete the proof of Theorem 3.1. □

5. Conclusions and Open Problems

In the paper, we consider the generalized linear mode with FCA processes, which includes many special cases, such as an ordinary regression model, an ordinary generalized regression model, a linear regression model with constant coefficient autoregressive processes, time-dependent and function coefficient autoregressive processes, constant coefficient autoregressive processes, time-dependent or time-varying autoregressive processes, and a linear

regression model with functional coefficient autoregressive processes. And then we obtain the QML estimators for some unknown parameters in the generalized linear mode model and extend some estimators. At last, we use pseudo LR method to investigate three hypothesis tests of interest and obtain the asymptotic chi-squares distributions of statistics.

However, several lines of future work remain open.

(1) It is well known that a conventional time series can be regarded as the solution to a differential equation of integer order with the excitation of white noise in mathematics, and a fractal time series can be regarded as the solution to a differential equation of fractional order with a white noise in the domain of stochastic processes (see [25]). In the paper, $\{\varepsilon_t\}$ is a conventional nonlinear time series. We may investigate some hypothesis tests by pseudo LR method when the $\{\varepsilon_t\}$ is a fractal time series (the idea is given by an anonymous reviewer). In particular, we assume that

$$\sum_{i=0}^{p} a_{p-i} D^{v_i} \varepsilon_t = \eta_t, \tag{5.1}$$

where $v_p, v_{p-1}, \ldots, v_0$ is strictly decreasing sequence of nonnegative numbers, a_i is a constant sequence, and D^v is the Riemann-Liouville integral operator of order $v > 0$ given by

$$D^v h(t) = \frac{1}{\Gamma(v)} \int_0^t (t-u)^{v-1} h(u) du, \tag{5.2}$$

where Γ is the Gamma function, and $h(t)$ is a piecewise continuous on $(0, \infty)$ and integrable on any finite subinterval of $[0, \infty)$ (See [25, 26]). Fractal time series may have a heavy-tailed probability distribution function and has been applied various fields of sciences and technologies (see [25, 27–32]). Thus it is very significant to investigate various regression models with fractal time series errors, including regression model (1.1) with (5.1).

(2) We maybe investigate the others hypothesis tests, for example:

H_{04}: $f_t(\theta) = 0, g(u) = \mathrm{u}, \sigma_0^2 > 0$;

H_{05}: $f_t(\theta) = \theta, g(u) = 0, \sigma_0^2 > 0$;

H_{06}: $f_t(\theta) = 0, g(u) = e^u/(1+e^u), \sigma_0^2 > 0$;

H_{07}: $f_t(\theta) = a_t$ and $g(u)$ is a continuous function, $\sigma_0^2 > 0$;

H_{08}: $f_t(\theta) = a_t, g(u) = u, \sigma_0^2 > 0$;

H_{09}: $f_t(\theta) = a_t, g(u) = e^u/(1+e^u), \sigma_0^2 > 0$.

Acknowledgments

The authors would like to thank the anonymous referees for their valuable comments which have led to this much improved version of the paper. The paper was supported by Scientific Research Item of Department of Education, Hubei (no. D20112503), Scientific Research Item of Ministry of Education, China (no. 209078), and Natural Science Foundation of China (no. 11071022, 11101174).

References

[1] Z. D. Bai and M. Guo, "A paradox in least-squares estimation of linear regression models," *Statistics & Probability Letters*, vol. 42, no. 2, pp. 167–174, 1999.

[2] Y. Li and H. Yang, "A new stochastic mixed ridge estimator in linear regression model," *Statistical Papers*, vol. 51, no. 2, pp. 315–323, 2010.

[3] A. E. Hoerl and R. W. Kennard, "Ridge regression: Biased estimation for nonorthogonal problems," *Technometrics*, vol. 12, pp. 55–67, 1970.

[4] X. Chen, "Consistency of LS estimates of multiple regression under a lower order moment condition," *Science in China Series A*, vol. 38, no. 12, pp. 1420–1431, 1995.

[5] T. W. Anderson and J. B. Taylor, "Strong consistency of least squares estimates in normal linear regression," *The Annals of Statistics*, vol. 4, no. 4, pp. 788–790, 1976.

[6] G. González-Rodríguez, A. Blanco, N. Corral, and A. Colubi, "Least squares estimation of linear regression models for convex compact random sets," *Advances in Data Analysis and Classification*, vol. 1, no. 1, pp. 67–81, 2007.

[7] H. Cui, "On asymptotics of t-type regression estimation in multiple linear model," *Science in China Series A*, vol. 47, no. 4, pp. 628–639, 2004.

[8] M. Q. Wang, L. X. Song, and X. G. Wang, "Bridge estimation for generalized linear models with a diverging number of parameters," *Statistics & Probability Letters*, vol. 80, no. 21-22, pp. 1584–1596, 2010.

[9] L. C. Chien and T. S. Tsou, "Deletion diagnostics for generalized linear models using the adjusted Poisson likelihood function," *Journal of Statistical Planning and Inference*, vol. 141, no. 6, pp. 2044–2054, 2011.

[10] L. Fahrmeir and H. Kaufmann, "Consistency and asymptotic normality of the maximum likelihood estimator in generalized linear models," *The Annals of Statistics*, vol. 13, no. 1, pp. 342–368, 1985.

[11] Z. H. Xiao and L. Q. Liu, "Laws of iterated logarithm for quasi-maximum likelihood estimator in generalized linear model," *Journal of Statistical Planning and Inference*, vol. 138, no. 3, pp. 611–617, 2008.

[12] Y. Bai, W. K. Fung, and Z. Zhu, "Weighted empirical likelihood for generalized linear models with longitudinal data," *Journal of Statistical Planning and Inference*, vol. 140, no. 11, pp. 3446–3456, 2010.

[13] S. G. Zhao and Y. Liao, "The weak consistency of maximum likelihood estimators in generalized linear models," *Science in China A*, vol. 37, no. 11, pp. 1368–1376, 2007.

[14] P. Pere, "Adjusted estimates and Wald statistics for the AT(1) model with constant," *Journal of Econometrics*, vol. 98, no. 2, pp. 335–363, 2000.

[15] R. A. Maller, "Asymptotics of regressions with stationary and nonstationary residuals," *Stochastic Processes and Their Applications*, vol. 105, no. 1, pp. 33–67, 2003.

[16] W. A. Fuller, *Introduction to Statistical Time Series*, John Wiley & Sons, New York, NY, USA, 2nd edition, 1996.

[17] G. H. Kwoun and Y. Yajima, "On an autoregressive model with time-dependent coefficients," *Annals of the Institute of Statistical Mathematics*, vol. 38, no. 2, pp. 297–309, 1986.

[18] J. S. White, "The limiting distribution of the serial correlation coefficient in the explosive case," *Annals of Mathematical Statistics*, vol. 29, pp. 1188–1197, 1958.

[19] J. S. White, "The limiting distribution of the serial correlation coefficient in the explosive case—II," *Annals of Mathematical Statistics*, vol. 30, pp. 831–834, 1959.

[20] J. D. Hamilton, *Time Series Analysis*, Princeton University Press, Princeton, NJ, USA, 1994.

[21] F. Carsoule and P. H. Franses, "A note on monitoring time-varying parameters in an autoregression," *International Journal for Theoretical and Applied Statistics*, vol. 57, no. 1, pp. 51–62, 2003.

[22] R. Azrak and G. Mélard, "Asymptotic properties of quasi-maximum likelihood estimators for ARMA models with time-dependent coefficients," *Statistical Inference for Stochastic Processes*, vol. 9, no. 3, pp. 279–330, 2006.

[23] R. Dahlhaus, "Fitting time series models to nonstationary processes," *The Annals of Statistics*, vol. 25, no. 1, pp. 1–37, 1997.

[24] H. Hu, "QML estimators in linear regression models with functional coefficient autoregressive processes," *Mathematical Problems in Engineering*, vol. 2010, Article ID 956907, 30 pages, 2010.

[25] M. Li, "Fractal time series—a tutorial review," *Mathematical Problems in Engineering*, vol. 2010, Article ID 157264, 26 pages, 2010.

[26] Y. S. Mishura, *Stochastic Calculus for Fractional Brownian Motion and Related Processes*, vol. 1929 of *Lecture Notes in Mathematics*, Springer, Berlin, Germany, 2008.

[27] M. Li and W. Zhao, "Visiting power laws in cyber-physical networking systems," *Mathematical Problems in Engineering*, vol. 2012, Article ID 302786, 13 pages, 2012.
[28] M. Li, C. Cattani, and S. Y. Chen, "Viewing sea level by a one-dimensional random function with long memory," *Mathematical Problems in Engineering*, vol. 2011, Article ID 654284, 13 pages, 2011.
[29] C. Cattani, "Fractals and hidden symmetries in DNA," *Mathematical Problems in Engineering*, vol. 2010, Article ID 507056, 31 pages, 2010.
[30] J. Lévy-Véhel and E. Lutton, *Fractals in Engineering*, Springer, 1st edition, 2005.
[31] V. Pisarenko and M. Rodkin, *Heavy-Tailed Distributions in Disaster Analysis*, Springer, 2010.
[32] H. Sheng, Y.-Q. Chen, and T.-S. Qiu, *Fractional Processes and Fractional Order Signal Processing*, Springer, 2012.

Hindawi Publishing Corporation
Mathematical Problems in Engineering
Volume 2012, Article ID 296407, 14 pages
doi:10.1155/2012/296407

Research Article

Detection and Recognition of Abnormal Running Behavior in Surveillance Video

Ying-Ying Zhu,[1] Yan-Yan Zhu,[1] Wen Zhen-Kun,[1] Wen-Sheng Chen,[2] and Qiang Huang[1]

[1] *College of Computer and Software, Shenzhen University, Shenzhen 518060, China*
[2] *College of Mathematics and Computational Science, Shenzhen University, Shenzhen 518060, China*

Correspondence should be addressed to Qiang Huang, jameshq@szu.edu.cn

Received 15 January 2012; Accepted 14 February 2012

Academic Editor: Ming Li

Abnormal running behavior frequently happen in robbery cases and other criminal cases. In order to identity these abnormal behaviors a method to detect and recognize abnormal running behavior, is presented based on spatiotemporal parameters. Meanwhile, to obtain more accurate spatiotemporal parameters and improve the real-time performance of the algorithm, a multitarget tracking algorithm, based on the intersection area among the minimum enclosing rectangle of the moving objects, is presented. The algorithm can judge and exclude effectively the intersection of multitarget and the interference, which makes the tracking algorithm more accurate and of better robustness. Experimental results show that the combination of these two algorithms can detect and recognize effectively the abnormal running behavior in surveillance videos.

1. Introduction

In most of the existing video surveillance systems, moving objects only were detected and tracked, which lacked to detect and recognize their behaviors in the surveillance scene. However, the purpose of monitoring the scene is to detect and analyze the unusual event or person's abnormal behavior in real life. In a long video sequence, such works handled manually are neither practical nor efficient, and the video surveillance system has already lost its original intention for preventing and actively intervening and almost become a tool of providing video evidence afterwards. The intelligent detection of abnormal behavior not only can detect abnormal behavior and inform the staffs to prevent illegal activities in time, but also can save a lot of storage space and avoid the staffs finding and collecting massively evidence after the illegal actions had happened.

At present, the methods of detecting abnormal behavior always have analyzed the continuous motion trail of moving object. First of all, the areas that change in the current frame have been identified, and the objects (people) of the region has been tracked in real-time. Secondly, velocity, acceleration, motion direction, and so on has been computed on the basis of the state information that was founded in each frame, and state models have been established. Finally, state parameters of the test video have been matched with the precalibrated parameters of the model in which the normal and reference sequence of events have been contained, and then abnormal events can be detected under the degree of match [1, 2]. Shape, motion and other information have been extracted from image sequence through a predetermined criteria. Based on above-mentioned information, the normal behavior model has been defined by using artificial or semisupervised methods, which usually have modeled the state represented by the features of the image sequences with HMM, and then observation has been considered as abnormal behavior if they do not match the normal behavior model [3, 4]. However, the unpredictable and infrequent characteristics of abnormal behaviors have limited the supervised learning methods, because these methods have needed a large number of training samples. The complexity of events and actions often make a simple event model not enough to express a wide range of abnormal behaviors [5, 6].

In [7, 8], video documents were divided into some segments according to some rules, then extracting features from each subvideo were composed of a vector to represent this sub-video. The method of clustering and similarity measure was adapted to those vectors, and then the behavior in a sub-video would be considered as abnormal if the subvideo had less categories. But the computation would dramatically increase as the number of categories increased. It was very difficult that identifying abnormal behavior kept real time. Jian-hao and Li [9] proposed a method to identify abnormal behavior, such as robbery, fighting and chasing, in surveillance videos. The method recognized these behaviors according to the disorder of velocity, and direction of these behaviors. However, the method could not distinguish the three abnormal behaviors. Cheng et al. [10] proposed a method to detect and describe periodic motions, which can be used to characterize periodic motion of a nonrigid moving object, such as human running behavior. Furthermore, to identify the human running behavior, they defined a descriptor derived from their periodic motion description. However, it could not classify these running behaviors.

In order to satisfy the real-time performance in the surveillance system, this paper proposes a method that detects the abnormal running behavior on the basis of spatio-temporal parameters in surveillance videos. First of all, we extract foreground objects from videos based on Mixture Gaussian Model and Frame Subtraction [11, 12] and binarize the images. The algorithm for extract foreground involves nonlinear systems [13–15]. In addition, we obtain a clearer foreground image with morphological processing. Furthermore, in order to satisfy the real-time requirement, this paper presents a multitarget tracking algorithm that is based on the intersection area among the minimum enclosing rectangles, which can effectively track multiple objects in the case of shelter. Finally, the abnormal running behavior can be detected through spatio-temporal relationship. Experimental results show the effective and the real-time performance of the proposed algorithm.

This paper is organized as follows. In Section 2, the definitions of the normal running behavior and the abnormal behavior are presented. In Section 3, the method of multitarget tracking is described in detail. In Section 4, the approach to recognize abnormal running behavior is described. In Section 5, experimental results based on the surveillance video database are shown, and the conclusion is given in Section 6.

2. Definition of Running Behaviors

Abnormal running behaviors frequently happened in robbery cases and other criminal cases. In order to distinguish between the abnormal running and the normal running, we first present the definition of the two behaviors as follow.

Definition 2.1 (normal running). The object gradually accelerates from the state of walking or being stationary and then reaches even greater than the speed of normal running after a certain long time, or the object's speed moving into the video scene is greater than the speed of normal running. We define the above-mentioned action as the Normal Running Behavior. It can be represented by the following equation:

$$\text{isRun} = \begin{cases} 1 & (V_0 \le V_{\text{walk}},\ V_t > V_{\text{run}},\ t > T_{\text{run}}) \| (V_0 \ge V_{\text{run}}), \\ 0 & \text{else.} \end{cases} \tag{2.1}$$

Definition 2.2 (abnormal running). The object suddenly accelerates from the state of walk or stationary and then reaches even greater than the speed of normal running after a certain short time, which is defined as Abnormal Running Behavior. It can be written as:

$$\text{isAbnormal} = \begin{cases} 1 & V_0 \le V_{\text{walk}},\ V_t > V_{\text{run}},\ t < T_{\text{ab}} \\ 0 & \text{else,} \end{cases} \tag{2.2}$$

where V_0, V_t are the initial velocity and the instantaneous velocity of the interested object, respectively, and $V_{\text{walk}}, V_{\text{run}}$ are the speed of walk and the speed of normal running, separately. In additional, t is the time interval of an object from the speed less than V_{walk} to the speed V_t. When the speed $V_t > V_{\text{run}}$, T_{run} is a time threshold used to determine whether the motion of object is the normal running, T_{ab} is also a time threshold used to determine whether the motion of object is the abnormal running, and there is $T_{\text{ab}} > T_{\text{run}}$. Diagrams of the behavior are shown in Figures 1 and 2.

In Figures 1 and 2, t_1 is the start time and t_2 is the moment that the speed of moving object reaches the V_{run} value. The difference between Figures 1 and 2 is that $t_2 - t_1 > T_{\text{run}}$ existed in Figure 1, while there is $t_2 - t_1 < T_{\text{ab}}$ in Figure 2. From this we have two conclusions: the key to distinguish the run behavior from the nonrun behavior is the speed of moving target; while the key to differentiate normal running from abnormal running is the moment at which moving targets achieve the speed of running.

3. Target Tracking under Shelter

3.1. The Basic Idea of the Method

Between the two adjacent images, the position and the contour of the same object are only changing a little in general, so the object's region in the two images is often intersected with each other [16, 17]. It is an important feature in continuous video sequences. The feature is exploited to track object in continuous video sequences in this paper, which is also used to detect moving objects in the algorithm of frame subtraction. In the following we will discuss the fundamental ideas of this paper in detail.

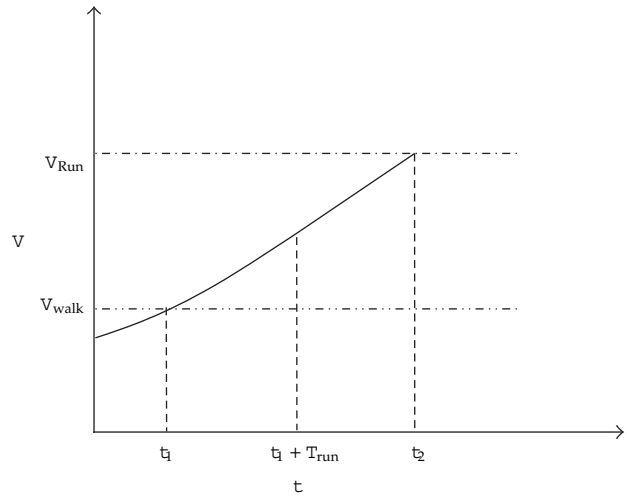

Figure 1: Normal running.

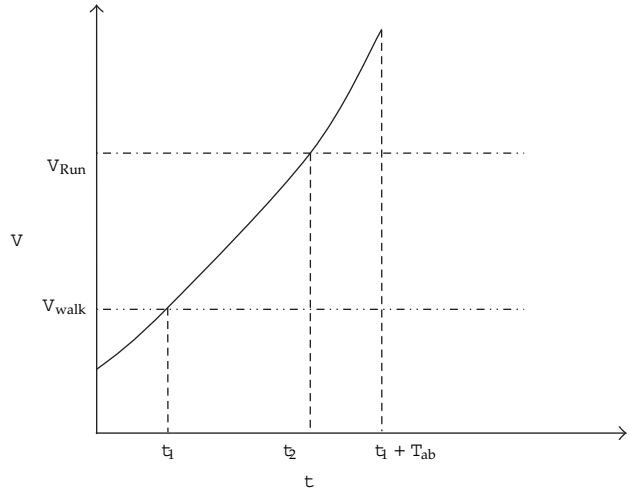

Figure 2: Abnormal running.

In this paper, a moving object is marked with the minimum enclosing rectangle which is represented as Rect $I(I.x, I.y, I.\text{width}, I.\text{Height})$, and $(I.x, I.y)$ refers to coordinates of the upper left corner. $(I.\text{width}, I.\text{Height})$ refers to the width and the height of the rectangle. Thus the moving object's centroid can be calculated as the following formula:

$$CI.x = I.x + \frac{I.\text{width}}{2}, \tag{3.1}$$

$$CI.\text{y} = I.\text{y} + \frac{I.\text{height}}{2}. \tag{3.2}$$

In accordance with (3.1) and (3.2), we can obtain the centroid $CI(CI.x, CI.y)$ of the moving object. We assume that J which is represented as Rect $J(J.x, J.y, J.\text{witdth}, J.\text{Height})$ is a moving object in the $t-1$ frame. We consider that the moving object J intersects with I, a moving object, in the t frame if they satisfy the following formulas:

$$|CI.x - CJ.x| \leq \frac{I.\text{width}}{2} + \frac{J.\text{width}}{2}, \tag{3.3}$$

$$\left|CI.y - CJ.y\right| \leq \frac{I.\text{height}}{2} + \frac{J.\text{height}}{2}, \tag{3.4}$$

$$\frac{\text{Aea}(\text{Rect } I \& \text{Rect } J)}{\min \text{ Aea}(\text{Rect } I, \text{Rect } J)} \geq r. \tag{3.5}$$

Actually the object I intersects with the object J if they satisfy the (3.3) and (3.4), while the object's position does not always have much change in the two adjacent images, so that the intersection area between the rectangle of Rect I and Rect J has the property that is represented as (3.5). In this paper, Rect I and Rect J are considered as the intersection unless they meet (3.3), (3.4), and (3.5) simultaneously. Shelter often occurs in surveillance scenes, because there are always multiple moving objects, so (3.5) can exclude a small part of the shelter which always impacts on the object tracking.

The shelter often happens in multitarget tracking in which objects may be sheltered by others or themselves, or by the stationary object in the background. The degree of the shelter is always different. The object's shelter can be divided into two stages. Firstly, the shelter occurring means that the target information is lost more and more during this period, which is shown as two or more rectangle boxes merged. Secondly, the shelter begins disappearing, and the target information is gradually restored, which are shown as the rectangle box separated into two or more rectangle boxes.

Therefore, when the block is occurring, this approach is to merge the blocked objects into a new object tracking and to record the histogram information of the sheltered objects in the previous frame. When the shelter is disappearing, to recognize the separated object, the separated rectangular box matches the recorded histogram of the tracked target.

3.2. The Exclusion of Interference

The interference in the moving object detection phase generally has two features. One is small size, and the other is the short survival time. In the former case, since we are only interested in people in video images and the people size in video images is generally not too small, so we can use a threshold to remove small object. According to data from several experimental results, we remove the object if its target area is less than 30 pixels. In the latter case, we have designed the list of temporary tracked objects, *m_TempObjectList*, and the list of tracked objects, *m_TrackedObjectList*, which are shown in Figure 3.

The node structures of the two lists are same. Each node records the corresponding history information of the moving target, such as the information of tracking process or the tracking information of behaviors analysis. These nodes are called tracked objects. There are differences in the two lists. *m_TempObjectList* records the moving object in scenes whose existence time does not exceed a certain threshold, and *m_TrackedObjectList* records the stable moving object whose existence time reaches a certain threshold.

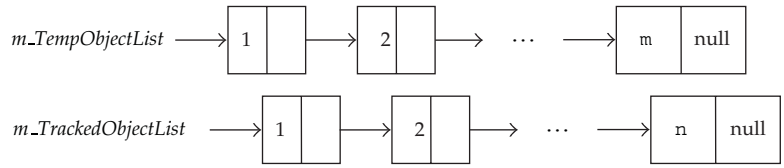

Figure 3: The list of temporary tracked object and tracked object.

According to many experimental results, only when the existence time of the moving object reaches 5 frames, then the moving object is inserted into *m_TrackedObjectList* and deleted from *m_TempObjectList*. This method can exclude short-term interference in the surveillance video. Meanwhile, in order to avoid the interference in which the objects appear in part, we only deal with the object that has entered completely into the scene.

3.3. The Proposed Algorithm

Algorithm 3.1. Multitarget tracking algorithm.
Input. The list of moving objects extracted from the current frame.

Step 1. We get a node from the *m_TempObjectList* or *m_TrackedObjectList*. If there are moving objects in the list of moving objects with the node that satisfies the formulae (3.3), (3.4), and (3.5), then those moving objects are recorded as associated objects in the node. The node is recorded as associated node in those moving objects too. If there are some nodes which are not handled in the *m_TempObjectList* or the *m_TrackedObjectList*, then go to Step 1. Otherwise, go to Step 2.

Step 2. We get a node from the *m_TempObjectList* and the *m_TrackedObjectList* and count the number of associated objects of the node. If $n = 0$, then goto Step 3, else if $n = 1$, then go to Step 4, else go to Step 5. If every node in the *m_TempObjectList* and the *m_TrackedObjectList* has been processed, then go to Step 6.

Step 3. $n = 0$ shows the tracked objects has disappeared in the current frame, if it belongs to *m_TempObjectList*, then it is deleted from *m_TempObjectList*. Otherwise if it is inserted into *m_TempObjectList* and deleted from *m_TrackedObjectList*, go to Step 2.

Step 4. $n = 1$ means that there is only one object associated with the node. If there are more associated nodes recorded in the associated object, then the shelter algorithm will begin. Otherwise, the node is updated with the information of the associated object. Go to Step 2.

Step 5. $n > 1$ indicates that there are more associated objects, so the approach of the shelter disappearing is utilized. Go to Step 2.

Step 6. If there are not objects associated with any node in the *m_TempObjectList* and the *m_TempObjectList,* then a new node is generated for the object, and the node is inserted into the *m_TempObjectList*. Go to Step 7.

Step 7. Update the *m_TempObjectList* and the *m_TrackedObjectList*. Delete the node whose existence time is more than *5* frames from the *m_TempObjectList* and insert it into the *m_TrackedObjectList*.

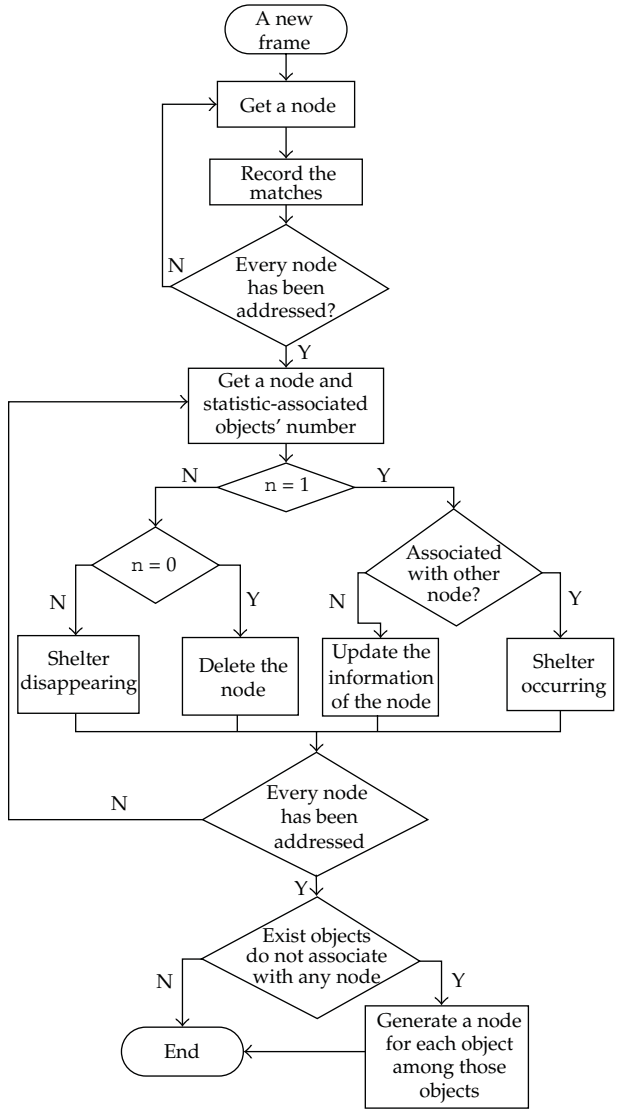

Figure 4: The main flow of multitarget tracking method.

Figure 4 shows the main flow chart of the algorithm. Mean shift and Particle Filter are the most popular tracking algorithms in the intelligent video surveillance system. Comparing with Mean shift tracking algorithm and Particle Filter tracking algorithm, the proposed multitarget tracking algorithm has the following advantages.

(1) In the tracking result, regardless of the shelter, Particle Filter tracking results are more accurate than Mean shift, and Particle Filter is less affected by the background. Mean shift can track fast moving targets, but it is vulnerable to the background that is similar to the tracking target. And it can easily cause the vibration of the tracking window, which results in the tracking result being not stable. But our algorithm is less affected by the background as well as Particle Filter, and our algorithm can exclude two typical interferences in the surveillance video. Particle Filter and Mean

shift cannot track the object which is entirely sheltered, but our algorithm can do this.

(2) About the time complexity, Particle Filter is more complex than Mean shift. The time complexity of Particle Filter is $O(K^2N^2)$, where K is the number of moving objects in the current frame, and N is the number of particles that distributed to moving objects [18]. The time complexity of Mean shift is $O(Nk_hC_s)$, where N is the average number of iterations per frame, k_h is the number of pixel of target in the window of nuclear function, and is C_s the cost of arithmetic operations, such as an addition operation [19]. However, the time complexity of the proposed multitarget tracking algorithm is $O(K^2)$, where K is the number of moving objects in the current frame.

4. Detection of Abnormal Running Behavior

4.1. Detection of Running Behavior

According to the conclusion in the second part, the key to distinguish the running behavior or nonrunning behavior is the speed of the moving object. The instantaneous speeds of the targets can be simply obtained from $v_{\text{video}} = s_k - s_{k-1}$, where s_k, s_{k-1} is the target's centroid in the frame of k and $k-1$, respectively. But it has not taken into account the actual action. People may appear into the surveillance video scene from different angles, and the distance between man and the camera may be changing. In addition, the focal lengths of cameras may often vary. Although people were standing in the same position, if its location was relatively far away from the camera, his picture will be small. On the contrary it will be relatively large. Moreover, the focal length has the same impact on the picture size of man in the video images. Thus we can see that v_{video} is related with the camera focal length and the distance between man and camera, for which we use the following formula to revise v_{video}:

$$v = \alpha \times \frac{v_{\text{video}}}{\sqrt{\min \text{ Aea}(\text{Rect } I, \text{Rect } I')}}, \tag{4.1}$$

where Rect I, Rect I' is the enclosing rectangle of the moving object I in two adjacent frames, respectively. And $\alpha = 27$ is a const, v_{video}, v'_{video} is the instantaneous speed of object I in the corresponding conditions of Rect I, Rect I', respectively. As Rect$I$ is similar to Rect I', $v_{\text{video}}/\sqrt{\text{area}(\text{Rect } I)} = v'_{\text{video}}/\sqrt{\text{area}(\text{Rect } I')}$. From this we can see that if the actual speeds of an object into surveillance scene are same, $v_{\text{video}}/\sqrt{\text{area}(\text{Rect } I)}$ is same as the target area, even if in different shooting conditions. Therefore, the speed revised by (4.1) is reliable.

However, there are many reasons leading to the instantaneous speed being not reliable. First of all, the human motions are a complex system with a high degree of freedom and nonlinear characteristics. Secondly, the position and the contour of the object will have little change between the two adjacent images in general. Nevertheless, there may be some interference in the phase of extracting moving targets. It will lead to the centroid position if the target have not changed, even in the opposite direction. It makes the centroid and the instantaneous speed not accurate with formula (3.1). To reduce the influence of the unreliable factors, we use the average speed in a short time to distinct running or not. The average speed of the targets can be obtained from $\overline{v} = (\text{v}_{k_1} + \cdots + \text{v}_{k_2})/(k_2 - k_1)$, where k_2 and k_1 is frame number.

4.2. Recognition between Normal and Abnormal Running

Distinction of abnormal running is carried out under the condition of, $V_t > V_{\text{run}}$. Only when the speed of the moving target has reached the V_{run}, we determine whether the object running is normal running or not. According to Definition 2.2, if the speed of the moving target achieves the running speed, the key to distinguish whether it is abnormal running is the time of t. If it is abnormal running, there are $t < T_{\text{ab}}$ and $V_0 \leq V_{\text{walk}}$. According to the Newton Leibniz Theorem, there are

$$\begin{aligned} V_t - V_0 &= \int a\,dt = \overline{a}t \Longrightarrow t = \frac{(V_t - V_0)}{\overline{a}} \\ & t < T_{\text{ab}}, \\ & V_0 \leq V_{\text{walk}}, \quad V_t > V_{\text{run}} \\ & \overline{a} > \frac{(V_{\text{run}} - V_{\text{walk}})}{T_{\text{ab}}}, \end{aligned} \tag{4.2}$$

where V_{run}, V_{walk}, and T_{ab} are consts, so $(V_{\text{run}} - V_{\text{walk}})/T_{\text{ab}}$ is a const too, which is abbreviated as AMIN in this paper. Therefore, it can be distinguished between abnormal and normal running by judging whether $\overline{a}$ is greater than AMIN.

4.3. The Proposed Recognition Algorithm

Based on the above analysis, Definition 2.2 reduces to the following formula:

$$\text{isAbnormal} = \begin{cases} 1 & \overline{V} > V_{\text{run}},\ \overline{a} > \text{AMIN}, \\ 0 & \text{else}. \end{cases} \tag{4.3}$$

In accordance with the above formula, determining whether the target behavior is abnormal running, we only need to judge whether $\overline{V}$ and $\overline{a}$ of the moving target meet a certain condition. In the light of many experimental results, the threshold of $\overline{V}$ and $\overline{a}$ is set to 4.0 and 0.4, separately. Thus we get the criterion for detecting and recognizing abnormal.

Algorithm 4.1. recognition algorithm for abnormal running.
Input. The list of moving objects extracted from current frame.

Step 1. The moving targets in the current frame are tracked with Algorithm 3.1, and then *m_TrackedObjectList* is got. Go to Step 2.

Step 2. Get a tracked object from *m_TrackedObjectList and* calculate the average speed $\overline{v}$ of the object in 5 frames, if $\overline{v} > V_{\text{run}}$ then go to Step 3, else go to Step 4.

Step 3. Calculating the average acceleration $\overline{a}$ of the object in 5 frames, if $\overline{a} >$ AMIN then the object is identified as abnormal, otherwise go to Step 4.

Step 4. If there are tracked objects in the *m_TrackedObjectList* have not been access then go to Step 2, else end.

Figure 5 shows the main flow chart of the algorithm.

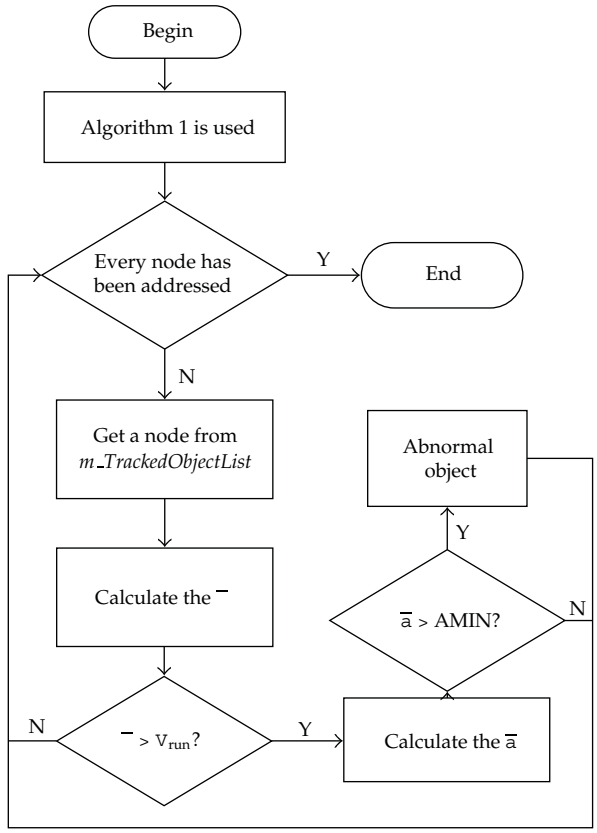

Figure 5: The main flow of recognition algorithm for abnormal running.

5. Experimental Results

Our algorithms are implemented using the OpenCV library with C++ interface, which has been tested and evaluated in simple surveillance scenes and complicated surveillance scenes from open surveillance datasets PETS 2007 [20]. Objects are modeled as rectangular bounding boxes with two colors. If the object is an abnormal object, then we identify it with black box and red "running" will appear on the box above, otherwise with red box, no "running". Besides, the red font upper left corner of the image shows the frame number. and the number of the objects, what is more, the green line in the image stands for the trajectory of the objects.

5.1. The Selection of V_{run} and AMIN

Figure 6(a) shows the relationship between the performance of the proposed algorithm and the value of threshold V_{run}. And Figure 6(b) shows the relationship between the performance of the algorithm and the threshold value of AMIN too. According to Figure 6, we conclude that the best threshold of V_{run} is 4.0, and the optimal threshold of AMIN is 0.4.

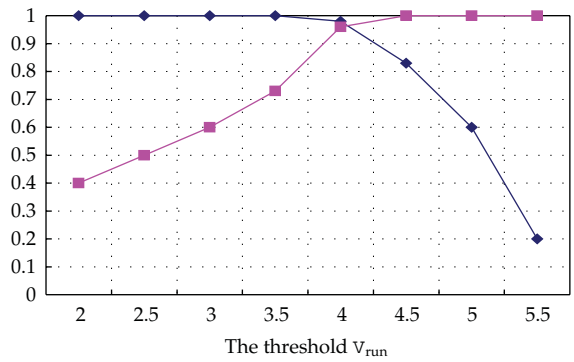

(a) The threshold V_{run}

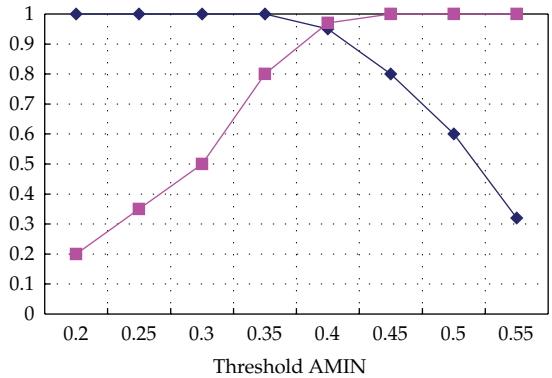

(b) The threshold AMIN

Figure 6: The detection of performance at different threshold values.

5.2. In Simple Surveillance Scenes

The first test case is to detect abnormal running in a simple scene with single person. Figure 6 shows the result. In Figure 7(a), the existence time of the target is less than 5 frame, so that its behavior is not judged in frame 425. But in Figure 7(b), the average speed of the person reaches $\overline{v} = 5.34$ which is more than 4.0, and the average acceleration of the person is $\overline{a} = 0.889$ which is more than 0.4 too, and we can see that $\overline{v}$ and $\overline{a}$ meet the criterion for judging abnormal running, so the person is an abnormal target in the frame of 433.

5.3. In Complicated Surveillance Scenes

Figures 8 and 9 illustrate two complicated cases of abnormal running detection, respectively. In Figure 8, although there is more than one object, but shelter did not occurred between the objects, yet shelter happened in Figure 8.

(a) The frame of 425 (b) The frame of 433

Figure 7: Detection of abnormal running in simple surveillance scenes.

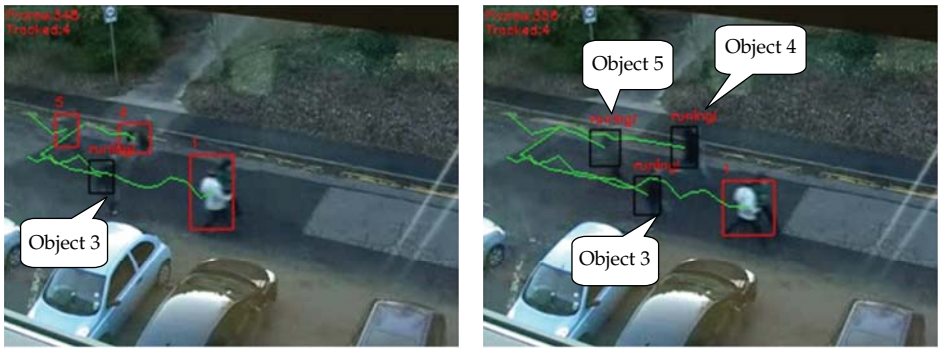

(a) The frame of 348 (b) The frame of 356

Figure 8: Without shelter.

In Figure 8(a), the average speed of the person (referred to as object 1) is $\overline{v} = 5.42$ which is more than 4.0, but his average acceleration $\overline{a} = -0.05$, which is less than 0.4, so the person 1 is not an abnormal target in the frame 65. Meanwhile, the average speed of another person (referred to as object 3) is $\overline{v} = 7.50$ and its average acceleration is $\overline{a} = 1.87$, so object 3 is an abnormal target. Besides, the existence time of object 4 and object 5 is both less than 5, so that their behaviors are not judged in the frame 348. In Figure 8(b), the average speed of object 1 is $\overline{v} = 7.9$, but its average acceleration is $\overline{a} = 0.17$, so object 1 is not an abnormal target. While the average speed of object 3 is $\overline{v} = 7.00$ and its average acceleration is $\overline{a} = 1.40$, the average speed of object 4 is $\overline{v} = 4.85$ and its average acceleration is $\overline{a} = 1.21$, and the average speed of the object 5 is $\overline{v} = 5.00$ and its average acceleration is $\overline{a} = 1.69$, so as we have seen, object 3, object 4 and object 5 are all identified as abnormal targets in frame 356.

In Figure 9(a), the average speed of the object 2 is $\overline{v} = 3.49$, and is less than 4.0, so it is not an abnormal target. Object 3 behavior is not judged because of its existence time which is less than 5 frames. In Figure 9(b), serious shelter happened, which results in object 2 and object 3 merged into a new object 4, so we only need judge object 4, at this time the average speed of object 4 is $\overline{v} = 4.29$, and its average acceleration is $\overline{a} = 0.71$, so object 4 is identified as an abnormal target. Experimental results show that this algorithm can accurately detect the abnormal running behavior in different scenes.

(a) The frame of 44 (b) The frame of 76

Figure 9: With shelter.

6. Conclusion

Abnormal running frequently happened in robbery cases and other criminal cases. In order to identity such abnormal behavior in real time, this paper proposed a method on the basis of spatio-temporal parameters which can detect accurately the abnormal running. Meanwhile, to obtain precise spatiotemporal parameters and improve the real-time performance of the proposed algorithm, this paper proposed a multitarget tracking algorithm that is based on the intersection area among the minimum enclosing rectangle of the moving objects. The simple and real-time algorithm can effectively judge the intersection among objects and exclude the interference. In addition, two means of excluding interference are adopted in the multitarget tracking, which can exclude the objects which are too small or stay too short in scenes. Thus, the complexity of multitarget tracking is reduced significantly, and the accuracy is improved.

Acknowledgments

This work was partially supported by Natural Science Foundation of China under Grant no. 61170326, Natural Science Foundation of Guangdong Province under Grant no. 9151806001000011, Science & Technology Planning Project of Shenzhen City (JC200903120115A, 0015533011100512097), and Public Technical Service Platform of Shenzhen (0015533054100524069).

References

[1] M. A. Geng-yu and L. I. N. Xue-yin, "Unexpected human behavior recognition in image sequences using multiple features," in *Proceedings of the 20th International Conference on Pattern Recognition (ICPR '10)*, pp. 368–371, Istanbul, Turkey, August 2010.

[2] K. Sudo, T. Osawa, K. Wakabayashi, and H. Koike, "Detecting the degree of anomaly in security video," in *Proceedings of the IAPR Conference on Machine Vision Applications (MVA '07)*, pp. 3–7, Tokyo, Japan, May 2007.

[3] D. Matern, A. P. Condurache, and A. Mertins, *Linear Prediction Based Mixture Models for Event Detection in Video Sequences*, Springer, Berlin, Germany, 2011.

[4] P. L. M. Bouttefroy, A. Beghdadi, A. Bouzerdoum, and S. L. Phung, "Markov random fields for abnormal behavior detection on highways," in *Proceedings of the Visual Information Processing (EUVIP '10)*, 2nd European Workshop, pp. 149–154, Paris, France, July 2010.

[5] M. Li and W. Zhao, "Visiting power laws in cyber-physical networking systems," *Mathematical Problems in Engineering*, vol. 2012, Article ID 302786, 13 pages, 2012.
[6] M. Li, C. Cattani, and S. Y. Chen, "Viewing sea level by a one-dimensional random function with long memory," *Mathematical Problems in Engineering*, vol. 2011, Article ID 654284, 13 pages, 2011.
[7] D. Zhang, D. Gatica-Perez, S. Bengio, and I. Mccowan, "Semi-supervised adapted HMMs for unusual event detection," in *Proceedings of the IEEE Computer Society Conference on Computer Vision and Pattern Recognition (CVPR '05)*, pp. 611–618, June 2005.
[8] V. Reddy, C. Sanderson, and B. C. Lovell, "Improved anomaly detection in crowded scenes via cell-based analysis of foreground speed, size and texture," in *Proceedings of the IEEE Computer Society Conference on Computer Vision and Pattern Recognition Workshops*, pp. 55–61, June 2011.
[9] D. U. Jian-hao and X. U. Li, "Abnormal behavior detection based on regional optical flow," *Journal of Zhejiang University*, vol. 45, no. 7, pp. 1161–1166, 2011.
[10] F. Cheng, W. J. Christmas, and J. Kittler, "Detection and description of human running behavior in sports video multimedia database," in *Proceedings of the 11th International Conference on Image Analysis and Processing*, pp. 366–371, Palermo, Italy, September 2001.
[11] L. Xin, L. Hui, Q. Zhen-ping, and G. Xu-tao, "Adaptive background modeling based on mixture Gaussian model," *Journal of Image and Graphics*, vol. 13, no. 4, pp. 729–734, 2008.
[12] J. Chen, Q. Lin, and Q. Hu, "Application of novel clonal algorithm in multiobjective optimization," *International Journal of Information Technology and Decision Making*, vol. 9, no. 2, pp. 239–266, 2010.
[13] Z. Liao, S. Hu, D. Sun, and W. Chen, "Enclosed laplacian operator of nonlinear anisotropic diffusion to preserve singularities and delete isolated points in image smoothing," *Mathematical Problems in Engineering*, vol. 2011, Article ID 749456, 15 pages, 2011.
[14] S. Hu, Z. Liao, D. Sun, and W. Chen, "A numerical method for preserving curve edges in nonlinear anisotropic smoothing," *Mathematical Problems in Engineering*, vol. 2011, Article ID 186507, 14 pages, 2011.
[15] Z. Liao, S. Hu, and W. Chen, "Determining neighborhoods of image pixels automatically for adaptive image denoising using nonlinear time series analysis," *Mathematical Problems in Engineering*, vol. 2010, Article ID 914564, 14 pages, 2010.
[16] Z. Liao, S. Hu, M. Li, and W. Chen, "Noise estimation for single-slice sinogram of low-dose X-ray computed tomography using homogenous patch," *Mathematical Problems in Engineering*, vol. 2012, Article ID 696212, 2012.
[17] J. Lian-Hua, G. Z. Hui, and J. Mi, "Review of multi-target tracking," *Computer System & Application*, vol. 19, no. 12, p. 271, 2010.
[18] L. Chenguang and C. Dansong, "Interactive particle filter based algorithm for tracking multiple objects in videos ," *Acta Electronica Sinica*, pp. 260–267, 2011.
[19] N. S. Peng, J. Yang, D. K. Zhou, and Z. Liu, "Mean-shift tracking with adaptive model update mechanism," *Journal of Data Acquisition and Processing*, vol. 20, no. 2, pp. 125–129, 2005.
[20] http://groups.inf.ed.ac.uk/vision/BEHAVEDATA/INTERACTIONS/.

Hindawi Publishing Corporation
Mathematical Problems in Engineering
Volume 2012, Article ID 710690, 16 pages
doi:10.1155/2012/710690

Research Article

Automatic Regulation Time Series for Industry Processes

Tain-Sou Tsay

Department of Aeronautical Engineering, National Formosa University, Huwei, Yunlin 63208, Taiwan

Correspondence should be addressed to Tain-Sou Tsay, tstsay@nfu.edu.tw

Received 28 January 2012; Accepted 20 March 2012

Academic Editor: Ming Li

A nonlinear digital control scheme is proposed for analyses and designs of stable industry processes. It is derived from the converging characteristic of a specified numerical time series. The ratios of neighbourhoods of the series are formulated as a function of the output of the plant and the reference input command and will be converted to be unities after the output has tracked the reference input command. Lead compensations are also found by another numerical time series to speed up the system responses on the online adjusting manner. A servosystem, a time-delay system, a high-order system, a very-high-order system, and a 2×2 multivariable aircraft gas turbine engine are used to illustrate effectiveness of the proposed nonlinear digital controller. Comparisons with other conventional methods are also made.

1. Introduction

For unit feedback discrete-time control systems, the control sequences are usually functions of the difference between the sampled reference input and output of the plant [1–5]. The discrete-time control sequence can be generated by Finite Impulse Response (FIR) filter or Infinite Impulse Response (IIR) filter. The input of FIR or IIR filter is the difference between the sampled reference input and output of the plant. The output of FIR or IIR will be the input of the plant. In general, they are linear controllers.

In this literature, a nonlinear discrete-time control sequence described by periodic numerical series $G(jT_S)$ is proposed for analyses and designs of industry processes. They are sampled-data feedback control systems. T_S represents the sampling interval. The ratios of $G((k+1)T_S)$ to $G(kT_S)$ of the series are formulated as a function of the reference input command and the output of the plant. The value of $G(kT_S)$ is the control input of the plant at time intervals between $(k-1)T_S$ and kT_S. Thus, the considered system is closed as a feedback control system by use of $G(jT_S)$. It will be seen that the output of the plant tracks the reference

input command exactly after ratios $G((k+1)T_S)/G(kT_S)$ of the series being converted to unities. It implies that $G(kT_S)$ will be converted to a steady-state value for a constant reference input applied. The stability of the closed-loop system is guaranteed by selecting the proper function of ratios $G((k+1)T_S)/G(kT_S)$. This function can be called as "Regulation Function." It will be proven that the considered system using $G(kT_S)$ becomes a negative feedback control system for a stable plant [4].

Note that it needs not integration to get zero tracking error, and performance of controlled systems are dependent on selected functions of $G((k+1)T_S)/G(kT_S)$. Furthermore, an adaptive limitation for $G(kT_S)$ can be applied also to minimize the control effort and get better performance. Controlled results will be compared with conventional famous PI and PID controllers [6–15]. In this work, measurement noises of plant outputs are not considered. It is worthwhile to include recent developments of fractional-order systems and controls [16, 17] in the proposed nonlinear automatic regulation time series. They have been applied to signal processing [18], Cyber-physical networking system [19, 20], PMSM position servo system [21], and optimal control [22].

In following sections, basic concepts of the proposed nonlinear discrete-time control sequence are discussed first, and then a servo system, a time-delay system, a high-order system, a very-high-order system, and a 2×2 multivariable aircraft gas turbine examples are used to illustrate their tracking behaviour and performance. Simulating results will show that the proposed nonlinear digital controller gives another possible way for analyses and designs of industry processes. Design results of the fourth example give the proposed method can also be applied to multivariable feedback control systems.

2. The Basic Approach

2.1. Automatic Regulation Time Series

A numerical series with time interval T_S [1–5] can be written as in the form of

$$G(jT_S), \quad j = 1, 2, 3, \ldots, n, n+1, \ldots, \tag{2.1}$$

where $G(jT_S)$ represents a constant value between time interval from $(j-1)T_S$ and jT_S. For simplicity, the representation of $G(jT_S)$ will be replaced by $G(j)$ in the following evaluations. The ratios $G(j+1)/G(j)$ of the series are defined as in the form of

$$F(j) = \frac{G(j+1)}{G(j)}, \quad j = 1, 2, 3, \ldots, n, n+1, \ldots. \tag{2.2}$$

Equation (2.2) gives the value of $G(n+1)$ approaches to be a constant value when the value of $F(n)$ approaches to be unity. Now, the problem for closing the considered system is to find the formula of $F(j)$ which is the function of the reference input command R and the output of the plant Y. $G(n+1)$ is used as the input of the considered system. Considering a series given below,

$$G(n+1) = \left[\sum_{i=0}^{m} a_i \left(\frac{R(n)}{Y_S(n)}\right)^i\right] G(n), \tag{2.3}$$

where $R(n)$ represents the reference input command and $Y_S(n)$ represents the nonzero sampled output of the plant at the sampling interval nT_S. Note that this non-zero constraint will be removed later by level shifting. Equation (2.3) is a possible way to close the considered system as a sampled-data feedback control system. Assuming the reference input command has been tracked by applying control effort $G(j)$, (2.3) becomes

$$G(n+1) = \sum_{i=0}^{m} a_i G(n). \tag{2.4}$$

For steady-state condition, $G(n+1)$ approaches to be a constant value, and it gives

$$\sum_{i=0}^{m} a_i = 1. \tag{2.5}$$

Rearranging (2.3) and taking the derivative of it with respect to $Y_S(n)/R(n)$, one has

$$F(n) = \sum_{i=0}^{m} a_i \left(\frac{Y_S(n)}{R(n)} \right)^{-i}, \tag{2.6}$$

$$\frac{\partial F(n)}{\partial (Y_S(n)/R(n))} = -\sum_{i=0}^{m} i a_i \left(\frac{Y_S(n)}{R(n)} \right)^{-1-i}. \tag{2.7}$$

The sufficient but not necessary condition for (2.7) less than zero is $a_i > 0$ for $Y_S(n)/R(n) \cong 1$ and (2.6) can be rewritten as in the form of

$$F(n) = \sum_{i=0}^{m} a_i \left| \frac{Y_S(n)}{R(n)} \right|^{-i}. \tag{2.8}$$

$a_i > 0$ will be used in the following evaluations. Negative value of (2.7) represents the closed-loop system using (2.3) activated as a negative feedback system around the equilibrium condition; that is, $Y_S(n) = R(n)$. This statement will be illustrated and discussed by a graph in the next paragraph. The first-order polynomial described in (2.3) can be written as in the form of

$$G(n+1) = \left[\beta \left| \frac{R(n)}{Y_S(n)} \right| + 1 - \beta \right] G(n), \tag{2.9}$$

where β satisfies constrains stated above and becomes an adjustable parameter. Thus, the ratios $F(n)$ become

$$F(n) = \beta \left| \frac{R(n)}{Y_S(n)} \right| + 1 - \beta. \tag{2.10}$$

$F(n)$ can be called as "Regulation Function" also. Similarly, the third-order representation of $F(n)$ is in the form of

$$F(n) = \alpha \left| \frac{Y_S(n)}{R(n)} \right|^{-3} + \gamma \left| \frac{Y_S(n)}{R(n)} \right|^{-1} + 1 - \alpha - \gamma, \tag{2.11}$$

where $0 < \alpha$ and $0 < \gamma$.

Taking the derivative of (2.10) with respect to $Y_S(n) = R(n)$, one has

$$\frac{\partial F(n)}{\partial (Y_S(n)/R(n))} = -\beta \left(\frac{Y_S(n)}{R(n)} \right)^{-2}. \tag{2.12}$$

For negative value of (2.12), the value of β must be greater than zero. This implies the range of β is $0 < \beta < 1$. The suitability of the proposed nonlinear adaptive digital controller is based on this negative regulation characteristic. Figure 1 shows ratios $F(n)$ versus $R(n)/Y_S(n)$ represented by (2.9) for $\beta = 0.9, 0.7, 0.5, 0.3$ and 0.1, respectively.

Figure 1 shows that the value of $F(n)$ is less than one for that of $Y_S(n)$ greater than that of $R(n)$, then the value of $G(n+1)$ will be decreased; the value of $F(n)$ is greater than one for that of $Y_S(n)$ less than that of $R(n)$, and the value of $G(n+1)$ will be increased. This implies that the controlled system connected using (2.9) will be regulated to the equilibrium point $(Y_S(n)/R(n) = 1)$ and gives a negative feedback control system for deviation from the equilibrium point. From Figure 1, it can be seen that one can adjust β to get desired regulating slope; that is, regulating characteristic. Certainly, other tracking functions can be formulated and proposed also for the considered system, if its derivative with respect to $Y_S(n)/R(n)$ is negative. Similar to the derivation of (2.12), (2.11) gives

$$\frac{\partial F(n)}{\partial (Y_S(n)/R(n))} = -\left\{ \gamma \left(\frac{Y_S(n)}{R(n)} \right)^{-2} + 3\alpha \left(\frac{Y_S(n)}{R(n)} \right)^{-4} \right\}, \tag{2.13}$$

where $0 < \alpha$ and $0 < \gamma$.

The constraint of non-zero $Y_S(n)$ can be removed by $R(n)/Y_S(n)$ of (2.9) replaced by $(R(n) + Y_o)/(Y_S(n) + Y_o)$. Y_o is a positive value and represents the negative maximal control swing. The modified equation of (2.9) becomes

$$G(n+1) = \left\{ \beta \left| \frac{R(n) + Y_o}{Y_S(n) + Y_o} \right| + 1 - \beta \right\} G(n). \tag{2.14}$$

Equation (2.14) implies ratios $G(n+1)/G(n)$ are in the form of

$$F(n) = \left[\beta \left| \frac{R(n) + Y_o}{Y_S(n) + Y_o} \right| + 1 - \beta \right], \quad n = 1, 2, 3, \ldots, j, j+1, \ldots. \tag{2.15}$$

Control inputs of the plant are in the form of

$$u(n+1) = G(n+1) - \frac{Y_o}{P(0)} \tag{2.16}$$

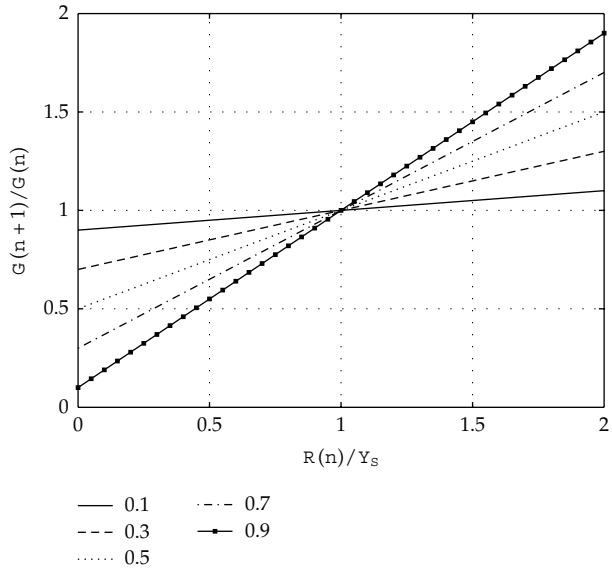

Figure 1: $G(n+1)/G(n)$ Versus R/Y_S for $\beta = 0.9, 0.7, 0.5, 0.3$, and 0.1.

for the negative swing control using positive values of β, $G(n)$, and $F(n)$. Equation (2.14) gives negative regulation characteristics also for $R(n) = Y_S(n)$ is corresponding to $R(n)+Y_o = Y_S(n) + Y_o$. Similar to the evaluation of (2.12), the derivative of (2.15) becomes

$$\frac{\partial F(n)}{\partial((Y_S(n)+Y_o)/(R(n)+Y_o))} = -\beta\left(\frac{Y_S(n)+Y_o}{R(n)+Y_o}\right)^{-2}. \tag{2.17}$$

Figure 2 shows the connected system configuration using (2.14) and (2.16) in which U is the sampled with hold output of the controller. The values of $G(n)$ and $F(n)$ will be all positive for the summation of $Y_S(n)$ and Y_o (or R and Y_o) is greater than zero with specified values of Y_o. All positive values will give the better continuity and regulating characteristic of the time series. Naturally, absolute value of $(R(n)+Y_o)/(Y_S(n)+Y_o)$ can be used in (2.14) to guarantee positive of $G(n)$ and $F(n)$ for negative of $R(n)$.

2.2. Control Effort Limitation

An adaptive value of Y_o can be selected at $|R(n)|$ for the system is well controlled. Then (2.14) and (2.16) can be rewritten as

$$G(n+1) = \left\{\beta\left|\frac{R(n)+|R(n)|}{Y_S(n)+|R(n)|}\right| + 1 - \beta\right\}G(n), \tag{2.18}$$

$$u(n+1) = G(n+1) - \frac{|R(n)|}{P(0)}, \tag{2.19}$$

respectively. The maximal value of $G(n)$ can be limited by an adaptive constraint $|R(n) + |R(n)||$ to minimize the control effort. The control input U of the plant is now described by (2.19).

Note that the singularity of (2.18) must be avoided when $Y_S(n) + |R(n)| = 0$. It is easy to replace $Y_S(n) + |R(n)| = 0$ by a small value. A small value of $G(n)$ is selected also to avoid null time series. Figure 3 shows an equivalent block diagram of Figure 2 using constraint of $G(n)$ and singularity avoidance of $Y_S(n) + |R(n)| = 0$. The constrain of $G(n)$ cannot be only for minimizing the control effort but also for improving system performance.

2.3. Phase Lead Compensation

A conventional digital filter $C(z)$ in Figure 3 can be applied for filtering $G(n)$, if it is necessary. In general, phase lead is used for speeding up the time response. The first-order phase lead can be expressed as

$$C(z) = \left.\frac{T_n s + 1}{T_n s/\rho + 1}\right|_{s=(2/T_S)((z-1)/(z+1))} \tag{2.20}$$

for $\rho > 1$. The parameter T_n can be found by another numerical time series. It is

$$\begin{aligned} W(n+1) &= \left[\eta\left(\frac{T_c}{T_{cs}}\right)^j + 1 - \eta\right] W(n), \\ T_n &= W(n+1), \end{aligned} \tag{2.21}$$

where T_c is the time constant of the closed loop system and T_{cs} is the wanted time constant.

Considering a illustrating example [6] is shown in Figure 3, in which $P(s)$ is in the form of

$$P(s) = \frac{30}{s^2 + 10s + 30}. \tag{2.22}$$

DC gain of $P(s)$ is unity. The sampling period T_S is selected to be equal to 0.1 second for illustrating variations of $G(n)$ and $F(n)$. Time responses of the overall system using the nonlinear digital controller for $\beta = 0.5$, $Y_o = |R(n)|$ and $C(z) = 1$ are shown in Figure 4. Magnitudes of reference inputs between 0 and 5 seconds are equal to 1, between 5 and 10 seconds are equal to −0.7, between 10 and 14 seconds are equal to 0.5, and between 14 and 17 seconds are equal to −0.3, in which gives reference input $R(n)$ (dash line), output Y (solid line), time series $G(n)$ (dotted line), and ratios $F(n)$ (dash-dotted line) of $G(n)$. Figure 4 shows that all values of $G(n)$ and $F(n)$ are positive while the value of output Y is tracking the negative value of the reference input $R(n)$. The value of $R(n)$ can be positive or negative.

Figure 4 shows also that ratios $F(n)$ are converted to be unities quickly; that is, the controlled output tracks the reference input quickly. The proposed method gives a good performance and zero steady-state error without integration. Note that maximal values of $G(n)$ are set to be $|R(n) + |R(n)||$ for better performance and minimal the control effort. Equation (2.14) gives that $F(n)$ will be converted to 0.5 for zero input ($R(n) = 0$) and $\beta = 0.5$. Equation (2.14) and Figure 1 give that the less the value of β is, the larger the regulation slope will be. $\beta = 0.5$ is the optimal value for the considered system.

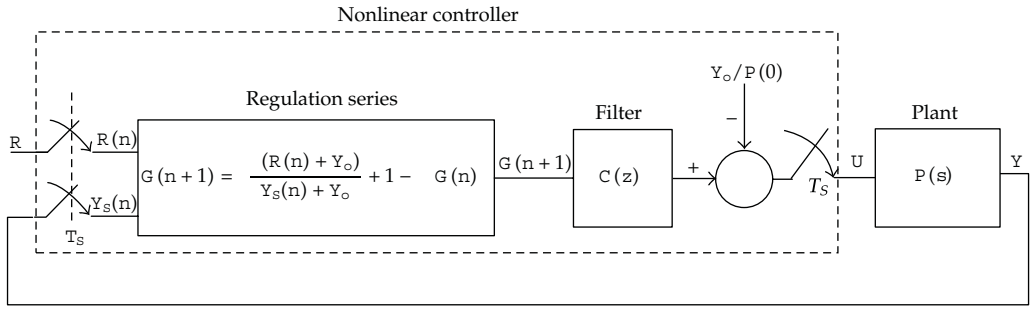

Figure 2: A nonlinear digital controller using automatic regulation time series.

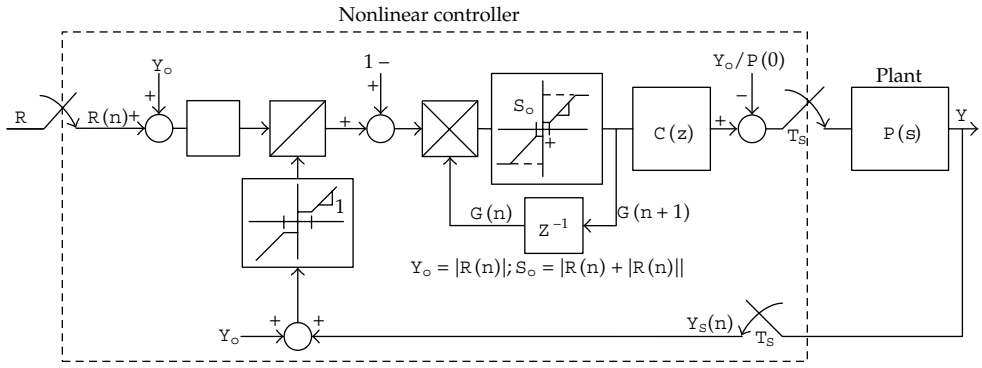

Figure 3: Equivalent block diagram of Figure 2 using $G(n)$ limitations and singularity avoidance of (2.18).

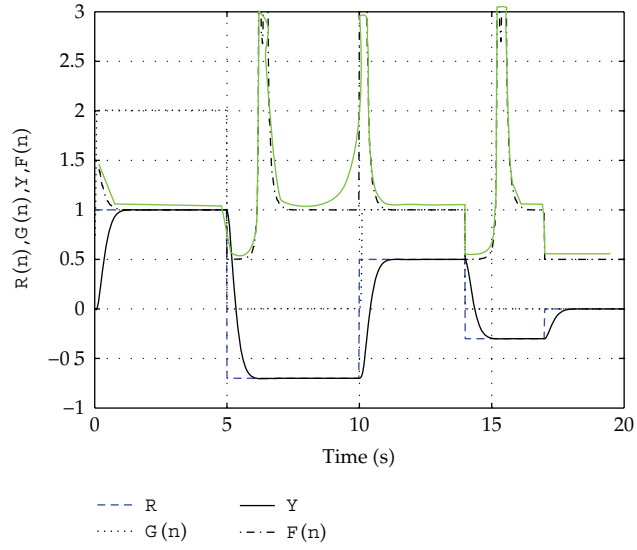

Figure 4: Time responses of the illustrating example for $\beta = 0.50$ and $T_S = 0.1$ sec.

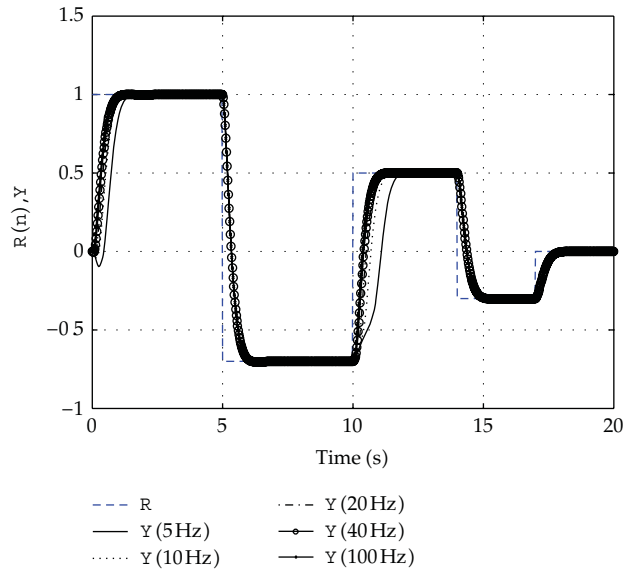

Figure 5: Time responses of the illustrating example for $\beta = 0.50$ and *sampling frequency* equating to 100, 40, 20, 10, and 5 Hz, respectively.

Figure 5 shows time responses for $\beta = 0.50$ and sampling frequency equal to 100, 40, 20, 10, and 5 Hz, respectively. It shows that 40 Hz (i.e., $T_S = 25$ ms) is fast enough for the considered system. Figure 6 shows comparisons with a phase-lead compensator $C(z)$ which is included in the control loop. The phase-lead compensator $C(z)$ is in the form of

$$C(z) = \left.\frac{0.15923s + 1}{0.03185s + 1}\right|_{s = (2/T_S)((z-1)/(z+1))}. \tag{2.23}$$

It can speed up the time responses while keeping system performance.

The proposed control scheme using numerical time series will be applied to three numerical SISO (single-input single-output) examples in next section on online adjusting manner. Equation (2.21) will be used for finding phase-lead compensators $C(z)$ to meet design specifications.

3. Numerical Examples

Example 3.1. Consider a stable plant that has the transfer function [7, 8]

$$P_1(s) = \frac{e^{-s}}{(s+1)^2}. \tag{3.1}$$

It has pure time delay of 1 second. The specification for time constant $T_{cs} = 1.85$ sec is selected. Parameters of (2.18) and (2.21) are $\beta = 0.7$, $T_S = 25$ ms, $\rho = 50$, $\eta = 0.9$, and $j = 1$. Figure 7

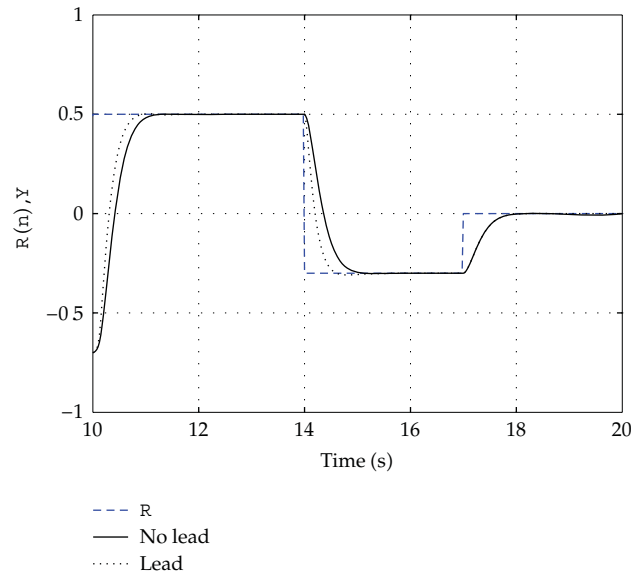

Figure 6: Time responses of the illustrating example with/without $C(z)$ for $\beta = 0.5$, $T_S = 25$ ms.

shows online adjusting processes for finding $C(z)$. The initial guess of T_n is equal to 1.00 and converted to 0.5195 after third adjusting processes. The found lead compensator is

$$C(z) = \left.\frac{0.5195s + 1}{0.5195s/\rho + 1}\right|_{s=(2/T_S)((z-1)/(z+1))}. \tag{3.2}$$

Time constants of each step are 1.4107, 1.8488, 1.8498, and 1.8500. Figure 7 shows the proposed method provides an automatic regulation procedure to get wanted design specifications. It gives good performance and zero steady-state error.

Simulation results of the proposed method and four other methods are presented for comparisons. They are Ziegler-Nichols method [9–12] for finding PI and PID compensators, Tan et al. [13, 14] for finding PID compensator, and Majhi [7, 8] for finding PI compensator. The controller is in the form of

$$u(t) = K_p e(t) + K_i \int e(t)dt + K_d \frac{d}{dt} e(t). \tag{3.3}$$

Parameters of four found compensators are given below:

(1) ZN(PI): $K_p = 1.240$ and $K_i = 0.251$;

(2) ZN(PID): $K_p = 1.6367$, $K_i = 0.4187$, and $K_d = 0.5972$;

(3) Tan's(PID): $K_p = 0.620$, $K_i = 0.5636$, and $K_d = 0.1705$;

(4) Majhi's(PI): $K_p = 0.864$ and $K_i = 0.3653$.

Integral of the Square Error (ISE) and Integral of the Absolute Error (IAE) are given in Table 1. Time responses are shown in Figure 8. From Table 1 and Figure 8, one can see that the proposed method gives faster and better performance than those of other methods presented.

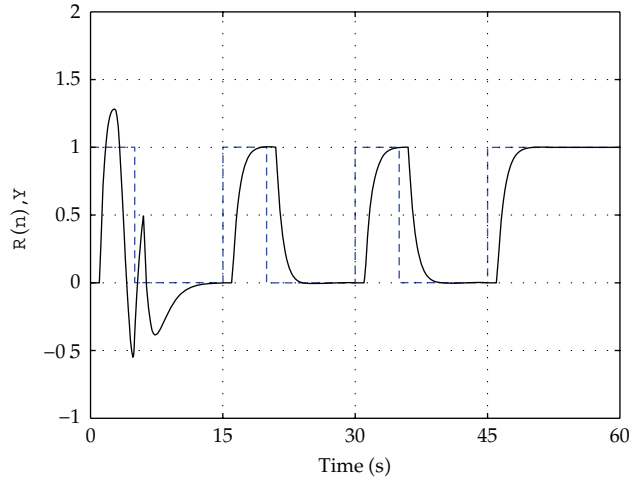

Figure 7: Time responses of Example 3.1 for finding $C(z)$.

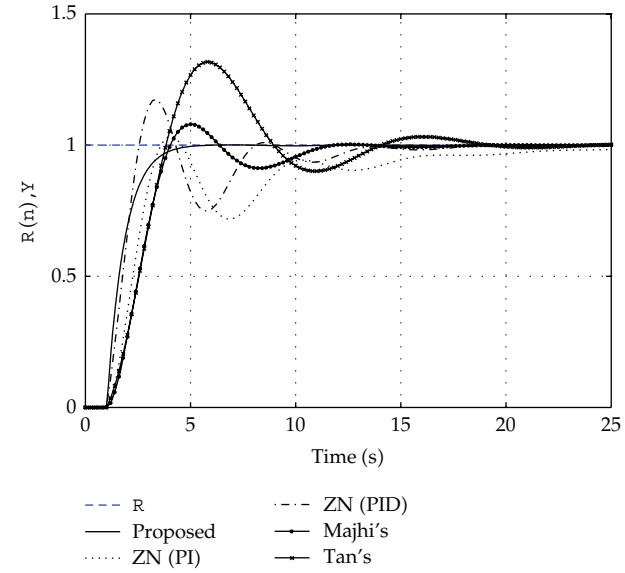

Figure 8: Time responses of Example 3.1 using different control methods.

Table 1: IAE and ISE errors of Example 3.1 using different control methods.

Methods	Proposed	ZN(PI)	ZN(PID)	Tan's	Majhi's
ISE	1.4610	2.2675	1.7694	2.2471	2.4654
IAE	1.8726	4.0107	2.8757	3.0725	4.0659

Example 3.2. Consider a sixth order plant [7, 8]

$$P_2(s) = \frac{1}{(s+1)^6}. \tag{3.4}$$

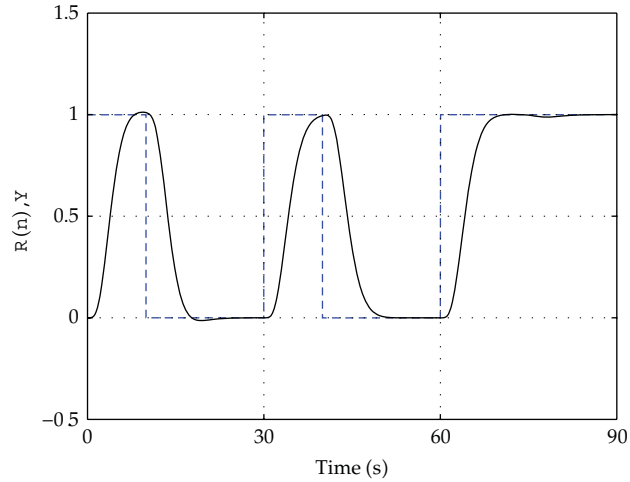

Figure 9: Time responses of Example 3.2 for finding $C(z)$.

Table 2: IAE and ISE errors of Example 3.2 using different control methods.

Methods	Proposed	ZN(PI)	ZN(PID)	Ho's	Majhi's
ISE	3.3895	5.335	4.023	5.215	3.746
IAE	4.4798	9.279	6.492	7.219	5.425

The specification of time constant $T_{cs} = 4.8$ sec is selected. Parameters of (2.18) and (2.21) are $\beta = 0.5$, $T_S = 25$ ms, $\rho = 50$, $\eta = 0.9$, and $j = 3$. The initial guess of T_n is equal to 1.0 and converted to 0.7759 after second adjusting process. The found lead compensator is

$$C(z) = \left.\frac{0.7759s + 1}{0.7759s/\rho + 1}\right|_{s=(2/T_S)((z-1)/(z+1))}. \tag{3.5}$$

Figure 9 shows on-line adjusting processes for finding $C(z)$ to meet $T_{cs} = 4.8$ sec. Simulation results of the proposed and four other methods are presented for comparisons. They are Ziegler-Nichols rule [9–12] for finding PI and PID compensators, Ho et al. [15] for finding PID compensator, and Majhi [7, 8] for finding PI compensator. Parameters of five found compensators are given below:

(1) ZN(PI): $K_p = 1.079$ and $K_i = 0.110$;

(2) ZN(PID): $K_p = 1.4248$, $K_i = 0.1838$, and $K_D = 1.360$;

(3) Majhi's(PI): $K_p = 0.7736$, and $K_i = 0.1547$;

(4) Ho's(PID): $K(s) = 1.3(1 + 0.189/s + 1.3s/(0.13s + 1))$.

Integral of the Square Error (ISE) and Integral of the Absolute Error (IAE) are given in Table 2. Time responses are shown in Figure 10. From Table 2 and Figure 10, one can see that the proposed method gives faster and better performance than those of other methods.

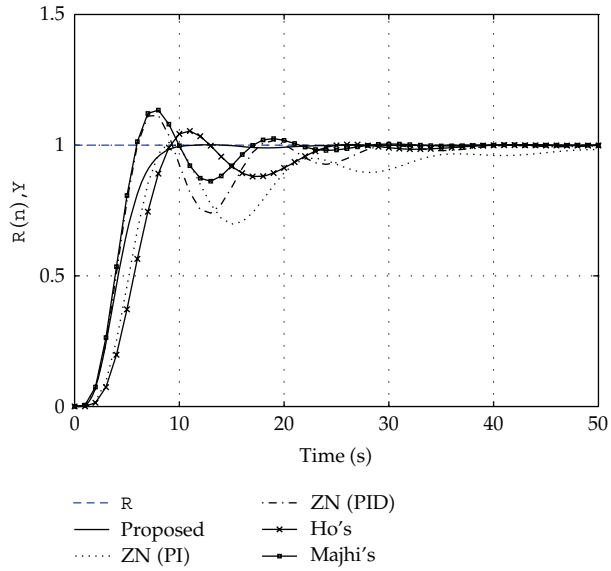

Figure 10: Time responses of Example 3.2 using different control methods.

Example 3.3. Consider the very-high-order plant [7, 8]:

$$P_3(s) = \frac{1}{(s+1)^{20}}. \tag{3.6}$$

The design specification for time constant $T_{cs} = 19.0$ sec is selected. Parameters of (2.18) and (2.21) are $\beta = 0.5$, $T_S = 25$ ms, $\rho = 50$, $\eta = 0.9$, and $j = 3$. The initial guess of T_n is equal to 1.00 and converted to 0.9586 after the fourth adjusting process. The found lead compensator is

$$C(z) = \left.\frac{0.9586\,s+1}{0.9586\,s/\rho+1}\right|_{s=(2/T_S)((z-1)/(z+1))}. \tag{3.7}$$

Figure 11 shows time response of the controlled system, which gives reference input $R(n)$ (dash line), output Y (solid line), time series $G(n)$ (dotted line), and ratios $F(n)$ (dash-dotted line) of $G(n)$. It gives good performance and zero steady-state errors. Figure 11 shows the considered plant is a large time-lag system. The high order system model is usually used to describe the industry process for replacing pure time delay (e.g., $e^{-T_d s}$) such that conventional analysis and design techniques can be applied [7, 8]. Figure 11 shows the proposed method can be applied to a large time-delayed system.

Final results and four other methods are presented for comparison and show the merit of the proposed method. They are Ziegler-Nichols method [9–12] for finding PI and PID compensators, Zhuang and Atherton [23] for finding PI compensator, and Majhi [7, 8] for finding PI compensator. Parameters of four found compensators are given below:

(1) ZN(PI): $K_p = 0.585$ and $K_i = 0.0305$;

(2) ZN(PID): $K_p = 0.77256$,$K_i = 0.05088$, and $K_d = 4.9135$;

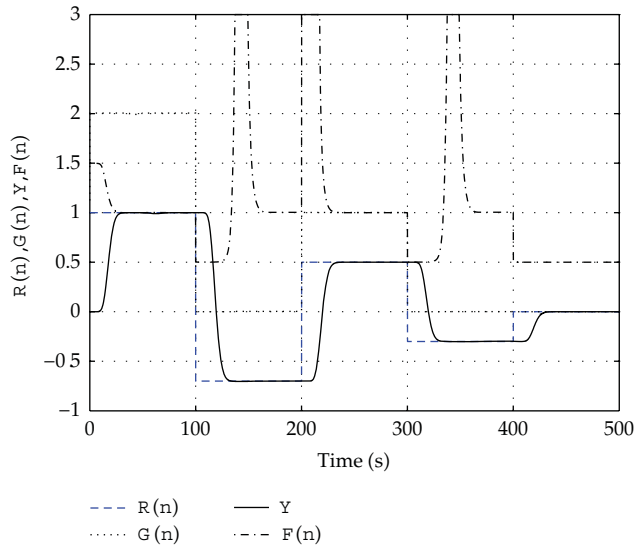

Figure 11: Time responses of Example 3.3 with $C(z)$ for $\beta = 0.5$; $T_S = 25$ ms.

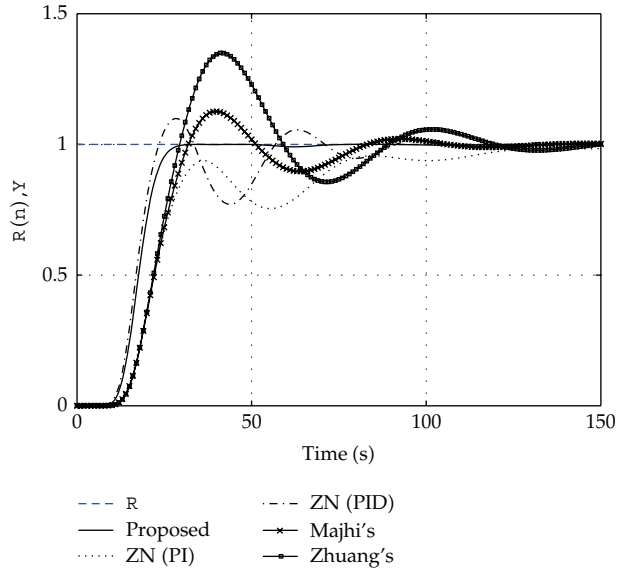

Figure 12: Time responses of Example 3.3 using different control methods.

(3) Majhi's(PI): $K_p = 0.5097$ and $K_i = 0.0443$;

(4) Zhuang's(PI): $K_p = 0.473$ and $K_i = 0.058$.

Time responses are shown in Figure 12. Table 3 gives integration of absolute error (IAE) and integration of square error (ISE) of them. From Table 3 and Figure 12, one can see that the proposed method gives better performance than those of other methods.

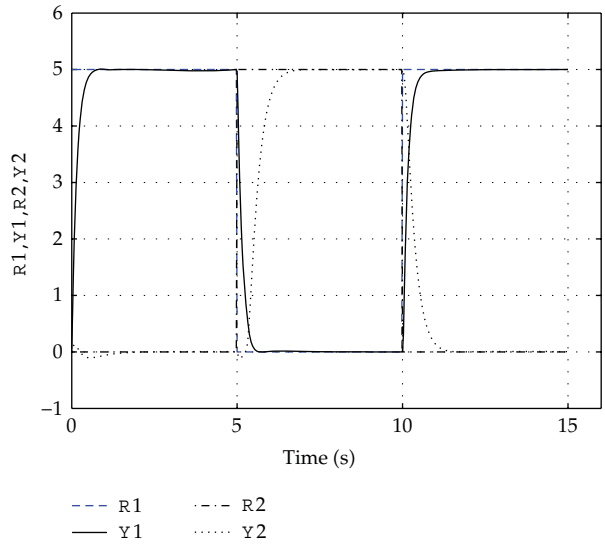

Figure 13: Time responses of Example 3.4 for $\beta = 0.5$ and $T_S = 25$ ms.

Table 3: IAE and ISE errors of Example 3.3 using different control methods.

Methods	Proposed	ZN(PI)	ZN(PID)	Majji's	Zhuang's
ISE	15.7313	21.2271	16.2160	20.1908	21.8142
IAE	18.0892	32.7084	22.9707	26.8295	32.9125

Example 3.4. Consider a gas turbine engine with plant transfer function matrix [24–26]:

$$P_4(s) = \frac{1}{\Delta(s)} \begin{bmatrix} 2533 + 1515.33s + 14.9s^2 & 1805947 + 1132094.7s + 95150s^2 \\ 12268.8 + 8642.68s + 85.2s^2 & 2525880 + 1492588s + 124000s^2 \end{bmatrix}, \tag{3.8}$$

where $\Delta(s) = 2525 + 3502.7s + 1357.3s^2 + 113.22s^3 + s^4$. It is a 2×2 multivariable plant. The steady-state gain of open loop $P_4(s)$ is in the form of

$$P_4(0) = \begin{bmatrix} 1.00316 & 715.2265 \\ 4.85893 & 1000.3485 \end{bmatrix}. \tag{3.9}$$

A pre-compensating matrix $P_4^{-1}(0)$ is first applied to decouple the plant in low-frequency band. Then, two digital filters are used in the diagonal to filter outputs of two time series for speeding up transient responses. They are in the form of

$$\begin{aligned} C_1(z) &= \left.\frac{0.75s + 1}{0.15s + 1}\right|_{s=(2/T_S)((z-1)/(z+1))}, \\ C_2(z) &= \left.\frac{0.60s + 1}{0.25s + 1}\right|_{s=(2/T_S)((z-1)/(z+1))}, \end{aligned} \tag{3.10}$$

where $T_S = 25\,\text{ms}$ is the sampling period. Figure 13 shows time responses of this controlled system for $\beta = 0.5$. It shows that the proposed control scheme can be applied to the multivariable feedback control system also.

4. Conclusions

In this literature, a new nonlinear digital controller has been proposed for analyses and designs of industry processes. They are sampled-data feedback control systems. It was applied to four simple and complicated numerical examples to get good performance and zero steady-state errors. No integrations of tracking errors are needed to get zero steady-state errors. Lead compensations are also found by another numerical time series to speed up the system responses on the on-line adjusting manner. From simulation and comparison results with other famous control methods, it can be seen that the proposed method provides another possible control scheme for sampled-data feedback control systems, and it is worthwhile to find other regulation $F(n)$ to get better performance.

References

[1] K. Ogata, *Discrete-Time Control System*, Prentice-Hall, Englewood Cliffs, NJ, USA, 1994.

[2] B. C. Kuo, *Digital Control Systems*, 1995.

[3] C. L. Phillips and H. T. Nagle, *Digital Control System Analyses and Designs*, Prentice-Hall, Englewood Cliffs, NJ, USA, 1994.

[4] G. F. Franklin and J. D Powelll, *Feedback Control Dynamics*, Addison-Wesley Publishing Company, 1986.

[5] G. F. Franklin, J. D. Powell, and M. L. Workman, *Digital Control of Dynamics*, Ellis-Kagle Press, Half Moon Bay, Calif, USa, 2006.

[6] G. S. Buja and A. Souliaev, "A variable structure controller," *IEEE Transactions on Automatic Control*, vol. 33, no. 2, pp. 206–209, 1988.

[7] S. Majhi and D. P. Atherton, "Autotuning and controller design for processes with small time delays," *IEE Proceedings D*, vol. 146, no. 5, pp. 415–425, 1999.

[8] S. Majhi, "On-line PI control of stable processes," *Journal of Process Control*, vol. 15, no. 8, pp. 859–867, 2005.

[9] J. G. Ziegler and N. B. Nichols, "Optimum settings for automatic controllers," *Transactions of ASME*, vol. 65, pp. 759–768, 1942.

[10] K. J. Åström and T. Hägglund, "Revisiting the Ziegler-Nichols step response method for PID control," *Journal of Process Control*, vol. 14, no. 6, pp. 635–650, 2004.

[11] K. J. Åström and C. C. Hang, "Towards intelligent PID control," *Automatica*, vol. 28, pp. 1–9, 1991.

[12] K. J. Åström and T. Hägglund, "Automatic tuning of simple regulators with specifications on phase and amplitude margins," *Automatica*, vol. 20, no. 5, pp. 645–651, 1984.

[13] K. K. Tan, T. H. Lee, and X. Jiang, "Robust on-line relay automatic tuning of PID control systems," *ISA Transactions*, vol. 39, no. 2, pp. 219–232, 2000.

[14] K. K. Tan, T. H. Lee, and X. Jiang, "On-line relay identification, assessment and tuning of PID controller," *Journal of Process Control*, vol. 11, no. 5, pp. 483–496, 2001.

[15] W. K. Ho, C. C. Hang, and L. S. Cao, "Tuning of PID controllers based on gain and phase margin specifications," *Automatica*, vol. 31, no. 3, pp. 497–502, 1995.

[16] C. A. Monje, Y. Q. Chen, B. M. Vinagre, D. Xue, and V. Feliu, *Fractional Order Systems and Controls—Fundamentals and Applications*, Springer, 2010.

[17] M. Li, "Fractal time series—a tutorial review," *Mathematical Problems in Engineering*, Article ID 157264, 26 pages, 2010.

[18] H. Sheng, Y. Q. Chen, and T. S. Qiu, *Fractional Processes and Fractional Order Signal Processing*, Springer, 2012.

[19] C. Tricaud and Y. Q. Chen, *Optimal Mobile Sensing and Actuation Policies in Cyber-Physical Systems*, Springer, 2012.

[20] M. Li and W. Zhao, "Visiting power laws in cyber-physical networking system," *Mathematical Problems in Engineering*, vol. 2012, Article ID 302786, 13 pages, 2012.

[21] Y. Luo, Y. Chen, H. S. Ahn, and Y. Pi, "Fractional order robust control for cogging effect compensation in PMSM position servo systems: stability analysis and experiments," *Control Engineering Practice*, vol. 18, no. 9, pp. 1022–1036, 2010.

[22] C. Tricaud and Y. Chen, "An approximate method for numerically solving fractional order optimal control problems of general form," *Computers & Mathematics with Applications*, vol. 59, no. 5, pp. 1644–1655, 2010.

[23] M. Zhuang and D. P. Atherton, "Automatic tuning of optimum PID controllers," *IEE Proceedings D*, vol. 140, no. 3, pp. 216–224, 1993.

[24] D. Q. Mayne, "The design of linear multi-variable systems," *Automatics*, vol. 9, pp. 201–207, 1973.

[25] D. Q. Mayne, "Sequential design of linear multivariable systems," *Proceedings of the Institution of Electrical Engineers*, vol. 126, no. 6, pp. 568–572, 1979.

[26] T. S. Tsay, "A sequential design method for multivariable feedback control systems," *WSEAS Transactions on Systems*, vol. 8, no. 12, pp. 1294–1304, 2009.

Hindawi Publishing Corporation
Mathematical Problems in Engineering
Volume 2012, Article ID 951584, 22 pages
doi:10.1155/2012/951584

Research Article

Online Health Management for Complex Nonlinear Systems Based on Hidden Semi-Markov Model Using Sequential Monte Carlo Methods

Qinming Liu and Ming Dong

Department of Operations Management, Antai College of Economics & Management, Shanghai Jiao Tong University, 535 Fahua Zhen Road, Shanghai 200052, China

Correspondence should be addressed to Ming Dong, mdong@sjtu.edu.cn

Received 13 January 2012; Accepted 15 February 2012

Academic Editor: Ming Li

Health management for a complex nonlinear system is becoming more important for condition-based maintenance and minimizing the related risks and costs over its entire life. However, a complex nonlinear system often operates under dynamically operational and environmental conditions, and it subjects to high levels of uncertainty and unpredictability so that effective methods for online health management are still few now. This paper combines hidden semi-Markov model (HSMM) with sequential Monte Carlo (SMC) methods. HSMM is used to obtain the transition probabilities among health states and health state durations of a complex nonlinear system, while the SMC method is adopted to decrease the computational and space complexity, and describe the probability relationships between multiple health states and monitored observations of a complex nonlinear system. This paper proposes a novel method of multisteps ahead health recognition based on joint probability distribution for health management of a complex nonlinear system. Moreover, a new online health prognostic method is developed. A real case study is used to demonstrate the implementation and potential applications of the proposed methods for online health management of complex nonlinear systems.

1. Introduction

With the rapid development of modern economy, the manufacturing industry increasingly needs to operate equipment at high reliability, low environmental risks, and human safety. The technological development has resulted in increasing complexity in both industrial machinery and production systems. It is difficult or almost impossible to identify and predict failure conditions in a timely manner. In a complex nonlinear system, high maintenance cost and uncertain downtime are often caused by system's failures. Health management for

a complex nonlinear system has a significant impact on the profitability of a business. So system's health diagnosis and prognosis implementing CBM (condition-based maintenance) become a basic and desirable requirement in many application domains, where safety, reliability, and availability of systems are considered critically [1]. Health management involves evaluating the current system condition, observing the future system condition and predicting the system residual useful life (RUL) before the failures.

In the system health management framework, health prognosis is a complex process and it is particularly difficult when the system under study is operating in the real time environment. Traditional linear methods such as ARIMA (autoregressive integrated moving average) cannot precisely predict the system health. For this reason, the study on online health management has attracted much attention. Some prognostic models have been introduced and developed with various degrees of success. Usually, three categories of nonlinear prognostic methods can be classified to obtain system health prognosis, including physical models, data-driven models, and model-driven models.

With intelligent monitoring systems, physical models are useful to account for different operating conditions. They integrate physical features of a system for monitoring. Therefore, the functional mappings between the drifting parameters and the selected prognostic features can be established. Kacprzynski et al. [2] proposed a helicopter gear prognosis method that fused physics of failure modeling and relevant diagnostic information. Oppenheimer and Loparo [3] applied a physical model to estimate residual useful lifetime based on the crack growth law. These methods applied physical modeling and advanced parametric identification techniques, along with failure detection and prognosis algorithm for estimating the time to failure of complex nonlinear systems. The limitations of these models are their higher costs and lower accuracy. Furthermore, it is very difficult to build a good physical model.

Data-driven methods use the monitored data to predict the health of complex nonlinear systems. Li [4] gave a tutorial review about fractal time series that was substantially different from the conventional time series in its statistic properties such as heavy-tailed probability distribution functions and slowly decayed autocorrelation functions. M. Li and J. Y. Li [5] addressed the particularity of the predictability of long-range dependence series and presented a generalized mean square error in the domain of generalized functions to prove the existence of long-range dependence series prediction. Li et al. [6] introduced the concept of one-dimensional random functions with long-range dependence based on a specific class of processes called the Cauchy-class process and presented the power spectrum density function of the Cauchy-class process in the closed form. Li and Zhao [7] addressed the power laws related to some physical systems and discussed that power-law-type data may be governed by stochastically differential equations of fractional order. Chen et al. [8] proposed a novel kernel machine-based rank-lifting regularized discriminant analysis method for nonlinear problems. However, the slow convergence and local minimum value are main drawbacks of these models and the computational explosion problems will occur when the number of observations increases dramatically. All disadvantages limit these models in the applications of online equipment health management.

Model-based prognostic methods rely on the use of a mathematical model to represent the degradation behavior of the system. A main nonlinear time series method of model-driven methods called hidden Markov model has been quite effective for health prognosis. Zhou et al. [9] applied a new method for real time failure prognosis, by combining the capabilities of the HMM and the belief rule base. However, only ordinary HMM techniques are adopted and the inherent limitations within HMM still exist in their models. By allowing

one state to generate a sequence of observations and have an explicit distribution for the duration of states, the HMM is generalized to HSMM. The HSMM has been an active research topic since the late 1980s. It has attracted considerable research attention in some fields [10–13]. Dong and He [14] presented an integrated framework based on HSMM for multisensors equipment diagnosis and prognosis. And in [15], they proposed a segmental hidden semi-Markov model for prognosis and diagnosis of the equipment. The HSMM has very rich mathematical structures and can form the solid theoretical foundation for use. Thus, HSMM has been effective for the health management of systems. However, the major drawback of HSMM is that recognizing and training processes of HSMM are often time consuming which is disadvantageous when real time prognosis is required. So HSMM is only applied to the offline equipment health prediction. The improvement for traditional HSMM is needed for online health management of complex nonlinear systems.

The SMC method could decrease the computational and space complexity. And if the mathematical model or statistical model of a system is known, the filter based methods including SMC method can predict the health by estimating states or parameters of systems. The SMC method can also recognize the hidden failures of complex nonlinear systems. Unfortunately, when the mathematical models or the statistical models of systems are difficult to obtain, the SMC method is not applied to predict the health of systems. However, HSMM has very rich mathematical structures. So we combine the SMC method with HSMM in this paper. HSMM is used to obtain the transition probabilities among health states and health state durations of a complex nonlinear system, while the SMC method is adopted to decrease the computational and space complexity and describe the probability relationships between multiple health states and monitored observations of a complex nonlinear system. This paper proposes a novel multistep ahead recognition algorithm based on the joint probability distribution for health management of complex nonlinear systems. The proposed method has a better mathematical structure and better performance for real time prognosis. It can also decrease the computational complexity for health prognosis. Moreover, it overcomes the offline only constraint of the HSMM Viterbi algorithm and can recognize the health states in real time. Thus, it is effective for online health management of complex nonlinear systems.

This paper aims to develop a new method for online health management of complex nonlinear systems. The paper is organized as follows. In Sections 2 and 3, the theories of HSMM and SMC methods are introduced. Section 4 proposes a joint multistep ahead health recognition algorithm based on HSMM using SMC methods and develops the corresponding online health prognostic algorithm for complex nonlinear systems. In Section 5, a case study for online health management of a complex nonlinear system is provided. Finally, conclusions are drawn in Section 6.

2. Hidden Semi-Markov Model

A HSMM is constructed by adding the state duration into the well-defined HMM structures. Unlike a state in a standard HMM, a state in HSMM generates a segment of observations, as opposed to a single observation in the HMM. The states in a segmental hidden semi-Markov model are called macrostates (i.e., segments). Each macrostate consists of several single states, which are called microstates [15]. Suppose that a macrostate sequence has n segments and let q_i be the time index of the endpoint of the ith segment $(0 \leq i \leq n-1)$. The segments are illustrated in Figure 1.

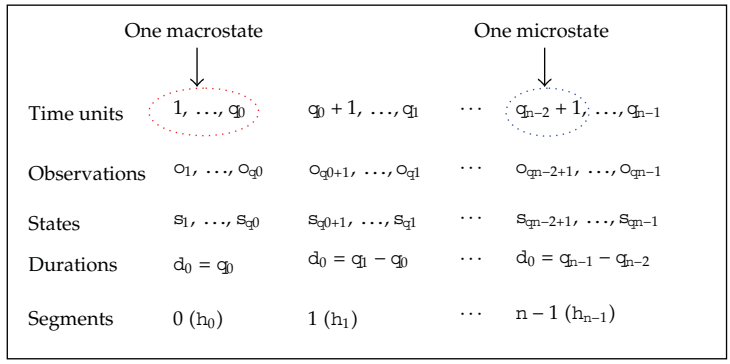

Figure 1: Mapping of microstates and macrostates for a general HSMM.

For the ith macrostate, the observations are $o_{q_{i-1}+1}, \ldots, o_{q_i}$, respectively, and they have the same macrostate labels as follows:

$$s_{q_{i-1}+1} = s_{q_{i-2}+1} = \cdots = s_{q_i} = h_i. \tag{2.1}$$

In this paper, the monitored observations are continuous signals. In order to deal with the continuous observations, instead of the discrete-state situation, the continuous-state situation is adopted. The HSMM can establish a rational relationship between the states and observations. For some nonlinear problems, the state space model of HSMM can be described as follows

$$\begin{aligned} x_n &\sim g(x_n \mid x_{n-1}, \Lambda), \\ y_n &\sim h(y_n \mid x_n, \Lambda). \end{aligned} \tag{2.2}$$

Based on the state space model, a standard HSMM can be established as follows:

$$\begin{aligned} x_n &\sim p(x_n \mid x_{n-1}, A), \\ y_n &\sim h(y_n \mid x_n, B), \\ d_i &\sim N(d_i \mid u_i, \sigma_i), \quad 0 \le d \le D. \end{aligned} \tag{2.3}$$

For convenience, the above equation can be rewritten as follows:

$$\begin{aligned} x_n &\sim p(x_n \mid x_{n-1}), \\ y_n &\sim q(y_n \mid x_n), \\ d_i &\sim N(d_i \mid u_i, \sigma_i), \quad 0 \le d \le D, \end{aligned} \tag{2.4}$$

where Λ is the parameter set of HSMM in the state space model. d_i is the duration of the state i and D is the maximum state duration. u_i and σ_i are the duration mean and variance of state i, respectively. $x_n \in S$ is a hidden state at time n ($S = \{s_1, s_2, \ldots, s_N\}$ is the hidden state set with N elements). $x_n \sim g_n(x_n \mid x_{n-1}, A)$ is the system model and depends on

the state transition probability $A = \{a_{ij}\}$, $(a_{ij} = P(x_t = s_j \mid x_{t-1} = s_i))$. $y_n \sim h_n(y_n \mid x_{n-1}, B)$ is the observation model $(y_n \in O)$ and $O = \{o_1, o_2, \ldots, o_T\}$ is the observation sequence with T elements. $B = \{b_i(o),\ 1 \le i \le N\}$ is the conditional probability distribution of observation $(b_i(o) = p(y_n \mid x_n = s_i))$.

Besides, there is an initial state distribution π $(\pi_i = p(x_1 = s_i),\ 1 \le i \le N)$. It can be seen that an HSMM can be described by λ $(\lambda = \{A, B, D, \pi\})$. In real applications, there are three basic problems associated with an HSMM.

(1) Evaluation (*Also Called Classification*). Given the observation sequence $O = o_1 o_2 \cdots o_T$, and an HSMM λ, what is the probability of the observation sequence given the model (i.e., $P(O \mid \lambda)$)? The solution of this problem is obtained by using the forward-backward algorithm.

(2) Decoding (*Also Called Recognition*). Given the observation sequence $O = o_1 o_2 \cdots o_T$, and an HSMM λ, what sequence of hidden states $S = (s_1, s_2, \ldots, s_N)$ most probably generates the given sequence of observations? This problem is solved by using the Viterbi algorithm. Here, a novel algorithm is used to solve this problem.

(3) Learning (*Also Called Training*). How to adjust the model parameters $\lambda = \{A, B, D, \pi\}$ to maximize $P(O \mid \lambda)$? This problem is solved by using the Baum-Welch algorithm.

Different algorithms have been developed for the above three problems. The details of three problems and the corresponding algorithms can be found in Rabiner [16] and Dong and He [15].

3. Sequential Monte Carlo Methods

Sequential Monte Carlo method has been introduced in the 1960s, and it is a significant and powerful methodology for coping with difficult nonlinear problems. The key idea of the SMC method is to represent the posterior density function by a set of random samples with associated weights and compute recognition probability based on these samples.

Let $\{x^i_{n-1}, w^i_{n-1}\}_{i=1}^{N_s}$ denote the sample from importance function, and let w^i_{n-1} denote the weights of particles $(x^i_{n-1}\ (i = 1, 2, \ldots, N_s))$, and N_s is the number of particles for the computation. Then, $p(x_{n-1} \mid y_{0:n-1})$ can be approximated as follows:

$$p(x_{n-1} \mid y_{0:n-1}) \approx \sum_{i=1}^{N} w^i_{n-1} \delta\left(x_{n-1} - x^i_{n-1}\right), \tag{3.1}$$

where $w^i_{n-1} \propto p(x^i_{0:n-1} \mid y_{0:n-1}) / q(x^i_{0:n-1} \mid y_{0:n-1})$, $\sum_{i=1}^{N} w^i_{n-1} = 1$, $q(x^i_{0:n-1} \mid y_{0:n-1})$ is the importance probability density, and the $\delta(\cdot)$ is Dirac delta function [17].

With the increase of new observation data, in order to obtain the new sample $(x^i_{0:n} \sim q(x_{0:n} \mid y_{0:n}))$, the new data $(x^i_n \sim q(x_n \mid x^i_{0:n-1}, y_{0:n}))$ can be added into the old sample $(x^i_{0:n-1} \sim q(x_{0:n-1} \mid y_{0:n-1}))$. And, the weights of particles x^i_n can be obtained as follows:

$$\tilde{w}^i_n = \frac{p(x^i_n \mid x^i_{n-1}) p(y_n \mid x^i_n)}{q(x^i_n \mid x^i_{0:n-1}, y_{0:n})} w^i_{n-1}. \tag{3.2}$$

So the posterior probability density of x_n can be written as follows:

$$p(x_n \mid y_{0:n}) = \sum_{i=1}^{N} w_n^i \delta\left(x_n - x_n^i\right). \tag{3.3}$$

However, the choice of the importance density function is critical for the performance of the SMC method. In the paper, the a priori probability density function is chosen as the importance density function and it is written as follows:

$$q\left(x_n^i \mid x_{0:n-1}^i, y_{0:n}\right) = p\left(x_k^i \mid x_{k-1}^i\right). \tag{3.4}$$

From (3.2) and (3.4), we can obtain

$$\tilde{w}_n^i = p\left(y_n \mid x_n^{(i)}\right) w_{n-1}^{(i)}, \qquad w_n^{(i)} = \frac{\tilde{w}_n^i}{\sum_{i=1}^{N} \tilde{w}_n^i}. \tag{3.5}$$

In the sequential importance sampling implementation of SMC methods, since most particles have negligible weights after a few iterations, the main difficulty is the degeneracy problem [18]. Several researchers have developed methods to overcome the degeneracy in the particle population $\widehat{N}_{\text{eff}}$, which is an estimation of the effective sample size N_{eff} [18, 19]. N_{eff} and $\widehat{N}_{\text{eff}}$ can be approximated as follows:

$$N_{\text{eff}} = N * \left(1 + \text{var}\left(w_n^{(i)}\right)^{-1}\right), \qquad \widehat{N}_{\text{eff}} = \left(\sum_{i=1}^{N_s} \left(w_n^{(i)}\right)^2\right)^{-1}. \tag{3.6}$$

In (3.6), if the valid sample N_{eff} becomes smaller, the degeneracy of SMC methods becomes more serious. But, whenever $\widehat{N}_{\text{eff}}$ is smaller than N_{thres}, a resampling algorithm will be applied to eliminate the particles with small weights, and it also reserves the computational impacts on the optimal results in those having large weights [18].

After the resampling procedure, the new particle population $(\{\tilde{x}_{0:n}^{(i)}\}_{i=1,\ldots,N})$ is an independent and identically distributed sample of the empirical distribution; thus, the weights are reset to $\tilde{w}_n^i = N^{-1}$ and we have

$$p(x_n \mid y_{0:n}) = \sum_{i=1}^{N} w_n^i \delta\left(x_n - x_n^i\right) = \frac{1}{N} \sum_{i=1}^{N} \delta\left(x_n - x_n^i\right). \tag{3.7}$$

4. Online Prognosis Model for Complex Nonlinear Systems

The health management for complex nonlinear systems uses both state transition relations and duration information to predict the evolving trend or estimate the remaining useful life. In the previous sections, the HSMM given by (2.4) is considered and its parameters are obtained through the training algorithm in which state duration probabilities are estimated on the trellis of observations and states. In this section, the framework for online health management of a system is described.

Firstly, a novel algorithm for online health recognition of a system based on HSMM is proposed by using SMC method and its computational framework is given. Then,

the collected sensor data is used as the input of the proposed model. With the state information obtained from the proposed method, an online health prognostic model for a system is proposed. The intention is to apply SMC method to make joint multisteps ahead health recognition with all available information. The principle of SMC-based HSMM involves two main phases, as shown in Figure 2. For a complex nonlinear system, the learning phase will generate an appropriate model and an exploitation phase will recognize its current health condition and predict its RUL. In the first phase, which is achieved offline, the raw data provided by the sensors is processed for HSMM training. The second phase, which is an online one, exploits the trained models for recognizing the current system state (by using the following proposed method) and computing the corresponding RUL.

In the following, the data processing algorithm is described first. Then, a novel HSMM-based algorithm for online health recognition of complex nonlinear systems using SMC methods is proposed, and the computational framework is given. Finally, with the state information obtained from the proposed method, the online health prognostic model for complex nonlinear systems is proposed.

4.1. Data Processing Algorithm

The data processing algorithm includes feature extraction using wavelets and vector quantization. The feature extraction is described first. Since the structures of each part are different, when a system fails, it often generates a large number of nonstationary signals. The performance of output signals in each frequency band is different. The wavelet analytical method can automatically decompose different frequency signals into different frequency bands, which can increase the time-frequency resolution and realize failure feature extraction. The failure feature extraction algorithm using wavelet can be described as follows.

Step 1. The vibration signals can be decomposed into V-layers wavelet, and coefficients $(X_j\,(j = 1, 2, \ldots, 2^V))$ of 2^V frequency bands from low frequency to high frequency of the V-layers are extracted, respectively.

Step 2. Reconstruct the wavelet package coefficients and extract each frequency band signal $S_j\,(j = 1, 2, \ldots, 2^V)$.

Step 3. The total energy of each frequency band signal is computed by the following equation:

$$E_j = \int \left|S_j(t)\right|^2 dt = \sum_{k=1}^{n} \left|x_{jk}\right|^2, \tag{4.1}$$

where $x_{jk}\,(j = 1, 2, \ldots, 2^V,\ k = 1, 2, \ldots, n)$ is the amplitude of discrete points for reconstructing signals.

Step 4. Construct and normalize feature vector as follows:

$$E = \left(\sum_{j=1}^{2^V} \left|E_j\right|^2\right)^{1/2}. \tag{4.2}$$

So the feature vector F equals F' (i.e., $F' = (E_1, E_2, \ldots, E_2^V)/E$).

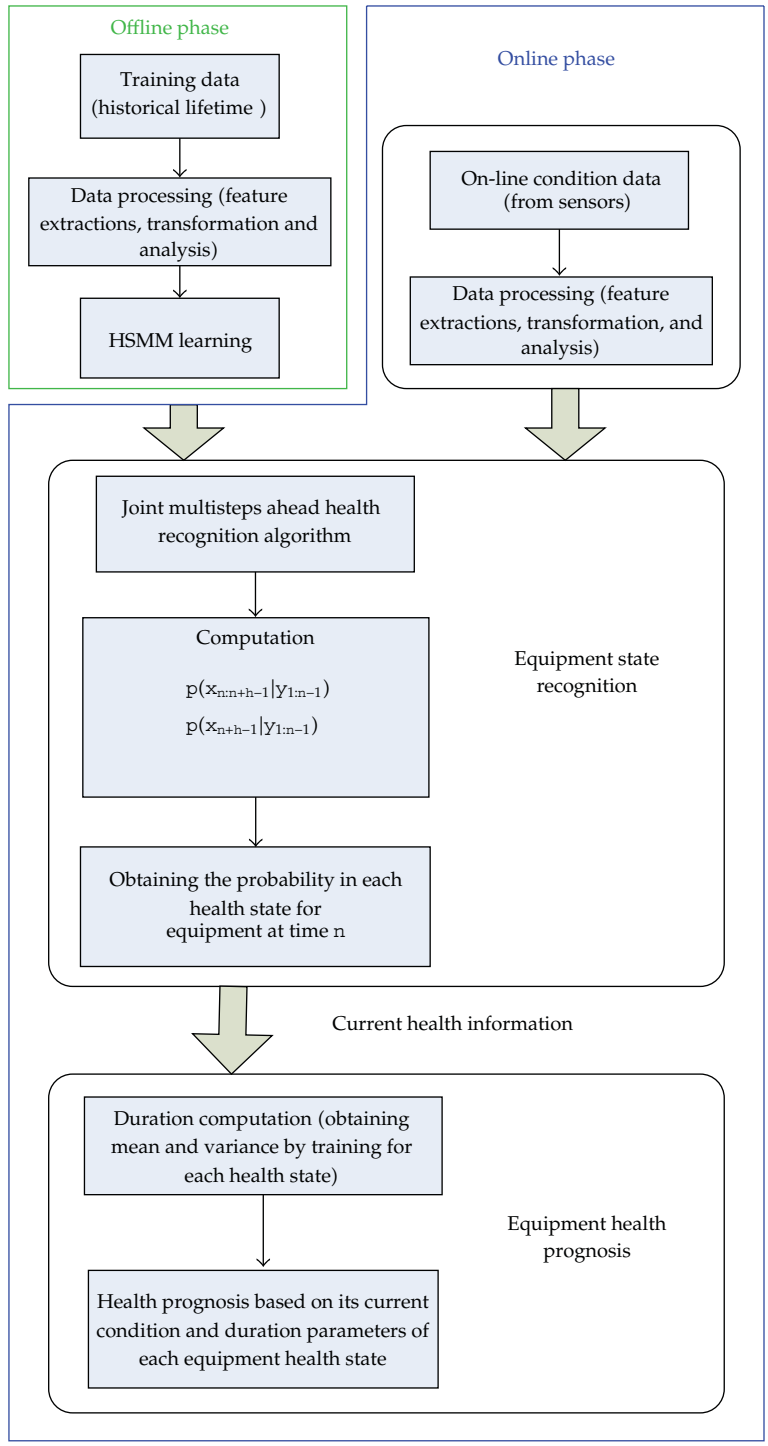

Figure 2: Fault prognosis scheme of HSMM-based SMC method.

The feature vector must be quantized before the wavelet fault feature vector is used for HSMM training. The self-organizing feature maps (SOMs) are often used for vector quantization. The SOMs simulates self-organizing feature maps function of the brain's nervous system, it is a competitive learning network, and the learning process is unsupervised and self-organized [20].

4.2. Joint Multisteps Ahead Health Recognition for Systems Using SMC in HSMM

One purpose of the paper is to offer the appropriate methods for real time recognition of health states and RUL prognosis as a continuous function of time. A new HSMM-based SMC method is applied to address the recognition problems of HSMM. Currently, the primary concerns in HSMM are two aspects: one-step ahead health recognition of states by estimating the probability distribution $p(x_n \mid y_{1:n-1})$ and multistep ahead health recognition of states by estimating the probability distribution $p(x_{n+h} \mid y_{1:n-1})$ [18]. However, the recognizing trajectories of $p(x_n \mid y_{1:n-1})$ and $p(x_{n+h} \mid y_{1:n-1})$ may be incredible due to neglecting the consistency principle of HSMM. The consistency is very important and required for many cases. Therefore, a novel method of multistep ahead state health recognition based on joint probability distribution $p(x_{n:n+h} \mid y_{1:n-1})$, which provides the most possible recognition for the recognizing trajectory, is proposed. In order to illustrate the superiority of the proposed method, the proposed joint multisteps ahead algorithm will be compared with the general multistep ahead algorithm and one-step ahead algorithm on the aspect of prognostic accuracy.

In the following, the SMC method is used for joint multistep ahead health recognition given all available information up to time $n-1$. The joint multistep ahead health recognition method is capable of capturing the relationship between hidden states and observations of a system. By combining the capabilities of HSMM and SMC method, a new health recognition algorithm is proposed here to recognize the hidden failure online. And HSMM can provide rich mathematical structures for health management of complex nonlinear systems.

This health recognition algorithm is related to the one-step ahead health recognition. The state probability density function of the one-step ahead health recognition can be obtained by a recursive manner based on Algorithm 4.1. Suppose that the state pdf $p(x_{n-1} \mid y_{1:n-1})$ can be approximated by $\{x^{(i)}_{0:n-1}, w^i_{n-1}\}_{i=1}^{N_s}$, as it is shown as follows:

$$p(x_{n-1} \mid y_{1:n-1}) = \sum_{i=1}^{N_s} w^i_{n-1} \delta\left(x_{n-1} - x^i_{n-1}\right). \tag{4.3}$$

The state probability density $p(\hat{x}_n \mid y_{1:n-1})$ can be approximated with new samples evolved from $\{x^i_{0:n-1}, w^i_{n-1}\}_{i=1}^{N_s}$ (the symbol $\hat{}$ represents the recognized value). The procedure of the one-step ahead health recognition is described as follows.

Algorithm 4.1. Online one-step ahead health recognition is as follows

Step 1. Let $\hat{x}^i_n \sim p(\hat{x}_n \mid x^i_{n-1})$, then

$$p(\hat{x}_n \mid y_{1:n-1}) \approx \sum_{i=1}^{N_s} w^i_{n-1} \delta\left(\hat{x}_n - \hat{x}^i_n\right). \tag{4.4}$$

Step 2. Update the weights $\widehat{w}_n^i = p(y_n \mid \widehat{x}_n^i) w_{n-1}^i$, then

$$w_n^i = \frac{\widehat{w}_n^i}{\sum_{i=1}^{N_s} \widehat{w}_n^i}. \tag{4.5}$$

Step 3. Compute the state pdf as follows:

$$p(\widehat{x}_n \mid y_{1:n}) \approx \sum_{i=1}^{N_s} w_n^i \delta\left(\widehat{x}_n - \widehat{x}_n^i\right). \tag{4.6}$$

Then, we extend to the joint multistep ahead health recognition. Based on (2.4) and the current state recognition Algorithm 4.1, $p(x_{n-1} \mid y_{1:n-1})$ can be obtained. According to the conditional probability and chain rule of probability, we can obtain

$$p(\widehat{x}_{n:n+h-1} \mid y_{1:n-1}) = \prod_{j=0}^{h-1} p(\widehat{x}_{n+j} \mid y_{1:n-1}, \widehat{x}_{n:n+j-1}). \tag{4.7}$$

In the above equation, $p(\widehat{x}_{n+j} \mid y_{1:n-1}, \widehat{x}_{n:n+j-1})$, $j = 0, 1, \ldots, h-1$ is just one-step ahead health recognition probability and can be approximated by Algorithm 4.1 with $\{\widehat{x}_{n+h}^i x_{0:n-1}^i, w_{n+h-1}^i\}_{i=1}^{N_s}$ such that

$$p(x_{n+j} \mid y_{1:n}, x_{n:n+j-1}) = \sum_{i=1}^{N_s} w_{n+h}^i \delta\left(\widehat{x}_{n+h} - \widehat{x}_{n+h}^i\right). \tag{4.8}$$

The joint h-step ahead health recognition can be approximated by the particles with corresponding weights:

$$\left\{\left(\widehat{x}_n^{i_0}, \ldots, \widehat{x}_{n+h-1}^{i_{h-1}}\right), \left(\widehat{w}_{n-1}^{i_0}, \ldots, \widehat{w}_{n+h-2}^{i_{h-1}}\right)\right\}_{i_{0,\ldots,i_{h-1}}=1}^{N_s}. \tag{4.9}$$

And we have

$$p(\widehat{x}_{n:n+h-1} \mid y_{1:n-1}) = \sum_{i_0=1}^{N_s} \cdots \sum_{i_{h-1}=1}^{N_s} \left(\widehat{w}_{n-1}^{i_0}, \ldots, \widehat{w}_{n+h-2}^{i_{h-1}}\right) \delta\left(\widehat{x}_n - \widehat{x}_n^{i_0}, \ldots, \widehat{x}_{n+h-1} - \widehat{x}_{n+h-1}^{i_{h-1}}\right). \tag{4.10}$$

So the overall online joint multistep ahead health recognition algorithm can be described as follows.

Algorithm 4.2. Online joint multistep (h-steps) ahead health recognition is as follows.

Step 1. Based on Step 1 in Algorithm 4.1, we can obtain

$$p(\widehat{x}_n \mid y_{1:n-1}) \approx \sum_{i=1}^{N_s} w_{n-1}^i \delta\left(\widehat{x}_n - \widehat{x}_n^i\right). \tag{4.11}$$

Step 2. If $h = 1$, then go to Step 3, otherwise set $k = 1$.

Substep 1. Use the prognosis value $\{\hat{x}^i_{n+k-1}\}_{i=1}^{N_s}$ to update weights $\{w^i_{n+k-2}\}_{i=1}^{N_s}$, according to $w^i_{n+k-1} = p(\hat{y}^i_{n+k-1} \mid \hat{x}^i_{n+k-1}) w^i_{n+k-2}$, then we have

$$p(\hat{x}_{n+k-1} \mid y_{1:n-1}) \approx \sum_{i=1}^{N_s} w^i_{n+k-1} \delta\left(\hat{x}_{n+k-1} - \hat{x}^i_{n+k-1}\right). \tag{4.12}$$

Substep 2. Let $\hat{x}^i_{n+k} \sim p(\hat{x}_{n+k} \mid \hat{x}^i_{n+k-1})$, then

$$p(\hat{x}_{n+k} \mid y_{1:n-1}) \approx \sum_{i=1}^{N_s} w^i_{n+k-1} \delta\left(\hat{x}_{n+k} - \hat{x}^i_{n+k}\right). \tag{4.13}$$

Substep 3. Let $k = k + 1$. If $k = h$, then the joint h-step ahead prognosis can be obtained based on (4.10), and go to Step 3, otherwise return to Substep 1.

Step 3. When the online monitoring measurement y_n is available, update the weights $\hat{w}^i_n = p(y_n \mid \hat{x}^i_n) w^i_{n-1}$, and

$$p(\hat{x}_n \mid y_{1:n}) \approx \sum_{i=1}^{N_s} w^i_n \delta\left(\hat{x}_n - \hat{x}^i_n\right). \tag{4.14}$$

Based on Algorithm 4.2, for a given new sequence of continuously observed data, the state recognition probability of the current time can be obtained. Based on the state recognition probability, the RUL values of a complex nonlinear system at the current time can be predicted based on the prognostic algorithm.

Obviously, the relationship between joint multistep ahead health recognition and simple multistep ahead recognition is given as follows:

$$p(\hat{x}_{n+h-1} \mid y_{1:n-1}) = \sum_{\hat{x}_n} \cdots \sum_{\hat{x}_{n+h-1}} p(\hat{x}_{n:n+h-1} \mid y_{1:n-1}). \tag{4.15}$$

In the above equation, $p(\hat{x}_{n+h-1} \mid y_{1:n-1})$ is the marginal distribution of $p(\hat{x}_{n:n+h-1} \mid y_{1:n-1})$. The simple multistep ahead recognition is suitable for the situation where the health management of a system needs to be obtained at given time with lower accuracy. However, the joint multistep ahead health recognition algorithm is much better for online health management of a system due to the ability of keeping the Markov consistency in HSMM.

After obtaining the state recognition probability of a system, the health state change point needs to be determined. The health state change point is defined as the point at which the system changes from health state x_l to health state x_{l+1}. Through the health state change point detection, the time from the system's current condition to the health state change point can be estimated, as the health state change point corresponds to the switching from health state x_l to health state x_{l+1} in the model and the determination of health state change point can be obtained in the following way: apply the joint multistep ahead health recognition

	S_1	S_2	S_3	$\cdots$	S_{l-1}	S_1	S_{l+1}	$\cdots$	S_{T-1}	S_T
$S^{(2)}$	x_1	x_{l+1}	x_{l+1}	...	x_{l+1}	x_{l+1}	x_{l+1}	...	x_{l+1}	x_{l+1}
$S^{(3)}$	x_1	x_1	x_{l+1}	$\cdots$	x_{l+1}	x_{l+1}	x_{l+1}	$\cdots$	x_{l+1}	x_{l+1}
					$\cdots$					x_{l+1}
$S^{(1)}$	x_1	x_1	x_1	...	x_1	x_{l+1}	x_{l+1}	...	x_{l+1}	x_{l+1}
					$\cdots$					x_{l+1}
S^L	x_1	x_1	x_1	$\cdots$	x_1	x_1	x_1	$\cdots$	x_1	x_{l+1}

Figure 3: The recognized state sequences for a system having two health states.

algorithm online when new observations are obtained. If the value of $p(S_l = x_{l+1} \mid y_{1:l-1})$ is increasing up to time l and becomes the maximum at time l, then l will be the health state change point.

For new observations $y_1 y_2 \cdots y_T$ and two system health states, the recognized state sequences of a system for computing RUL are shown in Figure 3. From Figure 3, it can be seen that each state sequence will provide the location recognition of the health state change point. Moreover, the probability of a system staying in the state based on Algorithm 4.2 can be recognized and the RUL values of a system can be computed.

4.3. Online Health Prognosis Model for Complex Nonlinear Systems

For the health prognosis of a system, its purpose is to predict the progression of a failure condition in order to estimate the RUL of a system. Assuming that the system will go through health states s_i $(i = 1, 2, \ldots, n-1)$ before entering the failure state $F(s_n)$. And let $D(s_i)$ denote the expected duration of a system at health state s_i. Once the system enters health state s_i, its RUL will equal the summation of the residual useful duration of a system staying at health state s_i and the residual useful duration of system staying in the future health states before failure. This type of prognostic structure is shown in Figure 4. Let $\widehat{D}(s_i^{(l)})$ denote the residual duration of a system staying in health state s_i at the lth observation time point. Then, we can obtain

$$\begin{aligned} D(s_i) &= \mu(s_i) + \rho\sigma^2(s_i), \\ \rho &= \frac{\left(\text{life time} - \sum_{i=1}^{N} \mu(s_i)\right)}{\sum_{i=1}^{N} \sigma^2(s_i)}, \\ \widehat{D}\left(s_i^{(l)}\right) &= p(S_l = s_i \mid y_{1:l}) D(s_i), \end{aligned} \tag{4.16}$$

where $\mu(s_i)$ is the mean of duration probability function $p_i(d)$ of state s_i and $\sigma^2(s_i)$ is the variance of duration probability function $p_i(d)$ of state s_i. l represents the step length. $p(S_l = s_i \mid y_{1:l})$ denotes the state probability of s_i at the lth observation time point based on observation $y_{1:l}$.

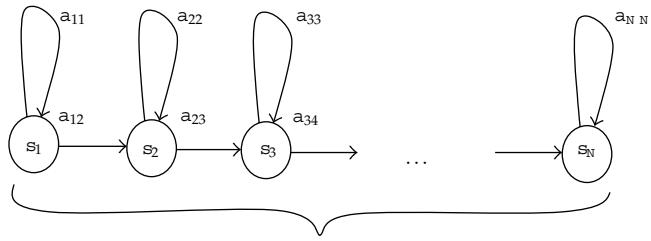

Figure 4: Prognostic structure based on HSMM using SMC method. Life time of a component = $D(s_1) + D(s_2) + D(s_3) + \cdots + D(s_N)$. $D(s_i)$: duration of a component staying at state s_i. s_1: health state 1 (baseline), s_2: health state 2 (contamination 1), ..., s_N: health state N (failure), a_{ij}: transition probability.

Based on (4.16), the RUL at the lth observation time point since a system stays at the health state s_i can be computed as follows:

$$\mathrm{RUL}^{(l)} = \widehat{D}\left(s_i^{(l)}\right) + \sum_{j=i+1}^{n-1} D(s_j). \tag{4.17}$$

By integrating (4.16) with (4.17), the RUL at the lth observation time point since a system enters health state s_i can be obtained.

4.4. Prognosis Algorithm

The proposed methods are used during the online phase in order to recognize health states and estimate the RUL values. In terms of the HSMM-based SMC method, the online health management procedure of a system can be described as follows.

Step 1. This step consists of learning the appropriate HSMM that best fits and represents the online observed sequence. Indeed, the observations are continuously fed into the set of learned (completely defined) models and a likelihood value is calculated in order to learn the appropriate model that will be used for the computation of the expected state duration and the initial state transition probability.

Step 2. This step is related to the recognition of the current state. Based on Algorithm 4.2, the pdf of state s_i at the lth observation time since a system enters state s_i can be computed with the online monitored data using joint multistep ahead health recognition algorithm. And the health state change point of a system can also be obtained.

Step 3. Based on Step 2, the residual duration of a system keeping the health state s_i at the lth observation time point can be computed based on (4.16).

Step 4. Based on (4.17), the RUL at the lth observation time point since a system enters health state s_i can be obtained.

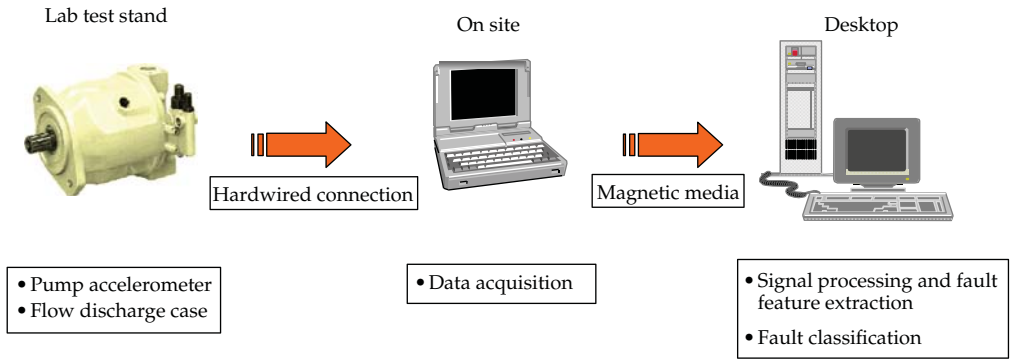

Figure 5: Schematic diagram of the experimental setup.

5. Case Study

To evaluate the performance of the HSMM-based SMC method for online health management of complex nonlinear systems, a real hydraulic pump health monitored application is used.

In the case study, the long-term wear test experiments were conducted at a research laboratory facility. In the test experiments, three pumps (pump 6, pump 24, and pump 82) were worn by running them using oil-containing dust. In other words, it is a seeding fault experiment and the deterioration of the three pumps does not follow a nature process. Each pump experienced four states: baseline (normal state), contamination 1 (5 mg of 20-um dust injected into the oil reservoir), contamination 2 (10 mg of 20-um dust injected into the oil reservoir), and failure (15 mg of 20-um dust injected into the oil reservoir). The contamination stages in this hydraulic pump wear test case study correspond to different stages of flow loss in the pumps. As the flow rate of a pump clearly indicates pump's health state, the contamination stages corresponding to different degrees of flow loss in a pump were defined as the health states of the pump in the test [15, 21].

Vibration signals were collected from a pump accelerometer that was positioned parallel to the axis of swash plate swivel axis and data was continuously sampled. Figure 5 shows the schematic diagram of the experimental setup. The pump used for testing in the experiments was a Back Hoe Loader: a 74 cc/rev variable displacement pump. The data was collected at a sample rate of 60 kHz with antialiasing filters from accelerometers designed to have a usable range of 10 kHz. In many cases, the most distinguished information is hidden in the frequency content of signals. So the time-frequency representation of signals is needed. In this case, the signals were processed using wavelet packet with Daubechies wavelet 10 (db10) and five decomposition levels as the db10 wavelet provide the most effective way to capture the fault information in the pump vibration data. The coefficients obtained by the wavelet packet decomposition were used as the inputs.

5.1. Hidden States and Probability Density of Parameters

For prognosis, the health changing mechanisms of a system usually involve several degraded states. From normal to failure, a system goes through a series of different degraded states

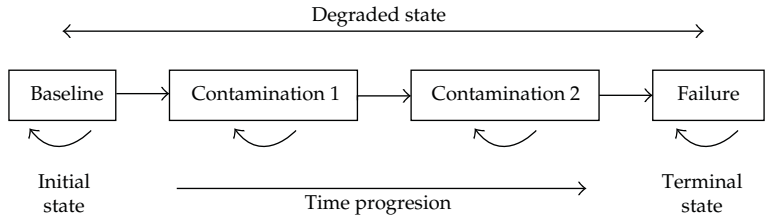

Figure 6: A HSMM scheme describing failure mechanism of a system.

and the certain transition relation among states is existed. There are four hidden states in this case study which are defined as baseline, contamination 1, contamination 2, and failure, respectively. The state transition process for the experiment is described by Figure 6.

There should be three probability distributions which will be modeled by the following sections, including the probability of state transition, the probability of state duration, and the probability of observation.

5.1.1. Probability of State Transitions

Assuming that A_{ij} is the jth element of the ith row of the transition matrix A, then the transition probability can be computed as follows:

$$A_{ij} = \frac{\left((1-\lambda)m_{ij} + \lambda\overline{A}_{ij}\right)}{\sum_{i=1}^{N}\left((1-\lambda)m_{ij} + \lambda\overline{A}_{ij}\right)}, \quad i,j = 1,2,3,4, \tag{5.1}$$

where the values of $\overline{A}_{ij}$ come from the expert knowledge, m_{ij} denotes the number of transitions from state x_j to x_i (m_{i0} is the count of occurrences of the state x_i). λ is used to control the weights between the expert knowledge and observation evidence.

5.1.2. Probability of State Duration

The duration probability distribution $p_i(d)$ can be modeled using the half-normal distribution and expressed as follows:

$$p_i(d) = \frac{1}{\sigma_i}\sqrt{\frac{2}{\pi}}\exp\left(-\frac{1}{2}\left(\frac{d-\mu_i}{\sigma_i}\right)\right), \quad i = 1,2,3,4, \tag{5.2}$$

where $\sigma^2(s_i)$ is the variance for the ith state and $\mu(s_i)$ is the mean for the ith state.

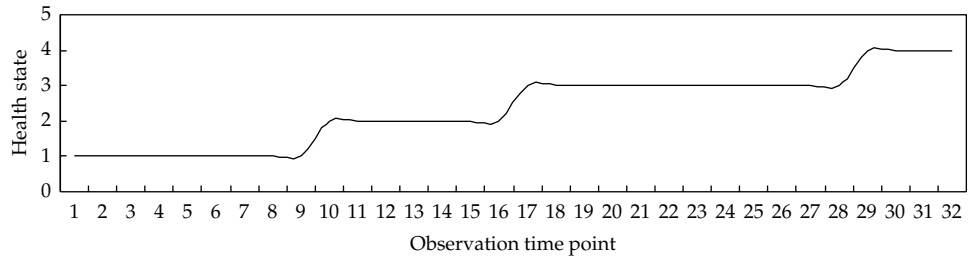

Figure 7: One sequence of the historical health data for a failure event.

5.1.3. Probability of Observations

For the observation sequences, two Gaussian mixtures for each state are chosen. Thus, the following probability density can be obtained:

$$b_i(o_t) = \sum_{k=1}^{2} \omega_{ik} N(o_t, u_{ik}, U_{ik}), \quad i = 1,2,3,4, \ k = 1,2, \tag{5.3}$$

where $N(o_t, u_{ik}, U_{ik}^2)$ is the kth mixture Gaussian distribution at state s_i. u_{ik}, U_{ik}^2, and ω_{ik} are the mean, variance, and mixture weight of the kth Gaussian distribution at state s_i, respectively. However, the weights must satisfy the following constraints:

$$\sum_{k=1}^{2} w_{ik} = 1 \quad w_{ik} \geq 0, \ i = 1,2,3,4, \ k = 1,2. \tag{5.4}$$

Based on Sections 2, 5.1.1 and 5.1.2, the parameters of HSMM can be described as follows:

$$\{A, B, D, \pi\} = \left\{ a_{ij}, u_{ik}, U_{ik}^2, w_{ik}, \mu_i, \sigma_i, \pi_i, 1 \leq i, \ j \leq 4, 1 \leq k \leq 2 \right\}. \tag{5.5}$$

5.2. Results and Discussion

For the health prognosis, the lifetime training data from three hydraulic pumps is used. An HSMM with four health states (baseline, contamination 1, contamination 2, and failure) can be trained. The initial transition probabilities among four health states are transition probabilities at the beginning of pump's running. And the expected values of the duration time in each state are also available through the training process. The results are given in Tables 1 and 2.

In this case study, we denote baseline state as s_1, contamination 1 state as s_2, contamination 2 state as s_3, failure state as s_4, and the states set as S ($S_l \in S$, and S_l denotes the health state at observation time point l). Historical health data for pumps, at each observation time point in one of the failure events, is shown in Figure 7. y-axis indicates the health state of a pump, where 1 means s_1, 2 means s_2, 3 means s_3, and 4 means s_4. It can be seen from Figure 7 that the health states for pumps are rigidly degrading over time.

Table 1: Transition probabilities among four health states.

State	Baseline	Contamination 1	Contamination 2	Failure
Baseline	0.9056	0.0879	0.0063	0.0002
Contamination 1	0	0.8491	0.1506	0.0003
Contamination 2	0	0	0.9129	0.0871
Failure	0	0	0	1

Table 2: Expected values of duration time for each health state.

State	Baseline	Contamination 1	Contamination 2	Failure
Exp. of duration	10.4549	9.7923	11.3375	—

Table 3: State density of 5 observation time points.

Observation time point (l)	State probability	Health state
1	0.8821	
2	0.8556	
3	0.7908	s_1
4	0.7744	
5	0.6379	

For testing the proposed methods, after the pumps enter baseline state, firstly, the 5 observation time points are used to compute the RUL and test the effectiveness. Based on Section 4.2, the state recognition probability of the pumps staying at health state "baseline" (i.e., $p(S_l = s_1 \mid y_{1:l-1}),\ l = 1, \ldots, 5$) can be computed and the results are given in Table 3.

Then, based on (4.16) and (4.17), the RUL values of 5 observation time points for pumps can be obtained. The comparison of the prognostic and actual RULs and their relative errors are provided in Table 4. It can be seen that the proposed methods are effective for online failure prognosis of pumps. The relative error is computed as follows:

$$\text{Error} = 100\% \times \frac{\left|\text{Actual RUL} - \text{Prognostic RUL}\right|}{\text{Actual RUL}}. \tag{5.6}$$

In order to determine whether the proposed methods have a better performance for online failure prognosis of pumps, the sample size is enlarged from 5 observation time points to 29 observation time points.

First, based on Algorithm 4.2, the observation step is set as 4 (i.e., $h = 4$, h is the observation steps) and the state is recognized after 4 observation time points.

Then, the state recognition probability is computed. The health state change point is obtained and the changing trends of the state probability with the observation time points are shown in Figure 8. Figures 8(a), 8(b), and 8(c) are the probability changing trends of states s_1, s_2, and s_3, respectively. Each health state of pumps is assumed to begin from the observation time point when the corresponding health state probability has the largest value. From Figure 8, it can be seen that the health state of pumps stays at state s_1 from the 6th observation time point to the 12th observation time point (see Figure 8(a)), the health state

Table 4: Prognostic and actual RUL (5 observation time points).

Actual RUL	Computed RUL	Relative error (%)
32.0000	30.3521	5.1498
31.0000	30.0746	2.9851
30.0000	29.3980	2.0067
29.0000	29.2262	0.7801
28.0000	27.7989	0.7181

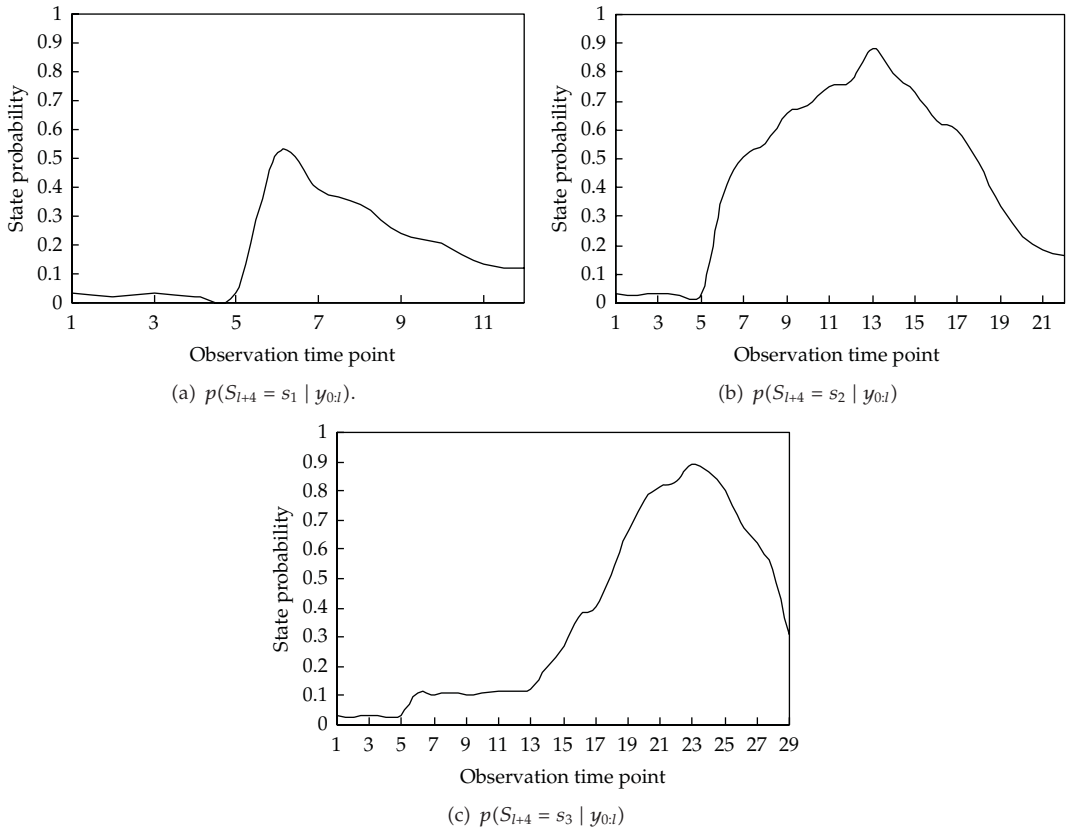

(a) $p(S_{l+4} = s_1 \mid y_{0:l})$.

(b) $p(S_{l+4} = s_2 \mid y_{0:l})$

(c) $p(S_{l+4} = s_3 \mid y_{0:l})$

Figure 8: Changing trends of the state probability.

of pumps stays at state s_2 from the 13th observation time point to the 22nd observation time point (see Figure 8(b)), and the health state of pumps stays at state s_3 from the 23rd observation time point to the 29th observation time point (see Figure 8(c)). Each health state probability for the corresponding observation time points can be found in Table 5.

From Table 5 and Figure 8(a), it can be seen when the observation time point is 5, the failure prognosis probability $p(S_{l+4} = s_1 \mid y_{0:l})$ suddenly begins to increase its values and when the observation time point is 6, the failure prognosis probability obtains the maximum value. And it progressively becomes stable from the 6th observation time point, so it indicates that the pumps have more failure possibility at about 6th observation time point. In fact, at the 6th observation time point, the health state of the pumps begins to change from the

Table 5: State prognosis probability.

Observation time point	State probability	Health state
3	0.0711	
4	0.0703	
5	0.0895	
6	0.5186	
7	0.3907	
8	0.3413	s_1
9	0.2379	
10	0.2092	
11	0.1327	
12	0.1203	
13	0.8792	
14	0.7982	
15	0.7328	
16	0.6307	
17	0.5961	
18	0.4841	s_2
19	0.3384	
20	0.2306	
21	0.1864	
22	0.1664	
23	0.8935	
24	0.8632	
25	0.8014	
26	0.6902	s_3
27	0.6187	
28	0.5341	
29	0.3062	

baseline. From Figure 8(b), it can be seen when the observation time point is 6, the failure prognosis probability $p(S_{l+4} = s_2 \mid y_{0:l})$ obviously begins to increase its values. When the observation time point is 7, the failure prognosis probability exceeds 0.5. It is shown that the failure mode of the pumps begins to shift into the second failure mode (contamination 1). In fact, the failure mode of the pumps lies in the contamination 1 at the 13th observation time point. From Figure 8(c), it can be seen when the observation time point is 13, the failure prognosis probability $p(S_{l+4} = s_3 \mid y_{0:l})$ obviously begins to increase its values. When the observation time point is 18, the failure prognosis probability exceeds 0.5. It is shown that the failure mode of the pumps begins to shift into the third fault mode (contamination 2). In fact, the failure mode of the pumps lies in the contamination 2 at the 23rd observation time point. It can also be seen that the simulation results are consistent with the actual states and the proposed methods of HSMM-based SMC method can be used to predict the evolution of the system.

Based on (4.16), each $\widehat{D}(s_i^{(l)})$ (l represents the observation time point and $i = 1, 2, 3$) can be computed. And the expected residual duration of the pumps staying at each health state can be obtained. According to (4.17) and the values of each $\widehat{D}(s_i^{(l)})$, the RUL can be obtained

Table 6: RUL prognostic comparison with 4 methods.

Actual RUL	HSMM (joint multisteps)	Relative error	HSMM (multisteps)	Relative error	HSMM (one-step)	Relative error	HSMM	Relative error
30.00	29.398	2.0067	29.3980	2.0067	29.3980	2.0067	30.2558	0.8527
26.00	25.2142	3.0224	28.5854	9.9438	27.8536	7.1291	29.9643	15.2473
22.00	22.5172	2.3507	26.0616	18.4618	25.3297	15.1352	29.7954	35.4336
17.00	17.5134	3.0199	15.3897	9.4721	18.3274	7.8085	19.4981	14.6947
15.00	16.0776	7.1837	13.7082	8.6119	17.6251	17.5009	19.2081	28.054
12.00	13.1625	9.6878	13.4892	12.4097	15.4476	28.7302	18.8666	57.2217
11.00	12.9667	17.879	13.3303	25.2653	14.3096	30.0869	10.2471	6.8445
9.00	9.7866	8.7401	13.2352	19.4156	13.5290	50.3224	10.0291	11.4344
5.00	6.0558	21.1166	8.0292	35.8459	7.0224	40.4490	9.7675	95.35
MAPE	8.3341 (%)		15.7147 (%)		22.1298 (%)		29.4592 (%)	

and the results of HSMM, multistep ahead and one-step ahead health recognition methods can be compared. The comparison between the prognostic and actual RUL is given in Table 6, and the comparison scheme is illustrated in Figure 9. The mean absolute percentage error (MAPE) is set as follows:

$$\text{MAPE} = \left(\frac{1}{n}\right) \sum_{i=1}^{n} \varepsilon_i, \tag{5.7}$$

where i is the observation time point and n is the total observation time points.

Based on Table 6, the relative error of the proposed methods between the prognostic RUL and actual RUL is quite small. So it indicates that the proposed method has a better performance for online failure prognosis of the pumps. And the MAPE of the proposed methods is smaller than that of HSMM [14], multistep ahead, and one-step ahead health recognition methods, respectively. So the prognostic accuracy of the proposed method is higher than that of the HSMM, multisteps ahead, and one-step ahead health recognition methods, respectively.

Through the overall case study, the sample of the pumps is modeled based on HSMM using SMC methods and the failure prognosis is implemented based on the available observations. The results show that the proposed methods have a better performance for online health management of a system, including prognostic effectiveness and accuracy. Furthermore, the computational complexity of the proposed methods is decreased compared with HSMM-based method [15] the prognostic accuracy is better than both multisteps ahead and one-step ahead health recognition methods. The proposed methods also reduce the computing storage space. This indicates that the proposed methods are more effective for online health management of complex nonlinear systems and could be used in the real time applications with large data sets.

6. Conclusions

Currently, prognosis is still in its infancy and the literature is yet to present a working model for effective prognosis, but a new trend is that more combination models are designed to

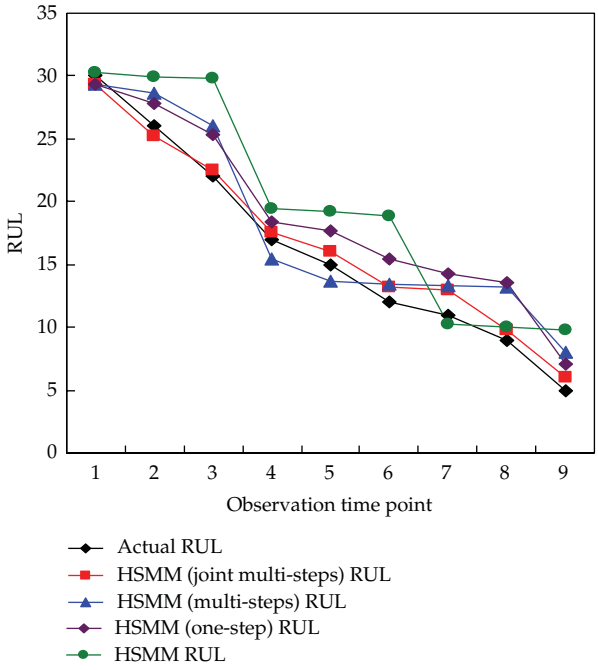

Figure 9: The results' comparison scheme for 4 methods.

deal with data extraction, data processing, and modeling for prognosis. In this paper, in order to obtain the health management of a system, the detailed models and algorithm of HSMM-based SMC method are proposed. Because it is difficult for a single method to obtain satisfied results online health management of a system, the novel online prognostic methods for a system are developed based on both the mathematical structure of HSMM and online features of SMC method, including online health recognition algorithm and online prognostic model. The methods can eliminate the disadvantages of each method, increase the prognostic accuracy, and utilize the advantages of each method. A case study is used to illustrate the superiority of the proposed methods. Through the comparisons among the proposed methods, HSMM, multisteps ahead, and one-step ahead health recognition algorithm, the results show that the proposed methods have a better performance and are more effective for online health management of complex nonlinear systems.

Acknowledgments

The work presented in this paper has been supported by Grants from the National Natural Science Foundation of China (71131005) and "Shu Guang" project (no. 09SG17) of Shanghai Municipal Education Commission and Shanghai Education Development Foundation.

References

[1] W. Wang, "A two-stage prognosis model in condition based maintenance," *European Journal of Operational Research*, vol. 182, no. 3, pp. 1177–1187, 2007.

[2] G. J. Kacprzynski, A. Sarlashkar, M. J. Roemer, A. Hess, and W. Hardman, "Predicting remaining life by fusing the physics of failure modeling with diagnostics," *JOM*, vol. 56, no. 3, pp. 29–35, 2004.

[3] C. H. Oppenheimer and K. A. Loparo, "Physically based diagnosis and prognosis of cracked rotor shafts," in *The International Society for Optical Engineering, Components and Systems Diagnostics, Progrnostics, and Health Management II*, vol. 4733 of *Proceedings of SPIE*, pp. 122–132, Orlando, Fla, USA, April 2002.
[4] M. Li, "Fractal time series—a tutorial review," *Mathematical Problems in Engineering*, vol. 2010, Article ID 157264, 26 pages, 2010.
[5] M. Li and J. Y. Li, "On the predictability of long-range dependent series," *Mathematical Problems in Engineering*, vol. 2010, Article ID 397454, 9 pages, 2010.
[6] M. Li, C. Cattani, and S. Y. Chen, "Viewing sea level by a one-dimensional random function with long memory," *Mathematical Problems in Engineering*, vol. 2011, Article ID 654284, 13 pages, 2011.
[7] M. Li and W. Zhao, "Visiting power laws in cyber-physical networking systems," *Mathematical Problems in Engineering*, vol. 2012, Article ID 302786, 13 pages, 2012.
[8] W. S. Chen, P. C. Yuen, and X. Xie, "Kernel machine-based rank-lifting regularized discriminant analysis method for face recognition," *Neurocomputing*, vol. 74, no. 17, pp. 2953–2960, 2011.
[9] Z. J. Zhou, C. H. Hu, D. L. Xu, M. Y. Chen, and D. H. Zhou, "A model for real-time failure prognosis based on hidden Markov model and belief rule base," *European Journal of Operational Research*, vol. 207, no. 1, pp. 269–283, 2010.
[10] C. Burge and S. Karlin, "Prediction of complete gene structures in human genomic DNA," *Journal of Molecular Biology*, vol. 268, no. 1, pp. 78–94, 1997.
[11] S. Deligne and F. Bimbot, "Inference of variable-length acoustic units for continuous speech recognition," in *Proceedings of the IEEE International Conference on Acoustics, Speech, and Signal Processing (ICASSP '97)*, pp. 1731–1734, April 1997.
[12] W. H. Majoros, M. Pertea, A. L. Delcher, and S. L. Salzberg, "Efficient decoding algorithms for generalized hidden Markov model gene finders," *BMC Bioinformatics*, vol. 6, article no. 16, 2005.
[13] M. Dong, "A tutorial on nonlinear time-series data mining in engineering asset health and reliability prediction: Concepts, models, and algorithms," *Mathematical Problems in Engineering*, vol. 2010, Article ID 175936, 22 pages, 2010.
[14] M. Dong and D. He, "Hidden semi-Markov model-based methodology for multi-sensor equipment health diagnosis and prognosis," *European Journal of Operational Research*, vol. 178, no. 3, pp. 858–878, 2007.
[15] M. Dong and D. He, "A segmental hidden semi-Markov model (HSMM)-based diagnostics and prognostics framework and methodology," *Mechanical Systems and Signal Processing*, vol. 21, no. 5, pp. 2248–2266, 2007.
[16] L. R. Rabiner, "Tutorial on hidden Markov models and selected applications in speech recognition," *Proceedings of the IEEE*, vol. 77, no. 2, pp. 257–286, 1989.
[17] Z. H. Tang and R. Q. Wang, "The research of definition and feature on Dirac delta function," *Journal of Liuzhou Vocational & Technical College*, vol. 9, no. 2, pp. 68–76, 2009.
[18] A. Doucet, S. Godsill, and C. Andrieu, "On sequential Monte Carlo sampling methods for Bayesian filtering," *Statistics and Computing*, vol. 10, no. 3, pp. 197–208, 2000.
[19] A. Kong, J. S. Liu, and W. H. Wong, "Sequential imputations and Bayesian missing data problems," *Journal of the American Statistical Association*, vol. 89, no. 425, pp. 278–288, 1994.
[20] T. Furukawa, "SOM of SOMs," *Neural Networks*, vol. 22, no. 4, pp. 463–478, 2009.
[21] K. M. Hancock and Q. Zhang, "A hybrid approach to hydraulic vane pump condition monitoring and fault detection," *Transactions of the ASABE*, vol. 49, no. 4, pp. 1203–1211, 2006.

Hindawi Publishing Corporation
Mathematical Problems in Engineering
Volume 2012, Article ID 305384, 12 pages
doi:10.1155/2012/305384

Research Article

A New Texture Synthesis Algorithm Based on Wavelet Packet Tree

Hsi Chin Hsin,[1] Tze-Yun Sung,[2] Yaw-Shih Shieh,[2] and Carlo Cattani[3]

[1] *Department of Computer Science and Information Engineering, National United University, Miaoli 36003, Taiwan*
[2] *Department of Electronics Engineering, Chung Hua University, Hsinchu City 30012, Taiwan*
[3] *Department of Mathematics, University of Salerno, Via Ponte Don Melillo, 84084 Fisciano, Italy*

Correspondence should be addressed to Tze-Yun Sung, bobsung@chu.edu.tw

Received 14 February 2012; Accepted 15 March 2012

Academic Editor: Ming Li

This paper presents an efficient texture synthesis based on wavelet packet tree (TSWPT). It has the advantage of using a multiresolution representation with a greater diversity of bases functions for the nonlinear time series applications such as fractal images. The input image is decomposed into wavelet packet coefficients, which are rearranged and organized to form hierarchical trees called wavelet packet trees. A 2-step matching, that is, coarse matching based on low-frequency wavelet packet coefficients followed by fine matching based on middle-high-frequency wavelet packet coefficients, is proposed for texture synthesis. Experimental results show that the TSWPT algorithm is preferable, especially in terms of computation time.

1. Introduction

Texture modeling can be effectively applied to a wide variety of natural surfaces such as plants, furs, skins, minerals, terrains, and fractal materials [1, 2] and is an important issue in cyber-physical systems [3–7]. Numerous techniques have been proposed for texture processing; one may refer to [8] for a complete survey.

Given an example texture, the goal of texture synthesis is to produce a visually similar image of any size. One may easily tile small textures to synthesize a larger image; however, there are some blocking effects near the tile edges [9]. Although some smoothing methods were proposed to reduce the blocking effects at the cost of computation time, it seems to be

limited in improvements, especially for structured textures [10]. Efros and Leung proposed a neighborhood matching method [11], in which each pixel of the synthesis image was obtained by searching the most similar one in the source image based on the user-defined neighboring pixels. Wei and Levoy took account of the order in which pixels were synthesized and proposed an order-independent search-based texture synthesis algorithm [12]. Instead of synthesizing one pixel at a time, a patch of pixels can be taken as a whole and synthesized by matching the overlap regions between neighboring patches [13–15]. To improve the synthesis speed, the multi-resolution approach has been widely used for texture analysis and synthesis [16, 17]; Fang and Lien developed a rapid image synthesis system by adopting a multi-resolution approach, which consisted of an analysis process and a synthesis process. It consumed most of the computation time in the analysis process; yet the speed of synthesis was very fast [16]. In [17], De Bonet proposed a scheme of generating the synthesis image by sampling the filtered outputs of a texture in the framework of Laplacian pyramid [18]. Burt adopted the Gaussian pyramid [19] to represent both the input texture and the synthesis image at multiple resolutions and synthesized the texture images from lower to higher resolutions [20].

Wavelet transform provides an efficient multi-resolution representation [21], in which the higher frequency components of an image are projected onto the shorter basis functions with higher spatial resolutions and the lower frequency components are projected onto the larger basis functions with higher spectral resolutions. Such a compact representation matches the characteristics of human visual system [22]. Wavelet theory has been successfully applied to many applications such as parameter estimation in fractal signals and images [23–29]. Yu et al. randomly sampled blocks of wavelet coefficients from the input texture to substitute that of the synthesis image [30]. Cui et al. adopted a 2-level wavelet transform and generated the synthesis image by minimizing the sum of squared distances between neighboring blocks of wavelet coefficients [31].

For images with textures, lots of wavelet coefficients are likely to be significant in the middle-high frequency subbands, which surely demand further decompositions for a more compact representation [32]. Note that wavelet transform only decomposes the low-frequency component of an image at each resolution. However, both the low-frequency and high-frequency components can be decomposed using wavelet packet transform, which provides more bases functions than wavelet transform [33]. In [34], we proposed an efficient scheme to organize the wavelet packet coefficients of an image into hierarchical trees called wavelet packet (WP) trees for image compression. In this paper, an efficient WP tree-based algorithm is proposed for the texture synthesis applications.

The remainder of this paper proceeds as follows. In Section 2, wavelet transform and wavelet packet transform are briefly reviewed. Section 3 describes the proposed scheme to synthesize a texture image based on the WP trees of an example texture. Experimental results are presented in Section 4. Conclusion can be found in Section 5.

2. Review of Wavelet Transform and Wavelet Packet Transform

Wavelet-transform- (WT-) based multiresolution analysis/synthesis has drawn a lot of attention to the signal/image/video applications. The extension of WT known as wavelet packet transform (WPT) provides a much larger family of bases functions with a more compact representation. In this section, a brief review of WT and WPT is given. For a more complete survey, we refer readers to [21].

2.1. Wavelet Transform

WT has a variety of desirable properties, for example, joint space-spatial frequency localization, self-similarity across subbands of the same orientation, and energy clustering within each subband. For a discrete signal at resolution ℓ, $S_\ell(n)$, the wavelet transform is defined as

$$\begin{aligned} S_{\ell+1}(n) &= \sum_k h(2n-k)\cdot S_\ell(k), \\ D_{\ell+1}(n) &= \sum_k g(2n-k)\cdot S_\ell(k), \end{aligned} \tag{2.1}$$

where

$$\begin{aligned} h(n) &= \langle \phi, \phi_{-1,-n} \rangle, \\ g(n) &= \langle \psi, \phi_{-1,-n} \rangle, \\ \phi_{-1,-n}(x) &= 2^{-1/2}\phi\left(2^{-1}x - n\right). \end{aligned} \tag{2.2}$$

ψ is a (mother) wavelet, ϕ is the corresponding scaling function, $S_{\ell+1}(n)$ is the approximation signal at the next coarser resolution $\ell+1$, $D_{\ell+1}(n)$ is the detail information between resolutions ℓ and $\ell+1$, $h(n)$ and $g(n)$ are low-pass filter and high-pass filter, respectively, and $\langle\cdot,\cdot\rangle$ is an inner product operator. $S_\ell(n)$ can be exactly reconstructed from $S_{\ell+1}(n)$ and $D_{\ell+1}(n)$ by using the following inverse wavelet transform (IWT):

$$S_\ell(n) = \sum_k \widetilde{h}(n-2k)\cdot S_{\ell+1}(k) + \sum_k \widetilde{g}(n-2k)\cdot D_{\ell+1}(k), \tag{2.3}$$

where $\widetilde{h}(n) = h(-n)$ and $\widetilde{g}(n) = g(-n)$.

For the image applications, 2D WT can be obtained by using a tensor product of two 1D WTs, horizontally followed by vertically or vice versa. Specifically, let $LL_0(m,n)$ be an image at the finest resolution 0, where m and n are indices for the vertical and horizontal orientations, respectively. The 2D WT of $LL_0(m,n)$ is as follows:

$$\begin{aligned} LL_1(m,n) &= \sum_i \sum_j h(i)\cdot h(j)\cdot LL_0(2m-i,2n-j), \\ LH_1(m,n) &= \sum_i \sum_j h(i)\cdot g(j)\cdot LL_0(2m-i,2n-j), \\ HL_1(m,n) &= \sum_i \sum_j g(i)\cdot h(j)\cdot LL_0(2m-i,2n-j), \\ HH_1(m,n) &= \sum_i \sum_j g(i)\cdot g(j)\cdot LL_0(2m-i,2n-j), \end{aligned} \tag{2.4}$$

where $LL_1(m,n)$ is the approximation image at the next coarser resolution 1, $LH_1(m,n)$, $HL_1(m,n)$, and $HH_1(m,n)$ are the detail images in the vertical, horizontal, and diagonal orientations, respectively. Figure 1 shows a 2-level 2D WT, where subbands LH_ℓ, HL_ℓ, HH_ℓ; $\ell = 1,2$, and LL_2 are delimited by solid lines. Similarly, 2D IWT can be obtained by using the tensor product of two 1D IWTs.

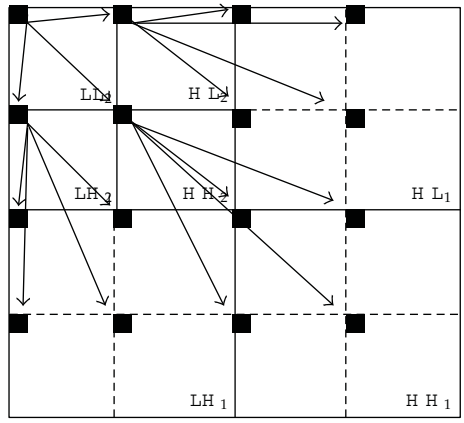

Figure 1: 2-level wavelet transform (solid boundaries), wavelet packet transform (dashed boundaries), and a wavelet packet tree with wavelet packet coefficients connected by arrows.

2.2. Wavelet Packet Transform

2D WT is only to decompose the lowest-frequency subband of an image in an iterative manner. More specifically, only the scaling coefficients are decomposed from higher to lower resolutions. However, for the texture applications, wavelet coefficients in the middle- and high-frequency subbands are likely to be significant, which needs to be taken into account to improve the multiresolution representation.

As one can see, both the low-frequency scaling coefficients and high-frequency wavelet coefficients of a signal, at any resolution, can be decomposed, which leads to wavelet packet transform (WPT), and a much larger family of bases functions can be produced [33]. Moreover, 2D WPT can be obtained by using a tensor product of two 1D WPTs. Figure 1 shows a 2-level 2D WPT, where all the wavelet subbands LH_1, HL_1, and HH_1, at resolution 1, are further decomposed into wavelet packet subbands delimited by dashed lines.

3. Wavelet-Packet-Tree-Based Texture Synthesis

Wavelet packet transform provides more bases functions, which leads to a more compact representation in comparison with wavelet transform. For the image-coding applications, we had proposed an efficient scheme to organize the wavelet packet (WP) coefficients of an image into hierarchical trees called WP trees [32]. In this section, we explore the key features of WP trees and propose a WP-tree-based algorithm for texture synthesis.

3.1. Wavelet Packet Tree

The WP coefficients of a sequence of wavelet coefficients $D_\ell(n)$, at resolution ℓ, are computed by

$$\begin{aligned} \tilde{D}_{\ell,1}(n) &= \sum_k h(2n-k)\cdot D_\ell(k), \\ \tilde{D}_{\ell,2}(n) &= \sum_k g(2n-k)\cdot D_\ell(k), \end{aligned} \tag{3.1}$$

which can be efficiently rearranged and concatenated by

$$\tilde{D}_{\ell}(n) = \begin{cases} \tilde{D}_{\ell,1}\left(\dfrac{n}{2}\right); & \text{even } n, \\ \tilde{D}_{\ell,2}\left(\dfrac{n-1}{2}\right); & \text{odd } n. \end{cases} \tag{3.2}$$

After the rearrangement and concatenation above, the dyadic relationship of wavelet coefficients across subbands is still valid and can be used to construct the dyadic WP trees of a signal. Similarly, the (2D) WP trees of an image can be obtained by rearranging the WP coefficients horizontally followed by vertically or vice versa. Figure 1 shows a 2-level WP tree with arrows connecting the related WP coefficients.

The key idea behind the construction of WP trees is based on the spatial relationships of WP coefficients. It has the same structure, that is, quad-tree structure, as the conventional wavelet trees. Furthermore, the number of high-energy wavelet coefficients can be significantly reduced through the use of wavelet packet transform. Take the rice image shown in Figure 5 as an example. The cumulative energy distribution (CED) of wavelet coefficients or WP coefficients is given by

$$\mathrm{CED}(n) = \frac{\sum_{i=1}^{n} |C(i)|}{\sum_{i=1}^{N} |C(i)|} \times 100\%, \tag{3.3}$$

where $|C(i)|, i = 1, 2, \ldots, N$, is the sorted magnitudes of wavelet coefficients or WP coefficients in descending order, n in is the number of coefficients, and N is the total number of coefficients. Figure 2 shows the CED curves of wavelet coefficients and WP coefficients, where the horizontal and vertical axes are the number of coefficients and percentage of energy, respectively. It is noted that the energy clustering of WP coefficients is more compact than wavelet coefficients. As a result, the WP-based representation is preferable to the wavelet-based representation for texture images.

3.2. Proposed Algorithm

As noted, the low-frequency WP coefficients retain the global information of an image, and the high-frequency WP coefficients contain the local detail. It is desirable to coarsely synthesize an image based on the low-frequency WP coefficients and then tune the intermediate synthesis result based on the high-frequency WP coefficients. Motivated by the fact above, we propose an efficient WP-tree-based texture synthesis algorithm using a two-step process: a coarse searching followed by a fine tuning. Figure 2 depicts a flowchart of the proposed algorithm. It is presented in steps as follows.

Step 1 (initialization). Decompose the source image by wavelet packet transform, rearrange the high-frequency WP coefficients, and construct the WP trees. Randomly select a WP tree from the source image, which is replicated in the upper left corner of the synthesis image.

Step 2 (coarse matching). For every WP tree to be synthesized, starting from the upper left corner to the lower right corner of the synthesis image, search the candidate WP trees from the source image by using a coarse matching with a tolerance as follows:

$$\begin{aligned}
\mathrm{CWP}_j &= \left\{\mathrm{WP}_{\mathrm{souce},i} \mid \mathrm{err}_{\mathrm{LFN}}(i,j) \le \mathrm{tol}_j,\ \forall i\right\},\\
\mathrm{tol}_j &= \min_i \mathrm{err}_{\mathrm{LFN}}(i,j)\cdot(1+T_r),\\
\mathrm{err}_{\mathrm{LFN}}(i,j) &= \sum_{p\in N_i, q\in N_j} \mathrm{dist}_{\mathrm{LFN}}(p,q),\\
\mathrm{dist}_{\mathrm{LFN}}(p,q) &= \sum_{m,n\in \mathrm{LFN}} \left(\mathrm{WP}_{\mathrm{source},p}(m,n) - \mathrm{WP}_{\mathrm{synthesis},q}(m,n)\right)^2,
\end{aligned} \tag{3.4}$$

where CWP_j is the set of candidate WP trees obtained from the source image for matching the synthesis WP tree $\mathrm{WP}_{\mathrm{synthesis},j}$, with the tolerance tol_j, T_r is a given threshold, $\mathrm{dist}_{\mathrm{LFN}}(p,q)$ is the distance between $\mathrm{WP}_{\mathrm{source},p}$ and $\mathrm{WP}_{\mathrm{synthesis},q}$ based on the low-frequency nodes (LFNs) of WP trees, and N_i and N_j are neighbors of $\mathrm{WP}_{\mathrm{source},i}$ and $\mathrm{WP}_{\mathrm{synthesis},j}$, respectively. Causal neighborhoods were used in our experiments.

Step 3 (fine matching). After the coarse matching in Step 2, the following fine matching is used to find the best WP tree based on the high-frequency nodes (HFNs) of the candidate WP trees.

$$\begin{aligned}
\mathrm{WP}_{\mathrm{synthesis},j} &= \mathrm{WP}_{\mathrm{source},i};\quad i = \arg\left(\min_i \mathrm{err}_{\mathrm{HFN}}(i,j)\right),\\
\mathrm{err}_{\mathrm{HFN}}(i,j) &= \sum_{p\in N_i, q\in N_j} \mathrm{dist}_{\mathrm{HFN}}(p,q),\\
\mathrm{dist}_{\mathrm{HFN}}(p,q) &= \sum_{m,n\in \mathrm{HFN}} \left(\mathrm{WP}_{\mathrm{source},p}(m,n) - \mathrm{WP}_{\mathrm{synthesis},q}(m,n)\right)^2,
\end{aligned} \tag{3.5}$$

where $\mathrm{WP}_{\mathrm{source},i} \in \mathrm{CWP}_j$ in (3.5).

Step 4. Repeat Step 2 followed by Step 3 until all the WP trees to be synthesized are obtained from the WP trees of the source image.

Step 5. Finally, the synthesis image is obtained by taking the inverse wavelet packet transform of the synthesis WP trees.

To reduce the synthesis time, one can easily modify Steps 2 and 3 by using patches of WP trees instead of single WP trees. Moreover, it is noted that lots of high-frequency WP coefficients are not significant, and only a small portion of middle-frequency WP coefficients are sufficient for the fine matching in Step 3. Thus, the proposed texture synthesis based on wavelet packet tree (TSWPT) algorithm is simple and computationally efficient. Flowchart of the TSWPT algorithm is shown in Figure 3.

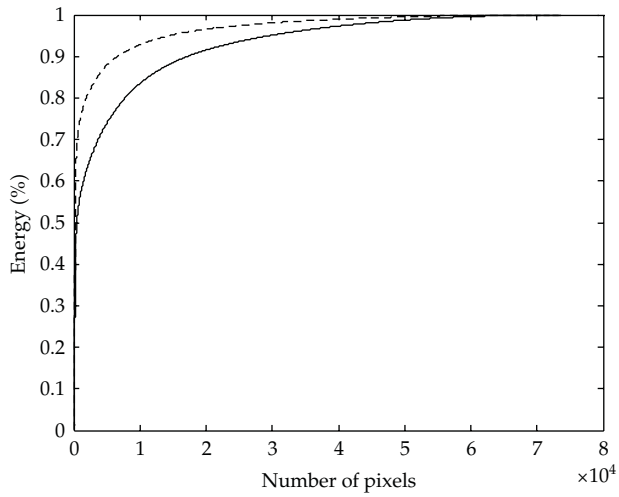

Figure 2: Cumulative energy distributions (CEDs) of the wavelet coefficients (solid line) and wavelet packet coefficients (dashed line) of the rice image shown in Figure 5.

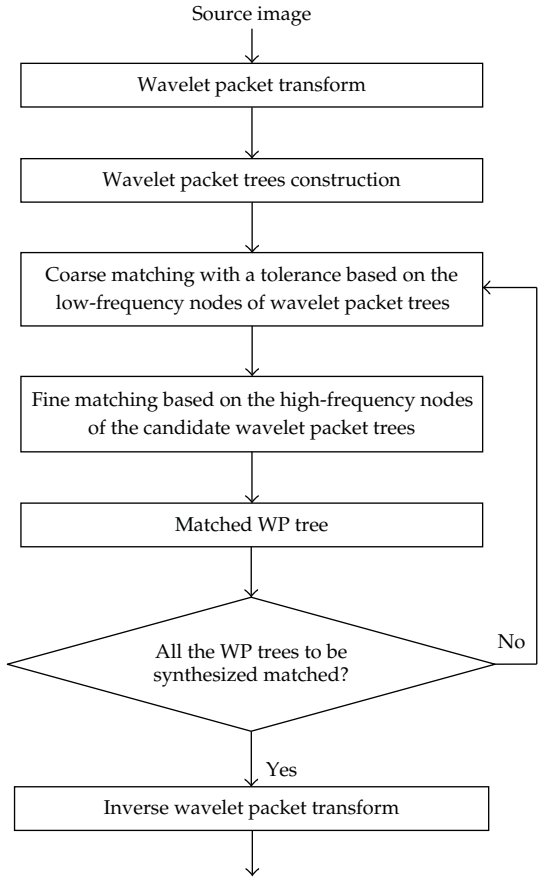

Figure 3: Flowchart of the TSWPT algorithm.

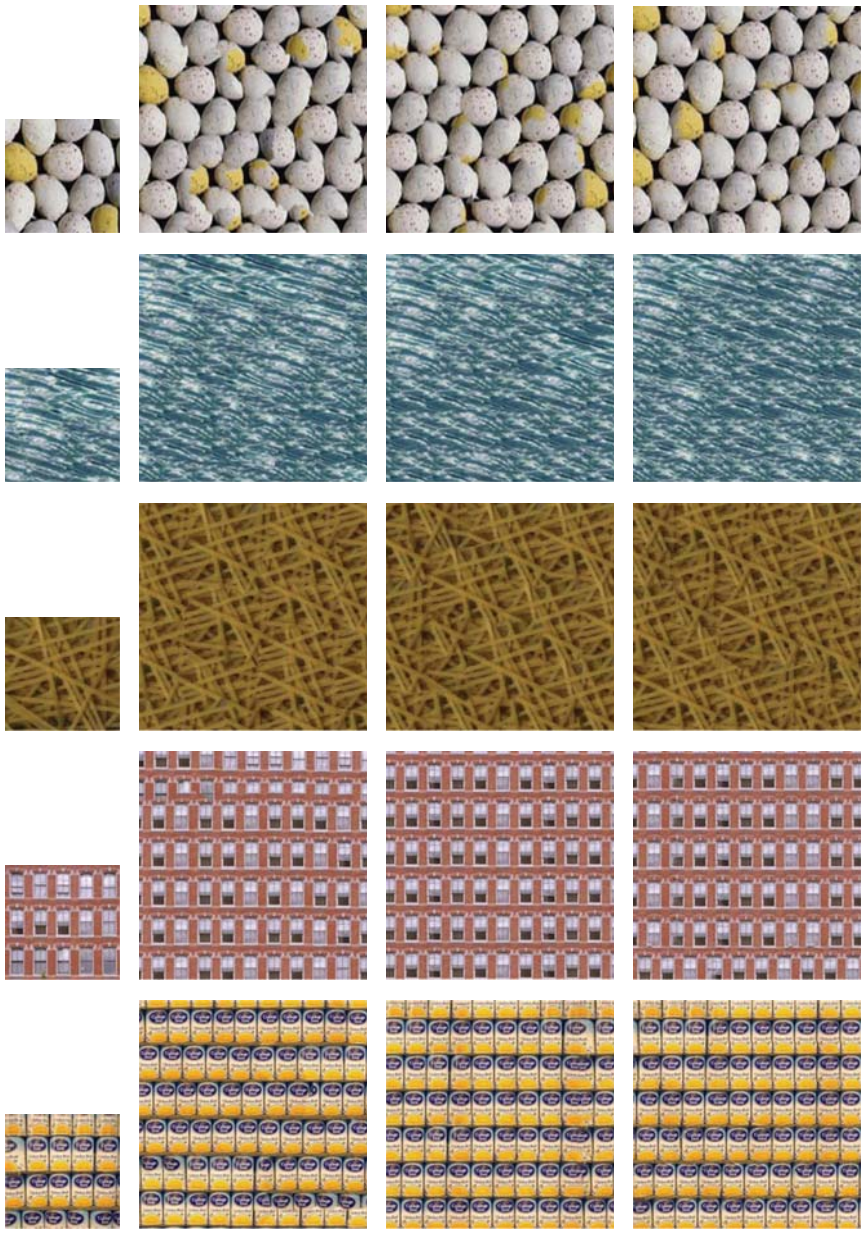

Figure 4: Visual comparison. Source images (1st column), synthesis images using Efros' algorithm [13] (2nd column), Cui's algorithm [31] (3rd column), and the TSWPT algorithm (4th column).

4. Experimental Results

In the first experiment, the size of source images is 128 × 128, which are shown in the 1st column of Figure 4; the size of synthesis images is 256 × 256. The TSWPT algorithm is applied to patches of WP trees in order to reduce computation time. The size of patches is 11 × 11, and the width of overlapped regions between neighboring patches is 3. The root nodes of WP trees, that is, WP coefficients in the lowest frequency subband, are used in the coarse matching

Figure 5: Synthesis images at double the size of the source image (top) using Efros' algorithm [13] (middle) and the TSWPT algorithm (bottom).

step to retain the global appearance of the input source image. Since the essential components of textures are mainly distributed in the middle-frequency subbands, the highest-frequency WP coefficients, that is, the leaf nodes of WP trees, can be ignored in the fine matching step. The biorthogonal 9/7 wavelet is used. The threshold value, T_r, is set to 0.1.

Two widely used algorithms, Efros' algorithm [13] and Cui's algorithm [31], were used for comparisons with the TSWPT algorithm. The synthesis results are shown in the 2nd, 3rd, and 4th columns of Figure 4, respectively. Visual inspection shows that TSWPT is comparable to Cui's algorithm and is preferable to Efros' algorithm. All the algorithms were implemented by Matlab without optimization in source codes. Table 1 shows the computation times running on PC with CPU of 1.7 GHz. It is noted that TSWPT is superior to both Efros' and Cui's algorithms.

In the second experiment, the sizes of source image and synthesis image are 192×128 and 384×256, respectively. All the settings are the same as the first experiment. The source image and synthesis results using Efros' algorithm and TSWPT are shown in Figure 5. It is shown that there are some blocking effects in the synthesis image using Efros' algorithm. However, blocking effects are likely to be eliminated by using the TSWPT algorithm due largely to the filtering operations of inverse wavelet packet transform in Step 5. Figure 6

Table 1: Comparison of computation times.

	Efros and freeman [13]	Cui et al. [31]	TSWPT
Image 1	3.784 s	0.703 s	0.416 s
Image 2	3.893 s	0.854 s	0.425 s
Image 3	3.939 s	0.810 s	0.404 s
Image 4	3.914 s	0.737 s	0.372 s
Image 5	3.891 s	0.731 s	0.392 s

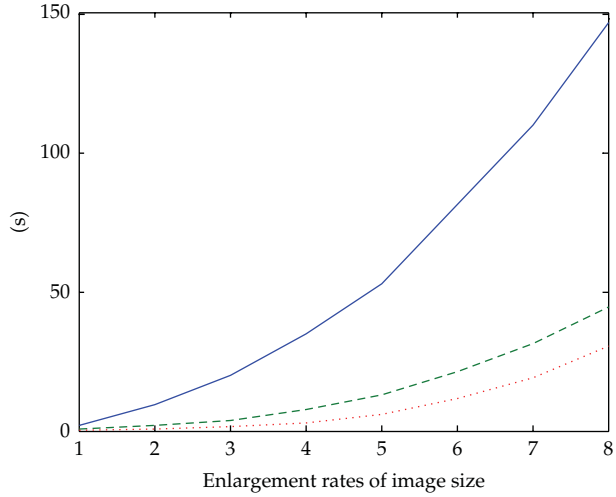

Figure 6: Synthesis times of the texture image (Figure 5) using Efros' algorithm [13] (solid line), Cui's algorithm [31] (dashed line), and the TSWPT algorithm (dotted line).

shows the computation times at various enlargement rates of image size. As one can see, the TSWPT algorithm outperforms both Efros' and Cui's algorithms.

5. Conclusion

The multi-resolution approach is suitable for texture synthesis in terms of computation time. Wavelet packet transform provides more bases functions than wavelet transform and therefore produces a more compact representation. We adopt wavelet packet transform to analyze the input texture and organize wavelet packet coefficients to form hierarchical trees called wavelet packet trees. The low-frequency nodes of wavelet packet trees contain the global characteristics of an image; the high-frequency nodes contain the local details. Thus, we propose texture synthesis based on wavelet packet tree (TSWPT). It has the advantage of saving computation time dramatically, and moreover, no training process is needed. Given a 128×128 texture, experimental results show that the computation time for synthesizing an 256×256 image is only a fraction of a second.

Acknowledgment

The National Science Council of Taiwan, under Grants NSC100-2628-E-239-002-MY2, supported this work.

References

[1] M. Li, "Fractal time series–a tutorial review," *Mathematical Problems in Engineering*, vol. 2010, Article ID 157264, 26 pages, 2010.

[2] C. Cattani, G. Pierro, and G. Altieri, "Entropy and multifractality for the myeloma multiple TET 2 gene," *Mathematical Problems in Engineering*, vol. 2012, Article ID 193761, 14 pages, 2012.

[3] M. Li and W. Zhao, "Visiting power laws in cyber-physical networking systems," *Mathematical Problems in Engineering*, vol. 2012, Article ID 302786, 13 pages, 2012.

[4] A. Hausner, "Simulating decorative mosaics," in *Computer Graphics Annual Conference (SIGGRAPH '01)*, pp. 573–580, August 2001.

[5] F. Neyret, "Modeling, animating, and rendering complex scenes using volumetric textures," *IEEE Transactions on Visualization and Computer Graphics*, vol. 4, no. 1, pp. 55–70, 1998.

[6] X. Tong, J. Zhang, L. Liu, X. Wang, B. Guo, and H. Y. Shum, "Synthesis of bidirectional texture functions on arbitrary surfaces," *ACM Transactions on Graphics*, vol. 21, no. 3, pp. 665–672, 2002.

[7] E. Risser, C. Han, R. Dahyot, and E. Grinspun, "Synthesizing structured image hybrids," *ACM Transactions on Graphics*, vol. 29, no. 4, article no. 85, 2010.

[8] N. Pietroni, P. Cignoni, M. Otaduy, and R. Scopigno, "Solid-texture synthesis: a survey," *IEEE Computer Graphics and Applications*, vol. 30, no. 4, pp. 74–89, 2010.

[9] Y. Xu, B. Guo, and H. Y. Shum, "Chaos mosaic: fast and memory efficient texture synthesis," MSR-TR-2000-32, Microsoft Research, 2000.

[10] J. Portilla and E. P. Simoncelli, "Parametric texture model based on joint statistics of complex wavelet coefficients," *International Journal of Computer Vision*, vol. 40, no. 1, pp. 49–71, 2000.

[11] A. A. Efros and T. K. Leung, "Texture synthesis by non-parametric sampling," in *7th IEEE International Conference on Computer Vision (ICCV '99)*, pp. 1033–1038, September 1999.

[12] L. Y. Wei and M. Levoy, "Order independent texture synthesis," Stanford Computer Science TR-2002-01, 2002.

[13] A. A. Efros and W. T. Freeman, "Image quilting for texture synthesis and transfer," in *Computer Graphics Annual Conference (SIGGRAPH '01)*, pp. 341–346, August 2001.

[14] L. Liang, C. Liu, Y. Xu, B. Guo, and H. Y. Shum, "Real-time texture synthesis using patch-based sampling," *ACM Transactions on Graphics*, vol. 20, no. 3, pp. 127–150, 2001.

[15] V. Kwatra, A. Schödl, I. Essa, G. Turk, and A. Bobick, "Graphcut textures: image and video synthesis using graph cuts," *ACM Transactions on Graphics*, vol. 22, no. 3, pp. 277–286, 2003.

[16] C.-W. Fang and J.-J. J. Lien, "Rapid image completion system using multiresolution patch-based directional and nondirectional approaches," *IEEE Transactions on Image Processing*, vol. 18, no. 12, pp. 2769–2779, 2009.

[17] J. S. De Bonet, "Multiresolution sampling procedure for analysis and synthesis of texture images," in *Conference on Computer Graphics (SIGGRAPH '97)*, pp. 361–368, August 1997.

[18] P. J. Burt and E. H. Adelson, "The laplacian pyramid as a compact image code," *IEEE Transactions on Communications*, vol. 31, no. 4, pp. 532–540, 1983.

[19] P. J. Burt, "Fast algorithms for estimating local image properties.," *Computer Vision, Graphics, & Image Processing*, vol. 21, no. 3, pp. 368–382, 1983.

[20] L. Y. Wei and M. Levoy, "Fast texture synthesis using tree-structured vector quantization," in *Computer Graphics Annual Conference (SIGGRAPH '00)*, pp. 479–488, July 2000.

[21] G. Strang and T. Nguyen, *Wavelets and Filter Banks*, Wellesley-Cambridge Press, Wellesley, Mass, USA, 1996.

[22] C. K. Su, H. C. Hsin, and S. F. Lin, "Wavelet tree classification and hybrid coding for image compression," *IEE Proceedings—Vision, Image, and Signal Processing*, vol. 152, no. 6, pp. 752–756, 2005.

[23] C. Cattani and J. Rushchitsky, *Wavelet and Wave Analysis as Applied to Materials with Micro or Nanostructure*, vol. 74 of *Series on Advances in Mathematics for Applied Sciences*, World Scientific, Hackensack, NJ, USA, 2007.

[24] Z. W. Liao, S. X. Hu, M. Li, and W. Chen, "Noise estimation for single-slice sinogram of low-dose X-ray computed tomography using homogenous patch," *Mathematical Problems in Engineering*, vol. 2012, Article ID 696212, 16 pages, 2012.

[25] M. Li, C. Cattani, and S. Y. Chen, "Viewing sea level by a one-dimensional random function with long memory," *Mathematical Problems in Engineering*, vol. 2011, Article ID 654284, 13 pages, 2011.

[26] J. W. Yanga, M. Li, Z. Chen, and Y. Chen, "Cutting affine invariant moments," *Mathematical Problems in Engineering*. In press.

[27] B. Chen and W.-S. Chen, "Noisy image segmentation based on wavelet transform and active contour model," *Applicable Analysis*, vol. 90, no. 8, pp. 1243–1255, 2011.

[28] B. Chen, P. C. Yuen, J. H. Lai, and W. S. Chen, "Image segmentation and selective smoothing based on variational framework," *Journal of Signal Processing Systems*, vol. 54, no. 1–3, pp. 145–158, 2009.

[29] B. Chen, Y. Li, and J. L. Cai, "Noisy image segmentation based on nonlinear diffusion equation model," *Applied Mathematical Modeling*, vol. 36, no. 3, pp. 1197–1208, 2012.

[30] Y. Yu, J. Luo, and C. W. Chen, "Multiresolution block sampling-based method for texture synthesis," in *16th International Conference on Pattern Recognition (ICPR '02)*, pp. 239–242, 2002.

[31] H. F. Cui, X. Zheng, and T. Ruan, "An efficient texture synthesis algorithm based on WT," in *7th International Conference on Machine Learning and Cybernetics (ICMLC '08)*, pp. 3472–3477, July 2008.

[32] T. Y. Sung and H. C. Hsin, "An efficient rearrangement of wavelet packet coefficients for embedded image coding based on SPIHT algorithm," *IEICE Transactions on Fundamentals of Electronics, Communications and Computer Sciences*, vol. E90-A, no. 9, pp. 2014–2020, 2007.

[33] N. M. Rajpoot, R. G. Wilson, F. G. Meyer, and R. R. Coifman, "Adaptive wavelet packet basis selection for zerotree image coding," *IEEE Transactions on Image Processing*, vol. 12, no. 12, pp. 1460–1472, 2003.

[34] H. C. Hsin and T. Y. Sung, "Adaptive selection and rearrangement of wavelet packets for quad-tree image coding," *IEICE Transactions on Fundamentals of Electronics, Communications and Computer Sciences*, vol. E91-A, no. 9, pp. 2655–2662, 2008.

Hindawi Publishing Corporation
Mathematical Problems in Engineering
Volume 2012, Article ID 690262, 11 pages
doi:10.1155/2012/690262

Research Article

Construction of Affine Invariant Functions in Spatial Domain

Jianwei Yang,[1] Yunjie Chen,[1] and Massimo Scalia[2]

[1] *School of Mathematics and Statistics, Nanjing University of Information Science and Technology, Nanjing 210044, China*
[2] *Department of Mathematics G. Castelnuovo, University of Rome la Sapienza, Piazzale, Aldo Moro 2, 00185 Rome, Italy*

Correspondence should be addressed to Jianwei Yang, yjianw2002@yahoo.com.cn

Received 17 January 2012; Accepted 9 March 2012

Academic Editor: Bin Fang

Affine invariant functions are constructed in spatial domain. Unlike the previous affine representation functions in transform domain, these functions are constructed directly on the object contour without any transformation. To eliminate the effect of the choice of points on the contour, an affine invariant function using seven points on the contour is constructed. For objects with several separable components, a closed curve is derived to construct the affine invariant functions. Several experiments have been conducted to evaluate the performance of the proposed method. Experimental results show that the constructed affine invariant functions can be used for object classification.

1. Introduction

Recognizing objects that are subjected to certain viewing transformation is important in the field of computer vision [1]. Affine transformation may be used as an approximation to viewpoint-related changes of objects [2–4]. Typical geometric transformation such as rotation, translation, scaling, and skewing are included in the affine transformation.

The extraction of affine invariant features plays a very important role in object recognition and has been found application in many fields such as shape recognition and retrieval [5, 6], watermarking [7], identification of aircrafts [1, 8], texture classification [9], image registration [10], and contour matching [11].

Many algorithms have been developed for affine invariant features extraction. Based on whether the features are extracted from the contour only or from the whole-shape region, the approaches can be classified into two main categories: region-based methods and contour-based methods [12]. For good overviews of the various techniques refer to [12–15].

Contour-based methods provide better data reduction, and the contour usually offers more shape information than interior content [12]. A number of contour-based methods have been introduced in recent years. *Affine invariant function* (AIF) in these papers is usually constructed in transform domain (see [1, 8, 16–20], etc.).

Due to the spatial and frequency localization property of wavelets, many wavelet-based algorithms have been developed for the extraction of affine invariant features. It is reported that these wavelet-based methods outperform Fourier descriptors [1, 8, 19]. In these methods, the object boundary is firstly analyzed by wavelet transform at different scales. The obtained approximation and detail signals are then used for the construction of AIF. The choice of the signals, the number of decomposition levels, and the wavelet functions used have all resulted in a number of different approaches. Many promising results have been reported; Alferez and Wang [21] proposed geometric and illumination invariants for object recognition depending on the details coefficients of dyadic wavelet decomposition. Tieng and Boles [19] have developed an approximation-detail AIF using one dyadic level only. Another AIF, the detail-detail representation function, was derived by Khalil and Bayoumi using a dyadic wavelet transform [1, 8]. The invariant function is computed by utilizing two, three, or four dyadic scale levels. Recently, AIF from the approximation coefficients has been developed by applying two different wavelet transforms with different wavelet basis [18]. The synthesized AIF is proposed by Lin and Fang [17] with the synthesized feature signals of the shape.

However, in all these methods, AIFs are constructed in transform domain. That is to say, the shape contour is firstly transformed by a linear operator (e.g., wavelet transform, Fourier transform, etc.). Then AIFs are constructed from the transformed contour. In this paper, we construct AIF directly by the shape contour without any transformation. Equidistant Points on the object contour are used to construct AIFs. To eliminate the effect of the choice of points on the contour, an AIF using seven points on the contour is constructed. In addition, the shape contour is not available [12] in many cases. For example, the image of Chinese character "Yang" as shown in Figure 3 consists of several components. AIFs can not be constructed from these objects. To address this problem, we derive a closed curve, which is called *general contour* (GC), from the object. GC is obtained by performing projections along lines with different polar angles. The GC derived from the affine transformed object is the same affine transformed version as that of the original object. AIFs can be constructed in spatial domain from the derived GC. Several experiments have been conducted to evaluate the performance of the proposed method. Experimental results show that the constructed affine invariant functions can be used for object classification.

The rest of the paper is organized as follows: in Section 2, some basic concepts about affine transform are introduced. AIFs are constructed in Section 3. The performance of the proposed method is evaluated experimentally in Section 4. Finally, some conclusion remarks are provided in Section 5.

2. Preliminaries

2.1. Affine Transformation

Consider a parametric point $\mathbf{x}(t) = [x(t), y(t)]^T$ with parameter t on the object contour. The affine transformation consists of a linear transformation and translation as follows:

$$\begin{aligned} \tilde{x}(t) &= a_{11}x(t) + a_{12}y(t) + b_1, \\ \tilde{y}(t) &= a_{21}x(t) + a_{22}y(t) + b_2. \end{aligned} \tag{2.1}$$

The above equations can be written with the following form:

$$\tilde{\mathbf{x}}(t) = \begin{bmatrix} a_{11} & a_{12} \\ a_{21} & a_{22} \end{bmatrix} \begin{bmatrix} x(t) \\ y(t) \end{bmatrix} + \begin{bmatrix} b_1 \\ b_2 \end{bmatrix} = \mathbf{A}\mathbf{x}(t) + \mathbf{b}, \tag{2.2}$$

where the nonsingular matrix $\mathbf{A}$ represents the scaling, rotation, skewing transformations, and the vector $\mathbf{b}$ corresponds to the translation.

If I is an affine invariant function and $\tilde{I}$ is the same invariant function calculated using the points under the affine transformations, then the relation between them can be formulated as

$$\tilde{I} = IJ^{w}, \tag{2.3}$$

where $J = \det(\mathbf{A})$ is the determination of the matrix $\mathbf{A}$. The exponent w of the power is called the weight of the invariance. If $w = 0$, the function I is called as absolute invariant. If $w \neq 0$, the function I is called a relative invariant.

2.2. *Affine Invariant Parameters*

To establish one-to-one relation between two contour, the object contour should be parameterized. The arc length parameter transforms linearly under any liner transformation up to the similarity transform including translation, rotation, and scaling. But, it is not a suitable parameter for the constructing affine invariant function.

There are two parameters which are liner under an affine transformation: the affine arc length [22] and the enclosed area [16]. The affine arc length τ is defined as follows:

$$\tau = \int \sqrt[3]{\dot{x}(t)\ddot{y}(t) - \ddot{x}(t)\dot{y}(t)}dt, \tag{2.4}$$

where $\dot{x}(t)$, $\dot{y}(t)$, and $\ddot{x}(t)$, $\ddot{y}(t)$ are the first and the second derivatives of $x(t)$, $y(t)$ with respect to the arc length parameter t. Arbter et al. [16] defined the enclosed area parameter σ as follows:

$$\sigma = \frac{1}{2}\int \left|x(t)\dot{y}(t) - y(t)\dot{x}(t)\right|dt. \tag{2.5}$$

These two parameters can be made completely invariant by simply normalizing them with respect to either the total affine arc length or the enclosed area of the contour. In the discrete case, the derivatives of x and y can be calculated using finite difference equations. To establish one-to-one relation between two parameter, the contour should be normalized and resampled as in [19]. In the experiments of this paper, we use the enclosed area as the parameter. In the discrete case, the parameterization should be normalized and resampled. The curve normalization approach used in this paper mainly composes of the following steps [23].

(i) For the discrete object contour $\{(x(t_k), y(t_k)) : k = 0, 1, 2, \ldots, N-1\}$, compute the total area of the object contour by the following formula

$$\mathrm{EAN} = \frac{1}{2}\sum_{k=0}^{N-1}\left|(x(t_k) - x_0)(y(t_{k+1}) - y_0) - (x(t_{k+1}) - x_0)(y(t_k) - y_0)\right|, \tag{2.6}$$

where $O(x_0, y_0)$ denotes the centroid of the object. Let the number of points on the contour after the parameterization be N too. Denote that $S_{\text{part}} = \text{EAN}/N$.

(ii) Select the starting point on object contour as the starting point $P_0(x'(\sigma_0), y'_0(\sigma_0))$ of the normalized curve. From $P_0(x'(\sigma_0), y'(\sigma_0))$ on object contour, search a point $P_1(x'(\sigma_1), y'(\sigma_1))$ along the contour, such that the area of each closed zone; namely, the polygon P_0OP_1 equals to S_{part}.

(iii) Using the same method, from point $P_1(x'(\sigma_1), y'(\sigma_1))$, calculate all the points $P_i(x'(\sigma_i), y'(\sigma_i))$, $i \in \{1, 2, \ldots, N-1\}$ along the object contour. $P_i(x'(\sigma_i), y'(\sigma_i))$, $i \in \{1, 2, \ldots, N-1\}$ along object contour.

In the experiments of this paper, the object contour or GC is normalized and resampled such that $N = 256$.

3. Affine Invariant Object Representation

In this part, we will derive invariant function from the normalized object contours. Correlation coefficient is used to measure the similarity of two AIFs. To construct AIFs from objects with several separable components, we convert the object into a closed curve by performing projections along lines with different polar angles.

3.1. AIFs Construct in Spatial Domain

Let $[x(\sigma), y(\sigma)]$, and $[\tilde{x}(\tilde{\sigma}), \tilde{y}(\tilde{\sigma})]$ be the parametric equations of two contours that differ only by an affine transformation. For simplicity, in this subsection, we assume that the starting points on both contours are identical. After normalizing and resampling, there is a one-to-one relation between σ and $\tilde{\sigma}$. We use the object centroid as the origin, then translation factor $\mathbf{b}$ is eliminated. Equation (2.2) can be written in matrix form as $\tilde{\mathbf{x}}(t) = \mathbf{A}\mathbf{x}(t)$.

Let γ be an arbitrary positive constant, then $[x(\sigma+\gamma), y(\sigma+\gamma)]$ is a shift version of $[x(\sigma), y(\sigma)]$. We define the following function:

$$\begin{aligned} S(\gamma, \sigma) &= x(\sigma)y(\sigma+\gamma) - y(\sigma)x(\sigma+\gamma) \\ &= \begin{vmatrix} x(\sigma) & x(\sigma+\gamma) \\ y(\sigma) & y(\sigma+\gamma) \end{vmatrix}, \end{aligned} \tag{3.1}$$

where $|\cdot|$ denotes determination of a matrix. As a result of normalizing and resampling, $[x(\sigma), y(\sigma)]$, $[\tilde{x}(\tilde{\sigma}), \tilde{y}(\tilde{\sigma})]$, and $[x(\sigma+\gamma), y(\sigma+\gamma)]$, $[\tilde{x}(\tilde{\sigma}+\gamma), \tilde{y}(\tilde{\sigma}+\gamma)]$ satisfy the following equation:

$$\begin{pmatrix} \tilde{x}(\tilde{\sigma}) \\ \tilde{y}(\tilde{\sigma}) \end{pmatrix} = \mathbf{A}\begin{pmatrix} x(\sigma) \\ y(\sigma) \end{pmatrix}, \qquad \begin{pmatrix} \tilde{x}(\tilde{\sigma}+\gamma) \\ \tilde{y}(\tilde{\sigma}+\gamma) \end{pmatrix} = \mathbf{A}\begin{pmatrix} x(\sigma+\gamma) \\ y(\sigma+\gamma) \end{pmatrix}. \tag{3.2}$$

It follows that

$$\tilde{S}(\gamma, \tilde{\sigma}) = \begin{vmatrix} \tilde{x}(\tilde{\sigma}) & \tilde{x}(\tilde{\sigma}+\gamma) \\ \tilde{y}(\tilde{\sigma}) & \tilde{y}(\tilde{\sigma}+\gamma) \end{vmatrix} = JS(\gamma, \sigma). \tag{3.3}$$

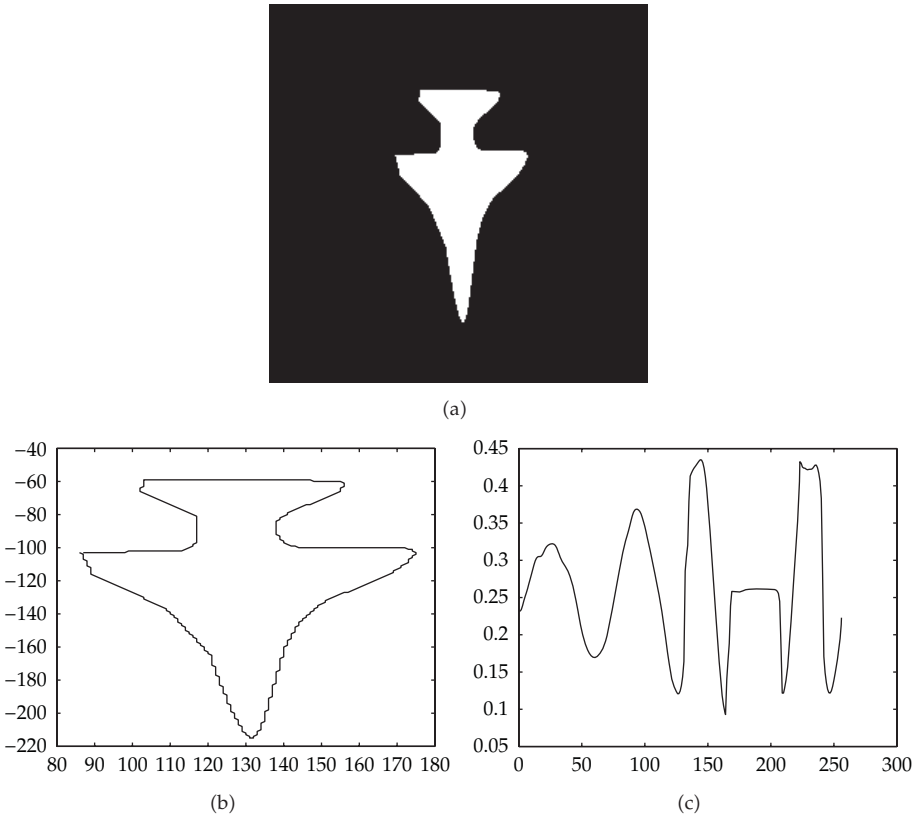

Figure 1: (a) A plane object. (b) The boundary of plane in (a). (c) The invariant function for the boundary in (b).

In other words, S given in (3.1) is a relative invariance function. To eliminate the factor $J = \det(\mathbf{A})$ in (3.3), $S(\gamma, \sigma)$ needs to be normalized. We normalize S as follows:

$$I_\gamma = \frac{S(\gamma, \sigma)}{\mathrm{EAN}}, \tag{3.4}$$

where EAN denotes enclosed area of the object contour as defined in (2.6). It follows from (3.3) that I_γ given in (3.4) is an AIF. In [1, 8, 16–20], the shape contour is firstly transformed by a linear operator (such as wavelet transform, Fourier transform, etc.). Then AIFs are constructed from the transformed contour. In our method, the AIF given in (3.4) is directly constructed from the shape contour without any transformation.

Figure 1(a) shows a plane object, and Figure 1(b) shows its boundary. Figure 1(c) shows the AIF defined in (3.3) associated with Figure 1(b). Figure 2(a) shows an affine transformation version of plane in Figure 1(a), and Figure 2(b) shows its boundary. Figure 2(c) shows the AIF derived from Figure 2(b). In Figures 1(c) and 2(c), γ is set to 32. Note that after affine transformation, the starting points of AIFs are different. We observe that Figure 2(c) is nearly a translated version of Figure 1(c).

Experimental results show that the choice of γ may affect the accuracy of the object classification based on I_γ. Some choice of γ may result in lower accuracy while other choice

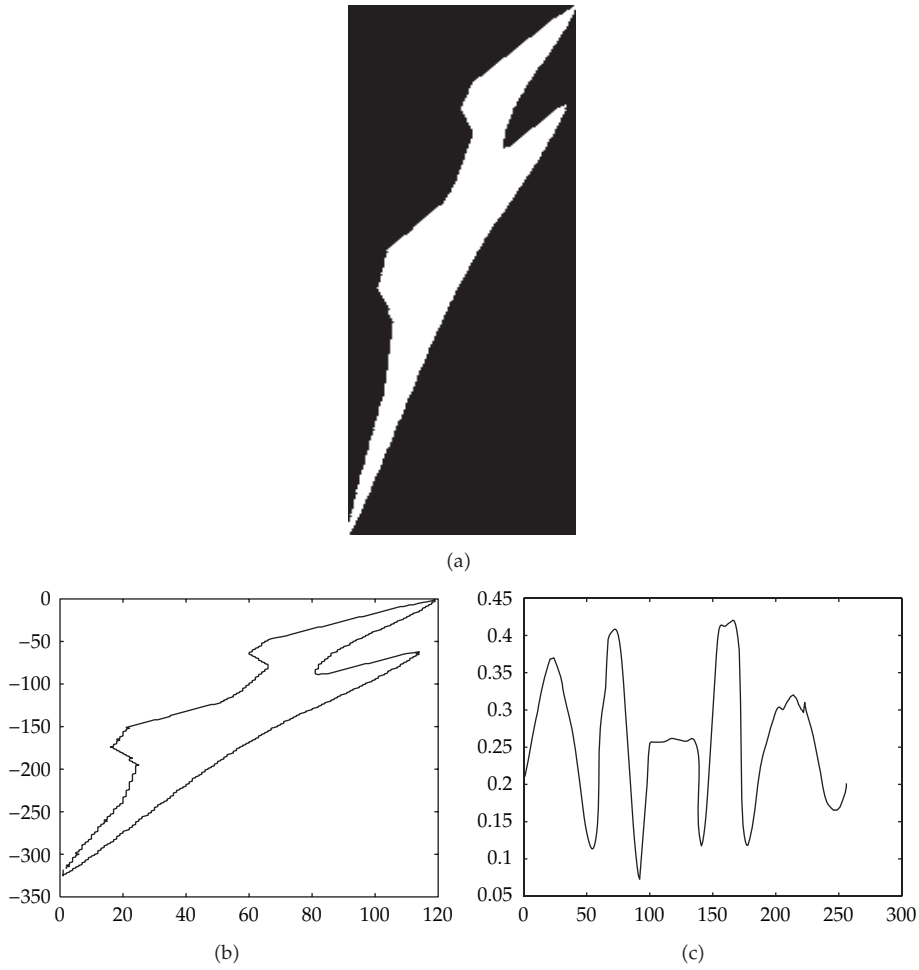

Figure 2: (a) An affine transformation version of Figure 1(a). (b) The boundary of plane in (a). (c) The AIF for the boundary in (b).

of γ may result in higher accuracy. To eliminate the effect of the choice of γ, we construct AIFs that involve more points on the object contour. In experiments of this paper, we use seven equidistant partition points of the object contour: $\gamma_1 = N/8$, $\gamma_2 = 2N/8, \ldots, \gamma_7 = 7N/8$ to construct AIF as follows:

$$\begin{aligned} H_{\gamma_1,\gamma_2,\ldots,\gamma_7} = {} & I_{\gamma_1} I_{\gamma_2} I_{\gamma_3} I_{\gamma_4} I_{\gamma_5} I_{\gamma_6} + I_{\gamma_1} I_{\gamma_2} I_{\gamma_3} I_{\gamma_4} I_{\gamma_5} I_{\gamma_7} \\ & + I_{\gamma_1} I_{\gamma_2} I_{\gamma_3} I_{\gamma_4} I_{\gamma_7} I_{\gamma_6} + I_{\gamma_1} I_{\gamma_2} I_{\gamma_3} I_{\gamma_7} I_{\gamma_5} I_{\gamma_6} \\ & + I_{\gamma_1} I_{\gamma_2} I_{\gamma_7} I_{\gamma_4} I_{\gamma_5} I_{\gamma_6} + I_{\gamma_1} I_{\gamma_7} I_{\gamma_3} I_{\gamma_4} I_{\gamma_5} I_{\gamma_6} \\ & + I_{\gamma_7} I_{\gamma_2} I_{\gamma_3} I_{\gamma_4} I_{\gamma_5} I_{\gamma_6}. \end{aligned} \tag{3.5}$$

Indeed, it can be shown that, for arbitrary constants: $\gamma_1, \gamma_2, \ldots, \gamma_n$, homogeneous polynomials in terms of $I_{\gamma_1}, I_{\gamma_2}, \ldots, I_{\gamma_n}$ are also AIFs.

3.2. Measurement of the Similarity between Two AIFs

We have seen from Figures 1(c) and 2(c) that affine transformation may result in a translated version of AIF. To eliminate the effect of starting point, one-dimensional Fourier transform can be applied to the obtained AIF. The invariance can be achieved by ignoring the phase in the coefficients and only keeping the magnitudes of the coefficients. This way has a lower computational complexity since that FFT is faster than shift matching [24].

In this paper, we construct AIFs in spatial domain. Therefore, to eliminate the effect of starting point, we use correlation coefficient as in [18] to measure the similarity between two AIFs. For two sequences I_k and I'_k, the normalized cross-correlation is defined as follows:

$$R_{I,I'}(l) = \frac{\sum_l \sum_k I_k I'_{k-l}}{\sqrt{\sum I_k^2 \sum I'^2_k}}. \tag{3.6}$$

One of sequences, I_k or I'_k is rendered periodically, then the maximum value of correlation is selected. Such an arrangement reduces the effect of the boundary starting point variation [18]. Consequently, translation invariant is achieved. Based on [25–27], some other approaches can be derived to eliminate the effect of starting point.

3.3. AIFs for Objects with Several Separable Components

AIFs given in (3.4) and (3.5) can be used to object contour. But, in real-life, many objects consist of several separable components (such as Chinese character "Yang" in Figure 3(a)). Object contours are not available for these objects. Consequently, AIFs given in Section 3.1 cannot be used to these objects. To address this problem, we convert the object into a closed curve by performing projection along lines with different polar angles (which is called central projection transformation in [28]). The obtained closed curve is called *general contour* (GC) in [29]. It can be proved that the GC extracted from the affine transformed object is also an affine transformed version of GC extracted from the original object. Consequently, AIFs given in Section 3.1 can be constructed based on the GC of the object. For example, Figure 3(b) shows the GC of Figure 3(a). Figure 3(c) shows the AIF derived from GC of Figure 3(a).

4. Experiment

In this section, we evaluate the discriminate ability of the proposed method. In the first experiment, we examine the proposed method by using some airplane images. Object contours can be derived from these images. In the second experiment, we evaluate the discriminate ability of the proposed method by using some Chinese characters. These characters have several separable components, and contours are not available for these objects.

In the following experiments, the classification accuracy is defined as

$$\eta = \frac{\delta}{\lambda} \times 100\%, \tag{4.1}$$

where δ denotes the number of correctly classified images, and λ denotes the total number of images applied in the test. Affine transformations are generated by the following matrix [1]:

$$A = k \begin{pmatrix} \cos\theta & -\sin\theta \\ \sin\theta & \cos\theta \end{pmatrix} \begin{pmatrix} a & b \\ 0 & \dfrac{1}{a} \end{pmatrix}, \tag{4.2}$$

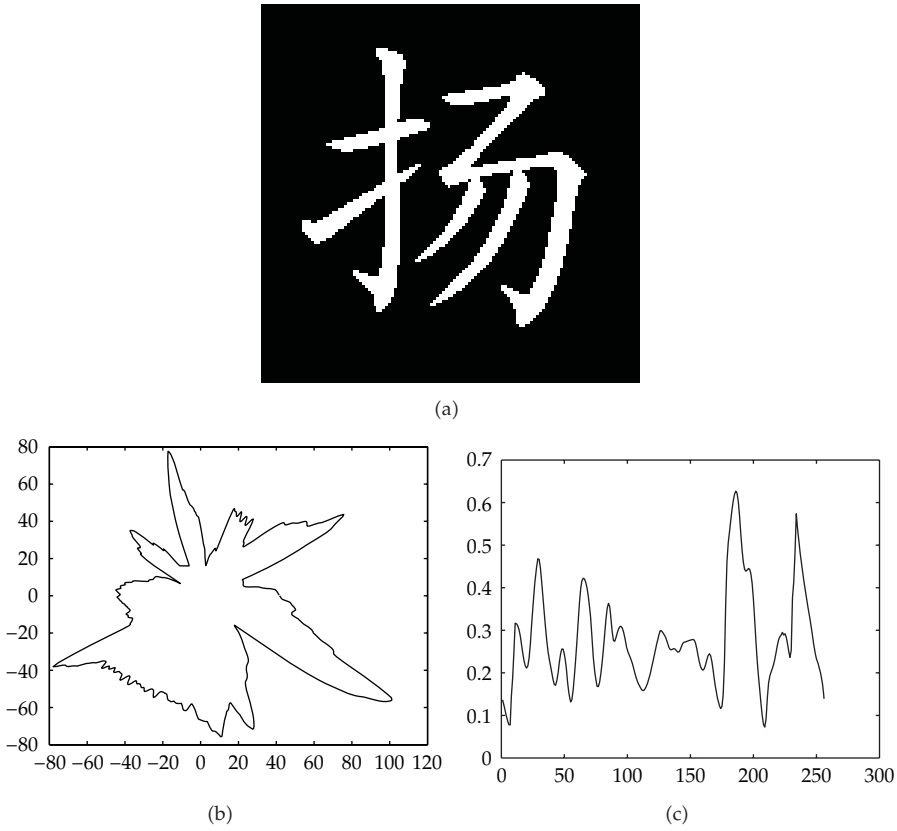

Figure 3: (a) The Chinese character "Yang". (b) GC of Chinese in (a). (c) The AIF for GC in (b).

where k, θ denote the scaling, rotation transformation, respectively, and a, b denote the skewing transformation. To each object, the affine transformations are generated by setting the parameters in (4.2) as follows: $k \in \{0.8, 1.2\}$, $\theta \in \{30, 90°, 150°, 210°, 270°, 330°\}$, $b \in \{-3/2, -1, -1/2, 0, 1/2, 1, 3/2\}$ and, $a \in \{1, 2\}$. Therefore, each image is transformed 168 times.

4.1. Air Plane Image Classification

The first experiment is conducted to classify the airplane images. Seven airplane images shown in Figure 4 are used as models in this experiment. Some of these models represent different objects but with similar contours, such as model 6 and model 7. They can be easily misclassified due to their similarity. We test the effect of the choice of the constant γ. The contour is normalized and resampled such that $N = 256$. We set $\gamma_1 = 32, \gamma_2 = 64, \ldots, \gamma_7 = 224$. To each airplane image, the affine transformations are generated by setting the parameters in (4.2) as aforementioned. Therefore, each image is transformed 168 times. That is to say, the test is repeated 1176 times. Table 1 shows the classification accuracy of different constants and that AIF is given in (3.5). It can be observed that different accuracies may be achieved with different γ. For example, the accuracy rates are very low for $\gamma_4 = 128$ and $\gamma_7 = 224$. To eliminate the effect of the choice γ, AIFs involved more points that can be used for object classification. In the rest of this paper, we use AIF given in (3.5) to extract affine invariant features.

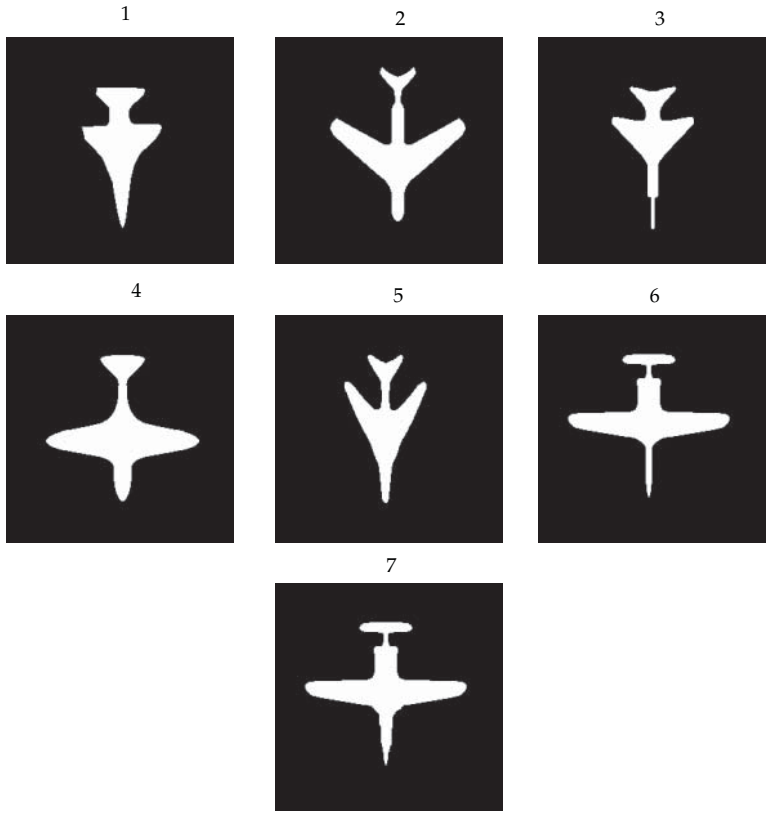

Figure 4: The airplane models.

Table 1: Classification accuracies for different γ under different affine transformations.

γ	32	64	96	128
Accuracy rates	90.05%	96.51%	93.03%	87.59%
γ	160	192	224	AIF in (3.5)
Accuracy rates	93.03%	96.51%	88.61%	92.52%

4.2. The Classification of Objects with Several Separable Components

In this experiments, we extract affine invariant features from objects with several separable components. 10 Chinese characters shown in Figure 4 are used as the database. These characters are with regular script font. The size of these characters is 128 × 128. Each of these characters consists of several separable components. Some characters have the same structures, but the number of strokes or the shape of specific stokes may be a little different. As aforementioned, each character image is transformed 168 times. That is to say, the test is repeated 1680 times. Experiments on Chinese characters in Figure 5 and their affine transformations show that 96.25% accurate classification can be achieved by using AIF given in (3.5).

Figure 5: Test characters used in the second experiment.

5. Conclusions

In this paper, we construct AIFs in spatial domain. Unlike the previous affine representation functions in transform domain, these AIFs are constructed directly on the object contour without any transformation. This technique is based upon object contours, parameterized by an affine invariant parameter, and shifting of the contour. To eliminate the effect of the choice of points on the contour, an AIF using seven points on the contour is constructed. For objects with several separable components, a closed curve is derived to construct the AIFs. Several experiments have been conducted to evaluate the performance of the proposed method.

Acknowledgments

This work was supported in part by the National Science Foundation under Grant 60973157, 61003209, in part by the Natural Science Foundation of Jiangsu Province Education Department under Grant 08KJB520004.

References

[1] M. I. Khalil and M. M. Bayoumi, "A dyadic wavelet affine invariant function for 2D shape recognition," *IEEE Transactions on Pattern Analysis and Machine Intelligence*, vol. 23, no. 10, pp. 1152–1164, 2001.

[2] M. K. Hu, "Visual pattern recognition by moment invariants," *IRE Transactions on Information Theory*, vol. 8, no. 2, pp. 179–187, 1962.

[3] J. Flusser and T. Suk, "Pattern recognition by affine moment invariants," *Pattern Recognition*, vol. 26, no. 1, pp. 167–174, 1993.

[4] T. Suk and J. Flusser, "Affine moment invariants generated by graph method," *Pattern Recognition*, vol. 44, no. 9, pp. 2047–2056, 2011.

[5] M. R. Daliri and V. Torre, "Robust symbolic representation for shape recognition and retrieval," *Pattern Recognition*, vol. 41, no. 5, pp. 1799–1815, 2008.

[6] P. L. E. Ekombo, N. Ennahnahi, M. Oumsis, and M. Meknassi, "Application of affine invariant fourier descriptor to shape based image retrieval," *International Journal of Computer Science and Network Security*, vol. 9, no. 7, pp. 240–247, 2009.

[7] X. B. Gao, C. Deng, X. Li, and D. Tao, "Geometric distortion insensitive image watermarking in affine covariant regions," *IEEE Transactions on Systems, Man and Cybernetics C*, vol. 40, no. 3, Article ID 5378648, pp. 278–286, 2010.

[8] M. I. Khalil and M. M. Bayoumi, "Affine invariants for object recognition using the wavelet transform," *Pattern Recognition Letters*, vol. 23, no. 1–3, pp. 57–72, 2002.

[9] G. Liu, Z. Lin, and Y. Yu, "Radon representation-based feature descriptor for texture classification," *IEEE Transactions on Image Processing*, vol. 18, no. 5, pp. 921–928, 2009.

[10] R. Matungka, Y. F. Zheng, and R. L. Ewing, "Image registration using adaptive polar transform," *IEEE Transactions on Image Processing*, vol. 18, no. 10, pp. 2340–2354, 2009.

[11] Y. Wang and E. K. Teoh, "2D affine-invariant contour matching using B-Spline model," *IEEE Transactions on Pattern Analysis and Machine Intelligence*, vol. 29, no. 10, pp. 1853–1858, 2007.

[12] D. Zhang and G. Lu, "Review of shape representation and description techniques," *Pattern Recognition*, vol. 37, no. 1, pp. 1–19, 2004.

[13] E. Rahtu, *A multiscale framework for affine invariant pattern recognition and registration*, Ph.D. thesis, University of OULU, Oulu, Finland, 2007.

[14] R. Veltkamp and M. Hagedoorn, "State-of the art in shape matching," Tech. Rep. UU-CS-1999, 1999.

[15] I. Weiss, "Geometric invariants and object recognition," *International Journal of Computer Vision*, vol. 10, no. 3, pp. 207–231, 1993.

[16] K. Arbter, W. E. Snyder, H. Burkhardt, and G. Hirzinger, "Application of affine-invariant Fourier descriptors to recognition of 3-D objects," *IEEE Transactions on Pattern Analysis and Machine Intelligence*, vol. 12, no. 7, pp. 640–647, 1990.

[17] W. S. Lin and C. H. Fang, "Synthesized affine invariant function for 2D shape recognition," *Pattern Recognition*, vol. 40, no. 7, pp. 1921–1928, 2007.

[18] I. El Rube, M. Ahmed, and M. Kamel, "Wavelet approximation-based affine invariant shape representation functions," *IEEE Transactions on Pattern Analysis and Machine Intelligence*, vol. 28, no. 2, pp. 323–327, 2006.

[19] Q. M. Tieng and W. W. Boles, "Wavelet-based affine invariant representation: a tool for recognizing planar objects in 3D space," *IEEE Transactions on Pattern Analysis and Machine Intelligence*, vol. 19, no. 8, pp. 846–857, 1997.

[20] G. Tzimiropoulos, N. Mitianoudis, and T. Stathaki, "Robust recognition of planar shapes under affine transforms using principal component analysis," *IEEE Signal Processing Letters*, vol. 14, no. 10, pp. 723–726, 2007.

[21] R. Alferez and Y. F. Wang, "Geometric and illumination invariants for object recognition," *IEEE Transactions on Pattern Analysis and Machine Intelligence*, vol. 21, no. 6, pp. 505–536, 1999.

[22] D. Cyganski and R. F. Vaz, "A linear signal decomposition approach to affine invariant contour identification," *SPIE: Intelligent Robots and Computer Vision X*, vol. 1607, pp. 98–109, 1991.

[23] M. Yang, K. Kpalma, and J. Ronsin, "Affine invariance contour desciptor based on the equal area normalization," *IAENG International Journal of Applied Mathematics*, vol. 36, no. 2, 2007.

[24] Y. W. Chen and C. L. Xu, "Rolling penetrate descriptor for shape-based image retrieval and object recognition," *Pattern Recognition Letters*, vol. 30, no. 9, pp. 799–804, 2009.

[25] M. Li, C. Cattani, and S. Y. Chen, "Viewing sea level by a one-dimensional random function with long memory," *Mathematical Problems in Engineering*, vol. 2011, Article ID 654284, 13 pages, 2011.

[26] M. Li and W. Zhao, "Visiting power laws in cyber-physical networking systems," *Mathematical Problems in Engineering*, vol. 2012, Article ID 302786, 13 pages, 2012.

[27] W. S. Chen, P. C. Yuen, and X. Xie, "Kernel machine-based rank-lifting regularized discriminant analysis method for face recognition," *Neurocomputing*, vol. 74, no. 17, pp. 2953–2960, 2011.

[28] Y. Y. Tang, Y. Tao, and E. C. M. Lam, "New method for feature extraction based on fractal behavior," *Pattern Recognition*, vol. 35, no. 5, pp. 1071–1081, 2002.

[29] J. Yang, Z. Chen, W. S. Chen, and Y. Chen, "Robust affine invariant descriptors," *Mathematical Problems in Engineering*, vol. 2011, Article ID 185303, 15 pages, 2011.

Hindawi Publishing Corporation
Mathematical Problems in Engineering
Volume 2012, Article ID 802152, 15 pages
doi:10.1155/2012/802152

Research Article

Location Updating Schemes for High-Speed Railway Cellular Communication Systems

Hao Wu, Tao Wang, and Zhangdui Zhong

State Key Laboratory of Rail Tra c Control and Safety, Beijing Jiaotong University, Beijing 100044, China

Correspondence should be addressed to Hao Wu, hwu@bjtu.edu.cn

Received 11 January 2012; Accepted 20 February 2012

Academic Editor: Ming Li

High-speed railway private cellular network provides voice and data services for passengers. It brings much signaling cost as a great many of mobile subscribers ask for location updating simultaneously. Moreover, it leads to plenty of control signaling channel requests. This paper presents two novel location updating schemes, that is, "clustering location management" and "mobile group location management" to solve the problems caused by the existing location updating scheme in high speed railway cellular private network. These two schemes can realize location updating without occupying more frequency resources. In addition, it does not impact the mobile subscribers' paging. Then it analyses the performance of two improved schemes, such as channel request number of stand-alone dedicated control channel (SDCCH), average waiting time of location updating, cost of location updating, and paging. The result indicates that both schemes can utilize the SDCCH channel resource effectively.

1. Introduction

With the constructing and opening of the high-speed railway lines, mobile users' demand of the voice, data, and other services in the high-speed train is gradually improved. Since the environment of the radio propagation is very complex, and it executes handover frequently during the calling procedure, mobile users have some problems, such as low communication quality, and high call drop rate. Although it can be solved through the construction of private networks for the high-speed railways [1, 2], some new problems are involved correspondingly. For example, there are a large number of mobile users in the same train. All mobile users will send the location update messages to the network at the same time. As a result, the signaling overhead will be increased, and it will even cause the congestion of signaling channel [3, 4]. The field test data also confirmed this. It can be found that most congested base stations locate at the border between the two location areas, and the congestion time is

concentrated within a brief period. Thus, in order to ensure the success of location update, more frequencies should be allocated even if the requirement of voice service in the private network is less. Obviously it is a waste of the network resources. In this paper, to reduce the cost of the location updating and improve the performance of communication system, we propose "clustering location management" scheme and "mobile group location management" scheme used in mobile communication system for passenger dedicated lines, and it may ensure the mobile users to execute location update successfully and not to affect the normal paging process.

There are three types of approaches for location update procedure: time-based, movement-based, and distance-based update schemes [5]. Each type has its advantages suitable for special applications. In order to improve the performance of location management, the improved methods based on those schemes are proposed in the literatures [6–13], such as hybrid location update scheme [6], dynamic location management scheme based on movement-state [7], interoperation of identity management [8], and two-level pointer forwarding strategy for location management in PCS networks [9]. According to the move trend of train, some mobile location management schemes have also been proposed. For instance, a method was proposed in [10], which divided the users into different groups based on their move speed and used the corresponding location management scheme to improve paging efficiency. In [11], a hybrid method based on self-organization mobile network and GSM network has been presented, but the complexity of implementation is increased. According to the characteristics of railway communication, a group location management method based on the group ID (GID) and virtual visit location register (VVLR) is proposed in [12]. To meet the requirement of mobility of base-station in military communication, an enhanced mechanism for relay-based group mobility by extending the IEEE 802.16 m specification on relay is proposed in [13]. However, the methods described in [12, 13] both need to add some mobile base-station equipments, and the internal communication in a group still occupied the network resource, it brings a great challenge to the mobile communication network. Several location management strategies to reduce the cost of location management in mobile networks are presented in [14–16].

For the above reasons, we propose two location update schemes not taking additional frequency resource, and the improved schemes may ensure all the users on the high-speed train to finish location update. For the specific application, we mainly consider two schemes. The first scheme is called "clustering location management" scheme, in which mobile users will be divided into multiple groups to execute location update separately. The second scheme considers the mobile users in a carriage as an integral unit (group), and a particular device (group head) executes location update as the representative of the whole group, which is called "mobile group location management" scheme. This paper is organized as follows: in Section 2, the principles of two improved location schemes are described. In Section 3, the further analysis and performance comparison of the existing scheme and improved schemes are given. Finally the conclusion is obtained in Section 4.

2. Principle Description of Two Improved Schemes

2.1. Clustering Location Management Scheme

The basic idea of clustering location management (CLM) scheme is to divide the mobile subscribers (MSs) with high-speed movement into two or more clusters according to their

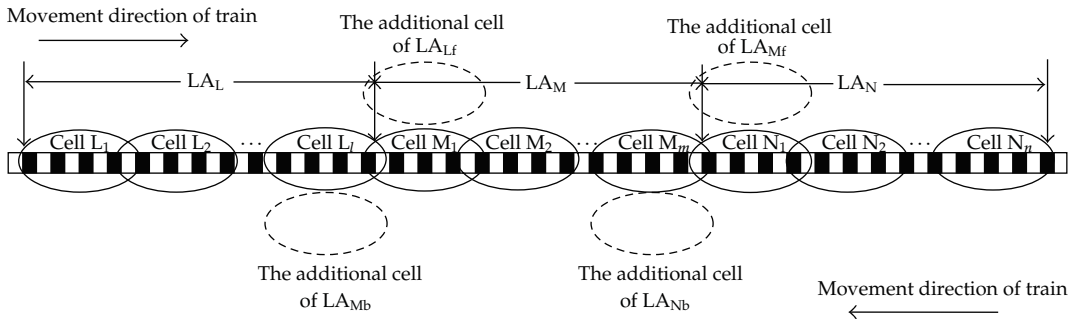

Figure 1: location area and virtual location area.

identification, such as international mobile subscriber identity (IMSI), and then the MSs in each cluster perform location updating in turns. Thus, it can reduce the number of MSs who need location updating in unit time, decreasing the network resource requirement. Meanwhile, through the virtual location area, it can guarantee the paging of those MSs who have not carried out the location updating yet, so as to reduce the call failure probability and improve the reliability of communication.

To take two user clusters clustering in GSM system as an example, according to the difference number of the end bit of IMSI, the odd number MSs is clustering as Cluster 1, the even number MSs is clustering as Cluster 2. When mobile stations find that the current location area code (LAC) is different from the previous registered LAC, they will request a location updating. Considering the different clusters, the network side let the MSs of Cluster 1 carry out the normal location updating procedure, but the updating request of the MSs of Cluster 2 will not be accepted temporarily. After the timer reaches the default time T, then the MSs of Cluster 2 perform the location updating procedure. The value of the default time T is related with the speed of train and the cell radius, T should not be longer than the train travel time for a cell, namely, it should guarantee the MSs of Cluster 1 to complete the location updating within T.

Considering the network coverage along the railway is linear in general, as shown in Figure 1, supposed that LA_L, LA_M, and LA_N are three adjacent location areas, which are l cells in LA_L, m cells in LA_M, and n cells in LA_N. After adopting the CLM scheme, during the location updating phase of Cluster 1, if the MS in Cluster 2 has an incoming call, it will be missed because the MSs in Cluster 2 have not performed location updating yet. Hence, we put forward a concept of virtual location area for paging the MSs in Cluster 2 during Cluster 1 updating phase. The virtual location areas are recorded in the database of network side, and it contains all cells in the original location area and adds an adjacent cell, which is in the target location area. In this case, if the MS in Cluster 2 has an incoming call, it will page MSs in the virtual location area. As shown in Figure 1, when the train travels from left to right, LA_{Lf}, which is the virtual location area of LA_L, is defined as all cells in $LA_L$and cell M_1, and LA_{Mf}, which is the virtual location area of LA_M, is defined as all cells in LA_M and cell N_1. Similarly, when the train travels from right to left, LA_{Mb}, which is the virtual location area of LA_M, is defined as all cells in LA_M and cell L_1, and LA_{Nb}, which is the virtual location area of LA_N, is defined as all cells in LA_M and cell M_m.

By use of the virtual location area, the MSs who are waiting for location updating will not miss the incoming calls. For example, when MSs move from LA_M into LA_N, before the timer time t reaches the default time T, the MSs of Cluster 2 are located in cell N_1, which

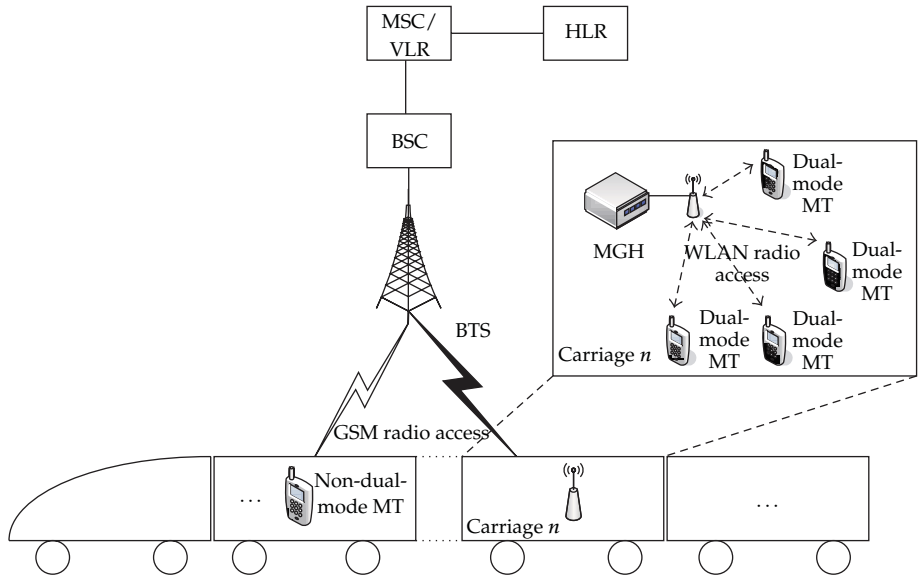

Figure 2: Network architecture of the group location management.

belongs to LA_N, but their location information is still LA_M; when the MS of Cluster 2 has an incoming call, the network will page the MS in the virtual location area $LA_{Mf,}$ including cell M_1, M_2, …, M_m and cell N_1, so the called MS will not miss the incoming call. Note that the paging procedure of the MSs in Cluster 2 is as usual.

If the number of MSs is very large, to avoid the call failure caused by too many location updates, the MSs can be divided into more clusters, each cluster carries out the location updating procedure in turns. However, the virtual location areas for each cluster must be redefined, the specific rules of which can be decided by the network operators.

2.2. Mobile Group Location Management Scheme

To implement the mobile group location management (MGLM) scheme, we need to configure some network devices in each railway carriage to build WLANs, as shown in Figure 2. Each WLAN's coverage range is limited within a carriage, and it should be equipped with a device as the mobile group head (MGH), which is responsible for the management of mobile terminals and performs the integrated location updating with representing the group. MGH comprises a wireless access point (AP), a cellular communication transceiver, and MGH register for storage the registered information of group members, as shown in Figure 3. The mobile terminals have dual mode, which means they support both cellular network wireless transceiver function and Wi-Fi function; hence, they have the ability to access to the WLAN.

In our MGLM scheme, we take GSM network as an example. It includes several processes: the group formation, dissolution and update process, intramobile switching center/visitor location register (MSC/VLR) group location updating procedure, inter-MSC/VLR group location updating procedure. As for the group location updating, it is in relative terms of traditional GSM location updating, the traditional GSM location updating is requested by MSs, each update just updates one MS's information, but the group location updating is

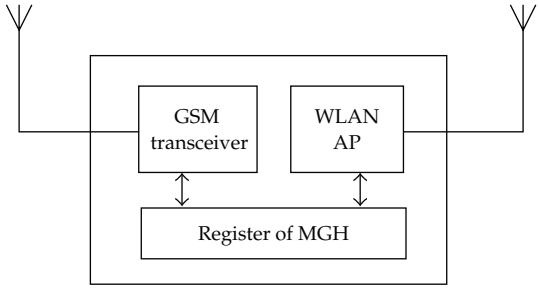

Figure 3: The inner structure of the mobile group head.

requested by the MGH, and it may update the location information of all MSs managed by the MGH. Apparently, the updating efficiency of MGLM scheme is much higher than the traditional ways. The details of those processes are as follows.

2.2.1. Group Formation, Dissolution, and Update Process

As the train sets off from the origin station, the WLANs in the carriages are enabled, the AP in MGH periodically sends member-joining notification message to MSs, the MSs in the carriage establish association with AP through the WLAN and are formed as an integral unit (group). The MGH is taken as the whole group representative, and the ordinary MSs are regarded as the group members. The specific process related to group formation, dissolution, and update includes the following steps.

(1) The AP in MGH sends the checking signal with a period of T_{AP} in the wireless coverage range, usually inside a railway carriage. Mobile group head register stores every MS's IMSI number or temporary mobile subscriber identity (TMSI) number, each TMSI is correspondent to an IMSI;

(2) When the mobile terminals (MTs) within WLAN signal coverage range receives the checking signal, they reply their own IMSI (or TMSI) number, and then apply for joining the group;

(3) After receiving the reply of each MS, the MGH registers the IMSI (or TMSI) number and sequence number of each MS, then returns a confirmation message and sequence number to the MS; when the MS receives the confirmation message, it means that MS has joined the group and knows its sequence number in the group;

(4) MGH checks the change of member in the carriage every T_{AP} cycle regularly, when MGH finds new member joining the group, it registers the new MS information and returns the corresponding message and sequence number;

(5) After sending the period checking signal, if the MGH has not received the IMSI (or TMSI), it thinks that the MS has left the group and then cancels the MS group registration information.

2.2.2. Intra-MSC/VLR Group Location Updating Procedure [17]

The intra-MSC/VLR group location updating procedure is shown in Figure 4.

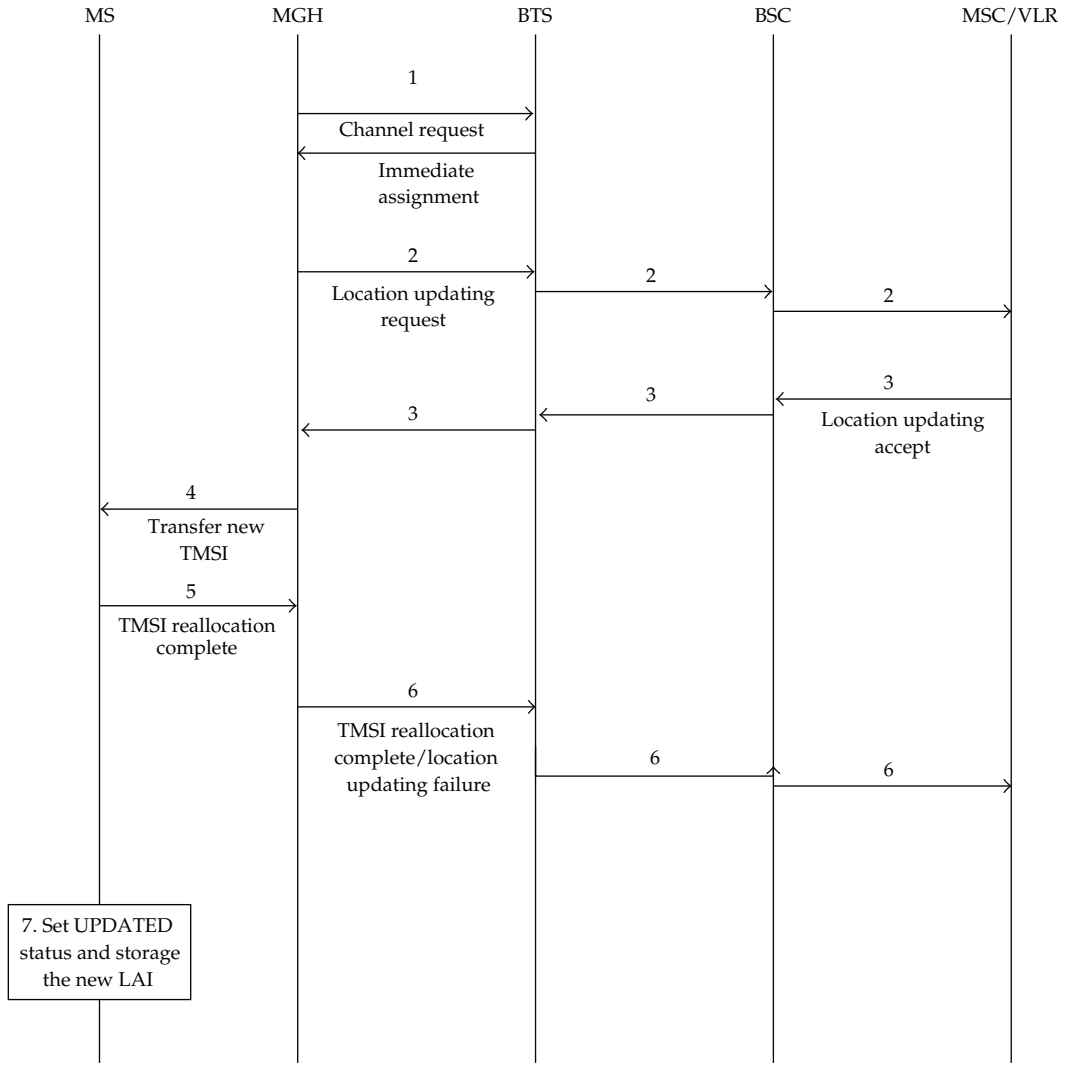

Figure 4: Intra-MSC/VLR group location updating procedure.

(1) The MGH sends the "channel request" message to BTS on random access channel (RACH), the priority of this message is higher than those sent from the ordinary MSs', so the base station (BTS) responds to the "immediate assignment" message on a stand-alone dedicated control channel (SDCCH);

(2) The MGH sends the "location updating request" message to the network, which includes each MS's IMSI (or TMSI) number and old location area identify (LAI) in sequence. The location updating request is forwarded to the MSC/VLR;

(3) The VLR stores each MS's new LAI, assigns a new TMSI to each MS, and then sends the new TMSI table aligned in sequence via "location updating accept" message to the MGH;

(4) The MGH receives the new TMSI table and forwards the message including the new MS's TMSI via WLAN, then each MS updates its location information and TMSI;

(5) The MSs in the group replies the "TMSI reallocation complete" acknowledgement message to the MGH through the WLAN, if the MGH does not receive the acknowledgement message of some MS, the MS location updating failure is considered;

(6) The MGH replies back "TMSI reallocation complete" or "location updating failure" message of each MS to the network in sequence, MSC receives the message and releases the channel link. For the MSs failed in location updating, the network responds their "location updating message" messages sent to the BTS individually, the location updating procedure is the same as the traditional one;

(7) After completing the location updating, the mobile station sets SIM card's update status to UPDATED (latest) and storages the new LAI.

2.2.3. Inter-MSC/VLR Group Location Updating Procedure [17]

The inter-MSC/VLR group location updating procedure is shown in Figure 5, in this case MSs move from VLR1 to VLR2.

(1) The MGH sends the "channel request" message to BTS on random access channel (RACH), the priority of this message is higher than those sent from the ordinary MSs', the base station (BTS) responds to the "immediate assignment" message on a stand-alone dedicated control channel (SDCCH);

(2) The MGH sends the "location updating request" message to the network, which includes each MS's IMSI (or TMSI) number and old location area identify (LAI) in sequence. The location updating request is forwarded to the VLR2 via MSC2;

(3) The new VLR2 inquires to the old VLR1 the authentication parameters and identity of each MS;

(4) The old VLR1 sends the new identity and authentication parameters of each MS to the new VLR2 in sequence, including IMSI, RAND, SRES, and Kc;

(5) The new VLR2 assigns a new TMSI to each MS, then sends the new TMSI table aligned in sequence via "location updating accept" message to the MGH, if necessary, it will send encrypted mode;

(6) The MGH receives the new TMSI table and forwards the message including the new MS's TMSI via WLAN, then each MS updates its location information and TMSI;

(7) The MSs in the group replies the "TMSI reallocation complete" acknowledgement message to the MGH through the WLAN, if the MGH does not receive the acknowledgement message of some MS, the MS location updating failure is considered;

(8) The MGH replies back "TMSI reallocation complete" or "location updating failure" message of each MS to the network in sequence, MSC1 receives the message and releases the channel link. For the MSs failed in location updating, the network responds their "location updating message" messages sent to the BTS individually, the location updating procedure is the same as the traditional one;

(9) The new VLR2 notifies the HLR each mobile resides, then the HLR sends the MS's information to the new VLR2, and the old VLR1is told to delete the data of that MS;

(10) After completing the location updating, the mobile station sets SIM card's update status to UPDATED (latest) and stores the new LAI.

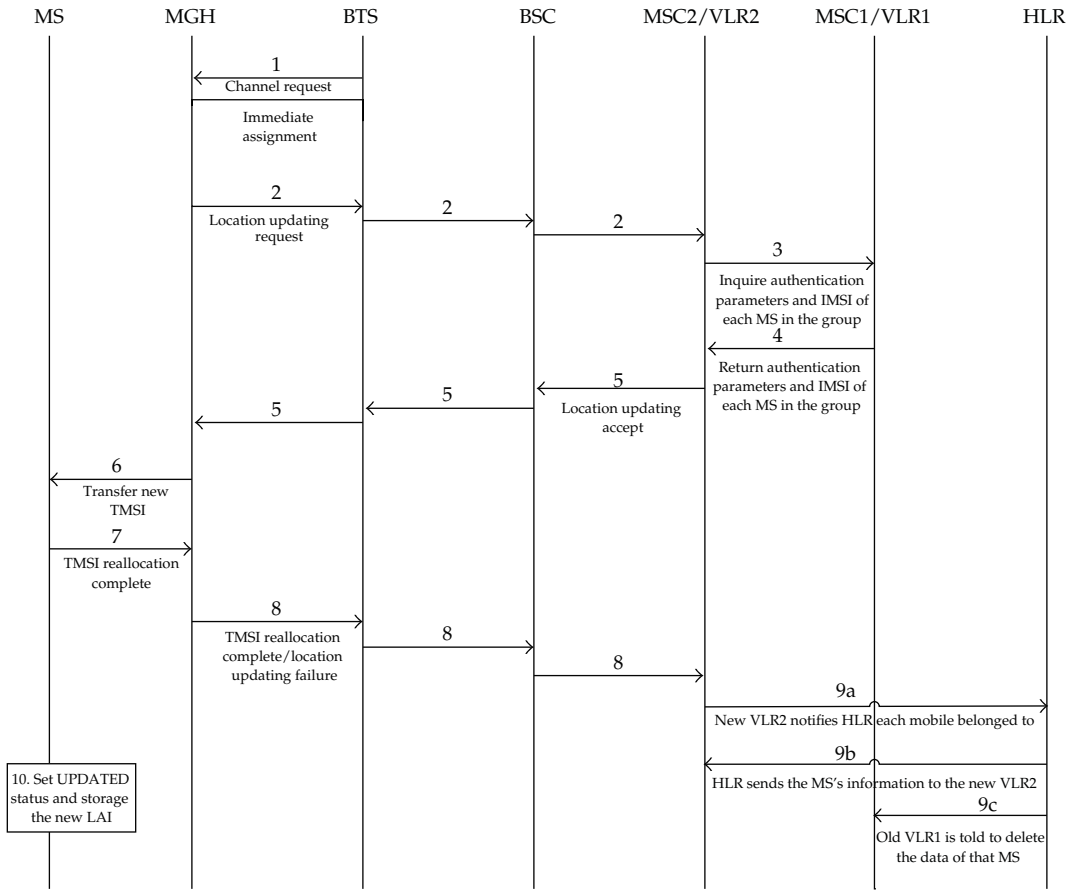

Figure 5: Inter-MSC/VLR group location updating procedure.

3. Performance Analysis

3.1. Parameter Hypothesis

Generally speaking, the minimum interval between two trains in one way is about 10 km. Considering that most of the high-speed railway is double-tracked, there are at most two passenger trains within the 20 km range. Each train has k ($k = 8 \sim 16$) carriages, and each carriage may carry 75 passengers; hence, total number of passengers per train is $Q = 600 \sim 1200$, in which the number of GSM mobile subscriber is about 60%, that is, the biggest number of MSs to perform location updating once is $2 \times Q \times 60\% = 1.2Q$; supposing each line traffic is 0.02 Er1, then the total traffic is $1.2Q \times 0.02 = 0.024Q$ Erl. According to a radio channel call loss rate 2% to design, the least channel number and SDCCH channel number needed per cell is shown in Table 1, due to the LAC boundary of the private network needed to provide enough channel resources to complete location updating and routing updating, consequently the increased number of SDCCHs is 3.2–4 times of the number of traffic channel [1, 2].

Based on the analysis of signaling, a location update occupies SDCCH average 3 s; considering the time from an SDCCH be released (i.e., CHANNEL RELEASE ACK is received) to be reassigned, a normal location updating total time is about 3.5 s.

Table 1: Number of passenger versus the number of TCH and SDCCH.

The number of passengers per train Q	Traffic (Erl)	The number of TCH N (radio loss rate 2%)	The number of SDCCHs S per normal cell	The number of SDCCHs $S_{\mathrm{LAC}} = 4N$ per cell in the private network
600	14.4	22	32	88
700	16.8	25	32	88
800	19.2	27	32	88
900	21.6	30	40	96
1000	24	33	40	96
1100	26.4	36	48	144
1200	28.8	37	48	148

3.2. Performance Analysis of Traditional Location Management Scheme

In the traditional location management scheme, the cost of location updating and paging per MS on the train in a unit time is represented by C_T:

$$C_T = \eta C_{\mathrm{LU}} + \lambda_C C_P, \tag{3.1}$$

where $\eta = v/R$ is the location updating rate; v indicates the speed of train; R expresses the average distance between location boundaries; C_{LU} indicates the average location updating cost of each MS; λ_C is the call arrival rate, that is, the arrived calling number of each MS per unit time; C_P represents the average paging cost of each MS:

$$C_P = x \cdot C_{\mathrm{Pcell}}, \tag{3.2}$$

where x indicates the average number of cells in an LA and C_{Pcell} represents the paging cost of each cell, here supposed the average distance over an LA is about $R = 100\,\mathrm{km}$ including average 10 cells, $v = 300\,\mathrm{km/h}$, $\lambda_C = 0.5/\mathrm{h}$. Supposing that the passengers in a train is Q, $1.2Q$ expresses the total location updating number of MSs at the same time, thus the total cost of all location management per unit time is represented by $C_T{}'$, and

$$C_T{}' = 1.2Q\left(\eta C_{\mathrm{LU}} + \lambda_C C_P\right). \tag{3.3}$$

If SDCCH is congested, the average location updating time is increased, which can be obtained by M/M/C model [18–21]. Supposing the average waiting time per MS is W_q, as shown in (3.4):

$$W_q = \frac{1}{c\mu\left(1 - (\lambda/c\mu)\right)^2} p_c, \tag{3.4}$$

where c represents available SDCCH number and μ represents the number of location updates in a unit time (1 s) completed in one SDCCH. Considering that a normal location updating total time is about 3.5 s, the average service rate is $\mu = 1/3.5$, and λ represents the average arrived rate of location updating. Since the triggering time of the location updating is very

short, we suppose that all MSs start location updating procedure within 1 min, $\lambda = 1.2Q/60$. p_c and the traffic degree ρ are related to SDCCH number c and the steady-state probability p_0:

$$\begin{aligned} p_c &= \frac{1}{c!} \cdot \rho^c \cdot p_0, \\ \rho &= \frac{\lambda}{\mu}, \\ p_0 &= \left[\sum_{k=0}^{c-1} \frac{1}{k!} \rho^k = \frac{\rho^c}{c!(1-\rho_c)} \right]^{-1}, \\ \rho_c &= \frac{\lambda}{c\mu} < 1, \end{aligned} \tag{3.5}$$

where k represents the number of MSs, that is, $1.2Q$, from the above equations, the number of MSs is more, the number of SDCCHs is less, thus the SDCCH is more congested, and the average waiting time of MS for location updating is much longer.

3.3. Performance Analysis of CLM Scheme

In the improved CLM scheme, MSs are divided into n clusters. The cost of the location updating is the same as the cost of traditional location management scheme, although the cost of paging is increased, the performance of radio resource utilization rate and the average waiting time of location updating is improved. Please refer to [22–25]:

$$\frac{C_{\mathrm{LU}}}{C_{\mathrm{Pcell}}} = 17. \tag{3.6}$$

As we know, the cost of location updating occupies too much proportion of the total cost of location management; therefore, a little increase of paging cost will bring little effect to the total cost of location management. Supposing C_{Pcell} is the unit cost, we may calculate C_{LU} and C_P via formulas (3.6) and (3.2), respectively; moreover, we may analyze the cost of the location updating and the cost of paging and the total cost.

Through clustering, the number of SDCCHs can be reduced greatly. From Figure 6, we can see that the CLM scheme with 48 SDCCHs can acquire the similar waiting time performance of traditional scheme with 88 SDCCHs, which reduces a great amount of the SDCCH channel consumption. And the more the number of the SDCCH is, the shorter the average waiting time is. Observed in Figure 6, we may choose the appropriate number of SDCCHs to be assigned. When $n = 1$, which means no clustering, it needs at least 88 SDCCHs [1]; when $n = 2$, the number of SDCCHs can be set to 48; when $n = 3$, the number of SDCCHs can be set to 40; when $n = 4$, the number of SDCCHs can be just set to 32. Hence, it can greatly reduce the SDCCH channel resource by clustering and further enhance the QoS quality of MSs. Using the same number of SDCCHs, the more clusters in CLM, the shorter the average waiting time is. For example when SDCCH = 88, the average waiting time of the traditional scheme (i.e., $n = 1$) is 0.215653 s, and when SDCCH = 56, the average waiting time of CLM for $n = 2$ is just 0.15365 s, consequently, the CLM scheme can achieve a better performance.

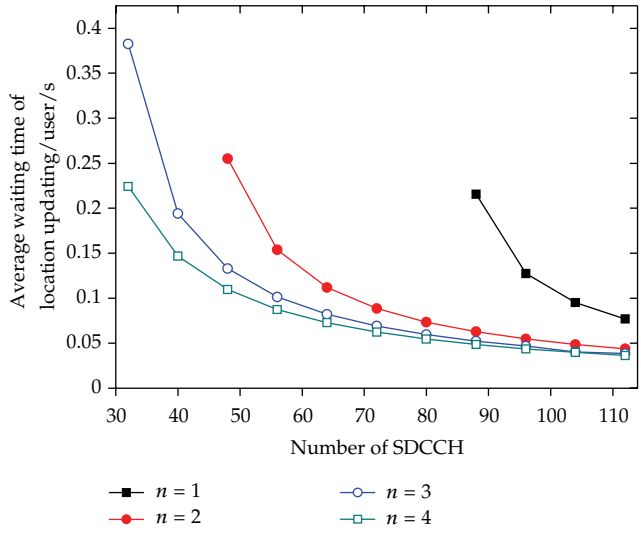

Figure 6: The average waiting time of location updating.

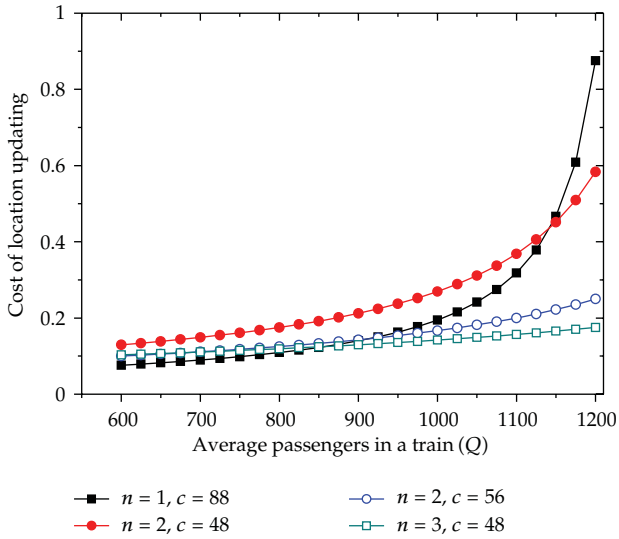

Figure 7: The cost of location updating (n represents the number of clusters, c represents the number of SDCCHs).

Figure 7 describes the performance comparison of the cost of the location updating between traditional scheme and the CLM scheme. Seen from the graph, no matter whether clustering, the general trend of the location updating cost is increased as the number of MSs. When no clustering (i.e., $n = 1$), if the number of MSs is less than 850, the updating cost is a little better than CLM scheme, but its number of SDCCHs far outweighs the CLM scheme; whereas when the total passengers is nearly 1200, the cost of location updating for no clustering increases significantly. When using the same number SDCCH, the more clusters;

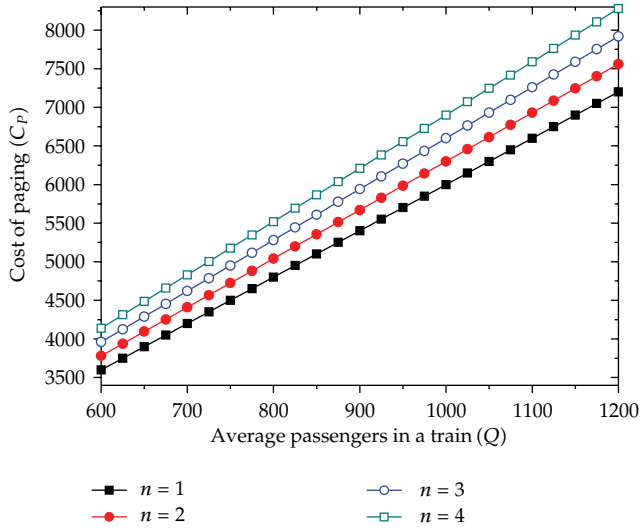

Figure 8: The cost of paging.

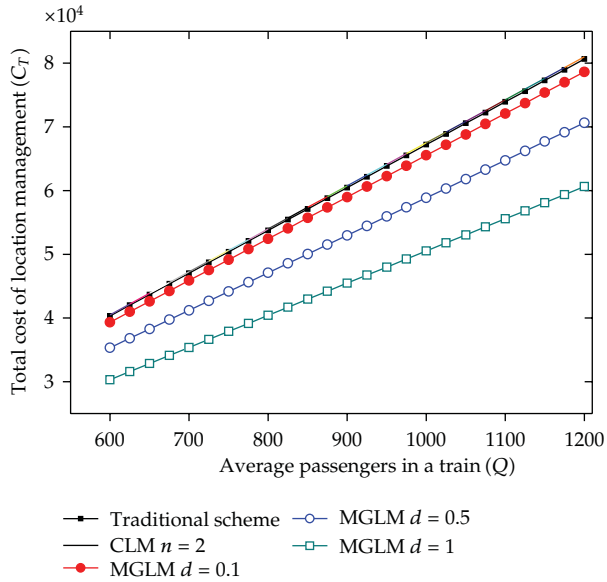

Figure 9: The total cost comparison of the three location management schemes.

the less cost of location updating. When using the same number of clusters n, the more SDCCHs are assigned, the less cost of location updating is.

Figure 8 is the paging cost performance comparison between the traditional scheme and the CLM scheme. We can see that the more clusters, the higher paging cost is increased, but usually the value of n could be 2 or 3 in practical application, and the paging cost only occupies a small proportion of the cost of location management.

Hence, it can be concluded that on the basis of saving SDCCH resource, the CLM scheme can acquire the similar average waiting time and total location management cost performance of the traditional scheme.

3.4. Performance Analysis of MGLM Scheme

In MGLM scheme, we suppose that there are $d * 1.2Q$ $(0 < d < 1)$ MSs with dual-mode terminals joining into the group, the other users cannot join into the group due to mobility or without dual-mode terminals. The definition Q is the same as 3.2; d represents the proportion of MSs in the group. According to the basic principle of the MGLM scheme, the decreasing percentage of SDCCH is in proportion to the percentage of MSs joining in the group, for instance, when $d = 0.5$, the amount of SDCCHs is decreased from 88 to 44. However when $d > 0.5$, to meet the requirement of calling, the number of SDCCHs is not suitable for decreasing. From the specific procedure of the MGLM scheme, we know the overhead of the MGLM scheme includes the overhead of the initial group registration procedure C_g, the overhead of the group location updating procedure $C_{\text{LU\_G}}$, the overhead of paging C_P, and the overhead of group cancellation procedure C_c. Since the group registration does not involve the mobile network resources, it will be neglected, and the group cancellation procedure can be equivalent to the cost of a location updating. Assuming there are 75 passengers in each carriage, where $75d$ MSs with the dual-mode terminal join the group update management, hence the cost of location updating includes two parts: the cost of dual-mode users $C_{\text{LU\_G}}$ and the cost of ordinary users C_{LU}. The calculation of the LA cost for ordinary users is the same as the calculation in traditional scheme, to see (3.6); the LA cost of other dual-mode users can be derived by the signaling:

$$\frac{C_{\text{LU\_G}}}{C_{\text{Pcell}}} \approx 12.36. \tag{3.7}$$

Hence, the total cost of MGLM is

$$C_{T\_G}{}' = 1.2Q \cdot d \cdot (\eta + 1) C_{\text{LU\_G}} + 1.2Q \cdot (1 - d) \cdot \eta C_{\text{LU}} + 1.2Q \cdot \lambda_c C_P, \tag{3.8}$$

where the cost of paging C_p is the same as the one in the traditional management scheme. The cost of the location management comparison is depicted in Figure 9.

Figure 9 shows that the total cost of the CLM is higher than the tradition scheme's, this is because the virtual paging area introduced by CLM leads to the increase of paging cost. Whereas the total cost of the MGLM is relatively low, and with the number increase of MSs joining in the group, its total cost decreases more and more. The reason is that the group location updating may reduce the updating cost greatly. Obviously, we do not consider the equipment cost in MGLM in this paper.

4. Conclusions

In this paper, two kinds of location updating schemes for high-speed railway private network are provided, that is, clustering location management (CLM) and mobile group location management (MGLM). The performance analysis and comparison results of traditional scheme,

CLM and MGLM schemes are also given. From the results we may conclude that both the two improved location updating schemes can reduce the number of SDCCHs greatly. For example, with CLM scheme, it may decrease the number of location updating per unit time more than 50%, and it can acquire much better performance with 56 SDCCHs than traditional scheme with 88 SDCCHs. Consequently, it saves the SDCCH resource greatly. Meanwhile, through adopting the virtual location area, it can guarantee the paging of MSs and reduce the call failure probability and improve the reliability of communication. However, the CLM scheme may increase the complexity of network management. From the view of decreasing radio resource and the cost of location updating, the MGLM scheme is the best choice, in which the decreasing extent of SDCCH is related with the percentage of MSs joining in the group, for instance, when $d = 0.5$, the amount of SDCCHs is decreased from 88 to 44. Since the members of carriage can perform group location updating by the MGH, the cost of the location updating is decreased greatly; but it needs to add the MGH device in each carriage and leads to much change in both the network side and the mobile terminals, the complexity of MGLM is the highest in 3 schemes. In conclusion, the railway private cellular network operator may take a suitable location management improved scheme to decrease the location updating average waiting time and utilize the radio resource effectively.

Acknowledgment

This paper is supported by the State Key Laboratory of Rail Traffic Control and Safety (Contract no. RCS2010ZZ004), Beijing Jiaotong University. This paper is also supported by Program for Changjiang Scholars and Innovative Research Team in University under Grant no. IRT0949 and the Joint State Key Program of the National Natural Science Foundation of China and the National Railway Ministry of China (Grant no. 60830001). And it is supported in part by the Chinese National Programs for High Technology Research and Development (863) Project 2009AA110302.

References

[1] Y. Wei-guang, G. Hai-ping, and H. Hin-yang, "Discussion about the private network planning and optimazation of high-speed railway," *Telecommunications Science*, vol. 22, no. 3, pp. 94–98, 2008 (Chinese).

[2] L. Fu-xin, X. Ying, and L. Wen-peng, "Study on mobile network coverage scheme of high speed railway," *Designning Techniques of Posts and Telecommunications*, vol. 22, no. 9, pp. 20–24, 2008 (Chinese).

[3] Y. Zhang and M. Fujise, "Location management congestion problem in wireless networks," *IEEE Transactions on Vehicular Technology*, vol. 56, no. 2, pp. 942–954, 2007.

[4] M. Li and W. Zhao, "Visiting power laws in cyber-physical networking systems," *Mathematical Problems in Engineering*, vol. 2012, Article ID 302786, 13 pages, 2012.

[5] N. E. Kruijt, D. Sparreboom, F. C. Schoute, and R. Prasad, "Location management strategies for cellular mobile networks," *Electronics and Communication Engineering Journal*, vol. 10, no. 2, pp. 64–72, 1998.

[6] G. Y. Lee, Y. Lee, and Z. J. Haas, "Hybrid location-update scheme for mobile networks," *IEEE Trans actions on Vehicular Technology*, vol. 58, no. 1, pp. 338–348, 2009.

[7] C. Peng, Y. Xue-jun, and H. Zai-lu, "A dynamic location management scheme based on movement-state," *ACTA Telectronica Sinica*, vol. 30, no. 7, pp. 1038–1040, 2002 (Chinese).

[8] J. Chen, G. Wu, and Z. Ji, "Secure interoperation of identity managements among different circles of trust," *Computer Standards and Interfaces*, vol. 33, no. 6, pp. 533–540, 2011.

[9] W. Ma and Y. Fang, "Two-level pointer forwarding strategy for location management in PCS networks," *IEEE Transactions on Mobile Computing*, vol. 1, no. 1, pp. 32–45, 2002.

[10] Y. W. Chung, "Performance analysis of movement-based group location management for mobile stations riding on transportation systems in cellular systems," in *Proceedings of the 11th IEEE/IPSJ International Symposium on Applications and the Internet (SAINT '11)*, pp. 333–337, Munich, Germany, 2011.
[11] W. Fu-Rong, X. Lai, and W. Hao, "A group location management method based on hybird mobile network," People's Republic of China: ZL101001414A, July, 2007.
[12] I. Han and D.-H. Cho, "Group location management for mobile subscribers on transportation systems in mobile communication networks," *IEEE Transactions on Vehicular Technology*, vol. 53, no. 1, pp. 181–191, 2004.
[13] R. Balakrishnan, X. Yang, M. Venkatachalam, and I. F. Akyildiz, "Mobile relay and group mobility for 4G WiMAX networks," in *Proceedings of the IEEE Wireless Communications and Networking Conference (WCNC '11)*, pp. 1224–1229, Quintana Roo, Mexico, March 2011.
[14] Z. Mao, "An intra-LA location update strategy for reducing paging cost," *IEEE Communications Letters*, vol. 6, no. 8, pp. 334–336, 2002.
[15] P. G. Escalle, V. C. Giner, and J. M. Oltra, "Reducing location update and paging costs in a PCS network," *IEEE Transactions on Wireless Communications*, vol. 1, no. 1, pp. 200–208, 2002.
[16] R. Munadi, M. Ismail, M. Abdullah, and N. Misran, "Location management cost reduction using fuzzy logic in cellular radio network," in *Proceedings of the IEEE International Conference on Space Science and Communication (IconSpace '11)*, pp. 165–169, Penang, Malaysia, 2011.
[17] GSM 03.12, Digital cellular telecommunications system (Phase 2+); Location registration procedures, 1995.
[18] S. V. Subramanian and R. Dutta, "Performance measurements and analysis of M/M/C queuing model based sip proxy servers in local and wide area networks," in *Proceedings of the 2nd International Conference on Advances in Recent Technologies in Communication and Computing (ARTCom '10)*, pp. 306–310, Kerala, India, October 2010.
[19] M. Li and W. Zhao, "Representation of a stochastic traffic bound," *IEEE Transactions on Parallel and Distributed Systems*, vol. 21, no. 9, pp. 1368–1372, 2010.
[20] M. Li, C. Cattani, and S. Y. Chen, "Viewing sea level by a one-dimensional random function with long memory," *Mathematical Problems in Engineering*, vol. 2011, Article ID 654284, 13 pages, 2011.
[21] G. Ren-yong, "A rule of updating position in microscopic pedestrian model," in *Proceedings of the International Conference on Optoelectronics and Image Processing (ICOIP '10)*, vol. 1, pp. 120–123, Haiko, China, November, 2010.
[22] E. Martin, G. Lin, M. Weber, P. Pesti, and M. Woodward, "Unified analytical models for location management costs and optimum design of location areas," in *Proceedings of the 5th International Conference on Collaborative Computing: Networking, Applications and Worksharing (CollaborateCom '09)*, pp. 1–10, IEEE Press, Washington, DC, USA, November 2009.
[23] Z. Liao, S. Hu, and W. Chen, "Determining neighborhoods of image pixels automatically for adaptive image denoising using nonlinear time series analysis," *Mathematical Problems in Engineering*, vol. 2010, Article ID 914564, 14 pages, 2010.
[24] W.-S. Chen, P. C. Yuen, and X. Xie, "Kernel machine-based rank-lifting regularized discriminant analysis method for face recognition," *Neurocomputing*, vol. 74, no. 17, pp. 2953–2960, 2011.
[25] J. Yang, Z. Chen, W.-S. Chen, and Y. Chen, "Robust affine invariant descriptors," *Mathematical Problems in Engineering*, vol. 2011, Article ID 185303, 15 pages, 2011.

Hindawi Publishing Corporation
Mathematical Problems in Engineering
Volume 2012, Article ID 767613, 15 pages
doi:10.1155/2012/767613

Research Article

Image Denoising Based on Dilated Singularity Prior

Shaoxiang Hu,[1] Zhiwu Liao,[2] and Wufan Chen[1]

[1] *School of Automation Engineering, University of Electronic Science and Technology of China, Chengdu 610054, China*
[2] *Visual Computing and Virtual Reality Key Laboratory of Sichuan Province, Sichuan Normal University, Chengdu 610066, China*

Correspondence should be addressed to Zhiwu Liao, liaozhiwu@163.com
and Wufan Chen, chenwufan@hotmail.com

Received 19 January 2012; Accepted 21 February 2012

Academic Editor: Ming Li

In order to preserve singularities in denoising, we propose a new scheme by adding dilated singularity prior to noisy images. The singularities are detected by canny operator firstly and then dilated using mathematical morphology for finding pixels "near" singularities instead of "on" singularities. The denoising results for pixels near singularities are obtained by nonlocal means in spatial domain to preserve singularities while the denoising results for pixels in smooth regions are obtained by EM algorithm constrained by a mask formed by downsampled spatial image with dilated singularity prior to suiting the sizes of the subbands of wavelets. The final denoised results are got by combining the above two results. Experimental results show that the scheme can preserve singularity well with relatively high PSNR and good visual quality.

1. Introduction

How to preserve edges and textures in image denoising is a very difficult and important topic. Many efforts focus on this topic for a long time. The most straight way to image denoising while preserving singularities is adaptive methods [1, 2], which suggest that denoising should be carried on local regions. However, preserving singularities requires the size of local area to be small while denoising requires the size of local area to be large, which makes it become a trade-off problem.

Recently, Buades et al. argue that the small size of local area is not a requirement for preserving singularities in image denoising. That is, if correct similar pixels can be found through their similar local areas, singularity preserving denoising can be achieved by simple mean smoothing [3]. Nonlocal means has very good performance in maintaining the borders

and textures than most of existing methods. Based on it, some improved algorithms are proposed [4–10]. However, its computation cost is very high.

Although some denoising methods on spatial domain, such as nonlocal means and its improvements, nonlinear anisotropic diffusion, and fractional calculus can provide satisfied denoising results, most of them suffer from high computation burden [9, 11–20]. Thus, some researchers suggest that wavelets can be used to reduce the computation cost and suppress noises.

Some works on wavelet domain propose that threshold values should be selected according to statistical rules; the type of these methods is called shrinkage denoising. In [21], the threshold is determined by SURE shrinkage, which has better performance than threshold selected by Baysian rule. However, all coefficients in a subband are considered as independent identical distributed (iid) variables, and this is considered an unreal assumption.

In order to improve the performance of shrinkages, some schemes focus on how to describe the residual dependencies among wavelet coefficients [22–26]. In [22], the authors present a tree structure to describe the dependency among the wavelet coefficients. Recently, [23] proposes that trivariates should be used for three subbands of wavelet coefficients.

Both methods can provide improved denoising results than independent model for wavelet coefficients, but they do not consider the difference between pixels near singularities and in smooth regions. That is, they think that the coefficients near singularities are the same as they are in smooth regions. Intuitively, it is wrong.

We suggest that the dependency among wavelet coefficients should be considered both on their local energy and their object labels [26]. However, object labels cannot be assigned correctly in serious noise especially in high-frequency subbands.

Most recently, following block similarity proposed in [3], a denoised method based on collaborative filtering and wavelets is proposed. It obtains great success in its high value of peak signal noise ratio (PSNR). However, estimating real levels both of singularity points and smooth points with large regions leads it has very high computation complexity.

In summary, there are two popular methods to preserve singularities in denoising: one is local area similarity proposed in [3] and then improved by many efforts; the other is adaptive denoising in small local regions. The former has good performance in preserving singularities but suffers from its high computation complexity while the latter has low computation complexity and good performance in smooth regions but blurs the singularities.

It reminds us that if we can distinguish points near singularities from the points in smooth regions correctly and design different denoising schemes for these two types of points separately, singularities can be preserved in denoising. Following this idea, dilated singularity prior is posed to find points "near" singularities instead of "on" singularities. After distinguishing pixels near singularities from pixels in smooth regions, the real level for pixels in smooth regions can be estimated by a smooth version of noisy image. By combining these two different denoising methods together, we can obtain good denoising results.

The detailed framework will be introduced as follows. The second section in this paper will introduce backgrounds, the third section introduces how to build mask, and the fourth section describes the denoising framework. Section 5 is the experimental results and discussion. Section 6 gives conclusions, and, finally, there is the acknowledgment part.

2. Backgrounds

In this section, we will introduce terms, notations, and concepts for image denoising, wavelets, and GMM.

2.1. Image Denoising

An image x is regarded as a realization of a random field X. In these terms, the image denoising problem can be rephrased as follows: given a noisy image, estimate for real gray level of each pixel.

Let the original image be $\{x_{i,j}\}$, $i, j = 1, \ldots, N$, where N is some integer power of 2 and (i, j) is the pixel coordinate of the image. The image has been corrupted by additive noise and one observation

$$y_{i,j} = x_{i,j} + n_{i,j}, \tag{2.1}$$

where $n_{i,j}$ is an iid variable as normal $N(0, \sigma_n^2)$ and independent to $x_{i,j}$. The goal is to remove the noise from $y_{i,j}$ and obtain an estimate $\widehat{x}_{i,j}$ of $x_{i,j}$ which minimizes the mean squared error (MSE):

$$\mathrm{MSE}(\widehat{x}) = \frac{1}{N^2} \sum_{i,j=1}^{N} \left[\widehat{x}_{i,j} - x_{i,j}\right]^2. \tag{2.2}$$

Thus, the minimum MSE estimate would be the conditional mean estimate of a Gaussian signal with Gausssian noise

$$E\left[X_{i,j} \mid Y_{i,j}\right] = \frac{\sigma^2_{X_{i,j}}}{\sigma^2_{X_{i,j}} + \sigma_n^2} y_{i,j}, \tag{2.3}$$

where $X_{i,j}$ and $Y_{i,j}$ are the random variables of $x_{i,j}$ and $y_{i,j}$ respectively.

However, only one observation (a noisy image) provides for us to estimate real gray levels for the image. Thus we have to share statistical information among image pixels. One common method used in adaptive denoising assuming pixels in a local region is iid variables. However, since local regions have singularities, iid variable assumption leads to blurred edges and textures.

Intuitively, pixels with more similar real gray levels have higher probability for identical distribution. Thus more plausible way for selecting iid pixels converts to find pixels with similar real gray levels in a local region.

However, finding pixels with similar real gray levels in noise is very difficult. In this paper, we use singularities detected in spatial domain combined with a mask built on LL subband of wavelets to help us find similar pixels in a local region. The whole framework will be given in Section 4.

2.2. Wavelets and Gaussian Mixture Model (GMM) [21]

Let $W = wx$, W denote the matrix of wavelet coefficients of x, where w is the 2D dyadic orthogonal wavelet transform operator. It is convenient to group wavelet coefficients into groups or subbands of different scales and orientations, where, for example, the label HL_1

refers to those coefficients at the first scale of decomposition which are the output of the high-pass filter in the horizontal direction and the low-pass filter in the vertical direction. The subbands $\mathrm{HH}_k, \mathrm{HL}_k, \mathrm{LH}_k$, $k = 1, 2, \ldots, J$ are called the details, where k is the scale, with J being the largest (or coarsest) scale in the decomposition, and a subband at scale k has size $N/2k \times N/2k$. The subband LL_J is the low-resolution residual. Wavelets lead to a natural structure of the wavelet coefficients into three subbands representing the horizontal, vertical, and diagonal edges.

The coefficients of DWTs of many real-world images tend to be sparse, with just a few nonzero coefficients containing most of the image energy. This property, combined with our view of the image as a realization from a family or distribution of signal, leads to a simple model for an individual wavelet coefficient. Hence, the marginal density of each wavelet coefficient is typically described by a peaky and heavy-tailed non-Gaussian density.

Such densities are well approximated by a two-component Gaussian mixture model [21], and its overall pdf is given by

$$f_{W_{i,j}}(\omega_{i,j}) = \sum_{m=0}^{1} P_{S_{i,j}} Y_{W_{i,j}|S_{i,j}}(\omega_{i,j} \mid S_{i,j} = m). \tag{2.4}$$

In general, a 2-state Gaussian mixture model for a random variable $W_{i,j}$ consists of

(1) discrete random state variable $S_{i,j}$ taking the value $S_{i,j} \in \{0, 1\}$ according to the probability mass function (pmf);

(2) means and variances of Gaussian distributions.

In most applications of mixture models, the value $\omega_{i,j}$, can be observed, but the value of the state variable is not; we say that the value of $S_{i,j}$ is hidden. Although each wavelet coefficient $W_{i,j}$ is conditionally Gaussian given its state variable $S_{i,j}$, the wavelet coefficient has an overall non-Gaussian density due to the randomness of $S_{i,j}$.

2.3. EM Algorithm

EM algorithm is a kind of Max-likelihood Estimation (MLE) algorithm whose target is to find a set of hidden states to maximize the probability of observations. If the initial values for parameters are known, EM iterates between estimating the probability for the state (Expectation) and updating the model given the state probabilities (Maximization).

The normal form of the E step and M step of EM algorithm is as follows.

Expectation (E):

$$P_{S_{i,j}|W_{i,j}}(m \mid \omega_{i,j}) = \frac{P_{S_{i,j}}(m) P_{W_{i,j}|S_{i,j}}(\omega_{i,j} \mid m)}{\sum_{m=0}^{1} P_{S_{i,j}}(m) P_{W_{i,j}|S_{i,j}}(\omega_{i,j} \mid m)}. \tag{2.5}$$

Maximization (M):

$$P_{S_{i,j}}(m) = \frac{1}{N}\sum_{t,k} P_{S_{t,k}|W_{t,k}}(m \mid \omega_{t,k}),$$
$$\sigma^2_{i,j,m} = \frac{1}{NP_{S_{i,j}}(m)}\sum_{t,k} \omega^2_{t,k} P_{S_{t,k}|W_{t,k}}(m \mid \omega_{t,k}), \tag{2.6}$$

where N is the samples of an image.

3. Designing Mask

Just as discussed in Section 2.1, image denoising using statistical theory has to find similar pixels as iid variables. However, pixels near singularities have very different statistical properties to pixels in smooth regions. Thus, if two types of pixels, pixels near singularities and pixels in smooth regions, can be parted correctly, iid variables can be selected from the pixels with identical type labels. Based on this idea, we present a method to find similar pixels by posing dilated singularity prior. That is, singularity prior and its dilated version are used to find pixels near singularities while other pixels are considered as in smooth regions.

However, polluted gray levels will also lead to noisy wavelet coefficients in the details of wavelets, which hampers us to detect singularities and measure the similarity among wavelet coefficients correctly. Therefore, posing singularity prior and finding similar pixels in the details of wavelets cannot be carried on directly using the details of wavelets.

One solution for these difficulties is to design a mask and then apply it to the details of wavelets for image denoising. In this section, we will discuss the method to design the mask in detail.

3.1. Dilated Singularity Prior

Pixels near singularities are different to the pixels in smooth regions. Thus if we can find the pixels near singularities correctly and handle them separately, the singularities can be preserved in denoising. On the other side, smoothing only among pixels in smooth regions, which is implemented by abandoning pixels near singularities, can help us reduce the outliers in estimate. Moreover, parting pixels to different groups can help us design different denoising methods separately according to their different statistical properties. Thus it can get satisfying denoising results for both groups.

However, in noise, singularities in the details of wavelets cannot be detected correctly. Moreover, the low-resolution residual of wavelets is an oversmoothing version for the noisy image, which blurs many important weak singularities, such as some textures and degraded edges. Therefore, singularities cannot be detected from the subbands of the wavelets directly. In this paper, the singularities are located in spatial domain using canny operator and then downsampled to suit the size of different subbands of wavelets.

It should be indicated that although some pixels near singularities have similar real gray levels to nearby pixels in smooth regions, they have different statistical natures to the pixels in nearby smooth region. Thus, we need find pixels *near* singularities instead of *on* singularities. Based on this consideration, the detected singularities by canny are dilated using mathematical morph operator.

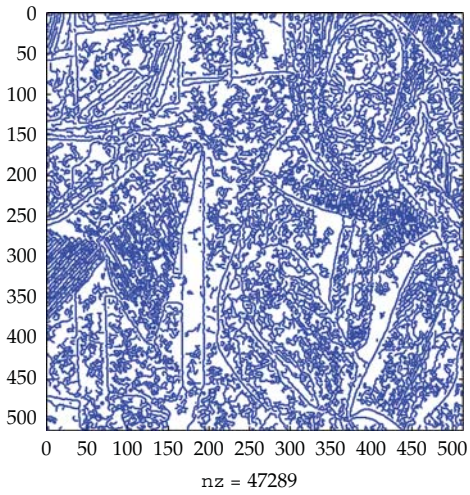

(a) Step 1: the singularities detected by canny in noisy barbara

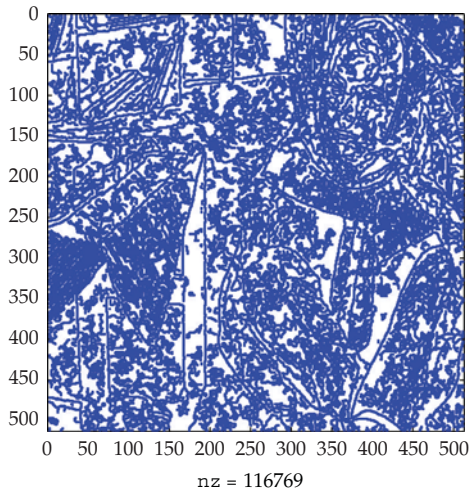

(b) Step 2: the dilated singularities

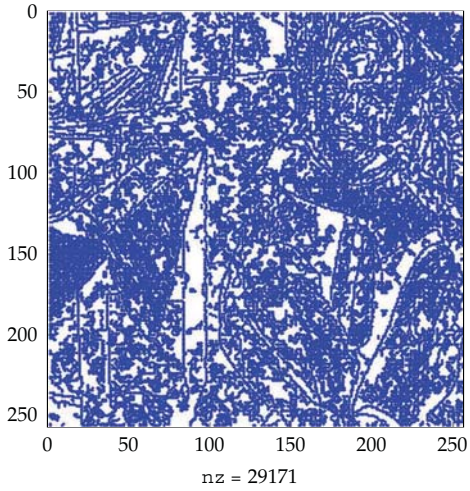

(c) Step 3: the downsampled dilated singularity prior

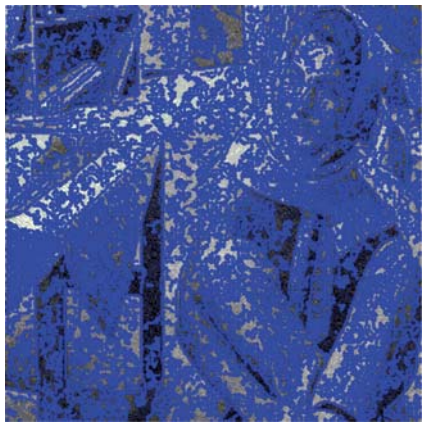

(d) The mask composed by LL_1 and singularity prior

Figure 1: The steps for locating singularity prior and making the mask. (a)–(c) three steps for locating singularity prior in Section 3.1; (d) the mask in Section 3.2.

In summary, procedures for posing singularity prior are

(1) detecting singularities in the noisy image using canny operator;

(2) dilating singularities using mathematical morphology operator;

(3) downsampling singularity image obtained in procedure 2 to form singularity prior for different subbands of wavelets.

One example for these three steps of noisy 512 × 512 barbara whose noise variance is 0.01 is shown in Figures 1(a)–1(c).

3.2. Designing Mask

After parting pixels into two groups by posing dilated singularity prior, we have to measure the similarity for two groups correctly in noise. However, even having posed singularity prior, measuring similarity among pixels in smooth regions correctly in the details of wavelets is very difficult because of noise influence in high frequency.

Fortunately, the low-resolution residual of wavelets can provide a downsampled smoother version for noisy images. Thus, if the singularity prior is posed to the low-resolution residual of wavelets, the similarity among pixels in smooth regions can be measured correctly by the coefficients of the low-resolution residual. Based on this discussion, the mask for the details of wavelets is designed as posing singularity prior to the low resolution of wavelets.

Figures 1(a)–1(c) show the steps for building the singularity prior for pixels in smooth regions, and the final mask is shown in Figure 1(d).

4. The Framework

In this section, we will discuss the framework for the proposed method, whose flow chart is shown in Figure 2. In Figure 2, the squares without shadow represent the method used in this framework while the shaded squares represent the processing results for the methods, and $\oplus$ represents combining two squares together. The dashed frame with a title frame "Mask" is the steps for designing masks for different pixel groups presented in Section 3.

The proposed method is based on a novel idea of preserving singularities by processing pixels near singularities and in smooth regions separately. The steps for denoising to different types of pixels are shown in Figure 2 as the two dashed frames with number 1 and 2 in two triangles where number 1 indicates the denoising steps for pixels in smooth regions and number 2 indicates denoising steps for pixels near singularities. Both methods will be discussed detailedly in this section.

4.1. Denoising for Pixels Near Singularities

In order to preserve singularities, the pixels near singularities located by dilated singularity prior should be processed alone. Since LL subband of wavelets will blur the singularities while the details of wavelets will magnify the influence of noises, the denoising for pixels near singularities should be carried on spatial domain directly. In this subsection, we will present the denoising method for pixels near singularities.

For each pixel $y_{i,j}$ of image, after imposing dilated singularity prior, it has a one and only one label $f_{i,j}$ and $f_{i,j} \in \{0,1\}$, where 0 represents "non-singularity" and 1 represents "near singularity."

Essentially, the most important procedure for image denoising is how to select similar points from image pixels. Similar pixels selected according to their block similarity are proposed in [3] recently. In this framework, the block is defined as a square with fixed size centered at the consideration pixel. In our method, the similarity among two pixels $y_{i,j}$, $y_{s,t}$ with labels $f_{i,j} = 1$ and $f_{s,t} = 1$ can be measured by two 7×7 blocks centered at (i, j) and (s, t):

$$S(y_{i,j}, y_{s,t}) = \sum_{k=-3,l=-3}^{k=3,l=3} \left\| y_{i-k,j-l} - y_{s-k,t-l} \right\|_2 e^{-(k^2+l^2)/2\sigma^2}. \tag{4.1}$$

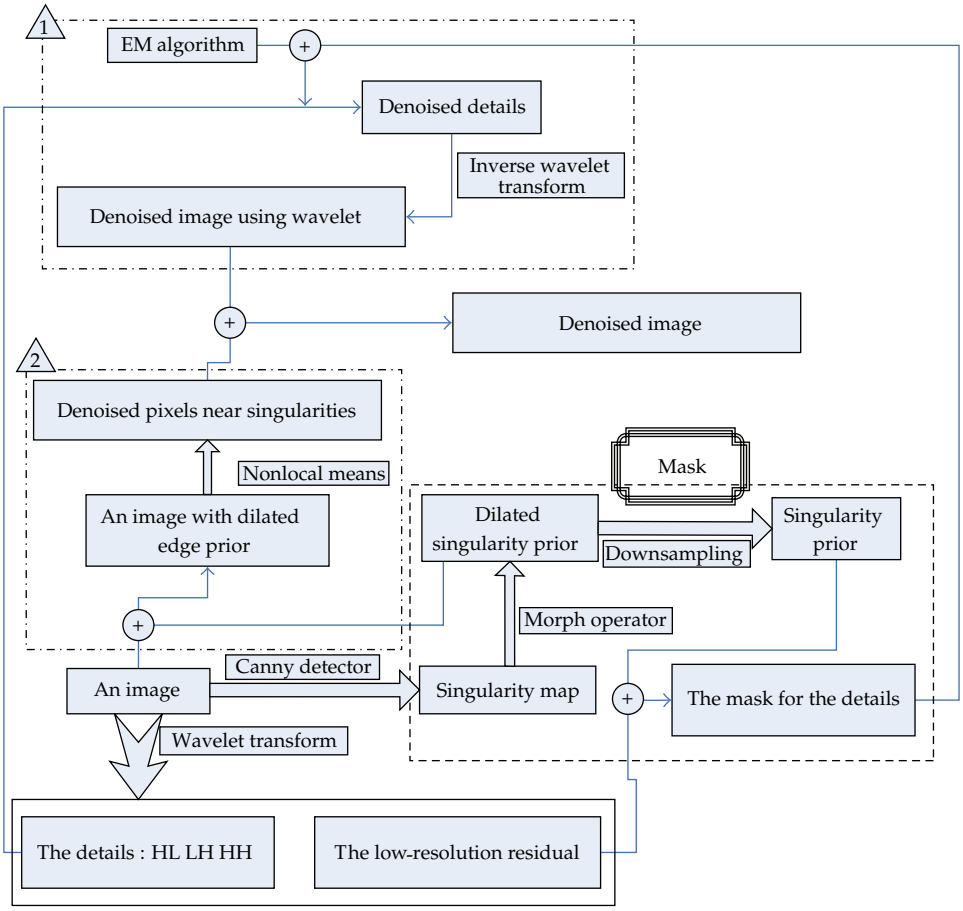

Figure 2: The flowchart of proposed method.

Thus, for each pixel $y_{i,j}$ with $f_{i,j} = 1$, searches in a 21×21 window to find its similar pixels whose similarity between itself and $y_{i,j}$ is below a predefined threshold T:

$$\chi(s,t) = \begin{cases} 1 : S(y_{i,j}, y_{s,t}) \leq T, \\ 0 : S(y_{i,j}, y_{s,t}) > T. \end{cases} \tag{4.2}$$

Thus the estimate of the real gray level of $y_{i,j}$ is

$$\hat{y}_{i,j} = \frac{1}{n} \sum_{k,l=-10}^{k,l=10} y_{i-k,j-l} \chi(i-k, j-l) f_{i-k,j-l}, \tag{4.3}$$

where

$$n = \sum_{k,l=-10}^{k,l=10} \chi(i-k, j-l) f_{i-k,j-l}. \tag{4.4}$$

Since $\chi(i-k, j-l)$ and $f_{i-k,j-l}$ are two indicator functions, we can combine them as

$$\chi(i-k, j-l) = \begin{cases} 1 : S(y_{i,j}, y_{i-k,j-l}) \le T, \ f_{i-k,j-l} = 1, \\ 0 : \text{otherwise.} \end{cases} \tag{4.5}$$

Therefore, (4.3) becomes

$$\widehat{y}_{i,j} = \frac{1}{n} \sum_{k,l=-10}^{k,l=10} y_{i-k,j-l} \chi(i-k, j-l), \tag{4.6}$$

where

$$n = \sum_{k,l=-10}^{k,l=10} \chi(i-k, j-l). \tag{4.7}$$

According to the above discussion, the denoising steps for pixels near singularities are as follows.

(1) **Initialization:** give T, compute $f_{i,j}$ for all image pixels according to dilated singularity prior.

(2) **For an image pixel** (i, j) **with** $f_{i,j} = 1$

(a) for $k = -10 : 10$, $l = -10 : 10$
compute $S(y_{i,j}, y_{i-k,j-l})$ using (4.1), for all $f_{i-k,j-l} = 1$,

(b) if $S \le T$, $\chi(i-k, j-l) = 1$
otherwise, $\chi(i-k, j-l) = 0$,

(c) compute $\widehat{y}_{i,j}$ using (4.6).

(3) **Repeat step 2 a – c** until all image pixels have been processed.

4.2. Denoising for Pixels in Smooth Regions

Wavelets, which are based on the idea that a linear, invertible transform will represent the image by the sparse wavelet coefficients whose structure is "simpler" to process, are a powerful tool to reduce the complexity.

However, in noise, there are two difficulties: one is the singularities cannot be located correctly in all subbands; the other is how to find similar pixels in the details of wavelets. In order to solve the above two problems, a mask will be built in the LL subbands and spatial domain together whose detailed algorithm is discussed in Section 3. That is, locate prior in spatial domain and then downsample and pose it to the LL subband to form the mask. Therefore, the real values of the details of wavelets can be estimated based on the mask.

Let $W^t_{i,j,k}$ denote a coefficient of wavelet, where $t \in \{0, 1, 2, 3\}$ and 0, 1, 2, 3 represent the LL, HL, LH, and HH subband, respectively, and k represents the decomposition scale.

Since the mask is built by posing singularity prior to the LL subband of each scale, we can give a label $\iota_{i,j,k}$ for a pixel $W^0_{i,j,k}$ in LL subband and $\iota_{i,j,k} \in \{0,1\}$, where 0 represents "non-singularity" and 1 represents "near singularity". Thus $\iota_{i,j,k}$s combined with $W^0_{i,j,k}$s forms the mask to measure the similarity between each pair of wavelet coefficients.

In our method, $W^t_{i,j,k}$, $t = 0,1,2,3$, is considered as a random variable with GMM distribution

$$P_{W^t_{i,j,k}}\left(\omega^t_{i,j,k}\right) = \sum_{m=0}^{1} P_{S^t_{i,j,k}} \Upsilon_{W^t_{i,j,k}|S^t_{i,j,k}}\left(\omega^t_{i,j,k} \mid S^t_{i,j,k} = m\right), \tag{4.8}$$

where $i, j = 1, \ldots, N/2^k$, $t = 0,1,2,3$.

Thus if the parameters $\Theta = \{P_{S^t_{i,j,k}=m}, \sigma^t_{m,i,j,k}, m = 0,1\}$ where $\sigma^t_{m,i,j,k}, m = 0,1$ are two standard deviations of Gaussian components, have known. The real value of $W^t_{i,j,k}$ can be estimated as

$$\widehat{\omega}^t_{i,j,k} = \sum_{m=0}^{1} P\left(S^t_{i,j,k} = m \mid \omega, \Theta\right) \frac{\left[\left(\sigma^t_{m,i,j,k}\right)^2 - \sigma_n^2\right]_+}{\left(\sigma^t_{m,i,j,k}\right)^2}, \tag{4.9}$$

where

$$\left[\left(\sigma^t_{m,i,j,k}\right)^2 - \sigma_n^2\right]_+ = \begin{cases} \left[\left(\sigma^t_{m,i,j,k}\right)^2 - \sigma_n^2\right] & : \left[\left(\sigma^t_{m,i,j,k}\right)^2 - \sigma_n^2\right] \geq 0, \\ 0 & : \text{otherwise.} \end{cases} \tag{4.10}$$

However, only one observation is for W; thus we have to share statistical information to estimate parameter Θ. Generally, the statistical information should be shared among iid variables. Pixels with small spatial distance and similar real values are iid variables which is a plausible assumption. Then we will discuss how to find pixels with small distance and similar real values in the details of wavelets. Since the following steps are processed in a subband and one scale, we will omit index t for $t = 1,2,3$, k for above notations for the sake of simple explanation.

The similar pixels of $W_{i,j}$ can be selected from a $(2\nu+1)\times(2\nu+1)$ window with measure of similarity

$$\gamma(\omega_{i,j}, \omega_{s,t}) = \left\|\omega^0_{i,j} - \omega^0_{s,t}\right\|_2 \times \phi\left(\omega^0_{i,j}, \omega^0_{s,t}\right), \tag{4.11}$$

where $\omega^0_{i,j}$ and $\omega^0_{s,t}$ are values of (i,j) and (s,t) in the LL subband, respectively; the $\phi(\omega^0_{i,j}, \omega^0_{s,t})$ is a binary value function

$$\phi\left(\omega^0_{i,j}, \omega^0_{s,t}\right) = \begin{cases} 1 : \iota_{i,j} = \iota_{s,t}, \\ 0 : \text{otherwise.} \end{cases} \tag{4.12}$$

Then by using similarity measure defined in (4.11) we can find similar points in a $(2\nu+1)\times(2\nu+1)$ centered at (i,j)

$$\Phi_{i,j}=\left\{(s,t)\mid \gamma\left(\omega_{i,j},\omega_{s,t}\right)\neq 0,\gamma\left(\omega_{i,j},\omega_{s,t}\right)\leq\tau,|s-i|\leq\nu,\left|t-j\right|\leq\nu\right\}. \tag{4.13}$$

Thus the parameter Θ can be estimated using EM algorithm in the collection $\Phi_{i,j}$.

Expectation (E):

$$P_{S_{i,j}|W_{i,j}}\left(m\mid\omega_{i,j}\right)=\frac{P_{S_{i,j}}(m)P_{W_{i,j}|S_{i,j}}\left(\omega_{i,j}\mid m\right)}{\sum_{m=0}^{1}P_{S_{i,j}}(m)P_{W_{i,j}|S_{i,j}}\left(\omega_{i,j}\mid m\right)}. \tag{4.14}$$

Maximization (M):

$$\begin{aligned}P_{S_{i,j}}(m)&=\frac{1}{\left|\Phi_{i,j}\right|}\sum_{s,t,(s,t)\in\phi}P_{S_{s,t}|W_{s,t}}(m\mid\omega_{s,t}),\\ \sigma^2_{i,j,m}&=\frac{1}{\left|\Phi_{i,j}\right|P_{S_{i,j}}(m)}\sum_{s,t,(s,t)\in\phi}\omega^2_{s,t}P_{S_{s,t}|W_{s,t}}(m\mid\omega_{s,t}),\end{aligned} \tag{4.15}$$

where $|\Phi_{i,j}|$ is the number of elements in $\Phi_{i,j}$.

In summary, the steps of denoising for pixels in smooth regions are

(1) *Initialization:* input scale J, dilated singularity prior F whose size is $N\times N$, and ν.

(2) *Build marks for the details of di erent scale using downsample (see Section 3).*

(3) *Find similar pixels for each* $W^t_{i,j,k}$: find similar points using (4.11) and then compute ϕ.

(4) *EM algorithm,* for each $W^t_{i,j,k}$, estimate parameter Θ using EM algorithm in (4.14)-(4.15).

(5) *Repeat Steps* (3)-(4) *until all wavelet coe cients have been processed.*

(6) *Inverse wavelet transform:* obtain denoised results using inverse wavelet transform for all processed coefficients.

(7) *Get final denoised image:* the final denoised image can be got by combining both denoising image together; that is, the real values for pixels near singularities are estimated using the method in Section 4.1, and the values for other pixels are estimated using steps (1)–(6).

5. Experimental Results

In order to compare our method with state-of-the-art methods and denoising methods using wavelets, the proposed method is compared with nonlocal means [3], BM3D [10], BLS-GSM [21], and HMT [22]. Nonlocal means [3] and BM3D [10] are two well-known state-of-the-art methods. That is, nonlocal means and BM3D find similar points using the block

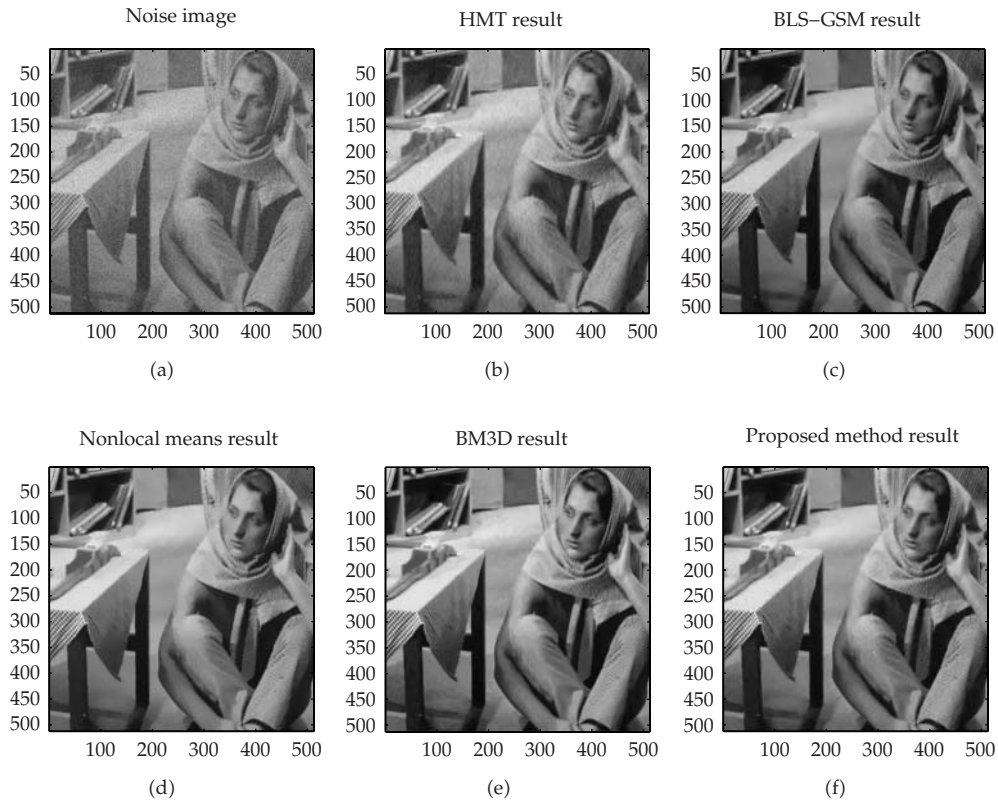

Figure 3: The noisy image is shown in (a) whose standard deviation of noise is 25, and the denoised results using different methods are shown in (b)–(f).

similarity between a pair of pixels, which is proposed firstly in [3]. BM3D designs a complex hierarchical scheme to get very high PSNR, which is usually used as benchmark in many denoising scheme.

Moreover, HMT which is presented in [22] is a famous wavelet denoising method capturing dependency among the details of wavelets using a tree structure while BLS-GSM is a wavelet denoising method using adaptive shrinkage and GMM.

Since the objective for presenting the denoised results of our method only focuses on whether adding singularity prior can improve the denoising performance, we use some simple tools for testing the potential of our new framework. The wavelet used in this paper is one scale "Haar"; similarity threshold τ, ν in $\Phi_{i,j}$ is from 14 to 28 and 3, respectively. Even by using this simple form, the proposed method has good performance both in PSNR and visual quality (see Figure 3). That is, its average PSNR only is 0.2 db lower than the nonlocal means [3]; the average PSNR for lena is 0.4 db lower than the BM3D, and for Barbara, it is 1.4 db lower than BM3D (see Table 1).

Although the values of PSNR for proposed method are lower than both nonlocal means and BM3D, considering both of them being state-of-art denoising methods and their computation complexity, PSNR of proposed method is an acceptable result. Moreover, the main objective for this paper only focuses on designing a new scheme to improve performance in singularity preserving by adding singularity prior in image denoising. We think the experimental results can demonstrate the potential of proposed method. Based on

Table 1: PSNR Comparison of HMT [22], BLS-GSM [21], nonlocal [3], BM3D [10], and the proposed method with simulated gaussian noisy image.

Image	Standard deviation of noise	HMT [22]	BLS-GSM [21]	Nonlocal [3]	BM3D [10]	Proposed method
Lena (512 × 512)	10	34.08	35.23	35.65	35.91	35.51
	15	31.89	33.50	34.12	34.26	33.85
	20	30.41	32.26	32.82	33.05	32.66
	25	29.36	31.30	31.89	32.09	31.71
Barbara (512 × 512)	10	31.62	33.13	34.06	34.93	33.74
	15	29.28	30.76	31.78	33.05	31.67
	20	27.81	29.10	30.41	31.72	30.16
	25	26.61	27.80	29.29	30.64	29.00

this framework, some different methods can be used to improve the performance further. For example, the performance can be improved by processing pixels near singularities using BM3D, using different wavelets, designing different denoising methods for pixels in smooth regions, or by designing more suitable singularity location tools, and so forth. However, discussion about how to improve our framework further is beyond the scope of this paper.

6. Conclusions

In this paper, we propose a new scheme to preserve singularities in image denoising by adding dilated singularities to noisy image. This scheme even that uses simple tools can get satisfying denoising results both in PSNR and visual quality. Since the scheme is based on the fact that pixels near singularities have different statistical properties to the pixels in the smooth regions, it is designed by parting the pixels into two groups using dilated singularity prior and handled pixels with different type labels separately. Dilated singularity prior used to locate the pixels "near" singularities instead of "on" singularities can help us obtain satisfied denoising results and reduce computation complexity. Moreover, denoising in smooth regions can be carried on a smoother version of the noisy image, called mask, since the pixels near singularities have been excluded. Based on the above well-designed framework, the proposed method can obtain good denoising results.

Acknowledgments

This paper is supported by the National Natural Science Foundation of China (no. 60873102), Major State Basic Research Development Program (no. 2010CB732501), and Open Foundation of Visual Computing and Virtual Reality Key Laboratory Of Sichuan Province (no. J2010N03). This work was supported by a grant from the National High Technology Research and Development Program of China (no. 2009AA12Z140).

References

[1] Z. Dengwen and C. Wengang, "Image denoising with an optimal threshold and neighbouring window," *Pattern Recognition Letters*, vol. 29, no. 11, pp. 1694–1697, 2008.

[2] D. Coupier, A. Desolneux, and B. Ycart, "Image denoising by statistical area thresholding," *Journal of Mathematical Imaging and Vision*, vol. 22, no. 2-3, pp. 183–197, 2005.
[3] A. Buades, B. Coll, and J. M. Morel, "Nonlocal image and movie denoising," *International Journal of Computer Vision*, vol. 76, no. 2, pp. 123–139, 2008, Special section: selection of papers for CVPR 2005, Guest Editors: C. Schmid, S. Soatto and C. Tomasi.
[4] Y.-L. Liu, J. Wang, X. Chen, Y.-W. Guo, and Q.-S. Peng, "A robust and fast non-local means algorithm for image denoising," *Journal of Computer Science and Technology*, vol. 23, no. 2, pp. 270–279, 2008.
[5] Z. Ji, Q. Chen, Q.-S. Sun, and D.-S. Xia, "A moment-based nonlocal-means algorithm for image denoising," *Information Processing Letters*, vol. 109, no. 23-24, pp. 1238–1244, 2009.
[6] V. Katkovnik, A. Foi, K. Egiazarian, and J. Astola, "From local kernel to nonlocal multiple-model image denoising," *International Journal of Computer Vision*, vol. 86, no. 1, pp. 1–32, 2010.
[7] A. Buades, B. Coll, and J. M. Morel, "Image denoising methods. A new nonlocal principle," *SIAM Review*, vol. 52, no. 1, pp. 113–147, 2010.
[8] Z. Liao, S. Hu, and W. Chen, "Determining neighborhoods of image pixels automatically for adaptive image denoising using nonlinear time series analysis," *Mathematical Problems in Engineering*, vol. 2010, Article ID 914564, 14 pages, 2010.
[9] Z. Liao, S. Hu, and W. Chen, "Determining neighborhoods of image pixels automatically for adaptive image denoising using nonlinear time series analysis," *Mathematical Problems in Engineering*, vol. 2011, Article ID 914564, 14 pages, 2010.
[10] K. Dabov, A. Foi, V. Katkovnik, and K. Egiazarian, "Image denoising by sparse 3-D transform-domain collaborative filtering," *IEEE Transactions on Image Processing*, vol. 16, no. 8, pp. 2080–2095, 2007.
[11] Z. Liao, S. Hu, M. Li, and W. Chen, "Noise estimation for single-slice sinogram of low-dose X-ray computed tomography using homogenous patch," *Mathematical Problems in Engineering*, vol. 2012, Article ID 696212, 16 pages, 2012.
[12] Z. Liao, S. Hu, D. Sun, and W. Chen, "Enclosed Laplacian operator of nonlinear anisotropic diffusion to preserve singularities and delete isolated points in image smoothing," *Mathematical Problems in Engineering*, vol. 2011, Article ID 749456, 15 pages, 2011.
[13] S. Hu, Z. Liao, D. Sun, and W. Chen, "A numerical method for preserving curve edges in nonlinear anisotropic smoothing," *Mathematical Problems in Engineering*, vol. 2011, Article ID 186507, 14 pages, 2011.
[14] B. Chen and W.-S. Chen, "Noisy image segmentation based on wavelet transform and active contour model," *Applicable Analysis*, vol. 90, no. 8, pp. 1243–1255, 2011.
[15] B. Chen, P. C. Yuen, J. H. Lai, and W. S. Chen, "Image segmentation and selective smoothing based on variational framework," *Journal of Signal Processing Systems*, vol. 54, no. 1–3, pp. 145–158, 2009.
[16] H. C. Hsin, T. Y. Sung, Y. S. Shieh, and C. Cattani, "Adaptive binary arithmetic coder-based image feature and segmentation in the compressed domain," *Mathematical Problems in Engineering*, vol. 2012, 14 pages, 2012.
[17] H. C. Hsin, T. Y. Sung, and Y. S. Shieh, "An adaptive coding pass scanning algorithm for optimal rate control in biomedical images," *Computational and Mathematical Methods in Medicine*, vol. 2012, Article ID 935914, 7 pages, 2012.
[18] M. Li and W. Zhao, "Visiting power laws in cyber-physical networking systems," *Mathematical Problems in Engineering*, vol. 2012, Article ID 302786, 13 pages, 2012.
[19] M. Li, C. Cattani, and S. Y. Chen, "Viewing sea level by a one-dimensional random function with long memory," *Mathematical Problems in Engineering*, vol. 2011, Article ID 654284, 13 pages, 2011.
[20] M. Li, "Fractal time series—a tutorial review," *Mathematical Problems in Engineering*, vol. 2010, Article ID 157264, 26 pages, 2010.
[21] J. Portilla, V. Strela, M. J. Wainwright, and E. P. Simoncelli, "Image denoising using scale mixtures of Gaussians in the wavelet domain," *IEEE Transactions on Image Processing*, vol. 12, no. 11, pp. 1338–1351, 2003.
[22] J. K. Romberg, H. Choi, and R. G. Baraniuk, "Bayesian tree-structured image modeling using wavelet-domain hidden Markov models," in *Mathematical Modeling, Bayesian Estimation, and Inverse Problems*, vol. 3816 of *Proceedings of SPIE*, pp. 31–44, Denver, Colo, USA, July 1999.
[23] H. Yu, L. Zhao, and H. Wang, "Image denoising using trivariate shrinkage filter in the wavelet domain and joint bilateral filter in the spatial domain," *IEEE Transactions on Image Processing*, vol. 18, no. 10, pp. 2364–2369, 2009.
[24] S. Y. Chen, H. Tong, and C. Cattani, "Markov models for image labeling," *Mathematical Problems in Engineering*, vol. 2012, Article ID 814356, 18 pages, 2012.

[25] S. Y. Chen, H. Tong, Z. Wang, S. Liu, M. Li, and B. Zhang, "Improved generalized belief propagation for vision processing," *Mathematical Problems in Engineering*, vol. 2011, Article ID 416963, 12 pages, 2011.

[26] Z. Liao and Y. Y. Tang, "Signal denoising using wavelets and block hidden Markov model," *International Journal of Pattern Recognition and Artificial Intelligence*, vol. 19, no. 5, pp. 681–700, 2005.

Hindawi Publishing Corporation
Mathematical Problems in Engineering
Volume 2012, Article ID 235929, 16 pages
doi:10.1155/2012/235929

Research Article

Design of Deep Belief Networks for Short-Term Prediction of Drought Index Using Data in the Huaihe River Basin

Junfei Chen,[1,2] Qiongji Jin,[1,2] and Jing Chao[3]

[1] *State Key Laboratory of Hydrology-Water Resources and Hydraulic Engineering, Hohai University, Nanjing 210098, China*
[2] *Business School, Hohai University, Nanjing 210098, China*
[3] *State Key Laboratory for Novel Software Technology, Nanjing University, Nanjing 210093, China*

Correspondence should be addressed to Junfei Chen, chenjunfei@yahoo.com.cn

Received 18 January 2012; Revised 20 February 2012; Accepted 21 February 2012

Academic Editor: Ming Li

With the global climate change, drought disasters occur frequently. Drought prediction is an important content for drought disaster management, planning and management of water resource systems of a river basin. In this study, a short-term drought prediction model based on deep belief networks (DBNs) is proposed to predict the time series of different time-scale standardized precipitation index (SPI). The DBN model is applied to predict the drought time series in the Huaihe River Basin, China. Compared with BP neural network, the DBN-based drought prediction model has shown better predictive skills than the BP neural network for the different time-scale SPI. This research can improve drought prediction technology and be helpful for water resources managers and decision makers in managing drought disasters.

1. Introduction

With the global environmental degradation and water resource shortages, droughts are becoming increasingly eye catching and have aroused the attention of many countries and regions. Drought is considered the most complex but least understood of all natural hazards, affecting more people than any other disasters [1]. In recent years, drought disasters continuously happened and caused serious impact on production and life in China. The losses caused by drought ranked the first in all natural hazards in China [2]. For example, in the extreme drought in Southwest China during 2009 to 2010, five provinces and cities suffered droughts which have seriously threatened people's life and economic production activities. The Chinese northern region also suffered severe drought in 2011. Long and

severe droughts have direct impacts on industrial production, people's lives, and ecological environment and even lead to desertification and other natural disasters. Droughts have become serious constraints to the sustainable development of Chinese society and economy [3, 4]. Drought prediction is an important content in the planning and management of water resource systems of a river basin. How to effectively monitor and forecast droughts has become the research focus, which can help to take effective strategies and measures to mitigate the damages of droughts.

There are some forecasting methods used in drought prediction fields. Lohani and Loganathan used a nonhomogeneous Markov chain model to characterize the stochastic behavior of drought, and an early-warning system in the form of a decision tree enumerating is proposed for drought management [5]. Jia et al. established a grey-time series combined method (GTCM) to predict annual precipitation of Huangcun Meteorological Observation, Daxing county, Beijing [6]. Yang et al. proposed a chaotic Bayesian method based on multiple criteria decision making to forecast nonlinear hydrological time series, which can be applied in drought forecast [7]. The predictability of drought severity from spatiotemporal varying indices of large-scale climate phenomena was studied by integrating linear and nonlinear statistical data models, and the model was used for the Murray-Darling Basin (MDB) in Australia [8]. Meteorological droughts were characterized using the standardized precipitation index (SPI) developed by McKee et al. [9]. Drought classes based on standardized precipitation index (SPI) values were derived by Markov chain model in Alentejo, Southern Portugal [10]. Peng et al. used weighted Markov chain to predict the future drought index, weighted by the standardized self-coefficients. The drought indexes of Nanjing city from 1959 to 2004 were a specific application with this method and satisfactory results were obtained [11]. SPI is calculated from monthly precipitation data collected from 36 weather stations in Guanzhong plain and Weibei tablelands, and the Markov chain model with weights was applied to predict SPI drought intensity by using standardized self-coefficients as weights [12]. The vegetation temperature condition index (VTCI) based on remote sensing data is used for drought monitoring. The ARIMA models were developed to simulate the VTCI series and be used in Guanzhong Plain in China [13]. The loglinear modeling for three-dimensional contingency tables was used for short-term prediction of drought severity classes. The results show that three-dimensional loglinear modeling of monthly drought class transitions is able to capture the trends for both drought initiation, establishment, and drought dissipation [14]. Mishra and Desai compared linear stochastic model (ARIMA/SARIMA), recursive multistep neural network (RMSNN), and direct multisteps neural network (DMSNN) for drought forecasting by using standardized precipitation index (SPI) series as drought index in the Kansabati River Basin in India [15]. Traditionally, forecasting research and practice has been dominated by conventional statistical methods. Recently, the study of long range or long memory has received many attentions in forecasting. Hurst developed a test for long-range dependence and found significant long-term correlations among fluctuations in the Nile's outflows and described these correlations in terms of power laws [16]. Mathematical models with long-range dependence were first introduced to statistics by Mandelbrot and his workers [17–19]. Long-range dependence is often encountered in practice, not only in hydrology, geophysics, and finance, but also in all fields of statistical applications [20–24]. Pelletier and Turcotte present power spectra of time-series data for tree ring width chronologies, atmospheric temperatures, river discharges, and precipitation averaged over hundreds of stations worldwide. They thought that long-range persistence can have a dramatic effect on the likelihood of severe hydrologic drought and computed recurrence intervals for droughts of different magnitudes,

durations, and coefficients of variation [25]. Radziejewski and Kundzewicz computed fractal dimensions of crossings of Warta flows by using a novel variant of the box-counting method, and spectral properties are compared between the time series of flows [26]. Li et al. computed long-range dependence (LRD) of sea level and thought that sea level is multiscaled and heavy tailed [27].

Recently, deep belief networks (DBNs) are proposed by Hinton. The DBN is a probabilistic generative model, the bottom layer is observable, and the multiple hidden layers are created by stacking multiple restricted Boltzmann machines (RBMs) on top of each other [28]. Hinton et al. derived a way to perform fast, greedy learning of deep belief networks (DBN) one layer at a time, with the top two layers forming an undirected bipartite graph [29]. DBNs and restricted Boltzmann machines (RBMs) have already been applied successfully to solve many problems [30]. Lee et al. present a convolutional deep belief networks and are used to scale the realistic image sizes [31]. A novel text classification approach based on deep belief networks is proposed, and the proposed method outperforms traditional classifier based on support vector machine [32]. Zhou et al. present a discriminative deep belief networks (DDBNs) to address the image classification problem with limited labeled data. Experiments on the artificial dataset and real image datasets show that DDBN outperforms most semisupervised algorithms [33]. Chao et al. proposed a deep belief network (DBN) to forecast the foreign exchange rate. In their experiments, both British pound/US dollar and Indian rupee/US dollar exchange rates are forecasted, and the results show that deep belief networks (DBNs) achieve better performance than feed-forward neural networks [34]. Deep learning techniques have also been shown to perform significantly better than other techniques for problems such as image classification and handwriting analysis [31].

In this paper, we propose a deep belief network (DBN) for short-term prediction of drought index. The aims of this study are to present and evaluate the performance of DBN model as a drought prediction method. This model was applied to forecast drought index using standardized precipitation index (SPI) series in the Huaihe River Basin, China. The results are compared and analyzed with BP neural network for demonstration of the validity of the DBN model. The remainder of the paper is organized as follows. In Section 2, the standardized precipitation index (SPI) and BP neural network are introduced, and the deep belief networks (DBN) model for drought index prediction is proposed. In Section 3, a case is studied, and discussions are arranged. Finally in Section 4, the main conclusions and a discussion for future work are given.

2. Methodology

2.1. Standardized Precipitation Index (SPI)

The SPI was formulated by Mckee et al. of the Colorado Climate Center in 1993. The purpose is to assign a single numeric value to the precipitation which can be compared across regions with markedly different climates [11]. The SPI is an index based on the probability of precipitation for any time scale. Technically, the SPI is the number of standard deviations that the observed value would deviate from the long-term mean, for a normally distributed random variable. The SPI can be computed for different time scales and can provide early warning of drought and help assess drought severity. The SPI is a probability index that considers only precipitation, while Palmer's indices are water balance indices that consider water supply (precipitation), demand (evapotranspiration), and loss (runoff). So, SPI is less

complex than PDSI [35]. Now, the standardized precipitation index (SPI) is widely accepted and used throughout the world [36]. The computing procedure of the SPI value is as follows [37, 38].

Assuming that a precipitation series of some time scale is x, then its probability density function of Γ distribution is expressed as

$$f(x) = \frac{1}{\beta^{\gamma}\Gamma(\gamma)} x^{\gamma-1} e^{-x/\beta}, \quad x > 0, \tag{2.1}$$

where $\Gamma(\gamma)$ is a gamma function and $\Gamma(\gamma) = \int_0^{\infty} x^{\gamma-1} e^{-x} dx$. β and γ are the shape parameter and the scale parameter, respectively, and $\beta > 0$, $\gamma > 0$. The precipitation value $x > 0$.

The shape and scale parameters can be estimated by the maximum likelihood method as follows:

$$\begin{aligned} \widehat{\gamma} &= \frac{1 + \sqrt{1 + 4A/3}}{4A}, \\ \widehat{\beta} &= \frac{\overline{x}}{\widehat{\gamma}}, \end{aligned} \tag{2.2}$$

where $A = \ln(\overline{x}) - (1/n) \sum_{i=1}^{n} \ln x_i$, n stands for the number of precipitation observations, x_i are the samples of the precipitation data, and $\overline{x}$ is the mean of these samples.

The gamma distribution is not defined for $x = 0$; however, the actual precipitation can be 0. Therefore, cumulative probability of precipitation for a certain time scale can be calculated using the following formula [38, 39]:

$$H(x) = u + (1 - u)F(x), \tag{2.3}$$

where $F(x) = (1/\Gamma(\widehat{\gamma})) \int_0^x t^{\widehat{\gamma}-1} e^{-t} dt$ and $t = x/\widehat{\beta}$. u is the probability of zero precipitation and can be calculated as m/n. m is the total number of precipitation series, and n is the number of zeros in the precipitation series.

The cumulative probability, $H(x)$, is then transformed to the standard normal random variable with mean as zero and variance as one. Following Edwards and Mckee [40] and Hughes and Saunders [41], SPI can be obtained as follows:

$$\mathrm{SPI} = \begin{cases} -\left(t - \dfrac{c_0 + c_1 t + c_2 t^2}{1 + d_1 t + d_2 t^2 + d_3 t^3} \right) & \text{for } 0 < H(x) \leq 0.5, \\ t - \dfrac{c_0 + c_1 t + c_2 t^2}{1 + d_1 t + d_2 t^2 + d_3 t^3} & \text{for } 0.5 < H(x) < 1, \end{cases} \tag{2.4}$$

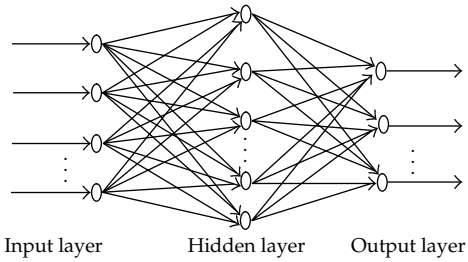

Figure 1: The structure of BP neural network.

where

$$t = \begin{cases} \sqrt{\ln\left(\dfrac{1}{(H^2(x))}\right)} & \text{for } 0 < H(x) \leq 0.5, \\ \sqrt{\ln\left(\dfrac{1}{(1-H(x))^2}\right)} & \text{for } 0.5 < H(x) < 1. \end{cases} \tag{2.5}$$

In (2.4), the c_i and d_i are parameters during the computing process and $c_0 = 2.515517$, $c_1 = 0.802853$, $c_2 = 0.010328$, $d_1 = 1.432788$, $d_2 = 0.189269$, and $d_3 = 0.001308$.

According to SPI, drought can be classified. When the value of SPI is continuously negative, a drought event occurs. The event ends when the SPI becomes positive.

2.2. Backpropagation Neural Network (BPNN)

The BP neural network is a kind of multilayer feed-forward networks with training by error backpropagation algorithm [42]. It is a kind of supervised learning neural network, the principle behind which involves using the steepest gradient descent method to reach any small approximation. A general model of the BP neural network has a structure as described in Figure 1.

In Figure 1, there are three layers contained in BP: input layer, hidden layer, and output layer. Two nodes of each adjacent layer are directly connected, which is called a link. Each link has a weighted value presenting the relational degree between two nodes. The algorithm of BP neural network is to input the training samples from the input layer and then obtain the calculation output through the operation of corresponding thresholds, functions, and connection weights between nodes [42, 43]. The node function has usually selected S-type function as follows:

$$f(x) = \frac{1}{1 + e^{-x/Q}}. \tag{2.6}$$

The Q in the equation is a Sigmoid parameter which is the form of adjusted activation function, and the specific algorithm is introduced in [44]. The output error is obtained by the comparison between the calculation output and the sample output. If the error does not meet the requirements, the network weights and thresholds usually are adjusted along the

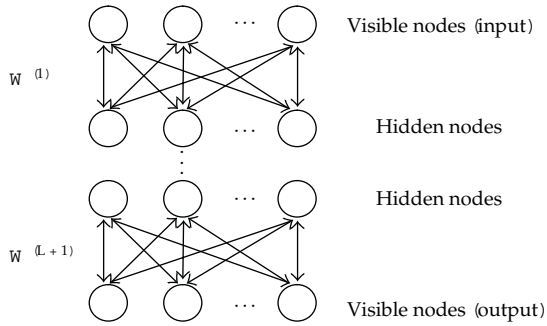

Figure 2: A DBN structure with L hidden layers.

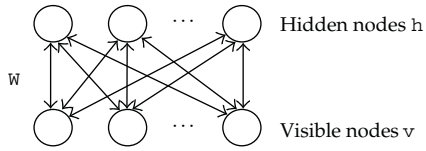

Figure 3: A RBM structure.

negative gradient direction of network error and finally reach the minimum network error [45]. The number of hidden layer nodes is firstly determined by employing an empirical formula in the design stage and finally adjusted by comparing the efficiencies of different numbers of hidden layer nodes in neural network training stage [46].

2.3. Deep Belief Networks

A deep belief network (DBN) is a generative model with an input layer and an output layer, separated by many layers of hidden stochastic units. The multilayer neural network can efficiently be trained by composing RBMs using the feature activations of one layer as the training data for the next. Figure 2 shows an example of a DBN structure [28].

Usually a DBN consists of two kinds of different layers. They are visible layer and hidden layer. Visible layers contain input nodes and output nodes, and hidden layers contain hidden nodes. Hinton et al. proposed a greedy layerwise unsupervised learning algorithm for DBNs which is based on sequence training with restricted Boltzmann machines (RBMs) [28, 34]. A restricted Boltzmann machine (RBM) is composed of two different layers of units, with weighted connection between them. It consists of one layer of visible nodes (neurons) and one layer of hidden units. Figure 3 shows an RBM structure. Nodes in each layer have no connections between them and are connected to all other units in another layer. Connections between nodes are bidirectional and symmetric. Restricted Boltzmann machines (RBMs) have been used as generative models of many different types of data including labeled or unlabeled images windows of mel-cepstral coefficients that represent speech, and so on. Their most important use is as learning modules that are composed to form deep belief nets [28].

Let v_i and h_j represent the states of visible node i and hidden node j, respectively. For binary state nodes, that is, v_i and $h_j \in \{0,1\}$, the state of h_j is set to 1 with probabilities [47]:

$$p_{h_j} = p(h_j = 1 \mid v) = \sigma\left(b_j + \sum_i w_{ij} v_i\right), \tag{2.7}$$

where $\sigma(x)$ is the logistic sigmoid function $1/(1+\exp(-x))$, b_j is the bias of j, and v_i is the binary state. w_{ij} is the weight between v_i and h_j. After binary states have been chosen for the hidden units, then set the state of v_i to be 1 with probability

$$p_{v_i} = p(v_i = 1 \mid h) = \sigma\left(b_i + \sum_j w_{ij} h_j\right). \tag{2.8}$$

The training process of the RBM is described as follows. Firstly, a training sample is presented to the visible nodes, and the $\{v_i\}$ is obtained. Then the hidden nodes state that $\{h_j\}$ are sampled according to probabilities in (2.7). This process is repeated once more to update the visible and then the hidden nodes, and the one-step "reconstructed" states v_i' and h_j' are obtained. The update in a weight is given as follows:

$$\Delta w_{ij} = \eta\left(\langle v_i h_j \rangle - \left\langle v_i' h_j' \right\rangle\right), \tag{2.9}$$

where η is the learning rate, and $\langle \cdot \rangle$ refers to the expectation of the training data.

A continuous restricted Boltzmann machine (CRBM) is considered by Chao et al. [34] and Chen and Murray [48]. Suppose the inputs nodes with state $\{s_i\}$, then the output nodes s_j can be computed as follows:

$$s_j = \varphi_j\left(\sum_i w_{ij} s_i + \sigma \cdot N_j(0,1)\right), \tag{2.10}$$

where $\varphi_j(x)$ is a sigmoid function with lower and upper asymptotes at θ_L and θ_H, $\varphi_j(x_j) = \theta_L + (\theta_H - \theta_L)\cdot(1/(1+e^{-a_j x_j}))$. $N_j(0,1)$ represents a unit Gaussian. σ is a constant, and parameter a_j is a "noise-control" parameter which controls the slope of the sigmoid function [49]. The update equations for w_{ij} and a_j are

$$\begin{aligned} \Delta w_{ij} &= \eta_w\left(\langle s_i s_j \rangle - \left\langle s_i' s_j' \right\rangle\right), \\ \Delta a_j &= \frac{\eta_a}{a_j^2}\left(\left\langle s_j^2 \right\rangle - \left\langle s_j'^2 \right\rangle\right), \end{aligned} \tag{2.11}$$

where η_w and η_a represent the learning rates, s_j' denotes the one-step sampled state of node j, and $\langle \cdot \rangle$ refers to the expectation of the training data. We train sequentially as many RBMs

as the number of hidden layers in the DBN to construct a DBN model. We adopt the learning algorithm according to [28, 34, 50]. The method of stacking CRBMs makes it possible to train many layers of hidden units efficiently and is one of the most common deep learning strategies. As each new layer is added, the overall generative model gets better. This process of learning is continued until a prescribed number of hidden layers in the DBN have been trained. In order to apply DBN model to drought prediction using SPI series, the DBN model with two hidden layers is selected in this paper. The main steps using DBN model for drought index prediction are as follows.

Step 1. Compute the different time-scale SPI series by precipitation data.

The different time-scale SPI series are computed by precipitation data by the description method in Section 2.1, and different time-scale SPI series are obtained.

Step 2. Normalize the SPI series by formula (2.12) as follows:

$$\mathrm{SPI}' = \frac{\mathrm{SPI} - \mathrm{SPI}_{\min}}{\mathrm{SPI}_{\max} - \mathrm{SPI}_{\min}}, \tag{2.12}$$

where SPI' and SPI represent the normalized and original SPI data, respectively. The $\mathrm{SPI}_{\min}$ represents the minimum value of the corresponding SPI series, and $\mathrm{SPI}_{\max}$ represents the maximum value of the corresponding SPI series.

Step 3. Determine the optimal network structure by experiments.

Determine the number of input nodes, the numbers of the first hidden and second hidden nodes, and weight coefficients by learning algorithm. The data of SPI series are split into two parts. The first part is used as a training sample, and the rest is used as a testing sample. During the training process, the network structures for different time-scale SPI series are determined according to the criterion of smallest RMSE and MAE.

Step 4. Forecast drought index based on DBN model and results analysis.

3. Case Study

3.1. Experimental Design

We use four data sets of precipitation in the experiments. Four hydrologic stations were considered in this study. They are Bengbu, Fuyang, Xuchang, and Zhumadian in Huaihe River Basin which is located in the eastern part of China. Data sets contain monthly precipitation during 1958–2006. These data are used to calculate four different time scales of standardized precipitation index (SPI), that is, SPI3, SPI6, SPI9, and SPI12. Taking the SPI3 as an example, all of the SPI sets are divided into two parts. The observations during 1958–1999 are as training set, and the remaining observations during 2000–2006 are as testing set.

Our purpose of this research is to explore if the DBN model can be used well in drought prediction by using the monthly rainfall data of four hydrologic stations from January 1958 to 2006 to calculate different time scales of SPI in Huaihe River Basin.

Table 1: The CRBM results of Bengbu SPI3.

Number of input nodes	Number of hidden nodes	RMSE	MAE	Number of input nodes	Number of hidden nodes	RMSE	MAE
2	5	0.1270	0.0980	7	5	0.1107	0.0869
	10	0.1276	0.0983		10	0.1114	0.0877
	15	0.1306	0.1002		15	0.1113	0.0878
	20	0.1276	0.0983		20	0.1113	0.0877
	25	0.1274	0.0982		25	0.1123	0.0885
3	5	0.1270	0.0987	8	5	0.1113	0.0865
	10	0.1293	0.1000		10	0.1120	0.0871
	15	0.1272	0.0988		15	0.1115	0.0866
	20	0.1274	0.0989		20	0.1117	0.0869
	25	0.1273	0.0988		25	0.1097	0.0864
4	5	0.1292	0.0993	9	5	0.1105	0.0863
	10	0.1291	0.0990		10	0.1117	0.0876
	15	0.1283	0.0988		15	0.1119	0.0876
	20	0.1301	0.0995		20	0.1120	0.0876
	25	0.1286	0.0992		25	0.1181	0.0945
5	5	0.1225	0.0929	10	5	0.1112	0.0874
	10	0.1230	0.0927		10	0.1116	0.0875
	15	0.1235	0.0931		15	0.1123	0.0884
	20	0.1232	0.0928		20	0.1115	0.0885
	25	0.1248	0.0939		25	0.1121	0.0886
6	5	0.1235	0.0931				
	10	0.1239	0.0930				
	15	0.1236	0.0934				
	20	0.1235	0.0930				
	25	0.1244	0.0942				

In this paper, we use two criteria to evaluate the performance of a DBN in drought forecasting. They are root mean square error (RMSE) and mean absolute error (MAE). The formulas of this two predictive accuracy measures are listed as follows:

$$\begin{aligned} \text{RMSE} &= \sqrt{\frac{\sum_{i=1}^{T}\left(y_i - y_i'\right)^2}{T}}, \\ \text{MAE} &= \frac{\sum_{i=1}^{T}\left|y_i - y_i'\right|}{T}, \end{aligned} \tag{3.1}$$

where y_i is the observations of SPI, y_i' is the predicted SPI values, and T is the total number of predictions.

Table 2: The DBN results of Bengbu SPI3.

Number of input nodes	Number of first hidden nodes	Number of second hidden nodes	RMSE	MAE	Number of input nodes	Number of first hidden nodes	Number of second hidden nodes	RMSE	MAE
		5	0.6924	0.5497			5	0.6905	0.5510
		10	0.6911	0.5567			10	0.6842	0.5425
	5	15	0.7103	0.5787		5	15	0.6858	0.5473
		20	0.7006	0.5712			20	0.7138	0.5860
		25	0.8051	0.6858			25	0.7068	0.5769
		5	0.7048	0.5702			5	0.6881	0.5472
		10	0.6911	0.5506			10	0.6899	0.5479
	10	15	0.6962	0.5616		10	15	0.6954	0.5548
		20	0.7147	0.5874			20	0.7090	0.5775
		25	0.7749	0.6606			25	0.7032	0.5805
		5	0.6852	0.5453			5	0.6930	0.5545
		10	0.6926	0.5596			10	0.7165	0.5887
8	15	15	0.6969	0.5636	9	15	15	0.7300	0.6106
		20	0.7265	0.6113			20	0.7218	0.6070
		25	0.7316	0.6236			25	0.7488	0.6375
		5	0.7224	0.6001			5	0.6915	0.5516
		10	0.6923	0.5525			10	0.6962	0.5592
	20	15	0.7152	0.5940		20	15	0.7407	0.6245
		20	0.6955	0.5560			20	0.7140	0.5885
		25	0.7794	0.6679			25	0.7309	0.6136
		5	0.6935	0.5570			5	0.6919	0.5563
		10	0.6877	0.5496			10	0.7013	0.5637
	25	15	0.7037	0.5761		25	15	0.6949	0.5617
		20	0.7470	0.6322			20	0.7669	0.6566
		25	0.7174	0.5868			25	0.7214	0.6104

We use the learning sample to find an optimal network structure for these four different time-scales SPI. Taking the SPI3 of Bengbu data as an example, we explain how to determine an optimal network structure. In our experiment, the DBN has two hidden layers. The key for our experiment is to determine the numbers of input and hidden nodes. We determine the optimal number of input nodes and two hidden layer nodes by experiments. On one hand, neural networks with too few hidden nodes may not have enough power to model the data. On the other hand, neural networks with too many hidden nodes may lead to overfitting problems and finally result in poor forecasting performance [30]. In our experiment, the number of input nodes and hidden nodes of the DBN network structures is selected by experimentation. The number of input nodes ranges from 2 to 10. Because the forecasting performance of neural networks is not as sensitive to the number of hidden nodes as to the number of input nodes, so the number of hidden nodes is selected by five levels, that is, 5, 10, 15, 20, and 25. We did the experiment for 45 times to find the optimal structure of DBN. We compared the RMSE and MAE, and we determined the number of every layer node. The results are shown in Table 1.

Table 3: The optimal network structures of DBN.

SPI series	Station	Number of input nodes	Number of first hidden nodes	Number of second hidden nodes
SPI3	Bengbu	9	5	10
	Fuyang	8	20	15
	Xuchang	8	20	15
	Zhumadian	8	20	15
SPI6	Bengbu	10	5	10
	Fuyang	7	5	5
	Xuchang	7	5	5
	Zhumadian	8	5	5
SPI9	Bengbu	10	5	5
	Fuyang	7	5	5
	Xuchang	6	5	5
	Zhumadian	10	5	15
SPI12	Bengbu	8	5	5
	Fuyang	10	5	5
	Xuchang	9	5	5
	Zhumadian	10	5	5

In Table 1, we find when the CRBM structure is 8-25, the RMSE is the smallest, and when the CRBM structure is 9-5, the MAE is the smallest. We can find that the most optimal structure is most likely to appear when the number of input nodes is 8 or 9. Then we do the next step. The results of the next step have just been shown in Table 2. We can find that the best DBN structure is 9-5-10-1. That is, the DBN has 9 input nodes, 5 nodes in the first hidden layer, 10 nodes in the second hidden layer, and 1 output node, and the RMSE and MAE are the smallest of all.

According to above processes, we can determine the optimal structures of DBN for the four stations and different time-scale SPI series. We try nine levels of input nodes from 2 to 10 in combination with five hidden nodes (5, 10, 15, 20, and 25) for CRBM training. We can find the optimal network structure in a similar way for all of the SPI series. The optimal network structures of DBN for the different four stations and different time-scale SPI series are shown in Table 3.

3.2. Results and Discussion

In this paper, the DBN and BP neural network model are used for forecasting the different time-scale SPI series, and the results of their prediction are compared. The quantitative performance evaluations of DBN and BP neural network are carried out by using RMSE and MAE. The results are shown in Table 4.

We can find that the prediction errors of the DBN are smaller than the prediction errors of BP neural network in Table 4. The errors results demonstrate that DBN model is suitable for the drought prediction in the Huaihe River Basin. DBN model can obtain smaller RMSE and MAE compared with BP neural network. With the change of the time scale of SPI from little to large, the RMSE and MAE become smaller. That is, the fitting

Table 4: The comparison of RMSE and MAE between BP and DBN.

Station	Model	Errors	SPI3	SPI6	SPI9	SPI12
Bengbu	DBN	RMSE	0.6842	0.6592	0.5355	0.4797
		MAE	0.5425	0.5274	0.3959	0.3553
	BP neural network	RMSE	0.9897	0.6987	0.5899	0.5809
		MAE	0.7564	0.5523	0.4157	0.4532
Fuyang	DBN	RMSE	0.8112	0.6634	0.5590	0.5620
		MAE	0.6527	0.4812	0.3923	0.4282
	BP neural network	RMSE	1.0876	0.8022	0.8032	0.5773
		MAE	0.8202	0.5867	0.5509	0.4080
Xuchang	DBN	RMSE	0.7258	0.5764	0.5262	0.4236
		MAE	0.5714	0.4342	0.3880	0.2976
	BP neural network	RMSE	0.8223	0.6938	0.6783	0.4454
		MAE	0.6786	0.5411	0.4725	0.3268
Zhumadian	DBN	RMSE	0.7794	0.6239	0.5686	0.4990
		MAE	0.6276	0.4792	0.3811	0.3504
	BP neural network	RMSE	1.0780	0.7956	0.7996	0.4474
		MAE	0.8147	0.6336	0.5365	0.3144

results of SPI12 are better than SPI9, SPI9 is better than SPI6, and SPI6 is better than SPI3. In a word, DBN has a higher precision in drought prediction based on SPI than BP neural network.

Figure 4 shows the test results of SPI3, SPI6, SPI9, and SPI12 of Bengbu station. It is obvious that the prediction values of different time-scale SPI series are very close to the actual ones. The comparison results between observations and predicted data of Fuyang station, Xuchang station, and Zhumadian station are shown in Figures 5, 6, and 7 using DBN and BP neural network for SPI6 series.

From Figures 5, 6, and 7, the predicted data of SPI based on DBN model agreed with observations very well. The majority of DBN outputs are nearer to the real SPI values than those of BP neural network. The results show that the DBN model is appropriate for short term of drought index and can obtain higher precision.

4. Conclusion

In this paper, we proposed a deep belief network (DBN) for short-time drought index prediction. The forecasting model based on DBN is used to forecast different time-scale SPI series of four stations in Huaihe River Basin, China. Compared with the BP neural network, the DBN-based model is more reliable and efficient for short-term prediction of drought index. The errors results show that the DBN model outperforms the BP neural network. This study shows that the DBN model is a useful tool for drought prediction. Due to the complexity of the formation mechanism of the drought disasters and the long memory of hydrological data, some new method which can deal with long-range dependence will be

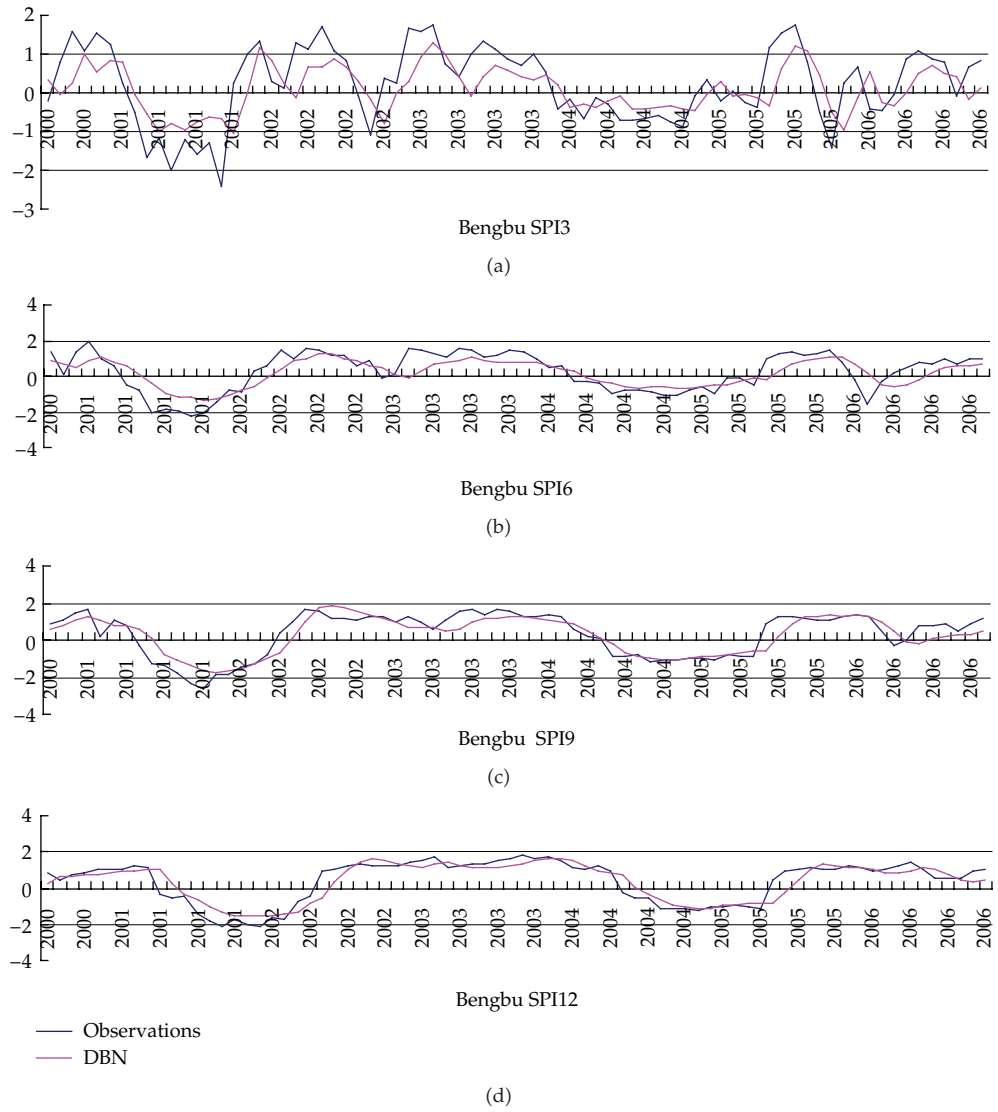

Figure 4: Results comparison between observations and predicted data using DBN for different time-scale SPI series of Bengbu station.

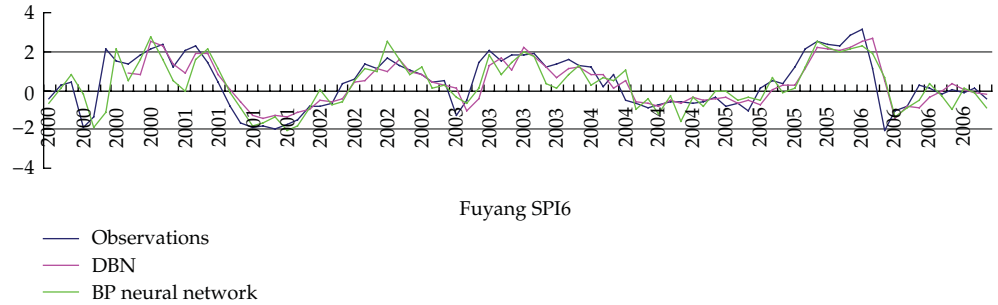

Figure 5: A comparison of DBN and BP neural network for SPI6 series of Fuyang station.

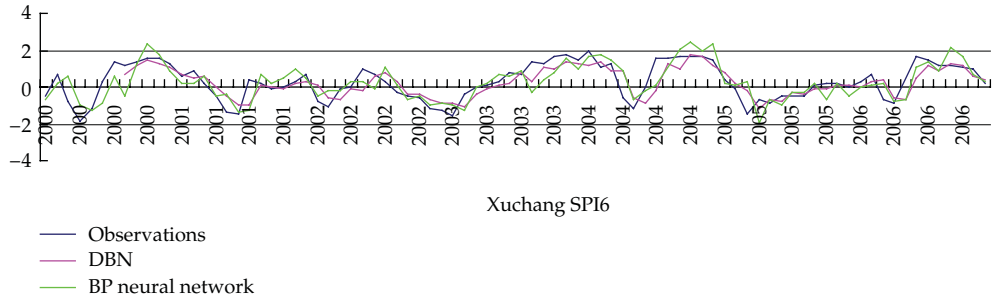

Figure 6: A comparison of DBN and BP neural network for SPI6 series of Xuchang station.

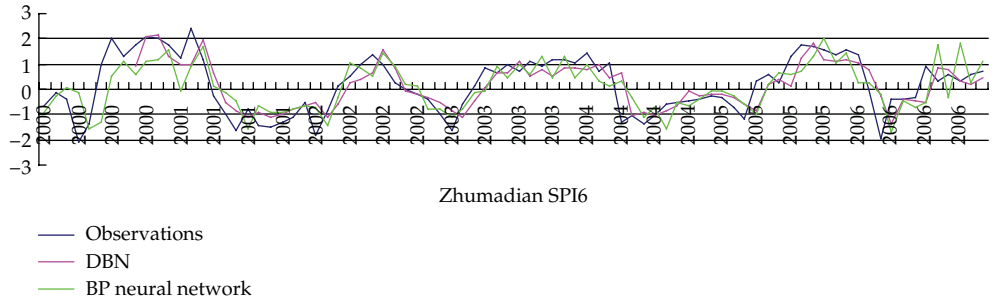

Figure 7: A Comparison of DBN and BP neural network for SPI6 series of Zhumadian station.

thought about, and further studies are needed to deal with more complex situations for drought prediction.

Acknowledgments

This work was supported partially by the National Society Science Fund of China (09CJY020), the National Nature Science Foundation of China (90924027), the Special Fund of State Key Laboratory of Hydrology-Water Resources and Hydraulic Engineering, China (2011585312), Public-Interest Industry Project of Chinese Ministry of Water Resources (200801027), the Science and Technology Projects of Yunnan Province (2010CA013), the Fundamental Research Funds for the Central Universities of Hohai University, and 2010 Jiangsu Province Qing Lan Project.

References

[1] D. A. Wilhite, "Drought as a natural hazard: concepts and definitions," in *Drought: A Global Assessment*, D. A. Wilhite, Ed., Routledge Hazards and Disasters Series, Routledge, New York, NY, USA, 2000.

[2] G. Hagman, *Prevention Better than Cure: Report on Human and Environmental Disasters in the Third World*, Swedish Red Cross, Stockholm, Sweden, 1984.

[3] L. C. Song, Z. Y. Deng, and A. X. Dong, *Drought Disaster*, China Meteorological Press, Beijing, China, 2003.

[4] R. H. Huang, C. Y. Li, and S. W. Wang, *Climatic Disasters*, China Meteorological Press, Beijing, China, 2003.

[5] V. K. Lohani and G. V. Loganathan, "An early warning system for drought management using the Palmer Drought Index," *Journal of the American Water Resources Association*, vol. 33, no. 6, pp. 1375–1386, 1997.

[6] H. F. Jia, Y. Q. Zheng, Y. Y. Ding, and B. Cao, "Grey-time series combined forecasting model and its application in annual precipitation," *Systems Engineering-Theory & Practice*, vol. 8, pp. 122–126, 1998.

[7] X. H. Yang, D. X. She, Z. F. Yang, Q. H. Tang, and J. Q. Li, "Chaotic bayesian method based on multiple criteria decision making (MCDM) for forecasting nonlinear hydrological time series," *International Journal of Nonlinear Sciences and Numerical Simulation*, vol. 10, no. 11-12, pp. 1595–1610, 2009.

[8] A. P. Barros and G. J. Bowden, "Toward long-lead operational forecasts of drought: an experimental study in the Murray-Darling River Basin," *Journal of Hydrology*, vol. 357, no. 3-4, pp. 349–367, 2008.

[9] T. B. McKee, N. J. Doeskin,, and J. Kleist, "The relationship of drought frequency and duration to time scales," in *Proceedings of the 8th Conference on Applied Climatology*, pp. 179–184, American Meteorological Society, Boston, Mass, USA, 1993.

[10] A. A. Paulo, E. Ferreira, C. Coelho, and L. S. Pereira, "Drought class transition analysis through Markov and Loglinear models, an approach to early warning," *Agricultural Water Management*, vol. 77, no. 1–3, pp. 59–81, 2005.

[11] S. Z. Peng, Z. Wei, C. Y. Dou, and J. Z. Xu, "Model for evaluating the regional drought index with the weighted Markov chain and its application," *Xitong Gongcheng Lilun yu Shijian/System Engineering Theory and Practice*, vol. 29, no. 9, pp. 173–178, 2009.

[12] Y. J. Wang, J. M. Liu, P. X. Wang et al., "Prediction of drought occurrence based on the standardized precipitation index and the Markov chain model with weights," *Agricultural Research in the Arid Areas*, vol. 5, pp. 198–203, 2007.

[13] P. Han, P. X. Wang, S. Y. Zhang, and D. H. Zhu, "Drought forecasting based on the remote sensing data using ARIMA models," *Mathematical and Computer Modelling*, vol. 51, no. 11-12, pp. 1398–1403, 2010.

[14] E. E. Moreira, C. A. Coelho, A. A. Paulo, L. S. Pereira, and J. T. Mexia, "SPI-based drought category prediction using loglinear models," *Journal of Hydrology*, vol. 354, no. 1–4, pp. 116–130, 2008.

[15] A. K. Mishra and V. R. Desai, "Drought forecasting using feed-forward recursive neural network," *Ecological Modelling*, vol. 198, no. 1-2, pp. 127–138, 2006.

[16] H. E. Hurst, "Long term storage capacity of reservoirs," *Transactions of the American Society of Civil Engineers*, vol. 116, pp. 770–799, 1951.

[17] B. B. Mandelbrot and J. R. Wallis, "Noah, Joseph and operational hydrology," *Water Resource Research*, vol. 4, pp. 908–918, 1968.

[18] B. B. Mandelbrot and J. R. Wallis, "Computer experiments with fractional Gaussian noises," *Water Resource Research*, vol. 5, pp. 228–267, 1969.

[19] B. B. Mandelbrot and J. W. Van Ness, "Fractional Brownian motions, fractional noises and applications," *SIAM Review*, vol. 10, pp. 422–437, 1968.

[20] J. Beran, " Statistical method for data with long-range dependence," *Statistical Science*, vol. 7, no. 4, pp. 404–416, 1992.

[21] M. Li and J. Y. Li, "On the predictability of long-range dependent series," *Mathematical Problems in Engineering*, vol. 2010, Article ID 397454, 2010.

[22] M. Li, "Fractal time series—a tutorial review," *Mathematical Problems in Engineering*, Article ID 157264, 26 pages, 2010.

[23] M. Li and S. C. Lim, "Modeling network traffic using generalized Cauchy process," *Physica A*, vol. 387, no. 11, pp. 2584–2594, 2008.

[24] M. Li and W. Zhao, "Visiting power laws in cyber-physical networking systems," *Mathematical Problems in Engineering*, vol. 2012, Article ID 302786, 13 pages, 2012.

[25] J. D. Pelletier and D. L. Turcotte, "Long-range persistence in climatological and hydrological time series: analysis, modeling and application to drought hazard assessment," *Journal of Hydrology*, vol. 203, no. 1–4, pp. 198–208, 1997.

[26] M. Radziejewski and Z. W. Kundzewicz, "Fractal analysis of flow of the river Warta," *Journal of Hydrology*, vol. 200, no. 1–4, pp. 280–294, 1997.

[27] M. Li, C. Cattani, and S. Y. Chen, "Viewing sea level by a one-dimensional random function with long memory," *Mathematical Problems in Engineering*, vol. 2011, Article ID 654284, 2011.

[28] G. E. Hinton, S. Osindero, and Y. W. Teh, "A fast learning algorithm for deep belief nets," *Neural Computation*, vol. 18, no. 7, pp. 1527–1554, 2006.

[29] Y. Kang and S. Choi, "Restricted deep belief networks for multi-view learning," in *Proceedings of the European Conference on Machine Learning and Principles and Practice of Knowledge Discovery in Databases (ECML PKDD '11)*, vol. 6912 of *Lecture Notes in Computer Science*, pp. 130–145, 2011.
[30] G. E. Hinton and R. R. Salakhutdinov, "Reducing the dimensionality of data with neural networks," *Science*, vol. 313, no. 5786, pp. 504–507, 2006.
[31] H. Lee, R. Grosse, R. Ranganath, and A. Y. Ng, "Convolutional deep belief networks for scalable unsupervised learning of hierarchical representations," in *Proceedings of the 26th International Conference On Machine Learning (ICML '09)*, pp. 609–616, June 2009.
[32] T. Liu, "A novel text classification approach based on deep belief network," in *Proceedings of the 17th International Conference on Neural Information Processing (ICONIP '10)*, vol. 6443 of *Lecture Notes in Computer Science*, pp. 314–321, 2010.
[33] S. Zhou, Q. Chen, and X. Wang, "Discriminative Deep Belief networks for image classification," in *Proceedings of the 17th IEEE International Conference on Image Processing (ICIP '10)*, pp. 1561–1564, Hong Kong, 2010.
[34] J. Chao, F. Shen, and J. Zhao, "Forecasting exchange rate with deep belief networks," in *Proceedings of the International Joint Conference on Neural Networks (IJCNN '11)*, pp. 1259–1266, San Jose, Calif, USA, 2011.
[35] L. Zhai and Q. Feng, "Spatial and temporal pattern of precipitation and drought in Gansu Province, Northwest China," *Natural Hazards*, vol. 49, no. 1, pp. 1–24, 2009.
[36] H. Wu, M. D. Svoboda, M. J. Hayes, D. A. Wilhite, and F. Wen, "Appropriate application of the Standardized Precipitation Index in arid locations and dry seasons," *International Journal of Climatology*, vol. 27, no. 1, pp. 65–79, 2007.
[37] Y. P. Xu, S. J. Lin, Y. Huang, Q. Q. Zhang, and Q. H. Ran, "Drought analysis using multi-scale standardized precipitation index in the Han River Basin, China," *Journal of Zhejiang University*, vol. 12, no. 6, pp. 483–494, 2011.
[38] N. B. Guttman, "Accepting the standardized precipitation index: a calculation algorithm," *Journal of the American Water Resources Association*, vol. 35, no. 2, pp. 311–322, 1999.
[39] S. M. Vicente-Serrano, "Differences in spatial patterns of drought on different time scales: an analysis of the Iberian Peninsula," *Water Resources Management*, vol. 20, no. 1, pp. 37–60, 2006.
[40] D. C. Edwards and T. B. McKee, "Characteristics of 20th Century drought in the United States at multiple time scales," Climatology Report 97-2, Colorado State University, Fort Collins, Colo, USA, 1997.
[41] B. Lloyd-Hughes and M. A. Saunders, "A drought climatology for Europe," *International Journal of Climatology*, vol. 22, no. 13, pp. 1571–1592, 2002.
[42] L. Zhang and G. Subbarayan, "An evaluation of back-propagation neural networks for the optimal design of structural systems: part I. Training procedures," *Computer Methods in Applied Mechanics and Engineering*, vol. 191, no. 25-26, pp. 2873–2886, 2002.
[43] L. H. Jiang, A. G. Wang, N. Y. Tian, W. C. Zhang, and Q. L. Fan, "BP neural network of continuous casting technological parameters and secondary dendrite arm spacing of spring steel," *Journal of Iron and Steel Research International*, vol. 18, no. 8, pp. 25–29, 2011.
[44] Q. Y. Tang and M. G. Feng, *DPS Data Processing System for Trial Design, Statistical Analysis and Data Mining*, Chinese Science Press, 2007.
[45] M. C. Wang, Y. H. Yan, Y. L. Han et al., "Application of neural network in the surface quality testing of cool rolled strip," *Machinery*, vol. 12, p. 71, 2006 (Chinese).
[46] Z. X. Ge and Z. Q. Sun, *Neural Network Theory and MATLAB R2007 Realization*, Electronic Industry Press, Beijing, China, 2007.
[47] V. Nair and G. E. Hinton, "Rectified linear units improve Restricted Boltzmann machines," in *Proceedings of the 27th International Conference on Machine Learning (ICML '10)*, pp. 807–814, June 2010.
[48] H. Chen and A. F. Murray, "A continuous restricted Boltzmann machine with hardware-amenable learning algorithm," in *Proceedings of the 12th International Conference on Artificial Neural Networks (ICANN '02)*, pp. 358–363, Madrid, Spain, 2002.
[49] B. J. Frey, "Continuous sigmoidal belief networks trained using slice sampling," *Advance in Neural Information processing Systems*, vol. 9, pp. 452–458, 1997.
[50] G. E. Hinton, "Learning multiple layers of representation," *Trends in Cognitive Sciences*, vol. 11, no. 10, pp. 428–434, 2007.

Hindawi Publishing Corporation
Mathematical Problems in Engineering
Volume 2012, Article ID 515296, 13 pages
doi:10.1155/2012/515296

Research Article

Data Matrix Code Location Based on Finder Pattern Detection and Bar Code Border Fitting

Qiang Huang,[1] Wen-Sheng Chen,[1,2] Xiao-Yan Huang,[1] and Ying-Ying Zhu[1]

[1] *College of Computer Science and Software Engineering, Shenzhen University, Shenzhen 518060, China*
[2] *College of Mathematics and Computational Science, Shenzhen University, Shenzhen 518060, China*

Correspondence should be addressed to Ying-Ying Zhu, zhuyy@szu.edu.cn

Received 25 November 2011; Accepted 7 January 2012

Academic Editor: Bin Fang

The 2-D bar code possesses large capacity of data, strong ability for error correction, and high safety, which boosts the 2-D bar code recognition technology being widely used and developed fast. This paper presents a novel algorithm for locating data matrix code based on finder pattern detection and bar code border fitting. The proposed method mainly involves three stages. It first extracts candidate regions that may contain a data matrix code by morphological processing and then locates the data matrix code roughly by detecting "L" finder pattern and the dashed border on the candidate regions. Finally, the lines fitted with the border points are used as the borders of data matrix code. A number of data matrix code images with complexity background are selected for evaluations. Experimental results show that the proposed algorithm exhibits better performance under complex background and other undesirable conditions.

1. Introduction

2-D bar code consists of a certain white and black geometric modules that alternately arrange in the vertical and horizontal directions according to certain rules (see Figure 1), and it is a symbol with large capacity for storing information. As the 2-D bar code with smallest size in the world, data matrix code is widely applied to electronic product components. 2-D bar code recognition technology shows great commercial value, and at present, most COTS (commercial of the shell) recognition algorithms are proprietary and protected by patents, so the 2-D bar code recognition technology is in a great demand for researching.

How to locate a 2-D bar code quickly and precisely in an image with complex background, poor illumination or other undesirable condition is crucial to the recognition process. For data matrix code location, many kinds of location algorithms have been

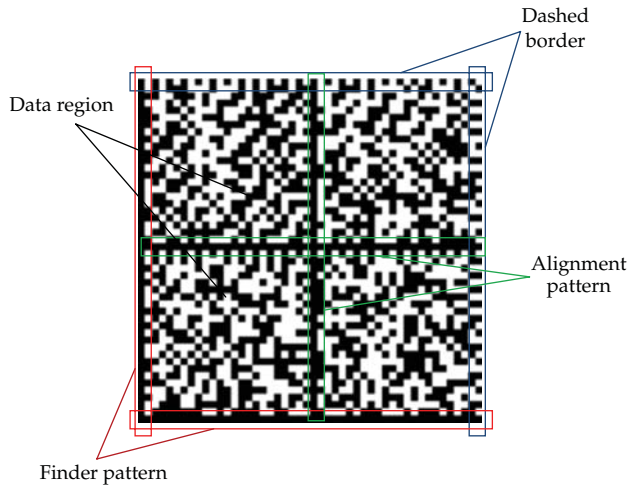

Figure 1: Data matrix code symbol.

proposed. Donghong et al. [1] proposed an algorithm based on Radon transform, which mainly locates data matrix code by the "L" finder pattern and dashed border detection. This algorithm has high precision and works well for the data matrix code within high density but is very time consuming and is not suitable to be applied to real-time application. Chenguang et al. [2] proposed the locating algorithm based on Hough transform. This algorithm is very time consuming and space consuming though it can reduce the consumption by a second Hough transformation. What's worse, this algorithm has low precision for the complex background. Wenting and Zhi [3] discussed the method of locating data matrix code based on convex algorithm, which determines the 3 vertexes of the "L" finder pattern according to the convex of the edge points of the bar code. This algorithm is simple and fast but requires that background is clean and the bar code gets no stained and complete. There are other locating algorithms [4, 5] and are solely appropriate for specific situation, such as simple background situation, good illumination condition, and low density. In reality, the bar code images are always accompanied with complex background, and furthermore the images might get stained, incomplete, or printed in high density. Under these undesirable conditions, most of the algorithms mentioned above do not work effectively or are not demanded for higher processing power and more storage space, which cannot satisfy most real-time application. The location problem of 2-D barcode involves nonlinear systems [6, 7].

In this paper, we propose a data matrix code location algorithm based on finder pattern detection and bar code border fitting, which is proved by extensive experiments to be effectively and fast. In this algorithm, the finder pattern is detected mainly based on line segment detection and combination. Some work has been done for finding "L" finder pattern by segment detection, such as reference [8–12]. About line segment detection, Grompone Von Gioi et al. [13] proposed a linear-time algorithm called line segment detector (LSD), which requires no parameter tuning and gives accurate results. The LSD algorithm has improved the line segment finder proposed by Burns et al. [14] and combined with a validation criterion inspired from Desolneux et al. [15, 16]. In this paper, the LSD algorithm is utilized to detect the "L" finder pattern, and an introduction of LSD is given in the related work section. About border fitting, the most important step is straight line fitting. An effective straight line fitting

solution is proposed by Fischler and Bolles called RANSAC [17] algorithm, which will be used to fit the bar code borders.

The remainder of this paper will be organized as followings. Section 2 is the introduction of the related algorithm about line segment detection. Section 3 will give details of the proposed data matrix code location algorithm. Section 4 comments on the experimental results and Section 5 concludes the paper.

2. Related Work

LSD is a linear-time line segment detector, which draws and improves the idea of Burns et al. (see [14]) that defines a line segment as a region which only concerning the gradient information, and combines the validation criterion inspired from Desolneux et al. (see [15, 16]). This algorithm is implemented in 4 steps.

Step 1 (finding the line-support regions). This method defines a line segment as a region called line-support region, which is a cluster of points in a connected region that sharing roughly the same gradient orientation angle and whose gradient magnitude is greater than a threshold. To get the line-support region, a region-grow algorithm is applied. Firstly, a pseudoordering is done. The pixels whose gradient magnitude value is larger than threshold ρ are classified into a finite number of bins according to their gradient magnitude value, then the pixels from higher bins are visited first and pixels in lower bins later; secondly, each region starts with one pixel and initializes the line-support region angle with the first pixel's gradient angle, if an adjacent pixel is under the condition as inequality (2.1), add it to the line-support region and update the line-support region angle as formula (2.2). Repeat the steps until there is no pixel that can be added to the line-support region.

$$\operatorname{abs}\left(\operatorname{angle}\left(\overline{\mathrm{p}}\right) - \theta_{\mathrm{region}}\right) < \tau, \tag{2.1}$$

where $\overline{\mathrm{p}}$ is the adjacent pixel, $\tau = 22.5^{\circ}$ is the threshold of the difference between adjacent pixel's angle and line-support region angle.

$$\theta_{\mathrm{region}} = \arctan\left(\frac{\sum_i \sin\left(\mathrm{ang}_i\right)}{\sum_i \cos\left(\mathrm{ang}_i\right)}\right). \tag{2.2}$$

Step 2 (finding the rectangular approximation of every line-support regions). A line segment that associated with a line-support region is defined as a rectangle which is the rectangular approximation of the line-support region. Parameters, such as center, orientation angle, length, and width, can be used to describe a line segment, see Figure 2. In LSD algorithm, instead of using the mean level-line angle as the line angle, which may lead to erroneous line angle estimation, the first inertia axis orientation is used to be the line segment orientation. The centroid of mass of the rectangular approximate is selected as the center, when the gradient magnitude is used as pixel's mass. The length and width are chosen in the way that covers the line-support region.

Step 3 (validation of each potential line segment). After getting the rectangular approximations of line-support region, it is necessary to validate each approximation a line segment

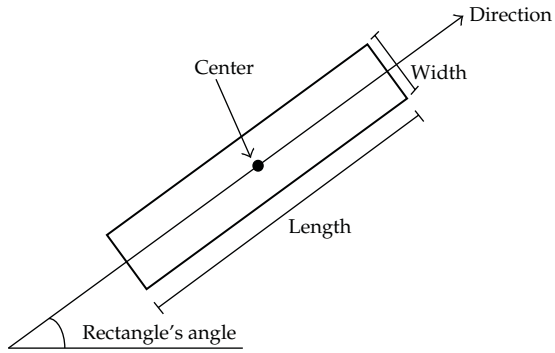

Figure 2: Line segments are characterized by a rectangle determined by its center point, angle, length, and width.

or not according to the number of aligned point and the total number of pixels of each approximation. Aligned point is defined as the pixel whose gradient angle is the same to the line segment angle up to the tolerance τ.

Suppose that image background has the Gaussian white noise model H_0, more formally, an image X under the background model H_0 is a random image (defined on the grid $\Gamma = [1, N] \times [1, M] \subset Z^2$) such that:

(1) for all $m \in \Gamma$, angle$(\nabla X(m))$ is uniformly distributed over $[0, 2\pi]$.

(2) The family $\{\text{angle}(\nabla X(m))\}_{m\in\Gamma}$ is composed of independent random variables.

Under the model H_0, image is isotropic flat zones, while straight edges are exactly the opposite: highly anisotropic zones. Thus, in practice, a set of pixels will not be accepted as a line segment if it could have been formed by an isotropic process. This algorithm defines the Number of False Alarms of a rectangle $r \in R$ in an image x, as

$$\text{NFA}(r, x) = \#R \cdot IP_{H_0}[k(r, X) \geq k(r, x)]. \tag{2.3}$$

In the formula (2.3), X is a random image under model H_0, $\#R$ is the total number of potential rectangle (line segment) in image X, $k(r, X)$, and $k(r, x)$ represent the number of aligned points in rectangle in image X and image x, respectively, $IP_{H_0}[k(r, X) \geq k(r, x)]$ is the probability that $k(r, X)$ greater than or equal to $k(r, x)$.

The smaller the NFA value is, the more significant the rectangle r is. Consider one pixel accuracy, there are N^4 potential line segments in a $N \times N$ image for the start point and end point both have N^2 possible, but in practice, line segment's width can be at most N pixels, thus $\#R = N^5$. Under the model H_0 and a tolerance $\tau = \pi p$ for the difference between aligned point gradient angle and line segment angle, $p = \tau/\pi$ is the probability of that a given point is an aligned point. Each pixel's gradient is independent in rectangle, so the number of aligned point $k(r)$ obey binomial distribution, thus,

$$IP_{H_0}[k(r, X) \geq k(r, x)] = b(n(r), k(r), p), \tag{2.4}$$

where $b(n,k,p) = \sum_{i=k}^{n}(n/i)p^i(1-p)^{n-i}$, finally, NFA is easy to be calculated:

$$\mathrm{NFA}(r) = N^5 \cdot b\big(n(r), k(r), p\big). \tag{2.5}$$

The NFA is the key to validate the rectangle as a line segment or not, if NFA is less than a threshold ε, then the rectangle is accepted as a ε-meaningful line segment, vice, the rectangle is not a line segment. This method is almost independent of ε (actually logarithmic). Thus, this algorithm let $\varepsilon = 1$ thoroughly as advised by Fuchao (see [17]).

Step 4 (improved the approximations of line-support region and validate them). In Step 3, the best rectangular approximation of a line-support region is the one that gives the smallest NFA value, in order to get a better NFA, the LSD algorithm tries to adjust the width of the approximation and the probability p. Five dyadic precision steps are considered before adjusting the rectangle width and again five dyadic precision steps afterward. Repeat Steps 2 and 3 and keep the rectangular approximation with best NFA value as the final line segment.

3. The Proposed Location Algorithm

Observed the data matrix code, the "L" finder pattern and the dashed border make data matrix code distinct from other 2-D bar codes or objects, so the first idea that comes to mind is to locate the data matrix code by detecting the "L" finder pattern and dashed border, but this procedure may lead to an imprecise location when there exists a perspective distortion in the bar code image or the image get stained or obscured (these situations happen frequently). Therefore, it needs to locate the bar code more precisely. In this paper, we utilize some edge points of data matrix code to fit 4 straight lines as the 4 borders of the bar code and finally achieve accurate positioning with their intersections (4 vertexes).

The location steps discussed above are the main steps of the location algorithm, which consume most of processing time, and the computation time is closely related to the size of the image. Normally, the bar code region is only a small part of the image, it is necessary to extract the bar code from the image to facilitate the follow-up location. In this way, it not only reduces the cost of computation but also enhances the antijamming capability of the algorithm for the extraction of bar code removes most of the background. After the extraction of candidate regions (may include a data matrix code), the location algorithm is applied on them to complete the whole location. The whole data matrix code location procedure is shown in Figure 3.

3.1. Extraction of Data Matrix Code Candidate Region

In general, 2-D barcodes consist of staggered white and black modules and have vast closely spaced edges, while other objects or background in the image has few sparse edges. This characteristic is utilized to extract candidate regions in 3 steps:

Step 1 (edge detection, remove most of the background by canny edge detection). The proposed algorithm chooses canny operator to do edge detection because it can get more complete edges by restraining the nonmaximum value and connecting the inconsecutive edges with mathematical morphology. Canny operator gets a good tradeoff between noise suppression and edge detection. In the standard canny edge detection, the first step is the

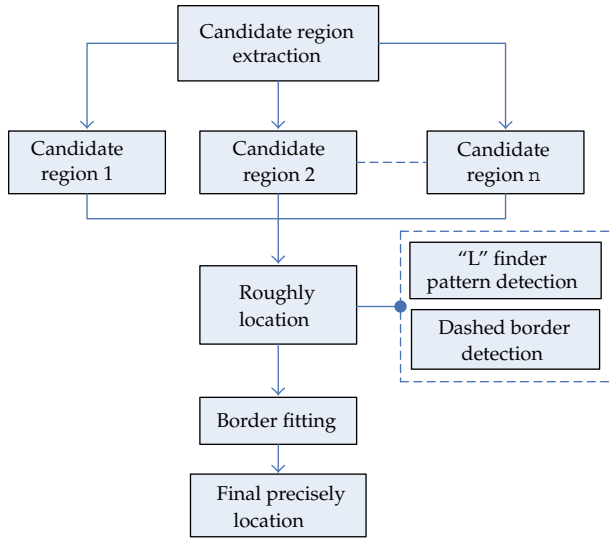

Figure 3: Data matrix code location algorithm flowchart.

Gaussian filtering which is used to remove noise, but in this application, we ignore this step to save time bringing little impact on subsequent processing.

Step 2 (morphological processing, highlight the bar code region by dilate operation and open operation). The dilate operation fills bar code but expands bar code boundary at the same time, which may lead to connection of bar code and other objects (such as text). So open operation is used to separate these small adhesions. The result is susceptible to the shape and size of the structure element. Actually, 2-D barcode module always has the size of 3 to 8 pixels in rectangle shape, so the structure elements are defined as follows.

$$\begin{array}{|c|c|c|c|}\hline 1 & 1 & 1 & 1 \\ \hline 1 & 1 & 1 & 1 \\ \hline 1 & 1 & 1 & 1 \\ \hline 1 & 1 & 1 & 1 \\ \hline \end{array}$$

Dilate structure element: 4×4 rectangle

$$\begin{array}{|c|c|c|c|c|}\hline 1 & 1 & 1 & 1 & 1 \\ \hline 1 & 1 & 1 & 1 & 1 \\ \hline 1 & 1 & 1 & 1 & 1 \\ \hline 1 & 1 & 1 & 1 & 1 \\ \hline 1 & 1 & 1 & 1 & 1 \\ \hline \end{array}$$

Open structure element: 5×5 rectangle

(3.1)

Step 3 (contour analysis, filter candidate regions with contour perimeter and area). Mark every connected region: $\{R_1, R_2, \ldots, R_n\}$ and extract the contour: $\{C_1, C_2, \ldots, C_n\}$, then filter the connected regions with their perimeter and area:

$$\text{candidate\_regions} = \{R_i \mid \text{Perimeter}(C_i) > \tau_1 \;\&\&\; \text{Area}(R_i) > \tau_2\}. \tag{3.2}$$

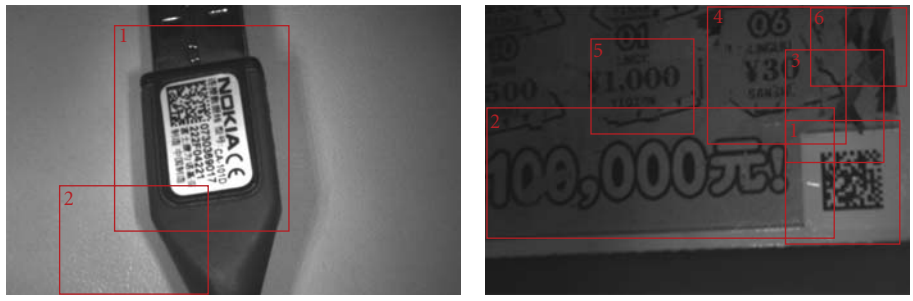

(a) (b)

Figure 4: Extraction of bar code candidate region.

To make sure that the whole bar code is included in the candidate region, the bounding box of the candidate is calculated and expanded. The experimental results are shown in Figure 4.

3.2. Preliminary Location Based on Finder Pattern

Based on the data matrix code feature analysis mentioned above, it can quickly determine whether there is a data matrix code or not in a candidate region and obtain the approximate location of data matrix code by detecting the "L" finder pattern. Detection of dashed border helps determine the top and right boundary position of data matrix code. In this paper, "L" finder pattern and the dashed border are detected to preliminarily locate data matrix.

3.2.1. "L" Finder Pattern Detection

L-detection is relatively complex, but an "L" finder pattern can be regards as two segments, and there are many mature line segment detection algorithms. The LSD algorithm (introduced in Section 2) proposed by Grompone Von Gioi et al. [13] is utilized to detect line segment. Consider that Step 4 of LSD is not very meaningful for large and well-contrasted line segments (the "L" finder pattern of data matrix code is always well contrasted) and time consuming within repeat of Steps 2 and 3, our algorithm ignores this step to save time. The detection result is shown in Figure 5.

An "L" finder pattern can be detected by combining the appropriate line segments. Assume that the line segments obtained in a candidate region are: $\{l_1, l_2, \ldots, l_n\}$, a line segment is described with its two endpoints as: $l_i = \{p_{i1}, p_{i2}\}$. Normally, if two line segments are belong to the same "L" finder pattern, then $\text{angle}(l_i, l_j) = 90°$, $i, j = 1, 2, \ldots n$. But this assumption no longer holds when the image has perspective deformation. Extensive experiments have demonstrated that the angle usually ranges from 60° to 120°. A constrain about the segments' length ratio that the length of the long line segment can not exceed 5 times the length of the short one is added. Therefore, combination of line segments can be implemented as in Algorithm 1.

Inevitably, some pseudo-L will be detected, so an "L" finder pattern will be abandoned if the postprocessing cannot locate a data matrix code. The approximate location of 3 vertexes (two endpoints and an intersection of "L") can be obtained from the "L" finder pattern to locate data matrix code roughly just as Figure 5(c).

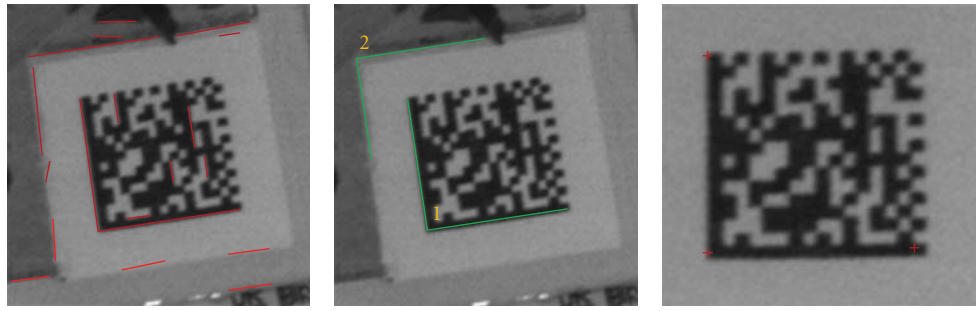

(a) (b) (c)

Figure 5: "L" finder pattern detection (a) shows the result of line segment detection; (b) combine the appropriate segments to an "L"; (c) roughly location using the 3 vertexes.

For each l_i $(i = 1 : n)$
If l_i is not marked
Search in $D_{p_{i1}}$ and $D_{p_{i2}}$ to find l_j; // $D_{p_{i1}}$ and $D_{p_{i2}}$ are Neighborhoods of p_{i1} and p_{i2}.
If l_j is not marked && $60° < \text{angle}(l_i, l_j) < 120°$
&& $\max\{\text{len}(l_i), \text{len}(l_j)\} / \min\{\text{len}(l_i), \text{len}(l_j)\} < 5$ // $\text{len}(l_i)$ and $\text{len}(l_j)$ are the lengths of l_i and l_j
Combine l_i and l_j into an "L";
Mark l_i and l_j;
End
End
End

Algorithm 1

3.2.2. Dashed Border Detection

Composed by alternating black modules and white modules, the dashed border has a lot of edges. On the other hand, the dashed border is roughly parallel to the "L" finder pattern. Detecting a dashed border by scanning edge point in the direction paralleling to "L" in two steps.

Step 1 (determine a detecting region). A quadruple: $\{x, y, \text{width}, \text{height}\}$ is used to defined the detecting region, where x and y are coordinates of the start point of the scanning, width and height are scanning arranged paralleling to "L" (see Figure 6). The 3 vertexes of the "L" are $p_1(x_1, y_1)$, $p_2(x_2, y_2)$, and $p_3(x_3, y_3)$, and the lengths of the two segments of "L" are len_1 and len_2. $\text{len}_1 > \text{len}_2$, then the detection regions are

$$\begin{aligned} \text{detect\_reg}_{\text{upper}} &= \{x_1 - \tau, y_1 - \tau,\ \text{len}_1 + 2\tau,\ \text{len}_1 - \text{len}_2 + 2\tau\}, \\ \text{detect\_reg}_{\text{right}} &= \{x_3 + \tau, y_3 + \tau,\ \text{len}_1 - \text{len}_2 + 2\tau, \text{len}_1 + 2\tau\}, \end{aligned} \tag{3.3}$$

where τ is an adjustable parameter.

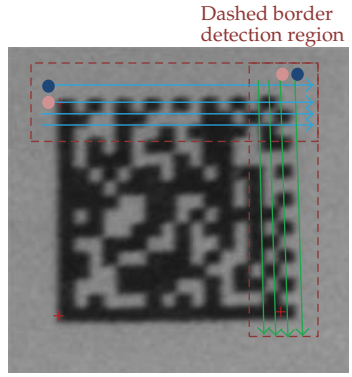

Figure 6: Dashed border detection.

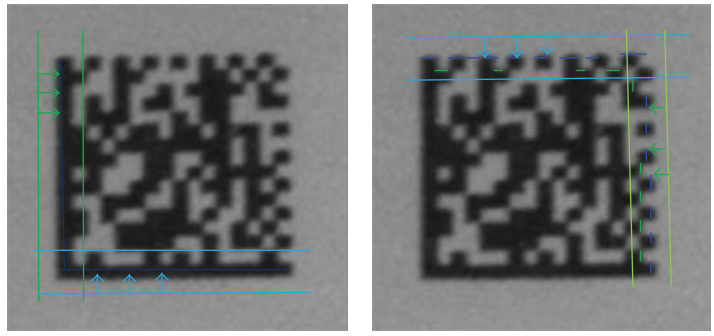

(a) (b)

Figure 7: Scan border points.

Step 2. Progressively scan edge points in the direction paralleling to the horizontal line segment of "L" in detect_reg$_{\text{upper}}$ and count the number of edge points. The row with the most edge points is kept as the horizontal dashed border. The row with the least edge points is kept as static region. The vertical dashed border is detected in the same way.

3.3. Border Fitting

The 3 vertexes obtained from the "L" finder pattern can only roughly locate data matrix code, even, the location is wrong when the "L" gets stained or partly covered and the detection of the dashed borders is not precise. So it is necessary to get more information for further location. In this paper, the 4 borders will be fitted to finally locate data matrix code in 3 steps.

Step 1 (scan border points). Border point is defined as the first edge point from outside to inside in the direction perpendicular to bar code's border. The scanning range is around the bar code borders with an offset (such as 5 pixels). An example has been demonstrated in Figure 7, 4 sets of border points can be obtained: border_point$_{\text{left}}$, border_point$_{\text{right}}$, border_point$_{\text{upper}}$, and border_point$_{\text{lower}}$.

Step 2 (fit borders). In mathematics, it is usually to describe a straight line by equality [18]: $y = kx + b$, but it cannot work when the straight line is perpendicular to the x axis, the slope k tends to be infinity, thus we use Hesse paradigm to describe a straight line: $ax + by + c = 0$, in fact, it is a excessive parametric expression, 2 points can determine a straight line while there are 3 parameters in the equality, so a constraint is added: $a^2 + b^2 = 1$.

In order to fit a straight line in a set of point: $\{p_1(x_1, y_1), p_2(x_2, y_2), \ldots, p_n(x_n, y_n)\}$, the sum of the distance from each point to the straight line: $e^2 = \sum_i^n (a_i + by_i + c)^2$ should be minimized. Therefore, the straight line fitting can be converted into distance minimization problem. But if $a = b = c = 0$, the equality above will get a zero measurement error. To avoid this problem, the constraint condition $a^2 + b^2 = 1$ would be added as a Lagrangian multiplier:

$$e^2 = \sum_i^n \left(ax_i + by_i + c\right)^2 + \lambda\left(a^2 + b^2 - 1\right)n. \tag{3.4}$$

The minimization problem can be expressed as:

$$(a, b, c) = \arg\left(\min\left(e^2\right)\right). \tag{3.5}$$

Solve (3.5):

$$\frac{a}{b} = -\frac{s_{xy}}{s_{xx}} = -\frac{s_{yy}}{s_{xy}}, \qquad c = -\left(a\overline{x} + b\overline{y}\right) \tag{3.6}$$

to avoid the situation that $a/b = -0/0$, accept the proposition that with greater value:

$$\begin{aligned} &\text{if } s_{yy} \geq s_{xx}, \quad \frac{a}{b} = -\frac{s_{yy}}{s_{xy}}, \quad \text{then } a = -\frac{s_{yy}}{\sqrt{{s_{yy}}^2 + {s_{xy}}^2}}, \quad b = -\frac{s_{xy}}{\sqrt{{s_{yy}}^2 + {s_{xy}}^2}}; \\ &\text{if } s_{yy} < s_{xx}, \quad \frac{a}{b} = -\frac{s_{xy}}{s_{xx}}, \quad \text{then } a = -\frac{s_{xy}}{\sqrt{{s_{xx}}^2 + {s_{xy}}^2}}, \quad b = -\frac{s_{xx}}{\sqrt{{s_{xx}}^2 + {s_{xy}}^2}}. \end{aligned} \tag{3.7}$$

In the formulas above:

$$\begin{gathered} \overline{x} = \frac{1}{n}\sum_i^n x_i, \qquad \overline{y} = \frac{1}{n}\sum_i^n y_i, \\ s_{xx} = \sum_i^n (x_i - \overline{x})^2, \qquad s_{yy} = \sum_i^n (y_i - \overline{y})^2, \qquad s_{xy} = \sum_i^n (x_i - \overline{x})(y_i - \overline{y}). \end{gathered} \tag{3.8}$$

Once the values of parameter a, b, c are determined, a straight line is fitted. Let us consider the points in the set, some outliers must deviate the straight line which fitted by minimizing the distance from points to it. An effective solution is the mature and typical RANSAC algorithms. This algorithm selects minimum quality of points (such as 2 points)

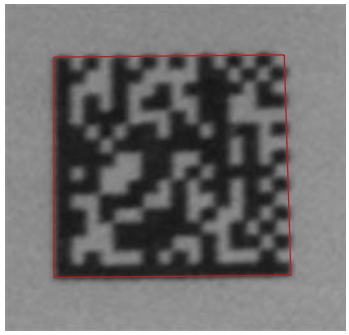

Figure 8: Precisely location.

randomly to fit a straight line, and then check the proposition of outliers. Repeat this procedure until the proposition of outliers reaches level less than a threshold such as 1%, and the straight line with minimum proposition of outliers is kept, finally used these certain 2 points and their inliers to fit the final straight line. The robustness RANSAC is used in this paper to fit 4 borders with the 4 set of border points obtained in Step 1.

Step 3 (obtain 4 vertexes of data matrix code precisely). After the Step 2, 4 straight lines l_{left}, l_{upper}, l_{right}, and l_{lower}, have been fitted and then calculate their intersections to obtain data matrix code position. The Figure 8 shows the final precise location.

4. Experimental Results

In order to verify the performance of the proposed algorithm, we conduct experiments on the images under different conditions (such as complex background, perspective distortion) and give four representative experimental results. All the experiments run on the ARM 11 hardware platform, and all test images have the resolution of 752 × 480. Figures 9(a)~9(d) are the four original test images. Figure 9(a) is the mobile phone battery image with a data matrix code. Around the data matrix code, there are some texts and other objects closed to the bar code, which bring great interference to bar code location. Figure 9(b) is an USB data cable connector image with a data matrix code. The size of the USB connector is small and the size of data matrix code is even smaller. Also, there are lots of texts very closed to the data matrix code. Figure 9(c) is an award ticket image with a data matrix code; the image is dim with bad illumination. Figure 9(d) is an image of the printed data matrix code, some perspective distortions exist in the image because of the tilt angle when taking photo.

Figures 9(e)~9(h) are the experimental results of data matrix code location. It can be seen that the proposed location method works effectively and precisely. Figure 9(e) shows that the proposed algorithm has good robustness to interference brought by complex background. Figure 9(f) demonstrates that the algorithm has high precise for the small size of data matrix code. Figures 9(g) and 9(h) reveal that the proposed algorithm can achieve good performance even under bad illumination or distortion conditions.

Moreover, the proposed algorithm costs no more than 100 ms in these experiments, which can completely satisfy the demand of real-time application, and it is especially suitable for embedded device.

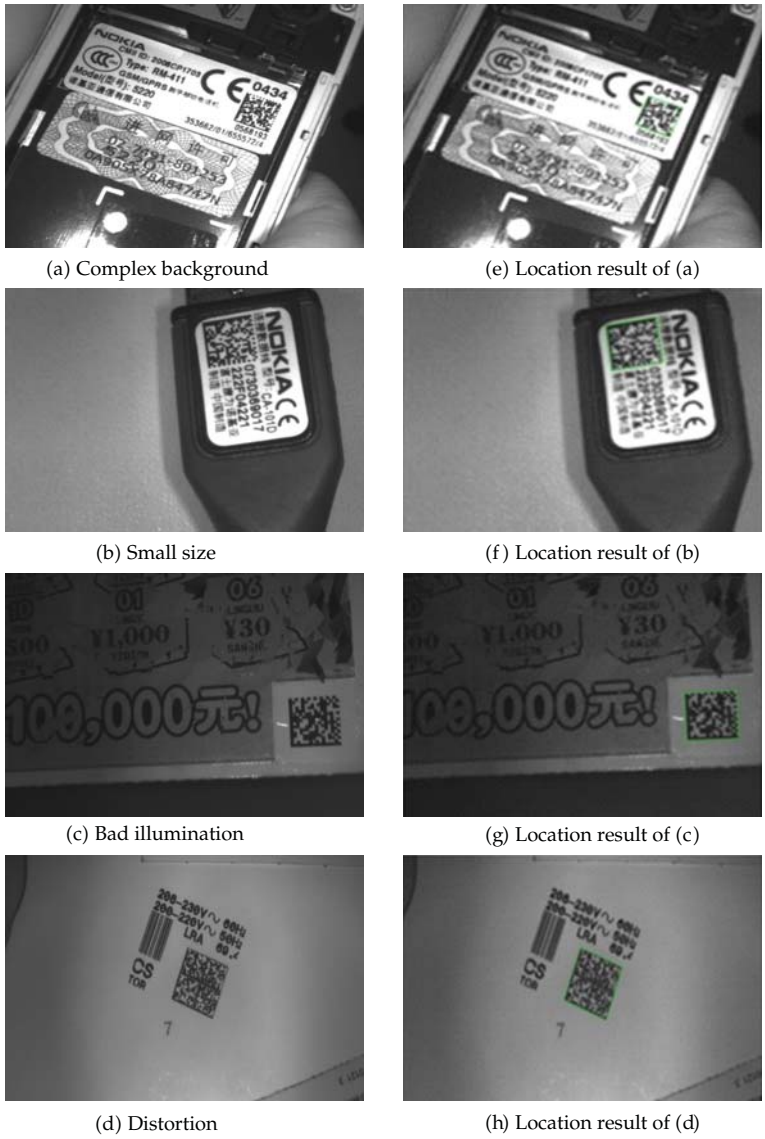

(a) Complex background (e) Location result of (a)

(b) Small size (f) Location result of (b)

(c) Bad illumination (g) Location result of (c)

(d) Distortion (h) Location result of (d)

Figure 9: Data Matrix code precise locations.

5. Conclusions

A data matrix code location algorithm is proposed in this paper, which utilizes the obvious features of "L" finder pattern and dashed border of data matrix code. This algorithm provides 3 advantages compared to those algorithms mentioned. (1) First: robustness, it locates data matrix code on candidate regions excluding most of interference from background. The two most important algorithms, namely, LSD and RANSAC, are used to achieve high robustness under complexity background conditions. (2) Second: it has high accuracy, preliminarily location by finder pattern, and then accurate location by fitting border lines. (3) It is suitable for real-time application. Extraction of candidate region greatly reduces the operating area of location algorithm, which saves a lot of time. Instead of using the time-consuming Hough

transformation algorithm to detect line segment, the linear-time LSD algorithm is used. The proposed method is evaluated on four images with complex background or distortion. The experimental results show that our proposed algorithm gives good performance.

Acknowledgments

This work was partially supported by Natural Science Foundation of China under Grant no. (60501026, 60873168), foundation for combination of industry and academy in Shenzhen under Grant no. SY200806270120A and Science & Technology Planning Project of Shenzhen City (JC200903130300A), and the Opening Project of Guangdong Province Key Laboratory of Computational Science of Sun Yat-Sen University (201106002).

References

[1] H. Donghong, T. Hui, and C. Xinmeng, "Radon transformation applied in two dimensional barcode image recognition," *Journal of Wuhan University*, vol. 5, pp. 584–588, 2005.
[2] Z. Chenguang, Y. Na, and H. Rukun, "study of two dimensional barcode identification technology based on HOUGH transform," *Journal of Changchun Normal University*, vol. 4, pp. 94–98, 2007.
[3] C. Wenting and L. Zhi, "Two dimensional barcode localization algorithm based on convex," *Journal of Zhejiang University*, vol. 46, pp. 669–672, 2008.
[4] M. Li and W. Zhao, "Visiting power laws in cyber-physical networking systems," *Mathematical Problems in Engineering*, vol. 2012, Article ID 302786, 13 pages, 2012.
[5] M. Li, C. Cattani, and S. Y. Chen, "Viewing sea level by a one-dimensional random function with long memory," *Mathematical Problems in Engineering*, vol. 2011, Article ID 654284, 13 pages, 2011.
[6] M. Li, "Fractal time series—a tutorial review," *Mathematical Problems in Engineering*, vol. 2010, Article ID 157264, 26 pages, 2010.
[7] Z. Liao, S. Hu, D. Sun, and W. Chen, "Enclosed Laplacian operator of nonlinear anisotropic diffusion to preserve singularities and delete isolated points in image smoothing," *Mathematical Problems in Engineering*, vol. 2011, Article ID 749456, 15 pages, 2011.
[8] X. You and Y. Y. Tang, "Wavelet-based approach to character skeleton," *IEEE Transactions on Image Processing*, vol. 16, no. 5, pp. 1220–1231, 2007.
[9] W. Zhang, Q. M. J. Wu, G. Wang, X. You, and Y. Wang, "Image matching using enclosed region detector," *Journal of Visual Communication and Image Representation*, vol. 21, no. 4, pp. 271–282, 2010.
[10] J. Huang, X. You, Y. Y. Tang, L. Du, and Y. Yuan, "A novel iris segmentation using radial-suppression edge detection," *Signal Processing*, vol. 89, no. 12, pp. 2630–2643, 2009.
[11] P. L. Palmer, J. Kittler, and M. Petrou, "An optimizing line finder using a hough transform algorithm," *Computer Vision and Image Understanding*, vol. 67, no. 1, pp. 1–23, 1997.
[12] H. Kato, K. T. Tan, and D. Chai, "Development of a novel finder pattern for effective color 2D-barcode detection," in *Proceedings of the International Symposium on Parallel and Distributed Processing with Applications (ISPA '08)*, pp. 1006–1013, December 2008.
[13] R. Grompone Von Gioi, J. Jakubowicz, J. M. Morel, and G. Randall, "LSD: a fast line segment detector with a false detection control," *IEEE Transactions on Pattern Analysis and Machine Intelligence*, vol. 32, no. 4, Article ID 4731268, pp. 722–732, 2010.
[14] J. B. Burns, A. R. Hanson, and E. M. Riseman, "Extracting straight lines," *IEEE Transactions on Pattern Analysis and Machine Intelligence*, vol. 8, no. 4, pp. 425–455, 1986.
[15] A. Desolneux, L. Moisan, and J. M. Morel, "Meaningful alignments," *International Journal of Computer Vision*, vol. 40, no. 1, pp. 7–23, 2000.
[16] A. Desolneux, L. Moisan, and J. M. Morel, "Computational gestalts and perception thresholds," *Journal of Physiology Paris*, vol. 97, no. 2-3, pp. 311–324, 2003.
[17] W. Fuchao, *Mathematical Method in Computer Vision*, Science Press, Beijing, China, 2008.
[18] C. Steger and M. Ulrich, *Machine Vision Algorithms and Applications*, Tsinghua University Press, 2008.

Hindawi Publishing Corporation
Mathematical Problems in Engineering
Volume 2012, Article ID 194953, 20 pages
doi:10.1155/2012/194953

Research Article

A Combined Approach on RBC Image Segmentation through Shape Feature Extraction

Ruihu Wang[1,2] and Bin Fang[1]

[1] *College of Computer Science, Chongqing University, Chongqing 400030, China*
[2] *Department of Science and Technology, Chongqing University of Arts and Sciences, Chongqing 402160, China*

Correspondence should be addressed to Bin Fang, fb@cqu.edu.cn

Received 11 November 2011; Accepted 26 December 2011

Academic Editor: Ming Li

The classification of erythrocyte plays an important role in clinic diagnosis. In terms of the fact that the shape deformability of red blood cell brings more difficulty in detecting and recognize for operating automatically, we believed that the recovered 3D shape surface feature would give more information than traditional 2D intensity image processing methods. This paper proposed a combined approach for complex surface segmentation of red blood cell based on shape-from-shading technique and multiscale surface fitting. By means of the image irradiance equation under SEM imaging condition, the 3D height field could be recovered from the varied shading. Afterwards the depth maps of each point on the surfaces were applied to calculate Gaussian curvature and mean curvature, which were used to produce surface-type label image. Accordingly the surface was segmented into different parts through multiscale bivariate polynomials function fitting. The experimental results showed that this approach was easily implemented and promising.

1. Introduction

The erythrocyte shape deformability is critical to the filterability of blood. It has drawn considerable attentions into the pathology research in clinical relevant blood diseases. Unfortunately, the diagnosing is usually performed by a human expert, and it shows some drawbacks such as time-cost consuming and inaccuracy. Conventionally, the experts deal with erythrocyte images segmentation issue with 2D gray scale image. However, in order to obtain a satisfied performance, the classification and recognition should be based on the real shape of RBCs. In fact, the shape feature of red blood cell provides more useful information for diagnosing accurately than intensity level image. So it is necessary to take the shape

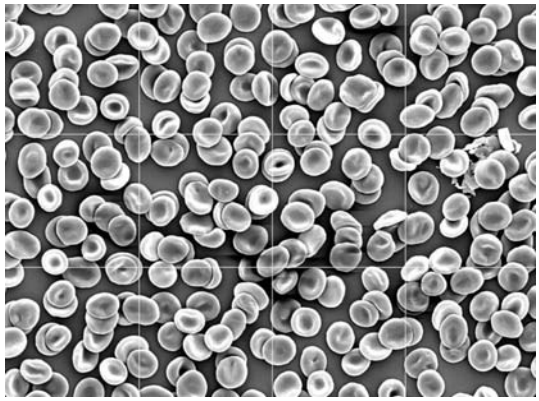

Figure 1: A typical SEM image of red blood cells.

information into consideration in this real problem. For our experiments, we use a database of 100 RBC images obtained by scanned electron microscope rather than optical imaging system. In [1], Egerton elaborated the operation principle of SEM, which creates images that are particularly easy to implement because the brightness in it is a function of the slope of the specimen at that point and forms a varied shading image. It is unlike the optical and transmission electron microscope, whose brightness depends on the thickness and optical and electron density instead.

In [2], Russ mentioned that many of the two-dimensional images have been sectioned through three-dimensional structures. This is especially true in the various types of microscopy, where either polished flat planes or cut thin sections are needed in order to form the images in the first place. But the specimens thus sampled are three dimensional, and the goal of microscopists is to understand the three-dimensional structure. Some works have been done on optical blood cell images with traditional 2D methods [3–5]. In order to detect and classify malaria parasites in images of Giemsa-stained blood slides, Di Ruberto et al. proposed a morphological approach to evaluate the parasitaemia of the blood. They segmented the cells (red and white) from the background firstly and then detected and classified the parasites infecting them [3, 6]. Equally with malaria parasite detection mentioned above, Kumarasmy et al. presented an automated method for the robust analysis of RBC images via Gestalt laws [4], and Mandal et al. presented a segmentation method of blood smear images using normalized cut [5]. As we well know that, noise estimation is a challenge problem for complex structures of images, Liao et al. presented a method determining neighborhoods of the image pixels automatically with adaptive denoising and estimate noise for a single-slice sonogram of low-dose CT based on the homogenous patches centered at a special pixel. In their method, the noisy image is viewed as an observation of a nonlinear time series. The true state of the NTS must be recovered from the observation to realize image denoising [7, 8]. Furthermore, Hu et al. proposed an image smoothing using nonlinear anisotropic diffusion [9]. They suggested that the diffusion should be performed both among the time variants and spatial variant.

Figure 1 shows a typical example of such kind of red blood cell images captured by SEM with which we are going to deal. They were obtained at 600 times magnification using a scanned electron microscope. As shown in Figure 1, there are some outstanding

characteristics about this image which make our problem be significant and challenging. On the one hand, the image represents very highly good quality with varied shading illuminated by light source. On the other hand, some light gridlines are superimposed in the image. The gridlines were added for the sake of manual counting. In addition, those cells' shape takes on lots of irregular deformation, which is the primary problem we have to solve to segment effectively. As we well know, image segmentation is the bridge to classification properly. We aimed to develop a satisfied algorithm to classify the red blood cells into different groups accurately. And also we believed that conventional segmentation methods based on gray value could be unsuitable to this case. In this paper we proposed a new strategy to segment RBC image according to surface feature extraction. At first, we have to estimate the distribution of erythrocyte shapes from scanned electron microscope. Then each cell's three-dimension shape was reconstructed as 3D height field using shape-from-shading technique. Lastly we implement multiscale surface fitting segmentation algorithm to partition the cells based on the depth data acquired in the previous procedures.

This paper is organized as follow. Firstly the preliminary work including system framework and image preprocessing are introduced in Section 2. In Section 3, a guided contour tracing method was used to extract the boundary and center point information. Accordingly all pixels of each cell which is located on the top of overlapped cells can be further obtained, whose intensity tone is disposed as shading information. The 3-D reconstruction of each cell is introduced in Section 4. We deduced an image irradiance equation under SEM imaging condition with linear approximation. Shape-from-shading technique is applied in this project, such as shape-from-shading technique using linear approximation. The next section is about to divide surface into several different types after computing mean curvature and Gaussian curvature. Multiscale surface fitting segmentation algorithm is proposed in Section 6 which involves seed extraction, region growing, and so on. In the end, Section 7 draws some conclusions and expects a few future works.

2. Image Preprocessing and System Framework

As shown in Figure 2(a), there existed some bright gridlines superimposed on the original image, which have some side effects on the subsequent work. As mentioned before, the images show perfect quality other than these lines, which is used to count and classification manually. The system we developed here is to relieve human from exhausted hand work and run automatically. Additionally, in terms of the shading information being critical in our case, we regard the lines as noise and we have to remove them before recovering the 3D shape from gray tone image.

2.1. System Framework

We describe the system framework in Algorithm 1.

2.2. Image Processing Using Median Filtering Locally

As time consumption is sensitive during RBCs classification, we make use of median filter to get rid of the gridlines. The median filter is a smoothing technique that causes minimal edge

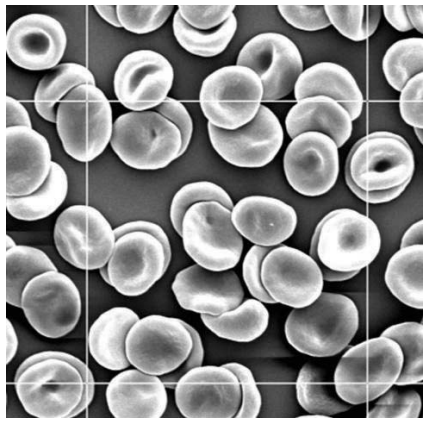

(a) Gridline superimposed image

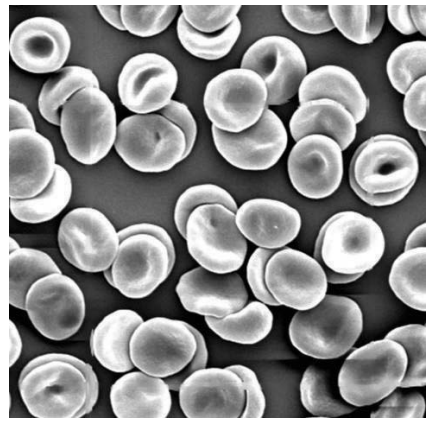

(b) Denoising using median locally

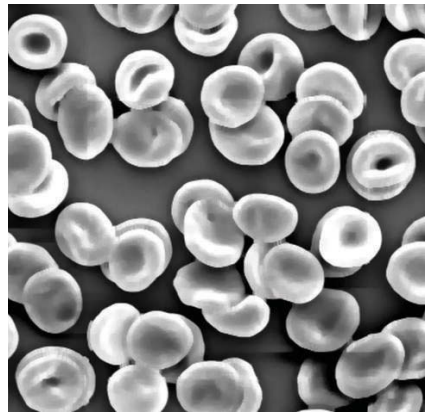

(c) Denoising using median filter directly on the whole image

Figure 2: RBC image preprocessing.

blurring, which involves replacing the pixel value at each point in an image by the median of the pixel values in a neighborhood about the point:

$$g(x,y) = \operatorname{med}\{f(x-k,y-l),(k,l \in W)\}, \tag{2.1}$$

where $f(x,y)$ is the original image and $g(x,y)$ is median filtered image, respectively. W is a 2-dimensional 7*7 template.

Figure 2(a) shows a scaled original RBC image with four white gridlines superimposed on it. The denoised image after median filtering directly on whole image is presented in Figure 2(c), in which the lines are removed successfully. However, the edges of cell image have been blurred and brightness changed at the same time. Consequently the issue of inaccuracy would arise from the change, because the recovered shape is relied on

1. Image Denoising
1.1 Find the rough position of each grid line;
1.2 Remove the noise using median filtering locally.
2. Cell Extraction Individually
2.1 Guided boundary contour tracing;
2.2 Cell Extraction through 4-neighborhood region growing.
3. Shape from Shading Using Linear Approximation
3.1 Image Irradiance Equation Deduction;
3.2 3-D Shape Reconstructing.
4. Computing RBC shape surface feature
4.1Compute mean curvature and Gaussian curvature using image convolution;
4.2 Set a threshold for this two curvature.
5: Segmentation through multiscale surface fitting
More details is in Section 6: Experiment.

Algorithm 1

the irradiance mostly. Fortunately we can detect the exact positions where those lines are by horizontal and vertical projection using

$$\sum_{i \oplus j} Q(i,j), \tag{2.2}$$

respectively, where $Q(i,j)$ only represents those pixels whose gray value is approximately equal to the pixels in those white gridlines. $i \oplus j$ means that only horizontal pixels are computed when sum on i and vertical pixels are projected when sum on j as well. Experimental results show that, while determining the exact positions of vertical lines, the points located in the range of $i \in [253, 259]$ or $[509, 517]$ have to be considered only. And those points whose j coordinate is in the range of $j \in [253, 259]$, $[509, 515]$, $[765, 771]$ have to be dealt with when impose median filtering locally.

As a result, this local median filtering method leads to a handily approach, namely filling locally combined with median filtering, 7*7 structure element defined. The improved result is shown in Figure 2(b), in which all the cells keep the same shading information as the original image and the gridlines have been removed successfully as well.

3. Tracing Contour and Cell Extraction Individually

3.1. Guided Contour Tracing

Vromen and McCane [10] proposed a method named contour-tracing-based approach to the problem of finding the boundary of red blood cells in a scanned electron microscope image automatically. As shown in the above Figure 1, there are considerable overlapped cells. We are just only interested in estimating the distribution of different erythrocyte shapes from SEM image rather than the accurate counting number. So it makes sense to assume that the distribution of overlapped cells is identical to the overall distribution. Consequently only those top-level cells are needed to be detected and recognized. At the very beginning, the most possible direction is chosen by taking the prior information of tracing into account so

far. Since the cell contours are likely elliptical, it would be reasonable to fit a conic shape to the path. A parameterized second-degree polynomial over the last n points was modeled the local curvature:

$$\begin{aligned} x(t) &= at^2 + bt + c, \\ y(t) &= et^2 + ft + g. \end{aligned} \tag{3.1}$$

The best fitting polynomial was calculated through a number of data points using least squares. In order to increase accuracy and decrease computation, consider only the directions with angles in a certain window around the predicted direction. This was represented with a set of unit vector $u_i \in U$:

$$U = \left\{ \left(\cos(\alpha_i + \beta), \sin(\alpha_i + \beta)\right) \mid \beta_{\min} \leq \beta \leq \beta_{\max} \right\}, \tag{3.2}$$

where α_i is the angle of the predicted tangent. In our application β is uniformly sampled between $\beta_{\min} = -(\pi/2)$ and $\beta_{\max} = (\pi/2)$.

Figure 3(a) shows the scaled 256*256 RBC image, and the contours after guided tracing are presented in Figure 3(b). There are 7 traced contours in Figure 3(b) which are located on top level of overlapped cell image. All of the contour information is stored as attributes in an XML file. It also contains the locus of each point on the boundary.

3.2. Cell Extraction Individually

As shown in Figure 4, there is a break point marked by a white circle in each traced boundary, which would result in a wrong region when growing we should fill them as a complete boundary point before growing. If the number of neighbors around a predicted boundary point is less than three under 8-connectivity, we consider it as a break point. The relationships between the two break points and how they break with each other are shown in Figure 5.

According to the extracted cell contours' information, we can grow each cell starting at center point regionally to get the entire cell image. The algorithms can be described in Algorithm 2.

The resulting image of region growing subject to contour boundary is shown in Figure 3(c). After growing regionally, we got the number of pixels which make the whole image and their gray level value. In Table 1, there are 7 cell contours that have been extracted altogether, where CENTER_X and CENTER_Y are the cell's center point coordinates and PIXELS denotes the pixels number involved in each cell.

4. Shape from Shading Using Linear Approximation

4.1. Shape from Shading and PDE

The "shape from shading" problem, namely, SFS, is to recover the 3-D shape of a surface from a gray-level monochrome image. In the 1970s Horn firstly proposed the approach to reconstruct the original shape from a varied shading image, which associated with obtaining a solution of a nonlinear first-order partial differential equation (PDE), that is, brightness

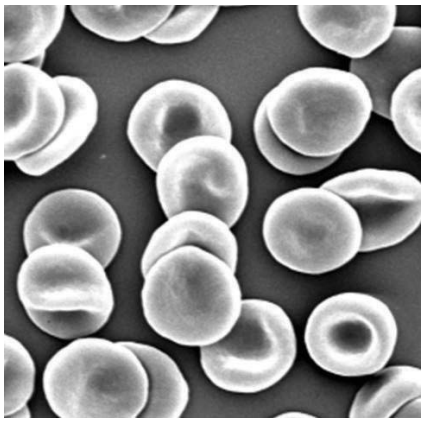

(a) Scaled 256*256 image

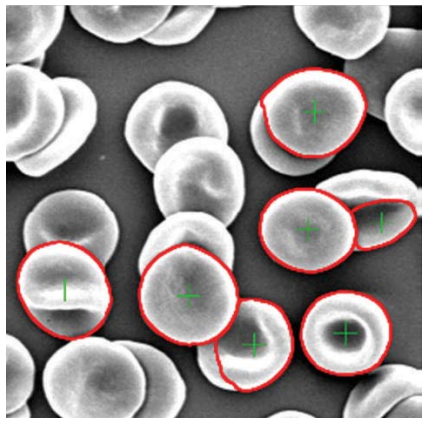

(b) Contour after guided tracing

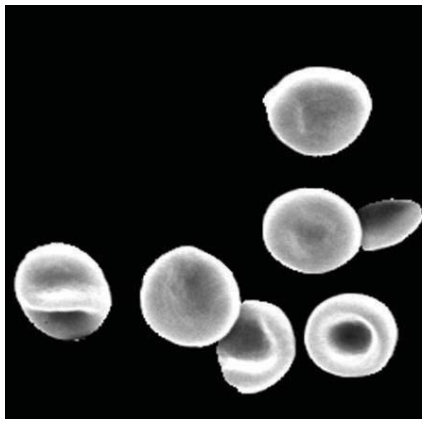

(c) Extracted cells

Figure 3: Cell image extracted using contour tracing.

Figure 4: Break point in cells boundary.

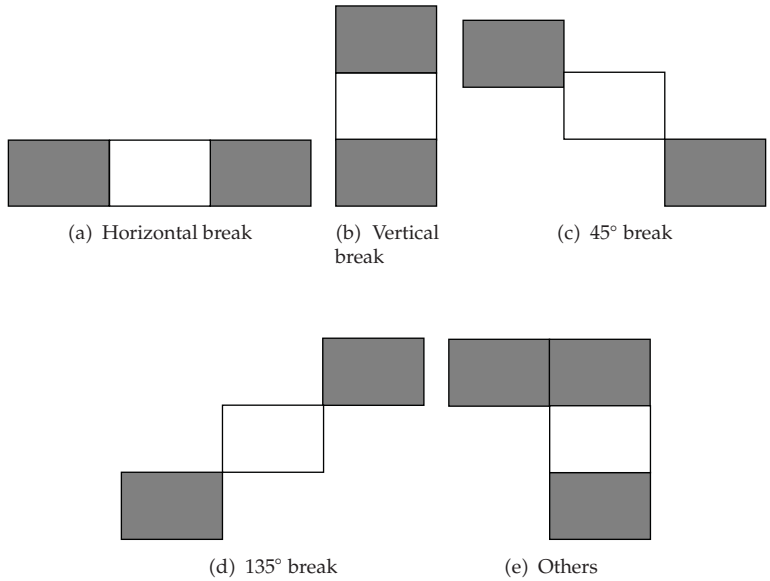

Figure 5: Five different types of break points.

1. Draw some key points for region growing
Collect the center points and contour points from the extracted contour which is stored in a XML data file.
2. Region Growing
2.1 Set the center point as a seed;
2.2 Grow the cell from the seed in the way of 4 connectivity neighborhoods till touch certain point on contour;
2.3 Store the pixels' information into a XML file attributed by position and gray level as tree nodes.
3. Continue to calculate cell pixels included in next contour
4. If All cells have been extracted successfully, then exit
5. Else return 1

Algorithm 2: Region growing algorithm.

equation. From then on, a number of articles have emerged which come up with various kinds of methods to strive to implement this technique into real or artificial synthetic images.

This PDE equation arises from the

$$I(x_1, x_2) = R(n(x_1, x_2)). \tag{4.1}$$

(x_1, x_2) is the coordinates of a point x in the image. The brightness equation connects the reflectance map (R) to the brightness image (I). Almost all the shape-from-shading methods at the exception of an extremely small number of papers [11–13] assume that the scene model

Table 1: Contours' information of traced cells.

No.	Center_X	Center_Y	Pixels
1	37.884	175.931	2697
2	114.131	179.526	2927
3	191.346	65.3348	2777
4	187.606	138.718	2516
5	154.363	209.667	2027
6	211.253	202.634	2359
7	233.308	134.118	953

is Lambertian. The reflectance map is the cosine of the angle between the light vector $\mathbf{L}(x)$ and the normal vector $\mathbf{n}(x)$ to the surface:

$$R = \cos(L, n) = \frac{L}{|L|} \cdot \frac{n}{|n|}, \tag{4.2}$$

where R, **L,** and **n** depend on (x_1, x_2) [14].

Shape from shading is a fundamental issue in computer vision, and considerable research has been performed [15, 16] in trying to solve this problem including methods of medical image processing. In [17], the authors applied their method to an endoscopic image of a normal stomach and showed the result obtained by generic algorithm in the perspective case with the light source at the optical center, which is not suitable for SEM. Tankus et al. in their papers [18–20] suggested the reconstruction algorithm under an assumption of perspective shape from shading. Deguchi and Okatani [21] accomplished shape reconstruction from an endoscope image by shape-from-shading technique for a point light source at the projection center.

4.2. Reflectance Map under SEM Imaging Condition

Jones and Taylor [22] proposed that SEM imaging process is particularly appropriate for SFS, since it allows us to make the simplifying assumptions that the projection is orthographic and the "light source" is at infinity. The Lambertian reflectance function is given by

$$R(p, q) = \eta\ \hat{n} \cdot \hat{I}, \tag{4.3}$$

where $\hat{n} = (-p, -q, 1)/\sqrt{p^2 + q^2 + 1}$ is the unit normal vector, $\hat{I}$ is a unit vector in the direction of the light source, and η is the surface albedo.

The SEM reflectance function is based upon the theoretical prediction that the number of electron emitted from a surface in the SEM is proportional to the secant of the angle between the illumination direction and the surface normal. The reflectance function is denoted by [22]

$$R(p, q) = \frac{\eta}{\hat{n} \cdot \hat{I}}. \tag{4.4}$$

In this paper, we assume that the image is formed by orthographic projection, because the object specimen examined by SEM is very small in comparison to distance from light source.

4.3. Linear Approximation

In [23], the authors believed that the linearity of the reflectance map in the depth Z, instead of p and q, is more appropriate in some cases. They presented a method for computing depth from a single-shaded image by employing the discrete approximations for p and q using finite differences and linearly approximating the reflectance in $Z(x,y)$. It gave good results for the spherical surface and can be applied to any reflectance function.

In this paper we aim to recover the red blood cell's shape of an image captured by SEM based on linear approximation. It is extended to solve such a problem assumed orthographic projection and derive the implementation equations with the reflectance function inverse to Lambertian reflectance function.

Image irradiance equation (**IRE**) indicates the relationship between reflection function and image irradiance. The recovered shape can be represented by depth map Z, normal (nx, ny, nz), or surface gradient (p,q). The radiance of surface patch depends on gradient, light source location, and reflectance property. The gray level of a pixel in the image is determined by light direction and normal vector, assumed Lambertian model, which can be denoted by **IRE**:

$$E(x,y) = R(p,q) = \frac{1 + pp_s + qq_s}{\sqrt{1+p^2+q^2}\sqrt{1+p_s^2+q_s^2}}, \tag{4.5}$$

where $E(x,y)$ is a gray level at pixel (x,y), $p = \partial z/\partial x$ and $q = \partial z/\partial y$, and $(p_s, q_s, 1)$ is the illumination direction.

By approximating the p and q discretely, we get

$$\begin{aligned} p &= \frac{\partial z}{\partial x} = Z(x,y) - Z(x-1,y), \\ q &= \frac{\partial z}{\partial y} = Z(x,y) - Z(x,y-1). \end{aligned} \tag{4.6}$$

According to (4.6), the reflection function can be rewritten as

$$\begin{aligned} 0 &= f(E(x,y), Z(x,y), Z(x-1,y), Z(x,y-1)) \\ &= E(x,y) - R(Z(x,y) - Z(x-1,y), Z(x,y) - Z(x,y-1)). \end{aligned} \tag{4.7}$$

Under the assumption of the point (x,y) and image E is given, the linear approximation of function f with respect to Z^{n-1} after *Jacobi iteration* method is:

$$\begin{aligned} 0 &= f(Z(x,y)) \\ &\approx f\left(Z^{n-1}(x,y)\right) + \left(Z(x,y) - Z^{n-1}(x,y)\right) \frac{d}{dZ(x,y)} f\left(Z^{n-1}(x,y)\right). \end{aligned} \tag{4.8}$$

The nth iterative result $Z^n(x,y)$ can be denoted by

$$Z^n(x,y) = Z^{n-1}(x,y) + \frac{-f(Z^{n-1}(x,y))}{(d/dZ(x,y))f(Z^{n-1}(x,y))}. \tag{4.9}$$

As mentioned previously, the reflection function is inversal to Lambertian model under the condition of SEM imaging. Equation (4.5) is transformed into

$$R(p,q) = \frac{\sqrt{1+p^2+q^2}\sqrt{1+p_s^2+q_s^2}}{1+pp_s+qq_s}. \tag{4.10}$$

Now we compute the partial derivatives of p and q with R:

$$\begin{aligned}
\frac{\partial R(p,q)}{\partial p} &= \sqrt{1+p_s^2+q_s^2}\,\frac{p(1+pp_s+qq_s)-(1+p^2+q^2)\cdot p_s}{(1+pp_s+qq_s)^2\sqrt{1+p^2+q^2}},\\
\frac{\partial R(p,q)}{\partial q} &= \sqrt{1+p_s^2+q_s^2}\,\frac{q(1+pp_s+qq_s)-(1+p^2+q^2)\cdot q_s}{(1+pp_s+qq_s)^2\sqrt{1+p^2+q^2}}.
\end{aligned} \tag{4.11}$$

So,

$$\frac{\partial R}{\partial p}+\frac{\partial R}{\partial q} = \frac{\sqrt{1+p_s^2+q_s^2}((p+q)(1+pp_s+qq_s)-(1+p^2+q^2)\cdot(p_s+q_s))}{(1+pp_s+qq_s)^2\sqrt{1+p^2+q^2}}. \tag{4.12}$$

The right part of (4.9) is rewritten as

$$\begin{aligned}
\frac{d}{dZ(x,y)}f\left(Z^{n-1}(x,y)\right) &= \frac{\partial R}{\partial p}+\frac{\partial R}{\partial q}\\
&= \frac{\sqrt{1+p_s^2+q_s^2}((p+q)(1+pp_s+qq_s)-(1+p^2+q^2)\cdot(p_s+q_s))}{(1+pp_s+qq_s)^2\sqrt{1+p^2+q^2}}.
\end{aligned} \tag{4.13}$$

We use the shape-from-shading method with linear approximation to reconstruct the red blood cell's 3-D shape as in Figure 6.

5. Curvature Calculation

There are 8 different types of surface altogether, namely peak, pit, ridge, valley, flat, minimal surface, saddle ridge, and saddle valley. The surface type of each data point on a scene object can be designated by the signs of mean curvature and Gaussian curvature uniquely. Both of these two curvatures can be calculated by local convolution [24, 25]. Each data point in a

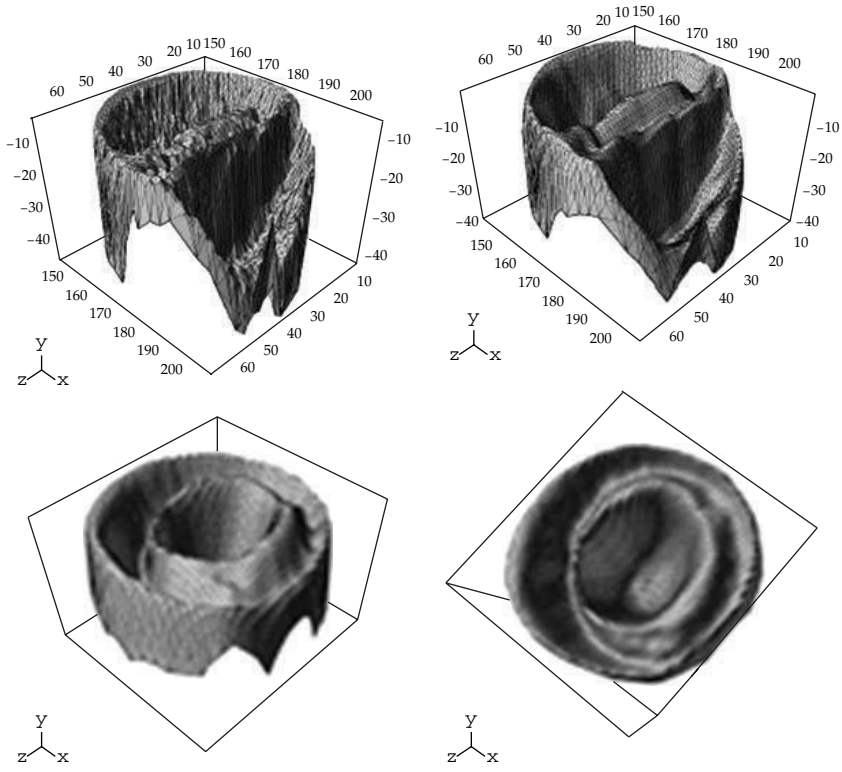

(a) Original shape (b) Filtered smooth shape

Figure 6: Reconstructed RBC 3D shape.

given window N^*N is associated with a 2-dimensional position (u, v) from the set $U \times U$, where

$$U = \left\{ -\frac{N-1}{2}, \ldots, -1, 0, 1, \ldots, \frac{N-1}{2} \right\} \tag{5.1}$$

and N is odd.

The following discrete orthogonal polynomials provide local biquadratic surface fitting capability:

$$\phi_0(u) = 1, \qquad \phi_1(u) = u, \qquad \phi_2(u) = u^2 - \frac{M(M+1)}{3}, \tag{5.2}$$

where $M = (N-1)/2$. The biquadratic is the minimal degree polynomial surface type needed to estimate the first and second partial derivatives. A corresponding set of $b_i(u)$ functions is

the normalized versions of the orthogonal polynomials $\phi_i(u)$ given by $b_i(u) = \phi_i(u)/P_i(M)$, where the $P_i(M)$ are normalizing constants. The three normalization constants are given by

$$\begin{aligned} P_0(M) &= N, \\ P_1(M) &= \frac{2}{3}M^3 + M^2 + \frac{1}{3}M, \\ P_2(M) &= \frac{8}{45}M^5 + \frac{4}{9}M^4 + \frac{2}{9}M^3 - \frac{1}{9}M^2 - \frac{1}{15}M. \end{aligned} \tag{5.3}$$

Defining a set of surface G in R^3 space, $G \subset R^3$, which can be parameterized by

$$G = \left\{ g(u,v) = \begin{bmatrix} g_1(u,v) \\ g_2(u,v) \\ g_3(u,v) \end{bmatrix} : \begin{matrix} u_{\min} < u < u_{\max} \\ v_{\min} < v < v_{\max} \end{matrix} \right\}. \tag{5.4}$$

Before implementing the surface-fitting segmentation algorithm, the surface types have to be divided at first, which is based on mean curvature and Gaussian curvature. The computation of mean curvature and Gaussian curvature of digital surface is approximated by partial derivative estimation, which is calculated via the appropriate 2D image convolution (denoted by $*$):

$$\begin{aligned} g_u &= D_u * S * g, \qquad g_v = D_v * S * g, \\ g_{uu} &= D_{uu} * S * g, \qquad g_{uv} = D_{uv} * S * g, \qquad g_{vv} = D_{vv} * S * g, \end{aligned} \tag{5.5}$$

where $S = \vec{s}\,\vec{s}^{\,T}$ is a 7×7 binomial smoothing window:

$$\begin{aligned} \vec{s} &= \frac{1}{64}\begin{bmatrix} 1 & 6 & 15 & 20 & 15 & 6 & 1 \end{bmatrix}, \\ [D_u] &= \vec{d}_0\,\vec{d}_1^{\,T}, \qquad [D_v] = \vec{d}_1\,\vec{d}_0^{\,T}, \\ [D_{uu}] &= \vec{d}_0\,\vec{d}_2^{\,T}, \qquad [D_{uv}] = \vec{d}_1\,\vec{d}_1^{\,T}, \qquad [D_{vv}] = \vec{d}_2\,\vec{d}_0^{\,T}, \end{aligned} \tag{5.6}$$

where

$$\begin{aligned} \vec{d}_0 &= \frac{1}{7}\begin{bmatrix} 1 & 1 & 1 & 1 & 1 & 1 & 1 \end{bmatrix}^T, \\ \vec{d}_1 &= \frac{1}{28}\begin{bmatrix} -3 & -2 & -1 & 0 & 1 & 2 & 3 \end{bmatrix}^T, \\ \vec{d}_2 &= \frac{1}{84}\begin{bmatrix} 5 & 0 & -3 & -4 & -3 & 0 & 5 \end{bmatrix}^T. \end{aligned} \tag{5.7}$$

Table 2: Average and variance of mean curvature and gaussian curvature.

No.	Average of MC	Average of GC	Variance of MC	Variance of GC
1	−0.00358235	−0.0118867	0.0144467	0.0110893
2	0.0019092	−0.0031961	0.0007467	0.00135311
3	−0.00801067	−0.000136584	0.00776577	8.05916e−06
4	0.00362456	−0.00492172	0.00174206	0.00280074
5	4.11563e-05	−0.00502711	0.00281172	0.00672413
6	0.00774488	−0.00243966	0.0071536	0.000373712
7	0.00235231	−0.0132902	0.00192086	0.0311508

The mean curvature and Gaussian curvature can be calculated by partial derivative as follows:

$$H = \frac{\left(1+g_v^2\right)g_{uu} + \left(1+g_u^2\right)g_{vv} - 2g_u g_v g_{uv}}{2\left(\sqrt{1+g_u^2+g_v^2}\right)^3},$$
$$K = \frac{g_{uu}g_{vv} - g_{uv}^2}{\left(1+g_u^2+g_v^2\right)^2}. \tag{5.8}$$

Table 2 shows the average and variance of mean curvature and Gaussian curvature of the 7 extracted cells in Figure 3.

6. Experiment

6.1. Surface-Type-Based Image Segmentation

The fundamental formulation of region-based image segmentation is defined as

(1) $U_{i=1}^{n} R_i = R$;

(2) R_i is a connected region, $i = 1, 2, \ldots, n$;

(3) $R_i \cap R_j = \Phi$, for $\forall(i, j)$, $i \neq j$;

(4) $P(R_i) = TRUE$, $i = 1, 2, \ldots, n$;

(5) $P(R_i \cup R_j) = FALSE$, R_i is adjacent to R_j,

where $P(R_i)$ is a uniformity predicate defined on groups of connected pixels. R_i was grown regionally via 8-connected neighborhood. All the points in region R_i satisfy the same surface function. Different regions meet different surface fitting function.

The segmentation procedure is divided into two mainly different parts. Firstly we compute the surface-type label image by

$$T = 1 + 3\left(1 + 3\mathrm{sgn}_{\varepsilon_H}(H)\right) + \left(1 - 3\mathrm{sgn}_{\varepsilon_K}(K)\right), \tag{6.1}$$

where T denotes the surface type ranging from 1 to 9 as shown in Table 3.

Table 3: Surface type defined by mean and Gaussian curvature.

	$K > 0$	$K = 0$	$K < 0$
$H < 0$	Peak ($T = 1$)	Ridge ($T = 2$)	Saddle ridge ($T = 3$)
$H = 0$	None ($T = 4$)	Flat ($T = 5$)	Minimal surface ($T = 6$)
$H > 0$	Pit ($T = 7$)	Valley ($T = 8$)	Saddle valley ($T = 9$)

1. Initialization
1.1 Get the whole depth map image from the output of shape from shading procedure;
1.2 Obtaining the range image by filling the value of each pixel, which is associated with the current processing cell by depth data;
1.3 Compute an estimate of the noise variance at each pixel;
1.4 Computing mean curvature and Gaussian curvature through separable convolution;
1.5 Computing the surface type label image and find all connected components of each surface type label image, sort it to get histogram distribution;
1.6 Extracted seed region through erosion (contraction) operation.
2. Iterative variable order surface fitting
2.1 Perform surface fit from the lowest order, if it is OK using RMS error and region test;
2.2 Then goto 3;
2.3 Else increase the order and fit again;
2.4 if order >4, then return.
3. Region Growing
3.1 Find the new region consisting of compatible connected neighboring pixels.

Algorithm 3: Algorithm of multiscale segmentation through mapped depth.

We the define root mean square error (RMSE) as

$$\sigma_{S_N}^2 = \frac{1}{N} \sum_{(x,y)\in S_N} \left(z_{ij} - \Phi_{\vec{a}}(x,y)\right)^2, \tag{6.2}$$

to measure whether the difference between fitted value and original depth is confined to the range preset by a threshold as in Algorithm 3.

6.2. Algorithm

6.2.1. Experimental Result

In our experiment, we define the RMS fit error as $\varepsilon = \omega\sigma_{\text{img}}$, where σ_{img} means noise variance, and

$$\hat{z}(p) = \hat{f}\left(m^k, \vec{a}_l, x(p), y(p)\right) \tag{6.3}$$

is compared with

$$z(p) = \tilde{g}(x(p), y(p)), \tag{6.4}$$

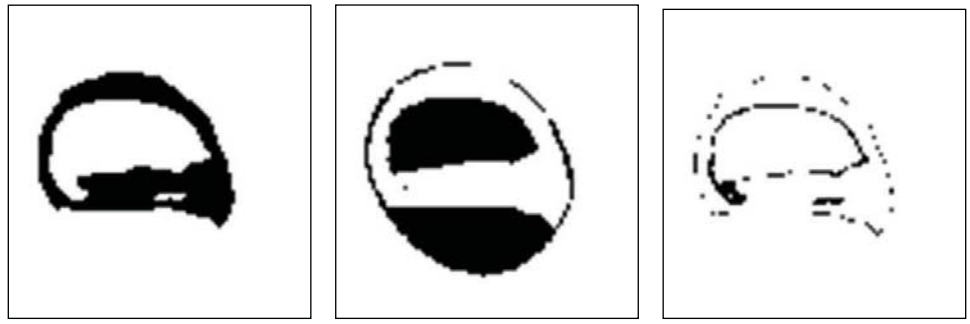

(a) Flat (b) Pit (c) Valley

Figure 7: Three surface-type components.

to see if the pixel p is compatible with the approximating surface function. If the magnitude of the difference between the function value and the digital surface value is less than the allowed tolerance value, denoted by $\omega_0 \cdot \varepsilon_l^k$, then the pixel p is added to the set of compatible pixels, denoted by $C(m_k, \vec{a}_l^k, \varepsilon_l^k)$, which are compatible with the surface fit to the region $\widehat{R}_l^k$. Otherwise, the pixel is incompatible and discarded. The result of this process is the compatible pixel list:

$$C\left(m_k, \vec{a}_l^k, \varepsilon_l^k\right) = p \in I : \left|\widehat{z}(p) - z(p)\right| \leq \omega_0 \varepsilon_l^k. \tag{6.5}$$

We choose $\omega_1 = 4.5$ and $\omega_0 = 8$ experimentally.

If we threshold the mean curvature and Gaussian curvature with an appropriate value, only three different surface type are remained among all cells. In our experiment, we choose

$$\begin{aligned} \varepsilon_H &= 0.0015, \\ \varepsilon_K &= 0.03 \end{aligned} \tag{6.6}$$

as the mean curvature and Gaussian curvature separately. The function of sgn in (6.1) is defined as

$$\operatorname{sgn}(H, K) = \begin{cases} 1 & (\varepsilon, +\infty) \\ 0 & (-\varepsilon, +\varepsilon) \\ -1 & (-\infty, -\varepsilon). \end{cases} \tag{6.7}$$

The three kinds of surface type are flat, pit, and valley, respectively, as shown in Figure 7.

Figure 8 represents the process of extracting seed region through erosion (contraction) operation. In order to implement the surface fitting segmentation algorithm, the seed region has to be obtained using erosion operation firstly. After several iteration, the pixel numbers of remained regions for growing are 32, 34, 45, 6 for these four region, respectively.

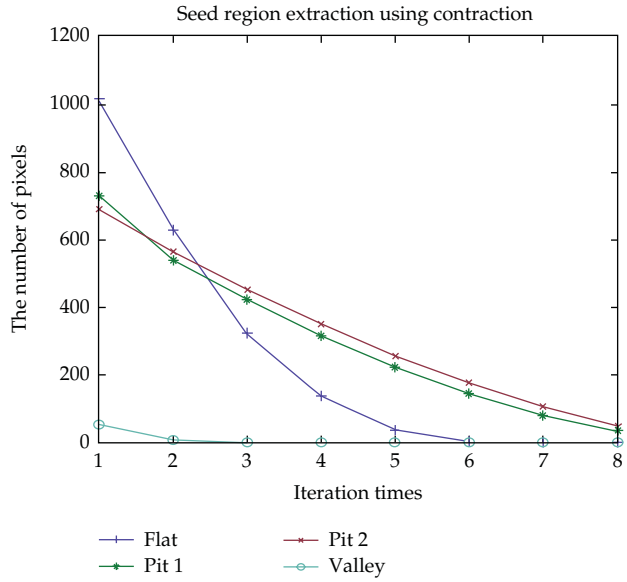

Figure 8: Contraction process to extract seed region of red blood cell.

Table 4: Accuracy of segmentation.

Category	Number of flat surfaces	Number of pit surfaces	Number of valley Surfaces	Accuracy
1	1	1	0	88.9%
2	1	2	0	93.3%
3	2	1	0	90.9%
4	0	1	0	100%
5	3	3	0	100%
6	2	2	1	100%
7	3	1	0	100%
8	2	2	0	94.6%
9	1	1	1	100%
10	2	1	1	100%
11	1	2	1	100%

In Figure 9, the cell is segmented into three isolated parts perfectly, which are obtained through fitting based on surface type.

6.3. Evaluation

In order to evaluate our proposed combined algorithm, we used a dataset containing 800 SEM images. These images are with resolution of 1024 by 768 pixels. For our evaluation, we ran the algorithm on 100 randomly selected images.

We divided the cells into different categories according to their distribution of surface type. Table 4 elaborated the segmentation accuracy of each category.

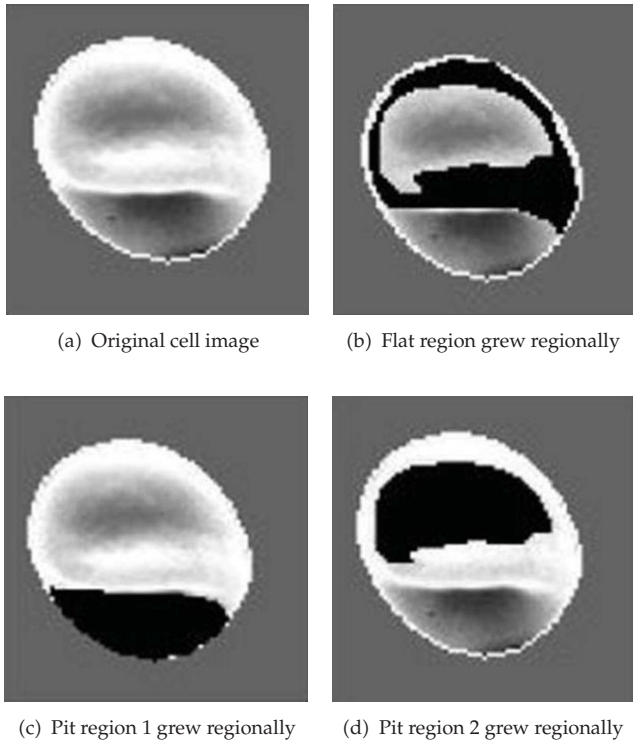

(a) Original cell image (b) Flat region grew regionally

(c) Pit region 1 grew regionally (d) Pit region 2 grew regionally

Figure 9: The segmentation result using surface fitting method.

7. Conclusion and Future Work

This paper is about how to reconstruct the 3D shape of red blood cell from gray tone images using scanned electronic microscope based on shape-from-shading technique, as well combined with linear approximation. The result of cell surface shape is given by height field. Our algorithm can be trivially transformed to various different kinds of reflection models. In Figure 7, the surface-type label image is given with cell number added manually. There are mainly three types of surfaces left after threshold. The distribution of count number of each surface type in every cell can present some useful information for classifying correctly, which will be trained as input data. In the end, we aim to construct a classifier by means of cascaded SVMs architecture to recognize whether the red blood cell is normal or not.

Acknowledgments

This work is sponsored by the National Key Technology R&D Program under Grant no. 2012BAI06B01, Science and Technology Foundations of Chongqing Municipal Education Commission under Grant no. KJ091216, and also by Excellent Science and Technology Program for Overseas Studying Talents of Chongqing Municipal Human Resources and Social Security Bureau under Grant no. 09958023.

References

[1] R. F. Egerton, *Physical Principes of Eletron Miscroscopy*, Springer, 2005.

[2] J. C. Russ, *The Image Processing Handbook*, CRC Press, Boca Raton, Fla, USA, 2007.

[3] C. Di Ruberto, A. Dempster, S. Khan, and B. Jarra, "Analysis of infected blood cell images using morphological operators," *Image and Vision Computing*, vol. 20, no. 2, pp. 133–146, 2002.

[4] S. K. Kumarasamy, S. H. Ong, and K. S. W. Tan, "Robust contour reconstruction of red blood cells and parasites in the automated identification of the stages of malarial infection," *Machine Vision and Applications*, vol. 22, no. 3, pp. 461–469, 2011.

[5] S. Mandal, A. Kumar, J. Chatterjee, M. Manjunatha, and A. K. Ray, "Segmentation of blood smear images using normalized cuts for detection of malarial parasites," in *Proceedings of the Annual IEEE India Conference: Green Energy, Computing and Communication (INDICON '10)*, pp. 1–4, Kolkata, India, 2010.

[6] C. Di Ruberto, A. Dempster, S. Khan, and B. Jarra, "Segmentation of blood images using morphological operators," in *Proceedings of the 15th International Conference on Pattern Recognition (ICPR '00)*, pp. 397–400, IEEE, Barcelona, Spain, 2000.

[7] Z. Liao, S. Hu, and W. Chen, "Determining neighborhoods of image pixels automatically for adaptive image denoising using nonlinear time series analysis," *Mathematical Problems in Engineering*, vol. 2010, Article ID 914564, 14 pages, 2010.

[8] Z. Liao, S. Hu, M. Li, and W. Chen, "Noise estimation for single-slice sinogram of low-dose X-ray computed tomography using homogenous patch," *Mathematical Problems in Engineering*, vol. 2012, Article ID 696212, 16 pages, 2012.

[9] S. Hu, Z. Liao, D. Sun, and W. Chen, "A numerical method for preserving curve edges in nonlinear anisotropic smoothing," *Mathematical Problems in Engineering*, vol. 2011, Article ID 186507, 14 pages, 2011.

[10] J. Vromen and B. McCane, "Red blood cell segmentation using guided contour tracing," in *Proceedings of the 18th Annual Colloquium of the Spatial Information Research Centre (SIRC '06)*, Dunedin, New Zealand, November 2006.

[11] S. Bakshi and Y. Yang, "Shape from shading for non-lambertain surfaces," in *Proceedings of the IEEE International Conference on Image Processing (ICIP '94)*, vol. 94, pp. 130–134, Austin, Tex, USA, 1994.

[12] K. M. Lee and C. C. J. Kuo, "Shape from shading with a generalized reflectance map model," *Computer Vision and Image Understanding*, vol. 67, no. 2, pp. 143–160, 1997.

[13] H. Ragheb and E. Hancock, "A probabilistic framework for specular shape–from-shading," *SIAM Journal of Numerical Analysis*, vol. 29, no. 3, pp. 867–884, 1992.

[14] E. Prados and O. Faugeras, "Shape from shading," in *Handbook of Mathematical Models in Computer Vision*, pp. 375–388, Springer, 2006.

[15] B. K. P. Horn and M. J. Brooks, "The variational approach to shape from shading," *Computer Vision, Graphics and Image Processing*, vol. 33, no. 2, pp. 174–208, 1986.

[16] R. Zhang, P.-S. Tsai, J. E. Cryer, and M. Shah, "Shape from shading: a survey," *IEEE Transactions on Pattern Analysis and Machine Intelligence*, vol. 21, no. 8, pp. 690–706, 1999.

[17] E. Prados, F. Camilli, and O. Faugeras, "A unifying and rigorous shape from shading method adapted to realistic data and applications," *Journal of Mathematical Imaging and Vision*, vol. 25, no. 3, pp. 307–328, 2006.

[18] A. Tankus, N. Sochen, and Y. Yeshurun, "Perspective shape-from-shading by fast marching," in *Proceedings of the IEEE Computer Society Conference on Computer Vision and Pattern Recognition (CVPR '04)*, pp. I43–I49, July 2004.

[19] A. Tankus, N. Sochen, and Y. Yeshurun, "A new perspective on shape-from-shading," in *Proceedings of the 9th IEEE International Conference on Computer Vision (ICCV '03)*, vol. 2, pp. 862–869, October 2003.

[20] A. Tankus, N. Sochen, and Y. Yeshurun, "Reconstruction of medical images by perspective shape-from-shading," in *Proceedings of the 17th International Conference on Pattern Recognition (ICPR '04)*, vol. 3, pp. 778–781, August 2004.

[21] K. Deguchi and T. Okatani, "Shape reconstruction from an endoscope image by shape-from-shading technique for a point light source at the projection center," in *Proceedings of the Workshop on Mathematical Methods in Biomedical Image Analysis*, pp. 290–298, IEEE, San Francisco, Calif, USA, June 1996.

[22] A. G. Jones and C. J. Taylor, "Robust shape from shading," *Image and Vision Computing*, vol. 12, no. 7, pp. 411–421, 1994.

[23] P.-S. Tsai and M. Shah, "Shape from shading using linear approximation," *Image and Vision Computing*, vol. 12, no. 8, pp. 487–498, 1994.
[24] P. J. Besl and R. C. Jain, *Surface in Range Image Understanding*, Springer, New York, NY, USA, 1988.
[25] P. J. Besl and R. C. Jain, "Segmentation through variable-order surface fitting," *IEEE Transactions on Pattern Analysis and Machine Intelligence*, vol. 10, no. 2, pp. 167–192, 1988.

Hindawi Publishing Corporation
Mathematical Problems in Engineering
Volume 2012, Article ID 717543, 12 pages
doi:10.1155/2012/717543

Research Article

Nonlinear Response of Vibrational Conveyers with Nonideal Vibration Exciter: Superharmonic and Subharmonic Resonance

H. Bayıroğlu,[1] G. F. Alışverişçi,[1] and G. Ünal[2]

[1] *Yıldız Technical University, 34349 Istanbul, Turkey*
[2] *Yeditepe University, 34755 Istanbul, Turkey*

Correspondence should be addressed to H. Bayıroğlu, hbayir@yildiz.edu.tr

Received 17 October 2011; Accepted 24 November 2011

Academic Editor: Swee Cheng Lim

Vibrational conveyers with a centrifugal vibration exciter transmit their load based on the jumping method. Common unbalanced-mass driver oscillates the trough. The motion is strictly related to the vibrational parameters. The transition over resonance of a vibratory system, excited by rotating unbalances, is important in terms of the maximum vibrational amplitude produced and the power demand on the drive for the crossover. The mechanical system is driven by the DC motor. In this study, the working ranges of oscillating shaking conveyers with nonideal vibration exciter have been analyzed analytically for superharmonic and subharmonic resonances by the method of multiple scales and numerically. The analytical results obtained in this study agree well with the numerical results.

1. Introduction

The load-carrying element of a horizontal shaking conveyer performs, as a rule, linear (or sometimes circular or elliptical) symmetrical harmonic oscillations—with a sinusoidal variation of exciting force. In vertical shaking conveyers, the load-carrying element performs double harmonic oscillations: linear along the vertical axis and rotational around that axis (i.e., longitudinal and torsional oscillations). Conveyer drives with centrifugal vibration exciters may have (1) a single unbalanced-mass, (2) two equal unbalancing masses, (3) a pendulum-type unbalanced-mass, (4) four unbalanced-masses in two shafts, (5) four rotating unbalanced-masses for three principal modes of oscillation, that is, linear, elliptical, and circular. To induce strictly oriented linear oscillations of the load-carrying element, the conveyer drive should be arranged so that the line of excitation force passes through the

inertial centre of the entire oscillating system. Nonideal drives find application in suspended and supported vibrational conveyers and feeders [1].

By the characteristics and adjustment of the elastic support elements (oscillating system), we can distinguish between shaking conveyers with a resonant, subresonant, and superresonant system.

A practical difficulty with unbalanced-mass exciters, observed as early as 1904 by A Sommerfeld, is that local instabilities may occur in operating speed of such devices.

Rocard [2], Mazert [3], Panovko, and I. I. Gubanova [4] have studied the problem of the stability of the unbalanced-mass exciter.

The first detailed study on the nonideal vibrating systems is presented by Kononenko. He obtained satisfactory results by the comparison of the experimental analysis and the approximated method [5].

After this publication, the nonideal problem was presented by Evan-Ivanowski [6] or Nayfeh and Mook [7]. These authors showed that sometimes dynamical coupling between energy sources and structural response that had not to be ignored in reel engineering problems.

Theorical studies and computations of Ganapathy and Parameswaran have indicated the beneficial effect of the "material load" during the starting and transition phase of an unbalanced-mass-driven vibrating conveyor [8].

Bolla et al. analyzed through the multiple scales method a response of a simplified nonideal and nonlinear vibrating system [9].

Götzendorfer in [10] presented a macromechanical model for the transport of granular matter on linear and horizontal conveyors subject to linear, circular or elliptic oscillations and compared it to experimental results [10].

2. The Governing Equations of the Motion

The equations of motion for the modified rocard system may be obtained by using Lagrange's equation

$$\frac{d}{dt}\left(\frac{\partial T}{\partial \dot{q}_i}\right) + \frac{\partial D}{\partial \dot{q}_i} - \frac{\partial T}{\partial q_i} + \frac{\partial V}{\partial q_i} = 0, \tag{2.1}$$

where T, the kinetic energy, is

$$T = \frac{1}{2}M\dot{y}^2 + \frac{1}{2}m\left[\left(\dot{y} + \dot{\theta}e\cos\theta\right)^2 + \left(\dot{\theta}e\sin\theta\right)^2\right] + \frac{1}{2}I_{\text{mot}}\dot{\theta}^2, \tag{2.2}$$

where e is the eccentricity of the mass m, m is the unbalanced-mass, M is the mass of the trough and the conveyed material on the trough of the conveyor, θ is the angle of rotation of the shafts carrying unbalanced-masses, I_{mot} is the moment of inertia of the rotating parts in the motor, V, the potential energy, is

$$V = \frac{1}{2}k_1y^2 + \frac{1}{4}k_2y^4 + mge(1 + \sin\theta), \tag{2.3}$$

where the constants k_1 and k_2 are the linear and nonlinear elastic coefficients, respectively, D, the Rayleigh dissipation function, is

$$D = \frac{1}{2}c\dot{y}^2 + \frac{1}{2}K(\omega_s - \dot{\theta}), \tag{2.4}$$

and q_i is the generalized coordinate. Applying Lagrange's equation for the two coordinates $q_i = y$ and $q_i = \theta$ gives the differential equations of motion

$$\begin{gathered} M\ddot{y} + m\ddot{y} + c\dot{y} + k_1 y + k_2 y^3 = me\left(\dot{\theta}^2 \sin\theta - \ddot{\theta}\cos\theta\right), \\ \left(\underbrace{I_{\text{mot}} + me^2}_{I_{\text{sys}}}\right)\ddot{\theta} + me\left(\ddot{y}\cos\theta + g\cos\theta\right) = \frac{1}{2}\left[\frac{\partial K}{\partial\dot{\theta}}(\dot{\theta} - \omega_s) + K\right]. \end{gathered} \tag{2.5}$$

Equation (2.5) can be rewritten as follows:

$$\ddot{y} + \omega_0^2 y = \varepsilon\left[-2\mu\dot{y} - \alpha y^3 - e\ddot{\theta}\cos\theta\right] + \kappa\left(\dot{\theta}^2 \sin\theta\right), \tag{2.6}$$

$$\ddot{\theta} = \varepsilon\left[-I\cos\theta(\ddot{y} + g) + E(\dot{\theta})\right], \tag{2.7}$$

where

$$\begin{gathered} I = \frac{(m+M)e}{I_{\text{sys}}}, \qquad \kappa = \frac{me}{m+M}, \qquad 2\mu = \frac{c}{m}, \qquad \alpha = \frac{k_2}{m}, \\ \frac{k_1}{m+M} = \omega_0^2, \qquad \frac{m}{m+M} = \varepsilon, \qquad E(\dot{\theta}) = \frac{(m+M)L(\dot{\theta})}{mI_{\text{sys}}}, \\ L(\dot{\theta}) = \frac{1}{2}\left[\frac{\partial K}{\partial\dot{\theta}}(\dot{\theta} - \omega_s) + K\right], \end{gathered} \tag{2.8}$$

where c is the damping coefficient of the vibrating conveyor, g is acceleration due to gravity, $I_{\text{sys}} = (I_m + I_M + I_{\text{mot}})$ is the total moment of inertia of all the rotating parts in the system, and ω_s is the synchronous angular speed of the induction motor [9]. K is the instantaneous drive torque available at the shafts. Note that E contains $L(\dot{\theta})$ that is the active torque generated by the electric circuit of the DC motor, shown in Figure 1.

3. Analytical Solution

Ideal system: if there is no coupling between motion of the rotor and vibrating system and $\dot{\theta}$ = constant ($\theta = \omega t$, $\ddot{\theta} = 0$), (2.6) becomes

$$\ddot{y} + \omega_0^2 y = \varepsilon\left[-2\mu\dot{y} - \alpha y^3\right] + \kappa\omega^2 \sin\omega t. \tag{3.1}$$

On the right side of the equation, a function of time is present.

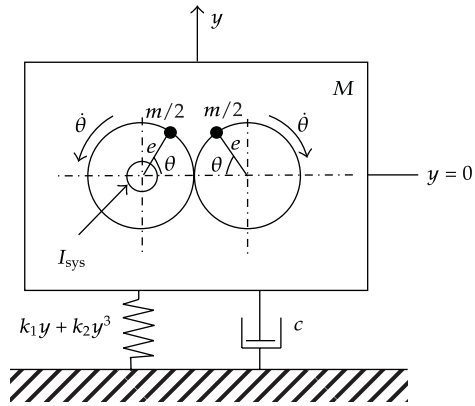

Figure 1: Vibrating model of the system.

Nonideal system:

$$\begin{aligned} \ddot{\theta} &= \varepsilon\left[-I\cos\theta\left(\ddot{y}+g\right)+E\left(\dot{\theta}\right)\right], \\ \ddot{y}+\omega_n^2 y &= \varepsilon\left[-2\mu\dot{y}-\alpha y^3-e\ddot{\theta}\cos\theta\right]+\kappa\left(\dot{\theta}^2\sin\theta\right), \end{aligned} \tag{3.2}$$

where $E(\dot{\theta}) = M_m(\dot{\theta}) - H(\dot{\theta})$ is the difference between the torque generated by the motor and the resistance torque. Function $E(\dot{\theta}) = u_1 - u_2\dot{\theta}$ is approximated by a straight line, where u_1 is a control parameter that can be changed according to the voltage, and u_2 is a constant parameter, characteristic for the model of the motor.

We will obtain an approximate analytical solution to (3.2) by using the multiple scales method:

$$\begin{aligned} \theta(t,\ \varepsilon) &\approx \theta_0(T_0,T_1)+\varepsilon\theta_1(T_0,T_1)+\varepsilon^2\theta_2(T_0,T_1), \\ y(t,\varepsilon) &\approx y_0(T_0,T_1)+\varepsilon y_1(T_0,T_1)+\varepsilon^2 y_2(T_0,T_1), \\ T_n &= \varepsilon^n t, \quad n=0,1,\ldots, \quad T_0=t, \quad T_1=\varepsilon t \end{aligned} \tag{3.3}$$

where the fast scale $T_0 = t$ and slow scale $T_1 = \varepsilon t$. The time derivatives transform according to

$$\begin{aligned} \frac{d}{dt} &= \frac{dT_0}{dt}\frac{\partial}{\partial T_0}+\frac{dT_1}{dt}\frac{\partial}{\partial T_1}+\cdots = D_0+\varepsilon D_1+\cdots \\ \frac{d^2}{dt^2} &= D_0^2+2\varepsilon D_0 D_1+\cdots, \end{aligned} \tag{3.4}$$

where $D_n = \partial/\partial T_n$, $(n = 0, 1, \ldots)$; then,

$$\begin{aligned} \dot{\theta} &= \frac{d\theta}{dt} \approx D_0\theta_0+\varepsilon(D_1\theta_0+D_0\theta_1)+\cdots, \\ \ddot{\theta} &= \frac{d^2\theta}{dt^2} \approx D_0^2\theta_0+\varepsilon\left(2D_0D_1\theta_0+D_0^2\theta_1\right)+\cdots, \end{aligned}$$

$$\dot{y} = \frac{dy}{dt} \approx D_0 y_0 + \varepsilon\left(D_1 y_0 + D_0 y_1\right) + \cdots,$$
$$\ddot{y} = \frac{d^2 y}{dt^2} \approx D_0^2 y_0 + \varepsilon\left(2D_0 D_1 y_0 + D_0^2 y_1\right) + \cdots. \tag{3.5}$$

Substituting (3.5) into (3.2), we will obtain

$$\begin{aligned} D_0^2\theta_0 &= \varepsilon\left[-2D_0D_1\theta_0 - D_0^2\theta_1 - I\cos\theta\left(D_0^2 y_0 + g\right) + E(\dot{\theta})\right], \\ D_0^2 y_0 &+ \varepsilon\left(2D_0D_1y_0 + D_0^2y_1\right) + \omega_n^2(y_0 + \varepsilon y_1) \\ &= \varepsilon\left[-2\mu D_0 y_0 - \alpha\left(y_0\right)^3 - eD_0^2\theta_0\cos\theta\right] + \kappa[D_0\theta_0 + \varepsilon(D_1\theta_0 + D_0\theta_1)]^2\sin\theta\Big], \end{aligned} \tag{3.6}$$

and equating coefficients of a like powers ε, we obtain

(i) for ε^0

$$\begin{aligned} D_0^2\theta_0 &= 0, \\ D_0^2 y_0 + \omega_0^2 y_0 &= \kappa(D_0\theta_0)^2\sin\theta, \end{aligned} \tag{3.7}$$

(ii) for ε^1

$$D_0^2\theta_1 = -2D_0D_1\theta_0 - I\cos\theta\left(D_0^2y_0 + g\right) + E(\dot{\theta}), \tag{3.8}$$

$$\begin{aligned} D_0^2 y_1 + \omega_0^2 y_1 = &-2D_0D_1y_0 - 2\mu D_0y_0 - \alpha\left(y_0\right)^3 - eD_0^2\theta_0\cos\theta \\ &+ \kappa\ 2D_0\theta_0(D_1\theta_0 + D_0\theta_1)\sin\theta. \end{aligned} \tag{3.9}$$

The solution of (3.7) can be written as

$$\theta_0 = BT_0 + \sigma T_1, \tag{3.10}$$

$$y_0 = \Lambda\sin(T_0\Omega) + A(T_1)e^{i\omega_0T_0} + \overline{A}(T_1)e^{-i\omega_0T_0}, \tag{3.11}$$

where

$$\begin{aligned} \cos(\theta_0 + \varepsilon\theta_1) = \cos(\theta_0) + O(\varepsilon), \qquad \sin(\theta_0 + \varepsilon\theta_1) = \sin(\theta_0) + O(\varepsilon), \\ \Lambda = \frac{-\kappa\Omega^2}{\left(\Omega^2 - \omega_0^2\right)}. \end{aligned} \tag{3.12}$$

Table 1: Vibrational conveyer parameters in SI units.

ε	α	μ	c	I	$e(m)$	E_1	E_0	g	ω_0	k_1	k_2	m	M
0.05	0.01	0.01	1	0.9	0.2	1.5	1.6	9.81	1	2 000	100	5	200

3.1. Subharmonic Resonances $\Omega \approx 3\omega_0$ *(Table 1)*

Near resonance:

$$D_0\theta_0 = \Omega, \tag{3.13}$$

$$\Omega = 3\omega_0 + \varepsilon\sigma. \tag{3.14}$$

The solution of (3.13) can be written as

$$\theta_0 = \Omega T_0 = 3\omega_0 T_0 + \sigma T_1. \tag{3.15}$$

Taking

$$A[T_1, T_2] = \frac{a[T_1]}{2} e^{i\beta[T_1]}, \tag{3.16}$$

where a and β are real, and substituting it into (3.11), we will obtain

$$\begin{aligned}
y_0 &= \frac{1}{2}e^{-iT_0\omega_0 - i\beta(T_1)}a(T_1) + \frac{1}{2}e^{iT_0\omega_0 + i\beta(T_1)}a(T_1) + \Lambda\sin(T_0\Omega),\\
\theta_1 &= \frac{1}{8\left(\Omega^3 - \Omega\omega_0^2\right)^2}e^{-i(T_0\omega_0+\beta(T_1))}\\
&\quad\times I\Big(-4\Omega^2\omega_0^2 a(T_1)\\
&\qquad\times\Big(\left(1 + e^{2i(T_0\omega_0+\beta(T_1))}\right)\left(\Omega^2 + \omega_0^2\right)\cos(T_0\Omega) - 2i\left(-1 + e^{2i(T_0\omega_0+\beta(T_1))}\right)\Omega\omega_0\sin(T_0\Omega)\Big)\\
&\qquad -2e^{i(T_0\omega_0+\beta(T_1))}\left(\Omega^2 - \omega_0^2\right)\cos(T_0\Omega)\left(-4g + \left(-\kappa\Omega^2 + \Lambda\omega_0^2\right)\sin(T_0\Omega)\right)\Big),\\
y_1 &= \Big(e^{-i(3T_0\Omega+4T_0\omega_0+3\beta(T_1))}\\
&\qquad\times\Big(-8e^{3i\beta(T_1)}\Omega\left(\Omega^3 + 3\Omega^2\omega_0 - \Omega\omega_0^2 - 3\omega_0^3\right)\\
&\qquad\quad\times\Big(ie^{iT_0(4\Omega+3\omega_0)}\omega_0^2\left(3\alpha\Lambda^3 + 8i\Lambda\mu\Omega + I\kappa^2\Omega^2 - I\kappa\Lambda\omega_0^2\right)\left(36\Omega^4 - 13\Omega^2\omega_0^2 + \omega_0^4\right)\\
&\qquad\qquad + ie^{iT_0(2\Omega+3\omega_0)}\omega_0^2\left(-3\alpha\Lambda^3 + 8i\Lambda\mu\Omega - I\kappa^2\Omega^2 + I\kappa\Lambda\omega_0^2\right)\left(36\Omega^4 - 13\Omega^2\omega_0^2 + \omega_0^4\right)\\
&\qquad\qquad + 4e^{iT_0(\Omega+3\omega_0)}gI\kappa\omega_0^2\left(9\Omega^4 - 10\Omega^2\omega_0^2 + \omega_0^4\right) + 4e^{iT_0(5\Omega+3\omega_0)}gI\kappa\omega_0^2
\end{aligned}$$

$$\times\left(9\Omega^4-10\Omega^2\omega_0^2+\omega_0^4\right)+8e^{3iT_0(\Omega+\omega_0)}gI\kappa\left(36\Omega^6-49\Omega^4\omega_0^2+14\Omega^2\omega_0^4-\omega_0^6\right)$$
$$-ie^{3iT_0(2\,\Omega+\omega_0)}\omega_0^2\left(4\Omega^4-5\Omega^2\omega_0^2+\omega_0^4\right)\left(\alpha\Lambda^3+I\kappa\left(\kappa\Omega^2-\Lambda\omega_0^2\right)\right)$$
$$-ie^{3iT_0\omega_0}\omega_0^2\left(4\Omega^4-5\Omega^2\omega_0^2+\omega_0^4\right)\left(-\alpha\Lambda^3+I\kappa\left(-\kappa\Omega^2+\Lambda\omega_0^2\right)\right)\Big)\Big)$$
$$+2e^{2i\beta(T_1)}\omega_0^2\left(36\Omega^5+108\Omega^4\omega_0^2-39\Omega^2\omega_0^3+\Omega\omega_0^4+3\omega_0^5\right)$$
$$\times\left(e^{iT_0(5\,\Omega+2\omega_0)}(\Omega+\omega_0)^2\left(2I\kappa\Omega\omega_0^2+3\alpha\Lambda^2(-\Omega+\omega_0)\right)\right.$$
$$+e^{i(T_0(\Omega+4\omega_0)+2\beta(T_1))}(\Omega+\omega_0)^2\left(2I\kappa\Omega\omega_0^2+3\alpha\Lambda^2(-\Omega+\omega_0)\right)$$
$$+e^{i(T_0(\Omega+2\omega_0)}(\Omega-\omega_0)^2\left(2I\kappa\Omega\omega_0^2-3\alpha\Lambda^2(\Omega+\omega_0)\right)+e^{i(5T_0\Omega+4T_0\omega_0+2\beta(T_1))}$$
$$\left.\times(\Omega-\omega_0)^2\left(2I\kappa\Omega\omega_0^2-3\alpha\Lambda^2(\Omega+\omega_0)\right)\right)a(T_1)+24ie^{i(T_0(2\,\Omega+\omega_0)+\beta(T_1))}\alpha$$
$$\times\Lambda\Omega\omega_0^2\left(-\left(-1-2e^{2i(T_0\omega_0+\beta(T_1))}+2e^{2i(T_0(\Omega+\omega_0)+\beta(T_1))}+e^{2i(T_0(\Omega+2\omega_0)+2\beta(T_1))}\right)\Omega\right.$$
$$\left.+\left(-1+6e^{2i(T_0\omega_0+\beta(T_1))}-6e^{2i(T_0(\Omega+\omega_0)+\beta(T_1))}+e^{2i(T_0(\Omega+2\omega_0)+2\beta(T_1))}\right)\omega_0\right)$$
$$\times\left(36\Omega^6-49\Omega^4\omega_0^2+14\Omega^2\omega_0^4-\omega_0^6\right)a(T_1)^2+e^{3iT_0\Omega}\left(1+e^{6i(T_0\omega_0+\beta(T_1))}\right)\alpha\Omega$$
$$\times\left(\Omega^2-\omega_0^2\right)^2\left(36\Omega^5+108\Omega^4\omega_0-13\Omega^3\omega_0^2-39\Omega^2\omega_0^2+\Omega\omega_0^4+3\omega_0^5\right)a(T_1)^3\Big)$$
$$\times(\cos(T_0\omega_0)+i\sin(T_0\omega_0)))/\left(64\,\Omega\left(6\Omega^2-5\,\Omega\omega_0+\omega_0^2\right)\right.$$
$$\times\left(-\Omega^2\omega_0+\omega_0^3\right)^2$$
$$\left.\times\left(6\Omega^3+23\Omega^2\omega_0+16\,\Omega\omega_0^2+3\omega_0^3\right)\right).$$

(3.17)

Secular terms will be eliminated from the particular solution of (3.8) if we choose A to be a solution of

$$-2\varepsilon\sigma'+E(\dot{\theta}). \tag{3.18}$$

In addition to the terms proportional to $e^{(\pm i\omega_0T_0)}$ or proportional to $e^{[\pm i(\Omega-2\omega_0)T_0]}$ there is another term that produces a secular term in (3.9). We express $(\Omega-2\omega_0)T_0$ in terms of ω_0T_0 according to

$$(\Omega-2\omega_0)T_0=\omega_0T_0+\varepsilon\sigma T_0=\omega_0T_0+\sigma T_1. \tag{3.19}$$

Table 2: Vibrational conveyer parameters in SI units.

ε	α	μ	c	I	$e(m)$	E_1	E_0	g	ω_0	k_1	k_2	m	M
0.05	0.01	0.01	1	0.9	0.2	1.5	1.6	9.81	10	200 000	100	5	200

3.2. *Superharmonic Resonances* $\Omega \approx (1/3)\omega_0$ ***(Table 2)***

We consider

$$3\,\Omega = \omega_0 + \varepsilon\sigma. \tag{3.20}$$

In addition to the terms proportional to $e^{(\pm i\omega_0 T_0)}$ in (3.9), there is another term that produces a secular term in (3.9). This is $-\alpha\Lambda^3 e^{(\pm 3i\Omega T_0)}$. T_0 eliminate the secular terms, we express $3\,\Omega T_0$ in terms of $\omega_0 T_0$ according to

$$3\,\Omega T_0 = (\omega_0 + \varepsilon\sigma)T_0 = \omega_0 T_0 + \sigma\varepsilon T_0 = \omega_0 T_0 + \sigma T_1. \tag{3.21}$$

Eliminating secular terms in equations, taking (3.16), and separating real and imaginary parts, the system of equations solved it is as follows [11]:

$$\begin{aligned}
y_0 &= \frac{1}{2}e^{-iT_0\omega_0 - i\beta(T_1)}a(T_1) + \frac{1}{2}e^{iT_0\omega_0 + i\beta(T_1)}a(T_1) + \Lambda\sin(T_0\Omega),\\
\theta_1 &= \frac{1}{8\left(\Omega^3 - \Omega\omega_0^2\right)^2}e^{-i(T_0\omega_0+\beta(T_1))}\\
&\quad\times I\Big(-4\Omega^2\omega_0^2 a(T_1)\\
&\quad\times\Big(\Big(1 + e^{2i(T_0\omega_0+\beta(T_1))}\Big)\left(\Omega^2 + \omega_0^2\right)\cos(T_0\Omega) - 2i\Big(-1 + e^{2i(T_0\omega_0+\beta(T_1))}\Big)\Omega\omega_0\sin(T_0\Omega)\Big)\\
&\quad-2e^{i(T_0\omega_0+\beta(T_1))}\left(\Omega^2 - \omega_0^2\right)\cos(T_0\Omega)\left(-4g + \left(-\kappa\Omega^2 + \Lambda\omega_0^2\right)\sin(T_0\Omega)\right)\Big),\\
y_1 &= \Big(e^{-i(2T_0\Omega + 5T_0\omega_0 + 3\beta(T_1))}\\
&\quad\times\Big(-8e^{3i\beta(T_1)}\Omega\Big(\Omega^4 - 10\Omega^2\omega_0^2 + 9\omega_0^4\Big)\\
&\quad\times\Big(4e^{iT_0(4\,\Omega+5\omega_0)}gI\kappa\omega_0^2\left(\Omega^2 - \omega_0^2\right) - 4e^{5iT_0\omega_0}gI\kappa\omega_0^2\left(-\Omega^2 + \omega_0^2\right)\\
&\quad+ ie^{iT_0(3\,\Omega+5\omega_0)}\omega_0^2\left(4\Omega^2 - \omega_0^2\right)\left(3\alpha\Lambda^3 + 8i\Lambda\mu\Omega + I\kappa^2\Omega^2 - I\kappa\Lambda\omega_0^2\right)\\
&\quad+ e^{iT_0(\Omega+5\omega_0)}\omega_0^2\left(-4\Omega^2 + \omega_0^2\right)\left(3i\alpha\Lambda^3 + 8\Lambda\mu\Omega + iI\kappa^2\Omega^2 - iI\kappa\Lambda\omega_0^2\right)\\
&\quad+ 8e^{iT_0(2\,\Omega+5\omega_0)}gI\kappa\left(4\Omega^4 - 5\Omega^4\omega_0^2 + \omega_0^4\right)\Big) + 2e^{2i\beta(T_1)}\omega_0^2\left(4\Omega^4 - 37\Omega^2\omega_0^2 + 9\omega_0\right)
\end{aligned}$$

$$\times \left(e^{4iT_0(\Omega+\omega_0)}(\Omega+\omega_0)^2\left(2I\kappa\Omega\omega_0^2+3\alpha\Lambda^2(-\Omega+\omega_0)\right)+e^{2i(3T_0\omega_0+\beta(T_1))}(\Omega+\omega_0)^2\right.$$
$$\times \left(2I\kappa\Omega\omega_0^2+3\alpha\Lambda^2(-\Omega+\omega_0)+e^{4iT_0\omega_0}(\Omega-\omega_0)^2\left(2I\kappa\Omega\omega_0^2-3\alpha\Lambda^2(\Omega+\omega_0)\right)\right.$$
$$\left.\left.+\ e^{2i(2T_0\Omega+3T_0\omega_0+\beta(T_1))}(\Omega-\omega_0)^2\left(2I\kappa\Omega\omega_0^2-3\alpha\Lambda^2(\Omega+\omega_0)\right)\right)a(T_1)\right.$$
$$-24ie^{i\beta(T_1)}\alpha\Lambda\Omega\omega_0^2\left(4\Omega^4-5\Omega^2\omega_0^2+\omega_0^4\right)$$
$$\times\left(2e^{i(3T_0\Omega+5T_0\omega_0+2\beta(T_1))}\left(\Omega^2-9\omega_0^2\right)-2e^{i(T_0(\Omega+5\omega_0)+2\beta(T_1))}\left(\Omega^2-9\omega_0^2\right)\right.$$
$$-e^{iT_0(\Omega+3\omega_0)}\left(\Omega^2-4\,\Omega\omega_0+3\omega_0^2\right)+e^{i(3T_0\Omega+7T_0\omega_0+4\beta(T_1))}\left(\Omega^2-4\,\Omega\omega_0+3\omega_0^2\right)$$
$$\left.+e^{3iT_0(\Omega+\omega_0)}\left(\Omega^2+4\,\Omega\omega_0+3\omega_0^2\right)-e^{i(T_0(\Omega+7\omega_0)+4\beta(T_1))}\right.$$
$$\times\left.\left(\Omega^2+4\,\Omega\omega_0+3\omega_0^2\right)\right)a(T_1)^2$$
$$+\left(e^{2iT_0(\Omega+\omega_0)}+e^{2i(T_0(\Omega+4\omega_0)+3\beta(T_1))}\right)\alpha\Omega\left(\Omega^2-\omega_0^2\right)^2$$
$$\left.\times\left(4\Omega^4-37\Omega^2\omega_0^2+9\omega_0^4\right)a(T_1)^3\right)\Big)\Big/\left(64\left(-\Omega^2\omega_0+\omega_0^3\right)^2\left(4\Omega^5-37\Omega^3\omega_0^2+9\,\Omega\omega_0^4\right)\right). \tag{3.22}$$

4. Stability Analysis

We analyzed in this system the stability (a,γ) in the equilibrium point, using (4.1), where F is the Jacobian matrix of (4.2), and $\gamma_{\text{sub}} = 3\beta[T_1]-T_1\sigma[T_1]$, $\gamma_{\text{sup}} = [\beta[T_1]-T_1\sigma[T_1]]$. Stability of the approximate solutions depends on the value of the eigenvalues of the Jacobian matrix F [12]. The solutions are unstable if the real part of the eigenvalues is positives Figures 2(a1) and 2(a2). Figure 2 shows the frequency-response curves for the subharmonic and superharmonic resonance of the unbalanced vibratory conveyor:

$$a'_{\text{sub}} = -\mu a-\frac{3}{8\omega_0}\alpha\Lambda a^2\cos[\gamma],$$
$$\gamma'_{\text{sub}} = -\frac{3\left(2I\kappa\Omega^2\omega_0^2+3\alpha\Lambda^2\left(-\Omega^2+\omega_0^2\right)\right)}{4\left(\Omega^2-\omega_0^2\right)\omega_0}+\frac{9}{8\omega_0}\alpha a^2-\frac{9}{8\omega_0}\alpha\Lambda a\sin[\gamma]-\sigma,$$
$$a'_{\text{sub}} = -\mu a-\frac{3}{8\omega_0}\left(\alpha\Lambda^3+I\kappa\left(\kappa\Omega^2-\Lambda\omega_0^2\right)\right)\cos[\gamma], \tag{4.1}$$
$$\gamma'_{\text{sub}} = -\frac{\left(2I\kappa\Omega^2\omega_0^2+3\alpha\Lambda^2\left(-\Omega^2+\omega_0^2\right)\right)}{4\left(\Omega^2-\omega_0^2\right)\omega_0}+\frac{3\alpha a^2}{8\omega_0}+\frac{\left(\alpha\Lambda^3+I\kappa\left(\kappa\Omega^2-\Lambda\omega_0^2\right)\right)\sin[\gamma]}{8\omega_0 a}-\sigma,$$
$$F = \left\{\partial_a f_1,\partial_\gamma f_1\right\},\left\{\partial_a f_2,\partial_\gamma f_2\right\},\quad f_1 = a',\ f_2 = \gamma'. \tag{4.2}$$

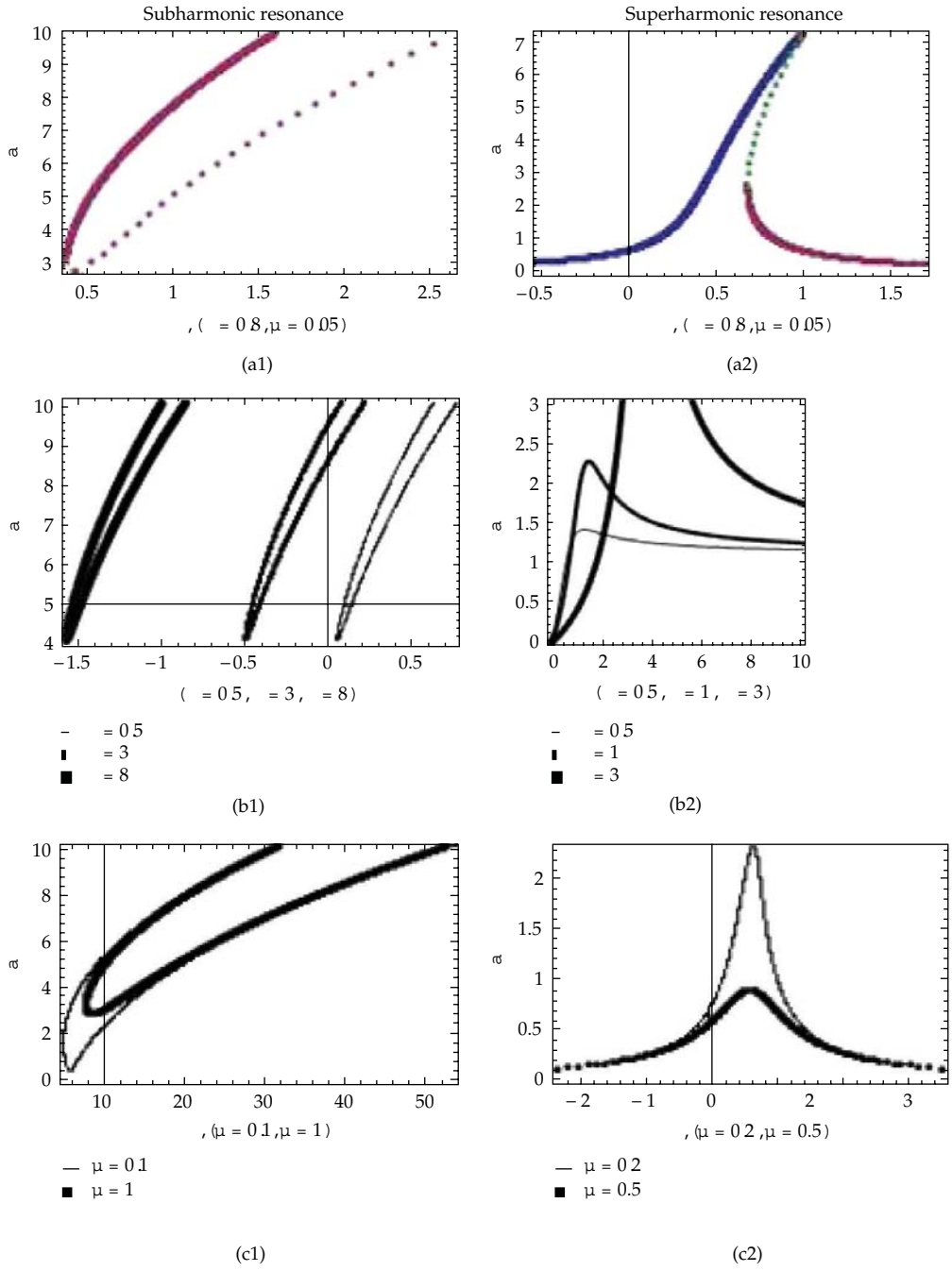

Figure 2: Subharmonic resonance and superharmonic resonance. (a) Frequency-response curves with stability, — stable, ⋯ unstable $\{(a_1) : a = 2.78\text{–}10, \sigma = 0.43258\text{–}2.62092$ and (a_2): $a = 2.73\text{–}7.21, \sigma = 0.6782\text{–}0.986448\}$, (b) effect of detuning parameter, and (c) effect of damping parameter.

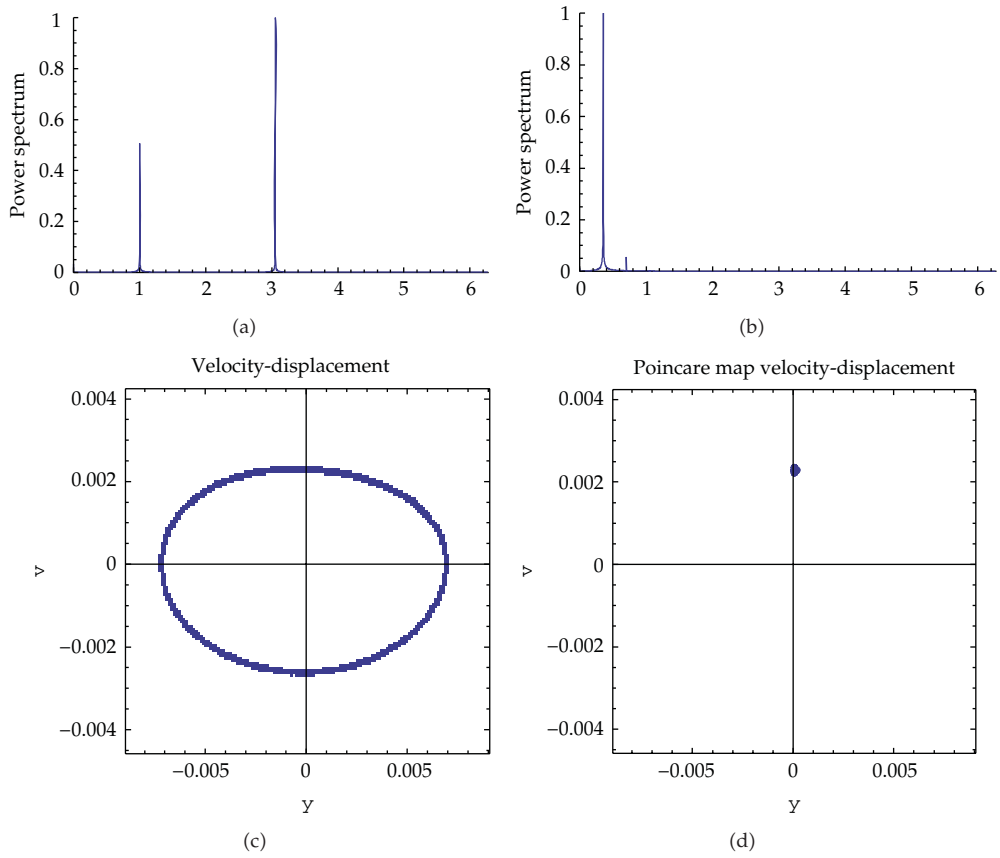

Figure 3: Subharmonic resonance: (a) power spectrum and superharmonic resonance, (b) power spectrum, (c) phase portrait, and (d) Poincaré sections.

5. Numerical Results

The numerical calculations of the vibrating system are performed with the help of the software Mathematica [13, 14]. We analyze the subharmonic resonance $\Omega \approx 3\omega_0$ and superharmonic resonance $3\,\Omega \approx \omega_0$. Figure 3 shows the power spectrum, phase portrait and the Poincaré map for superharmonic resonance and Figure 3 shows the power spectrum for superharmonic resonance.

6. Conclusions

The vibrating system is analyzed, analytically, and numerically for superharmonic and subharmonic resonance by the method of multiple scales. Very often in the motion of the system near resonance the jump phenomenon occurs. The frequency-response curves of the subharmonic resonance consist of two branches; the left one is stable and the right one is unstable (saddle node bifurcation). The frequency-response curves of the superharmonic resonance consist of three branches; the left one is stable, the middle one is unstable, and the right one is stable (pitchfork bifurcation). The stable motions of the oscillator are shown

with one peaks in the power spectrum for superharmonic resonance and with two peaks in the power spectrum for subharmonic resonance. Both analytical and numerical results that we have obtained are in good agreement. The system studied here exhibits chaotic behaviour in case of strong nonlinearity. This will be reported in the forthcoming paper. Furthermore, control methods in the passage through resonance await for future publication.

Acknowledgment

The authors greatly appreciate the comments of an anonymous referee.

References

[1] J. M. Balthazar, D. T. Mook, H. I. Weber et al., "An overview on non-ideal vibrations," *Mechanica*, vol. 38, no. 6, pp. 613–621, 2003.
[2] Y. Rocard, *General Dynamics of Vibrations*, Ungar, New York, NY, USA, 3rd edition, 1960.
[3] R. Mazert, *Mécanique Vibratoire*, C. Béranger, editor, Paris, France, 1955.
[4] Y. G. Panovko and I. I. Gubanova, *Stability and Oscillations of Elastic Systems*, Consultans Bureau, New York, NY, USA, 1965.
[5] V. O. Kononenko, *Vibrating Problems with a Limited Power Supply*, Iliffe, London, UK, 1969.
[6] R. M. Evan-Ivanowski, *Resonance Oscillations in Mechanical Systems*, Elsevier, Amsterdam, The Netherlands, 1976.
[7] A. H. Nayfeh and D. T. Mook, *Nonlinear Oscillations*, John Wiley & Sons, New York, NY, USA, 1979.
[8] S. Ganapathy and M. A. Parameswaran, "Transition over resonance and power requirements of an unbalanced mass-driven vibratory system," *Mechanism and Machine Theory*, vol. 21, no. 1, pp. 73–85, 1986.
[9] M. R. Bolla, J. M. Balthazar, J. L. P. Felix, and D. T. Mook, "On an approximate analytical solution to a nonlinear vibrating problem, excited by a nonideal motor," *Nonlinear Dynamics*, vol. 50, no. 4, pp. 841–847, 2007.
[10] A. Götzendorfer, *Vibrated granular matter: transport, fluidization, and patterns*, Ph.D. thesis, University Bayreuth, 2007.
[11] V. Piccirillo, J. M. Balthazar, and B. R. Pontes Jr., "Analytical study of the nonlinear behavior of a shape memory oscillator: part II-resonance secondary," *Nonlinear Dynamics*, vol. 60, no. 4, pp. 513–524, 2010.
[12] J. Awrejcewicz and C. H. Lamarque, *Bifurcation and Chaos in Nonsmooth Mechanical Systems*, World Scientific, River Edge, NJ, USA, 2003.
[13] A. H. Nayfeh and C. M. Chin, *Perturbation Methods with Mathematica*, Dynamics Press, Virgina, va, USA, 1999.
[14] S. Lynch, *Dynamical Systems with Applications Using Mathematica*, Birkhäauser, Boston, Mass, USA, 2007.

Hindawi Publishing Corporation
Mathematical Problems in Engineering
Volume 2012, Article ID 757018, 17 pages
doi:10.1155/2012/757018

Research Article

A Novel Fractional-Discrete-Cosine-Transform-Based Reversible Watermarking for Healthcare Information Management Systems

Lu-Ting Ko,[1] Jwu-E Chen,[1] Yaw-Shih Shieh,[2] Massimo Scalia,[3] and Tze-Yun Sung[2]

[1] *Department of Electrical Engineering, National Central University, Chungli 320-01, Taiwan*
[2] *Department of Electronics Engineering, Chung Hua University, Hsinchu 300-12, Taiwan*
[3] *Department of Mathematics "Guido Castelnuovo", Sapienza University of Rome, Piazzale Aldo Moro 2, 00185 Rome, Italy*

Correspondence should be addressed to Tze-Yun Sung, bobsung@chu.edu.tw

Received 7 November 2011; Accepted 30 November 2011

Academic Editor: Ming Li

Digital watermarking is a good tool for healthcare information management systems. The well-known quantization-index-modulation- (QIM-) based watermarking has its limitations as the host image will be destroyed; however, the recovery of medical image is essential to avoid misdiagnosis. A transparent yet reversible watermarking algorithm is required for medical image applications. In this paper, we propose a fractional-discrete-cosine-transform- (FDCT-) based watermarking to exactly reconstruct the host image. Experimental results show that the FDCT-based watermarking is preferable to the QIM-based watermarking for the medical image applications.

1. Introduction

In the healthcare information systems nowadays, one of the major challenges is a lack of complete access to patients' health information. Ideally, a comprehensive healthcare information system will provide the medical records including health insurance carriers, which are important for clinical decision making. There is sure to be a risk of misdiagnosis, delay of diagnosis, and improper treatments in case of insufficient medical information available [1].

Digital watermarking, which is a technique to embed imperceptible, important data called watermark into the host image, has been applied to the healthcare information

management systems [2–6]. However, it might cause the distortion problem regarding the recovery of the original host image. In order to protect the host image from being distorted, digital watermarking with legal and ethical functionalities is desirable especially for the medical images applications [7–10]. Specifically, any confidential data such as patients' diagnosis reports can be used as watermark and then embedded in the host image by using digital watermarking with an authorized utilization. Thus, digital watermarking can be used to facilitate healthcare information management systems.

Discrete cosine transform (DCT) has been adopted in various international standards, for example, JPEG, MPEG, and H.264 [11]. The miscellaneous DCT algorithms and architectures have been proposed [12–15]. The fractional discrete cosine transform (FDCT) [16, 17], which is a generalized DCT, is yet more applicable in the digital signal processing applications. In this paper, we propose a novel algorithm called the fractional-discrete-cosine-transform (FDCT-) based watermarking for the healthcare information management applications. In addition, the advantage of FDCT is to take account of the phenomena of image processing [18, 19], which is fundamental in nonlinear time series [20, 21] and fractal time series [22–25]. The remainder of the paper proceeds as follows. In Section 2, the type I fractional discrete cosine transform is reviewed. Section 3 describes the half discrete cosine transform. The proposed FDCT-based watermarking and experimental results on various medical images are presented in Section 4. The architecture of the half-DCT-based watermarking processor implemented by using FPGA (field programmable gate array) is given in Section 5. The conclusion can be found in Section 4.

2. Review of Type I Fractional Discrete Cosine Transform

For the sake of simplicity, let us take the 8-point, type I forward DCT as an example. The corresponding matrix can be expressed as follows [16, 17]

$$\mathbf{C} = \left\| \sqrt{\frac{2}{8-1}} \left[k_m k_n \cos\left(\frac{mn\pi}{8-1} \right) \right] \right\|, \tag{2.1}$$

where

$$k_m = \begin{cases} \dfrac{1}{\sqrt{2}}, & m = 1,\ m = 8, \\ 1, & 1 < m < 8, \end{cases}$$

$$k_n = \begin{cases} \dfrac{1}{\sqrt{2}}, & n = 1,\ n = 8, \\ 1, & 1 < n < 8, \end{cases} \tag{2.2}$$

$$m = 1, 2, 3, \ldots, 8, \quad n = 1, 2, 3, \ldots, 8.$$

It can be diagonalized by

$$\mathbf{C} = \mathbf{U}\mathbf{\Lambda}\mathbf{U}^T, \tag{2.3}$$

where $\mathbf{U}$ is an orthonormal matrix obtained from the eigenvectors of $\mathbf{C}$, which is given by

$$\mathbf{U} = \begin{bmatrix} -0.0854 & -0.3941 & -0.2698 & 0.3618 & -0.4605 & -0.2208 & 0.5689 & -0.2216 \\ -0.0279 & -0.0878 & 0.2942 & -0.4052 & -0.4381 & 0.3122 & 0.3273 & 0.5868 \\ 0.0859 & 0.6984 & -0.2412 & 0.0788 & -0.5416 & -0.3122 & -0.1721 & 0.1418 \\ 0.3807 & 0.4165 & 0.4627 & 0.3663 & 0.0691 & 0.3122 & 0.4141 & -0.2442 \\ -0.0454 & 0.3022 & -0.2725 & -0.4071 & 0.4507 & -0.3122 & 0.6014 & 0.0658 \\ -0.4867 & 0.1983 & 0.0220 & -0.4048 & -0.2402 & 0.3122 & 0.0113 & -0.6537 \\ 0.6633 & -0.2123 & 0.1550 & -0.4814 & -0.1927 & -0.3122 & -0.0790 & -0.3440 \\ -0.4010 & 0.0090 & 0.6852 & 0.0568 & 0 & -0.6053 & 0 & 0 \end{bmatrix}, \tag{2.4}$$

$\mathbf{\Lambda}$ is a diagonal matrix composed of the corresponding eigenvalues, which is given by

$$\mathbf{\Lambda} = \begin{bmatrix} -1 & 0 & 0 & 0 & 0 & 0 & 0 & 0 \\ 0 & -1 & 0 & 0 & 0 & 0 & 0 & 0 \\ 0 & 0 & -1 & 0 & 0 & 0 & 0 & 0 \\ 0 & 0 & 0 & -1 & 0 & 0 & 0 & 0 \\ 0 & 0 & 0 & 0 & 1 & 0 & 0 & 0 \\ 0 & 0 & 0 & 0 & 0 & 1 & 0 & 0 \\ 0 & 0 & 0 & 0 & 0 & 0 & 1 & 0 \\ 0 & 0 & 0 & 0 & 0 & 0 & 0 & 1 \end{bmatrix}, \tag{2.5}$$

and $\mathbf{U}^T$ is the transpose matrix of $\mathbf{U}$. Based on (2.3), the square of the DCT matrix can be written as

$$\mathbf{C}^2 = \mathbf{C} \cdot \mathbf{C} = \mathbf{U}\mathbf{\Lambda}\mathbf{U}^T\mathbf{U}\mathbf{\Lambda}\mathbf{U}^T = \mathbf{U}\mathbf{\Lambda}^2\mathbf{U}^T. \tag{2.6}$$

Similarly, we have

$$\mathbf{C}^\alpha = \mathbf{U}\mathbf{\Lambda}^\alpha\mathbf{U}^T, \tag{2.7}$$

where

$$\mathbf{\Lambda}^{\alpha} = \begin{bmatrix} \lambda_1^a & 0 & 0 & 0 & 0 & 0 & 0 & 0 \\ 0 & \lambda_2^a & 0 & 0 & 0 & 0 & 0 & 0 \\ 0 & 0 & \lambda_3^a & 0 & 0 & 0 & 0 & 0 \\ 0 & 0 & 0 & \lambda_4^a & 0 & 0 & 0 & 0 \\ 0 & 0 & 0 & 0 & \lambda_5^a & 0 & 0 & 0 \\ 0 & 0 & 0 & 0 & 0 & \lambda_6^a & 0 & 0 \\ 0 & 0 & 0 & 0 & 0 & 0 & \lambda_7^a & 0 \\ 0 & 0 & 0 & 0 & 0 & 0 & 0 & \lambda_8^a \end{bmatrix}, \tag{2.8}$$

α is a real fraction, $\lambda_n^a = e^{j(\theta_n + 2\pi q_n)a}$, $n = 1, 2, 3, \ldots, 8$, $\theta_1, \theta_2, \theta_3, \theta_4 = \pi$ and $\theta_5, \theta_6, \theta_7, \theta_8 = 0$, q_n is an element of generating sequence (GS) $\mathbf{q} = (q_1, q_2, \ldots, q_8)$, and q_n is an integer for $0 \leq q_n \leq 7$.

3. Half Discrete Cosine Transform

The half-DCT, that is, the FDCT with $\alpha = 1/2$ is obtained by

$$\sqrt{\mathbf{C}} = \mathbf{U}\mathbf{\Lambda}^{1/2}\mathbf{U}^T, \tag{3.1}$$

where

$$\mathbf{\Lambda}^{1/2} = \begin{bmatrix} j & 0 & 0 & 0 & 0 & 0 & 0 & 0 \\ 0 & j & 0 & 0 & 0 & 0 & 0 & 0 \\ 0 & 0 & j & 0 & 0 & 0 & 0 & 0 \\ 0 & 0 & 0 & j & 0 & 0 & 0 & 0 \\ 0 & 0 & 0 & 0 & 1 & 0 & 0 & 0 \\ 0 & 0 & 0 & 0 & 0 & 1 & 0 & 0 \\ 0 & 0 & 0 & 0 & 0 & 0 & 1 & 0 \\ 0 & 0 & 0 & 0 & 0 & 0 & 0 & 1 \end{bmatrix}. \tag{3.2}$$

The matrix $\mathbf{z}$, obtained by combining the 8-point half-DCT of $\mathbf{x}$ and $\mathbf{y}$ is defined as

$$\mathbf{z} = \mathbf{C}_1\mathbf{x} - \mathbf{C}_1\mathbf{y} = \mathbf{C}_1\mathbf{x} + \mathbf{C}_2\mathbf{y}, \tag{3.3}$$

where

$$\begin{aligned} \mathbf{C}_1 &= \mathbf{U}\mathbf{\Lambda}^{1/2}\mathbf{U}^T, \\ \mathbf{C}_2 &= -\mathbf{C}_1 = -\mathbf{U}\mathbf{\Lambda}^{(1/2)}\mathbf{U}^T. \end{aligned} \tag{3.4}$$

$\mathbf{U}$ is the orthonormal matrix given by

$$\begin{aligned}\mathbf{U} &= [\mathbf{u}_1, \mathbf{u}_2, \ldots, \mathbf{u}_n],\\ \mathbf{u}_m\mathbf{u}_n^T &= \begin{cases} 1, & m = n,\\ 0, & m \neq n. \end{cases}\end{aligned} \tag{3.5}$$

Let $\mathbf{U}_n$ be defined as

$$\mathbf{U}_n = \mathbf{u}_n\mathbf{u}_n^T \tag{3.6}$$

we have

$$\mathbf{U}_m\mathbf{U}_n = \left(\mathbf{u}_m\mathbf{u}_m^T\right)\left(\mathbf{u}_n\mathbf{u}_n^T\right) = \begin{cases} \mathbf{U}_n = \mathbf{u}_n\mathbf{u}_n^T, & m = n\\ 0, & m \neq n. \end{cases} \tag{3.7}$$

It is noted that $\mathbf{C}_1$ and $\mathbf{C}_2$ can be rewritten as

$$\begin{aligned}\mathbf{C}_1 &= \mathbf{U}\boldsymbol{\Lambda}^{1/2}\mathbf{U}^T = \mathbf{C}_R + j\mathbf{C}_I,\\ \mathbf{C}_2 &= -\mathbf{U}\boldsymbol{\Lambda}^{1/2}\mathbf{U}^T = \mathbf{C}_I + j\mathbf{C}_R,\end{aligned} \tag{3.8}$$

where

$$\mathbf{C}_R = \mathbf{U}_1 + \mathbf{U}_2 + \mathbf{U}_3 + \mathbf{U}_4, \tag{3.9}$$

$$\mathbf{C}_I = \mathbf{U}_5 + \mathbf{U}_6 + \mathbf{U}_7 + \mathbf{U}_8. \tag{3.10}$$

According to (3.7), (3.9) and (3.10) we have

$$\begin{aligned}\mathbf{C}_R\mathbf{C}_R &= \mathbf{C}_R,\\ \mathbf{C}_I\mathbf{C}_I &= \mathbf{C}_I,\\ \mathbf{C}_R\mathbf{C}_I &= 0,\\ \mathbf{C}_I\mathbf{C}_R &= 0,\\ \mathbf{C}_R + \mathbf{C}_I &= \mathbf{I},\\ \mathbf{C}_I - \mathbf{C}_R &= -(\mathbf{U}_1 + \mathbf{U}_2 + \mathbf{U}_3 + \mathbf{U}_4) + (\mathbf{U}_5 + \mathbf{U}_6 + \mathbf{U}_7 + \mathbf{U}_8) = \mathbf{C}.\end{aligned} \tag{3.11}$$

From (3.11), we have

$$\mathbf{z} = \left(\mathbf{C}_R + j\mathbf{C}_I\right)\mathbf{x} + \left(\mathbf{C}_I + j\mathbf{C}_R\right)\mathbf{y}. \tag{3.12}$$

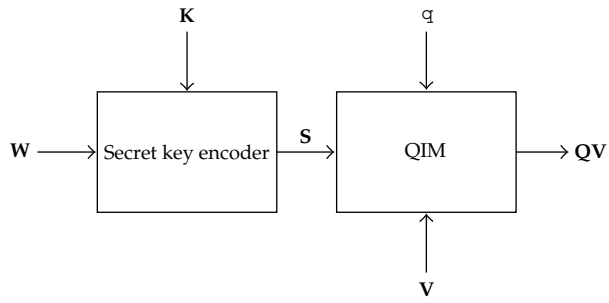

Figure 1: The conventional QIM-based watermarking (**W**: the watermark, **K**: the secret key, **S**: the coded watermark, q: the quantization step, **V**: the host image, and **QV**: the watermarked image).

Assume that

$$\begin{aligned}\mathbf{y} &= \mathbf{x} + \mathbf{y}',\\ \mathbf{z} &= (\mathbf{C}_R + j\mathbf{C}_I)\mathbf{x} + (\mathbf{C}_I + j\mathbf{C}_R)(\mathbf{x} + \mathbf{y}')\\ &= (\mathbf{C}_R + \mathbf{C}_I + j\mathbf{C}_R + j\mathbf{C}_I)\mathbf{x} + (\mathbf{C}_I + j\mathbf{C}_R)\mathbf{y}'\\ &= \mathbf{x} + \mathbf{C}_I\mathbf{y}' + j(\mathbf{x} + \mathbf{C}_R\mathbf{y}').\end{aligned} \tag{3.13}$$

Thus, $\mathbf{x}$ and $\mathbf{y}$ can be obtained from $\mathbf{z}$ as follows:

$$\begin{aligned}\mathrm{Re}\{\mathbf{z}\} - \mathrm{Im}\{\mathbf{z}\} = (\mathbf{x} + \mathbf{C}_I\mathbf{y}') - (\mathbf{x} + \mathbf{C}_R\mathbf{y}') = (\mathbf{C}_I - \mathbf{C}_R)\mathbf{y} &= \mathbf{C}\cdot\mathbf{y}',\\ \mathbf{y}' = \mathbf{C}^{-1}\cdot(\mathrm{Re}\{\mathbf{z}\} - \mathrm{Im}\{\mathbf{z}\}),&\\ \mathbf{x} = \mathrm{Re}\{\mathbf{z}\} - \mathbf{C}_I\mathbf{y}',&\\ \mathbf{x} = \mathrm{Im}\{\mathbf{z}\} - \mathbf{C}_R\mathbf{y}',&\\ \mathbf{y} = \mathbf{x} + \mathbf{y}'.&\end{aligned} \tag{3.14}$$

4. The Proposed Fractional-Discrete-Cosine-Transform-Based Watermarking

Both transparency and recovery of the host image are required for the medical applications. As the conventional quantization-index-modulation- (QIM-) [26] based watermarking is irreversible, we propose a novel FDCT- based algorithm for reversible watermarking.

4.1. Quantization Index Modulation

Figure 1 depicts the conventional QIM-based watermarking [26]. In which, $\mathbf{W}, \mathbf{K}, \mathbf{S}, \mathbf{V}$, and **QV** denote the watermark, the secret key, the coded watermark, the host image, and the watermarked image, respectively. For the sake of simplicity, let us consider the monochromatic images with 256 grey levels, and the size of the watermark is one-fourth

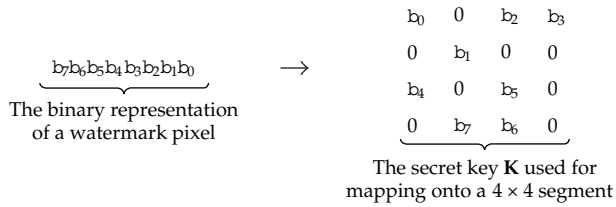

Figure 2: The secret key **K** used for mapping the watermark onto the host image.

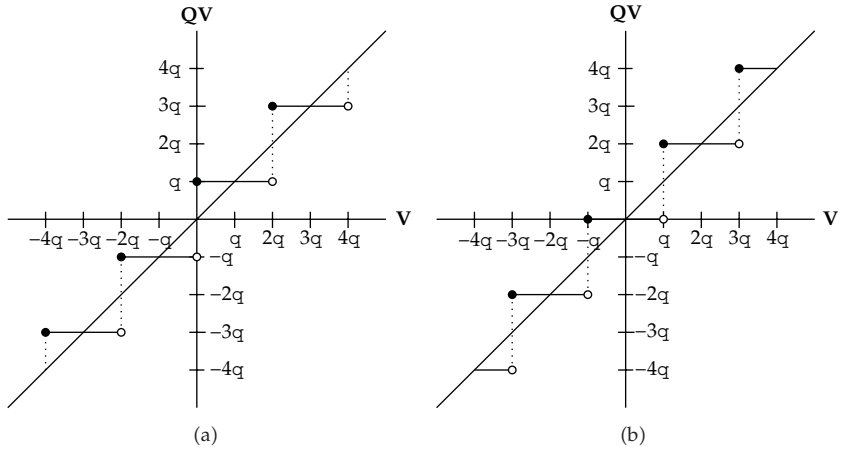

Figure 3: Operations of the QIM scheme for the coded watermark pixels being (a) bit 1 and (b) bit 0, respectively.

of that of the host image. The secret key is used to map the binary representation of the watermark onto the host image, for example, Figure 2 depicts the binary representation of a watermark pixel that is mapped onto a 4×4 segment using a given secret key.

Figure 3 shows the operation of the QIM block, in which the grey levels of the host image, **V**, ranging between $2c \cdot q$ and $(2c + 1) \cdot q$ will be quantized into $(2c + 1) \cdot q$ if the corresponding pixels of the coded watermark, **S**, are bit 1; otherwise they are quantized into $2c \cdot q$ if the corresponding pixels are bit 0. For the grey levels of **V** that are between $(2c + 1) \cdot q$ and $(2c + 2) \cdot q$, they will be quantized into $(2c + 1) \cdot q$ or $(2c + 2) \cdot q$ depending on the corresponding pixels of **S** being bit 1 or 0, respectively. Note that q denotes the quantization step, $0 \leq c < 255/(2 \cdot q)$, and c is an integer number.

It is noted that the watermarked image, **QV**, can be written as

$$QV(i,j) = \begin{cases} (2c+1)q & \text{if } V(i,j) \in \big((2c+0.5)q, (2c+1.5)q\big], \quad S(i,j) = 1, \\ (2c)q & \text{if } V(i,j) \in \big((2c-0.5)q, (2c+0.5)q\big], \quad S(i,j) = 0, \end{cases} \tag{4.1}$$

where (i, j) denotes the position index of pixels, and the coded watermark, **S**, can be obtained by

$$S(i,j) = \begin{cases} 1 & \text{if } QV(i,j) \in \big((2d+0.5)q, (2d+1.5)q\big], \\ 0 & \text{otherwise} \end{cases} \tag{4.2}$$

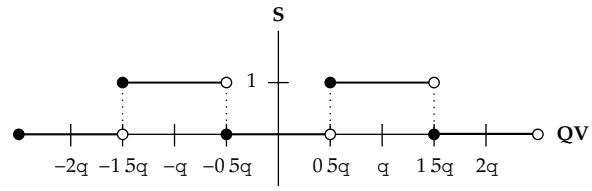

Figure 4: Operations of the inverse QIM scheme for the coded watermark pixels.

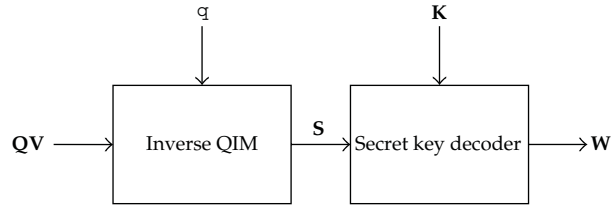

Figure 5: Extraction of the watermark, **W**, from the watermarked image, **QV**, based on the conventional QIM scheme.

as shown in Figure 4. Together with the secret key, **K**, the watermark, **W**, can be exactly extracted from the watermarked image, **QV**, as shown in Figure 5.

4.2. Proposed FDCT-Based Watermarking

According to (3.12), the half-DCT can be used to combine two real valued signals into a single, complex-valued signal. Let **x** and **y** in (3.12) be the host image and the watermark, respectively, and **z** the watermarked image. The watermark and host image can be extracted from **z** by using (3.14). Figure 6 depicts the proposed FDCT-based watermarking, where $\mathbf{W}, \mathbf{V}, \mathbf{S}, \mathbf{QV}, \mathbf{HV}_R$, and $\mathbf{HV}_I$ are the watermark, the host image, the secret key, the QIM watermarked image, and the watermarked images, R and I, respectively. According to (3.12), the half-DCT consists of two matrix multiplications as shown in Figure 7, where $\mathbf{C}_R$ and $\mathbf{C}_I$ are the half-DCT coefficient matrices for (3.9) and (3.10), respectively.

The original host image, **V**, and watermark, **W**, can be exactly reconstructed from the watermarked images: $\mathbf{HV}_R$ and $\mathbf{HV}_I$ as shown in Figures 8 and 9, where $\mathbf{C}_I$ is the corresponding half-DCT matrix and $\mathbf{C}^{-1}$ is the inverse DCT matrix.

4.3. Experimental Results on Medical Images

The proposed FDCT-based watermarking algorithm has been evaluated on various medical images. Figure 10 shows the test 256 × 256 images with 256 grey levels, namely, spine, chest, fetus and head obtained by magnetic resonance image (MRI), X-ray, ultrasound, and computed tomography (CT), respectively, which are used as host images. Figure 11 shows the 64 × 64 Lena image used as watermark with 256 grey levels.

The peak signal-to-noise ratio (PSNR) is used to evaluate the image quality [4, 8, 26], which is defined as

$$\mathrm{PSNR} = 20 \log\left(\frac{255}{\sqrt{\mathrm{MSE}}}\right), \tag{4.3}$$

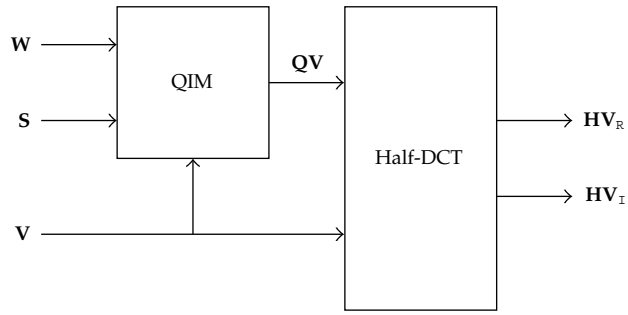

Figure 6: The proposed FDCT-based watermarking (**W**: the watermark, **V**: the host image, **S**: the secret key, **QV**: the QIM watermarked image, and $\mathbf{HV}_R$ and $\mathbf{HV}_I$: the watermarked images, R and I, resp.).

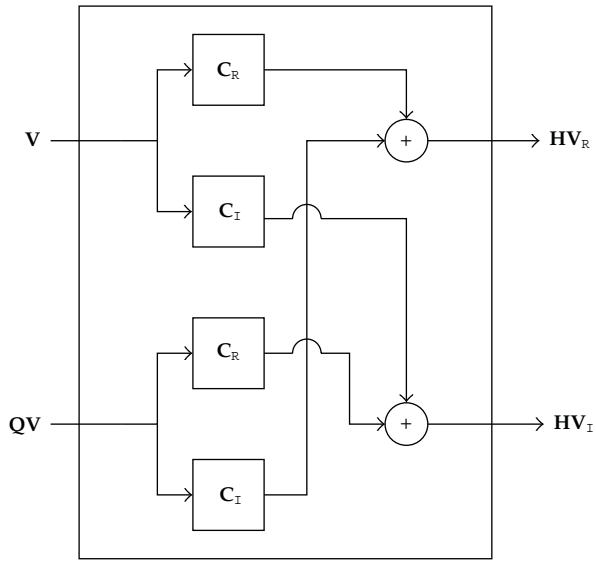

Figure 7: Data flow of the half-DCT operation (**V**: the host image, **QV**: the QIM watermarked images, $\mathbf{HV}_R$ and $\mathbf{HV}_I$: the watermarked image for real R and imaginary I, and $\mathbf{C}_R$ and $\mathbf{C}_I$: the corresponding half-DCT matrices.).

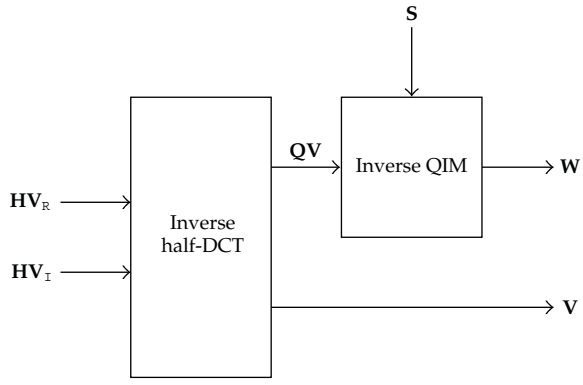

Figure 8: The proposed inverse FDCT-based watermarking for image extraction.

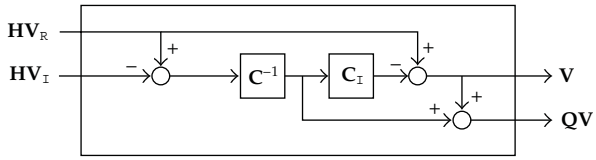

Figure 9: Data flow of the inverse half-DCT operation ($\mathbf{C}_I$: the corresponding half-DCT matrix and $\mathbf{C}^{-1}$: the inverse DCT matrix).

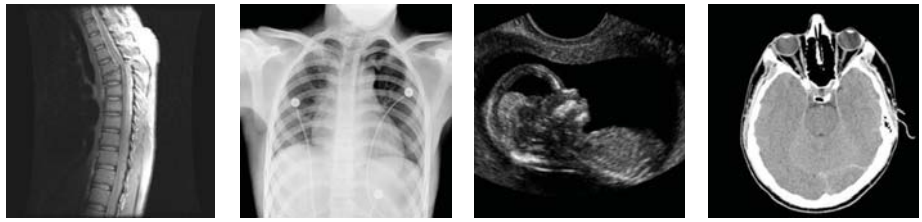

(a) (b) (c) (d)

Figure 10: The 256 × 256 host images with 256 grey levels: (a) spine (MRI), (b) chest (X-ray), (c) fetus (ultrasonic), and (d) head (CT).

Figure 11: The 64 × 64 Lena image with 256 grey levels used as watermarks.

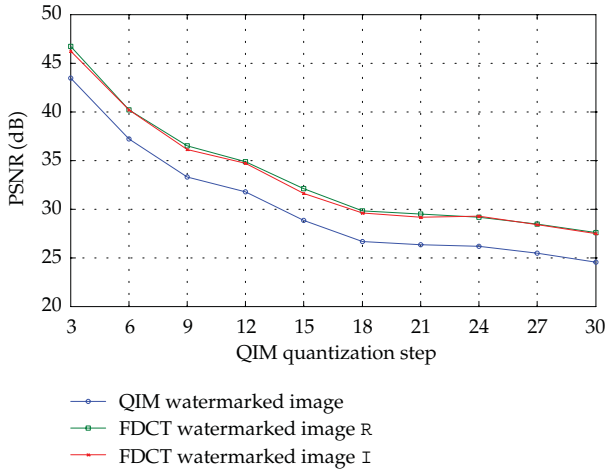

Figure 12: The PSNR of the watermarked image of the spine (MRI) at various QIM quantization steps.

where MSE denotes the mean square error. Figures 12, 13, 14, and 15 show the PSNR of the QIM watermarked image and FDCT watermarked images R and I of spine (MRI), chest (X-ray), fetus (ultrasonic), and head (CT) at various QIM quantization steps q. Figure 16 shows the QIM watermarked images (first row), the FDCT watermarked images, R (second row) and I (third row), and two extracted watermarks from the R and I watermarked images (fourth row) with QIM quantization step $q = 5$. It is noted that the FDCT watermarked images are more transparent than conventional QIM watermarked images, and the block effect of the

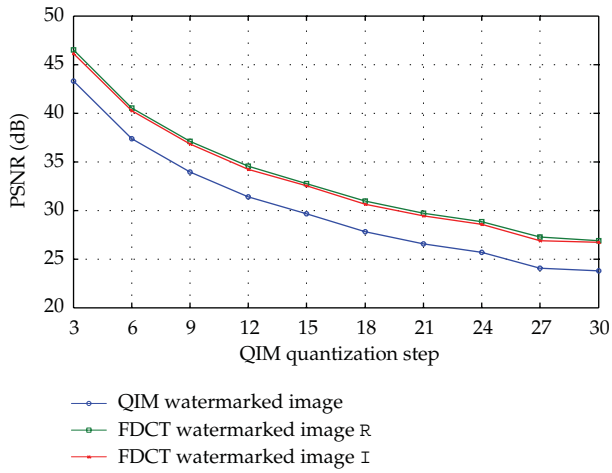

Figure 13: The PSNR of the watermarked image of the chest (X-ray) at various QIM quantization steps.

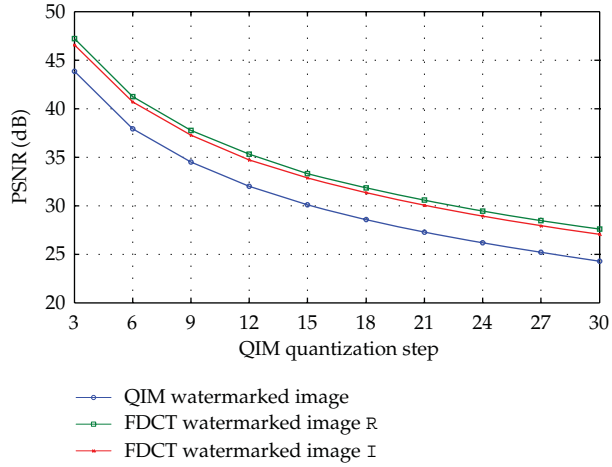

Figure 14: The PSNR of the watermarked image of the fetus (ultrasonic) at various QIM quantization steps.

Table 1: Comparison between this work and the related watermarking algorithms.

Items	Methods		
	Conventional QIM [26]	Nested QIM [8]	FDCT Watermarking
Watermarked image transparency	Poor	Good	Better
Reversible watermarking	No	Yes	Yes
Block effect	Yes	Yes	No

FDCT-based watermarking is eliminated. Table 1 shows the comparison between this work and the related watermarking algorithms [8, 26].

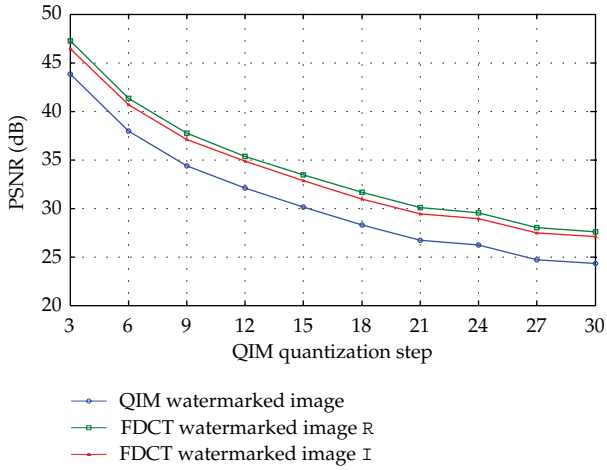

Figure 15: The PSNR of the watermarked image of the head (CT) at various QIM quantization steps.

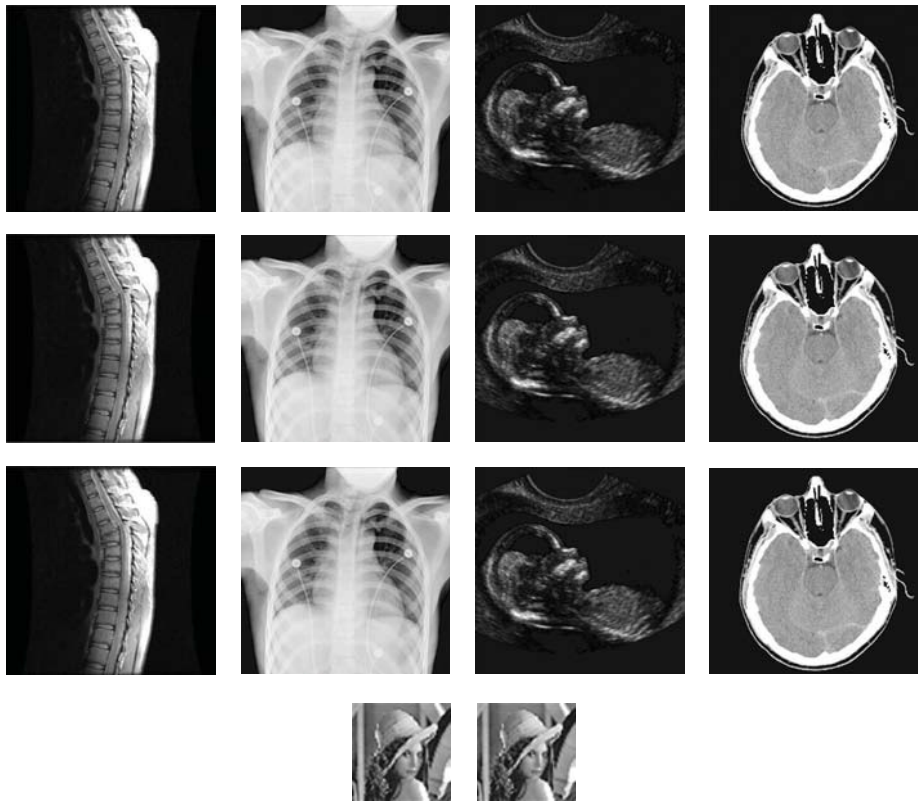

Figure 16: The QIM watermarked images (first row) and the FDCT watermarked images, R (second row) and I (third row), and two extracted watermarks: left one and right one (fourth row) are extracted from the R and I watermarked image, respectively, with QIM quantization step $q = 5$.

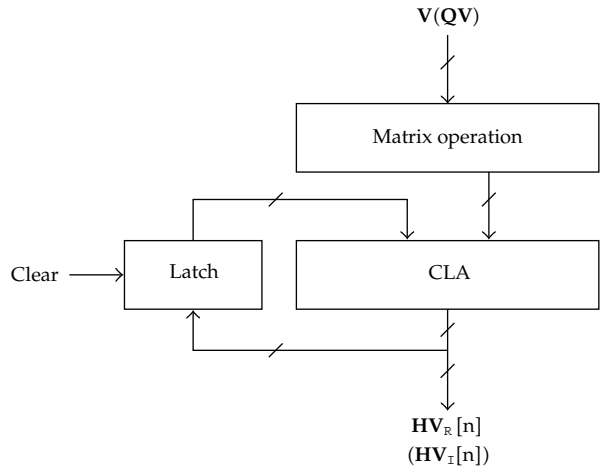

Figure 17: The architecture of the proposed 8-point half-DCT processor.

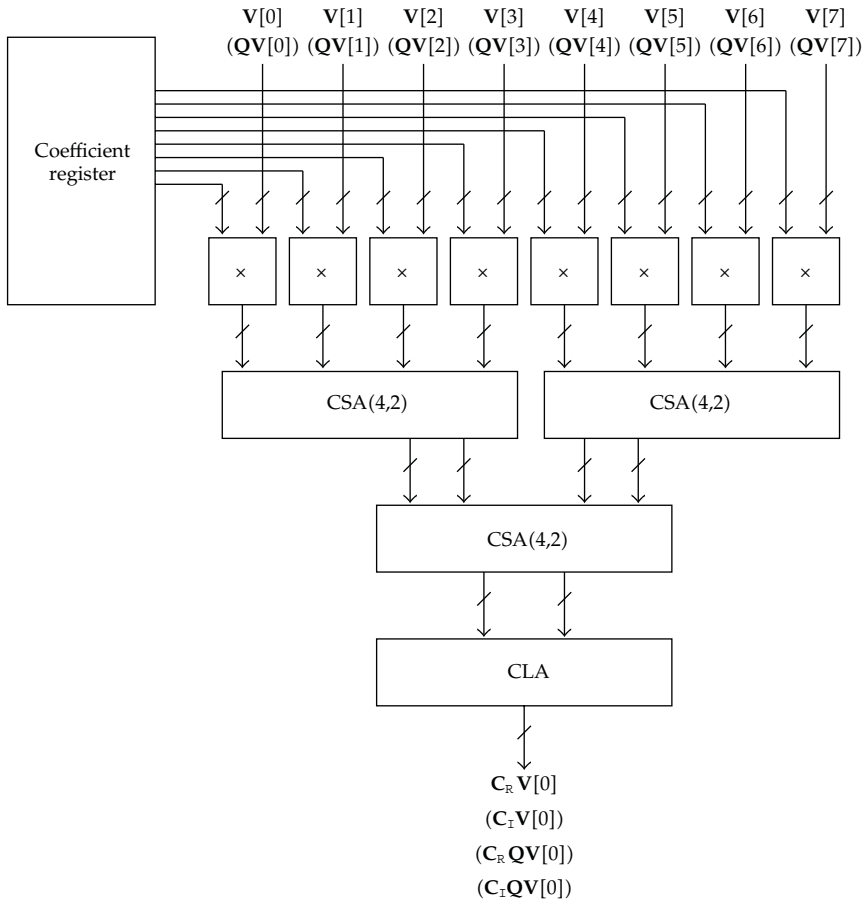

Figure 18: The matrix operation block in the proposed 8-point half-DCT and inverse half-DCT processor.

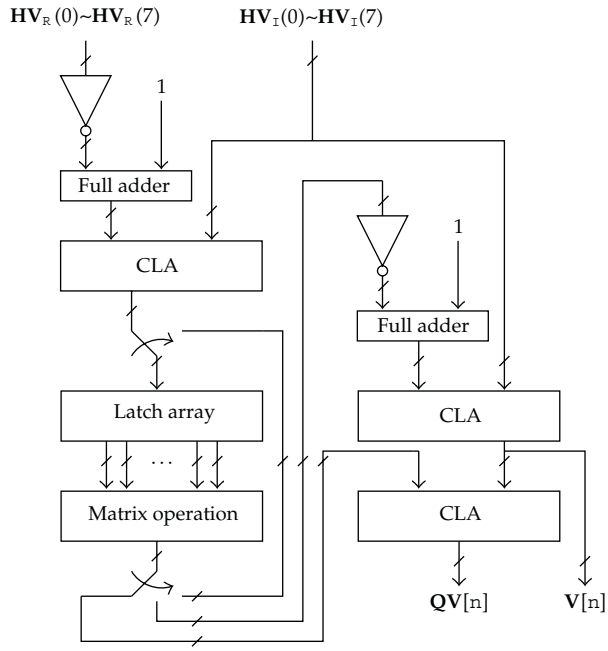

Figure 19: The architecture of the proposed 8-point inverse half-DCT processor.

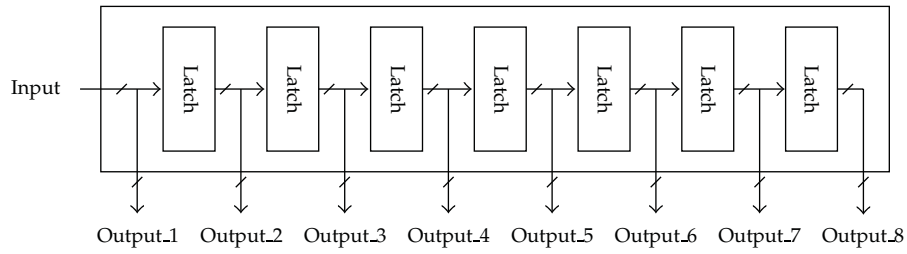

Figure 20: The latch array storing data for matrix operation.

5. FPGA Implementation of Half-DCT-Based Watermarking Processor

According to the data flow of the half-DCT shown in Figure 7, the architecture of the proposed 8-point half-DCT processor is shown in Figure 17. In which, the matrix operation block performs the matrix-vector multiplications of $\mathbf{C}_R \cdot \mathbf{V}$, $\mathbf{C}_I \cdot \mathbf{V}$, $\mathbf{C}_R \cdot \mathbf{QV}$ and $\mathbf{C}_I \cdot \mathbf{QV}$ shown in Figure 18, and the latch and CLA perform the addition operations of $\mathbf{C}_R \cdot \mathbf{V} + \mathbf{C}_I \cdot \mathbf{QV}$ and $\mathbf{C}_I \cdot \mathbf{V} + \mathbf{C}_R \cdot \mathbf{QV}$.

According to the data flow of the inverse half-DCT shown in Figure 9, the architecture of the proposed 8-point inverse half-DCT processor is shown in Figure 19. In which, the matrix operation block performs the matrix-vector multiplications of $\mathbf{C}^{-1} \cdot (\mathbf{HV}_R - \mathbf{HV}_I)$ and $\mathbf{C}_I \cdot (\mathbf{C}^{-1} \cdot (\mathbf{HV}_R - \mathbf{HV}_I))$. In the proposed 8-point inverse half-DCT processor as shown in Figure 19, the latch array storing data for matrix operation is shown in Figure 20.

The platform for architecture development and verification has been designed as well as implemented in order to evaluate the development cost. The architecture has been implemented on the Xilinx FPGA emulation board [27]. The Xilinx Spartan-3 FPGA has been

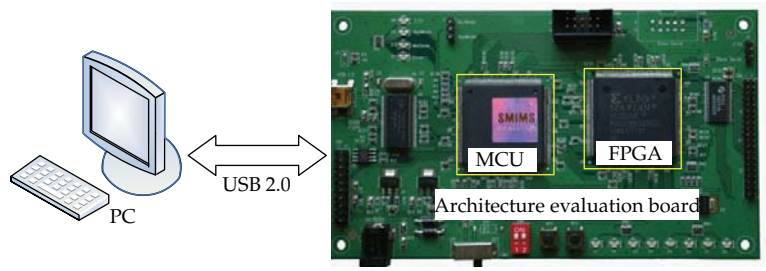

Figure 21: Block diagram and circuit board of the architecture development and verification platform for half-DCT-based watermarking processor.

integrated with the microcontroller (MCU) and I/O interface circuit (USB 2.0) to form the architecture development and verification platform. Figure 21 depicts block diagram and circuit board of the architecture development and evaluation platform, which can perform the prototype of special processor for half-DCT-based watermarking. In the architecture development and evaluation platform, the microcontroller reads data and commands from PC and writes the results back to PC by USB 2.0; the Xilinx Spartan-3 FPGA implements the proposed half-DCT processor. The hardware code written in Verilog is for PC with the ModelSim simulation tool [28] and Xilinx ISE smart compiler [29]. It is noted that the throughput can be improved by using the proposed architecture while the computation accuracy is the same as that obtained by using Matlab technical computing tool [30] with the same word length. Thus, the proposed programmable half-DCT architecture is able to improve the power consumption and computation speed significantly. Moreover, the reusable intellectual property (IP) 8×8 half-DCT/IDCT core has also been implemented in Verilog hardware description language [31] for the hardware realization. All the control signals are internally generated on-chip. The proposed half-DCT processor provides both high throughput and low gate count.

6. Conclusion

In this paper, a novel algorithm called the FDCT-based reversible watermarking has been proposed for medical image watermarking. The transparency of the watermarked image can be increased by taking advantage of the proposed watermarking. As the host image can be exactly reconstructed, it is suitable especially for the medical image applications. In addition, the elimination of block effect avoids detecting QIM coded watermarked image. Thus, the FDCT-based reversible watermarking is preferable to facilitate data management in healthcare information management systems.

References

[1] H. M. Chao, C. M. Hsu, and S. G. Miaou, "A data-hiding technique with authentication, integration, and confidentiality for electronic patient records," *IEEE Transactions on Information Technology in Biomedicine*, vol. 6, no. 1, pp. 46–53, 2002.

[2] U. R. Acharya, D. Anand, P. S. Bhat, and U. C. Niranjan, "Compact storage of medical images with patient information," *IEEE Transactions on Information Technology in Biomedicine*, vol. 5, no. 4, pp. 320–323, 2001.

[3] X. Kong and R. Feng, "Watermarking medical signals for telemedicine," *IEEE Transactions on Information Technology in Biomedicine*, vol. 5, no. 3, pp. 195–201, 2001.

[4] A. Giakoumaki, S. Pavlopoulos, and D. Koutsouris, "Multiple image watermarking applied to health information management," *IEEE Transactions on Information Technology in Biomedicine*, vol. 10, no. 4, pp. 722–732, 2006.
[5] S. Y. Chen and Q. Guan, "Parametric shape representation by a deformable NURBS model for cardiac functional measurements," *IEEE Transactions on Biomedical Engineering*, vol. 58, no. 3, part 1, pp. 480–487, 2011.
[6] M. Li, "Four transformation patterns of two-dimensional function on wavelet basis," *Int. J. Engineering and Interdisciplinary Mathematics*, vol. 1, no. 2, pp. 107–110, 2009.
[7] L. T. Ko, J. E. Chen, H. C. Hsin, Y. S. Shieh, and T. Y. Sung, "Haar-wavelet-based just noticeable distortion model for transparent watermark," *Mathematical Problems in Engineering*, vol. 2012, Article ID 635738, 14 pages, 2012.
[8] L. T. Ko, J. E. Chen, Y. S. Shieh, H. C. Hsin, and T. Y. Sung, "Nested quantization index modulation for reversible watermarking and its application to healthcare information management systems," *Computational and Mathematical Methods in Medicine*, vol. 2012, Article ID 839161, 8 pages, 2012.
[9] S. Y. Chen, H. Tong, Z. Wang, S. Liu, M. Li, and B. Zhang, "Improved generalized belief propagation for vision processing," *Mathematical Problems in Engineering*, vol. 2011, Article ID 416963, 12 pages, 2011.
[10] S. Y. Chen, H. Tong, and C. Cattani, "Markov models for image labeling," *Mathematical Problems in Engineering*, vol. 2012, Article ID 814356, 18 pages, 2012.
[11] K. R. Rao and P. Yip, *Discrete Cosine Transform: Algorithms, Advantages, Applications*, Academic Press, New York, NY, USA, 1990.
[12] L. T. Ko, J. E. Chen, H. C. Hsin, Y. S. Shieh, and T. Y. Sung, "A unified algorithm for subband-based discrete cosine transform," *Mathematical Problems in Engineering*, vol. 2012, Article ID 912194, 31 pages, 2012.
[13] T. Y. Sung, Y. S. Shieh, and H. C. Hsin, "An efficient VLSI linear array for DCT/IDCT using subband decomposition algorithm," *Mathematical Problems in Engineering*, vol. 2010, Article ID 185398, 21 pages, 2010.
[14] H. Huang, T. Y. Sung, and Y. S. Shieh, "A novel VLSI linear array for 2-D DCT/IDCT," in *Proceedings of the 3rd International Congress on Image and Signal Processing (CISP '10)*, vol. 8, pp. 3686–3690, Yantai, China, October 2010.
[15] T. Y. Sung, "Memory-efficient and high-performance 2-D DCT and IDCT processors based on CORDIC rotation," *WSEAS Transactions on Electronics*, vol. 3, no. 12, pp. 565–574, 2006.
[16] S. C. Pei and M. H. Yeh, "The discrete fractional cosine and sine transforms," *IEEE Transactions on Signal Processing*, vol. 49, no. 6, pp. 1198–1207, 2001.
[17] G. Cariolaro, T. Erseghe, and P. Kraniauskas, "The fractional discrete cosine transform," *IEEE Transactions on Signal Processing*, vol. 50, no. 4, pp. 902–911, 2002.
[18] Z. Liao, S. Hu, M. Li, and W. Chen, "Noise estimation for single-slice sinogram of low-dose X-Ray computed tomography using homogenous patch," *Mathematical Problems in Engineering*, vol. 2012, Article ID 696212, 16 pages, 2012.
[19] Z. Liao, S. Hu, D. Sun, and W. Chen, "Enclosed laplacian operator of nonlinear anisotropic diffusion to preserve singularities and delete isolated points in image smoothing," *Mathematical Problems in Engineering*, vol. 2011, Article ID 749456, 15 pages, 2011.
[20] C. Cattani and A. Kudreyko, "Application of periodized harmonic wavelets towards solution of eigenvalue problems for integral equations," *Mathematical Problems in Engineering*, vol. 2010, Article ID 570136, 8 pages, 2010.
[21] M. Li and W. Zhao, "Visiting power laws in cyber-physical networking systems," *Mathematical Problems in Engineering*, vol. 2012, Article ID 302786, 13 pages, 2012.
[22] M. Li, "Fractal time series—a tutorial review," *Mathematical Problems in Engineering*, vol. 2010, Article ID 157264, 26 pages, 2010.
[23] C. Cattani, "Harmonic wavelet approximation of random, fractal and high frequency signals," *Telecommunication Systems*, vol. 43, no. 3-4, pp. 207–217, 2010.
[24] M. Li, S. C. Lim, and S. Chen, "Exact solution of impulse response to a class of fractional oscillators and its stability," *Mathematical Problems in Engineering*, vol. 2011, Article ID 657839, 9 pages, 2011.
[25] E. G. Bakhoum and C. Toma, "Specific mathematical aspects of dynamics generated by coherence functions," *Mathematical Problems in Engineering*, vol. 2011, Article ID 436198, 10 pages, 2011.
[26] B. Chen and G. W. Wornell, "Quantization index modulation: a class of provably good methods for digital watermarking and information embedding," *IEEE Transactions on Information Theory*, vol. 47, no. 4, pp. 1423–1443, 2001.

[27] SMIMS Technology Corp, http://www.smims.com.
[28] Cadence design systems, http://www.cadence.com/products/pages/default.aspx.
[29] Xilinx FPGA products, http://www.xilinx.com/products/.
[30] MATLAB—The language of technical computing, http://www.mathworks.com/products/matlab/index.html.
[31] D. E. Thomas and P. R. Moorby, *The Verilog Hardware Description Language*, Baker & Taylor Books, 5th edition, 2002.

Hindawi Publishing Corporation
Mathematical Problems in Engineering
Volume 2012, Article ID 419319, 20 pages
doi:10.1155/2012/419319

Research Article

Bound Maxima as a Traffic Feature under DDOS Flood Attacks

Jie Xue,[1] Ming Li,[2] Wei Zhao,[3] and Sheng-Yong Chen[4]

[1] *Jiangsu Electronic Information Products Quality Supervision & Inspection Research Institute, China National Center for Quality Supervision and Test for the Internet of Things Products & Systems, No. 100, Jin-Shui Road, Wuxi 214073, China*
[2] *School of Information Science & Technology, East China Normal University, No. 500, Dong-Chuan Road, Shanghai 200241, China*
[3] *Department of Computer and Information Science, University of Macau Av. Padre Tomas Pereira, Taipa, Macau SAR, P.R., China*
[4] *College of Computer Science, Zhejiang University of Technology, Hangzhou 310023, China*

Correspondence should be addressed to Ming Li, ming_lihk@yahoo.com

Received 8 October 2011; Accepted 9 October 2011

Academic Editor: Thomas T. Yang

This paper gives a novel traffic feature for identifying abnormal variation of traffic under DDOS flood attacks. It is the histogram of the maxima of the bounded traffic rate on an interval-by-interval basis. We use it to experiment on the traffic data provided by MIT Lincoln Laboratory under Defense Advanced Research Projects Agency (DARPA) in 1999. The experimental results profitably enhance the evidences that traffic rate under DDOS attacks is statistically higher than that of normal traffic considerably. They show that the pattern of the histogram of the maxima of bounded rate of attack-contained traffic greatly differs from that of attack-free traffic. Besides, the present traffic feature is simple in mathematics and easy to use in practice.

1. Introduction

People nowadays are heavily dependent on the Internet that serves as an infrastructure in the modern society. However, distributed denial-of-service (DDOS) flood attackers remain great threats to it. By consuming resources of an attacked site, the victim may be overwhelmed such that it denies services it should offer or its service performances are significantly degraded. Therefore, intrusion detection system (ISD) for detecting DDOS flood attacks has been greatly desired.

There are two categories regarding IDSs. One is misuse detection and the other anomaly detection. Attacking alerts given by misuse detection is primarily based on a library of known signatures to match against network traffic, see, for example, [1–5]. Thus, attacking

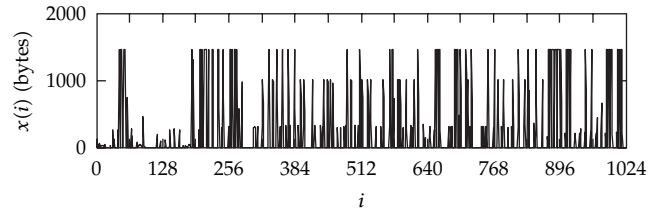

Figure 1: Time series: OM-W1-1-1999AF for the first 1024 points.

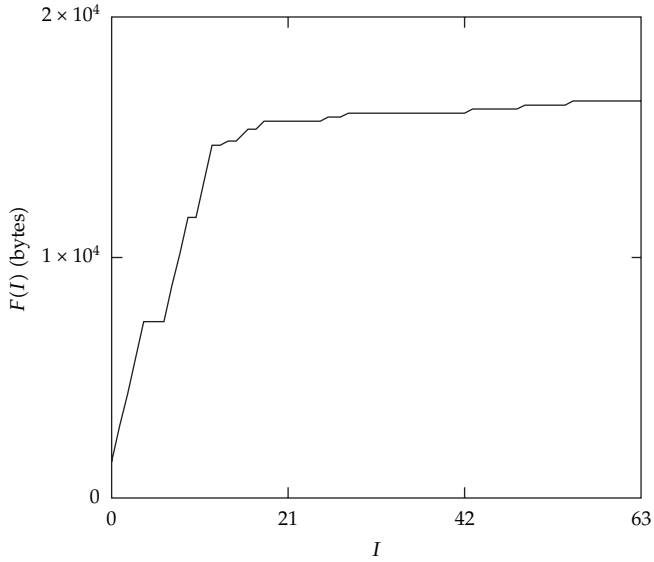

Figure 2: Traffic upper bound of OM-W1-1-1999AF for $0 \leq I \leq 63$.

with unknown signatures from new variants of an attack can escape from being detected by signature-based IDSs with the probability one, see, for example, [6], making such a category of IDSs at the protected site irrelevant. However, based on anomaly detection, abnormal variations of traffic are identified as potential intrusion so that this category of IDSs are particularly paid attention to for identifying new attacking, see, for example, [7–13]. For the simplicity, in what follows, the term IDS is in the sense of anomaly detection.

Noted that the detection accuracy is a key issue of an anomaly detector, see, for example, [14, 15]. To be effective, IDSs require appropriate features for accurately detecting an attack and distinguishing it from the normal activity as can be seen from [10, Section IV]. Hence, developing new traffic features for anomaly detection is essential.

The reference papers regarding traffic features for IDS use are wealthy. For example, 86 features for clustering normal activities are discussed in [9]. Note that a selected feature is methodology-dependent. In this regard, [16] uses packet head data. The paper [17] utilizes autocorrelation function of long-range dependent (LRD) traffic time series in packet size and [18] employs the Hurst parameter. Scherrer et al. adopt scaling properties of LRD traffic [19].

The traffic models used in [17–23] are in the sense of fractal. In general, fractal models might be somewhat complicated in practical application in engineering in comparison with the traffic feature proposed in this paper.

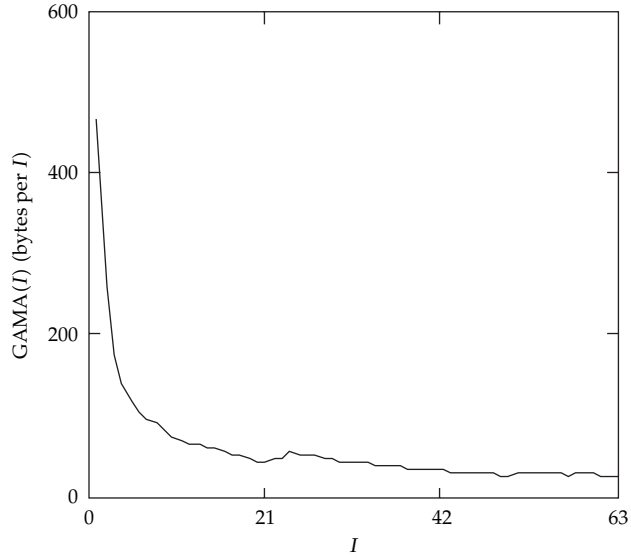

Figure 3: Traffic rate bound of OM-W1-1-1999AF for $0 \leq I \leq 63$.

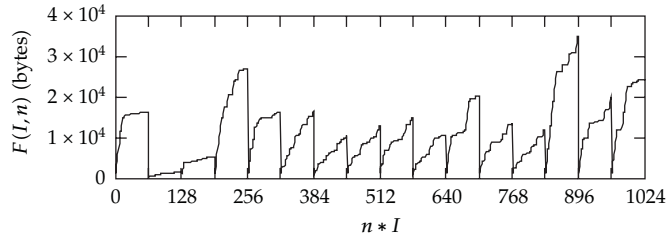

Figure 4: Traffic upper bound series for OM-W1-1-1999AF.

Recall that there are two categories in traffic modeling [24, Section XIV]. One is statistical modeling (e.g., LRD processes). The other bounded modeling, which has particular applications to modeling traffic at connection level, see, for example, [25–30]. Bounded models, in conjunction with a class of service disciplines, are feasible and relatively efficient in applications, such as connection admission control (CAC) in guaranteed quality-of-service (QoS). In addition, such models are simple in mathematics and relatively easy to be used in practice in comparison with fractal models. This paper aims at providing a new traffic feature for anomaly detection based on bounded modeling of traffic. The main contributions in this paper are as follows.

(i) We present the histogram of the maxima of bounded traffic rate on an interval-by-interval basis as a traffic feature for exhibiting abnormal variation of traffic under DDOS flood attacks.

(ii) The experimental results exhibit that the maxima of rate bound of attack-contained traffic is statistically greater than that of attack-free traffic drastically.

The rest of paper is organized as follows. Experimental data and related work are briefed in Section 2. The histogram of the maxima of traffic rate bound is proposed

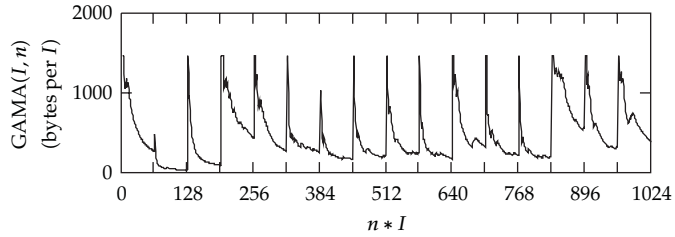

Figure 5: Traffic rate bound series for OM-W1-1-1999AF.

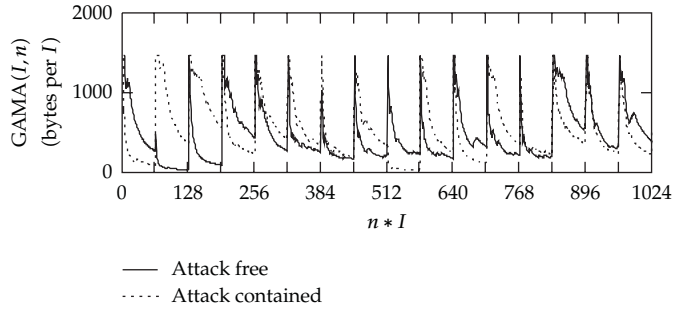

Figure 6: Traffic rate bound series. Solid lines for attack-free traffic OM-W1-1-1999AF. Dot lines for attack-contained traffic OM-W1-1-1999AC.

in Section 3. Experimental results are demonstrated in Section 4, which is followed by discussions and conclusions.

2. Experimental Data and Related Work

2.1. Experimental Data

While DDOS attacks continue to be a problem, there is currently not much quantitative data available for researchers to study the behaviors of DDOS flood attacks. The data in the 1998-1999 DARPA (http://www.ll.mit.edu/IST/ideval) are valuable but rare for public use though there are points worth further discussion [31]. Those data were obtained under the conditions of realistic background traffic and mean examples of realistic attacks [32, 33]. The used data sets in 1999 contain more than 200 instances and 58 attacks types, see, for details [34]. Two data sets are explained below.

2.1.1. Set One: Attack-Free Traffic (1999 Training Data—Week 1)

The first set of data containing 5 traces. We name them by OM-W1-i-1999AF ($i = 1, 2, 3, 4, 5$), meaning Outside-MIT-week1-i-1999-attack-free. Table 1 indicates the actual times at which the first packet and last one were extracted for each trace.

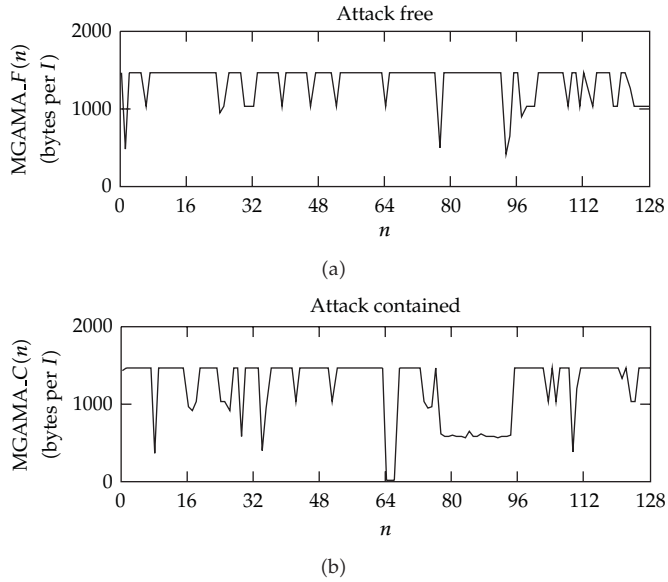

Figure 7: Maxima of traffic rate bound. (a) Maxima of GAMA(I, n) for OM-W1-1-1999AF. (b) Maxima of GAMA(I, n) for OM-W2-1-1999AC.

Table 1: Data set for attack-free traffic.

First Packet Time			Last Packet Time			Trace Name
Mon	Mar 1	08:00:02	Tue	Mar 2	06:00:02	OM-W1-1-1999AF
Tue	Mar 2	08:00:02	Wed	Mar 3	06:00:01	OM-W1-2-1999AF
Wed	Mar 3	08:00:03	Thu	Mar 4	06:00:01	OM-W1-3-1999AF
Thu	Mar 4	08:00:03	Fri	Mar 5	06:00:02	OM-W1-4-1999AF
Fri	Mar 5	08:00:02	Sat	Mar 6	06:00:02	OM-W1-5-1999AF

2.1.2. Set Two: Attack-Contained Traffic (1999 Training Data—Week 2)

Five traces are included in the second data set. They are named as OM-W2-i-1999AC (i = 1, 2, 3, 4, 5), implying Outside-MIT-week2-i-1999-attack contained. The actual times at which the first packet and last one were extracted for each trace are listed in Table 2.

2.2. Traffic Rate under DDOS Flood Attacks

Roughly, high rate is the radical feature of attack-contained traffic. The paper [35] reported the real events in 2000. He noticed that "the attacks inundated servers with 1 gigabit per second of incoming data, which is much more traffic than they were built to handle [35, page 12]." The analysis given by Moore et al. says that "to load the network, an attacker generally sends small packets as rapidly as possible since most network devices (both routers and NICs) are limited not by bandwidth but by packet processing rate [36, Section 2.1]." They infer that traffic rate is usually the best measure of network load during an attack. In short, computer scientists consider high rate as a basic feature of attack-contained traffic, also see, for example, [37–42]. The experimental results in this paper are simply for the data of the 1999 DARPA in the case of high-rate attacks.

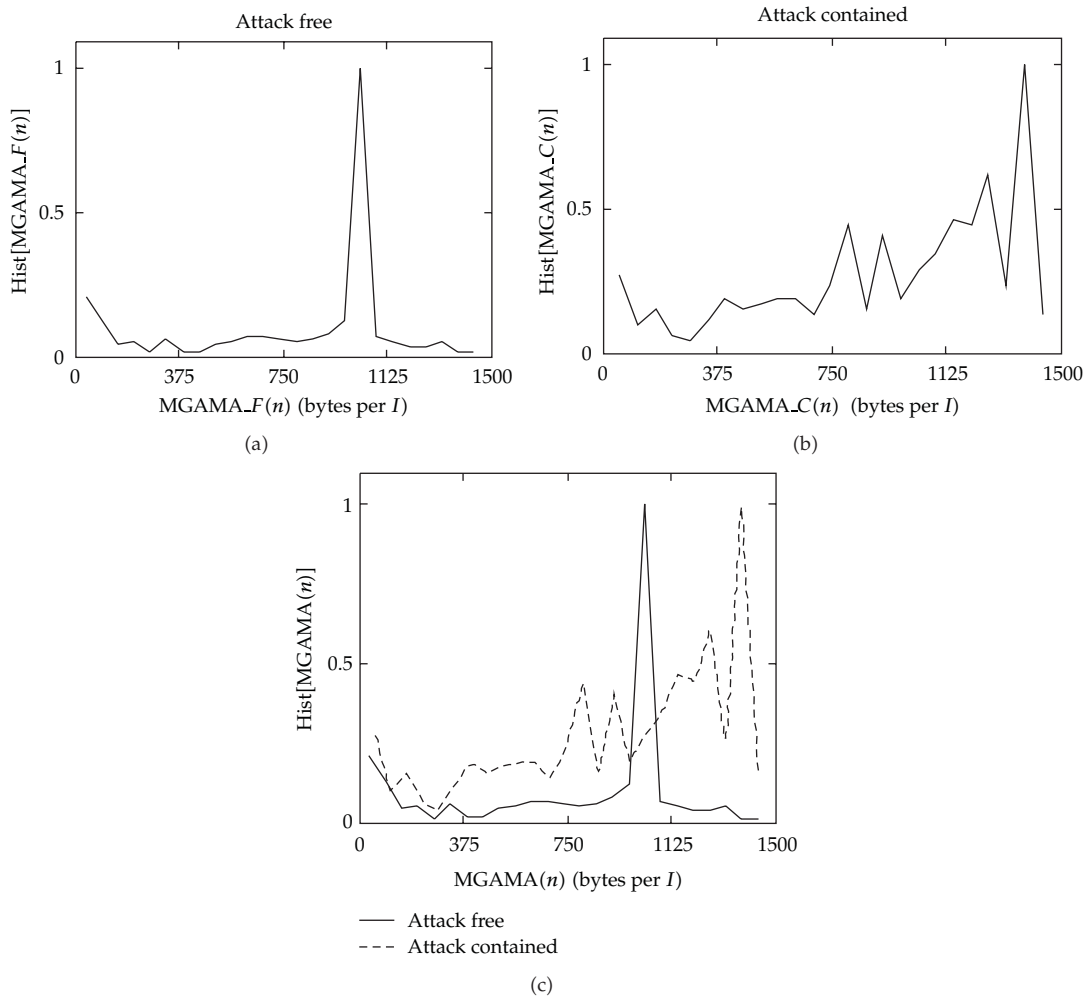

Figure 8: Histograms. (a) Hist[MGAMA_F(n)] of OM-W1-1-1999AF. (b) Hist[MGAMA_C(n)] of OM-W1-1-1999CF. (c) Comparison: Corr_FC = 0.01751.

Table 2: Data set for attack-contained traffic.

First Packet Time			Last Packet Time			Trace Name
Mon	Mar 8	08:00:01	Tue	Mar 9	06:00:49	OM-W2-1-1999AC
Tue	Mar 9	08:00:01	Wed	Mar 10	06:00:59	OM-W2-2-1999AC
Wed	Mar 10	08:00:03	Thu	Mar 11	06:00:01	OM-W2-3-1999AC
Thu	Mar 11	08:00:03	Fri	Mar 12	06:00:00	OM-W2-4-1999AC
Fri	Mar 12	08:00:02	Sat	Mar 13	06:00:00	OM-W2-5-1999AC

2.3. *Traffic Bounds*

In this subsection, we brief the deterministic bounds for accumulated traffic and traffic rate with the help of demonstrations using traffic traces OM-W1-1-1999AF and OM-W1-1-1999CF.

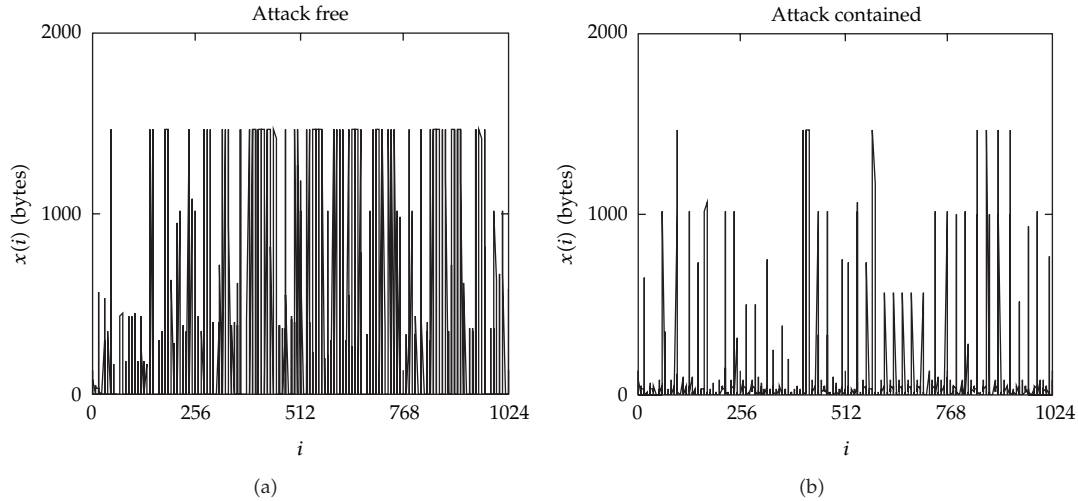

Figure 9: Time series of traffic traces. (a) The first 1024 points of OM-W1-2-1999AF. (b) The first 1024 points of OM-W2-2-1999AC.

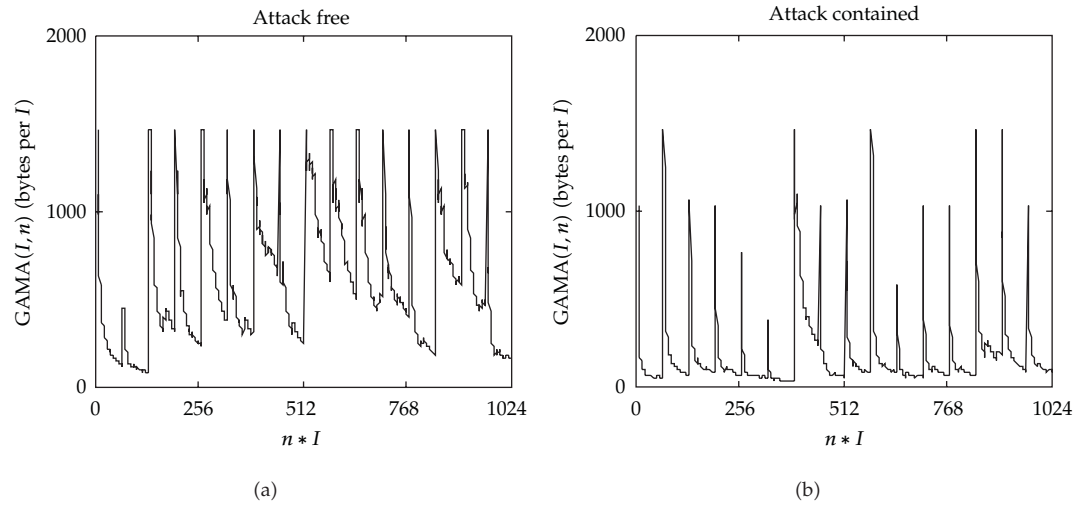

Figure 10: Series of traffic rate bound. (a) For OM-W1-2-1999AF. (b) For OM-W2-2-1999AC.

Let $x(t_i)$ be the series, indicating the number of bytes in the ith packet ($i = 0, 1, \ldots$) of arrival traffic at time t_i. Then, $x(i)$ is a discrete series, indicating the number of bytes in the ith packet of arrival traffic. Figure 1 shows a plot of $x(i)$ for the first 1024 points of OM-W1-1-1999AF.

According to [27, 43], an upper bound of arrival traffic $x(i)$ is given below.

Definition 2.1. Let $x(i)$ be the arrival traffic function. Then,

$$F(I) = \max_{i \geq 0}[x(i+I) - x(i)], \quad \text{for } i > 0,\ I > 0, \tag{2.1}$$

is called traffic upper bound of $x(i)$ over the duration of length I.

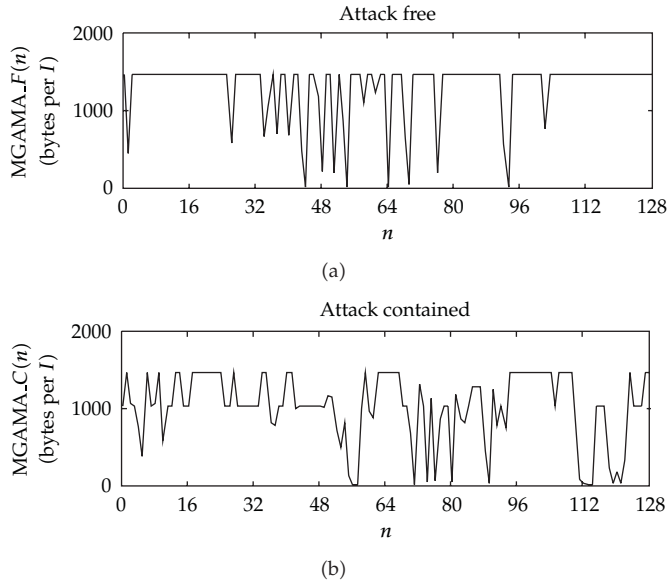

Figure 11: Series of the maxima of traffic rate bound. (a) For OM-W1-2-1999AF. (b) For OM-W2-2-1999AC.

Note 1. The physical meaning of $F(I)$ is that the accumulated amount of arrival traffic $x(i)$ over the duration of length I is upper bounded by $F(I)$. The unit of $F(I)$ is bytes. $F(I)$ is an increasing function in terms of I. Figure 2 indicates $F(I)$ of OM-W1-1-1999AF for $0 \leq I \leq 63$.

Definition 2.2. Let $x(i)$ be the arrival traffic function. Then,

$$\mathrm{GAMA}(I) = \frac{F(I)}{I} = \frac{\max_{i\geq 0}[x(i+I) - x(i)]}{I}, \quad \text{for } i > 0,\ I > 0, \tag{2.2}$$

is called upper bound of traffic rate (traffic rate bound for short) of $x(i)$.

Note 2. Equation (2.2) specifies that $\mathrm{GAMA}(I)$ is the maximum arrival rate at a specific point in the network over any duration of length I. The unit of $\mathrm{GAMA}(I)$ is defined as Bytes per I. $\mathrm{GAMA}(I)$ is a decreasing function in terms of I. Figure 3 demonstrates $\mathrm{GAMA}(I)$ of OM-W1-1-1999AF for $0 \leq I \leq 63$.

3. Histogram of Maxima of Traffic Rate Bound: A Feature for Identifying Abnormal Variation of Traffic under DDOS Attacks

In this section, we first introduce the time series of traffic rate bound. Then, we establish the maxima of traffic rate bound. Finally, we achieve the histogram of the maxima of traffic rate bound. The demonstrations with the experimental data are used for facilitating the discussions.

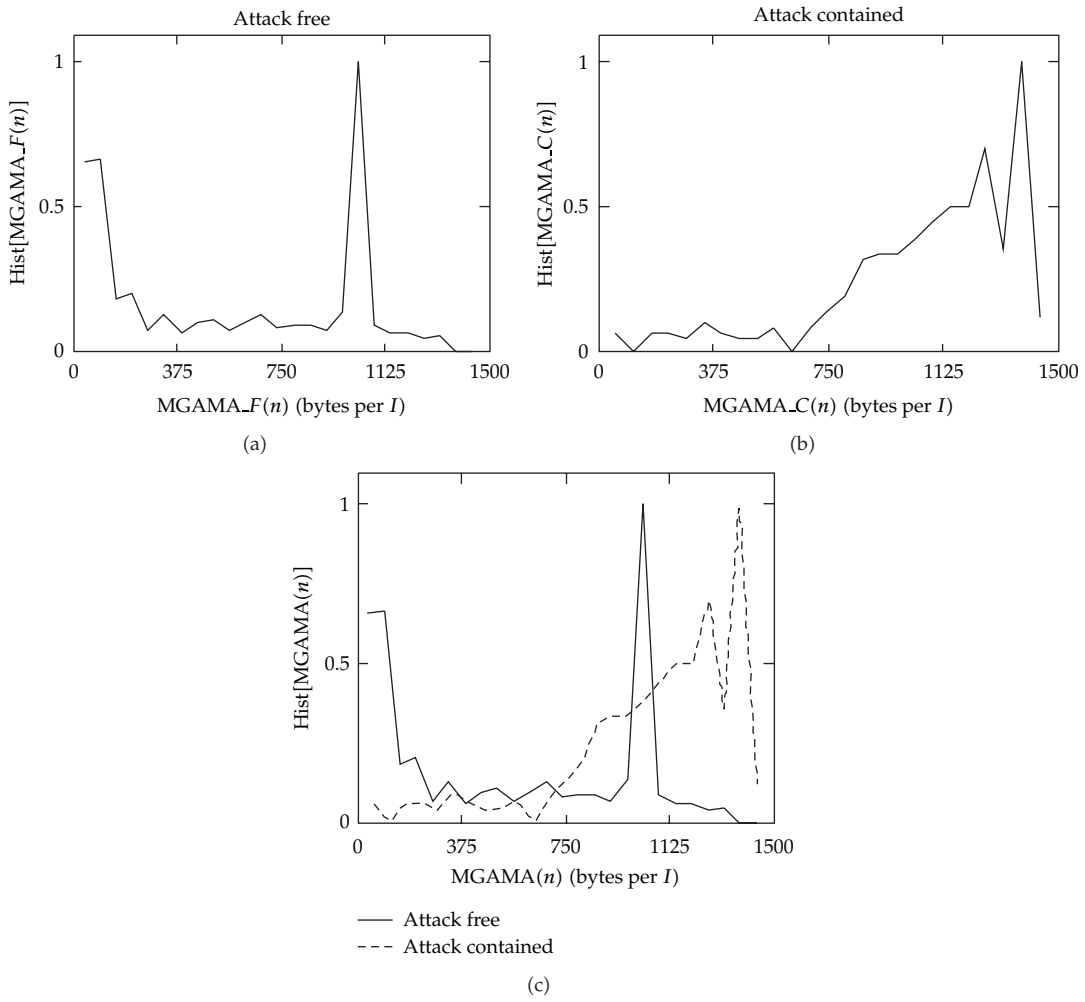

Figure 12: Histograms of the maxima of traffic rate bound. (a) For OM-W1-2-1999AF. (b) For OM-W2-2-1999AC. (c) Comparison: Corr_FC = 0.163261.

3.1. Traffic Bound Series

Theoretically, I can be any positively real number. In practice, however, I is selected as a finite positive integer. Fix the value of I and observe traffic bounds in the interval $((n-1)I,\ nI),\ n = 1, 2, \ldots, N$. Then, we express traffic bounds as a function in terms of the interval index n. Considering the index n, we express traffic upper bound by $F(I, n)$, which is a series.

Note that $x(i)$ is a stochastic series and so is $F(I, n)$. That is, $F(I, m) \neq F(I, n)$ for $m \neq n$. We term $F(I,\ n)$ traffic upper bound series. Similarly, we use GAMA(I, n) to represent traffic rate bound series. Figure 4 shows the traffic upper bound series. Figure 5 plots the rate bound series.

Since GAMA(I, n) is random, identification in a single interval is not enough. We use Figure 6 to explain this point of view. From Figure 6, we see that the rate bound of attack-contained traffic is greater than that of attack-free traffic in some intervals, for example, in the second and third intervals. However, it is less than the rate bound of attack-free traffic

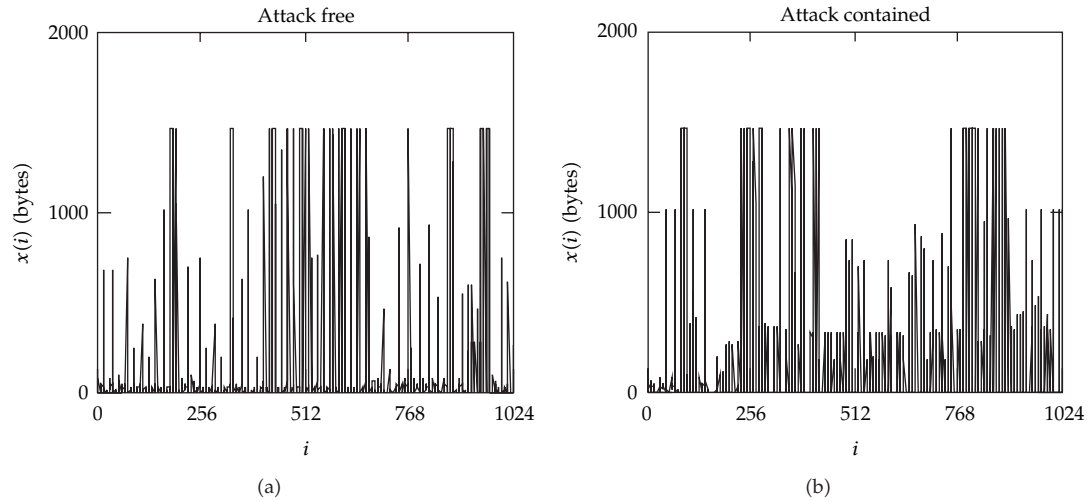

Figure 13: Time series of traffic traces. (a) The first 1024 points of OM-W1-3-1999AF. (b) The first 1024 points of OM-W2-3-1999AC.

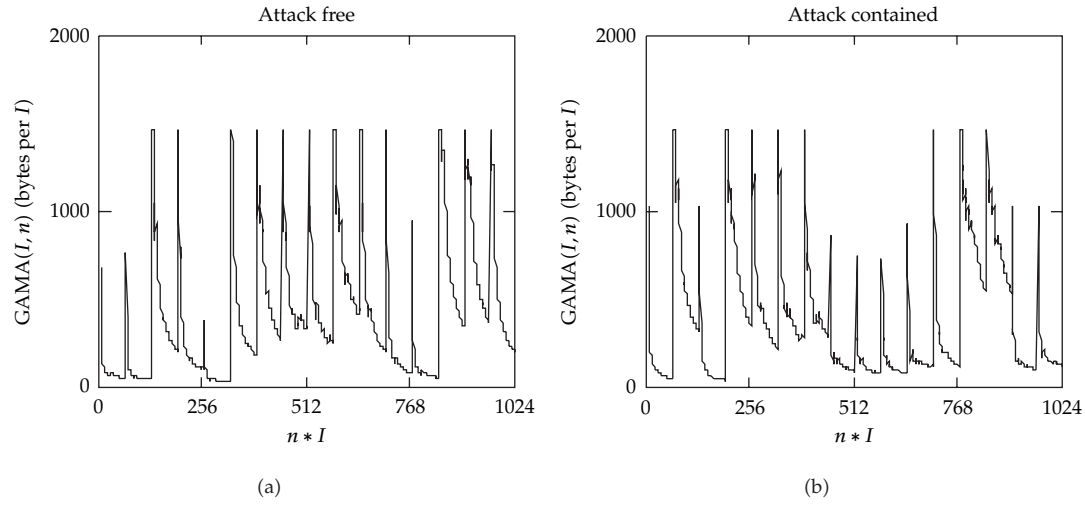

Figure 14: Series of traffic rate bound. (a) For OM-W1-3-1999AF. (b) For OM-W2-3-1999AC.

in some intervals, for example, in the first and fourth intervals. Therefore, we will study the issue how the bound series of traffic rate statistically varies under DDOS flood attacks. For this reason, we study the maxima of traffic rate bound.

3.2. Maxima of Traffic Rate Bound

Denote that

$$\mathrm{MGAMA}(n) = \mathrm{Max}[\mathrm{GAMA}(I,n)], \tag{3.1}$$

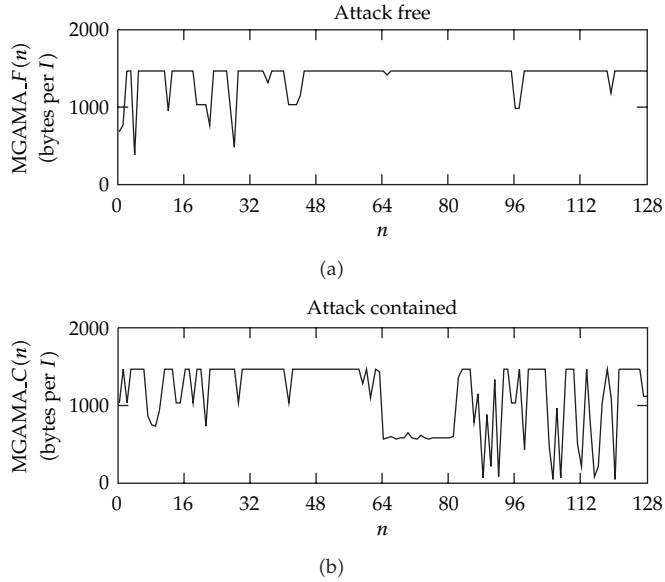

Figure 15: Series of the maxima of traffic rate bound. (a) Maxima of GAMA(I, n) for OM-W1-3-1999AF. (b) Maxima of GAMA(I, n) for OM-W2-3-1999AC.

over the index I in each interval $[(n-1)I,\ nI]$. Then, MGAMA(n) represents a series to describe the maximum value of GAMA(I, n) in each interval $[(n-1)I,\ nI]$. In other words, MGAMA(n) stands for the maxima of GAMA(I, n). The unit of MGAMA(n) is the same as that of GAMA(I, n). Here and below, we use the notation MGAMA_F(n) for attack-free traffic and MGAMA_C(n) for attack-contained traffic. Figures 7(a) and 7(b) give the plots of MGAMA_F(n) and MGAMA_C(n) for OM-W1-1-1999AF and OM-W2-1-1999AC, respectively.

3.3. *Histogram of Maxima*

Denote Hist[MGAMA_F(n)] and Hist[MGAMA_C(n)] as the histograms of MGAMA_F(n) and MGAMA_C(n), respectively. Then, they represent empirical distributions of MGAMA_F(n) and MGAMA_C(n). Figures 8(a) and 8(b) indicate the Hist[MGAMA_F(n)] and Hist[MGAMA_C(n)] for OM-W1-1-1999AF and OM-W1-1-1999CF, respectively. From Figure 8(c), we see that the pattern of Hist[MGAMA_F(n)] considerably differs from that of Hist[MGAMA_C(n)]. To investigate this phenomenon quantitatively, we need a measure to describe the similarity or dissimilarity between the pattern of Hist[MGAMA_F(n)] and that of Hist[MGAMA_C(n)], which will be explained in the next subsection.

3.4. *Correlation Coefficient Used as a Similarity Measure for Pattern Matching*

There are many measures to characterize the similarity or the dissimilarity of two patterns in the field of pattern matching, see, for example, [44, 45]. Among them, the correlation

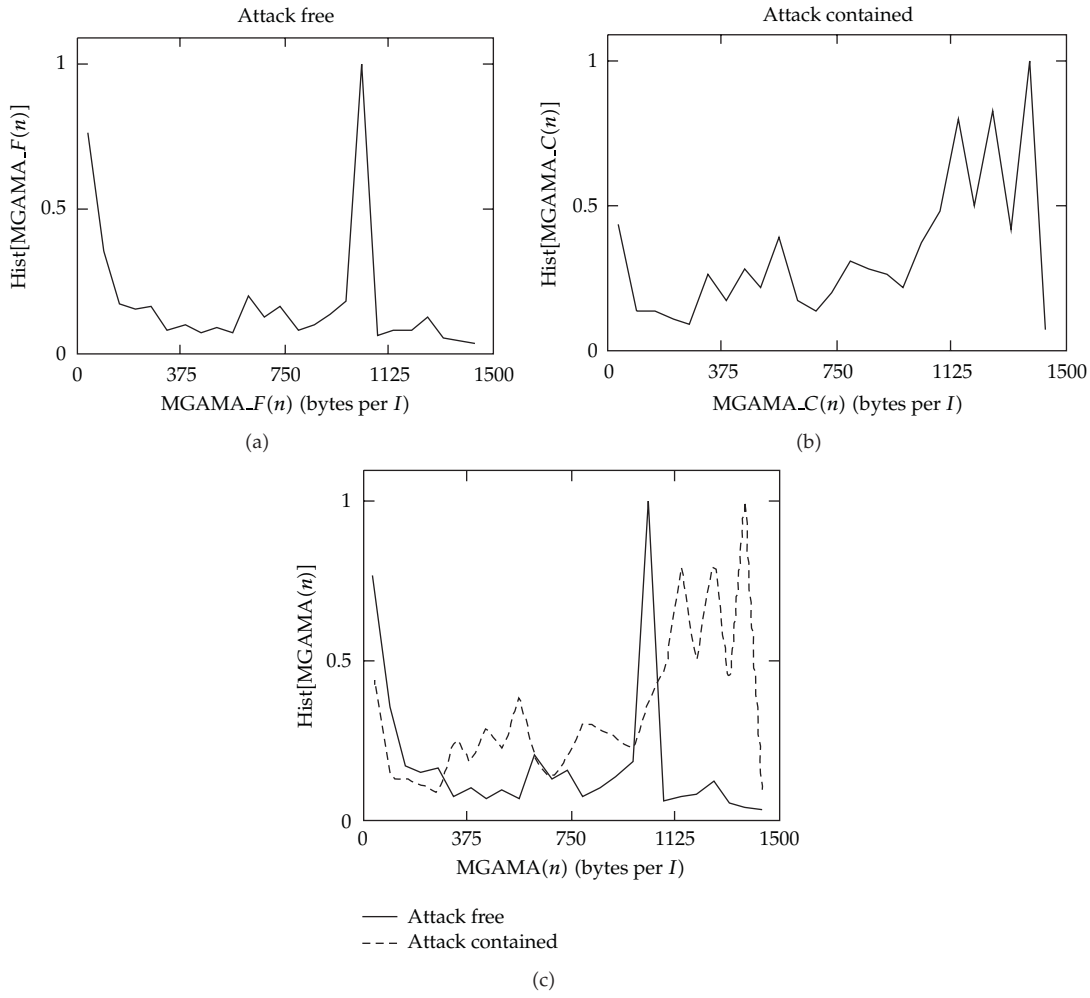

Figure 16: Histograms of the maxima of traffic rate bound. (a) For OM-W1-3-1999AF. (b) For OM-W2-3-1999AC. (c) Comparison: Corr_FC = 0.045515.

coefficient between two patterns is commonly used in engineering, see, for example, [46]. We use it to measure the pattern similarity in this research. Denote that

$$\text{Corr}_{\text{FC}} = \text{corr Hist MGAMA}_{\text{F}(n)} \text{ , Hist MGAMA}_{\text{C}(n)} \quad , \tag{3.2}$$

where corr implies the correlation operation.

It is known that $0 \leq \text{Corr\_FC} \leq 1$. The larger the value of Corr_FC the more similar between the pattern of Hist[MGAMA_F(n)] and that of Hist[MGAMA_C(n)]. Mathematically, the case of Corr_FC = 1 implies that the pattern of Hist[MGAMA_F(n)] is exactly the same as that of Hist[MGAMA_C(n)]. On the contrary, Corr_FC = 0 means that the pattern of Hist[MGAMA_F(n)] is totally different from that of MGAMA_C(n)]. From the point of view of engineering, however, the extreme case of either Corr_FC = 1 or Corr_FC = 0 does not make much sense due to errors and uncertainties in measurement and digital

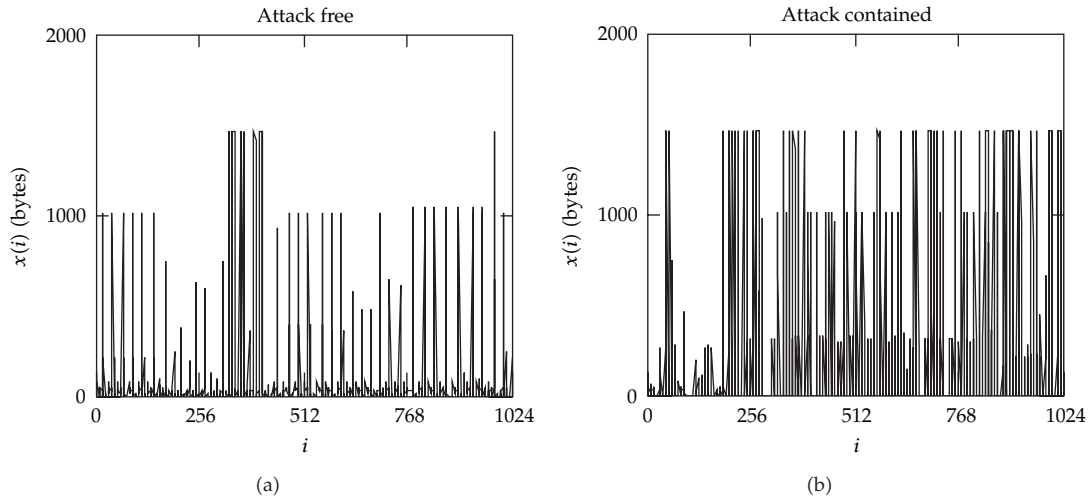

Figure 17: Time series of traffic traces. (a) The first 1024 points of OM-W1-4-1999AF. (b) The first 1024 points of OM-W2-4-1999AC.

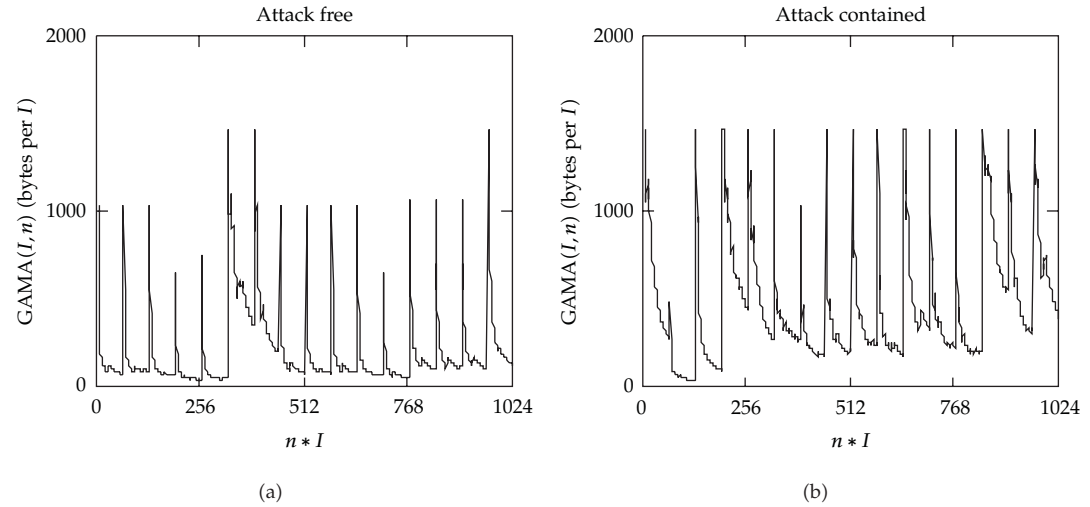

Figure 18: Series of traffic rate bound. (a) For OM-W1-4-1999AF. (b) For OM-W2-4-1999AC.

computation. In practical terms, one uses a threshold for Corr_FC to evaluate the similarity between two. The concrete value of the threshold depends on the requirement designed by researchers that but it is quite common to take 0.7 as the smallest value of the threshold for the pattern patching purpose. Suppose that we consider 0.8 as the threshold value. Then, we say that the pattern of Hist[MGAMA_F(n)] is similar to that of Hist[MGAMA_C(n)] if Corr_FC ≥ 0.8 and dissimilar otherwise.

By computing, we obtain Corr_FC = 0.01751 for OM-W1-1-1999AF and OM-W2-1-1999CF, implying the pattern of Hist[MGAMA_F(n)] considerably differs from that of Hist[MGAMA_C(n)] as indicated in Figure 8(c). We will further demonstrate this interesting phenomenon in the next section.

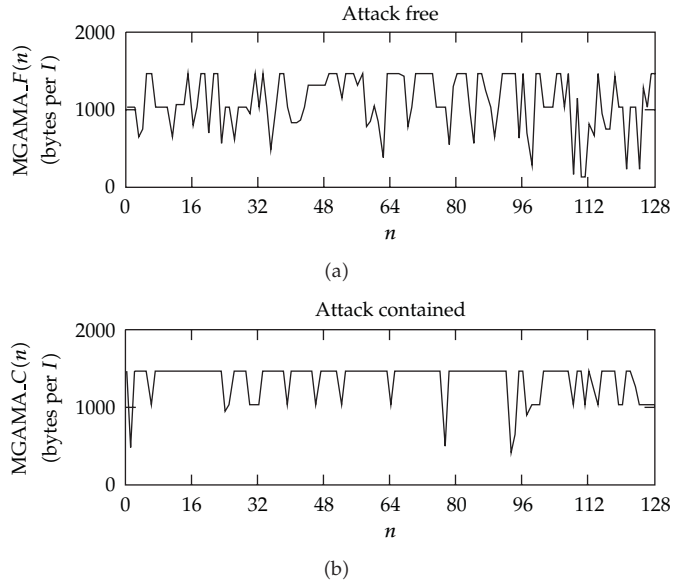

Figure 19: Series of the maxima of traffic rate bound. (a) Maxima of GAMA(I, n) for OM-W1-4-1999AF. (b) Maxima of GAMA(I, n) for OM-W2-4-1999AC.

4. Experimental Results

The value of Corr_FC for OM-W1-1-1999AF and OM-W2-1-1999CF has been mentioned above. In this section, we illustrate experimental results describing Corr_FC for OM-W1-2-1999AF and OM-W2-2-1999CF. The plots to illustrate Corr_FC for OM-W1-3-1999AF and OM-W2-3-1999CF, OM-W1-4-1999AF and OM-W2-4-1999CF, OM-W1-5-1999AF and OM-W2-5-1999CF and are listed in the appendices.

Figures 9(a) and 9(b) are the plots of the first 1024 points of OM-W1-2-1999AF and OM-W2-2-1999CF, respectively. Figures 10(a) and 10(b) indicate the series of traffic rate bound for OM-W1-2-1999AF and OM-W2-2-1999CF for $n = 0, 1, \ldots, 16$ with $I = 64$, respectively. Figures 11(a) and 11(b) demonstrate the maxima of rate bound for both traffic traces for $n = 0, 1, \ldots, 128$. Figures 12(a) and 12(b) show the histograms of the maxima of traffic rate bound for both traces. Figure 12(c) gives the comparison between two. By computation, we have Corr_FC = 0.163261, meaning that the pattern of Hist[MGAMA_F(n)] considerably differs from that of Hist[MGAMA_C(n)] for OM-W1-2-1999AF and OM-W2-2-1999AC.

Note that the values of Corr_FC for other three pairs of test traces, see Figures 16(c), 20(c), and 24(c), also exhibit that the pattern of Hist[MGAMA_F(n)] is noticeably different from that of Hist[MGAMA_C(n)]. We summarize the values of Corr_FC of all five pairs of traces in Table 3, which shows that Corr_FC < 0.2 for all pairs of test traces.

5. Discussions and Conclusions

The maxima of rate bound of attack-contained traffic is not always higher than that of attack-free traffic, see Figure 7. Statistically, however, it is higher than that of attack-free traffic

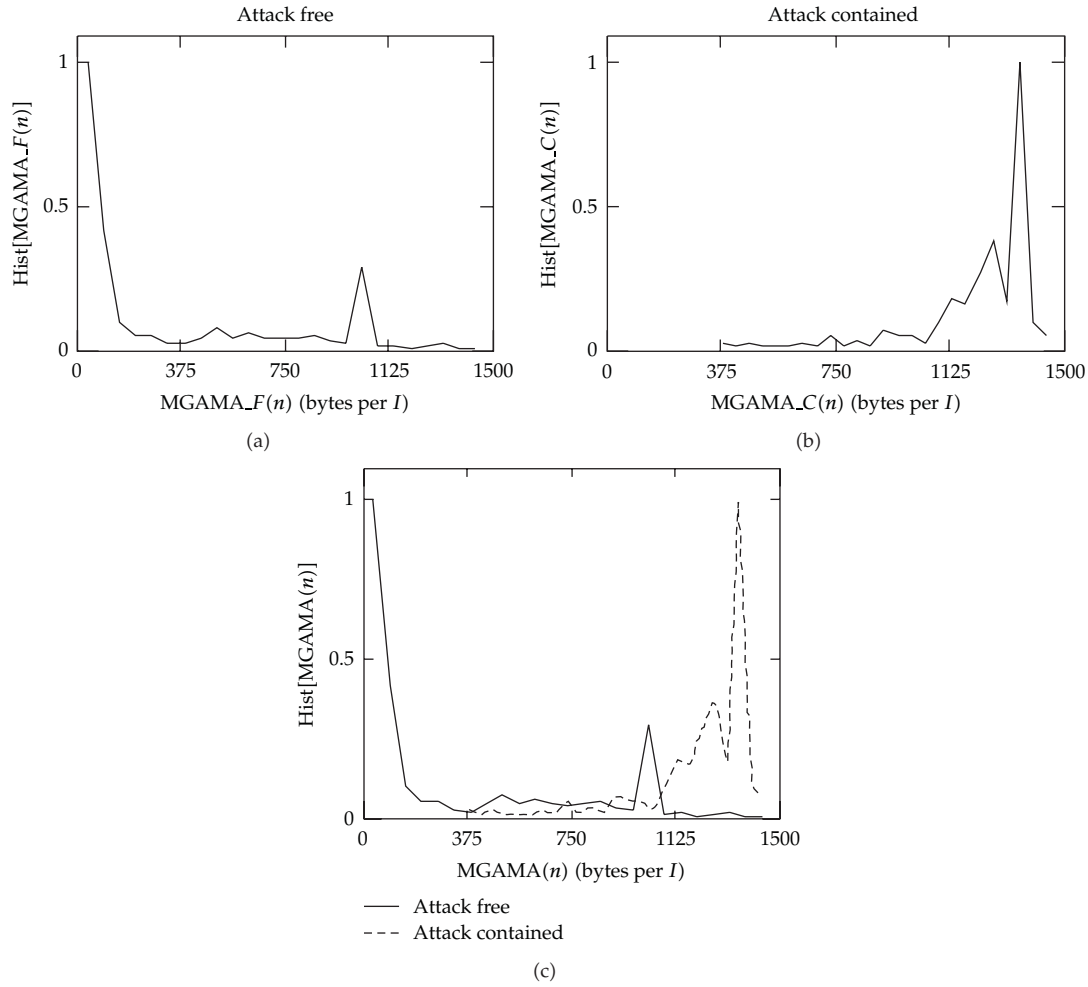

Figure 20: Histograms of the maxima of traffic rate bound. (a) For OM-W1-4-1999AF. (b) For OM-W2-4-1999AC. (c) Comparison: Corr_FC = 0.141885.

significantly as can be seen from the experimental results illustrated by Figures 8(c), 12(c), 16(c), 20(c), and 24(c). In addition, the results expressed in Table 3 indicate that the pattern of Hist[MGAMA_F(n)] is obviously different from that of Hist[MGAMA_C(n)]. Thus, the results in this paper suggest that the histogram of the maxima of traffic rate bound may yet be a traffic feature to distinctly identify abnormal variation of traffic under DDOS flood attacks.

In comparison with fractal model of traffic as discussed in [18, 19, 43], the present feature has an apparent advantage. Recall that statistical models like LRD processes, see, for example, [18, 19], are usually for traffic in the aggregate case, but there is lack of evidence to use them to characterize statistical patterns of real traffic at connection. As a matter of fact, finding statistical patterns of traffic at connection may be a tough task. To overcome difficulties in describing traffic at connection level, bounded modeling is introduced [25–29]. Thus, if we let $x_{j,k}(t)$ be all flows going through server k from input link j and let $F_{j,k}(I)$ be the maximum traffic constraint function of $x_{j,k}(t)$, the present analysis method of traffic

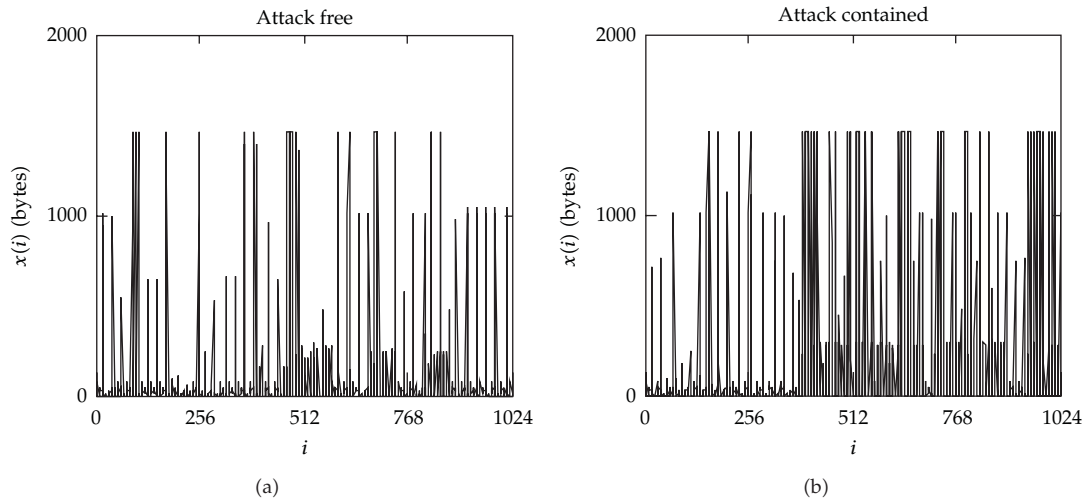

Figure 21: Time series of traffic traces. (a) The first 1024 points of OM-W1-5-1999AF. (b) The first 1024 points of OM-W2-5-1999AC.

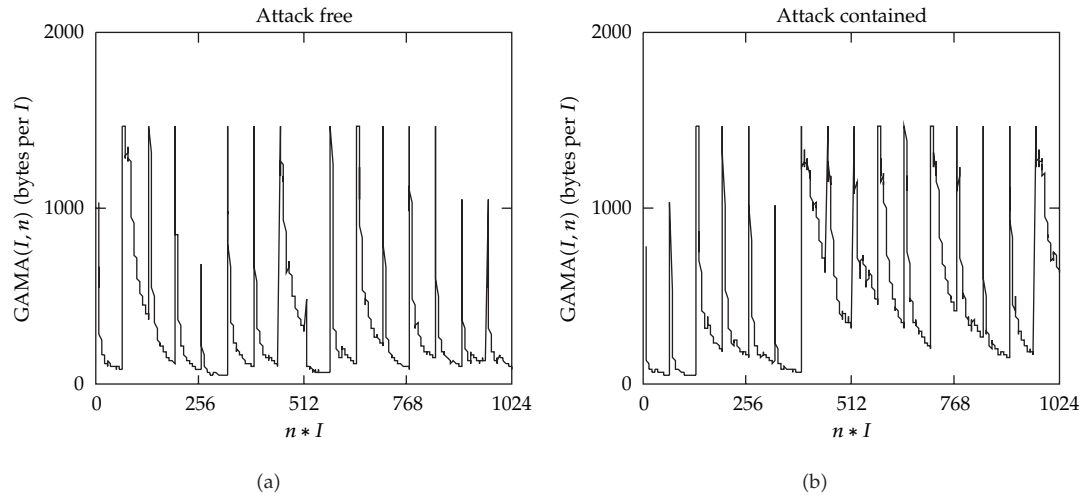

Figure 22: Series of traffic rate bound. (a) For OM-W1-5-1999AF. (b) For OM-W2-5-1999AC.

Table 3: Correlation coefficients between the pattern of Hist[MGAMA_F(n)] and that of Hist[MGAMA_C(n)] for 5 pairs of test traces.

Attack-free traffic traces	Attack-contained traffic traces	Corr_FC
OM-W1-1-1999AF	OM-W2-1-1999AC	0.01751
OM-W1-2-1999AF	OM-W2-2-1999AC	0.163261
OM-W1-3-1999AF	OM-W2-3-1999AC	0.045515
OM-W1-4-1999AF	OM-W2-4-1999AC	0.141885
OM-W1-5-1999AF	OM-W2-5-1999AC	0.177468

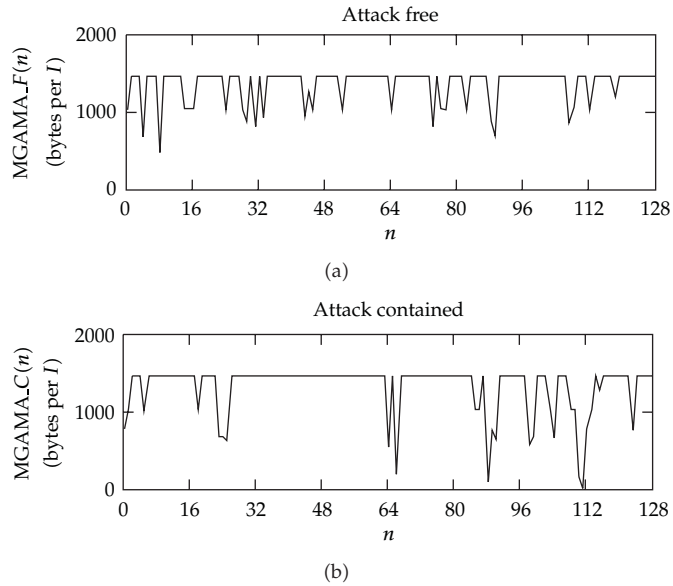

Figure 23: Series of the maxima of traffic rate. (a) Maxima of GAMA(I, n) for OM-W1-5-1999AF. (b) Maxima of GAMA(I, n) for OM-W2-5-1999AC.

is technically sound and usable for $x_{j,k}(t)$ but fractal models may not. Since the bounded models of traffic are mainly used at connection level in some applications, such as real-time admission control, it is clear that the present traffic feature for identifying abnormal variation of traffic under DDOS flood attacks can be extracted at early stage of attacks.

Appendices

These appendices gives experimental results for three pairs of traces. They are OM-W1-3-1999AF and OM-W2-3-1999CF, OM-W1-4-1999AF and OM-W2-4-1999CF, and OM-W1-5-1999AF and OM-W2-5-1999CF. The values of Corr_FC for each pair of traces are given in the captions of Figures 16(c), 20(c), and 24(c), respectively.

A. Experiments for OM-W1-3-1999AF and OM-W2-3-1999CF

See Figures 13, 14, 15, and 16.

B. Experiments for OM-W1-4-1999AF and OM-W2-4-1999CF

See Figures 17, 18, 19, and 20.

C. Experiments for OM-W1-5-1999AF and OM-W2-5-1999CF

See Figures 21, 22, 23, and 24.

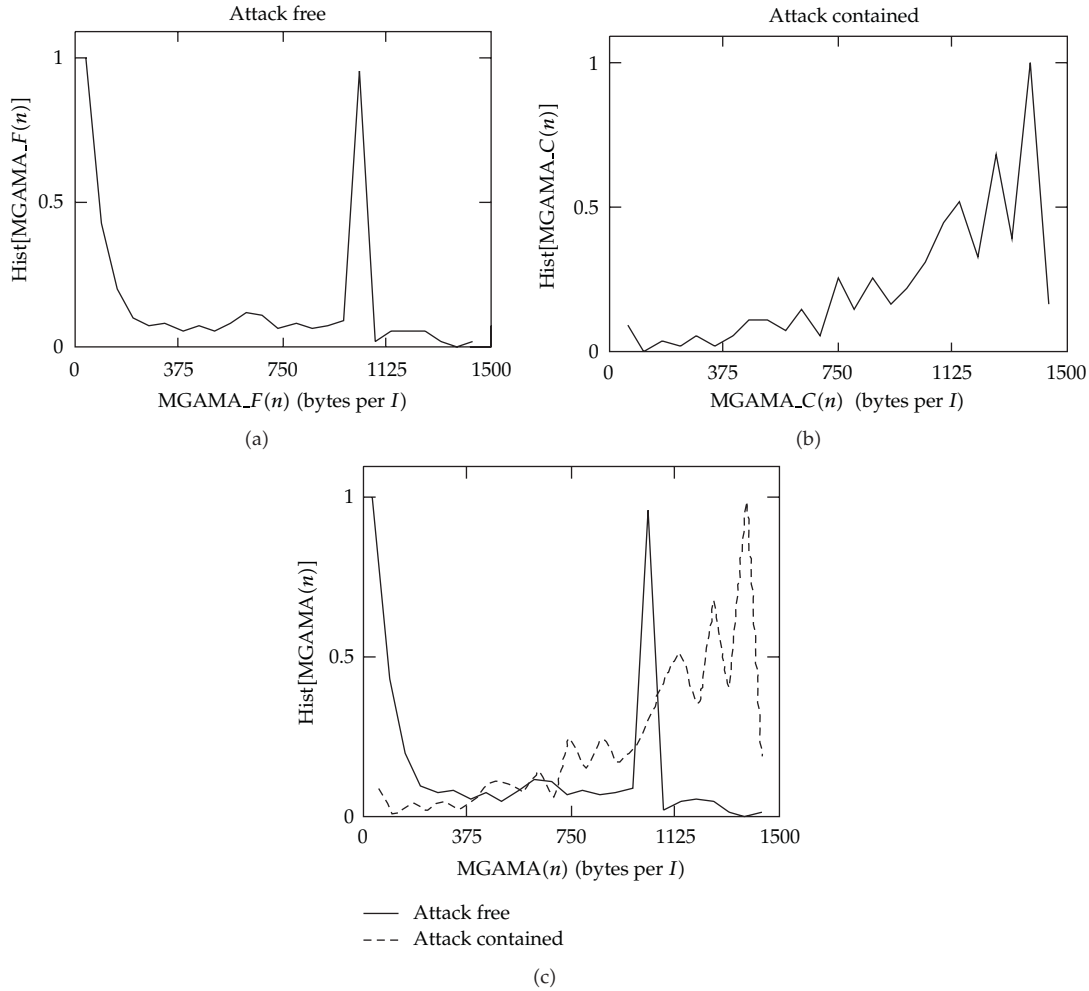

Figure 24: Histograms of the maxima of traffic rate bound. (a) For OM-W1-5-1999AF. (b) For OM-W2-5-1999AC. (c) Comparison: Corr_FC = 0.177468.

Acknowledgments

This work was supported in part by the 973 plan under the project number 2011CB302801/2011CB302802, by the National Natural Science Foundation of China under the project grant numbers, 60873264, 61070214, 61173096, by Zhejiang Provincial Natural Science Foundation of China (R1110679), and by the University of Macau.

References

[1] R. Shirey, *Internet Security Glossary*, RFC 2828, 2000.
[2] N. Hussain, *Measurement and spectral analysis of denial of service attacks*, Ph.D. dissertation, University of Southern California, 2005.
[3] S. Chebrolu, A. Abraham, and J. P. Thomas, "Feature deduction and ensemble design of intrusion detection systems," *Computers & Security*, vol. 24, no. 4, pp. 295–307, 2005.

[4] E. G. Amoroso, *Intrusion Detection: An Introduction to Internet Surveillance, Correlation, Traps, Trace Back, and Response*, Intrusion.Net Books, 1999.
[5] J. Mirkovic, S. Dietrich, D. Dittrich, and P. Reiher, *Internet Denial of Service: Attack and Defense Mechanisms*, Prentice Hall, 2004.
[6] K. Liston, "Intrusion Detection FAQ: can you explain traffic analysis and anomaly detection?" 2004, http://www.sans.org/security-resources/idfaq/anomaly_detection.php.
[7] E. Schultz, "Intrusion prevention," *Computers and Security*, vol. 23, no. 4, pp. 265–266, 2004.
[8] J. Leach, "TBSE—an engineering approach to the design of accurate and reliable security systems," *Computers and Security*, vol. 23, no. 1, pp. 265–266, 2004.
[9] S. H. Oh and W. S. Lee, "An anomaly intrusion detection method by clustering normal user behavior," *Computers and Security*, vol. 22, no. 7, pp. 596–612, 2003.
[10] F. Gong, "Deciphering detection techniques: part III denial of service detection," White Paper, McAfee Network Security Technologies Group, 2003.
[11] S. Sorensen, "Competitive overview of statistical anomaly detection," White Paper, Juniper Networks, 2004.
[12] S. B. Cho and H. J. Park, "Efficient anomaly detection by modeling privilege flows using hidden Markov model," *Computers and Security*, vol. 22, no. 1, pp. 45–55, 2003.
[13] S. Cho and S. Cha, "SAD: web session anomaly detection based on parameter estimation," *Computers and Security*, vol. 23, no. 7, pp. 312–319, 2004.
[14] R. A. Kemmerer and G. Vigna, "Intrusion detection: a brief history and overview," *Computer*, vol. 35, pp. 27–30, 2002.
[15] E. E. Schultz, "Representing information security fairly and accurately," *Computers and Security*, vol. 25, no. 4, p. 237, 2006.
[16] S. S. Kim, A. L. Narasimha Reddy, and M. Vannucci, "Detecting traffic anomalies through aggregate analysis of packet header data," *Lecture Notes in Computer Science*, vol. 3042, pp. 1047–1059, 2004.
[17] M. Li, "An approach to reliably identifying signs of DDOS flood attacks based on LRD traffic pattern recognition," *Computers and Security*, vol. 23, no. 7, pp. 549–558, 2004.
[18] M. Li, "Change trend of averaged Hurst parameter of traffic under DDOS flood attacks," *Computers and Security*, vol. 25, no. 3, pp. 213–220, 2006.
[19] A. Scherrer, N. Larrieu, P. Owezarski, P. Borgnat, and P. Abry, "Non-Gaussian and long memory statistical characterizations for Internet traffic with anomalies," *IEEE Transactions on Dependable and Secure Computing*, vol. 4, no. 1, pp. 56–70, 2007.
[20] B. Tsybakov and N. D. Georganas, "Self-similar processes in communications networks," *Institute of Electrical and Electronics Engineers. Transactions on Information Theory*, vol. 44, no. 5, pp. 1713–1725, 1998.
[21] M. Li, "Modeling autocorrelation functions of long-range dependent teletraffic series based on optimal approximation in Hilbert space-A further study," *Applied Mathematical Modelling*, vol. 31, no. 3, pp. 625–631, 2007.
[22] M. Li and S. C. Lim, "Modeling network traffic using generalized Cauchy process," *Physica A*, vol. 387, no. 11, pp. 2584–2594, 2008.
[23] M. Li and W. Zhao, "Detection of variations of local irregularity of traffic under DDOS flood attack," *Mathematical Problems in Engineering*, vol. 2008, Article ID 475878, 2008.
[24] H. Michiel and K. Laevens, "Teletraffic engineering in a broad-band era," *Proceedings of the IEEE*, vol. 85, no. 12, pp. 2007–2032, 1997.
[25] R. L. Cruz, "A calculus for network delay—I: network elements in isolation," *IEEE Transactions on Information Theory*, vol. 37, no. 1, pp. 114–131, 1991.
[26] J.-Y. Le Boudec, J. Yves, and T. Patrick, *Network Calculus, A Theory of Deterministic Queuing Systems for the Internet*, vol. 2050 of *Lecture Notes in Computer Science*, Springer, Berlin, Germany, 2001.
[27] S. Wang, D. Xuan, R. Bettati, and W. Zhao, "Providing absolute differentiated services for real-time applications in static-priority scheduling networks," *IEEE/ACM Transactions on Networking*, vol. 12, no. 2, pp. 326–339, 2004.
[28] M. Li and W. Zhao, "Representation of a stochastic traffic bound," *IEEE Transactions on Parallel and Distributed Systems*, vol. 21, no. 9, Article ID 5342414, pp. 1368–1372, 2010.
[29] M. Li and W. Zhao, "A model to partly but reliably distinguish DDOS flood traffic from aggregated one," *Mathematical Problems in Engineering*, vol. 2012, Article ID 860569, 12 pages, 2012.
[30] M. Li and W. Zhao, "Asymptotic identity in min-plus algebra: a report on CPNS," *Computational and Mathematical Methods in Medicine*, vol. 2012, Article ID 154038, 11 pages, 2012.

[31] J. McHugh, "Testing intrusion detection systems: a critique of the 1988 and 1999 DARPA intrusion detection system evaluations as performed by lincoln laboratory," *ACM Transactions Information System Security*, vol. 3, no. 4, pp. 262–294, 2000.

[32] J. W. Haines, L. M. Rossey, R. Lippmann, and R. K. Cunningharm, "Extending the DARPA off-line intrusion detection evaluations," in *Proceedings of the DARPA Information Survivability Conference and Exposition II*, vol. 1, pp. 77–88, IEEE, Anaheim, Calif, USA, 2001.

[33] L. Feinstein, D. Schnackenberg, R. Balupari, and D. Kindred, "Statistical approaches to DDoS attack detection and response," in *Proceedings of the DARPA Information Survivability Conference and Exposition*, vol. 1, pp. 303–314, Washington, DC, USA, 2003.

[34] R. Lippmann, J. W. Haines, D. J. Fried, J. Korba, and K. Das, "The 1999 DARPA off-line intrusion detection evaluation," *Computer Networks*, vol. 34, no. 4, pp. 579–595, 2000.

[35] L. Garber, "Denial-of-service attacks rip the internet," *Computer*, vol. 33, no. 4, pp. 12–17, 2000.

[36] D. Moore, G. M. Veolker, and S. Savage, "Inferring internet denial-of-service activity," in *Proceedings of the 10th USENIX Security Symposium*, 2001.

[37] R. Mahajan, S. M. Bellovin, and S. Floyd, "Controlling high bandwidth aggregates in the network," vol. 32, no. 3, pp. 62–73.

[38] A. Lakhina, M. Crovella, and C. Diot, "Characterization of network-wide anomalies in traffic flows," in *Proceedings of the ACM SIGCOMM Internet Measurement Conference (IMC '04)*, pp. 201–206, Sicily, Italy, October 2004.

[39] P. Barford and D. Plonka, "Characteristics of network traffic flow anomalies," in *Proceedings of the 1st ACM SIGCOMM Internet Measurement Workshop (IMW '01)*, pp. 69–73, San Francisco, Calif, USA, November 2001.

[40] V. A. Siris and F. Papagalou, "Application of anomaly detection algorithms for detecting SYN flooding attacks," *Computer Communications*, vol. 29, no. 9, pp. 1433–1442, 2006.

[41] H. Wang, D. Zhang, and K. G. Shin, "Detecting SYN flooding attacks," in *Proceedings of the 21st Annual Joint Conference of the IEEE Computer and Communications Societies*, pp. 1530–1539, New York, NY, USA, June 2002.

[42] M. Li, J. Li, and W. Zhao, " Simulation study of flood attacking of DDOS," in *Proceedings of the IEEE 3rd International Conference on Internet Computing in Science and Engineering (ICICSE '08)*, pp. 289–293, Harbin, China, 2008.

[43] R. Bettati, W. Zhao, and D. Teodor, "Real-time intrusion detection and suppression in ATM networks," in *Proceedings of the 1st USENIX Workshop on Intrusion Detection and Network Monitoring*, pp. 111–118, 1999.

[44] K. S. Fu, Ed., *Digital Pattern Recognition*, Springer, 2nd edition, 1980.

[45] M. Basseville, "Distance measures for signal processing and pattern recognition," *Signal Processing*, vol. 18, no. 4, pp. 349–369, 1989.

[46] M. Li, "An iteration method to adjusting random loading for a laboratory fatigue test," *International Journal of Fatigue*, vol. 27, no. 7, pp. 783–789, 2005.

Hindawi Publishing Corporation
Mathematical Problems in Engineering
Volume 2012, Article ID 490840, 14 pages
doi:10.1155/2012/490840

Research Article

Adaptive Binary Arithmetic Coder-Based Image Feature and Segmentation in the Compressed Domain

Hsi-Chin Hsin,[1] Tze-Yun Sung,[2] Yaw-Shih Shieh,[2] and Carlo Cattani[3]

[1] *Department of Computer Science and Information Engineering, National United University, Miaoli 36003, Taiwan*
[2] *Department of Electronics Engineering, Chung Hua University, Hsinchu City 30012, Taiwan*
[3] *Department of Mathematics, University of Salerno, Via Ponte Don Melillo, 84084 Fisciano, Italy*

Correspondence should be addressed to Tze-Yun Sung, bobsung@chu.edu.tw

Received 31 August 2011; Accepted 23 September 2011

Academic Editor: Ming Li

Image compression is necessary in various applications, especially for efficient transmission over a band-limited channel. It is thus desirable to be able to segment an image in the compressed domain directly such that the burden of decompressing computation can be avoided. Motivated by the adaptive binary arithmetic coder (MQ coder) of JPEG2000, we propose an efficient scheme to segment the feature vectors that are extracted from the code stream of an image. We modify the Compression-based Texture Merging (CTM) algorithm to alleviate the influence of overmerging problem by making use of the rate distortion information. Experimental results show that the MQ coder-based image segmentation is preferable in terms of the boundary displacement error (BDE) measure. It has the advantage of saving computational cost as the segmentation results even at low rates of bits per pixel (bpp) are satisfactory.

1. Introduction

Image segmentation is important in many applications, ranging from industrial monitoring to medical diagnosis. Among numerous techniques, the feature-based approach has received a lot of attention due largely to its computational efficiency [1]. However, the segmentation result is dependent on the selection of feature vectors [2–7]. Early research work on feature extraction is mainly at a single scale. It is noted that an image is decomposed into band-pass subimages by simple visual cortical cells in the human visual system (HVS) [8], which can be modeled by Gabor filters with spatial frequencies and orientations properly tuned

[9]. Wavelet transform (WT) provides an efficient multiresolution representation, in which the higher detail information of an image is projected onto the shorter basis function with higher spatial resolution, and the lower detail information is projected onto the larger basis function with higher spectral resolution. This property matches the characteristics of HVS [10]. Various WT-based schemes were proposed to extract image features at multiple scales [11–14]. In addition, the advantage of WT is to take account of the phenomena of multiscales [15–17], which is fundamental in nonlinear time series [18–20] and fractal time series [21].

With the rapid growth of multimedia technologies [22–25] and the Internet applications, image compression is still in great demand [26]. As one can see, it is desirable to extract image features in the compressed domain directly, such that the burden of decompressing an image can be avoided [14, 27, 28]. The Joint Photographic Expert Group (JPEG) standard shows satisfactory results at moderate compression rates. The JPEG2000 standard, which adopts WT as the underlying transform, is preferable for additional advantages, for example, embedded coding and progressive transmission [29, 30]. In embedded coding, the original image is coded into a single code stream, from which the decoded image at any bit rate can be obtained. For progressive transmission, which is especially beneficial to the image browsing and Internet streaming applications, JPEG2000 uses the postcompression rate distortion (PCRD) algorithm to arrange the code stream of an image in decreasing order of information importance [31]. It is based on the rate distortion theory; more specifically, the rate distortion slope (RDS) should be nonincreasing as the number of coding bits increases. For the image segmentation applications, two interesting questions are thus raised. (1) Is it possible that image segmentation can be carried out in the compressed domain such that the burden of decoding computations can be avoided? (2) Is there a common piece of information, based on which image features can be constructed at both encoder and decoder? If so, there is no need to transmit these features from encoder to decoder.

This paper presents an efficient scheme to segment an image in the compressed domain. It is a two-step algorithm. In the first step, the MQ coder-based image features are coarsely clustered into small regions known as superpixels by using the simple K-means algorithm. The inherently oversegmented superpiexels are merged recursively by using the Compression-based Texture Merging (CTM) algorithm [32]. In order to avoid over merging, we propose a simple RDS-based method to terminate CTM accordingly. The remainder of this paper proceeds as follows. In Section 2, the JPEG2000 standard is briefly reviewed. In Section 3, the modified CTM algorithm with the MQ coder-based image features is proposed to segment JPEG2000 images. Experimental results are presented in Section 4. Conclusion is given in Section 5.

2. Introduction to JPEG2000

The core of JPEG2000 is the embedded block coding with optimized truncation (EBCOT) algorithm [29], which adopts wavelet transform (WT) as the underlying method for subband decompositions. WT provides many desirable properties, for example, joint space-spatial frequency localization with orientation selectivity, self-similarity of wavelet coefficients across subbands of the same orientation, and energy clustering within each subband [10]. Among various WT-based image features, the commonly used are magnitude, energy, the generalized Gaussian distribution signature, and the cooccurrence measures [11–14].

EBCOT is a two-tier algorithm. Tier-1 consists of bit-plane coding (BPC) followed by arithmetic coding (AC). Tier-2 aims for optimal rate control. In BPC, three coding passes,

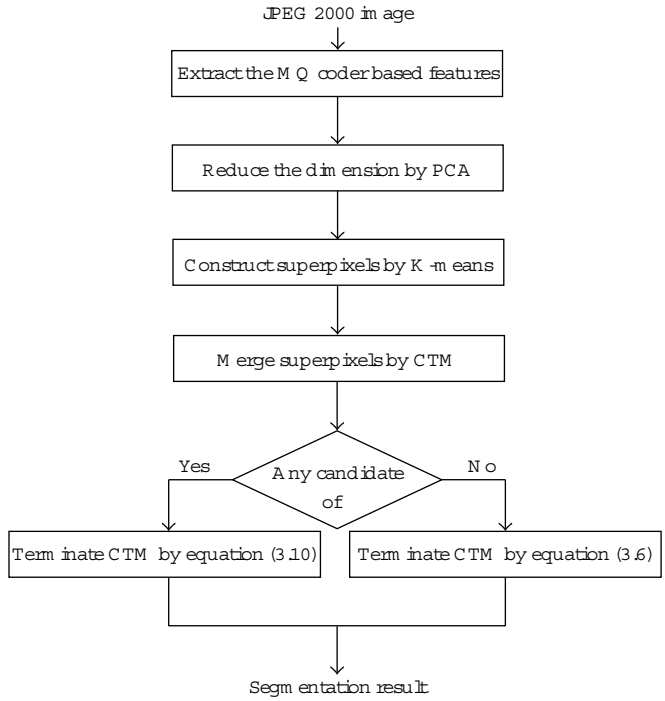

Figure 1: Flowchart of the proposed algorithm.

namely, the significance propagation (SP) pass, the magnitude refinement (MR) pass, and the clean up (CU) pass, are involved with four primitive coding operations, namely, the significance coding operation, the sign coding operation, the magnitude refinement coding operation, and the cleanup coding operation. For a wavelet coefficient that is currently insignificant, if any of the 8 neighboring coefficients are already significant, it is coded in the SP pass using the significance coding operation; otherwise, it is coded in the CU pass using the cleanup coding operation. If this coefficient becomes significant, the sign is coded immediately using the sign coding operation. In the MR pass, magnitudes of the significant coefficients are updated using the magnitude refinement coding operation. The output bit streams of coding passes can be further coded by using a context-based arithmetic coder known as the MQ coder to improve the compression performance. Based on the 8 neighboring coefficients, the MQ coder defines 18 context labels with their respective probability modes stored in the MQ table [29].

In JPEG2000, a large image can be partitioned into nonoverlapped subimages called tiles, each tile is decomposed into subbands by WT, each subband is divided into small blocks called code blocks, and each code block is independently coded from the most significant bit-plane to the least significant bit-plane. For optimal rate control, JPEG2000 adopts the postcompression rate distortion (PCRD) algorithm. Specifically, let $\{B_i\}$ be the code blocks of an image. The embedded code stream of B_i can be terminated at some point, say n_i, with a bit rate denoted by $R_i^{n_i}$; all the end points of coding passes are possible truncation points. PCRD selects the optimal truncation points to minimize the overall distortion: $D = \sum_i D_i^{n_i}$ subject to the rate constraint: $R = \sum_i R_i^{n_i} \leq R_c$, where $D_i^{n_i}$ denotes the distortion incurred by discarding the coding passes after n_i, and R_c is the target bit rate. It is noted that the

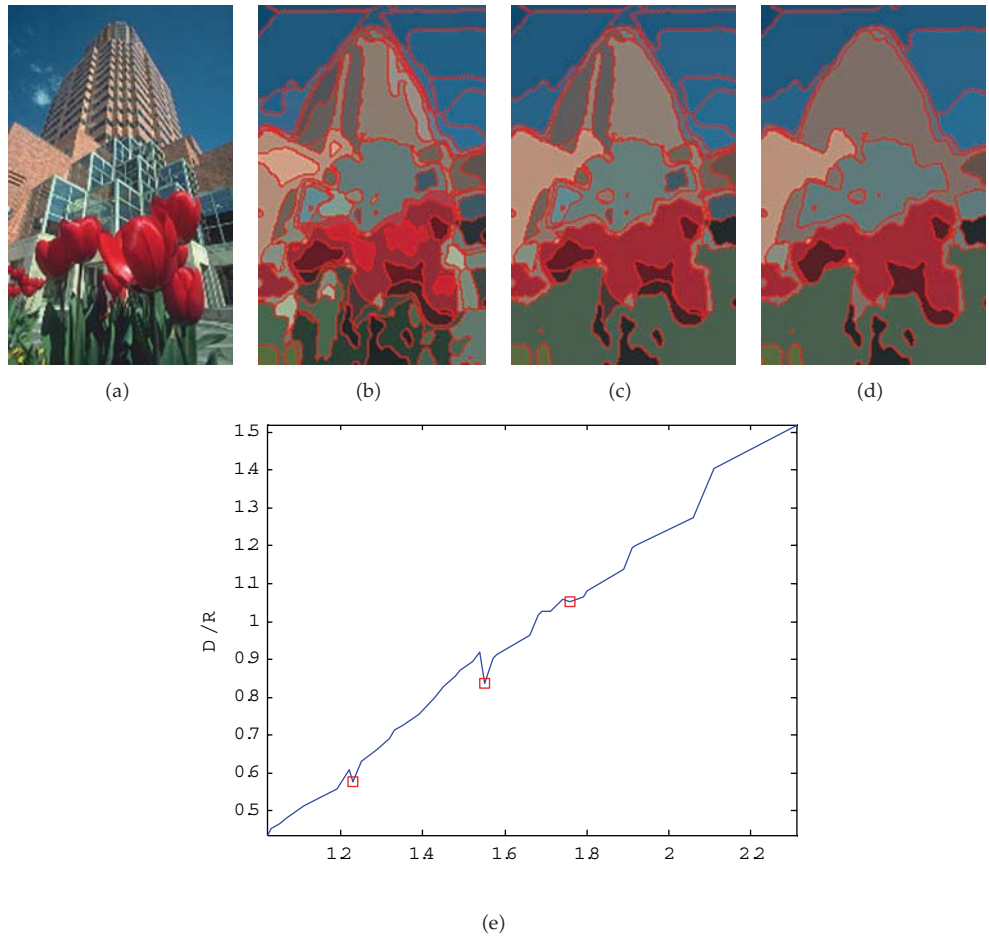

Figure 2: (a) Original image. (b) (d) Segmentation results with the first, second, and third candidates of ε. (e) Plot of the candidates of ε.

coding passes with nonincreasing rate distortion slopes (RDS) are candidates for the optimal truncation points. Based on the above, we propose an efficient scheme to segment JPEG2000 images in the following section.

3. Image Segmentation in the JPEG2000 Domain

In this section, we modify the Compression-based Texture Merging (CTM) algorithm [32] to segment the MQ coder-based image features [28] in an adaptive manner. As a result, the image segmentation task can be conducted in the JPEG2000 domain directly, and the burden of decompressing computation can be avoided.

3.1. The MQ Coder-Based Image Feature

The distribution of wavelet coefficients known as the wavelet histogram has been widely used for image segmentation. As the binary variables of wavelet coefficients are almost

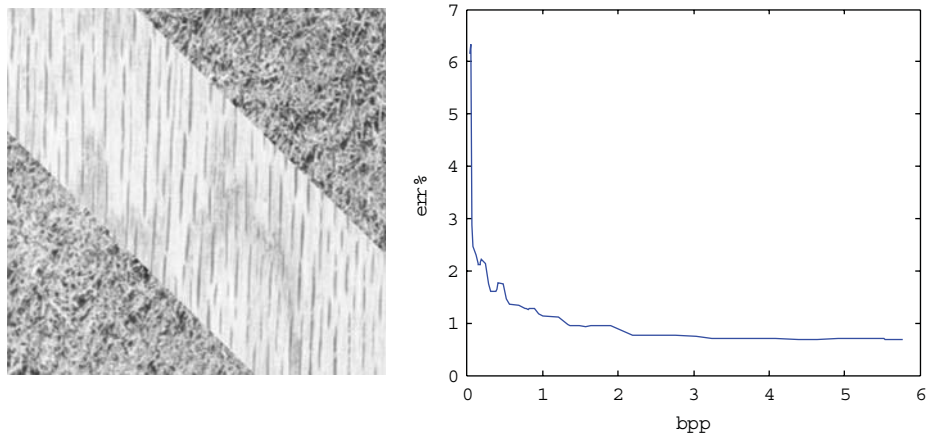

(a) (b)

Figure 3: Performance of the proposed algorithm at various bpp rates. (a) Test image. (b) Error rates in percentage at various bpp rates.

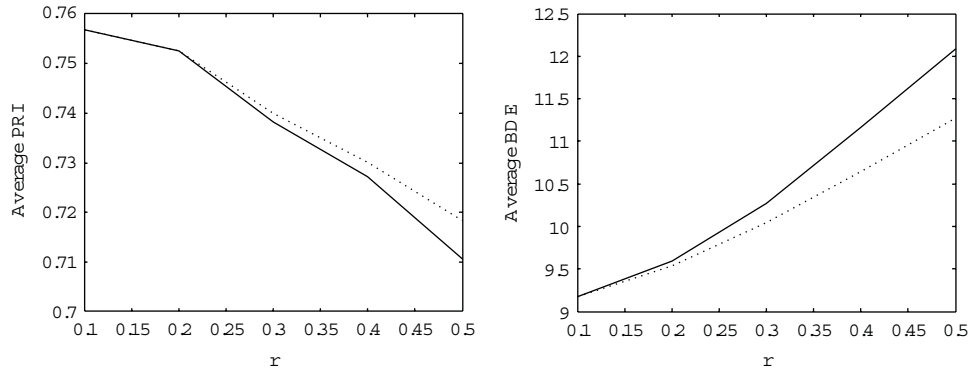

(a) (b)

Figure 4: Average (a) PRI and (b) BDE using CTM (solid line) and the modified CTM with the MQ coder-based image features (dotted line).

independent across bit-planes [14], the joint probability mass function (PMF) representing the wavelet histogram can be approximated as

$$P(|c| = x) = \prod_{i=0}^{n-1} P_i(x_i), \tag{3.1}$$

where x is the absolute value of a wavelet coefficient, c, which can be written by

$$x = \sum_{i=0}^{n-1} x_i \cdot 2^i; \quad x_i \in \{0,1\}, \tag{3.2}$$

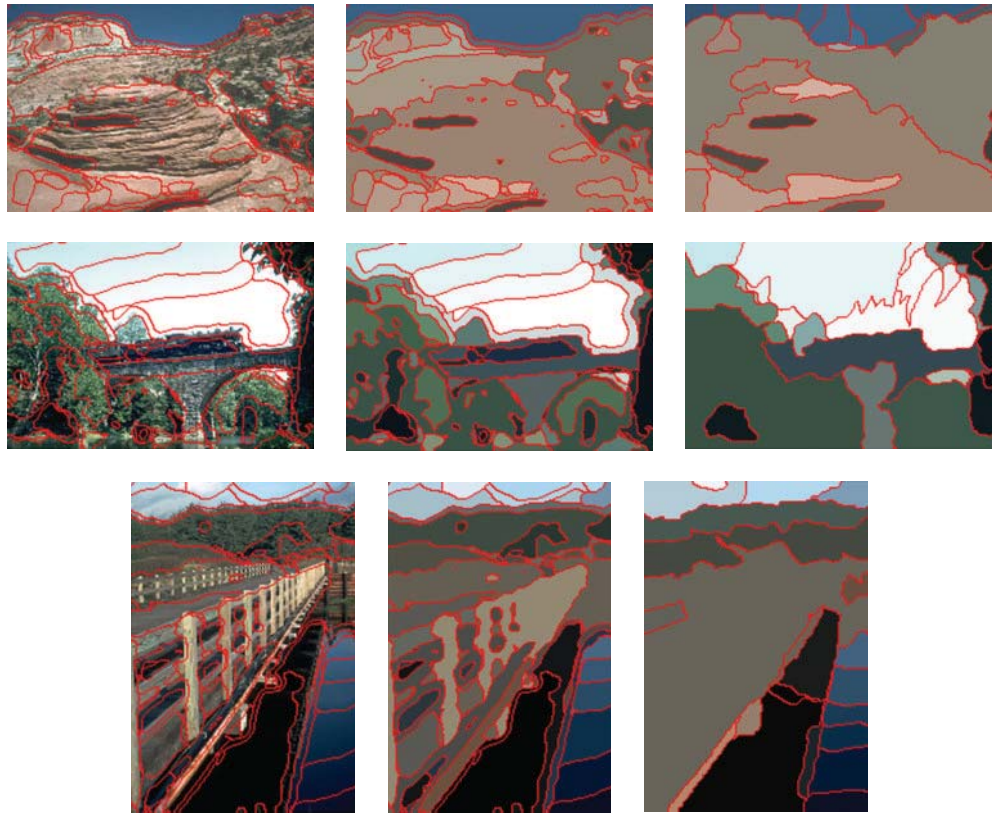

Figure 5: Landscape images: left column: original images with the boundaries obtained by using the proposed algorithm; middle and right columns: the segmentation results obtained by using the proposed algorithm and the CTM algorithm, respectively.

n is the number of bit-planes, and $P_i(\ )$ is the ith bit-plane's PMF. Based on the MQ table defined in JPEG2000, we proposed a simple scheme to estimate the local PMF [28]. Specifically, let $P_i(x_i = 1)$ be the probability of 1 bit for variable x_i on the ith bit-plane, which can be obtained from the MQ table as follows:

$$P_i(x_i = 1) = \begin{cases} \text{Qe\_Value} & \text{if MPS} = 0, \\ 1 - \text{Qe\_Value} & \text{if MPS} = 1, \end{cases} \tag{3.3}$$

where Qe_Value is the probability of less probable symbol (LPS) stored in the MQ table, and MPS stands for more probable symbol. Note that the set $\{P_i(x_i = 1);\ i = 0, \ldots, n-1\}$ obtained from the MQ table can be used to estimate the local PMF. As the MQ table is available at both encoder and decoder, there is no need to transmit the overhead information to construct the MQ features.

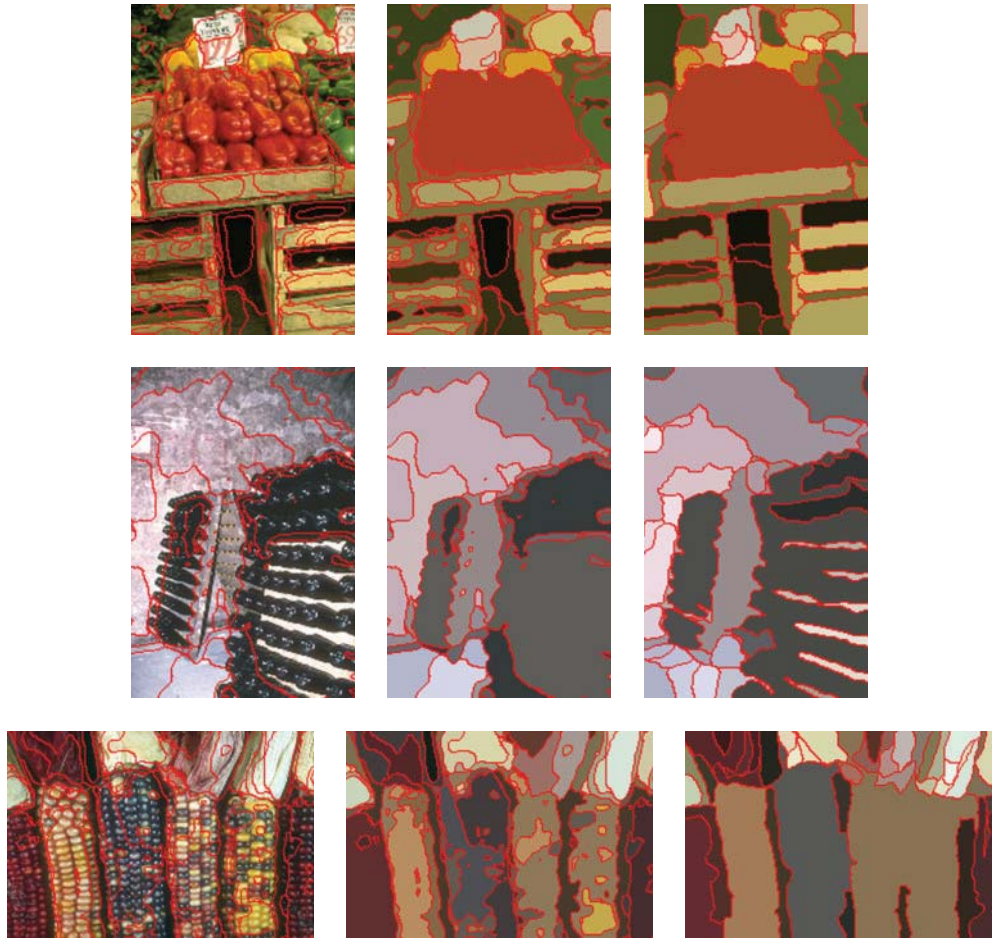

Figure 6: Objects images: left column: original images with the boundaries obtained by using the proposed algorithm; middle and right columns: the segmentation results obtained by using the proposed algorithm and the CTM algorithm, respectively.

3.2. The Modified CTM Algorithm

In this section, we modify the CTM algorithm [32] to segment the MQ feature vectors of an image. With a set of MQ feature vectors, the number of coding bits can be approximated as

$$L(\varepsilon) = \frac{N+D}{2}\log_2 \det\left(I + \frac{D}{\varepsilon^2 N}\Sigma\right) + \frac{D}{2}\log_2\left(1 + \frac{\mu^T\mu}{\varepsilon^2}\right), \tag{3.4}$$

where μ is the mean vector, Σ is the covariance matrix, ε is the distortion incurred, D is the feature dimension, and N is the number of feature vectors. For K sets of MQ feature vectors, the total number of coding bits is given by

$$L_{\text{tot}}(\varepsilon) = \sum_{i=1}^{K} L_i(\varepsilon) - N_i \log_2 \frac{N_i}{N}, \tag{3.5}$$

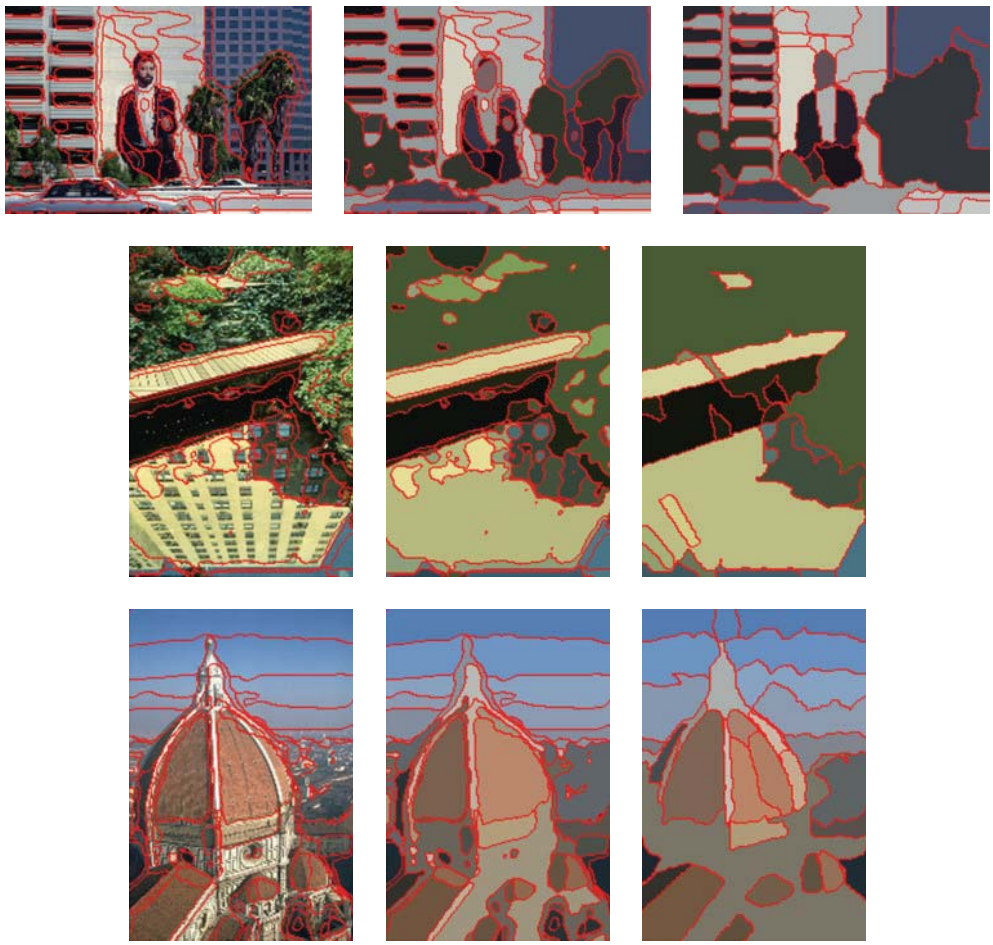

Figure 7: Urban images: left column: original images with the boundaries obtained by using the proposed algorithm; middle and right columns: the segmentation results obtained by using the proposed algorithm and the CTM algorithm, respectively.

where $L_i(\varepsilon)$ and N_i are the number of coding bits obtained by (3.4) and the number of MQ feature vectors in the i*th* set, respectively, and N is the total number of MQ feature vectors, that is, $N = \sum_{i=1}^{K} N_i$. The idea behind CTM is to merge two sets of feature vectors such that the coding bits can be reduced maximally. The pairwise merging procedure of CTM is performed iteratively until no merge can reduce the coding bits any more. As mentioned in [32], the termination of CTM is dependent on the distortion parameter, ε, which can be determined by

$$\varepsilon = \min\ \varepsilon : d(\varepsilon) \quad \gamma\ , \tag{3.6}$$

where $d(\varepsilon)$ is the distance between a pair of segments with respect to ε.

Motivated by the rate distortion theory, which has been widely used in embedded image coding for optimal rate control, we propose a simple scheme to determine the candidates of ε. Specifically, for a sequence of increasing distortion values: $\varepsilon_1 < \varepsilon_2 < \cdots$, the

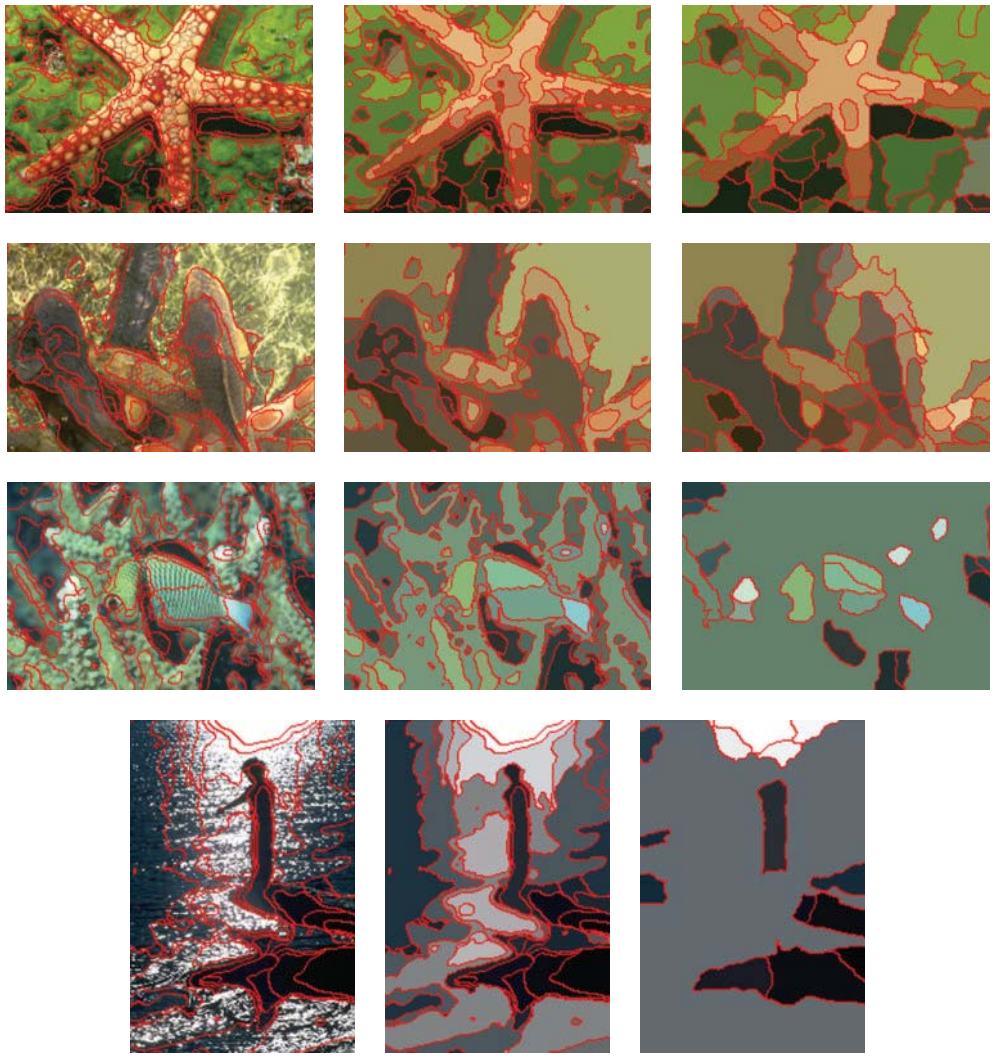

Figure 8: Water images: left column: original images with the boundaries obtained by using the proposed algorithm; middle and right columns: the segmentation results obtained by using the proposed algorithm and the CTM algorithm, respectively.

number of segments and the total number of coding bits are monotonically decreasing, that is, $K_1 > K_2 > \cdots$ and $L_{\text{tot}}(\varepsilon_1) > L_{\text{tot}}(\varepsilon_2) > \cdots$. The rate distortion slope (RDS) is thus defined as

$$S(\varepsilon_i) = \frac{\Delta D_i}{\Delta R_i}, \tag{3.7}$$

where

$$\begin{aligned} \Delta R_i &= \frac{L_{\text{tot}}(\varepsilon_{i-1}) - L_{\text{tot}}(\varepsilon_i)}{N}, \\ \Delta D_i &= \varepsilon_{\text{i}} - \varepsilon_{\text{i-1}}, \end{aligned} \tag{3.8}$$

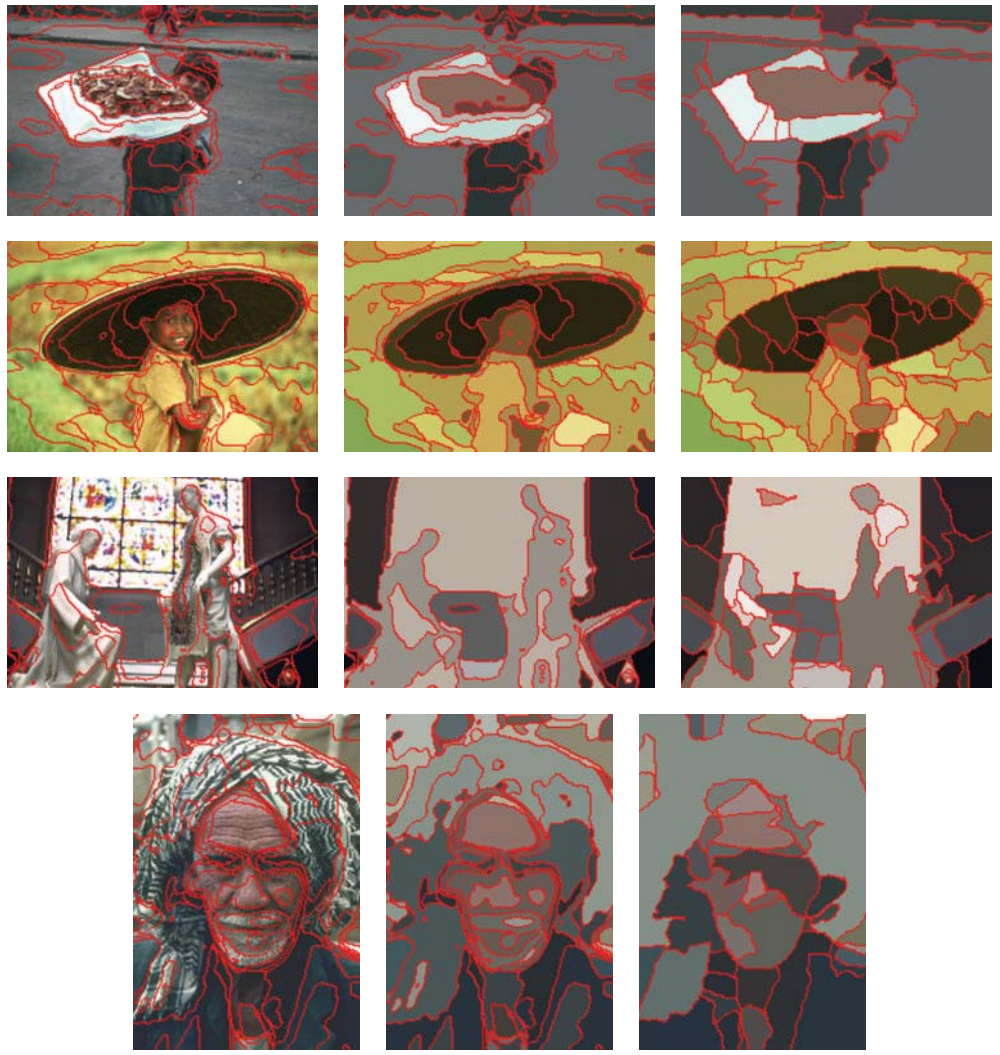

Figure 9: Portraits images: left column: original images with the boundaries obtained by using the proposed algorithm; middle and right columns: the segmentation results obtained by using the proposed algorithm and the CTM algorithm, respectively.

and N is the number of MQ feature vectors. As RDS should be nondecreasing, that is,

$$S(\varepsilon_i) \quad S(\varepsilon_{i+1}) \quad \text{for } \varepsilon_i < \varepsilon_{i+1}, \tag{3.9}$$

if $S(\varepsilon_i) > S(\varepsilon_{i+1})$, ε_i can be considered as a candidate to terminate the merging process of CTM. Thus, we modify the selection of ε as follows:

$$\varepsilon = \max_i \ \varepsilon_i : S(\varepsilon_i) > S(\varepsilon_{i+1}), d(\varepsilon_i) \quad \gamma \ . \tag{3.10}$$

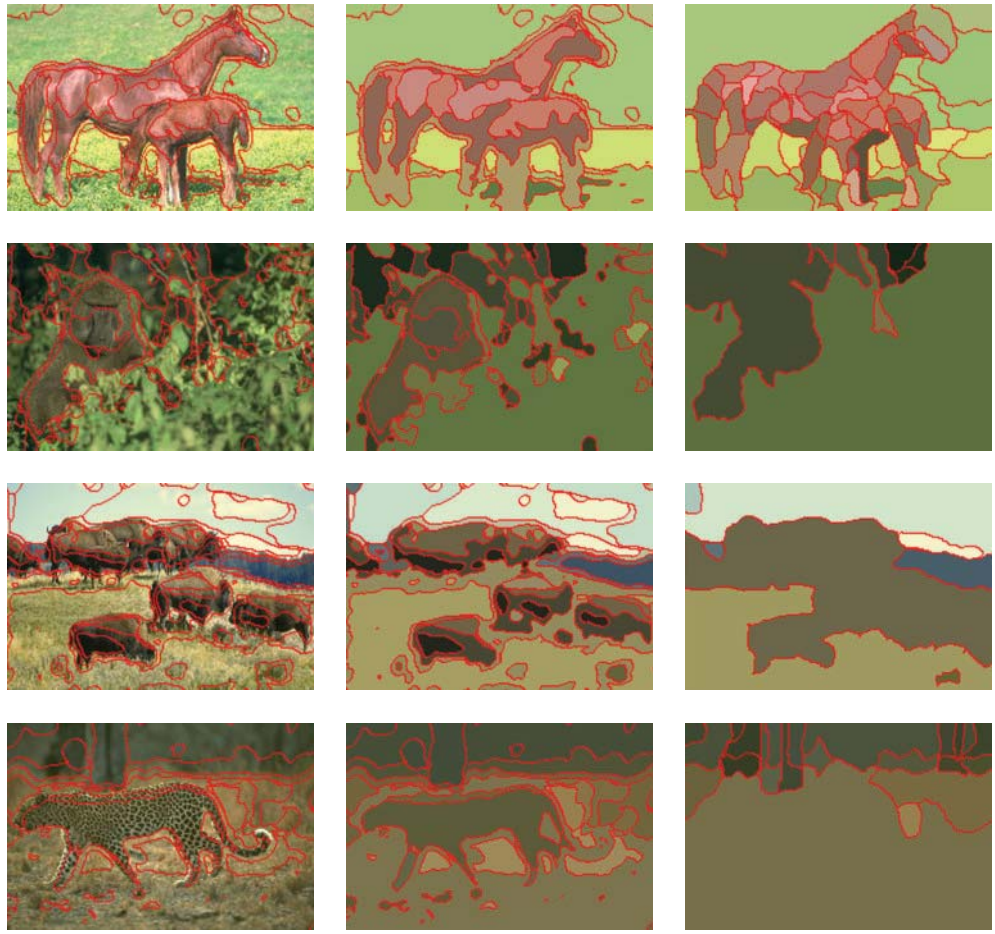

Figure 10: Animals images: left column: original images with the boundaries obtained by using the proposed algorithm; middle and right columns: the segmentation results obtained by using the proposed algorithm and the CTM algorithm, respectively.

Figure 1 depicts flowchart of the modified CTM with the RDS-based adaptive selection of ε , where the MQ coder-based image features are projected into a low-dimensional space via principal component analysis (PCA) in order to reduce the computational cost further, and the initial superpixels are obtained by using the simple K-means algorithm. Take the image shown in Figure 2(a) as an example; the candidates of ε are shown in Figure 2(e), where the horizontal and vertical axes are the distortion and the RDS values, respectively. Figures 2(b)–2(d) show the segmentation results with the first, second, and third candidates of ε. As one can see, the rate distortion information can be used to avoid overmerging of CTM.

4. Experimental Results

The proposed algorithm has been extensively evaluated on the Berkeley database [33]. The 9/7-wavelet filters adopted by JPEG2000 are used to extract the MQ coder-based image

Table 1: Average PRI and BDE on the Berkeley image database.

Measure	The proposed algorithm	CTM	Mean-shift	NCuts
Average PRI	0.757	0.756	0.755	0.723
Average BDE	9.2	9.4	9.7	9.6

features. The number of initial superpixels is set to 50. In addition to visual inspection, the boundary displacement error (BDE) and the probabilistic Rand index (PRI) [34] are used for quantitative evaluation. The segmentation results are compared with CTM, Mean-Shift and NCuts. In Mean-Shift, the parameters h_s and h_r are set to 13 and 19, respectively; in NCuts, the number of segments is 20. The threshold γ of CTM is set to 0.1, as suggested in [32].

We first evaluate the segmentation performance at various compression rates. Figure 3(a) shows a test image with two Brodatz textures, namely, wood and grass. Figure 3(b) depicts percentages of errors at various rates of bits per pixel (bpp). It is noted that the segmentation results even at low bpp rates are satisfactory; thus, a small portion of code stream is sufficient for the segmentation task. It has the advantage of saving transmission time, computational cost, and memory space, which are desirable especially for the Internet applications.

Table 1 shows the BDE and PRI performances compared to CTM, Mean-Shift, and NCuts. The proposed algorithm is preferable in terms of the average BDE.

The improvements in PRI and BDE using (3.10) are shown in Figures 4(a) and 4(b), respectively, where the horizontal axis is the threshold: γ. It is shown that the proposed algorithm is more robust by taking account of the rate distortion information to avoid overmerging.

Figures 5, 6, 7, 8, 9, and 10 are representative of the Landscape, Objects, Urban, Water, Portraits, and Animals images in the Berkeley database. The original images are shown in the left column. The segmentation results by using the proposed algorithm and the CTM algorithm are given in the middle and right columns, respectively. It is noted that, for images with high-detail contents, the proposed algorithm improves the segmentation results visually.

5. Conclusion

The MQ coder provides effective probability models, which is available at both encoder and decoder and therefore can be used to extract image features in the JPEG2000 domain directly. As a result, no overhead transmission is necessary to extract the feature vectors, and moreover the burden of decompressing a JPEG2000 image can be avoided. Based on the MQ coder, an efficient scheme of segmenting an image has been proposed. In order to avoid overmerging, the CTM algorithm has been modified by taking account of the rate distortion information. The proposed algorithm has been evaluated on images with Brodatz textures and the Berkeley image database. It is shown that the segmentation results at low-middle bpp rates are rather promising. In addition, for images with high-detail contents, the proposed algorithm is preferable in terms of the average BDE measure and visual comparison.

Acknowledgments

The authors are grateful to the maintainers of the Berkeley image database. The National Science Council of Taiwan under Grants NSC100-2628-E-239-002-MY2 supported this work.

References

[1] A. K. Jain, "Data clustering: 50 years beyond K-means," *Pattern Recognition Letters*, vol. 31, no. 8, pp. 651–666, 2010.

[2] N. A. M. Isa, S. A. Salamah, and U. K. Ngah, "Adaptive fuzzy moving K-means clustering algorithm for image segmentation," *IEEE Transactions on Consumer Electronics*, vol. 55, no. 4, pp. 2145–2153, 2009.

[3] S. K. Mitra and J. F. Kaiser, *Handbook for Digital Signal Processing*, John Wiley & Sons, New York, NY, USA, 1993.

[4] J. S. Bendat and A. G. Piersol, *Random Data: Analysis and Measurement Procedure*, John Wiley & Sons, New York, NY, USA, 3rd edition, 2000.

[5] M. Li, W. S. Chen, and L. Han, "Correlation matching method for the weak stationarity test of LRD traffic," *Telecommunication Systems*, vol. 43, no. 3-4, pp. 181–195, 2010.

[6] M. Li and W. Zhao, "Variance bound of ACF estimation of one block of fGn with LRD," *Mathematical Problems in Engineering*, vol. 2010, Article ID 560429, 14 pages, 2010.

[7] M. Li, "A method for requiring block size for spectrum measurement of ocean surface waves," *IEEE Transactions on Instrumentation and Measurement*, vol. 55, no. 6, pp. 2207–2215, 2006.

[8] T. N. Tan and A. G. Constantinides, "Texture analysis based on a human visual model," in *Proceedings of the IEEE International Conference on Acoustics, Speech, and Signal Processing (ICASSP '90)*, vol. 4, pp. 2137–2140, Albuquerque, NM, USA, April 1990.

[9] D. E. Ilea and P. F. Whelan, "CTex—an adaptive unsupervised segmentation algorithm based on color-texture coherence," *IEEE Transactions on Image Processing*, vol. 17, no. 10, pp. 1926–1939, 2008.

[10] S. Mallat, *A Wavelet Tour of Signal Processing*, Elsevier/Academic Press, Amsterdam, The Netherlands, 3rd edition, 2009.

[11] M. K. Bashar, N. Ohnishi, and K. Agusa, "A new texture representation approach based on local feature saliency," *Pattern Recognition and Image Analysis*, vol. 17, no. 1, pp. 11–24, 2007.

[12] C. M. Pun and M. C. Lee, "Extraction of shift invariant wavelet features for classification of images with different sizes," *IEEE Transactions on Pattern Analysis and Machine Intelligence*, vol. 26, no. 9, pp. 1228–1233, 2004.

[13] J. Sun, D. Gu, S. Zhang, and Y. Chen, "Hidden Markov Bayesian texture segmentation using complex wavelet transform," *IEE Proceedings: Vision, Image and Signal Processing*, vol. 151, no. 3, pp. 215–223, 2004.

[14] M. H. Pi, C. S. Tong, S. K. Choy, and H. Zhang, "A fast and effective model for wavelet subband histograms and its application in texture image retrieval," *IEEE Transactions on Image Processing*, vol. 15, no. 10, pp. 3078–3088, 2006.

[15] M. Li, W. Zhao, and S. Chen, "MBm-based scalings of traffic propagated in internet," *Mathematical Problems in Engineering*, vol. 2011, Article ID 389803, 21 pages, 2011.

[16] M. Li and W. Zhao, "Representation of a stochastic traffic bound," *IEEE Transactions on Parallel and Distributed Systems*, vol. 21, no. 9, pp. 1368–1372, 2010.

[17] M. Li, "Generation of teletraffic of generalized Cauchy type," *Physica Scripta*, vol. 81, no. 2, Article ID 025007, 2010.

[18] H. Kantz and T. Schreiber, *Nonlinear Time Series Analysis*, Cambridge University Press, Cambridge, UK, 2nd edition, 2004.

[19] T. Schreiber, "Interdisciplinary application of nonlinear time series methods," *Physics Report*, vol. 308, no. 1, pp. 1–64, 1999.

[20] B. J. West, E. L. Geneston, and P. Grigolini, "Maximizing information exchange between complex networks," *Physics Reports*, vol. 468, no. 1–3, pp. 1–99, 2008.

[21] M. Li, "Fractal time series—a tutorial review," *Mathematical Problems in Engineering*, vol. 2010, Article ID 157264, 26 pages, 2010.

[22] S. Y. Chen, H. Tong, and C. Cattani, "Markov models for image labeling," *Mathematical Problems in Engineering*, vol. 2011, Article ID 814356, 18 pages, 2011.

[23] S. Y. Chen, H. Tong, Z. Wang, S. Liu, M. Li, and B. Zhang, "Improved generalized belief propagation for vision processing," *Mathematical Problems in Engineering*, vol. 2011, Article ID 416963, 12 pages, 2011.

[24] S. Y. Chen, J. Zhang, Q. Guan, and S. Liu, "Detection and amendment of shape distortions based on moment invariants for active shape models," *IET Image Processing*, vol. 5, no. 3, pp. 273–285, 2011.

[25] F. R. Alexander, P. V. Juan, and S. Hichem, "Estimating quality bounds of JPEG 2000 compressed leukocytes images," in *Proceedings of the 2nd Mexican Conference on Pattern Recognition*, pp. 27–29, The National Institute of Astrophysics, Puebla, Mexico, 2010.

[26] T. Y. Sung and H. C. Hsin, "A hybrid image coder based on SPIHT algorithm with embedded block coding," *IEICE Transactions on Fundamentals of Electronics, Communications and Computer Sciences*, vol. E90-A, no. 12, pp. 2979–2984, 2007.
[27] F. Zargari, A. Mosleh, and M. Ghanbari, "A fast and efficient compressed domain JPEG2000 image retrieval method," *IEEE Transactions on Consumer Electronics*, vol. 54, no. 4, pp. 1886–1893, 2008.
[28] H.-C. Hsin, "Texture segmentation in the joint photographic expert group 2000 domain," *IET Image Processing*, vol. 5, no. 6, pp. 554–559, 2011.
[29] T. Acharya and P. S. Tsai, *JPEG2000 Standard for Image Compression*, John Wiley & Sons, New York, NY, USA, 2005.
[30] F. Auli-Llinas, J. Serra-Sagristà, and J. Bartrina-Rapesta, "Enhanced JPEG2000 quality scalability through block-wise layer truncation," *EURASIP Journal on Advances in Signal Processing*, vol. 2010, Article ID 803542, 11 pages, 2010.
[31] A. K. Gupta, S. Nooshabadi, and D. Taubman, "Novel distortion estimation technique for hardware-based JPEG2000 encoder system," *IEEE Transactions on Circuits and Systems for Video Technology*, vol. 17, no. 7, pp. 918–923, 2007.
[32] A. Y. Yang, J. Wright, Y. Ma, and S. S. Sastry, "Unsupervised segmentation of natural images via lossy data compression," *Computer Vision and Image Understanding*, vol. 110, no. 2, pp. 212–225, 2008.
[33] http://www.eecs.berkeley.edu/ yang/software/lossy_segmentation/.
[34] R. Unnikrishnan, C. Pantofaru, and M. Hebert, "Toward objective evaluation of image segmentation algorithms," *IEEE Transactions on Pattern Analysis and Machine Intelligence*, vol. 29, no. 6, pp. 929–944, 2007.

Hindawi Publishing Corporation
Mathematical Problems in Engineering
Volume 2012, Article ID 191902, 10 pages
doi:10.1155/2012/191902

Research Article

DNA Optimization Threshold Autoregressive Prediction Model and Its Application in Ice Condition Time Series

Xiao-Hua Yang[1] and Yu-Qi Li[2]

[1] State Key Laboratory of Water Environment Simulation, School of Environment, Beijing Normal University, Beijing 100875, China
[2] School of Geography and Remote Sensing Science, Beijing Normal University, Beijing 100875, China

Correspondence should be addressed to Xiao-Hua Yang, xiaohuayang@bnu.edu.cn

Received 24 August 2011; Accepted 18 September 2011

Academic Editor: Carlo Cattani

There are many parameters which are very difficult to calibrate in the threshold autoregressive prediction model for nonlinear time series. The threshold value, autoregressive coefficients, and the delay time are key parameters in the threshold autoregressive prediction model. To improve prediction precision and reduce the uncertainties in the determination of the above parameters, a new DNA (deoxyribonucleic acid) optimization threshold autoregressive prediction model (DNAOTARPM) is proposed by combining threshold autoregressive method and DNA optimization method. The above optimal parameters are selected by minimizing objective function. Realice condition time series at Bohai are taken to validate the new method. The prediction results indicate that the new method can choose the above optimal parameters in prediction process. Compared with improved genetic algorithm threshold autoregressive prediction model (IGATARPM) and standard genetic algorithm threshold autoregressive prediction model (SGATARPM), DNAOTARPM has higher precision and faster convergence speed for predicting nonlinear ice condition time series.

1. Introduction

Many natural phenomena, such as ice condition, runoff, are usually nonlinear, complex, and dynamic processes. Prediction of ice conditions is of primary importance for weather forecasting, agriculture, geosciences, and marine transportation safety. The simulation of the nonlinear time series was very difficult with the traditional deterministic mathematic models, which cause new challenges to calibrate the parameters [1, 2]. There are many methods for predicting nonlinear time series [3–10]. Threshold autoregressive (TAR) models are typically

applied to time series data as an extension of autoregressive models for higher degree of flexibility in model parameters through a regime switching behavior. TAR models were introduced by Tong and Li in 1977 and more fully developed in the seminal paper [11]. The threshold autoregressive model is a special case of Tong's general threshold autoregressive models. The latter allows the threshold variable to be very flexible, such as an exogenous time series in the open-loop threshold autoregressive system [11–13]. For a comprehensive review of developments over the 30 years since the birth of the model, see Tong [14]. However, the uncertainties in determining the parameters of the threshold variables, autoregressive coefficients, and the delay time exist in the developed threshold autoregressive model. So as to improve the prediction accuracy, the key problem is how to determine the parameters in the prediction model.

The global optimization in determining all the parameters is intractable mathematically. Once an objective function has many local extreme points, the traditional optimization methods may not obtain the global optimal solution. A genetic algorithm (GA) based on the genetic evolution of a species was proposed by Holland [15]. GA is a global optimization algorithm. However, the computational amount is very large and premature convergence phenomena exist in GA [16–20]. Recently, Adleman [21] showed that DNA can be used to solve a computationally hard problem. Many scientists used DNA computation to solve real problems [22–24].

In this study, DNA optimization threshold autoregressive prediction model (DNAO-TARPM) is presented to determine the parameters and to improve the calculation precision for predicting ice condition time series. In order to validate the new method, some real ice condition time series are used.

2. DNA Optimization Threshold Autoregressive Prediction Model (DNAOTARPM)

The TAR model is a tool for predicting future values in time series assuming that the behavior of the time series changes once the time series shifts to a different regime. The switch from one regime to another depends on the p past values of the x series. The model consists of k autoregressive (AR) parts for each different regime. The model is usually referred to as the TAR (k,p) model where k is the number of regimes and p is the order of the autoregressive part. Since those can differ between regimes, the p portion is sometimes dropped and models are denoted simply as TAR (k). A k-regime TAR $(d;p_1,p_2,\ldots,p_k)$ model for time series $x(i)$ $(i=1,2,\ldots,n)$ has the form

$$x(i)=\begin{cases}b_{j,0}+\sum_{l=1}^{p_j} b_{j,l}\,x(i-l)+e_{j,i}, & r_{j-1}\le x(i-d)<r_j,\\ j=1,2,\ldots,k,\end{cases} \tag{2.1}$$

where $r_0=-\infty$, $r_k=+\infty$, r_j $(j=1,2,\ldots,k-1)$ are $k-1$ nontrivial threshold parameters dividing the domain into k different regimes; d is the delay time parameter, $b_{j,l}$ is the regressive coefficients in the jth regime, $e_{j,i}$ stands for white-noise error term with constant variance, and p_j is the autoregressive order in the jth regime of the model. The threshold parameters satisfy the constraint:

$$-\infty=r_0<r_1<r_2<\cdots<r_{k-1}<r_k=+\infty. \tag{2.2}$$

Here $d, k, r_1, r_2, \ldots, r_{k-1}, p_1, p_2, \ldots, p_k$, and $b_{j,l}$ are parameters in TAR model. It is very difficult to determine these parameters with the traditional methods.

In this paper, we use DNA optimization method to determine the parameters and improve model accuracy. The new model, DNA optimization threshold autoregressive prediction method (DNAOTARPM), is described as follows.

Step 1 Determine the delay time d and the number of regressive coefficients. The delay time d is determined by the autocorrelation function method [21]. The autocorrelation function $R(j)$ for delay time j is calculated as

$$R(j) = \frac{\sum_{i=j+1}^{n} (x_i - m_x)(x_{i-j} - m_x)}{\sum_{i=1}^{n} (x_i - m_x)^2}, \qquad m_x = \sum_{i=1}^{n} \frac{x_i}{n}. \tag{2.3}$$

The delay time d is selected when autocorrelation function $R(j)$ [25] satisfies the following condition:

$$R(j) < R1(j), R2(j), \tag{2.4}$$

$$R1(j) = \frac{-1 - u_{\alpha/2} \cdot \sqrt{n-j-1}}{n-j}, \quad R2(j) = \frac{-1 + u_{\alpha/2} \cdot \sqrt{n-j-1}}{n-j}, \tag{2.5}$$

where $u_{\alpha/2}$ is the upper $100 \cdot \alpha/2$ percentage point of the normal distribution for $1-\alpha$ confidence level. The number of regressive coefficients $p_1 = \max\{j, l = 1,2,\ldots,k\}$. Some of the j values are regarded as the delay time.

Step 2 Determine the number and ranges of threshold parameters. Considering a set $\{x_i, x_{i-d} \mid i = 1,2,3,\ldots; d = 1,2,\ldots\}$ from the time series $\{i = 1,2,\ldots,n\}$, we divide x_{i-d} into s regimes $(s > k)$. Suppose there are N_j number of x_{i-d} in the jth part, and the corresponding x_i is regarded as $x_{i,j}$. In the jth part, the conditional expectation of x_i given the event $X = x_{i-d}$ is

$$E\left(\frac{x_i}{x_{i-d}}\right)_j = \sum_{i=1}^{N_j} \frac{x_{i,j}}{N_j}, \quad j = 1,2,\ldots,s; d = 1,2,\ldots. \tag{2.6}$$

Let x_{i-d} be horizontal axis, and let $E(x_i/x_{i-d})$ be vertical axis; we can get the scatter plots. When the scatter plots are piecewise linear map, we can estimate the number and ranges of threshold parameters. The piecewise number of piecewise linear map is the number of threshold parameters, and the ranges of the piecewise points are the ranges of threshold parameters.

Step 3 Construct the objective function . The parameter estimation for DNAOTARPM can be obtained by the following objective function, namely, the mean of least residual absolute value sum :

$$\mathrm{Min}\, f\ f(r_1, r_2, \ldots, r_{k-1}; b_{j,l}) \quad \frac{\sum_i |x_i - \hat{x}_i|}{n}. \tag{2.7}$$

Step 4 Solve objective function by DNA optimization method . Solving the parameters of $r_1, r_2, \ldots, r_{k-1}; b_{j,l}$, $j = 1,2,\ldots,k$; $l = 1,2,\ldots,p_j$, in the optimization objective function 2.7 is one nonlinear optimization problem . It is rather difficult to deal with it using a traditional optimization method. The above optimal model can be solved by the following DNA optimization method 24 . The k-regime prediction formula will be seen in the following application part in detail.

If we solve objective function 2.7 with improved genetic algorithm , we call the method improved genetic algorithm 18 threshold autoregressive prediction method IGATARPM , and if we solve objective function 2.7 with standard genetic optimization method 15 , we call the method standard genetic algorithm threshold autoregressive prediction method SGATARPM .

3. DNA Optimization Method (DNAOM)

Consider the following optimization problem :

$$\begin{aligned} &\mathrm{Min}\ f(c_1, c_2, \ldots, c_p) \\ &\text{st. } a_j \le c_j \le b_j \text{ for } j = 1,2,\ldots,p, \end{aligned} \tag{3.1}$$

where $c = \{c_j, j = 1,2,\ldots,p\}$, c_j is a parameter to be optimized, f is an objective function, and $f \ge 0$, $[a_j, b_j]$ is the range of c_j.

The procedure of DNAOM is shown as follows 25 .

Step 1 DNA encoding . Suppose DNA-encoding length is m in every parameter, the jth parameter range is the interval $[a_j, b_j]$, and then each interval is divided into $2^m - 1$ subintervals:

$$c_j = a_j + \delta_j \cdot (2^m - 1) \cdot h_j, \tag{3.2}$$

where the length of subinterval of the jth parameter $h_j = (b_j - a_j)/(2^m - 1)$ is constant. The searching location $I_j = \delta_j \cdot (2^m - 1)$ is an integer, and $0 \le I_j < 2^m$, δ_j is a random variable, and $0 \le \delta_j \le 1$, for $j = 1,2,\ldots,p$.

The DNA code array of the jth parameter is denoted by the grid points of $\{d_{j,k} \mid k = 1,2,\ldots,m\}$ for every individual:

$$I_j = \sum_{k=1}^{m} d_{j,k} \cdot 2^{k-1}. \tag{3.3}$$

DNAOM's process operates on a population of individuals also called DNA code array, strings, or chromosomes. Each individual represents a potential solution to the problem. For corresponding 1×1 T, 1×0 A, 0×1 G, 0×0 C. The first position value "1" or "0" expresses the position of DNA code and the second position value "1" or "0" expresses the true value of binary code and the value of DNA code.

Step 2 creating the initial population. To cover the whole solution space and to avoid individuals entering into the same region, large uniformity random population is selected in this algorithm. Once the initial father population has been generated, the decoding and fitness evaluation should be done.

Step 3 evaluating fitness value of each individual. The smaller the value f_i is, the higher the fitness of its corresponding ith chromosome is $i = 1,2,\ldots,N$. So the fitness function of ith chromosome is defined as follows:

$$F_i = \frac{1}{f_i^2 + 1.0}. \tag{3.4}$$

Step 4 selection. Select chromosome pairs randomly depending on their fitness value from the initial population. Two groups of N-chromosomes $d_1(j,k,i)$ and $d_2(j,k,i)$, are gotten $j = 1,2,\ldots,p$; $k = 1,2,\ldots,m$; $i = 1,2,\ldots,N$.

Step 5 two-point crossover and two-point mutation. Perform crossover and mutation on chromosomes the same as GA.

Step 6 DNA evolution. Repeat Steps 3–6 until the evolution times $q = Q$. Q is the total evolution times or the termination condition is satisfied.

Step 7 accelerating cycle. The parameter ranges of n_e-excellent individuals obtained by Q-times of the DNA-encoded optimal evolution alternating are regarded as the new ranges of the parameters, and then the whole process is back to the DNA-encoding. The DNAOM computation is over until the algorithm running times reaches the designed T times or there exists an optimal chromosome C_{fit} whose fitness satisfies a given criterion. In the former case the C_{fit} is the fittest chromosome or the most excellent chromosome in the population. That is, the chromosome C_{fit} represents the solution [25].

The parameters of the DNAOM are selected as follows. The length $m = 10$, population size $N = 100$, the number of excellent individuals $n_e = 10$, the times of evolution alternating $Q = 3$, the crossover probability $p_c = 1.0$, and the mutation probability $p_m = 0.5$.

4. Application in Ice Condition Time Series

The real ice condition time series in this study are chosen as the annual ice condition at Bohai in China for the period of 1966 to 1994 (29 years) [25]. For the ice condition time series, the first modeling data set is the data during the period of 1966 to 1993 (28 years). The prediction lead time is the year of 1970–1994 (25 years).

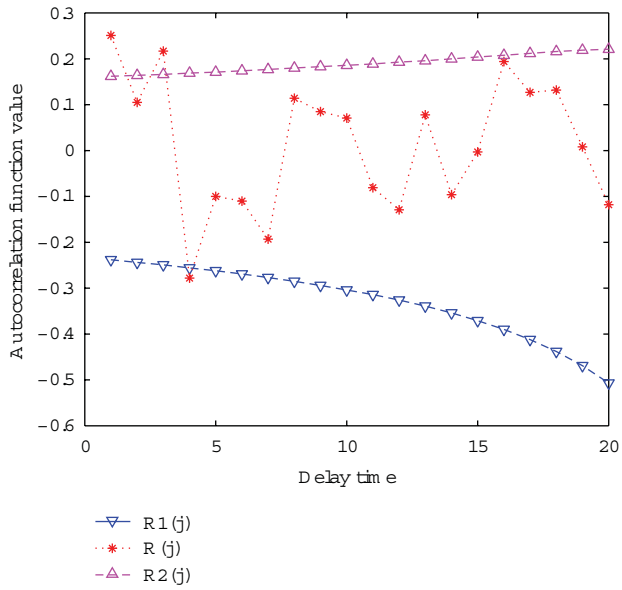

Figure 1: The autocorrelation function figure for the observed time series.

4.1. The Autocorrelation Function $R(j)$ for Delay Time j

The changes of the autocorrelation functions for the time series are presented at the confidence level 70% in Figure 1.

From Figure 1, we can see that only the values of $R(1), R(3), R(4)$ satisfy condition (2.4). So the delay time d is 1, 3, or 4 in DNAOTARPM.

4.2. The Number and Ranges of Threshold Parameters

The number and ranges of threshold parameters of the above ice condition time series are determined by the conditional expectation of $x(i)$ given the event $X(x(i-d))$. The scatter plot of the conditional expectation is shown in Figure 2.

From Figure 2, we can see that there are two piecewise linear maps, and the piecewise point is around the mean value of the time series. So we suppose $y(i) = x(i) - \text{mean value}$, and the k-regime TAR$(d; p_1, p_2, \ldots, p_k)$ model has the following form for $d = 1, 3, 4$:

$$y(i) = \begin{cases} b_{1,1}\, y(i-1) \cdots b_{1,3}\, y(i-3) \cdots b_{1,4}\, y(i-4), & y(i-d) \le r_1, \\ b_{2,1}\, y(i-1) \cdots b_{2,3}\, y(i-3) \cdots b_{2,4}\, y(i-4), & y(i-d) > r_1, \end{cases} \tag{4.1}$$

$$x(i) = y(i) + \text{mean value}.$$

The parameters of $r_1, b_{j,l}$ $(j = 1, 2;\ l = 1, 3, 4)$ are required in this model. In this work, the three parameters are estimated with respect to one criterion, namely, the mean of least residual absolute value sum shown in (2.6).

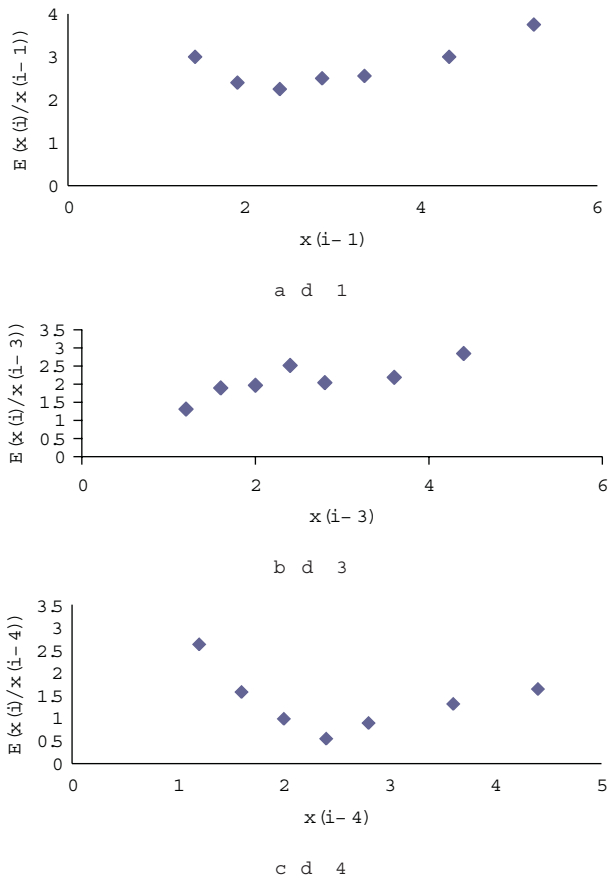

Figure 2: The scatter plot of the conditional expectation: a $E\,x\,i/x\,i-1\ :x\,i-1$; b $E\,x\,i/x\,i-3\ :x\,i-3$; c $E\,x\,i/x\,i-4\ :x\,i-4$.

4.3. Result Comparison between DNAOTARPM, IGATARPM, and SGATARPM

The time series were predicted by DNAOTARPM, IGATARPM, and SGATARPM, respectively.

Mean least residual absolute value sum f is 0.5737 for DNAOTARPM. The evaluation number of the objective function is 900. The computational results of the above model are given in Table 1.

For IGATARPM, the evaluation number of the objective function is 2700, and the prediction error f is 0.6016.

For SGATARPM, the evaluation number of the objective function is 2700, and the prediction error f is 0.6380.

From Table 1, we can see that prediction results for DNAOTARPM are better than those with the other methods. The prediction results of the practical example are shown in Figure 3 with different methods.

From Table 1 and Figure 3, we can see that the results achieved with our DNAOTARPM method are satisfactory in global optimum and prediction precision.

Table 1: The comparison of the prediction results for DNAOTARPM, IGATARPM, and SGATARPM at Bohai.

Methods	Parameters							Objective function minimum f
	r_1	$b_{1,1}$	$b_{1,3}$	$b_{1,4}$	$b_{2,1}$	$b_{2,3}$	$b_{2,4}$	
	$[-1.0,1.0]$	$[-0.5,0.5]$	$[-0.5,0.5]$	$[-0.5,0.5]$	$[-0.5,0.5]$	$[-0.5,0.5]$	$[-0.5,0.5]$	
DNAO-TARPM	−0.02	0.34	0.24	−0.36	0.13	0.39	−0.46	0.5737
IGA-TARPM	−0.75	0.12	0.40	−0.20	0.20	0.28	−0.44	0.6016
SGA-TARPM	0.90	0.26	0.33	−0.50	−0.06	−0.35	0.36	0.6380

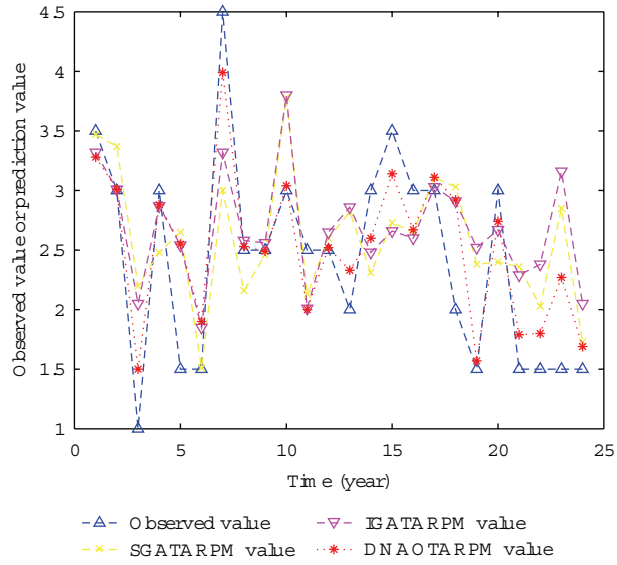

Figure 3: Comparison of prediction results with DNAOTARPM, IGATARPM, and SGATARPM at Bohai.

Compared with IGATARPM and SGATARPM, DNAOTARPM has a faster convergence speed and higher precision. And it is useful for parameter optimization of the nonlinear ice condition time series model.

5. Conclusions

In order to improve prediction precision and reduce the uncertainties in determination of the parameters for forecasting nonlinear ice condition time series, a new DNA optimization threshold autoregressive prediction model DNAOTARPM is proposed in this paper. The ice condition time series at Bohai in China are studied by using DNAOTARPM. The main conclusions are given as follows.

1. DNAOTARPM is established by using DNA optimization method and threshold autoregressive model. The delay time d is selected with autocorrelation function, and the results indicate x_{i-1}, x_{i-3}, x_{i-4} have significant influence on the ice condition time series $\quad 0.30$ at Bohai.

2 DNA optimization method is proposed for optimizing all parameters in DNAO-TARPM model. The optimal parameters, that is, the threshold value, autoregressive coefficients, and the delay time, are obtained for predicting the ice condition time series at Bohai by using DNA optimization method.

3 The prediction errors are 0.5737, 0.6016, and 0.6380 with DNAOTARPM, IGATARPM, and SGATARPM at Bohai, respectively. DNAOTARPM can reduce the calculation errors. It provides a new way to forecast nonlinear ice condition time series.

4 The evaluation number of the objective function is 900, 2700, and 2700 with DNAOTARPM, IGATARPM, and SGATARPM at Bohai, respectively. Compared with IGATARPM and SGATARPM, DNAOTARPM model has a faster convergence speed. The new model DNAOTARPM can be used in predicting other nonlinear systems in the future and its theory will be further studied.

Acknowledgments

The present work is supported by the Program for the National Basic Research Program of China (no. 2010CB951104), the Project of National Natural Science Foundation of China (nos. 50939001 and 51079004), the Specialized Research Fund for the Doctoral Tutor Program of Higher Education (no. 20100003110024), and the Program for Changjiang Scholars and Innovative Research Team in University (no. IRT0809).

References

1 X. H. Yang, D. X. She, Z. F. Yang, Q. H. Tang, and J. Q. Li, "Chaotic Bayesian method based on multiple criteria decision making (MCDM) for forecasting nonlinear hydrological time series," International Journal of Nonlinear Sciences and Numerical Simulation, vol. 10, no. 11-12, pp. 1595–1610, 2009.

2 M. Li, "Modeling autocorrelation functions of long-range dependent teletraffic series based on optimal approximation in Hilbert space-A further study," Applied Mathematical Modelling, vol. 31, no. 3, pp. 625–631, 2007.

3 C. T. Cheng, C. P. Ou, and K. W. Chau, "Combining a fuzzy optimal model with a genetic algorithm to solve multi-objective rainfall-runoff model calibration," Journal of Hydrology, vol. 268, no. 1–4, pp. 72–86, 2002.

4 W. Jia, B. Ling, K. W. Chau, and L. Heutte, "Palmprint identification using restricted fusion," Applied Mathematics and Computation, vol. 205, no. 2, pp. 927–934, 2008.

5 K. W. Chau, "Particle swarm optimization training algorithm for ANNs in stage prediction of Shing Mun River," Journal of Hydrology, vol. 329, no. 3-4, pp. 363–367, 2006.

6 N. Muttil and K. W. Chau, "Neural network and genetic programming for modelling coastal algal blooms," International Journal of Environment and Pollution, vol. 28, no. 3-4, pp. 223–238, 2006.

7 C. T. Cheng, K. W. Chau, and Y. Z. Pei, "A hybrid adaptive time-delay neural network model for multi-step-ahead prediction of sunspot activity," International Journal of Environment and Pollution, vol. 28, no. 3-4, pp. 364–381, 2006.

8 E. I. Debolskaya, "Numerical modeling the turbulent structure of flows under ice," Water Resources, vol. 27, no. 2, pp. 144–151, 2000.

9 E. I. Debolskaya, V. K. Debolskii, and M. V. Derbenev, "Numerical modeling of pollutant distribution at catastrophic floding in conditions of ice difficulties," Water Resources, vol. 34, no. 6, pp. 673–681, 2007.

10 A. M. Wasantha Lai and H. T. Shen, "Mathematics model for river ice processes," Journal of Hydraulic Engineering, vol. 117, no. 7, pp. 851–867, 1991.

11 H. Tong and K. S. Li, "Threshold autoregression, limit cycles and cyclical data," Journal of the Royal Statistical Society, Series B, vol. 42, pp. 245–292, 1980.

12 H. Tong, Threshold Models in Nonlinear Time Series Analysis, vol. 21 of Lecture Notes in Statistics, Springer, New York, NY, USA, 1983.
13 H. Tong, "Birth of the threshold time series model," Statistica Sinica, vol. 17, no. 1, pp. 8–14, 2007.
14 H. Tong, "Threshold models in time series analysis—30 years on with discussions by P. Whittle, M. Rosenblatt, B. E. Hansen, P. Brockwell, N. I. Samia and F. Battaglia," Statistics and Its Interface, vol. 4, pp. 107–136, 2011.
15 J. H. Holland, Adaptation in Natural and Artificial Systems, University of Michigan Press, Ann Arbor, Mich, USA, 1975.
16 K. Chau, "Calibration of flow and water quality modeling using genetic algorithm," in AI: Advances in Artificial Intelligence, vol. 2557 of Lecture Notes in Computer Science, p. 720, Springer, Berlin, Germany, 2002.
17 K. W. Chau, "A two-stage dynamic model on allocation of construction facilities with genetic algorithm," Automation in Construction, vol. 13, no. 4, pp. 481–490, 2004.
18 J. Andre, P. Siarry, and T. Dognon, "An improvement of the standard genetic algorithm fighting premature convergence in continuous optimization," Advances in Engineering Software, vol. 32, no. 1, pp. 49–60, 2001.
19 X. H. Yang, Z. F. Yang, and Z. Y. Shen, "GHHAGA for environmental system optimization," Journal of Environmental Informatics, vol. 5, no. 1, pp. 36–41, 2006.
20 X. H. Yang, Z. F. Yang, G. H. Lu, and J. Li, "A gray-encoded, hybrid-accelerated, genetic algorithm for global optimizations in dynamical systems," Communications in Nonlinear Science and Numerical Simulation, vol. 10, no. 4, pp. 355–363, 2005.
21 L. M. Adleman, "Molecular computation of solutions to combinatorial problems," Science, vol. 266, no. 5187, pp. 1021–1024, 1994.
22 C. W. Yeh, C. P. Chu, and K. R. Wu, "Molecular solutions to the binary integer programming problem based on DNA computation," BioSystems, vol. 83, no. 1, pp. 56–66, 2006.
23 R. J. Lipton, "DNA solution of hard computational problems," Science, vol. 268, pp. 542–545, 1995.
24 X. H. Yang and J. Q. Li, "DNA accelerating evolutionary algorithm and its application in the parameter optimization of Muskingum routing model," in Proceedings of the The 6th International Conference on Natural Computation and the 7th International Conference on Fuzzy Systems and Knowledge Discovery, vol. 8, pp. 3914–3917, Yantai, China, 2010.
25 X. H. Yang and Z. Y. Shen, Intelligent algorithms and their applications in resource and environment system modeling, Beijing Normal University Press, Beijing, China, 2005.